

JOSEPH YOUSSEF SAAB JUNIOR

**TRAILING-EDGE NOISE – DEVELOPMENT AND APPLICATION OF A
NOISE PREDICTION TOOL FOR THE ASSESSMENT AND DESIGN
OF WIND TURBINE AIRFOILS.**

V.1

São Paulo

2016

JOSEPH YOUSSEF SAAB JUNIOR

**RUÍDO DE BORDO DE FUGA – DESENVOLVIMENTO E APLICAÇÃO
DE FERRAMENTA PARA AVALIAÇÃO E PROJETO DE
AEROFÓLIOS PARA TURBINAS EÓLICAS.**

Tese apresentada à Escola Politécnica da
Universidade de São Paulo para obtenção
do título de Doutor em Ciências.

Área de Concentração:
Engenharia Mecânica de Energia e Fluidos

Orientador:
Prof. Dr. Marcos de Mattos Pimenta

V.1

São Paulo
2016

JOSEPH YOUSSEF SAAB JUNIOR

**TRAILING-EDGE NOISE – DEVELOPMENT AND APPLICATION OF A
NOISE PREDICTION TOOL FOR THE ASSESSMENT AND DESIGN
OF WIND TURBINE AIRFOILS.**

Thesis submitted to the Escola Politécnica da
Universidade de São Paulo, in partial fulfillment of
the requirements for the degree of Doctor in
Science.

Area of Knowledge:
Mechanical Engineering – Energy and Fluids.

Thesis Advisor:
Prof. Dr. Marcos de Mattos Pimenta

V.1

São Paulo
2016

Catálogo-na-publicação

Saab Jr., Joseph Youssif

Trailing-edge Noise - Development and Application of a Noise Prediction Tool for the Assessment and Design of Wind Turbine Airfoils. / J. Y. Saab Jr. - São Paulo, 2016.

547 p.

Tese (Doutorado) - Escola Politécnica da Universidade de São Paulo. Departamento de Engenharia Mecânica.

1.Trailing-edge noise 2.Wind Turbine Noise 3.PNoise 4.SP Airfoils
5.BPM Noise prediction model I.Universidade de São Paulo. Escola Politécnica. Departamento de Engenharia Mecânica II.t.

Este trabalho é dedicado à minha fonte permanente de inspiração, motivação e carinho: minha incrível família.

À Denise, Mauro e Fernando.

AGRADECIMENTOS

Agradeço inicialmente aos meus queridos e saudosos Pais.

Ao meu orientador e professor de longa data, Dr. Marcos de Mattos Pimenta, meu agradecimento e admiração pelas brilhantes aulas e inspiradoras conversas que tivemos. Que sua erudição nessa área possa continuar motivando muitos engenheiros, no presente e no futuro.

Ao Professor Dr. Sylvio Bistafa, da EPUSP, pela introdução ao mundo da acústica.

Aos Professores Doutores Jayme Pinto Ortiz, Fábio Saltara, Antônio Luiz Pacífico e Jurandir Itizo Yanagihara, da EPUSP, por sugestões importantes para melhoria do trabalho, pela revisão do artigo publicado e pelo auxílio da formalização do projeto de colaboração com a TU Berlin.

Aos Engenheiros Dr. Georgios Pechlivanoglou e David Marten, da Technische Universität Berlin, pela confiança que permitiu estabelecer a parceria entre a Poli-USP e a TU Berlin.

Ao Dr. Erik Sloth, atualmente na Vestas Wind Systems, pelas discussões iniciais sobre os principais problemas que afetam a indústria de turbinas eólicas.

Às demais indústrias e entidades presentes ao evento AWEA-2012, que aceitaram colaborar com a entrevista e pesquisa realizadas no começo do trabalho, direcionando-o para o desenvolvimento de uma ferramenta específica, voltada à solução de um problema real da indústria eólica. Entre tais entidades encontram-se, em ordem alfabética: Bladerna, General Electric Renewable Energy, IMPSA Wind, Iowa State University, Kenersys, LM Wind Power, Nordex Systems, Siemens Energy, Suzlon, e WE4CE.

Aos Professores do Instituto EESS, que dividiram comigo seu conhecimento sobre Mecânica dos Fluidos Computacional (CFD) ao longo de três intensos semestres de especialização.

Aos programadores Ricardo Marques Moreno e Nikolai Moesus, pela ajuda na integração do módulo de ruído de aerofólio (PNoise) ao software QBlade, nas versões v0.8 (beta) e v0.95 (*release público*), respectivamente.

Aos meus colegas da Escola de Engenharia Mauá e à memória do saudoso mestre, amigo e incentivador, Prof. Otávio de Mattos Silveiras.

Agradeço, por fim, a todos aqueles que contribuíram direta e indiretamente para a realização desse trabalho.

*“Science can amuse and fascinate us all,
but it is engineering that changes the world.”*

Isaac Assimov

ABSTRACT

This report concerns the research, design, implementation and application of an airfoil trailing-edge noise prediction tool in the development of new, quieter airfoil for large-size wind turbine application. The tool is aimed at enabling comparative acoustic performance assessment of airfoils during the early development cycle of new blades and rotors for wind turbine applications. The ultimate goal is to enable the development of quieter wind turbines by the Wind Energy Industry. The task was accomplished by developing software that is simultaneously suitable for comparative design, computationally efficient and user-friendly. The tool was integrated into a state-of-the-art wind turbine design and analysis code that may be downloaded from the web, in compiled or source code form, under general public licensing, at no charge. During the development, an extensive review of the existing airfoil trailing-edge noise prediction models was accomplished, and the semi-empirical BPM model was selected and modified to cope with generic airfoil geometry. The intrinsic accuracy of the original noise prediction model was evaluated as well as its sensitivity to the turbulence length scale parameter, with restrictions imposed accordingly. The criterion allowed comparison of performance of both CFD-RANS and a hybrid solver (XFLR5) on the calculation of the turbulent boundary layer data, with the eventual adjustment and selection of the latter. After all the elements for assembling the method had been selected and the code specified, a collaboration project was made effective between Poli-USP and TU-Berlin, which allowed the seamless coupling of the new airfoil TE noise module, "PNoise", to the popular wind turbine design/analysis integrated environment, "QBlade". After implementation, the code calculation routines were thoroughly verified and then used in the development of a family of "silent profiles" with good relative acoustic and aerodynamic performance. The sample airfoil development study closed the initial design cycle of the new tool and illustrated its ability to fulfill the originally intended purpose of enabling the design of new, quieter blades and rotors for the advancement of the Wind Energy Industry with limited environmental footprint.

Keywords: Airfoil self-noise. Trailing-edge noise prediction. Wind turbine noise. BPM. QBlade. PNoise. Silent Profiles. SP airfoils.

RESUMO

Este trabalho descreve a pesquisa de elementos iniciais, o projeto, a implantação e a aplicação de uma ferramenta de predição de ruído de bordo de fuga, no desenvolvimento de aerofólios mais silenciosos para turbinas eólicas de grande porte. O objetivo imediato da ferramenta é permitir a comparação de desempenho acústico relativo entre aerofólios no início do ciclo de projeto de novas pás e rotores de turbinas eólicas. O objetivo mais amplo é possibilitar o projeto de turbinas eólicas mais silenciosas, mas de desempenho aerodinâmico preservado, pela indústria da Energia Eólica. A consecução desses objetivos demandou o desenvolvimento de uma ferramenta que reunisse, simultaneamente, resolução comparativa, eficiência computacional e interface amigável, devido à natureza iterativa do projeto preliminar de um novo rotor. A ferramenta foi integrada a um ambiente avançado de projeto e análise de turbinas eólicas, de código aberto, que pode ser livremente baixado na Web. Durante a pesquisa foi realizada uma ampla revisão dos modelos existentes para predição de ruído de bordo de fuga, com a seleção do modelo semi-empírico BPM, que foi modificado para lidar com geometrias genéricas. A precisão intrínseca do modelo original foi avaliada, assim como sua sensibilidade ao parâmetro de escala de turbulência transversal, com restrições sendo impostas a esse parâmetro em decorrência da análise. Esse critério permitiu a comparação de resultados de cálculo provenientes de método CFD-RANS e de método híbrido (XFLR5) de solução da camada limite turbulenta, com a escolha do último. Após a seleção de todos os elementos do método e especificação do código, uma parceria foi estabelecida entre a Poli-USP e a TU-Berlin, que permitiu a adição de um novo módulo de ruído de bordo de fuga, denominado “PNoise”, ao ambiente de projeto e análise integrado de turbinas eólicas “QBlade”. Após a adição, as rotinas de cálculo foram criteriosamente verificadas e, em seguida, aplicadas ao desenvolvimento de aerofólios mais silenciosos, com bons resultados acústicos e aerodinâmicos relativos a uma geometria de referência. Esse desenvolvimento ilustrou a capacidade da ferramenta de cumprir a missão para a qual foi inicialmente projetada, qual seja, permitir à Indústria desenvolver pás mais silenciosas que irão colaborar com o avanço da energia eólica através da limitação do seu impacto ambiental.

Palavras-chave: Ruído de aerofólio. Predição de ruído de bordo de fuga. Ruído de Turbina Eólica. BPM. QBlade. PNoise. Aerofólios SP.

Observação: A redação deste trabalho na língua Inglesa tornou-se necessária em função da colaboração efetivada com a TU Berlin e foi previamente autorizada pela CPG, com base na solicitação encaminhada em 28/03/2012.

LIST OF FIGURES

Figure 1-1 Wind-generated electricity penetration in the energy matrix of 20 countries with the greatest cumulative installed WP capacity by the end of 2011 (Wiser & Bolinger, 2012).	2
Figure 1-2 Electricity generation costs in the USA from gas and wind at 9% cost of capital (current) and 8% cost of capital (2020), two price projections. EIA = Energy Information Administration scenario; CES= proposed Clean Energy Standard scenario (Wind Power - Special Report, 2012).	3
Figure 1-3 - World Cumulative Installed Wind Power Capacity between 1980 and 2012 (Rooney, 2013).	4
Figure 1-4 Brazilian domestic electricity supply, by source (EPE, 2012)	4
Figure 1-5 - Installed capacity evolution in Brazil for the Wind Energy (ABEEÓLICA, 2016).	6
Figure 1-6 Contribution of individual components to the total sound power level of a Wind turbine (Pinder, 1992).	7
Figure 1-7 3-D plot of the available mechanical power P_{mec} for a WT, Eqn. (1-1), for wind speeds from 0 to 30 m/s and rotor diameters from 0 to 300 m. Theoretical Betz limit used for C_p and sea-level, standard day density.	8
Figure 1-8 Approximate utility-grade blade length growth over time (Ashwill, C. 2008).	9
Figure 1-9 A General Electric 50.5 m prototype blade transported by truck over a bridge, in Brazil (Ashwill, C. 2008).	10
Figure 1-10 Percentage of highly annoyed (%HA) people by vehicle and aircraft traffic as a function of Ldn (dB(A)). Source: adapted by (Bistafa, 2011), reproduced with permission.	20
Figure 1-11 Sound Pressure levels (1 minute averages) as a function of wind speed, for background noise and a small size WT (Migliore, van Dam, & Huskey, Acoustic Tests of Small Wind Turbines, 2003).	21
Figure 1-12 Typical spectral signature for a WT, overlaid in a standard human hearing threshold line, adapted from the work of T.H. Pedersen (Bowdler & Leventhall, 2011). Reproduced under permission.	23

Figure 1-13 A large scale WT manufacturer diagram stating that 300 m is the minimum distance for WT siting from residential areas.....	28
Figure 2-1 Basic geometry employed by BLAKE to study the wall jet incident on the TE of a semi-infinite plane (Blake, <i>Mechanics of Flow-Induced Sound and Vibration</i> , 1986 II), p. 726, adapted by (Wagner, Bareiß, & Guidati, <i>Wind Turbine Noise</i> , 1996).	36
Figure 2-2 Typical flow around a WT rotor blade (Wagner, Bareiß, & Guidati, <i>Wind Turbine Noise</i> , 1996).	38
Figure 2-3 Low-Frequency, narrow-band noise spectra for HAWTs with downwind (upper spectrum) and upwind (lower spectrum) rotors, at 150 m distance (Hubbard & Shepherd, 1990).....	40
Figure 2-4 – Swept area, hub height and other basic data for Siemens SWT-3.0-101 WT, the smallest onshore WT of the D3 (direct-drive, 3 MW) series, offered by the manufacturer (Siemens, 2013).....	42
Figure 2-5 – Wind velocity spectrum for short and long term at Brookhaven, NY, at 100 m height, as measured by Van der Hooft (1957) and reported by (Burton, Sharpe, Jenkins, & Bossanyi, 2008). The abscissas axis represents the periods, in log scale.	43
Figure 2-6 - Average distribution, over 5 minutes, of noise sources that contribute to total SPL, as observed 32.5 m upwind, at the height of the hub, for an AOC WT in steady 8 m/s wind with no turbulent inflow noise (Moriarty & Migliore, <i>Semi-Empirical Aeroacoustic Noise Prediction Code for Wind Turbines</i> , 2003).....	46
Figure 2-7 - Average distribution, over many revolutions, of the noise source distribution in the azimuthal plane, for a typical, modern, large-size WT, projected over a picture of the WT, for illustration purposes only (Oerlemans, <i>Wind Turbine Noise: Primary Noise Sources</i> , 2011)	47
Figure 2-8 – The sound spectrum for a blunt TE NACA0012 airfoil, with spectral “hump” near 3 kHz (Brooks & Hodgson, 1981).	50
Figure 2-9 – Radiated sound for sharp and blunt TE NACA0012 airfoil, LE tripping (Brooks & Hodgson, 1981) data, adapted by (Blake, <i>Mechanics of Flow-Induced Sound and Vibration</i> , 1986 II).....	51
Figure 2-10 – Measured (continuous lines) broadband noise spectra for a U.S. Wind Power Inc. machine with blunt and sharp TE (Grosveld, 1985).	51

Figure 2-11 – A summary of airfoil TE shapes and relative tone noise amplitude, (Wagner, Bareiß, & Guidati, Wind Turbine Noise, 1996).	52
Figure 2-12 - Broadband noise prediction contributions, from different mechanism noise sources, at 100 m from a MOD-2 WT, operating in a 9.8 m/s wind and producing 1.5 MW (Grosveld, 1985).	55
Figure 2-13 - Calculated contributions of airfoil self-noise individual sources, for a WT blade, and the total SPL spectrum, after (Bareiss, Guidati, & Wagner, 1994).....	56
Figure 2-14 - A-weighted, 1/3 octave band spectrum from a large size, modern construction General Electric WT, with relative contributions from the most relevant flow-induced noise mechanisms (Petitjean, Drobiez, & Kinzie, 2011) for this kind of equipment.....	57
Figure 2-15 - A modern HAWT general layout with indication of the two most important linear dimensions: the hub height and the rotor diameter. Source: European Wind Energy Association.....	60
Figure 2-16 - A large rotor blade from a point of view close to the azimuthal plane, which allows for clearly identification of the blade twist along the span. Source: General Electric.	61
Figure 2-17 - The efficiency of the WT as a function of TSR (Hansen, 2008).	62
Figure 2-18 - Local flow velocities and angles for a blade section at radial distance r . (Hansen, 2008), p. 47.....	64
Figure 2-19 - The power production as a function of wind speed, with illustrations of typical cut-in and cut-out wind speeds for modern HAWTs. Source: AWEA.	65
Figure 2-20 - Comparison of power curves for 70 m diameter machines with (i) passive, stall-regulated, fixed speed; (ii) active, pitch-regulated, fixed speed and (iii) active, pitch-regulated variable speed modes. Source: (Burton, Jenkins, Sharpe, & Bossanyi, 2011), p. 350.	66
Figure 2-21 - The power production [kW] as a function of wind speed at hub height [m/s] for the Northern Power 100 WT, at sea level, 15 °C standard air density (Northern_Power, 2013).	68
Figure 2-22 - Self-noise spectra for the 0.3048 m –chord, NACA 0012 airfoil at zero angle of attach, for tripped boundary layer and freestream velocities	

between 31.7 to 71.3 <i>m/s</i> . Source: (Brooks, Pope, & Marcolini, Airfoil Self-Noise and Prediction, 1989), p.18.....	76
Figure 2-23 - Self-noise spectra for the 0.3048 m chord NACA 0012 airfoil, with tripped BL, at $\alpha_t = 14.4^\circ$, corrected $\alpha^* = 4.0^\circ$ and flow velocities of 39.6 and 71.3 <i>m/s</i> . Source: (Brooks, Pope, & Marcolini, Airfoil Self-Noise and Prediction, 1989), p. 19.....	77
Figure 2-24 - Self-noise spectra for the 0.3048 <i>m</i> -chord, NACA 0012 airfoil at zero angle of attach, for the natural transition case and freestream velocities between 31.7 to 71.3 <i>m/s</i> . Source: (Brooks, Pope, & Marcolini, Airfoil Self-Noise and Prediction, 1989), p.35.....	77
Figure 2-25 - Self-noise spectra for the 0.3048 m chord NACA 0012 airfoil, with natural transition BL, at $\alpha_t = 14.4^\circ$, corrected $\alpha^* = 4.0^\circ$ and flow velocities of 39.6 and 71.3 <i>m/s</i> . Source: (Brooks, Pope, & Marcolini, Airfoil Self-Noise and Prediction, 1989), p. 36.....	78
Figure 2-26 - Self-noise spectra for the Sikorsky airfoil at $\alpha_t = -0.4^\circ$ ($\alpha^* = 0^\circ$) from (Schlinker & Amiet, 1981), compared with prediction from the BPM model. Source: (Brooks, Pope, & Marcolini, Airfoil Self-Noise and Prediction, 1989), p.86.....	79
Figure 2-27 - Self-noise spectra for the Sikorsky airfoil at $\alpha_t = 7.6^\circ$ ($\alpha^* = 3.9^\circ$) from (Schlinker & Amiet, 1981), compared with prediction from the BPM model. Source: (Brooks, Pope, & Marcolini, Airfoil Self-Noise and Prediction, 1989), p.87.....	80
Figure 2-28 - The airfoil geometric parameters (Pechlivanoglou, Passive and Active Flow Control Solutions for Wind Turbine Blades, 2012).....	95
Figure 2-29 - The NACA 0012 airfoil (300 panels), plotted with the aid from XFOIL/XFLR5. Pressure Coefficient plotted over chord, for zero AOA and $Re = 1.5 \times 10^6$	97
Figure 2-30 – Symmetrical airfoil sections similar to the NACA 0012 airfoil, employed in helicopter rotors (Bell UH-1 Iroquois helicopter rotor). Photos: author @ USS Intrepid Museum, NYC, 2014.....	98
Figure 2-31 - The RISO A (upper plot), B (mid plot) and P (lower plot) series of airfoils. Source: adapted from (Burton, Jenkins, Sharpe, & Bossanyi, 2011), p. 117-118.....	102

Figure 2-32 - The NREL S830, S831 and S832 airfoil profiles for WT application. Source: (Somers & Tangler, The Airfoils S830, S831 and S832, 2005b), p. 19.....	106
Figure 2-33 - Other profiles of the NREL family of airfoils for stall-regulated or smaller WT blades, typical radial position on the blade and some design characteristics. Source: (Burton, Jenkins, Sharpe, & Bossanyi, 2011), p. 116.....	107
Figure 2-34 - TE noise resulting from different beveling of TEs, at $U=50$ m/s; $\delta=0.01$ m. (Wagner, Bareiß, & Guidati, Wind Turbine Noise, 1996).	112
Figure 2-35 – TE Serrations made from 2 mm thick aluminum foil, mounted to the outer 12.5 m of the blade, on the pressure side (Oerlemans, Wind Turbine Noise: Primary Noise Sources, 2011).	113
Figure 2-36 - Noise Spectra (average over all relevant wind speeds) for the baseline (unmodified), Sirocco (airfoil shape optimized) and serrated TE blades. Untripped, clean blades (Oerlemans, Fisher, Maeder, & Kögler, 2009).....	114
Figure 2-37 – Distance of Bird warning as a function of Whistle to ambient noise ratio and background noise level (Dooling, 2002).	118
Figure 2-39 - TE Noise Spectra for the S822 Airfoil at zero AOA, tripped (L) and untripped (R) conditions. Flow velocities: ___ 22,4 m/s; _- 32,0 m/s;47,9 m/s; _ _ 63,9 m/s. PWL = Sound Power Level. Source: (Migliore & Oerlemans, Wind Tunnel Aeoracoustic Tests of Six Airfoils for Use in Small Wind Turbines., 2003).....	120
Figure 2-40 - Normalized TE Noise Spectra for the S822 Airfoil (suction side) as a function of the chord-based Strouhal number, for tripped (L) and untripped (R) conditions. Flow velocities: ___ 22,4 m/s; _- 32,0 m/s;47,9 m/s; _ _ 63,9 m/s. Source: (Migliore & Oerlemans, Wind Tunnel Aeoracoustic Tests of Six Airfoils for Use in Small Wind Turbines., 2003).	121
Figure 2-41 - TE Noise Spectra for the NACA0012 Airfoil at 55,5 m/s, for tripped (L) and untripped (R) conditions. Data sources: -- NLR data (suction side); - - NASA data. Source: (Migliore & Oerlemans, Wind Tunnel Aeoracoustic Tests of Six Airfoils for Use in Small Wind Turbines., 2003)	122

Figure 2-42 - A-Weighted Overall TE Sound Power Level (PWL) for some tested airfoils (upper limits). Source: (Migliore & Oerlemans, Wind Tunnel Aeoracoustic Tests of Six Airfoils for Use in Small Wind Turbines., 2003).	123
Figure 2-43 - Airfoil section profile and table for direct (to scale) comparison of thickness distribution, maximum thickness and LE radius. B1-18 is not shown due to proprietary image. Source: (Devenport W. , et al., 2010), p. 43.....	125
Figure 2-44 - Location and lay out of the “soiling trip” applied to the LE of the DU6 airfoil. Source: (Devenport W. , et al., 2010), p. 46.	126
Figure 2-45 - One-twelfth octave bands spectrum derived from integration, for all NACA0012 airfoil self-noise sources, untripped flow at effective AOA of 4° (blue lines) and -4° (green lines). Source: (Devenport W. , et al., 2010).....	127
Figure 2-46 - Overall SPL as a function of aerodynamic parameters, for the tested geometrical variations of the DU-96 airfoil, at different AOA; (a) SPL as a function of cl/cd ; (b), SPL as a function of cl . Source: (Rautmann, Ewert, & Dierke, 2015).	129
Figure 2-47 - Typical structural arrangement of a blade section. Not to scale. Source: (Griffith, Ashwill, & Resor, Large Offshore Rotor Development: Design and Analysis of the SANDIA 100 m Wind Turbine Blade, 2012).....	134
Figure 2-48 - Typical spanwise arrangement of airfoils in a blade: (Griffith & Ashwill, The Sandia 100-m All-glass Baseline Wind Turbine Blade: SNL100-00, 2011).....	135
Figure 2-49 - Annular control volume employed in the BEM method. Source: (Hansen, 2008), p.45.	138
Figure 2-50 - Streamlines passing a rotor in the windmilling state, with axial pressures and velocities. Source: (Hansen, 2008), p.28.....	139
Figure 2-51 - Velocities triangles at the edges and relative velocity at the LE. Source: (Hansen, 2008), p.36 and 47.	140
Figure 2-52 - Forces perpendicular and normal to the rotor plane. Source: (Hansen, 2008), p.48.	141
Figure 2-53 - Rotor thrust coefficient, CT , as a function of axial induction factor. Source: (Hansen, 2008), p.33.....	144
Figure 2-54 - Thrust coefficient as a function of axial induction factor for the momentum theory, continuous line; Glauert’s correction Eqn. (3-16), dotted	

line; and Wilson and Walker correction Eqn. (3-17), dashed line. Source: (Hansen, 2008), p.54.	145
Figure 3-1 – General strategy pursued for the development of the TE noise code, its implementation, validation and later deployment in the search for quite airfoils.	147
Figure 3-2 - Typical blade chord distribution (planform) for 40-m to 60-m span blades, after (Griffin, 2001), p.6.	155
Figure 3-3 – Procedure devised for the geometric design of the WT under specified operating conditions.....	156
Figure 3-4 - Typical blade chord distribution (planform) adopted for the SNL-100, 100 m span blade (Griffith, Ashwill, & Resor, Large Offshore Rotor Development: Design and Analysis of the SANDIA 100 m Wind Turbine Blade, 2012).....	158
Figure 3-5 - The 3-D retarded coordinate system with origin at the TE of a thin plate representing the airfoil moving in rectilinear motion of velocity U in negative x_e axis direction. $\theta = \theta$; $\Psi = \phi$. Source: (Brooks, Pope, & Marcolini, Airfoil Self-Noise and Prediction, 1989), p. 107.	166
Figure 3-6 - Peak Strouhal number as a function of chord Reynolds number. Source: (Brooks, Pope, & Marcolini, Airfoil Self-Noise and Prediction, 1989), p. 53.....	167
Figure 3-7 - Peak Strouhal number as a function of angle of attack. Source: (Brooks, Pope, & Marcolini, Airfoil Self-Noise and Prediction, 1989), p. 58	167
Figure 3-8 - One-third octave spectral shape function A , as a function of Strouhal and Reynolds numbers, for zero AOA. Source: (Brooks, Pope, & Marcolini, Airfoil Self-Noise and Prediction, 1989), p. 55.....	168
Figure 3-9 - One-third octave spectral shape function B , as a function of Strouhal and Reynolds numbers, for large AOA, separated flow noise. Source: (Brooks, Pope, & Marcolini, Airfoil Self-Noise and Prediction, 1989), p. 55	170
Figure 3-10 - Peak scaled level for TBL-TE noise versus chord Reynolds number. Source: (Brooks, Pope, & Marcolini, Airfoil Self-Noise and Prediction, 1989), p. 53.....	171
Figure 3-11 - Scaled TBL-TE noise level as a function of AOA, subtracted from the zero-AOA level. Source: (Brooks, Pope, & Marcolini, Airfoil Self-Noise and Prediction, 1989), p. 59.....	172

Figure 3-12 - Variation of δ^*/c values as a function of Reynolds number, close to the airfoil TE, for experimental I, III (Brooks & Marcolini, 1985), numerical II (Glegg & Reba, 2010) and correlation IV (Schlichting & Gersten, 2003) determination methods.	179
Figure 3-13 - SPL1/3-prediction variation with δ^* -prediction variation, in the BPM TE noise model.	183
Figure 3-14 - XFOIL results for δ^* , calculated for tripped TBL in two different stations close to the NACA 0012 TE, at zero AOA, in the range $5 \times 10^5 \leq ReC \leq 2.6 \times 10^6$, compared with experimental data.	186
Figure 3-15 – XFLR5 results for δ^* , calculated for tripped and transition TBL, for the sharp TE NACA 0012, zero AOA, at station 1.0013C, in the range $5 \times 10^5 \leq ReC \leq 2.6 \times 10^6$ (Saab Jr & Pimenta, 2016).	188
Figure 3-16 - “D”-mesh with all-quad elements developed for the domain calculation in the Ansys ICEM software.	190
Figure 3-17 – TE mesh close up.	191
Figure 3-18 - The maximum distance from the wall to the first node inside the viscous sublayer was estimated with the flat plate theory and inserted as a restriction for the mesh generation, resulting in all first elements close to the surface to be within the sublayer, as verified later during post-processing.	191
Figure 3-19 - Typical behavior of the residues (rms) of the balance equations during a fully turbulent simulation (left), and a transition simulation (right). Case F displayed (intended for qualitative evaluation only).	193
Figure 3-20 - Velocity plot at station 0.96c of the airfoil, showing that the BL thickness at the TE is typically of the order of the airfoil chord $\delta \approx 1 m$, being unsuitable as an upper limit for the integration of the displacement thickness.	194
Figure 3-21 - TKE energy plot at station 1.001c, for the same simulation case of Fig. 4.3.2.3-6, showing the real TBL thickness at the TE to be of the order $\delta \cong 0.014 m$. A thousand points were employed in the construction of the TKE profile.	195
Figure 3-22 - CFD simulations results for fully turbulent and transition cases, compared to experimental data of Brooks, Marcolini, 1985, CFD data from	

Glegg, Reba, 2010, XFOIL simulations and Prandtl’s turbulent flat plate model.	196
Figure 3-23 – CFD simulation results for fully turbulent and transition cases, compared with experimental data of Brooks and Marcolini, 1985 (Saab Jr & Pimenta, 2016).....	197
Figure 3-24 - Refined meshes for the discretization error study. Upper mesh has 51% more elements and the lower mesh has 100% more elements than the original mesh.....	199
Figure 3-25 - Qblade V0.8 software original capabilities (Marten D. , Qblade Short Manual V0.8, 2014) and the proposed additional modules (blue frame) for 2-D and 3-D TE noise prediction capabilities.	206
Figure 4-1- Airfoil geometries (*) for all NREL “S” Series Airfoils employed in the 50 m length blade (S818->red; S830->green; S832->blue).	218
Figure 4-2 – Poli-100, general rotor geometry.....	219
Figure 4-3 - Airfoil section local chord Reynolds and Mach numbers (vertical axis), as a function of radial position over blade span (horizontal axis).	220
Figure 4-4 - Chord distribution and local pitch angle (vertical axis) for each section, calculated by the BEM method, for each airfoil section (horizontal axis) to work in ideal efficiency (maximum cl/cd ratio) throughout the blade span.	221
Figure 4-5 – The XFOIL/XFLR5 flow analysis definition screen.	225
Figure 4-6 – Input/output screen for the flow analysis of XFOIL/XFLR5. The angles and steps are selected at the right hand upper screen windows and the Euler number is plotted over the airfoil chord at the upper screen. At the lower screen, the profile is visible.	226
Figure 4-7 – This is the second output screen of the XFOIL/XFLR5 module, where the resulting polar diagram and other aerodynamic data may be verified. By selecting the indicated NOISE icon (red arrow), the code switches to the 2D TE noise module.	226
Figure 4-8 – Information resources for the user on the TE noise module are provided at the “?” menu, in “About Pnoise” option, and also in the “Noise Simulation” menu, option “Model Validity Hint”.	227
Figure 4-9 – Module copyright, General Public Licensing notices and references are available to the user.....	228

Figure 4-10 – Original (unmodified) Model validity is provided to the user.	228
Figure 4-11 - The input screen has two tabs. In the first one (shown) the airfoil geometric and flow information is input. Also the noise sources are selected and the directivity angles informed.....	229
Figure 4-12 – In the second tab, any combination of AOAs may be selected for any Polars available in the database.	230
Figure 4-13 - individual contributions of each source and the total SPL are displayed in different quadrants of the screen. Upper LH: OASPL; Upper RH: SPL_alpha; Lower LH: SPL_S; Lower RH: SPL_P.....	231
Figure 4-14 - For zero AOA flow and same conditions as in Fig. 11, item (a) of BPM paper: The upper graph is the spreadsheet output and it must be compared with the indicated calculated and measured spectra on the lower portion of the figure. Vertical axis=SPL (dB); Horizontal axis = Frequency (Hz), for all charts.....	235
Figure 4-15 - For AOA=4° (below switching angle) flow and same conditions as in Fig. 17, item (a) of BPM paper. The upper graph is the spreadsheet output and it must be compared with the indicated calculated and measured spectra on the lower portion of the figure. Vertical axis=SPL(dB); Horizontal axis = Frequency (Hz), for all charts	236
Figure 4-16 - For AOA=17,4° (above switching angle) flow and same conditions as in Fig. 42, item (a) of BPM paper. The upper graph is the spreadsheet output and it must be compared with the indicated calculated and measured spectra on the lower portion of the figure. Vertical axis=SPL (dB); Horizontal axis = Frequency (Hz), for all charts	237
Figure 4-17 – Initial data validation for the Virginia Tech (red dots) measurements, against BPM measurements (black lines) and BPM model calculations (black stars). $Re_c \approx 620,000$. Upper plot: zero AOA. Lower plot: 5.3° AOA. Source: (Devenport W. , et al., 2010), p.180.....	246
Figure 4-18 – PNoise inside Qblade v0.8, typical input screen for the validation attempt at higher Reynolds numbers and zero AOA.....	248
Figure 4-19 - PNoise inside QBlade v0.8, typical output screen for the validation attempt at higher Reynolds numbers and zero AOA. Lower, RH plot highlight is the resultant Sound Pressure Level (from both sources) at the 1,000 Hz band region.....	249

Figure 4-20 – Integrated spectrum for untripped NACA 0012 airfoil, at 0°, 2° and 4° for three different flow velocities for different wind tunnel data entries (different dates = different colors). (Devenport & Burdisso, Aeroacoustic Testing of Wind Turbine Airfoils, 2004), p. 189.	249
Figure 4-21 – Modified-BPM calculated spectra (color lines) for three different effective AOA, compared to VT data reference plot (thick, blackline).	250
Figure 4-22 – Recalculation of the SPL for the transition flow at zero AOA, with corrected directivity and distance data.	252
Figure 4-23 – VT data (black) versus predicted spectra. Overlap was forced by progressive reduction of the wetted TE length on the simulated blade segment.	254
Figure 4-24 - Integrated Spectrum for NACA 0012 airfoil at 0° effective AOA. Untripped (black) and tripped (red) spectra shown for the July, 2007 tunnel entry. Source: (Devenport W. , et al., 2010), p. 197.	255
Figure 4-25 - XFLR5 simulation input for 28 m/s, zero AOA and tripping at 5% upper and 10% lower surfaces.	256
Figure 4-26 – PNoise input screen for the simulation.	257
Figure 4-27 - Total TE-noise SPL calculated by the Modified-BPM method (upper plots), compared to VT measured spectrum (lower plots), for the NACA 0012 airfoil at 28 m/s, for 0° AOA with tripping at 5% chord, and 4° AOA with tripping at 5% chord for the suction side and 10% chord at the pressure side.	258
Figure 4-28 – The symmetric NACA 0012 airfoil profile (green) and the cambered NREL-Somers S831 airfoil profile (red).	260
Figure 4-29 – Modified-BPM model TE noise calculations for the tripped, S831 airfoil, at -2° and +5° AOA (upper plots) compared to the VT derived spectra (lower plots), for the same nominal conditions.	261
Figure 4-30 - Direct comparison of NASA wind tunnel acoustic data (Brooks, Pope, & Marcolini, Airfoil Self-Noise and Prediction, 1989), p.18, Fig. 11 (a), and Virginia Tech spectra derived from wind tunnel acoustic data (Devenport W. , et al., 2010), p.197 (red line, for 28 m/s), for a NACA 0012 airfoil at 0° AOA, tripped flow, and chord-based Reynolds number close to 1,500,000.	262
Figure 4-31 - The contour for the S830 airfoil (Copyright NREL-Somers).	265

Figure 4-32 – Coefficient of Pressure (Euler number) over normalized chord, for the baseline S830 airfoil, for the original ($ReC = 4,000,000$) and new operating conditions found at 85% radius of Poli-100 Wind Turbine ($ReC = 7,700,000$).	267
Figure 4-33 - S830 and NACA 0021 $cl\alpha$ curves at 7.7M Reynolds number.	269
Figure 4-34 - Typical input data for Aerodynamic analysis (all cases) in XFLR5 V6.06, with tripping at 5% chord over the suction side and 10% chord upper chord over the pressure side.	274
Figure 4-35 - Typical input data for Aeroacoustic analysis (different AOA and polar objects selected for each case) in the new 2D acoustic module of the QBlade software (PNoise).	274
Figure 4-36 - Typical graphical output of the sound pressure level spectra with the 2D acoustic module coupled to the QBlade software.	275
Figure 4-37 - Typical file output of the overall and 1/3 octave sound pressure level spectra with the 2D acoustic module coupled to the QBlade software.	275
Figure 4-38 – Overview of the baseline geometry (red) and the variations with more (blue) and less (green) LE radius simulated.	277
Figure 4-39 – Overview of the geometries with different suction side forward contour simulated.	278
Figure 4-40 – Overview of the geometries with different camber percentages.	280
Figure 4-41 – Overview of the geometries with different flap angles, after de-rotation.	281
Figure 4-42 – Overview showing the geometries with different maximum thickness positions along the chord line.	283
Figure 4-43 – Overview of the geometries with different suction (upper) side aft contour.	284
Figure 4-44 – Overview of the geometries with different LE gaps simulated.	286
Figure 4-45 - Overall acoustic and aerodynamic performance for Airfoil #100 (S830 original geometry and design conditions), the reference spline foil #109 (S830 splined foil at Poli-100 blade operating conditions) and all geometrical variations studied. Red line = original S830 OASPL level (94 dB). Blue line = Original S830 cl/cd max level (77.1). Orange line = original S830 A-weighted OASPL (80.3 dB(A)).	288

Figure 4-46 - Plot of OASPL x source graph for the higher velocity cases with the purpose of identifying priority sources.....	292
Figure 4-47 - Plot of SPL dB(A) x source graph for the higher velocity cases in order to investigate sources that contribute more to audible noise levels.	293
Figure 4-48 - The SP4621HP profile (red), with preserved original thickness in relation to the S830 airfoil (blue).	299
Figure 4-49 - The Polar diagrams for the S830 (red line = low Re; blue line = high Re) and the SP 4621HP (green line) airfoil. The cl/cd x AOA slope is slightly larger for the green curve in the circled graph.....	301
Figure 4-50 - The SP 4721LA profile, with preserved original thickness in relation to the S830 airfoil.	303
Figure 4-51 - The Polar diagrams for the S830 (green and blue) and the SP4621HP airfoil (yellow curve). Notice the flat-top curve of (cl/cd) x α diagram indicated by the red arrow.	304
Figure 4-52 - Friction coefficient over upper and lower surfaces for the SP 4621 – HP airfoil for untripped flow at AOA=6.4, Reynolds = 8,7 Million and $M=0.18$	309
Figure 4-53 - Audiograms from birds assembled by Dooling (Dooling, 2002), based on other references.	311
Figure 4-54 – Weighted and unweighted overall Sound Pressure Levels for the SP4621Hp and SP4721LA airfoils, compared with the baseline S830 airfoil.	315
Figure 4-55 - OASPL spectra for the baseline airfoil (S830) and for two developed airfoils.	316
Figure 4-56 A-Weighted SPL spectra for the baseline airfoil (S830) and for two geometric variations. SP4621HP and SP4721LA.	316
Figure 4-57 - Sound Pressure Level spectra for partially separated flow, SPL_{α} (dB).	317
Figure 4-58 - Aerodynamic efficiency (cl/cd) versus AOA.	318
Figure 4-59 – The Euler number along the chord for the upper and lower airfoil surfaces.	319
Figure 4-60 - Polar diagrams for the developed airfoils in tripped flow (black lines) and the polar diagram for the reference airfoil, S830 (in red).	321
Figure 4-61 - Comparison among noise radii from the different airfoils.	322

Figure 4-62 - Polar diagram (left) and other relevant diagrams for the SP4621HP airfoil for the local flow conditions on 8 discretized blade span sections 2.5 m wide, ranging from 55% to 90% of the POLI-100 WT blade.....	324
Figure 4-63 - Poli-100 WT upgraded with the SP4621HP airfoil for the radial stations from 55% to 90% radius, all other airfoils remaining unchanged from the baseline design.	325
Figure 4-64 - Coefficients output screen for the Poli-100 WT upgraded with the SP4621HP airfoil in selected radial stations. Coefficient of Power (Cp) at the upper left; Coefficient of Torque (Ct) at the upper right. The upgraded blade is plotted in red.....	326
Figure 4-65 - Coefficient of Power versus TSR for the original and upgraded Poli-100 WT.	326
Figure 4-66 - Power output screen for the Poli-100 WT upgraded with the SP4621HP airfoil in selected radial stations. The upgraded blade is plotted in red.....	327
Figure 4-67 - Coefficients of Power versus TSR for the original and upgraded Poli-100 WT.	327
Figure B-1 – Hydrodynamic near field, geometric near field and the far field (Bies & Hansen, 2009).	356
Figure B-2 – Graphical rendering of the acoustic field radiated by a monopole. Wolfram Mathematica Demonstration Program. Code author: Enrique Zeleny.	366
Figure B-3 – Graphical rendering of the acoustic field radiated by a dipole. Pressure fluctuation contour (left) and waves (right). Wolfram Demonstration Program. Code author: Enrique Zeleny.	369
Figure B-4 – A dipole source does not radiate an isotropic field. The directivity pattern derived from Eqn. B-56 shows two opposed lobes or regions where sound is well radiated and two regions where sound cancels. Picture: courtesy of Dr. Dan Russell, Grad. Prog. Acoustics, Penn State.	370
Figure B-5 – Constant sound pressure level (OASPL) contours for an AOC turbine, in steady 8 m/s operation. Source: (Moriarty & Migliore, Semi-Empirical Aeroacoustic Noise Prediction Code for Wind Turbines, 2003).....	370
Figure B-6 – Comparative directivity pattern for the far field of a monopole (a), dipole (b), lateral quadrupole (c) and longitudinal quadrupole (d). Although	

(b) and (d) display similar shapes for the far field, the waves at the same (r, t) have opposite phases for each lobe in the case of the dipole, and same phase for the longitudinal quadrupole (Russell, Titlow, & Bemmen, 1999).378
Figure B-7 – Graphical rendering of the acoustic far field radiated by a lateral quadrupole. Pressure fluctuation contour (left) and waves (right). Wolfram Demonstration Program. Code author: Enrique Zeleny.378
Figure B-8 – Definition of the coordinate system, of the moving surface implicitly defined $(fx, t = 0)$ and of the unit normal vector $(n = \nabla f)$ for the <i>FW-H</i> equation derivation. Illustration source: (Farassat, Derivation of Formulations 1 and 1A of Farassat, 2007).385
Figure C-1 – Histogram of Wind Speed versus frequency, 10-minute-averages, at 45 m height, at Sao Caetano do Sul, SP, overlapped with adjusted Weibull distribution (Reichenbach, Vieira, Yoshimura, & Telles, 2012).389
Figure C-2 – Rayleigh distribution plots of Eqn. (C-1), for wind averages of 6 m/s (blue line), 8 m/s (red line) and 10 m/s (golden line).389
Figure D-1 – Basic geometry employed by BLAKE to study the wall jet incident on the TE of a semi-infinite plane (Blake, Mechanics of Flow-Induced Sound and Vibration, 1986 II), p. 726, adapted by (Wagner, Bareiß, & Guidati, Wind Turbine Noise, 1996).391
Figure D-2 – Basic geometry employed by (Howe, 1978) and (Brooks & Hodgson, 1981), for identification of the convected turbulence incidence angle, β , in Eqn. (2.5.2-1). Source: (Brooks & Hodgson, 1981).395
Figure D-3 – TE noise spectra predicted based on measured surface pressure, compared to the theoretical prediction of Eqn. (2.5.2-2), for free stream velocities of 38.6 and 69.5 m/s. Experimental _____; prediction - - - - ; approximate prediction for low frequencies; and approximate prediction for turbulence convecting at 60% of U_0 + + + + +. Source: (Brooks & Hodgson, 1981).397
Figure D-4 – Normalized one-third octave spectra. All airfoils with tripped BL and $U = 71.3$ m/s. Source: (Brooks & Marcolini, 1985).399
Figure D-5 – WT Noise spectra for the MOD-2 WT, against prediction for inflow noise and TE noise. Source: (Lowson, 1993) Fig. 12a.404
Figure D-6 – WT Noise A-weighted spectra for the MOD-2 WT, against prediction for inflow noise and TE noise. Source: (Lowson, 1993) Fig. 12b.405

- Figure D-7 – Relative position between the observer and the blade segment for consideration of directivity function. Numbers from 1 to 5 indicate the following coordinate systems applied: 1- at the plate TE, as shown in the previous figure; 2- at the lifting line; 3- at the rotor shaft; 4- at the tower base, and 5- at the observer position. Source: (Fuglsang & Madsen, Implementation and Verification of an Aeroacoustic Noise Prediction Model for Wind Turbines, 1996), p.18.....408
- Figure D-8 – Experimental versus predicted A-weighted SPL [dB] for the Vestas V27 WT, at 8 m/s wind speed and 0.5° tip pitch. Source: (Fuglsang & Madsen, Implementation and Verification of an Aeroacoustic Noise Prediction Model for Wind Turbines, 1996), p.27.....409
- Figure D-9 – The six aluminum airfoil models employed by Migliore and Oerlemans (Migliore & Oerlemans, Wind Tunnel Aeroacoustic Tests of Six Airfoils for Use in Small Wind Turbines., 2003) in aeroacoustic tests: the Wortmann FX63-137, Selig S822 and S834, Selig-Donovan SD2030, Selig-Giguere SG6043 and Selig-Hanley SH3055. The white, composite-made NACA 0012, used as a benchmark, is at the center of the photograph.411
- Figure D-10 – The points with symbols represent measured wind tunnel test data and continuous lines represent the predicted spectra for similar flow conditions. Boundary layer “lightly tripped”. Source: (Moriarty & Migliore, Semi-Empirical Aeroacoustic Noise Prediction Code for Wind Turbines, 2003), p.8.....411
- Figure D-11 – Comparison of measured and predicted noise for the NACA 0012 airfoil at fixed 7.18° AOA along a range of Mach numbers. Source: (Moriarty & Migliore, Semi-Empirical Aeroacoustic Noise Prediction Code for Wind Turbines, 2003), p.8.....412
- Figure D-12 – Comparison of measured and predicted noise for the S822 airfoil at fixed Mach number of 0.038, as a function of AOA. The BL is “lightly tripped”. Source: (Moriarty & Migliore, Semi-Empirical Aeroacoustic Noise Prediction Code for Wind Turbines, 2003), p.10.413
- Figure D-13 – Comparison of measured and predicted noise for the AOC 15/50 WT in 8 m/s high turbulence wind. The BL is untripped. Source: (Moriarty & Migliore, Semi-Empirical Aeroacoustic Noise Prediction Code for Wind Turbines, 2003), p.13.....414

- Figure D-14 – Comparison of measured spectrum for the Bonus Combi 300 kW WT, at 8 m/s wind speed at hub height, with calculations for the same WT, but employing the NACA 0012 airfoil instead, for tripped and untripped BL. Source: (Zhu, 2004), p. 52 418
- Figure D-15 – Comparison of measured spectrum for the Bonus Combi 300 kW WT, at 8 m/s wind speed at hub height, with calculations for the same WT employing the NACA 634XX airfoil instead, for tripped and untripped BL. Source: (Zhu, 2004), p. 53 419
- Figure D-16 – Comparison of measured spectrum for the Bonus Combi 300 kW WT, at 8 m/s wind speed at hub height, with calculations for the original NACA 632XX, for tripped and untripped BL. Source: (Zhu, 2004), p. 53 419
- Figure D-17 – Comparison of measured NACA 0012 airfoil data with predicted noise spectra for different AOA, and Reynolds number of 1.1×10^6 . Source: (Moriarty P. , NAFNoise and FAST noise modules, 2008), p.21 421
- Figure D-18 – Comparison of measured of S822 airfoil data with predicted noise spectra for different AOA, and Reynolds number of 1.1×10^6 . Source: (Moriarty P. , NAFNoise and FAST noise modules, 2008), p.22 422
- Figure D-19 – Comparison of spectra predicted by Vargas' tool (LVNP) against experimental and theoretical prediction from (Brooks, Pope, & Marcolini, Airfoil Self-Noise and Prediction, 1989). Source: (Vargas L. d., 2008), p.46. 423
- Figure D-20 – Comparison of total and partial noise spectra predicted by Vargas' tool (LVNP) for the Bonus 300 WT (upper graph), against theoretical prediction from (Zhu, 2004) (lower graph), for the same equipment. Source: (Vargas L. d., 2008), p.50. 425
- Figure E-1 – Illustration of the production of TE noise. Source: (Wolf, Lutz, Würz, Stalnov, & Seifert, 2011). 428
- Figure E-2 – Comparison of Surface Pressure Spectra measured over a NACA 0015 Airfoil ($x/C = 0.567$), against calculation using the TNO model, with both XFOIL and CFD code EllipSys2-D, as a function of AOA. Source: (Bertanoglio, Madsen, & Bak, 2009). Data also available for higher Reynolds number in the reference, with similar conclusions..... 429
- Figure E-3 – Comparison of Surface Pressure Spectra measured (continuous lines) over a NACA 0012 Airfoil (Brooks & Hodgson, 1981) in three different

- sensor positions, against calculation using the TNO model, with both XFOIL and CFD code EllipSys2-D (lines with points). $Re = 2.9 \times 10^6$ and $\alpha = 0^\circ$. Source: (Bertanoglio, Madsen, & Bak, 2009).....430
- Figure E-4 – Comparison of Sound Pressure Level measured at LWT against prediction by the TNO model, at $Re = 1.6 \times 10^6$ and $cl = 1$. for a reference airfoil (a design employed in a WT), a new airfoil design and an airfoil that resulted from the DATA project. Source: (Lutz, Herrig, Würz, Kamruzzaman, & Krämer, 2007).....431
- Figure E-5 – Airfoils used for noise prediction and validation in (Moriarty, Guidati, & Migliore, Recent Improvement of a Semi-Empirical Aeroacoustic Prediction Code for Wind Turbines, 2004).433
- Figure E-6 – Measured (symbols) and predicted (lines) TE noise spectra for the NACA 0012 symmetrical airfoil at various AOA. Left: measurements plotted against TNO model prediction. Right, blue edge figure: measurements plotted against BPM model. See text for detail on models. $Re = 1.1 \times 10^6$. Source: (Moriarty, Guidati, & Migliore, Prediction of Turbulent Inflow and Trailing-Edge Noise for Wind Turbines, 2005), pages 11 and 14.434
- Figure E-7 – Measured (symbols) and predicted (lines) TE noise spectra for the SH3055 cambered airfoil at various AOA. Left: measurements plotted against TNO model prediction. Right, blue edge figure: measurements plotted against BPM model. See text for detail on models. $Re = 1.0 \times 10^6$. Source: (Moriarty, Guidati, & Migliore, Prediction of Turbulent Inflow and Trailing-Edge Noise for Wind Turbines, 2005), pages 12 and 15.435
- Figure E-8 – Comparison of $\delta^*/chord$ calculated with RANS, with experimental data from (Brooks & Hodgson, 1981) and (Brooks, Pope, & Marcolini, Airfoil Self-Noise and Prediction, 1989). $ReC = chord\ based\ Reynolds\ number$. Source: (Glegg & Reba, 2010), p. 1297.....438
- Figure E-9 – Comparison of SPL predicted spectrum (\circ) of the TE noise from a NACA 0012 airfoil (observer at 90° to the airfoil chord) against measurements from (Brooks & Hodgson, 1981) (+). Airfoil chord is 0.6096 m and flow speed is 69.5 m/s. Source: (Glegg & Reba, 2010), p. 1.298.438
- Figure E-10 – Comparison of SPL predicted spectrum (\circ) of the TE noise from a NACA 0012 airfoil (at 90° to the airfoil chord) against the empirical prediction

- of the BPM method (Brooks, Pope, & Marcolini, Airfoil Self-Noise and Prediction, 1989). Airfoil chord is 0.3028 m and flow speed is 39.6 m/s ; untripped (+); lightly tripped (\square); $ReC = \text{chord based Reynolds number}$. Source: (Glegg & Reba, 2010), p. 1298.....439
- Figure E-11 – The effect on the SPL spectrum, of the proposed empirical scaling law (a multiplier as a function of pressure gradient) over Λ_2 . Source: (Lutz, Herrig, Würz, Kamruzzaman, & Krämer, 2007), p. 782.....442
- Figure E-12 – The IAGNoise controlling interface flow diagram and its internal modules. Source: (Kamruzzaman, Meister, Lutz, Kühn, & Krämer, 2010).....444
- Figure E-13 – Noise sources parameters calculated by Xnoise (green dotted line), XEnoise (magenta dotted line), Rnoise (blue line with triangles), experimental data fed into the TNO-Blake model (orange dotted line) and experimental measurement (black line with squares). Source (Kamruzzaman M. , Lutz, Nübler, & Krämer, 2011).444
- Figure E-14 – Correlated anisotropy scale function $f_{22aniso}$ based on $Re\lambda$. Data from five different airfoil BL measurements at Reynolds number range $0.8 \times 10^6 - 3.0 \times 10^6$, varying AOA and BL tripping applied. Source (Kamruzzaman M. , Lutz, Herrig, & Krämer, 2012a), p. 56.....447
- Figure E-15 – Wind Tunnel TBL data (Exp. LWT) for a NACA 0012 at $Re = 1.5 \times 10^6$; $M = 0.166$; $y_1/c = 0.999$ and AOA of 0° and 4° , against RANS calculation by RNoise (Rnoise:SST), employing Menter's $SST\ k, \omega$ two-equation turbulence model. Source (Kamruzzaman M. , Lutz, Herrig, & Krämer, 2012a), p. 57.448
- Figure E-16 – Wind Tunnel TBL data (Model Exp.) for a NACA 0012 at $Re = 1.5 \times 10^6$; $M = 0.166$; $y_1/c \approx 1.004$, against RANS calculation by RNoise (Rnoise:SST), employing Menter's $SST\ k, \omega$ two-equation turbulence model. ε^* and Λf^* values are direct RANS-calculated values. ε and Λf values use a near-wall correction formula. Figures shown are for 0° AOA only, for clarity. Figures for 4° show similar trends, although authors state the correction presented better results for lower AOA. Source (Kamruzzaman M. , Lutz, Herrig, & Krämer, 2012a), p. 57.....450
- Figure E-17 – Noise sources parameters. Validation of the enhanced anisotropy scale function for TBL-TE noise prediction. NACA 0012 at $Re = 1.5 \times$

106; $M = 0.166$. AOA=0° (upper figure) and AOA=4° (lower figure). Experimental values (Exp. LWT); direct *SST* k, ω RANS-calculated values (Rnoise:SST/iso); *SST* k, ω RANS-calculated values corrected for both anisotropy and dissipation (Rnoise:SST/anisoRe); *Reynolds Stress Modeling RSM* RANS-calculated values (Rnoise:RSM/aniso). Source (Kamruzzaman M. , Lutz, Herrig, & Krämer, 2012a), p. 58-59.....451

- Figure E-18 – Comparison of the 1/3 octave band far-field noise spectrum measured (Exp. LWT), with that predicted by Rnoise with original TNO modeling (Rnoise/TNO); Rnoise with isotropic turbulence modeling (Rnoise/isoke) and RISOE with isotropic turbulence modeling (RISOE CFD). Airfoil: NACA 643-418. Source (Kamruzzaman M. , et al., 2012b), p. 56.....452
- Figure I-1 – Typical input screen of the PNoise for zero AOA calculation.462
- Figure I-2 – Typical output screen of the PNoise for zero AOA calculation.462

LIST OF TABLES

Table 1-1 - Selected Noise Limits for different Countries, SPL [dB] (GIPE, 2004). Reproduced under permission.	25
Table 1-2 - Criteria level for external environment evaluation, dB(A).	26
Table 2-1 – WT aerodynamic noise generation mechanisms (Rogers, Manwell, & Wright, 2006).	38
Table 2-2 – Typical eddy-size to chord-size ratios for some frequencies of audio noise emitted by turbulent eddies. Adapted (range enlarged) from (Wagner, Barei, & Guidati, Wind Turbine Noise, 1996).	44
Table 2-3 - Geometric characteristics of the rotor-blade for the SERI 7.9 m Airfoil Blade developed at Stanford University (Ong & Tsai, 2000).	60
Table 2-4 - Twist and chord as a function of radius, for a Nordtank NTK 500/51 Wind Turbine. Source: (Hansen, 2008), p. 58.	62
Table 2-5 - The A-weighted OASPL for the Northern Power 100 WT, at 30 m from the tower, at hub height. (Northern_Power, 2013)	66
Table 2-6 - Example of the bin method applied to the estimation of the total annual power output for a small size, 2.4 m diameter WT, with Rayleigh wind distribution and average annual wind speed of 12 m/s (GIPE, 2004).	68
Table 2-7 - Typical input required by Class II and Class III noise prediction models. Source: (Wagner, Barei, & Guidati, Wind Turbine Noise, 1996).	86
Table 2-8 - Modeled noise sources.	88
Table 2-9 - Type of theoretical base.	88
Table 2-10 - Type of noise field.	89
Table 2-11- WT geometry description required as input data.	89
Table 2-12 - Flow field data required as input	89
Table 2-13 - Turnaround time (TAT).	90
Table 2-14 - Accuracy class against experimental data.	90
Table 2-15 - Type of application domain (geometry validation).	91
Table 2-16 – Location of the observer.	91

Table 2-17 – Availability.	91
Table 2-18 – User-Friendliness.	92
Table 2-19 - Classification of all reviewed Semi-Empirical and Simplified-Theoretical WT noise prediction methods, in accordance with the proposed criteria.	93
Table 2-20 - Key design features for DU (Delft University) WT airfoils at Reynolds number of 3×10^6 . Source: (Timmer & van Rooji, 2003) p. 491.	101
Table 2-21 - More design features of the DU (Delft University) airfoils for WT blades. Source: (Burton, Jenkins, Sharpe, & Bossanyi, 2011), p. 119.	101
Table 2-22 – Airfoil design requirements for DU 95-W-180 / DU 96-W-180 outboard airfoil and wind tunnel test results. Source: (Timmer & van Rooji, 2003), p. 492.	101
Table 2-23 – Characteristics of the RISO A, B and P families of Airfoils for WT blades. Source: adapted from (Burton, Jenkins, Sharpe, & Bossanyi, 2011), p. 117-119.	103
Table 2-24 - Example of possible applications for the NREL Airfoil families. Source: (Burton, Jenkins, Sharpe, & Bossanyi, 2011), p. 115.	104
Table 2-25 - Airfoil design specifications employed in the development of NREL S830 (first column), S831(middle column) and S832 airfoils. Source: (Somers & Tangler, The Airfoils S830, S831 and S832, 2005b), p.15.	105
Table 2-26 - A summary of major published airfoils developed for pitch-controlled horizontal axis wind turbines and their aerodynamic theoretical characteristics.	109
Table 2-27 - Different methods proposed for the reduction of TE noise. Adapted from (Wagner, Bareiß, & Guidati, Wind Turbine Noise, 1996), p. 168.	112
Table 2-28 – Signal/Noise (S/N) in dB to be exceeded for detection of tones over noise for an average bird (Dooling, 2002), p.12.	117
Table 3-1 - Scaled up blade properties according to aerodynamic and gravitational scaling functions. The machine sizes of 10 MW and 15 MW were chosen as references for the larger blades designed in the context of the current research. Source: (Griffith, Ashwill, & Resor, Large Offshore Rotor Development: Design and Analysis of the SANDIA 100 m Wind Turbine Blade, 2012), SNL.	152
Table 3-2 - Operating conditions defined for the 87 m and 106.5-m-long blades.	157

Table 3-3 - Blade thickness distribution along the span and airfoil sections adopted for the SNL-100, 100 m span blade (Griffith, Ashwill, & Resor, Large Offshore Rotor Development: Design and Analysis of the SANDIA 100 m Wind Turbine Blade, 2012).	158
Table 3-4 - Displacement thickness data fit for experimental (I,III), CFD (II) and TBL correlation (IV).	180
Table 3-5 - Impact of δ^* variation, in SPL noise prediction, for a fixed $Re_c \approx 1.1 \times 10^6$, using different estimation approaches.	181
Table 3-6 – Cases tested in the XFOIL (XFLR5). Case A is based on Brooks and Hodgson, 1981. Cases B-H are based on Brooks and Marcolini, 1985. Case numbering is analog to (Glegg & Reba, 2010), p. 1297.	185
Table 3-7 - Relative error comparison for the XFOil results (tripped and transition TBL), for the sharp-TE NACA 0012 airfoil, in the range $5 \times 10^5 \leq Re_c \leq 1.5 \times 10^6$ (Saab Jr & Pimenta, 2016).	188
Table 3-8 - Flow parameters for the cases tested in CFD-RANS simulations, after chord normalization.	189
Table 3-9 – Relative error estimation for the CFD results (turbulent and transition TBL), for the sharp-TE NACA 0012 airfoil (Saab Jr & Pimenta, 2016).	197
Table 3-10 - Discretization error associated with the CFD solution of the fully turbulent regime simulation, case F.	200
Table 3-11 - Discretization error associated with the CFD solution of the transition regime simulation, case F.	201
Table 3-12 – Experimental, discretizations and CFD versus Experimental relative errors.	202
Table 3-13 - XFOIL results for δ^* , calculated for tripped and transition TBL, at station 0.98c of NACA 0012 TE, in the range $5 \times 10^5 \leq Re_c \leq 2.6 \times 10^6$ (Saab Jr & Pimenta, 2016).	203
Table 3-14 - The reviewed semi-empirical-based WT noise prediction methods (1-13), and the proposed method (14). N/A = Not Available.	209
Table 3-15 - Table of desirable requirements for a quiet airfoil aimed at 85% span of a large size HAWT, preserving aerodynamics performance.	212
Table 4-1 – Geometry details of the 50-m length blade of Poli-100 rotor.	219

Table 4-2 - Final operating conditions at each blade station for the 50-m length blade of Poli-100 WT, @ 12 m/s, TSR=7 and 16.4 rpm (typical output from the implemented BEM method).....	220
Table 4-3 - Sample output file of XFLR5 v6.06 inside QBlade, after modification to store $\delta * (D^*)$ for all AOA tested.	224
Table 4-4 – Sample of file output for the NACA0012 at zero AOA, with overall noise levels (weighted and unweighted) plus one third octave spectra weighted and unweighted.	232
Table 4-5 – XFLR5/XFOIL module calculation procedure verification table before and after modification.....	233
Table 4-6 – Verification table for the TE noise predicted for the zero AOA flow over the NACA 0012 airfoil.	238
Table 4-7 - Verification table for the TE noise predicted for the 4° AOA flow over the NACA 0012 airfoil.	239
Table 4-8 – Verification of SPL contributions for symmetrical AOA.....	240
Table 4-10 - Verification data for the 0° AOA calculation, with original BPM correlations for the displacement thickness.	241
Table 4-11 - Verification data for the 4° AOA calculation, with original BPM correlations for the displacement thickness	242
Table 4-12 - Verification data for the 12.5° AOA calculation, with original BPM correlations for the displacement thickness	242
Table 4-13 - Comparison of 0° AOA, transition flow results prior and after the directivity and distance adjustments.	252
Table 4-14 – Sensitivity tests for the SPL as a function of tripped or transition flow, for the S830 airfoil, at two different Reynolds numbers.	259
Table 4-15 - Simulated aerodynamic and aeroacoustics characteristics for the S830 airfoil at the original design point (Re = 4 million) and for the POLI-100 WT blade at 85% span (Re = 7.7 million), for tripped condition (XFLR5 V6.06 and QBlade V0.8 with 2D noise module).	265
Table 4-16 - $c_{l\alpha}$ [1/°] estimation based on XFLR5 output for the S830 and NACA 0021 airfoils at Reynolds number of 7.7M.....	269
Table 4-17 - Aerodynamic and aeroacoustic performance for the S830 original geometry and the geometrical variations employed in the sensitivity study	276

Table 4-18 - Classification of the geometrical modifications cases in relation to reference cases.	289
Table 4-19 - Aerodynamic and aeroacoustic performance of the SP4621HP dedicated WT airfoil when compared to the S830 in design condition and higher Reynolds number condition. Only differences in SPL should be considered.	298
Table 4-20 - Aerodynamic and aeroacoustic performance of the SP4721LA (case #163) dedicated WT airfoil when compared to the S830 in design condition (case #100) and higher Reynolds number condition (case # 109).	305
Table 4-21 - Comparison of airfoil characteristics with requirements.	320
Table 4-22 - cl_{max} difference between tripped and untripped flow for the reference (S830) and the newly developed airfoils. The differences are quite low, indicating good roughness tolerance.	321
Table 4-23 - Local Reynolds and Mach numbers calculated from the BEM method for the blade stations ranging from 55% to 90% radial position in the POLI-100 WT blade.	323
Table A-1 - WT manufacturers and industry direct survey at AWEA 2012.	349
Table D-1 – Input data for the Bonus Combi 300 kW WT, used as input to (Vargas L. d., 2008) and (Zhu, 2004) methods. Sources: (Vargas L. d., 2008), p.48; (Zhu, 2004), p.51.	423
Table F-1 - Sensitivity studies of $SPLW$ (A-Weighted SPL) as a function of the number of positions of the blade in the azimuthal plane. The total number of computed pressure values is $Np = N\beta \cdot NS \cdot Nf$. Source: (Vargas L. d., 2008), p.43.	455
Table H.1 – Airfoil distribution, with Reynolds and Mach numbers for the local flow as a function of radial station for the Poli-180, 177.10 m diameter, 10 MW (nominal) horizontal axis wind turbine.	459
Table H.2 – Airfoil distribution, with Reynolds and Mach numbers for the local flow as a function of radial station for the Poli-220, 217.84 m diameter, 15 MW (nominal) horizontal axis wind turbine.	460
Table I-2 – XFLR5 output with displacement thickness.	464
Table I-3 – Spreadsheet displacement thickness input cells.	465
Table I-4 – Spreadsheet output with spectral data for the zero AOA case.	465

Table I-5 – SPL contributions by source for zero AOA case (from the spreadsheet).....	466
Table I-6 – Final SPL comparison (overall and by source), in three selected 1/3 octave frequencies, including the peak frequency.	466
Table I – Calculation procedure verification for the displacement thickness value returned by different codes, measured over the Trailing Edge (1C). N/A = non applicable.....	510
Table II – Combinations (cases) of flow data sources and angles of attack for the verification and validation process.	512
TABLE III – RESULTS FROM QBLADE V0.95 CODE CALCULATION AGAINST VERIFICATION SPREADSHEET, FOR ZERO AOA.....	524
TABLE IV – RESULTS FROM QBLADE V0.95 CODE CALCULATION AGAINST VERIFICATION SPREADSHEET, FOR 4° AOA.	526
TABLE V – RESULTS FROM QBLADE V0.95 CODE CALCULATION AGAINST VERIFICATION SPREADSHEET, FOR 12.5° AOA.....	528
Table K-1 – Aerodynamic and Acoustic performance of NREL/Sommers 21% thick airfoils.	537

LIST OF ABBREVIATIONS AND ACRONYMS

Abbreviation	Meaning
a/b	Airborne (sound propagation)
ABNT	Associação Brasileira de Normas Técnicas
AM	Amplitude Modulation
AOA	Angle of Attack
ASME	The American Society of Mechanical Engineers
AWEA	American Wind Energy Association – USA
BEM	The Blade Element Momentum method
BL	Boundary Layer
BNDES	Banco Nacional de Desenvolvimento - Brasil
BPF	Blade-Passing Frequency (Hz)
BPM	Brooks, Pope, Marcolini, Airfoil Self Noise Prediction Model
BS	Bird-Saving (airfoil)
CAA	Computational Aeroacoustics
CFD	Computational Fluid Dynamics
CR	Community Reaction
dB	decibel
dB(A)	A-weighted decibel
dB(C)	C-weighted decibel
DU	Delft University – The Netherlands
D*	Displacement thickness (notation inside XFLR5 code)
EDDYBL	David C. Wilcox finite difference CFD code
EPA	Environmental Protection Agency
FAPESP	Fundação de Amparo à Pesquisa do Estado de São Paulo - Brasil
FFT	Fast Fourier Transform
FP	Flat Plate
FRP	Fibre-Reinforced Plastic.
FW-H	Ffowcs Williams and Hawkings equations for acoustic analogy
GE	General Electric Company
GUI	Graphical User Interface
GW	Gigawatt
HAWT	Horizontal Axis Wind Turbine
HP	High-Performance (airfoil)
IAG	Institute for Gas Dynamics and Aerodynamics – University of Stuttgart.
IEC	International Electrotechnical Commission
kW	Kilowatt
LA	Low A-weighted noise emission (airfoil)
LBL	Laminar Boundary Layer
LE	Leading Edge
LFN	Low Frequency Noise (Hz)

LH	Left Hand
MW	Megawatt
NACA	National Advisory Committee for Aeronautics – USA
NASA	National Air and Space Administration - USA
NBR	Norma Brasileira
NREL	National Renewable Energy Laboratory – Department of Energy - USA
NS	Navier Stokes (Equations)
OASPL	Overall Sound Pressure Level (dB)
Op. Point	XFLR5/XFOIL operational point object (polar data)
Poli – USP	Politechnic School - São Paulo State University - Brasil
PNoise	Poli-USP TE noise prediction code.
PROINFA	Programa de Incentivo às Fontes Alternativas de Energia Elétrica - Brasil
PSD	Power Spectral Density (of pressure)
QBlade	TU Berlin-developed, public domain, Wind Turbine Performance and Structural analysis software.
QMO	Quiet Mode of Operation (airfoil)
Q3D	Quasi Three Dimensional (method)
RANS	Reynolds-Averaged Navier Stokes (Equations)
RISO - DTU	Technical University of Denmark
RH	Right Hand
RMC	Right Mouse Click
RSM	Reynolds Stress Modeling (turbulence modeling)
R&D	Research and Development
s/b	Structure borne (sound propagation)
SIROCCO	Silent Rotors by Acoustic Optimization Project – Energy Research Center – The Netherlands - EU
SNL	Signal-to-noise Ratio
SP	Saab-Pimenta “Silent Profiles”
SPL	Sound Pressure Level (dB)
SPL_{1/3}	Sound Pressure Level for each 1/3 octave band (dB)
SPL_A	A-weighted Sound Pressure Level (dB)
SPL_α; SPL_α; SPL_{alpha}	Sound Pressure level (dB), contribution from the partially unattached flow at the suction side (noise deriving from AOA≠0.
SPL_p	Sound Pressure level (dB), contribution from the pressure side of the airfoil.
SPL_s	Sound Pressure level (dB), contribution from the suction side of the airfoil.
SPW	Sound Power Level (dB)
SST	Shear Stress Transport (turbulence modeling)
STE	Sharp Trailing Edge (airfoil)
TBL	Turbulent Boundary Layer
TBL-FP	Turbulent Boundary Layer, Flat Plate model
TBL-TE	Turbulent Boundary Layer at the Trailing Edge
TE	Trailing Edge
TEN	Trailing Edge Noise

TKE	Turbulent Kinetic Energy (per unit mass) (m^2/s^2)
TNO	Netherlands Organization for Applied Scientific Research
TPD	Institute of Applied Physics of the TNO
TSR	Tip-Speed Ratio
TU Berlin	Technische Universität Berlin
URANS	Unsteady Reynolds-Averaged Navier Stokes (Equations)
VS	Vortex Shedding (Frequency) (Hz)
VT	Virginia-Tech
W	watt
WPF	Wall Pressure Fluctuations
WPS	Wisconsin Public Service – USA
WT	Wind Turbine
WTN	Wind Turbine Noise
XFLR5	The XFOIL software with graphic user interface.
XFOIL	Hybrid, Potential Flow and Integral Boundary Layer Solver.
2-D, 2D	Two-Dimensional (method)
3-D, 3D	Three-Dimensional (method)
%HA	Percentage of Highly Annoyed People

LIST OF SYMBOLS

LATIN LETTERS

Letter	Meaning	Disambiguation, (section)	units
A	Empirical Spectral Shape Function for SPL, at zero angle of attack		
A'	Empirical Spectral Shape Function for SPL, at angle of attack above the switching angle		
A_b	Airfoil area		m^2
a	Axial induction factor		
a'	Tangential induction factor		
AOA	Angle of Attack		0
B	Empirical Spectral Shape Function for SPL, at angle of attack other than zero		
B	Stagnation Enthalpy	B.7	m^2/s^2
B	Number of Blades in the rotor	2.8	
b	Span of the airfoil in the considered section		m
C	Empirical Weibull scale factor		m/s
C_D	Blade drag coefficient		
C_J	Advance coefficient		
C_L	Blade lift coefficient		
C_n	Coefficient, normal force		
C_P	Power coefficient		
C_T	Coefficient, thrust		
C_t	Coefficient, tangential force		
C_f	Coefficient, friction		
C_θ	Rotational velocity in the wake		m/s
c	Airfoil chord		m
c_d	Section drag coefficient		
c_l	Section lift coefficient		
c_0	Acoustic wave speed		m/s
D	Wind Turbine Rotor diameter		m
\bar{D}	Directivity function, dipole		
\bar{D}_h	Directivity function, high frequency noise		
\bar{D}_l	Directivity function, low frequency noise		
d	Cylinder diameter		m

F	Prandtl's tip loss factor (BEM method)	
F_i	Force density of the fluctuating force field	N/m^3
$F(\mathbf{St})$	Universal spectral shape for the noise	
f	Sound or noise frequency	$1/s$
f_s	Frequency, vortex shedding	$1/s$
ft	foot	$0.3048\ m$
f_{peak}	Frequency, peak	$1/s$
$f(v)$	Frequency of occurrence of wind velocity v	
f_{22}^{aniso}	Semi empirical anisotropy scaling factor	m
$G(f)$	Spectral shape function for SPL	
$G(x)$	Green's Function	
$g(t)$	Non-harmonic function of a (pressure) signal	
$\tilde{g}(\omega)$	Fourier-Transform of the non-harmonic signal	
$H(x)$	Heaviside Function	
Hz	hertz	$1/s$
H_K	Kármán BL shape factor (δ^*/θ)	
h	Trailing Edge thickness	m
h/δ^*	Bluntness parameter	
I	Acoustic pressure intensity	w/m^2
in	inch	$0.0254m$
K	Function, empirical SPL	dB
K_2	Function K_1 for angle of attack other than zero	dB
K_1	Function, scaled SPL as a function of chord-based Reynolds number, for zero angle of attack	dB
k	Form factor for Weibull distribution	App. C
k	The wavenumber	$1/m$
k	Ratio of the specific heats	App. B only
\vec{k}	The wavevector	$1/m$
k_i	The wavevector component in direction i	$1/m$
k_T, k	Energy, turbulent kinetic, per unit mass	m^2/s^2
k, ω	Turbulence model, k = turbulent kinetic energy (TKE) (per mass unit); ω = energy dissipation rate per unit TKE	
$k - \omega$	Spectrum, wavenumber-frequency	
L	Spanwise extent of the wetted edge (also s)	m
$L_{A,eq}$	Equivalent Sound Pressure Level	$dB(A)$

L_{eq}	Equivalent Sound Pressure Level		dB
L_{10}	Exceedance level limit for 10% of the time		dB
L_{90}	Exceedance level limit for 90% of the time		dB
l	Length; characteristic source or turbulence dimension; height of turbulent stream.		m
M	Rotor torque	2.8 only	$N.m$
M, M_a	Mach number		
M_c	Mach number, eddy convection		
$M_{\bar{v}}$	Mach number, mean eddy convection		
M_r	Mach number, relative, of the source region		
M_{or}	Mach number, mean stream velocity, at position r		
$M_{\bar{v}r}$	Mach number, component of eddy convection velocity in the observer direction		
$M_{\bar{v}1}$	Mach number, component of eddy convection velocity normal to the edge plane		
N_s	Number of spanwise blade segments		
N_β	Number of blade angular positions in the azimuthal plane		
N_f	Number of frequencies in the spectrum		
P_{mech}	Available mechanical power		W
$P(k, \omega), P_{TE}$	wavenumber-frequency spectrum of the surface pressure fluctuation		
p_m	Pressure, mechanical		Pa
p_t	Pressure, thermodynamic		Pa
p'	Pressure, acoustic perturbation		Pa
$p(t)$	Time signal of acoustic pressure		Pa
$p'(t)$	Harmonic function of the acoustic pressure signal		Pa
p_N	Force, normal to the rotor plane		N
p_T	Force, tangential to the rotor plane		N
p_{ij}	Force per unit area tensor, acting from the surface into the fluid		Pa
\hat{p}_{ref}	Reference pressure, acoustic		$2 \times 10^{-5} Pa$
$\langle p \rangle, \hat{p}$	Root mean square of the acoustic pressure (effective pressure)		Pa
$\langle p^2 \rangle, \hat{p}^2$	Mean squared pressure, or effective pressure squared (proportional to sound intensity)		N^2/m^4
$Q(\vec{x}, t)$	Flow rate intensity of a source		$kg/m^3.s$
$\dot{q}(t)$	Mass Flow rate		kg/s^2

R	Rotor radius, total		m
R	Ideal gas model constant of the gas	B.5 only	$J/kg.K$
Re	Reynolds Number		
Re_c	Reynolds Number, chord-based		
r	Rotor, blade radial position		m
r	Distance from source to observer point, in the far field		m
r_e	Observer distance to source, retarded		m
r_0	Location of the source		m
r_0	Distance between the center of the eddy and the edge		m
SPL	Sound Pressure Level		dB
St	Strouhal Number		
St_1, St_{max}	Strouhal number, peak		
St_2	Strouhal number, peak, adjusted		
St_p	Strouhal number, pressure side		
St_s	Strouhal number, suction side		
$S(\omega), S(x, \omega), S_k(\omega)$	Sound pressure Power Spectral Density (sound field spectrum)		Pa
$SST k, \omega$	Menter's Turbulence model		
s	Span of edge, airfoil segment (also L)		m
T	Rotor thrust		N
Tu	Normalized turbulence intensity u'/U	2.2	
T_{ij}	Stress tensor		Pa
T_{ij}	Stress tensor, Lighthill tensor		Pa
TKE	Turbulent kinetic Energy (per unit mass)		m^2/s^2
TSR	Tip Speed Ratio (also λ)		
U	Velocity, local flow		m/s
\bar{U}	Mean wind velocity at hub height		m/s
U_c	Velocity, mean convective of WPF		m/s
U_0, U_1, U_∞, V_0	Velocity, freestream		m/s
$U_1(y_2)$	Velocity, streamwise mean		m/s
u	Velocity, of axial flow at rotor plane (uniform)		m/s
u_1	Velocity, wake (uniform)		m/s
u_i'	Particle velocity, perturbation		m/s
u_τ	Velocity, friction		m/s
$\langle u^2(y_2) \rangle$	Mean squared vertical velocity fluctuation (vertical Reynolds Stress).		m^2/s^2
V	Velocity, turbulent boundary layer convection		m/s
V_a	Corrected axial velocity		m/s
V_0	See U_0		m/s

V_{rel}	Velocity, wind relative	m/s
V_{rot}	Velocity, corrected rotational	m/s
v	Wind velocity	m/s
v'	Turbulence velocity, rms	m/s
v'^2	Mean squared turbulence velocity	m/s
W	Velocity, wake convection	m/s
x	Position of the observer in the sound field; position along airfoil chord.	m
x/c	Position, normalized by chord	
y_t	Coordinate, surface of the airfoil	m
y_1	Coordinate, wall parallel	m
y_2	Coordinate, wall normal	m
y^+	Distance, dimensionless, to wall (wall coordinates Reynolds number)	
	$y^+ = \frac{u_\tau \cdot y_2}{\nu}$	

GREEK LETTERS

Letter	Meaning	Disambiguation, (section)	units
α	Local angle of attack (AOA)		0
α	Normalized turbulence intensity u'/U	2.1.1.1; 2.5.2	
α_*	Angle of Attack, effective (corrected)		0
α_{stall}	Angle of Attack, stall		0
α_t	Angle of Attack, wind tunnel		0
$(\alpha_*)_0$	Angle, switching		0
β	Twist (angle) of the blade		0
β	Angle of incidence of the convecting turbulence and the edge plane	App. D	0
γ	Observer distance from source, normalized by source length		
γ_1	Edge length		cm
δ	Boundary layer thickness		m
δ	Dirac's Delta Function	App. B only	
δ^*	Displacement thickness		m
δ_0^*	Displacement thickness, zero AOA		m
δ_p^*	Displacement thickness, pressure side		m
δ_s^*	Displacement thickness, suction side		m
δ^*/c	Displacement thickness, normalized by chord		

ΔK_1	Empirical adjustment factor for K_1 function		<i>dB</i>
ε	Dissipation, turbulent kinetic energy rate, per unit mass		m^2/s^3
ε^*	Dissipation, turbulent kinetic energy rate, per unit mass, scalar, isotropic		m^2/s^3
θ	Directivity angle. Angle between the observer position and the chordwise airfoil plane.	See Fig. 2.1.	0
θ	Local pitch of the blade	2.3; 4.1	0
θ	Momentum Thickness (BL)	XFLR5/XFOIL results	
$\bar{\theta}$	Angle between the mean flow direction and the edge.	See Fig. 2.1	0
θ_e	Directivity angle. Angle between the observer position and the chordwise airfoil plane, retarded coordination system.		
θ_p	Variable pitch angle of the blade	2.8	0
Λ	Length, characteristic scale of the turbulence		<i>m</i>
Λ_2	Length, vertical TBL integral scale for the eddy field		<i>m</i>
λ	Tip Speed Ratio (also TSR)		
λ	wavelength		<i>m</i>
λ	Length, Taylor micro scale		<i>m</i>
μ	Viscosity, dynamic or first coefficient		<i>Pa.s</i>
ν	Viscosity, kinematic		m^2/s
ρ	Density, fluid	App. B	kg/m^3
ρ_0	Density, undisturbed fluid		kg/m^3
$\rho_0 c_0$	Impedance, acoustic, of the medium		$kg/m^2 s$
ρ'	Density, acoustic perturbation		kg/m^3
σ	Solidity ratio		
$\sigma(\vec{x}, t)$	Sound source, arbitrary		
τ	Time, emission or retarded		<i>s</i>
ϕ	Angle between the plane of rotation and the relative velocity.	2.3, 2.8	0
ϕ	Angle, directivity, between the observer and the edge plane, projected in the plane perpendicular to the edge.	See Fig 2-1	0
ϕ_e	Angle, directivity, between the observer and the edge plane, projected in the plane perpendicular to the edge, retarded coordinate system.		
ϕ_{22}	Spectrum, wavenumber-frequency, vertical velocity fluctuations		

$\tilde{\Phi}_{22}$	Spectrum, normalized, wavenumber-frequency, vertical velocity fluctuations	
$\phi_m(\omega, k_1)$	Spectrum, wavenumber-frequency, moving axis	
Ψ	Angle, TE beveling	0
ω	Frequency, angular or rotational speed	1/s
$\vec{\omega}$	Vorticity vector	1/s

OTHER SYMBOLS

Letter	Meaning	Disambiguation, (section)	units
\mathcal{K}	Bulk viscosity coefficient, $(\mathcal{L} + \frac{2}{3}\mu)$		<i>Pa.s</i>
\mathcal{L}	Lamé or second coefficient of viscosity		<i>Pa.s</i>
[]	Variable evaluated at the retarded time		
\square	Wave or D'Alembertian operator		

CONTENTS

1. INTRODUCTION.....	1
1.1 RELEVANCE OF SUBJECT	1
1.1.1 Wind Energy Advancement and Costs.	2
1.1.2 Wind Turbine Noise (WTN)	6
1.1.3 Relevance of Subject for the Industry.....	11
1.1.4 Academic Relevance.....	17
1.1.5 The impact of Wind Turbine Noise (WTN) on Humans and Fauna.	17
1.1.6 Regulations on Wind Turbine Noise	24
1.2 OBJECTIVES AND CONTRIBUTIONS.....	29
1.3 THESIS OUTLINE	31
2. AEROACOUSTIC THEORY AND APPLICATION	33
2.1 APLICATIONS OF AEROACOUSTIC THEORY TO WTN.....	33
2.1.1 Turbulent Flow-Induced Noise Mechanisms	34
2.1.2 Aerodynamic Noise Sources in Wind Turbine and Relevance in the Audio Range.....	37
2.1.3 Low-Frequency Noise	39
2.1.4 Inflow-Turbulence Noise.....	41
2.1.5 Airfoil Self-Noise.....	44
2.2 CONSIDERATIONS ON INFLOW TURBULENCE	58
2.3 THE UTILITY-SIZE HORIZONTAL AXIS WIND TURBINE (HAWT).....	59
2.3.1 The Annual Energy Output.....	67
2.4 MODELS AND METHODS FOR TRAILING EDGE NOISE PREDICTION AND THEIR IMPLEMENTATION.	69
2.4.1 Semi-Empirical Models.....	69

2.4.2 Simplified-Theoretical Models.	81
2.4.3 The Computational Aeroacoustic Methods.....	82
2.4.4 Noise Prediction Methods - Existing Classification.....	83
2.4.5 Noise Prediction Methods Classification	87
2.4.6 TE Noise Prediction Methods: A New Classification	92
2.5 AIRFOIL SECTIONS FOR HORIZONTAL-AXIS WIND TURBINES	95
2.5.1 AIRFOIL DEVELOPMENT AIMED MAINLY AT AERODYNAMIC EFFICIENCY	99
2.5.2 Specific Studies Concerning Airfoil Aerodynamic-Noise	110
2.5.3 Airfoil Geometry Studies Involving Optimization.....	129
2.6 WIND TURBINE BLADES.	134
2.7 THE XFOIL / XFLR5.	136
2.8 THE BLADE ELEMENT MOMENTUM (BEM) METHOD.....	138
2.8.1 BEM Method Corrections	143
2.9 THE QBLADE	146
3. METHODOLOGY	147
3.1 THE BEM METHOD IMPLEMENTATION.....	149
3.2 THE GEOMETRIES FOR THE LARGE-SIZE HORIZONTAL AXIS WIND TURBINES.....	151
3.2.2 The WT geometry and design point for the 50 m span, “Poli-100” WT blade.	153
3.2.3 The WT geometry and operating point for the 87 m (Poli-180) and 106.5 m (Poli-220) span blades.	157
3.3 THE MODIFIED BPM TRAILING EDGE NOISE CALCULATION METHOD.	159
3.3.1 The selection of the TE-noise prediction model and improvements.	159
3.3.2 Calculating procedures for the TBL-TE noise method.....	164
3.3.3 Original Displacement Thickness Correlations of the BPM model.	173
3.4 THE SELECTION OF THE FLOW SOLVER.	175

3.4.1 The selection of the method for solving the flow field.	175
3.5 IMPLEMENTATION OF THE METHOD.	204
3.5.1 Comparison and improvements over other methods.....	207
3.6 METHODOLOGY FOR THE INVESTIGATION OF QUIETER AIRFOILS FOR WT.	211
3.6.1 Requirements for the development airfoils with less overall and TE noise emission.....	211
3.6.2 Airfoil design methodology	213
3.6.3 General design procedure developed for a quieter airfoil section.	215
4. RESULTS AND DISCUSSION.....	216
4.1 TYPICAL OPERATING CONDITIONS CALCULATIONS FOR A LARGE SIZE HAWT	216
4.1.1 Operating Conditions for Airfoils at 85% Span of Large-Size HAWTs.....	216
4.1.2 Results for the 50 m length blade, and Poli-100 WT rotor.....	217
4.2 THE IMPLEMENTED TE NOISE PREDICTION METHOD.....	224
4.3 VERIFICATION AND VALIDATION OF THE IMPLEMENTED METHOD.....	233
4.3.1 – Validation of the spectral output.	234
4.3.2 – Verification of the calculation procedure.....	237
4.4 ATTEMPT TO EXTEND THE VALIDATION OF THE MODIFIED-BPM TE NOISE MODEL FOR HIGHER REYNOLDS NUMBERS AND GENERIC AIRFOIL GEOMETRY.	244
4.4.1 Naca 0012 airfoil, untripped flow for higher Reynolds numbers at zero to moderate AOA.	247
4.4.2 Naca 0012 tripped flow for higher Reynolds numbers at zero and moderate AOA.....	255
4.4.3 S831 airfoil tripped flow for higher Reynolds numbers at zero and moderate AOA.....	259
4.5 DEVELOPMENT OF A NEW FAMILY OF AIRFOILS FOR WT WITH REDUCED TE NOISE EMISSION AND PRESERVED AERODYNAMIC PERFORMANCE..	264

4.5.1 The S830 baseline geometry performance under the defined 50-m blade operating conditions.	264
4.5.2 Airfoil modification sensitivity analysis, for the 50 m blade under Poli-100 WT flow conditions.....	271
4.5.3 General Data Discussion.....	287
4.5.4 Profiles of quieter airfoils for the POLI-100 m 85% radial blade station...	296
4.5.5 – Aerodynamic Efficiency and Pressure Coefficient diagram (Euler number) comparison among the baseline and the SP4621HP and SP4721LA airfoils...	317
4.5.6 – Evaluation of proposed airfoil characteristics against the requirements.	319
5. CONCLUSIONS AND FURTHER DEVELOPMENT	328
REFERENCES.....	333
APPENDIX A – FIELD RESEARCH RESULTS	349
APPENDIX B – BASIC ACOUSTICS AND ACOUSTIC ANALOGY THEORIES, DISCUSSED AND COMMENTED.	351
B.1 SOUND POWER AND SOUND PRESSURE LEVELS	351
B.2 RADIATION FIELD OF A SOUND SOURCE	352
B.3 HARMONIC FUNCTIONS.....	357
B.4 FOURIER TRANSFORMS IN TIME AND SPACE	357
B.5 THE LINEAR WAVE EQUATION.....	359
B.5.1 The inhomogeneous linear wave equation	362
B.6 ELEMENTARY SOLUTIONS OF THE WAVE EQUATION	364
B.6.1 Monopoles	364
B.6.2 Dipoles.....	366
B.7 ACOUSTIC ANALOGY OF LIGHTHILL.....	371
B.7.1 Quadrupoles	373
B.7.2 The Powell-Howe theory of vortex sound	378
B.8 TIME, LENGTH, PRESSURE AND SOUND POWER SCALES.....	379
B.9 THE INFLUENCES OF BOUNDARIES	383

B.9.1 Ffowks Williams-Hawkings (FW-H) Equation and Farassat’s solutions..	384
B.9.2 The Influences of the Boundaries in the Frequency Domain	387
APPENDIX C - THE WIND.....	388
APPENDIX D – SEMI-EMPIRICAL NOISE PREDICTION MODELS AND METHODS - A DICUSSED REVIEW.	391
D.1 Grosveld’s Model.....	392
D.2 The Models from Howe, Brooks-Hodgson and Brooks-Marcolini.	393
D.3 Glegg’s Model	399
D.4 Lowson’s Model and Method.....	401
D.5 The IAG Method (I).....	405
D.6 The RISO Method.....	406
D.7 The NREL Method (I).....	410
D.8 Zhu’s (DTU) Method.....	416
D.9 The NAFNoise Method (NREL II)	420
D.10 The Vargas’ Method (LVNP).....	422
APPENDIX E – SIMPLIFIED-THEORETICAL NOISE PREDICTION MODELS AND METHODS - A DICUSSED REVIEW.	426
E.1 The TNO-Blake Model for Airfoil TE noise	426
E.2 The Moriarty-Guidati-Migliore Model and Method (2005).....	431
E.3 The Glegg-Reba Model.....	436
E.4 The IAGNoise Method (IAG II).....	440
APPENDIX F - THE “QUASI 3-D” METHOD FOR BLADE AND ROTOR NOISE PREDICTION FROM 2-D METHODS.	454
APPENDIX G – CONSIDERATIONS ON DESIGNING-FOR-NOISE AND SUGGESTIONS FOR LOCAL NOISE-REGULATIONS IMPROVEMENTS.....	457
APPENDIX H - THE TYPICAL OPERATING CONDITIONS FOR THE POLI-180 AND POLI-220 WIND TURBINES.	459
APPENDIX I - VERIFICATION OF THE AIRFOIL TRAILING-EDGE NOISE PREDICTION MODULE (PNOISE) INSIDE QBLADE V0.8	461

APPENDIX J - VERIFICATION AND VALIDATION OF THE AIRFOIL TRAILING- EDGE NOISE PREDICTION MODULE (PNOISE) INSIDE QBLADE V0.95	503
APPENDIX K - S830 AIRFOIL AERODYNAMIC AND AEROACOUSTIC PERFORMANCE IN RELATION TO OTHER NREL S-SERIES AIRFOILS	537

1. INTRODUCTION

The rapid expansion of Wind Energy worldwide is pushing the wind farms closer to the populated areas, where the noise annoying potential is higher, land availability is lower and the wind turbine noise (WTN) regulations are more stringent. The applicable noise regulations may be specific for WTN (e.g. USA, Europe) or of generic application (e.g. Brazil), but regardless of the type of restrictions imposed geographically, the wind turbine (WT) industry new equipment must be designed-for-noise in order to meet unrestricted market demand. The Wind Energy is the fastest growing type of renewable energy in the Brazilian market and domestic policy is imposing that an increasing share of the equipment be made locally. Despite the success of the national aeronautical industry in developing products with high technological content, most of the WT equipment being assembled in Brazil is designed overseas, with local manufacturing of blades and other parts. This research is expected to represent a small contribution towards the design and development of efficient, quieter WT airfoils and blades in Brazil and elsewhere.

1.1 RELEVANCE OF SUBJECT

“The problem of noise generation by low Mach number turbulent flows passing by the TE of a rigid lifting surface is of interest to aerospace, automobile, underwater and wind turbine acoustic communities” (Kamruzzaman M. , Lutz, Herrig, & Krämer, 2012a).

TE noise developing from the interaction with a turbulent boundary layer (TBL-TE noise) is an important research topic for the aeroacoustic community because the same noise radiation mechanism is present in a wide range of engineering flows, like aircraft high-lift systems, turbo machinery components, cooling fans and wind turbine blades (Herr & Kamruzzaman, 2013).

Also, according to Herr and Kamruzzaman (Herr & Kamruzzaman, 2013), the validation of methods to simulate TBL-TE noise are fundamental for low-noise profile

design and optimization, and also to assist the further development of noise reduction methodologies.

1.1.1 Wind Energy Advancement and Costs.

By the end of 2011, based on assumed country-specific capacity factors, the contribution of wind power to fulfil electricity demand was estimated to be around 29% in Denmark, 19% in Portugal, 19% in Spain and 18% in Ireland (Wiser & Bolinger, 2012), as shown in Figure 1-1. In the United States, the cumulative wind power capacity installed by the end of the same year was estimated to be roughly 3.3% of the nation's electricity demand, up from 0.9% at the end of 2006 (Wiser & Bolinger, 2012).

On a global basis, wind energy's contribution at the end of 2011 was estimated to be 2.9% of the electricity demand (Wiser & Bolinger, 2012). In Brazil, the wind energy contribution for domestic electricity production reached 0.5% by the end of 2011, after a 24% increase in one year (EPE, 2012) and 6.6% at the beginning of May, 2016 (ABEEÓLICA, 2016).

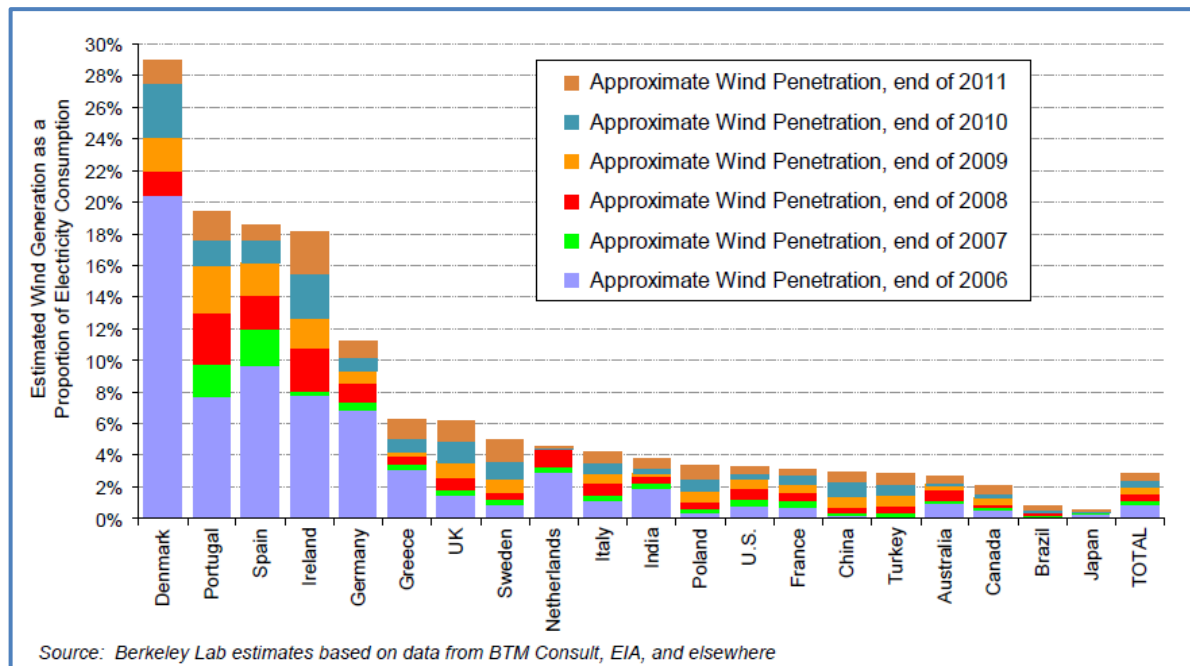


Figure 1-1 Wind-generated electricity penetration in the energy matrix of 20 countries with the greatest cumulative installed WP capacity by the end of 2011 (Wiser & Bolinger, 2012).

By the end of 2012 the global wind power total capacity exceeded 280,000 megawatts (MW), with wind farms generating carbon-free electricity in more than 80 countries, 24 of which have at least 1,000 MW of wind generated power. At the European level of consumption, the world's operating wind turbines could satisfy the residential electricity needs of 450 million people (Rooney, 2013).

To illustrate the large rate of expansion of this renewable resource, one can observe that the installed wind power capacity in Europe around 1996 was 3 GW and it was projected to increase to 30 GW by 2010 and to 100 GW by 2030 but this 100 GW target was to be met already in the 2011-2012 period (Bowdler & Leventhall, 2011). In the U.S. market, the installed capacity almost doubled from 2011 (6,703 MW) to 2012 (12,133 MW) and the projects in the pipeline, if materialized, could bring the installed capacity to 91,000 MW in 2020 (Wind Power - Special Report, 2012).

These numbers show growth rates that were expected neither in Europe by the beginning of the century, nor in North America, were the growth happened despite the all-time-low natural gas costs in the U. S. Market, as shown in Figure 1-2 and Figure 1-3.

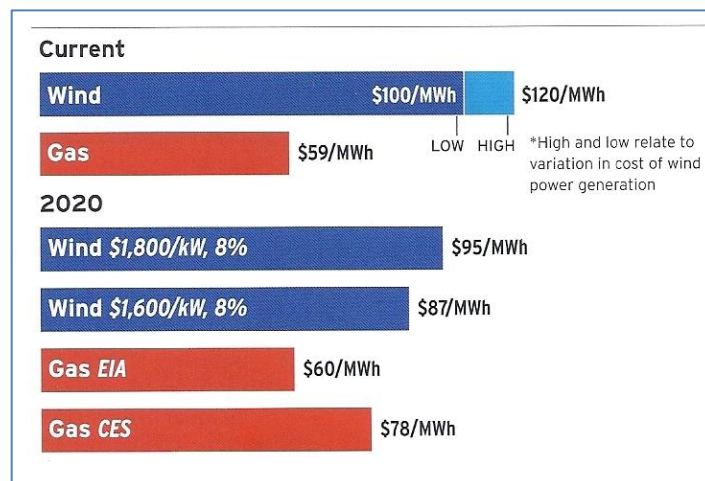


Figure 1-2 Electricity generation costs in the USA from gas and wind at 9% cost of capital (current) and 8% cost of capital (2020), two price projections. EIA = Energy Information Administration scenario; CES= proposed Clean Energy Standard scenario (Wind Power - Special Report, 2012).

The reason may lay in the fact that Wind energy expansion is not only cost-driven but also driven by environmental concerns and policy directives.

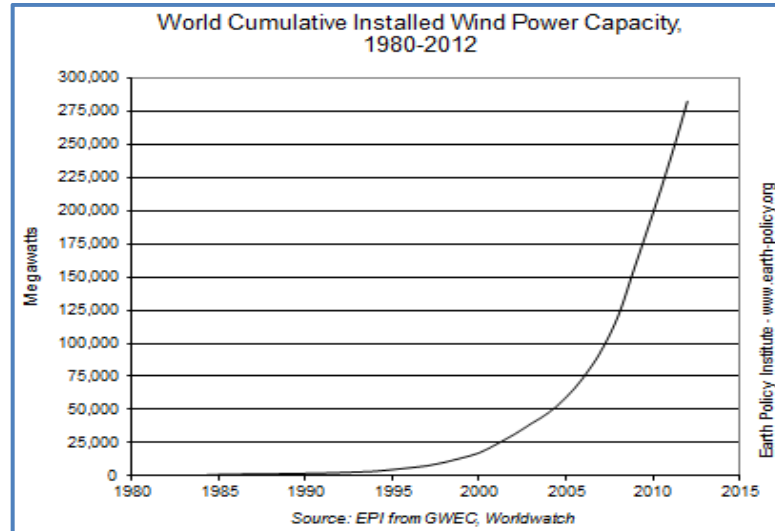


Figure 1-3 - World Cumulative Installed Wind Power Capacity between 1980 and 2012 (Rooney, 2013).

The Brazilian electricity¹ matrix is quite clean, as shown in Figure 1-4 with 81.9% of the supply coming from hydraulic power plants. Among the modern renewables (wind, solar, waves, etc.), excluding biomass, only the wind power generation model has grown significantly in the last 10 years (more than 47% per annum) to appear by itself in the current matrix, which is dominated by the hydraulic-originated supply.

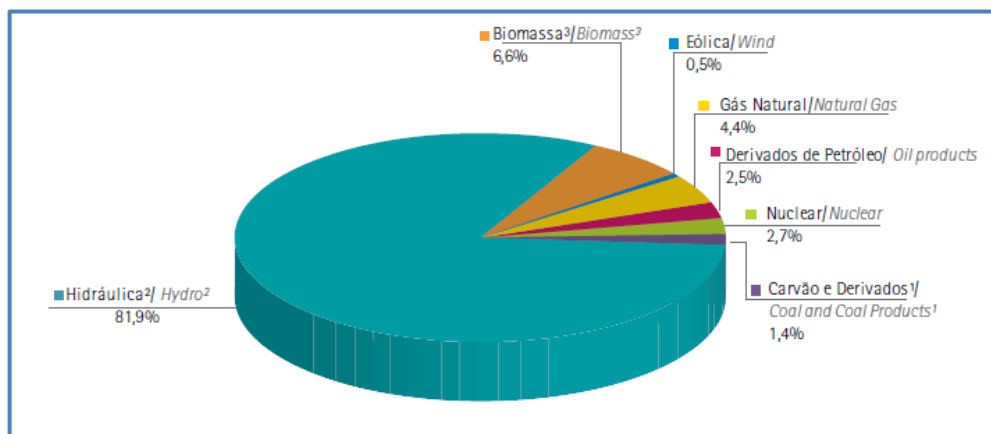


Figure 1-4 Brazilian domestic electricity supply, by source (EPE, 2012)

The total estimated hydraulic energy potential in Brazil is 136.8 GW among which just 28.1 GW is untapped. The current installed capacity is over 80 GW (EPE, 2012), and at the last 10-year-average growth rate for this production model, it could be fully

¹ The electricity matrix represented 16.7% of the total Brazilian energy matrix by the end of 2011 (EPE, 2012)

exploited by 2020. It is also important to acknowledge the fact that new hydraulic power plants to be commissioned in Brazil will have shallow reservoirs because of environmental considerations and thus, they will not deliver the utility in a steady, year-round fashion anymore, but with seasonal bias.

The need for rapid development of modern, renewable sources is established and the wind energy seems to be the choice of the Brazilian energy market. One of the plausible causes might be the complementary aspects of the hydro and wind forms of conversion. The Brazilian wind energy potential is estimated to be around 143 GW (França, 2011), about the same size of the hydraulic potential of the country and around 48% the estimated total wind energy potential for the US, of 300 GW (Wiser & Bolinger, 2012).

The first auction for selling electricity originated from wind power alone, undertaken by the Brazilian Federal Government, was held on December, 2009, with sales of 1,805.7 MW of installed capacity from 71 wind farms located in five States, in the Northeast and South of Brazil. The event clearly signaled that wind energy price had become competitive even in a country where hydraulic-grade, 'cheap' production cost² electricity is the benchmark:

“In this auction, 20-year contracts were signed, valid from July, 2012, at an average price of R\$ 148.39/MWh. As the price ceiling established in the auction was R\$ 189/MWh, the average final price represented a discount of 21.49%. In fact, this auction can be considered a success, since the contracted price of energy was well below the price established by PROINFA. You can associate this success to several factors, among which are the technological advancement of wind turbines, financing conditions associated with increased resources provided by large public banks such as BNDES, and tax incentives” (França, 2011).

The average cost of wind electricity in Brazil reached R\$ 198.59/MWh in 2016 and the capacity factor averaged 36.2% in 2015-2016 (ABEEÓLICA, 2016). More than 30% of the electricity needs of the northeastern States is provided for by the wind energy, with capacity factors peaking 56%, well above world averages.

² Because of a heavy taxation policy in the segment, cheap production costs do not necessarily translate into cheap electricity access prices for the industry or for the Brazilian citizens.

The installed capacity growth has been remarkable since 2011, as shown in Figure 1-5.

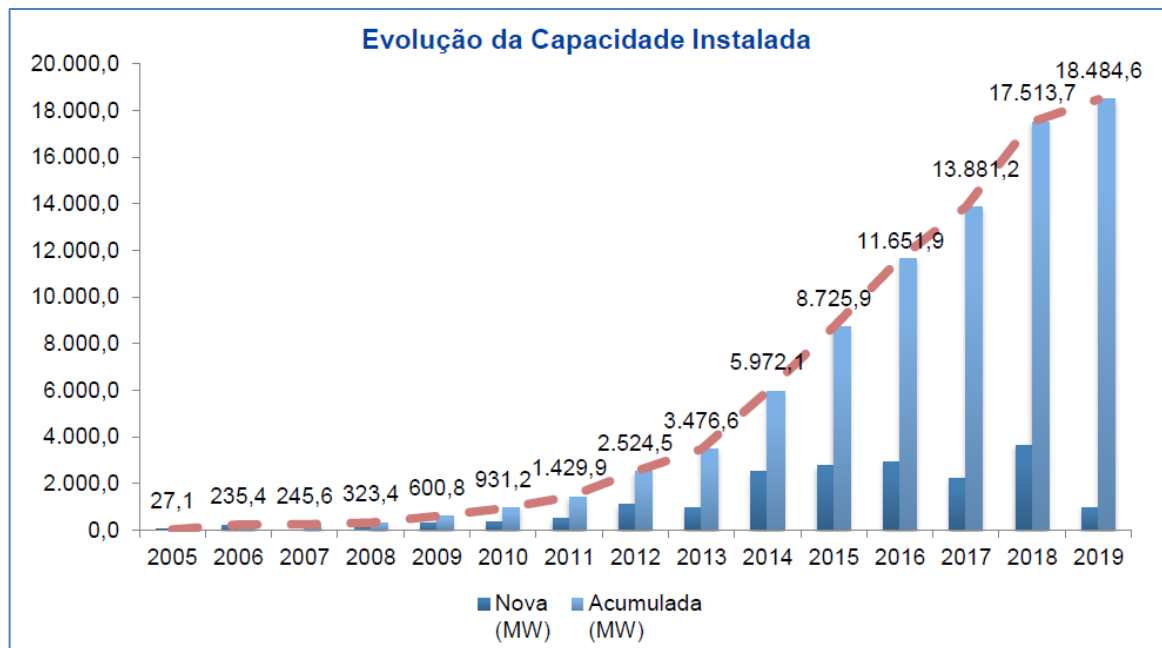


Figure 1-5 - Installed capacity evolution in Brazil for the Wind Energy (ABEEÓLICA, 2016).

1.1.2 Wind Turbine Noise (WTN)

“Noise emission is one of the major obstacles for a further spread of onshore wind turbines and significantly affects public acceptance” (Herrig, Wurz, Kamruzzaman, & Kramer, 2007).

A wind turbine radiates noise of mechanical and aerodynamic origins. Mechanical noise may originate in the generator and, in the case of indirect-drive units, from the gearbox. The mechanical noise is transmitted along the structure before it gets airborne, radiated from surfaces like the nacelle, the tower and the rotor blades.

Aerodynamic noise may be classified as *self-noise* or *interaction noise* (Blake, Mechanics of Flow-Induced Sound and Vibration, 1986 II). The aerodynamic noise is radiated from the blades and from the wake in the near-field region (the airfoil self-noise), and from the interaction of the rotor with inflow turbulence and tower wake (the interaction noise). With the general adoption of the WT rotor in an upwind position for Horizontal Axis Wind Turbine (HAWT) and also the more recent adoption of the direct-

drive system, the mechanical noises, illustrated in Figure 1-6, and the rotor/tower wake interaction problems have been minimized.

“Machinery noise can be reduced efficiently by well-known engineering methods, whereas reduction in aerodynamic noise still represents a problem. At present, manufacturers have been able to reduce the mechanical noise level below the aerodynamic noise, creating a situation that aerodynamic noise is the dominating noise mechanism” (WAGNER, BAREIß, GUIDATI, 1996, p.67).

Despite the many design configurations available for wind turbines, the bulk of the installed capacity in U.S., Europe and Brazil is delivered by the Horizontal Axis Wind Turbine (HAWT) type machines, whose reliability, performance and value are continuously improving.

“Decades of experience and investment in large stand-alone wind turbine technology (blade diameter > 20m) has culminated in a well-accepted form and mode of operation: three ‘pitch-control’ blades on a horizontal axis” (Stankovic, Campbell, & Harries, 2009)

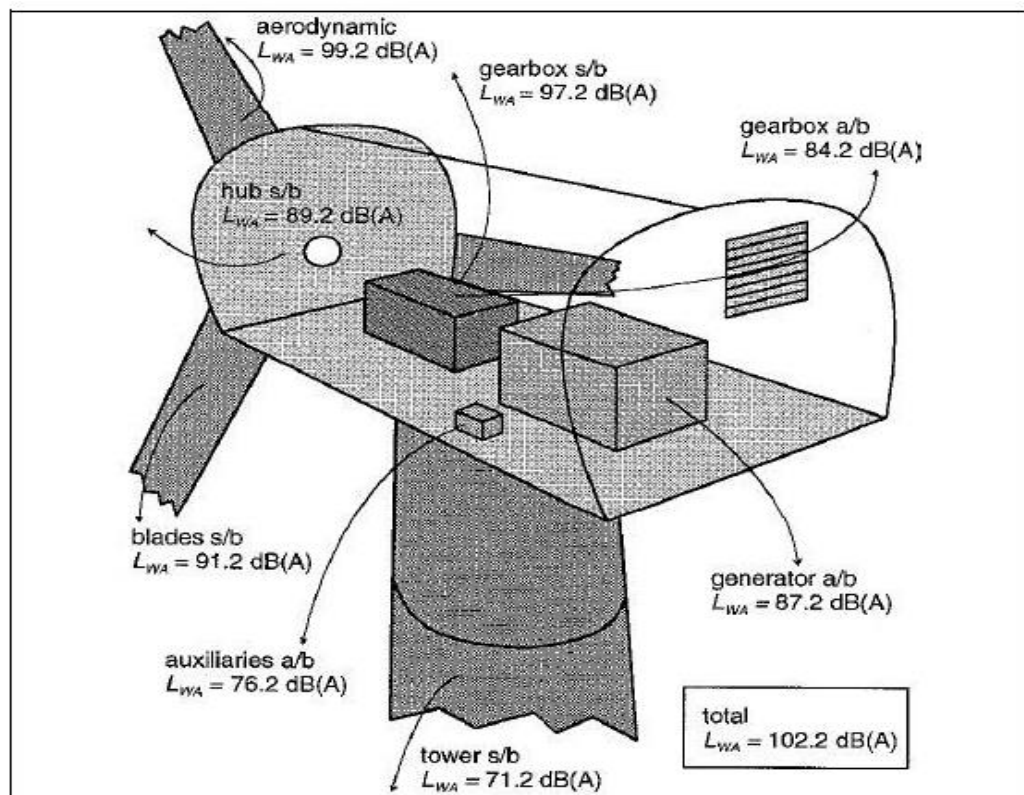


Figure 1-6 Contribution of individual components to the total sound power level of a Wind turbine (Pinder, 1992).

While the form of large-size, efficient WT is essentially fixed nowadays, rotor diameter is continuously increasing as a way of harvesting more wind power (Burton, Sharpe, Jenkins, & Bossanyi, 2008), as predicted by the equation of the available mechanical power for turbo machinery (Hansen, 2008):

$$P_{mech} = \frac{1}{2} C_p \rho_0 \pi R^2 U_\infty^3 \quad [W] \quad (1-1)$$

where C_p is the power coefficient, limited to 0.59 for unducted WT, the Betz Limit and R is the radius of the rotor. A typical modern, large-size WT, characteristic value for C_p is around 0.40 (Ragheb & Ragheb, 2011).

The available mechanical power is plotted in Figure 1-7, for a range of rotor diameter and wind speeds, for illustration purposes.

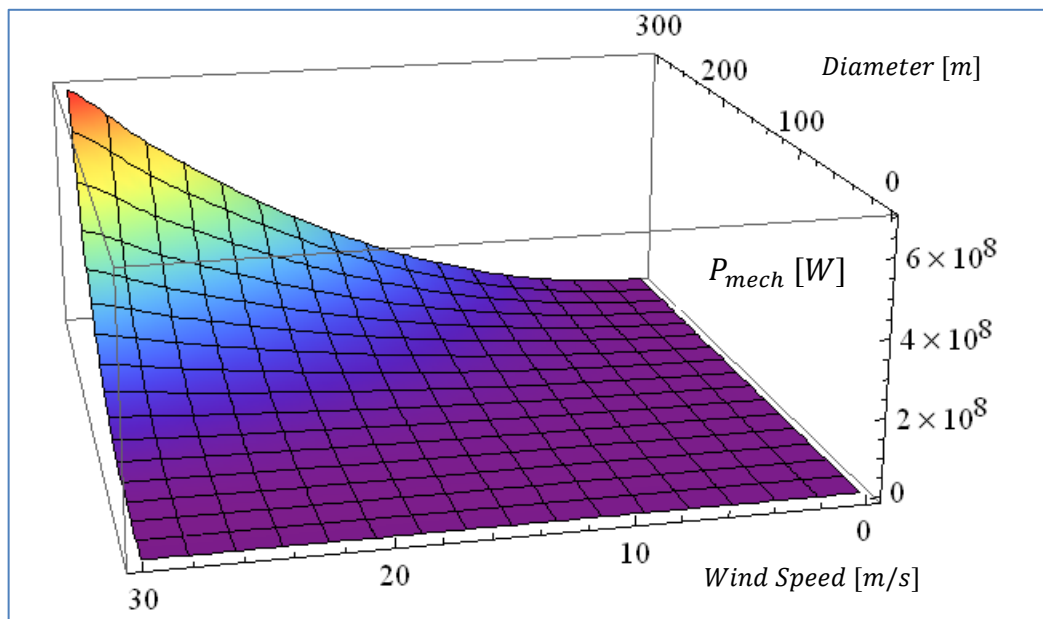


Figure 1-7 3-D plot of the available mechanical power P_{mec} for a WT, Eqn. (1-1), for wind speeds from 0 to 30 m/s and rotor diameters from 0 to 300 m. Theoretical Betz limit used for C_p and sea-level, standard day density.

In order to illustrate the rotor diameter growth over time, the experimental HAWT deployed by NASA in 1975 as a response to the first oil crisis (Wind Energy Research Reaps Rewards, 2006), had a 38 m diameter, 100 kW rotor, while one of the largest rotors operating presently (as of 2012) spans 150 m diameter, in a three bladed, 6.000

kW rotor, installed in France. The weight of each blade is 26 t and one such modern WT is capable of producing the power equivalent to the yearly requirements of 5,000+ households (LM Wind Power, 2012). Recently, Griffith et al. (Griffith, Ashwill, & Resor, Design and Analysis of the SANDIA 100 m Wind Turbine Blade, 2012) reported on the SANDIA LABS 100 m blade under development, which could lead the way for even larger machines.

According to Griffith et al. (Griffith, Ashwill, & Resor, Large Offshore Rotor Development: Design and Analysis of the SANDIA 100 m Wind Turbine Blade, 2012), “a consistent trend and technology development focus in commercial utility-grade wind turbine production throughout the years has been the growth in size of the rotor and lowered cost of energy”.

Figure 1-8 and Figure 1-9 further illustrate the tendency for larger rotor diameter in modern equipment.

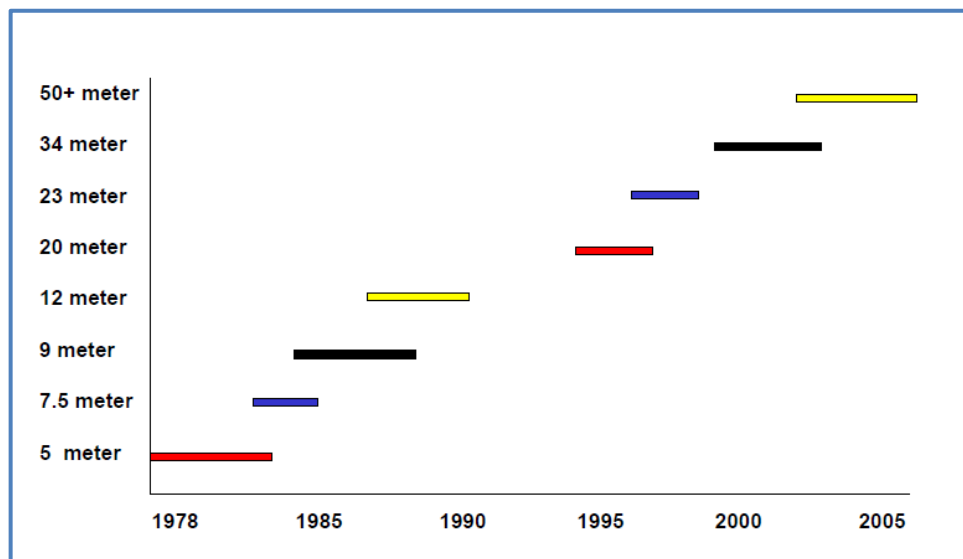


Figure 1-8 Approximate utility-grade blade length growth over time (Ashwill, C. 2008).



Figure 1-9 A General Electric 50.5 m prototype blade transported by truck over a bridge, in Brazil (Ashwill, C. 2008).

For the sake of the argument it will be assumed momentarily that the aerodynamic self-noise sources of a WT may be represented by dipole-type sources. Then, by employing a semi-infinite flat plate approximation for the WT blade airfoil, it can be shown analytically³ that the acoustic power, which is proportional to the square of the acoustic pressure, p , scales with the sixth power of the flow velocity: $p^2 \sim U^6$. This is an indication that while the power increases with the third power of the wind velocity, the aerodynamic noise will increase with the sixth power of the local wind velocity, bringing the technology to a stall.

For the modern lift-type WT, the ratio between the tangential velocity of the blade tip and the velocity of the approaching wind is in the range of 6 to 8 (Ragheb & Ragheb, 2011), with 7 being the most frequently reported value. This dimensionless ratio is a very important performance parameter, of which the power coefficient depends upon and is called *Tip Speed Ratio*, (TSR, λ).

$$TSR = \lambda = \frac{\text{blade tip tangential velocity}}{\text{wind velocity}} = \frac{\omega R}{U_{\infty}} \quad (1 - 2)$$

³ Assumed dipole source model, see (Norton & Karczub, 2003), p. 154.

For a 15 m/s approaching wind a WT with a TSR of 6 would operate with a tangential velocity close to 90 m/s at the tip of the blades, close to limits from where compressibility effects should be considered.

Because of this trend, blades sized only for performance will produce ever stronger sound power levels (SPW) and will demand ever growing sites (and related investments) for operating within acceptable noise levels measured at the households closest to the wind farm.

1.1.3 Relevance of Subject for the Industry

Airfoil self-noise is the total noise produced when an airfoil encounters smooth, non-turbulent inflow. It results from the interaction between the airfoil blade and the turbulence produced inside its own boundary layer and near wake (Brooks, Pope, & Marcolini, *Airfoil Self-Noise and Prediction*, 1989). The noise spectrum associated with airfoil self-noise is typically of broadband nature, but tonal components may arise due to laminar separation bubbles, blunt trailing edges or flow over slits and holes (Wagner, Bareiß, & Guidati, *Wind Turbine Noise*, 1996).

There are many self-noise producing mechanisms and a sizeable effort has been devoted to studying this subject in the recent past and in the present⁴. The studies generally aim at identifying noise source location; quantifying emission power levels associated with the source in the near field; quantifying immission pressure levels associated with the observer position in the far field; and trying to identify noise abatement techniques for use in the emission, transmission or immission phases. In the past, the main objects of study concerning airfoil noise were aircraft reciprocating-engine propellers, turbojet and turbofan-engine rotors, and helicopter rotor noise. At present most of those topics remain active but the scope has been broadened to include other subjects of interest, particularly Wind Turbine Noise.

⁴ Bibliographic research covering the 1975-2012 timeframe on the HighTech (Proquest) data base revealed 1,424 papers under “trailing edge noise” keywords. Nevertheless the number of trailing edge noise papers further associated with the “numerical methods” keywords is down to 47 papers only.

When the WT airfoil is large compared to the turbulent eddies typical length scale, the sound from the eddies will be scattered at the edges of the airfoil, producing “leading edge noise” due to inflow turbulence and “trailing edge noise” due to its own turbulent boundary layer (Oerlemans, Wind Turbine Noise: Primary Noise Sources, 2011).

Among the several airfoil self-noise emitting mechanisms identified to date, the Trailing Edge (TE) noise mechanism has been found to display a dipole nature⁵ (Brooks & Hodgson, 1981), and has been considered the main source of high-frequency noise ($750 \text{ Hz} < f < 2 \text{ kHz}$) for an airfoil in low angle-of-attach (AOA), low Mach number, smooth inflow regime (Brooks, Pope, & Marcolini, Airfoil Self-Noise and Prediction, 1989); (Wagner, Bareiß, & Guidati, Wind Turbine Noise, 1996).

Airfoil TE noise is the object of current investigation both in aeronautics⁶ and in the wind energy industry (Wagner, Bareiß, & Guidati, Wind Turbine Noise, 1996), (Bowdler & Leventhall, 2011).

The problem of TE noise emission is relevant for the fixed and rotary-wing aircraft industry but mainly it is of growing importance to the thriving Wind Turbine industry. The economy of scale brought about by larger rotor diameters, the advancement of this important renewable energy source in the world energy matrix and the concept of *distributed generation*⁷ in the wind energy industry, they all depend upon tools that will allow designing more efficient, quieter and larger WT Blades, in an affordable manner.

Since the airfoil self-noise acoustic pressure scales with the fifth or sixth power of the flow speed (depending upon the source being compact or non-compact as will be discussed later in detail), and stronger winds and larger area rotors both lead to increased local flow speed on the outboard section of the blades, one might expect a growing concern with the wind turbine noise as the equipment grows in size and wind energy increases its share in the world energy matrix.

⁵ Under certain conditions, i.e., when the airfoil may be considered a compact source.

⁶ As an example, between 2009 and 2011 an extensive research concerning all aspects of passenger acoustic cabin comfort was conducted at Poli-USP, funded by FAPESP and Embraer.

⁷ As of January 2013, 57% of the work-in-progress for the expansion of the electricity grid is behind schedule in Brazil (Domingos, 2013). This represents 238 lines and relay stations with problems, and at least 644 MW of hydraulic-generated electricity and 293 MW of wind-generated electricity that cannot be delivered to the grid.

It is not a matter of surprise then, that two of the largest issues the WT manufacturers are currently facing are the WTN and the wear (abrasion) of the blade composite material Leading Edge (LE) (Sloth, 2011)⁸. Both problems derive from the high tangential velocities attained at the blade outboard sections, even in mild wind conditions.

Designing for low noise is not quite a new concept or requirement in aeronautics. After the commissioning in service of aircraft powered by turbojets or low-bypass-ratio turbofan engines starting in the early 1950s (e.g. D.H. Comet, Boeing 707, Douglas DC-8), the first noise regulations for aircraft operations appeared by the end of the next decade, in 1969 (Da Silva, 2011). The work developed over the last 50 years has been centered mainly in jet-noise abatement and the progress has been so remarkable that it has been claimed that current jet noise for high-bypass-ratio turbofan engines is comparable to that of deployed main landing gear, flaps or slats at the same observer position (Orselli, 2011).

For the WT industry, on the other hand, designing for low noise emission is a new requirement and challenge, since most efforts have been historically aimed at improving aerodynamic performance since the first oil crisis.

An insight of the WT industry point of view concerning noise was obtained through a field research carried out by the authors during a Wind Energy Conference event (AWEA 2012⁹), when ten important WT industry players, including five large companies that altogether manufactured 55% of all U.S. installed wind power capacity¹⁰ completed a survey designed to understand the importance of WTN to their companies, the methods used for WTN prediction and also how soon in the product development cycle they considered the noise problem. The table in Appendix A shows all the questions and answers received during the survey.

Some of the most relevant conclusions drawn from the survey are:

- The subject “Wind Turbine Noise” was considered relevant by all respondents;

⁸ Two teleconferences were held between the author and Dr. Erik Sloth, Senior Specialist on Noise and Vibration for Suzlon Blade Tech., Denmark, in 2011.

⁹ American Wind Energy Association annual Conference, held in Atlanta, Ga.

¹⁰ As of the end of 2011.

- Although eight out of ten mentioned that they tried to predict WTN in the early design phase, six out of eight explained that they only assessed WTN through scale model testing or prototype testing, later in the design phase.
- Two of them still did not consider WTN during the development cycle, leaving the problem for siting experts.
- Seven out of ten manufacturers felt the need for better noise prediction methods to be employed at the early design stages.
- One of the participants pointed out that more accurate prediction in the early design phase depends upon performance parameters that usually will be available only later in the development process, so that predictive methods that could be used with more accuracy in the early design phase would be most welcome.

This means that, although acknowledged, the noise problem is not always dealt with at the source level and will have eventually to be dealt with later and in a more expensive way, in the propagation phase. The possible consequences of this approach will be discussed in more detail.

One large WT manufacturer expressed in his survey some needs that could be considered, in short, the objective of the present work:

“It would be desirable to have routines for estimating aero noise in the early phases, that could be later optimized via CFD in more advanced design phases. The better we can predict WTN, the easier we can assure our customers of the quality of our product. The industry lacks better predictive methods and also better ideas to lessen WTN”

On the other hand, as a contrast to the apparent general interest in the WTN subject, one company unveiled during the same conference its new 2.3 MW WT (126 m rotor) whose development did not consider noise emission as a design constraint. After building the first prototype the noise source level was assessed at “only¹¹” 103-104 dB (probably measured at one meter from the shaft, but not specified).

Many other approached companies did not respond to the survey and during the delivery interview they left a solid impression that WTN was still not integrated into their design processes at any level. Also, a post-survey interview with some of the respondents clarified that they believe to have acceptable guidelines for the use of

¹¹ The question was addressed by the authors directly to the company engineer at the end of his unveiling session.

RANS-CFD performance simulation, but not so much so for aero acoustic purposes. Also, it was noticed some possible confusion on the part of some of the respondents, concerning the difference between *noise prediction*¹² *models* and *noise propagation models*.

The European based companies that participated seemed more sensitive to the WTN problem than their counterparts from other regions. In fact, geographical and temporal considerations may provide an explanation for this fact. Some companies explained that their target markets (developing countries) have much less stringent noise restrictions and lack specific WTN legislation. In the case of the USA, although many States have specific and tight noise limits for WT, one Wind Energy consultant stated the following:

“we can still site the turbines pretty much in the middle of nowhere”

WTN seems, therefore, to be much less of a problem in the USA as it is in Europe, where the situation is quite diverse:

“Europeans, accustomed to greater population densities than the common in North America, are more tolerant of placing wind turbine in proximity to homes, businesses and public places. Commercial-scale wind turbines have been installed in parks, playgrounds, parking lots.....They can also be found alongside canals, dikes and breakwaters. In Germany it’s common to see wind turbines lining the autobahn, while in Denmark rail passengers can watch wind turbines spinning in fields adjacent to the tracks.” (GIPE, 2004)

Of special importance in the attended Conference, AWEA 2012, was the industry forum. It involved the largest WT manufacturers of the world and some regulating, R&D and control agencies in a broad debate. Mark Higgins, of the US Department of Energy, pointed out the need to increase efficiency by increasing rotor diameter, reducing aerodynamic losses, reducing siting barriers for WT, developing better predictive models, finding innovative technologies through computational tools, better knowledge of the boundary layer processes, stability and environmental issues. Roger Schonewald, from GE, showed that his new 103 m blade rotor is larger than a Boeing

¹² Noise Prediction Models are concerned with near-field sound pressure or sound power levels, while Noise Propagation Models are concerned with the sound pressure at the far field, only. Some of the latter models can be quite simple, such as the popular spherical divergence model.

747, the rotor area is larger than 2 acres and the blade tip speed is faster than the take-off speed of an F-18 fighter. Keith Longtin, also from GE, pointed out that, as rotors grow, the power produced by them also grows with the third power of the diameter, but the noise emitted grows with the fifth¹³ power. GE was at the time developing two WT testing facilities in the USA since they consider validation of models of utmost importance in the engineering learning curve.

With the focus momentarily turned to the elder sister of the WT industry, the aircraft manufacturing industry, for comparison purposes, it has been long known in that industry that most of the performance and operating costs of the airplane will be fixed in the first (conceptual) phase of the design (Raymer, 2006). The subsequent phases (preliminary and detail design) will challenge the designer with decreasing degrees of freedom, increasing manpower needs and increasing costs. Any changes made in the later design phases will cost much more for retrofitting into the conceptual project.

Assuming that this logic is applicable to the design of any complex system, it suggests that the WT industry practice should include design requirements concerning WTN still in the conceptual and preliminary design phases of the blades.

According to Wagner et al. (Wagner, Bareiß, & Guidati, Wind Turbine Noise, 1996), the industry is interested in how small modifications on airfoil geometry will influence in noise generation.

In closing, the technology for designing, controlling and decreasing airfoil noise emission seems to be still limited both in capacity and reach. Although most WT manufacturers acknowledge the importance of noise emission in their products and market, many of them dedicate their research and development towards performance and employ no more than good manufacturing practices towards noise emission. Some of them size the blade for structural and performance requirements only, and will measure the noise emission ex post in order to provide the sound pressure level (SPL) value at a certain rotor distance (as per applicable standards), to provide as guidance for the purchasing customer or siting team.

¹³ When the author refers generally to airfoil self-noise, the source model employed is the acoustic dipole and the scaling factor is $P \sim U^6$ as mentioned earlier, but when the author refers to TE noise only, the edge-scatter theory predicts that the suitable scaling factor is $P \sim U^5$, which is confirmed experimentally and will be discussed in greater detail.

1.1.4 Academic Relevance

At the Mechanical Engineering Department of EPUSP the subject has been motivated mainly by the noise research program developed in partnership with Embraer, concerning passenger cabin-comfort, turbofan-engine *jet-noise* prediction (Da Silva, 2011) and also more fundamental LES research on blunt bodies and low-Reynolds cylinder flow noise (Orselli, 2011).

It seemed reasonable to supplement the jet-noise and blunt body researches at the Department with an applied work on airfoil (slender body) aerodynamic noise in the context of a modern, renewable energy source.

Also, the theme is quite broad since it may also find application on airplane wing and fuselage aeroacoustics, with impact on the passenger annoyance level inside the cabin.

1.1.5 The impact of Wind Turbine Noise (WTN) on Humans and Fauna.

The data presented in the previous sections support a clear trend of continuous growth, both in size and number, of wind turbine equipment deployed worldwide.

Three negative impacts of the large scale HAWT equipment are frequently listed as the most relevant for the advancement of the technology: noise generation, visual pollution and wildlife impacts (Wagner, Bareiß, & Guidati, Wind Turbine Noise, 1996).

Wildlife impact has been deemed low (<1 of 30,000) compared to other human-erected structures and causes, such as buildings, communications towers, traffic, and house cats (NREL, 2005). However, the recent deactivation of 800 WT units at the Californian desert, even after repowering¹⁴ reduced the bird strike rate by 35% between 2006 and 2010, due to the reason that the units were putting at risk the life of many bird species,

¹⁴ Repowering, in the Wind Energy context, means replacing large numbers of old, inefficient Wind Turbines for a smaller number of new, higher efficiency machines.

including the protected American golden eagle (Lawton, 2015), clearly shows the relevance and impact of this subject.

In Brazil, there is a lack of studies quantifying the impact of wind farms on the avian fauna (Instituto Chico Mendes de Conservação da Biodiversidade, 2014) however, the recommendation is to avoid siting wind farms in areas of birds concentration or places permeated by the main migration routes. Out of the four main bird migration routes over Brazilian territory, the Atlantic Route - which extends from the Amapá State to the Rio Grande do Sul State shorelines - poses the major problem, because most of the country's wind farms are located along the same shorelines.

The visual pollution problem may be minimized by careful site planning and also by repowering, which significantly reduces the total number of WT units deployed (Hansen, 2008).

The noise generation problem, on the other hand, remains a crucial challenge for the wind energy industry. In fact, a detailed survey made in the Netherlands concluded that noise is often cited as the most annoying aspect of Wind Energy (Bowdler & Leventhall, 2011). This is further aggravated by the increasing size of commercial wind turbines

According to Gipe (2004), all WT create unwanted sound, or noise. The *swish* of the blades and other WT sounds are typically foreign to the rural settings where WT are most often used. The addition of new sounds, which most residents play no part in creating and do not receive direct benefit from, can be disturbing.

Some recent noise complaints in Brazil confirm completely this argument:

“At the peaceful Icarai, Ceará, the noise from the wind turbine blades has been annoying many citizens who live close to the wind farms. José Daniel lives close to the towers and was waking up in the middle of the night due to the noise and could not sleep again: ‘It’s been a complicated period but I am getting used to it’. Raimunda Martins dos Santos, 77, also suffered since the beginning of the wind turbines operation, some of which are at her backyard, among coconut, lemon and acerola trees: ‘Although there is some rhythm to it the blades are noisy’, complains Raimunda, who has a special daughter, deeply affected by the wind turbine blade noise, who kept everybody else restless in their home (Pereira, 19/June/2016).

Noise containing pure tones or impulsive sound is perceived as louder than broadband noise, which characterizes the flow around the turbine blades. Impulsive sounds (“*whop-whop*”) were typical of the two-bladed, downwind early models installed at Palm Springs, Ca, and led to many complaints about WTN. Although this kind of impulsive noise may be missed by the standard A-weighted sound measurements (GIPE, 2004), this fact helps explain why modern WT have a three bladed, upwind basic design.

Broadband sound is arguably more tolerable than impulsive, but a WT generates broadband noise in a continuous fashion for days and this helps make this trait of wind energy more annoying than any other (GIPE, 2004). The need to estimate a wind turbine noise impact derives from the mandatory local regulations on noise, which must be met before operation is authorized. Modern noise regulations tend to specify maximum levels that must not be exceeded for a minimum determined fraction of the total time, called *exceedance levels*¹⁵. For the purpose of comparing with the exceedance levels the WTN is often measured in equivalent level, L_{eq} , the equivalent, steady level sound pressure that produces the same total acoustic energy of the original sound, over its duration. Gipe (GIPE, 2004) also explains that for a sound to be considered intrusive by an observer, the judgment will depend upon (i) the nature of the noise (broadband, tonal or impulsive); (ii) the perception of the noise source (e.g. whether or not the observer likes WT); (iii) the distance from the source, and (iv) the activity of the observer (sleeping, working, etc.).

In fact, according to Bistafa (Bistafa, 2011), studies have shown a significant correlation between community discomfort (intrusion) and noise levels. The *community reaction* (CR) and percentage of *highly annoyed people* (%HA) are the descriptive variables used in studies to show the correlation, plotted against day-and-night sound pressure levels (L_{dn})¹⁶.

¹⁵ An exceedance level of 45 dB(A) L_{90} is stricter than a standard of 45 dB(A) L_{10} , because 90% of the time the noise must be below 45 dB(A).

¹⁶ L_{dn} is a sound level introduced by the EPA for the evaluation of noise in communities. It is similar to a L_{eq} over a 24 hours period, except that the equivalent level measured overnight has a 10 dB penalty increase.

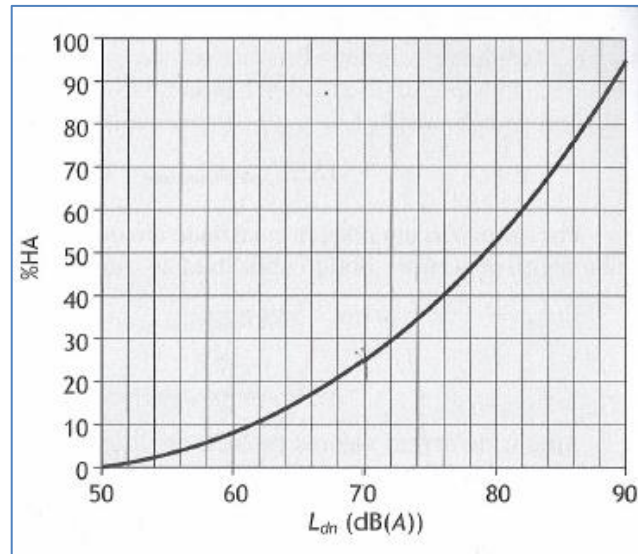


Figure 1-10 Percentage of highly annoyed (%HA) people by vehicle and aircraft traffic as a function of L_{dn} (dB(A)). Source: adapted by Bistafa (Bistafa, 2011), reproduced with permission.

Figure 1-10 above shows that a 60 dB(A) L_{dn} noise will heavily affect less than 10% of the community, while an 80 dB(A) L_{dn} noise will heavily affect more than 50% of the community. In fact, another reaction study (Bistafa, 2011) shows that a 10 dB(A) increase in L_{dn} will elicit strong community change in reaction, going, for instance, from periodic complaints to generalized complaints and threats of law suit. This is rather predictable as a 10 dB(A) increase in a noise source can be perceived as a doubling of loudness¹⁷. Also, Stankovic et al. (Stankovic, Campbell, & Harries, 2009), claim that a 5 dB(A) sound level change would probably be perceived by most people under normal listening conditions, although it would take ideal listening conditions to detect sound level differences of 2 or 3 dB(A). Both these observations will help us later define and propose a quality criteria for scaling variables employed in noise prediction methods.

As the background noise increases with wind speed, so does the WTN, making noise masking¹⁸ generally not possible, a fact clearly illustrated in Figure 1-11.

¹⁷ Loudness (audibilidade in Portuguese), is the psychoacoustic value associated by the humans with the sound pressure level, which is a physical value. Loudness is a subjective sensation that depends upon the frequency of the noise and is (subjectively) measured in *phons*. A *phon* unit does not keep the same relation to *dB* for all frequencies. For an observer to perceive a doubling of the sound pressure, the loudness has to increase by 10 *phons* to his perception, which translates into 10 *dB* in the 700 Hz to 2 KHz range of frequencies, approximately. For details, please see (Bistafa, 2011) pp 68-73.

¹⁸ Noise masking is a phenomena derived from the human ear physiology. Sound actuating the oval window of the inner ear, results in standing waves being set up on the basilar membrane. The amplitude

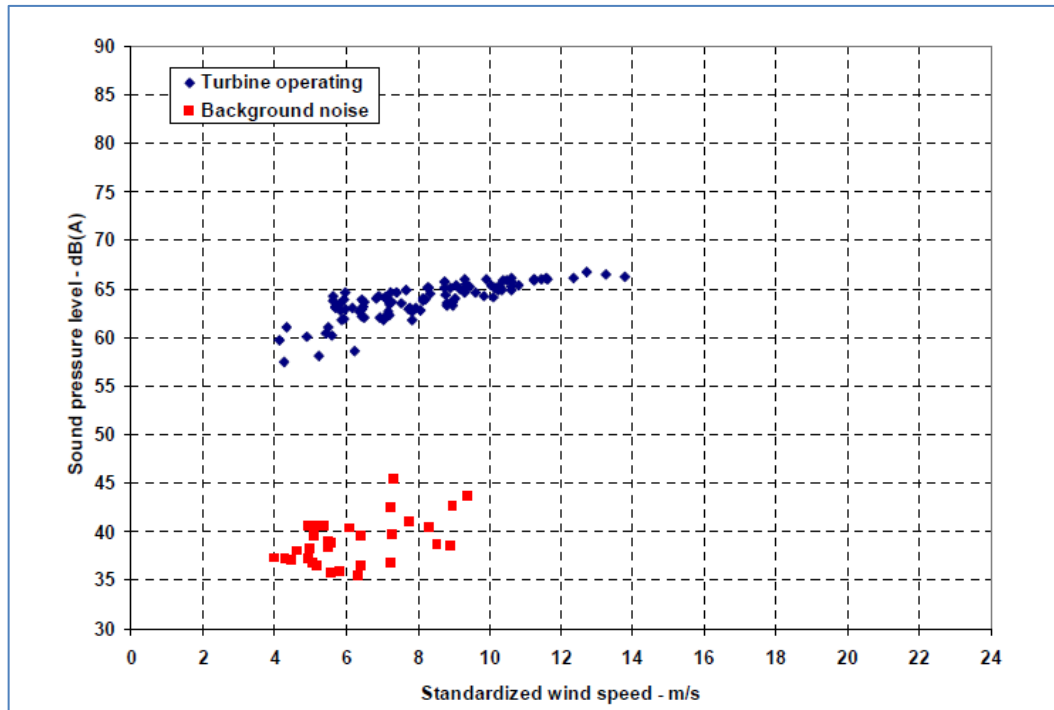


Figure 1-11 Sound Pressure levels (1 minute averages) as a function of wind speed, for background noise and a small size WT (Migliore, van Dam, & Huskey, Acoustic Tests of Small Wind Turbines, 2003).

In order to illustrate the consequences of the perceived noise by a nearby community, Gipe (GIPE, 2004) describes two interesting cases. Dan Win, a Danish WT manufacturer spent US\$ 750,000 to fix the noise levels coming from a 21-unit, 180 kW (each) wind farm near Kynby, Denmark. Despite many siting precautions and reducing operational speed below ideal, the noise at the nearest residence, a farm 220 m away, exceeded permissible levels and included a pure tone component¹⁹. After four years of correction rework the WTN emissions were reduced from 102 dB(A) to 95 dB(A), resulting in an acceptable noise level at the dwellings. Curiously,

“The engineers found that they could gain 4 dB(A) simply by sharpening the trailing edge of each blade, providing one of the most convincing demonstrations that trailing edge thickness is a significant factor in aerodynamic noise” (GIPE, 2004)

peak changes position for different frequencies (Everest & Pohlmann, 2009). Because of the continuous nature of the membrane and of the fact that low frequency tones generate activity over a larger area of the membrane, its displacement in response for low frequency tones also displace the hearing threshold, “masking” sounds of nearby frequencies (Bistafa, 2011).

¹⁹ A pure tone component penalizes the measured L_p in a further 5 or 10 dB(A), as shall be seen in the next section.

The other report is about the Wisconsin Public Service (WPS), which began receiving noise complaints after installing 14 Vestas V47 WTs in 1999. The WPS conducted a series of noise studies and ultimately had to make proposals to buy six homes to fix the problem, but only two owners accepted the offer. The initial project cost investment was overrun and the problem was not solved. These examples help to make the point that WTN should be dealt with in the beginning of the development phase of a new design, not later, in the field.

There has been also some discussion about the impact on human health of infrasound emitted by WT. In fact, Figure 1-12 shows typical spectra diagram for a WTN, analyzed with different frequency resolutions. The spectra are overlaid in a hearing threshold curve and it may be seen that, although the human being is not capable of hearing frequencies below 100 Hz, the amount of noise energy produced in that range looks significant at a first glance²⁰, in the overall noise signature for this type of equipment.

²⁰ In order to evaluate the importance of the Low Frequency Noise from a source, usually a C-weighting measurement is made and compared with an A-weighting measurement. If the reading is close for both filters, then there is little energy in the low frequencies. When the C reading is larger than the A reading by a significant amount (say 15-20 dB level difference) the spectrum is said to be dominated by the low frequency range (Bistafa, 2011).

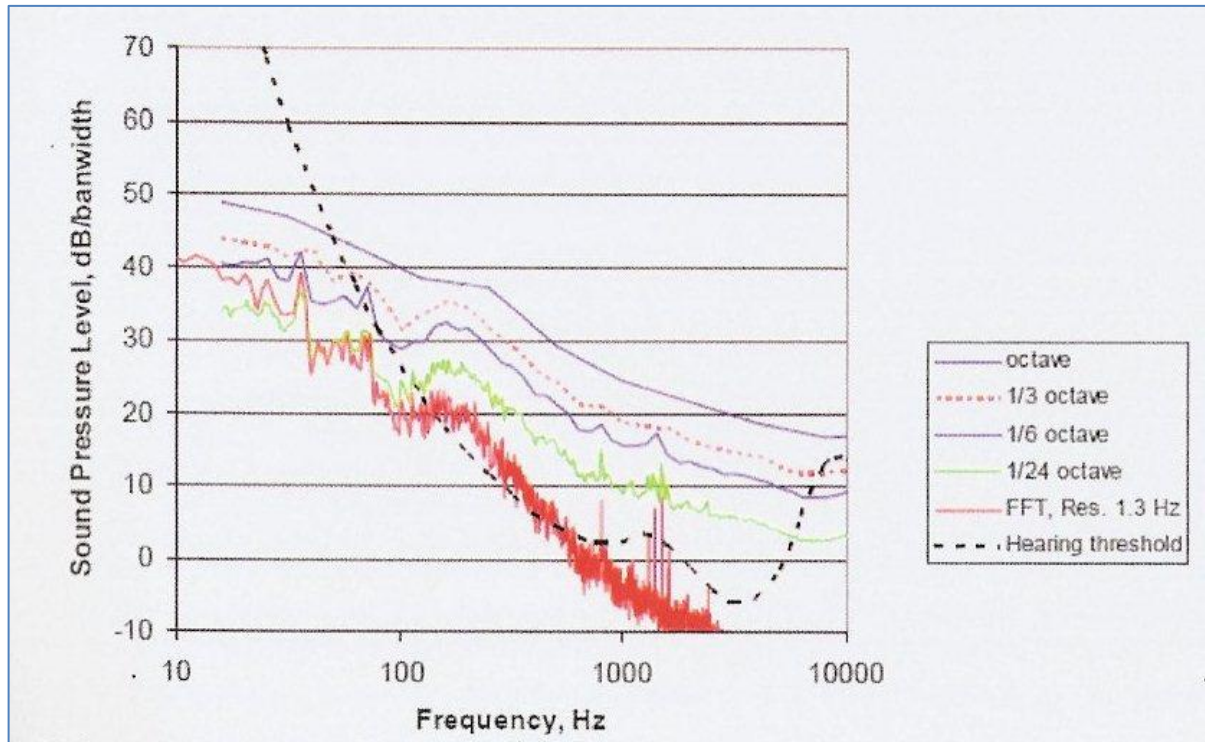


Figure 1-12 Typical spectral signature for a WT, overlaid in a standard human hearing threshold line, adapted from the work of T.H. Pedersen (Bowdler & Leventhall, 2011). Reproduced under permission.

A measurement of the apparent A-weighted and C-weighted sound power spectra, down to 4 Hz in some cases, for 78 wind turbines ranging in capacity from 75 kW to 3.6 MW was performed by Hessler (Hessler, 2011), who concluded that the C-A (C minus A) level difference was in the range of 11 dB. He further developed pressure spectra for the largest WT at “suitable” distance and compared to annoyance thresholds developed specifically for Low Frequency Noise (LFN), concluding that the spectra was 20 to 40 dB below the perception threshold and 20 to 30 dB lower than experienced by a passenger traveling in a modern car, at highway speeds, with an open window.

His conclusion is of restricted value for those concerned with the noise emitted by the source. While he may conclude that the WT LFN level is not an issue “at typical wind project buffer distances”, Figure 1-12 shows that the highest noise levels are present in the lower bands of the spectrum.

Factually, there is no current definitive evidence that, at normal WT noise emission levels, the infra-sound part of the noise spectrum has a significant impact over the population (Leventhall, 2013), although there is at least one theory concerning the

physiological effects of infra-sound produced by wind farm sites (Schomer, Erdreich, Boyle, & Pamidighatam, 2013).

Also, Wagner et al. (Wagner, Bareiß, & Guidati, Wind Turbine Noise, 1996), p. 77, show that the SPL at lower frequencies may couple with natural vibration frequencies of building windows, which might resonate in a broader spectrum.

Finally, a word about amplitude modulation (AM) in WTN. The UK Government published a research in 2007 (Bowdler & Leventhall, 2011) showing that noise complaints had been received for 20% of all the wind farms in UK. From the 14 complaints received, 13 had a description of a sound with a regular variation in level, or amplitude modulation (AM). The variation in level is at the rate of the Blade Passing Frequency (BPF), three times the rotation frequency for a three-bladed rotor, and the typical modulation depth (difference between the highest and lowest level) measured was up to 7 dB, but more usually about 3 dB. The AM research is quite open at this moment, as is the debate whether it is source or propagation driven. Many theories for explaining AM are available, including wind-shear effect.

1.1.6 Regulations on Wind Turbine Noise

Regulations on WTN appear in the form of noise-limiting ordinances and acceptable standards for measuring and evaluating WTN.

While in countries with a well-developed wind energy industry there are specific rules and regulations concerning WTN, in some others, general noise regulations and limitations apply. Also, the regulations may vary from state to state or even change at county or city level.

Noise limitations, regardless of general or specific types, exist in order to protect people health and well-being and they may have strong economic impact whether in a stand-alone WT siting or large farm siting projects as will be briefly shown.

The noise levels that WT enterprises must meet in Europe and USA are similar, differing mostly in the *exceedance levels* (GIPE, 2004). For instance, the 65 dB(A) L₁₀ WTN limit applicable in Minnesota for daytime, rural environment, means that the 65

dB(A) limit must be observed 10% of the time, while the 60 dB(A) L_{90} limit applicable in Palm Springs, day or night, rural area, means that the 60 dB(A) level cannot be exceeded for over 90% of the observed time.

In the Netherlands and Denmark, exceedance levels are expressed as equivalent levels, L_{eq} , defined earlier, as can be seen in Table 1-1.

Table 1-1 - Selected Noise Limits for different Countries, SPL [dB] (GIPE, 2004). Reproduced under permission.

Selected Noise Limits, Sound Pressure Levels in dBA		Commercial	Mixed	Residential	Rural
Germany					
Day		65	60	55	50
Night		50	45	40	35
Netherlands					
Day	L_{eq}		50	45	40
Night			40	35	30
Denmark ¹	L_{eq}			40	45
England ²					
High speed	L_{50}				45
Low speed	L_{50}				40
Minnesota					
Day	L_{50}	75	65	60	60
Night	L_{50}	75	65	50	50
Minnesota					
Day	L_{10}	80	70	65	65
Night	L_{10}	80	70	55	55
Kern County, Calif. ³	$L_{8.3}$			45	45
Riverside County, Calif.	L_{90}			45	
Palm Springs, Calif. ⁴	L_{90}			50	60

Notes: ¹ Not to exceed 45 dBA beyond 400 m from wind turbine.
² L_{50} approx. 350 m from the nearest turbine.
³ $L_{8.3}$, not to exceed 50 dBA.
⁴ 50 dBA if lot is actually used as residential.

Most community noise standards incorporate a penalty for pure tones, typically 5 dB. In Brazil there is currently no specific regulations concerning WTN and, like in many other countries, general noise regulations apply in that case. The maximum noise levels allowed are regulated by the Associação Brasileira de Normas Técnicas (ABNT), NBR 10151 Standard (Acústica - Avaliação do Ruído em Áreas Habitadas, Visando o Conforto da Comunidade), (NBR10151, 2000), with some limits illustrated in the table below.

Table 1-2 - Criteria level for external environment evaluation, dB(A).

Type of area	Criteria Level dB(A)	
	Day	Night
Farms and Countryland	40	35
Strictly residential urban area or hospital or school area	50	45
Mixed use, predominantly residential.	55	50
Mixed use, commercial and service prone.	60	55
Mixed use, recreational prone.	65	55
Industrial area (mostly)	70	60

More recent regulations applicable in many countries may be found summarized in Bowdler and Leventhall (Bowdler & Leventhall, 2011).

For the purpose of illustrating in a quantitative manner the impact of the regulations on the cost of a WT siting project, let us consider the simple van der Borg one parameter, linear model²¹ for WT Sound Power Level (SPW) noise production, (GIPE, 2004) p. 295:

$$SPW = 22 \cdot \log D + 65 \text{ dBA} \quad (1 - 3)$$

A 38 m diameter (D) rotor would produce a SPW of 100 dB(A) at 1 meter from the shaft, while a 150 m diameter machine would produce 113 dB(A). Since every increase of 3 dB means doubling the source power, growing the WT diameter from 38 to 150 m roughly increases the source power level sixteen times by this model and the sound pressure level at a fixed observer location, would increase four times.

The divergence of the Sound Pressure Level (SPL), from an omnidirectional noise source, far from the ground or reflective surfaces, propagating spherically without attenuation to distance r from the source, is (Bistafa, 2011):

$$SPL = SPW - 20 \cdot \log r - 11 \text{ dB} \quad (1 - 4)$$

By equating the SPL for the two different diameters and estimating the ratio of distances where the Sound Pressure Level will be the same for both sources, we will find a distance ratio of 1:4.5, which suggests that the larger diameter equipment will need 20 times more ground area for siting than the smaller diameter machine. In Brazil, the daytime Criteria Level (maximum limit) acceptable as per current standard

²¹ Van der Borg introduced two different correlations for L_w , this one being the one for second generation, quieter, WT.

(NBR10151, 2000), for acoustic comfort criteria in farmlands and fields, is 40 dB(A). By replacing this upper limit for SPL in the expression (1-4) one can obtain the linear distance r required from the closest dwelling in this simplified propagation model:

For the 38 m diameter WT:

$$40 = 100 - 20 \cdot \log r - 11 \text{ dB} \Rightarrow r = 10^{2.45} \cong 282 \text{ m}$$

For the 150 m diameter WT:

$$40 = 113 - 20 \cdot \log r - 11 \text{ dB} \Rightarrow r = 10^{3.10} \cong 1,259 \text{ m}$$

It becomes quite clear that the larger the WT, the farthest away it must be sited from dwellings in order to fulfill legal noise requirements. That translates into increased cost of acquisition of the real state, maintenance, access roads and also precludes the large size WT to come closer to the electricity end-user, which undermines the distributed generation concept.

Even a simplified noise prediction model can help the siting planners to evaluate the information provided by the WT manufacturers regarding allowable distance from households. The example shown in Figure 1-13, suggests a minimum separation distance of 300 m. However, that minimum distance would be enough separation only from small machines (38 m-diameter HAWT) as estimated by the calculations.

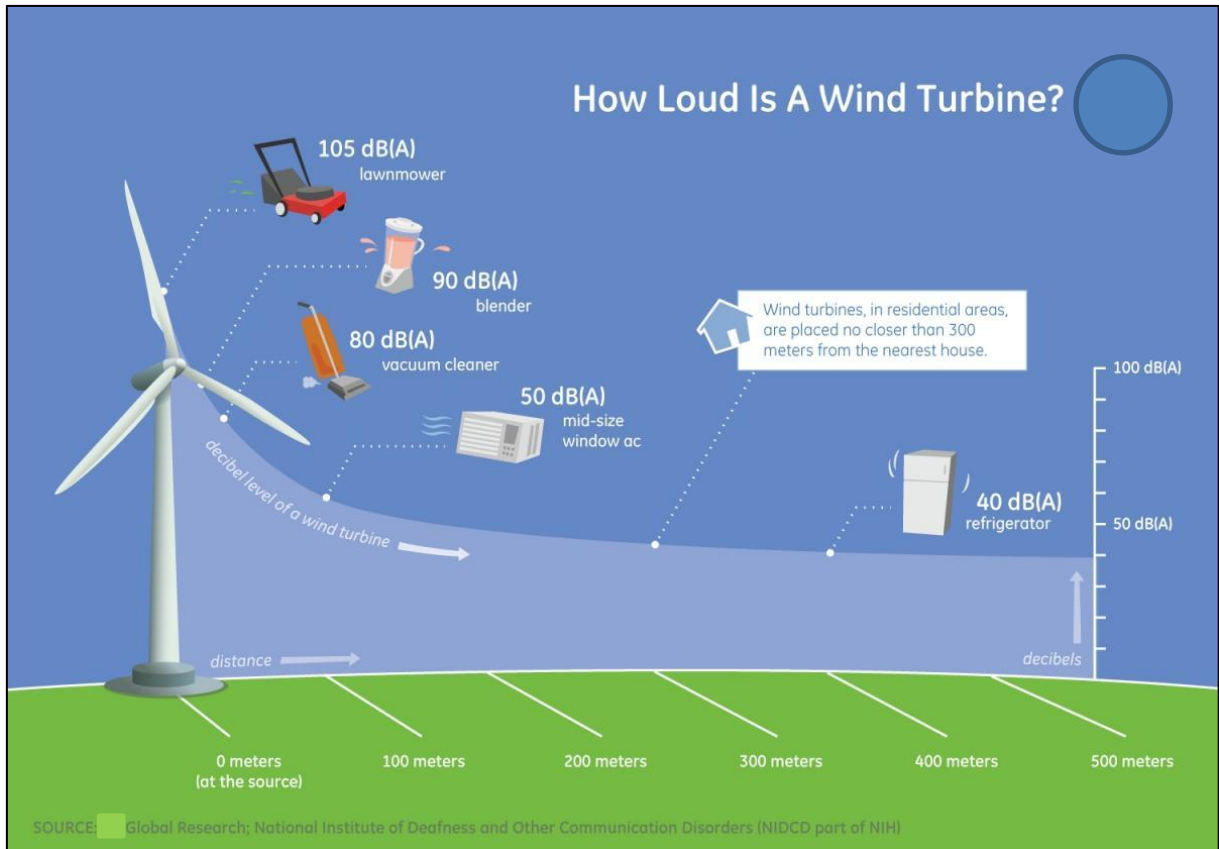


Figure 1-13 A large scale WT manufacturer diagram stating that 300 m is the minimum distance for WT siting from residential areas.

Noise levels at the observer (microphone, receiver, etc.) position must be assessed with calibrated equipment and approved noise measurement techniques in order to verify compliance in an acceptable manner. However, contrary to other power generation facilities whose noise is generally noticeable only during calm and still weather conditions, WT generates noise in competition with natural induced-sounds, as was clearly displayed in Figure 1-11. The background noise level then plays a major part in measuring WTN and one of the difficulties encountered has been the identification of the equipment-produced sound level, exclusive of background contamination, the key quantity sought after in such tests. A proposed procedure for compliance testing, developed based on extensive field experience, may be found in Bowdler and Leventhall (Bowdler & Leventhall, 2011).

As for the measurement of source power, at present only one dedicated standard exists for the purpose of measuring the sound power level of a single WT operating in isolation (Bowdler & Leventhall, 2011), the IEC 61400-11 (IEC61400-11, 2012). The

aim is to measure the sound power level under rigorously controlled conditions so that the sound emissions of different equipment can be compared on a consistent basis and to provide input data for modeling analysis. For the purpose of this measurement, a microphone is laid flat on a ground plate at a slant distance of $1 \frac{1}{2}$ rotor diameters. The measurements are made for wind speeds from 6 to 10 m/s (reference wind speeds measured 10 m above the ground level). At least three one-minute L_{Aeq} measurements must be obtained in each of the 5 wind speed bins, both for WT operating and off, for providing background noise reference. The sound pressure levels recorded are converted back to sound power level at the source based on the hemispherical surface area of the wave front at the microphone (Bowdler & Leventhall, 2011). The results are expressed as the overall A-weighted sound power level at each of the mandatory wind speeds along the 1/3 octave band frequency content, ideally at each speed. The test also includes a rather complicated process for evaluating the potential tonal content of the sound spectrum based on narrowband Fast-Fourier-Transform (FFT) measurements.

1.2 OBJECTIVES AND CONTRIBUTIONS

The main objective of this work is to provide the WT industry and researchers with a computationally efficient, high degree of freedom, friendly user graphic interface analysis tool that will allow the early noise assessment and design of quieter airfoil for WT equipment.

This is a quite broad undertaking and many relevant contributions had to be made along the way in order to make it possible.

- A field research with a relevant cross section of the WT industry was accomplished in order to determine the relevance and how the companies cope with the aeroacoustic noise problem.
- A broad revision of basic acoustics and noise sources was accomplished and will remain as a convenient source of reference.

- A thorough bibliographical research, spanning more than 25 years in the Wind Turbine Noise field, more specifically in the development of the semi-empirical and simplified theoretical models and methods was accomplished and commented, providing a broad review on the subject.
- A new set of evaluation dimensions was employed for comparing the WTN prediction methods discussed in the review and a broad classification table was assembled with all models and methods reviewed.
- A noise-restricting criterion is proposed for controlling the quality of the TBL integral parameters used as inputs in the semi-empirical scaling of airfoil self-noise models.
- The quality of prediction of TBL integral parameters for different numerical (XFLR5, RANS) methods is investigated in light of the proposed criteria. During RANS investigation, a detailed mesh sensitivity study was accomplished based on ASME methodology.
- Based on previous findings the elements were selected for the development of a modified-BPM TE noise prediction method and a collaboration was made effective with The Technische Universität Berlin (TU-Berlin), in order to add an airfoil self-noise prediction module to the QBlade software, an open source, graphic interface platform, distributed under General Public License (GPL).
- After implementation of the modified TE noise prediction method, a detailed verification and validation procedure was accomplished within the original model validation range.
- Since the real operating conditions of large-size Wind Turbines are not readily available in technical papers, wind energy books, or manufacturer catalogues, three large scale wind turbines were completely designed, from the aerodynamic point of view, allowing a reasonable assessment of the local operating conditions at each radial blade station, based on the application of the Blade Element Momentum (BEM) method.
- A validation of the TE noise prediction method was attempted beyond the original scope of the method (at larger Reynolds numbers), by comparing to experimental data at higher speeds, however, the validation extrapolation was not successful as a consequence of many shortcomings detailed discussed in the text and the method was considered suitable for comparative assessment, only.
- Based on the premise of physical-adherence of the BPM method, the effect of airfoil geometric characteristics is investigated and related to TE noise.
- A family of three new silent profile (SP) airfoils, including a bird-saving variant, is proposed with increased TE noise performance and preserved or increased aerodynamic performance in respect to the NREL S830 baseline airfoil.

After implementation of a flexible and user friendly tool, plus its deployment to develop a family of quieter airfoils, the ultimate goal of this work, i.e. to support the development of quieter WT equipment, has been completely fulfilled.

1.3 THESIS OUTLINE

For the reader uninitiated in the acoustic field, it is suggested to read the appendixes first, where the initial research that motivated the object of the current study is shown in Appendix A, followed by a broad, commented review of acoustics and noise sources in Appendix B, features of The Wind, in Appendix C, and self-noise models are reviewed in Appendixes D and E.

In the main body, the relevance of the subject from many standpoints is extensively treated in Section 1, human impact of noise and noise regulations are introduced, plus the research objectives are declared.

In Section 2, a general review of aeroacoustic theory is made as applicable to Wind Turbines covering both airfoil self-noise and inflow noise. The modern horizontal axis wind turbine morphology is then introduced followed by noise prediction methods, wind turbine noise mitigation technologies and an extensive review of airfoil research for wind turbines. The chapter also covers basic description of the numerical methods and codes used as tools in the research process.

Section 3 is dedicated to the methodology. In subsection 3.1, the method for determining the typical operating conditions for a large-size HAWT is described. In subsection 3.2 the essential elements for setting up the TE noise tool are selected. Subsection 3.3 discusses the planning for the XFLR5 modifications necessary to cope with the method. Subsection 3.4 details the methodology for the implementation of the modified-BPM TE noise prediction algorithm and the original model validity range. Subsections 3.5 and 3.6 discuss details of the software architecture for the implementation of the TE noise prediction code. Subsection 3.7 explains the methodology adopted for designing new, quieter airfoils.

In section 4 the results are displayed and also discussed, since the research is quite extensive. In section 4.1 the results are shown for the 50-m blade operating conditions. Section 4.2 shows the result of the implementation of a new method for classification of the WTN methods to sort all reviewed methods. In section 4.3 the validation and verification is accomplished for the original BPM TE noise model and a validation attempt is made for the method outside the original scope. Section 4.4 discusses a detailed sensitivity analysis for airfoil geometry versus TE noise and Section 4.5 discusses the development of a new family of “silent profiles”.

In section 5 the conclusions are presented, along with limitations and further development suggestions.

Further appendixes are provided on the detailed architecture planned for the 3-D noise module under development (Appendix G) and the typical operating conditions for still larger Wind Turbines (Appendix H).

2. AEROACOUSTIC THEORY AND APPLICATION

2.1 APPLICATIONS OF AEROACOUSTIC THEORY TO WTN

An extensive, commented revision of the basic concepts on sound and noise, the wave equation fundamental solutions and acoustic analogies is available to the reader in Appendix B.

The different aspects of the aeroacoustic theory may find different applications in the noise prediction engineering practice, depending upon the flow regimes and the dominant noise producing mechanisms. For instance, the steady, harmonic noise from a propeller is caused by steady loads at the rotating blades and occurs at multiples of the blade passing frequency (BPF). The mechanism of noise production is the displacement of air by the motion of the body, giving rise to monopole sound, and the forces acting from the body on the fluid, giving rise to dipole sound. Because it does not depend on the viscous flow interaction and can be calculated in a straightforward manner, this kind of noise is referred to as *deterministic noise*. This form of self-noise is called *Gutin noise* (Theodorsen & Regier, 1946) and may be computed with good accuracy, but it is not a significant noise source for current design HAWTs since, according to Blake (Blake, *Mechanics of Flow-Induced Sound and Vibration*, 1986 II), the Gutin noise is generally important at nearly sonic tip speeds (high Mach numbers).

There are also applications of the Ffowcs Williams & Hawkins (FW-H) equation (see Appendix B, Eqn. B-84) for the deterministic, harmonic fan noise, where the loads at the blades (source terms) are computed either using BEM methods (Hansen, 2008), (Burton, Sharpe, Jenkins, & Bossanyi, 2008) or *vortex-lattice methods* (Gupta & Leishman, 2005), which are inviscid in nature, and thus cannot model the source strengths coming from the interaction between the turbulence and the WT blade.

For the high-frequency noise originated from the turbulent flow, the Lighthill equation (Appendix B.7, Eqn. B-59) provides, in principle, the opportunity to obtain an exact

solution. However, knowing the source term for the solution of the Lighthill equation (the strength of the Lighthill tensor) implies having previously obtained the detailed solution for the turbulent flow field, which is almost never possible or practical, which prevents the direct noise computation.

For the application of the FW-H equation in the prediction of noise originated from the interaction between turbulence and the WT blades, the same difficulties arise and the procedures generally have to rely on a considerable amount of empirical input. For this reason, this type of noise is called *non-deterministic* or *semi-empirical* noise. For subsonic, turbulent flows interacting with the blades, the primary noise sources are the fluctuating Reynolds stresses (Lighthill tensor) originating quadrupole sound and the sound reflection and scattering in the presence of the rigid airfoil surface, which may give rise to dipole-type sound when the airfoil may be treated as a compact source.

The aeroacoustic theory formulations have led to the proposal of some noise prediction models and many noise prediction formulations or methods. Previous to a closer analysis of the models and methods of interest to WTN, it is necessary to discuss the key mechanisms of flow-induced noise and the nature of the spectra they produce. This shall be also followed by a discussion of the operating conditions of a typical WT rotor, a description of the TE model types, the technologies available for WTN mitigation and numerical codes.

2.1.1 Turbulent Flow-Induced Noise Mechanisms

A brief description of the general noise mechanisms induced by free turbulence and turbulence interacting with the airfoil will be made, along with dependence of sound intensity on Mach number and other flow parameters.

2.1.1.1 Noise from Free Turbulence

This subject was the original motivation of Lighthill's research, due to the increasing concern of noise emitted by jet propulsion²². In Appendix B the Lighthill analogy is explained and a solution is obtained for Lighthill inhomogeneous wave equation, with the aid of Green's Function, leading to the quadrupole-type source radiation. The pressure fluctuating field solution is also presented for time and frequency domains.

Lighthill (Lighthill, 1962) also deduced that for the jet noise, the acoustic intensity is proportional to the eighth power of the flow Mach number

$$I \propto \rho_0 c_0^3 M^8 \left(\frac{l}{r}\right)^2 \alpha^2 \quad (2 - 1)$$

where $M = U/c_0$, l is the typical dimension in the turbulent region, α is the normalized turbulence intensity and r is the distance from the source to the observer.

2.1.1.2 Noise from Turbulence Interaction with the Airfoil Edges

According to Oerlemans (Oerlemans, Wind Turbine Noise: Primary Noise Sources, 2011), the Mach number of the flow around the outboard part of a typical WT blade is of the order 0.2. From Eqn. (2 – 1) we may see that the resulting acoustic intensity from free turbulence at this small Mach number would be weak ($I \propto M^8$), leading to the conclusion that, for small Mach numbers, the radiated aerodynamic noise from an airfoil will be dominated by the interaction between the turbulence and the airfoil surface.

The subject was first formally treated by FW-Hall (Ffowcs-Williams & Hall, 1970) while investigating sound generation by turbulence in the vicinity of a scattering half-plane and was later treated in a more general approach by Blake (Blake, Mechanics of Flow-Induced Sound and Vibration, 1986 II). According to Blake, the sophistication of analytical modeling of flow-edge interactions evolved following the work of FW-Hall

²² Lighthill's Bakerian Lecture of 1961 (Lighthill, 1962) is very rich in historical details. One curious description is that, when the jet noise problem evolved from the civil aircraft operation arena, Britain was ahead of the World in both understanding and practical knowledge of noise generation and suppression, and that was due to the foresight and determination of the late Director of Scientific Research in Aeronautics, H.B. Irving, who, as early as 1949, toured the Country in an effort to engage scientists and engineers to study jet-noise theory and empirical methods for its suppression.

(Ffowcs-Williams & Hall, 1970), to include physically realistic acoustic and aerodynamic interactions, and so did the mathematical complexity of the models. In his development, it is assumed that (i) the disturbances created by the flow-edge interaction do not feed-back on the turbulence, i.e. the only interaction of importance is the acoustic one, and (ii) the size of a typical eddy scales on the typical dimension l of the turbulent region (see Figure 2-1).

The effect is therefore dependent on the turbulence length scale. For TE noise the turbulence length scales usually employed are the boundary layer thickness (Wagner, Bareiß, & Guidati, Wind Turbine Noise, 1996), or the displacement thickness, δ^* measured at the TE (Oerlemans, Wind Turbine Noise: Primary Noise Sources, 2011), and for inflow turbulence noise l is the scale of the incident eddies.

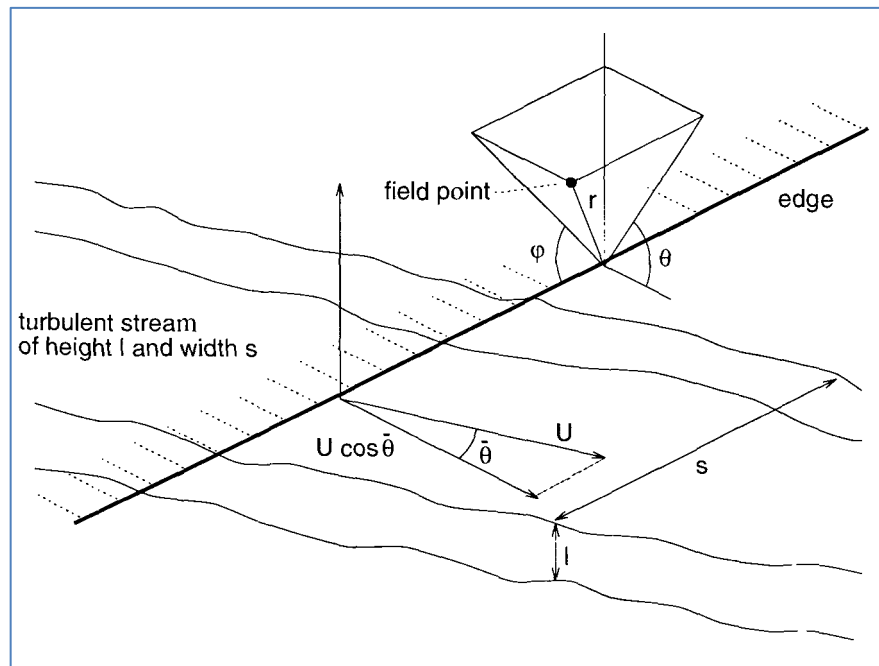


Figure 2-1 Basic geometry employed by BLAKE to study the wall jet incident on the TE of a semi-infinite plane (Blake, Mechanics of Flow-Induced Sound and Vibration, 1986 II), p. 726, adapted by (Wagner, Bareiß, & Guidati, Wind Turbine Noise, 1996).

The resulting acoustic intensity was found to depend on the fifth power of the flow Mach number, for non-compact source behavior

$$I \propto \rho_0 c_0^3 \cos^3(\bar{\theta}) M^5 \frac{sl}{r^2} \alpha^2 \cdot \sin(\varphi) \sin^2\left(\frac{\theta}{2}\right) \quad (2-2)$$

where α is the normalized turbulence intensity and the length scales and angles are depicted in Figure 2-1.

Equation (2-2) is valid for both Trailing Edge noise and Leading Edge noise (high-frequency inflow turbulence noise), with suitable turbulence length scales selected for each case, as highlighted above, and it is the basis of several edge-noise prediction models since it is the dominant type of noise source at low Mach number flows ($M < 1$).

However, when the incident eddies are much larger than the typical airfoil chord, $c \sim 1$ m, so will be the acoustic wavelength of the noise emitted ($f < 50$ Hz), and for this range of infrasound the airfoil may be considered a compact source (Oerlemans, Wind Turbine Noise: Primary Noise Sources, 2011). In that case the acoustic intensity will depend on the sixth power of the flow Mach number (Wagner, Bareiß, & Guidati, Wind Turbine Noise, 1996):

$$I \propto \rho_0 c_0^3 M^6 \left(\frac{A_b}{\Lambda r} \right) \alpha^2 \cdot \cos^2(\theta) \quad (2-3)$$

where A_b is the area of the airfoil, Λ is a characteristic length scale of the turbulence, and θ is the angle between the airfoil surface and the observer. The expression has a dipole-type directivity function.

2.1.2 Aerodynamic Noise Sources in Wind Turbine and Relevance in the Audio Range

In this and in the following sections a brief review of low Mach number sources of aerodynamic noise and their spectra will be presented based on the literature, so that their relative importance may be established based on energy and frequency considerations. Also, the specific mechanisms for LFN, Inflow turbulence noise and airfoil self-noise will be discussed in more detail in the WT operation context.

Figure 2-2 shows a typical flow around a WT rotor blade, with flow orientation, relevant phenomena and nomenclature, while Table 2-1 shows the nature of noise (airfoil self-noise or interaction noise) and the noise-producing mechanism associated with the flow.

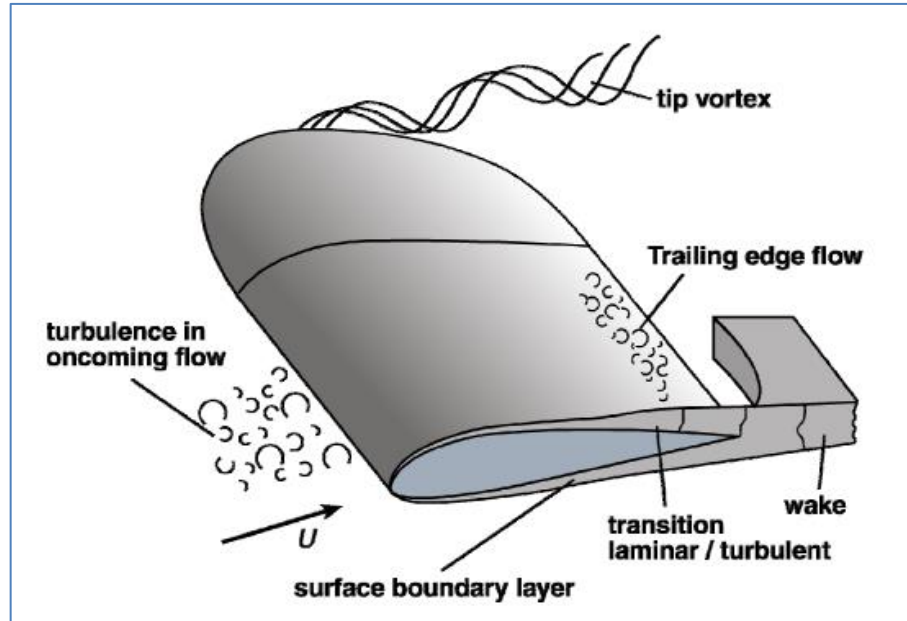


Figure 2-2 Typical flow around a WT rotor blade (Wagner, Bareiß, & Guidati, Wind Turbine Noise, 1996).

Table 2-1 – WT aerodynamic noise generation mechanisms (Rogers, Manwell, & Wright, 2006).

Type or indication	Mechanism	Main characteristics & importance
Low-frequency sound		
Steady thickness noise; steady loading noise	Rotation of blades or rotation of lifting surfaces	Frequency is related to blade passing frequency, not important at current rotational speeds
Unsteady loading noise	Passage of blades through tower velocity deficit or wakes	Frequency is related to blade passing frequency, small in cases of upwind rotors, though possibly contributing in case of wind farms
Inflow turbulence sound	Interaction of blades with atmospheric turbulence	Contributing to broadband noise; not yet fully quantified
Airfoil self-noise		
Trailing-edge noise	Interaction of boundary layer turbulence with blade trailing edge	Broadband, main source of high frequency noise ($770 \text{ Hz} < f < 2 \text{ kHz}$)
Tip noise	Interaction of tip turbulence with blade tip surface	Broadband; not fully understood
Stall, separation noise	Interaction of turbulence with blade surface	Broadband
Laminar boundary layer noise	Non-linear boundary layer instabilities interacting with the blade surface	Tonal, can be avoided
Blunt trailing edge noise	Vortex shedding at blunt trailing edge	Tonal, can be avoided
Noise from flow over holes, slits and intrusions	Unstable shear flows over holes and slits, vortex shedding from intrusions	Tonal, can be avoided

All self-noise causes listed in Table 2-1, including the Gutin noise (steady loading noise), are confirmed as the key sources by Blake (Blake, Mechanics of Flow-Induced Sound and Vibration, 1986 II), although Blake also identifies other types of important interaction-noise sources, for equipment operating at higher Mach numbers (e.g. ducted fan engines and helicopter rotors).

2.1.3 Low-Frequency Noise

In the case of WT, the origin of this noise occurs when the rotor blades flow through the wake generated by the tower, causing a rapid change in blade loading, which originate a dipole-type loading noise. This is why this class of noise is dependent on the BPF (Blade Passing Frequency) and relative position of rotor and tower.

If the local fluctuations are known, the noise can be found by the solution of the FW-H equation (B-84) or the Farassat loading noise equation (B-86).

For modern type HAWTs, with upwind rotors, the rotational speed is in the range of 18-60 rpm and for a 3 bladed rotor, this would translate into a BPF from 1 to 3 Hz. The frequency of the noise and its harmonics would cover the range from 1-150 Hz (Wagner, Bareiß, & Guidati, Wind Turbine Noise, 1996). Although these *discrete frequency noises* barely reach the audio range, their sound pressure levels can be high, as shown in Figure 2-3.

The typical LFN spectra for an upwind and a downwind rotor HAWT is displayed in Figure 2-3, where it is evident the higher SPL for the downwind rotor equipment, at least in part justifying its phase out, and the rotational harmonics, justifying the *discrete frequency noise* term used in the bibliography. Although mechanical noise is not the subject of this research, it is worth noting that direct generator drive has been implemented in many modern designs, eliminating the gearbox and, consequently, the generator drive shaft harmonic spikes seen in the spectrum of the upwind rotor equipment.

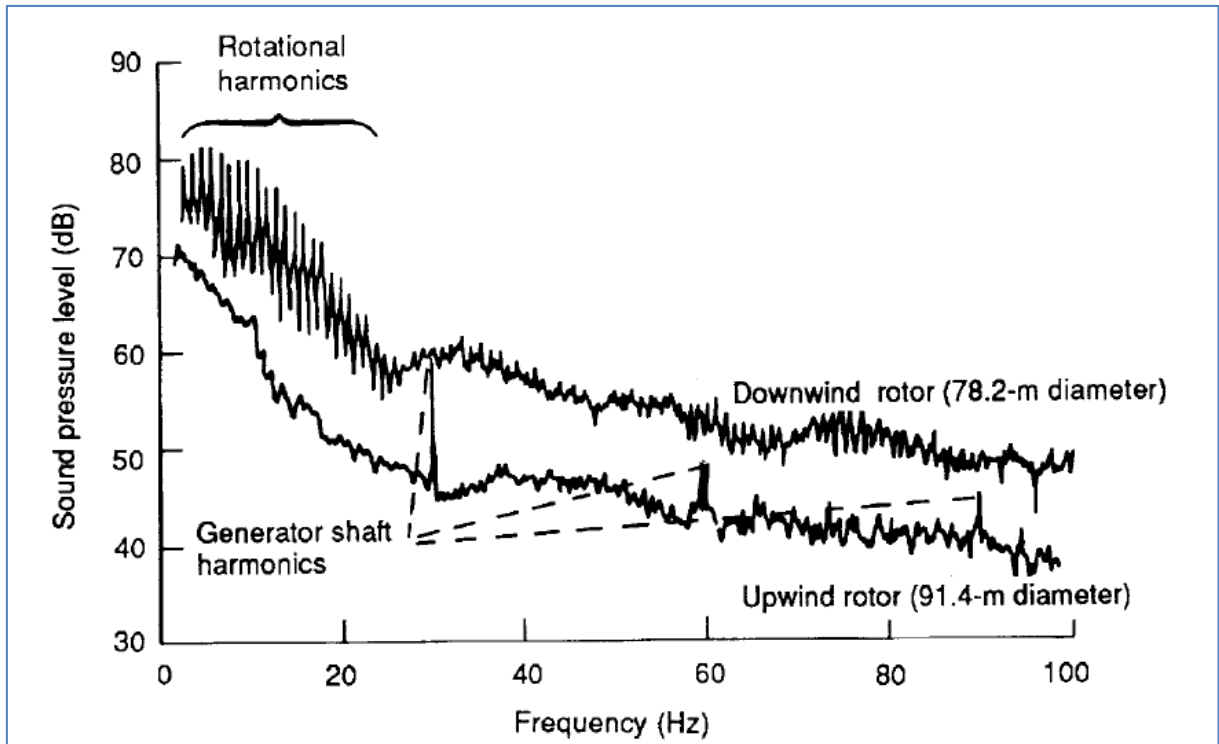


Figure 2-3 Low-Frequency, narrow-band noise spectra for HAWTs with downwind (upper spectrum) and upwind (lower spectrum) rotors, at 150 m distance (Hubbard & Shepherd, 1990).

Despite the relatively high SPL at low frequencies, the A-weighting acoustic filter employed during the noise measurements, as required by applicable standards, e.g. (IEC61400-11, 2012), would add negative gains from -70 dB (in the 10 Hz band) to -16 dB (in the 125 Hz band) over the sound pressure level measured, for each 1/3 octave band, in this range (Bistafa, 2011), p. 93, leaving only minor contributions to OASPL (dBA) from the LFN. For illustration purposes of this fact, see Figure 1-12 and notice that the part of the spectrum in this frequency range is almost completely outside human hearing threshold. Because of this fact and of comparison with other common sources of high intensity LFN present in the everyday day life, some authors claim that LFN does not play a relevant part on the WTN problem (Leventhall, 2013), while others pursue theories to establish causal effects that might explain real complaints from people who live nearby WT farms (Schomer, Erdreich, Boyle, & Pamidighatam, 2013). Also, Styles et al. (Styles, Westwood, Toon, Buckingham, & Marmo, 2011) explain that LFN from WT propagates through the ground for dozens of miles and affect the seismic monitoring stations network.

One possible element of liaison between WT LFN and neighboring restlessness is the possibility of human perception of vibrations induced in the buildings. For instance, Bistafa (Bistafa, 2011), p. 282, provides a chart where the critical frequency for typical construction panels can be easily determined as a function of panel thickness and material. Thicker panels have lower critical frequencies. As a matter of fact, Hubbard and Shepherd (Hubbard & Shepherd, 1990) explained long ago that one of the common ways for a person to sense noise-induced excitation of a house is through structural vibrations, a mode of observation particularly significant below the threshold of normal hearing. Because of their typical materials and dimensions, window panels seem particularly susceptible to WT LFN interaction.

2.1.4 Inflow-Turbulence Noise

According to Eisele et al. (Eisele, Pechlivanoglou, & Nayeri, 2013), the operational regime for WT blades is characterized by high atmospheric turbulence. The key parameters influencing the noise generation by inflow turbulence, however, have not been fully understood, but it is recognized that the shape of the airfoil and of the leading edge is of great importance (Wagner, Bareiß, & Guidati, Wind Turbine Noise, 1996).

It was mentioned in section 2.1.1.2 that the interaction mechanism among turbulent flow and the airfoil depend upon the turbulent length scale, which is, in the case of inflow-turbulence noise, the atmospheric turbulent scales.

As seen in Figure 2-4, the typical hub height of a modern, large size HAWT is in the range 75 - 100 m ($1,5 R - 2,0 R$).

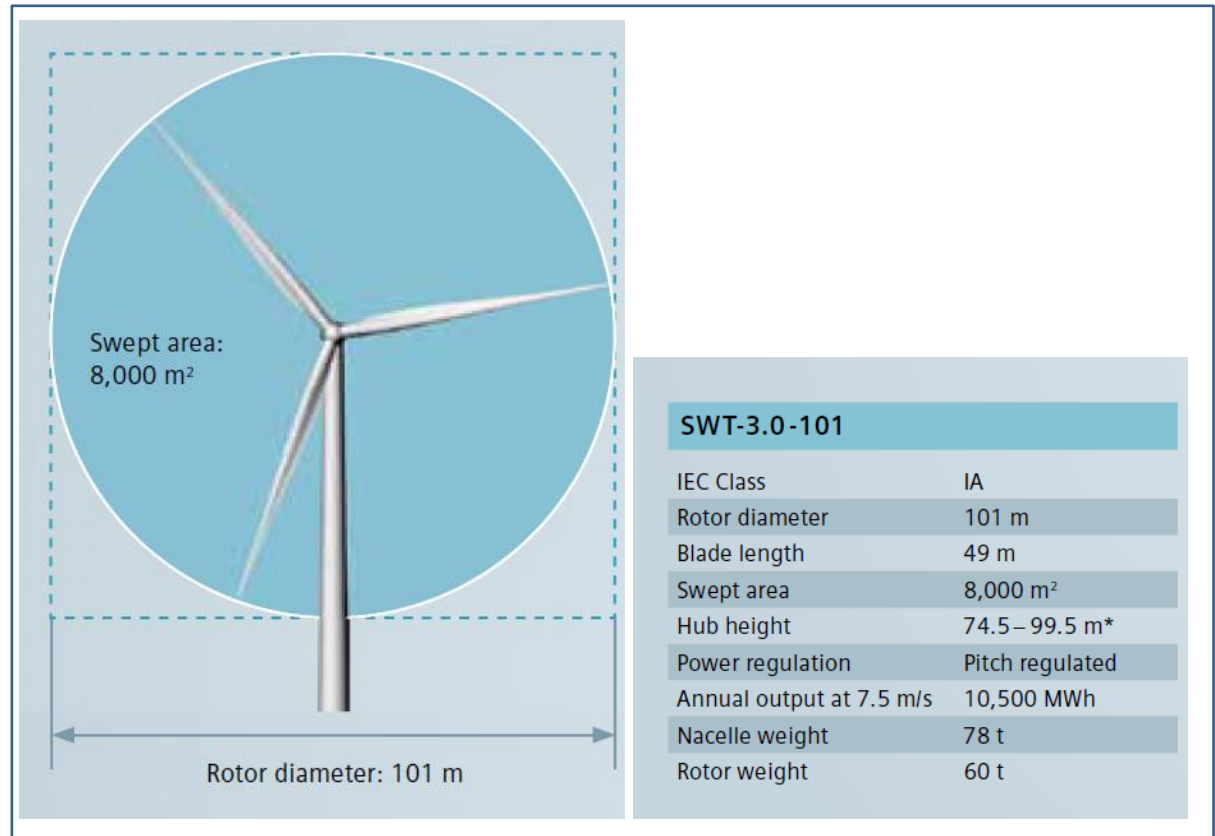


Figure 2-4 – Swept area, hub height and other basic data for Siemens SWT-3.0-101 WT, the smallest onshore WT of the D3 (direct-drive, 3 MW) series, offered by the manufacturer (Siemens, 2013).

For large scale turbulent flow, measurements of two point velocity correlations show that the velocity is appreciably correlated over distances comparable to the flow width (Pope, 2011), p. 178. This translates into the largest scales of turbulent motions scaling with the height of the WT. Because of the Richardson's concept of the energy cascade (Davidson, 2009), (Pope, 2011), the turbulence may be considered to be composed of eddies of different sizes, cascading from the integral, energy containing scale, to Kolmogorov's dissipative scale. In between, all intermediate "inertial range" scales are visited, by means of the vortex stretching mechanism. According to Pope (Pope, 2011), stability theory has been successful in explaining the structure of the large-scale motions, which support the view that these motions arise from the instabilities inherent in the various flows, as for the case of the atmospheric boundary layer.

In order to understand the distribution of wind energy at this typical tower height, the experimental data of Van der Hooft (1957), as reported by Burton et al. (Burton, Sharpe, Jenkins, & Bossanyi, 2008), may be employed. As shown in Figure 2-5, the energy peaks may be related to synoptic weather variation, daily variation and

turbulence itself. The peak around 1 minute period ($f \approx 0.02 \text{ Hz}$) is associated with real gust spectrum and is where the most intense energy is located in the short term measurements. The energy decreases with decreasing period (increasing frequency) and the decreasing model is typically proportional to $f^{-5/3}$ (Pope, 2011), p. 189, in the inertial range. Also Figure 2-5 shows that there is no relevant process in the atmosphere, at this measurement height, between 2 hours and 10 minutes periods. This is probably the reason why measurement standards recommend that wind speeds be averaged over the typical 10-minute intervals, to minimize measurement errors (IEC61400-12-1, 2005), (Measnet, 2009).

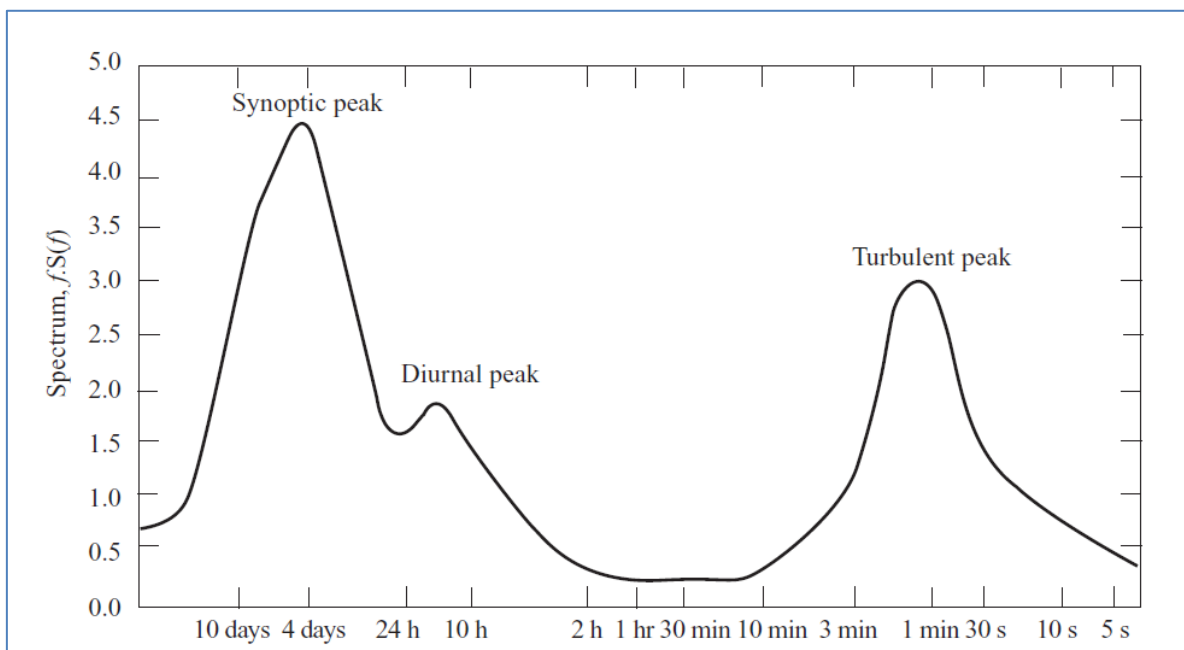


Figure 2-5 – Wind velocity spectrum for short and long term at Brookhaven, NY, at 100 m height, as measured by Van der Hoven (1957) and reported by (Burton, Sharpe, Jenkins, & Bossanyi, 2008). The abscissas axis represents the periods, in log scale.

According to Wagner et al. (Wagner, Bareiß, & Guidati, Wind Turbine Noise, 1996), if the local flow velocity at the blade is denoted by U , and the length scale of the turbulent eddy is Λ , the disturbances occur at frequency $f = U/\Lambda$, which will be approximately the same frequency of the radiated noise $f = c_0/\lambda$. The authors assembled a table similar to Table 2-2, where they estimated the eddy sizes that produced noise in some frequencies of the audio range for a WT operating at a Mach number of 0.25.

Table 2-2 – Typical eddy-size to chord-size ratios for some frequencies of audio noise emitted by turbulent eddies. Adapted (range enlarged) from (Wagner, Bareiß, & Guidati, Wind Turbine Noise, 1996).

Frequency [Hz]	$f = c_0/\lambda$	10	85	100	500	2000	4000	8000	16000
Wavelength [m]	$\lambda = c_0/f$	34.00	4.00	3.40	0.68	0.17	0.09	0.04	0.02
Eddy Size [m]	$\Lambda = U/f = U/c_0/\lambda = M \cdot \lambda$	8.5	1	0.85	0.17	0.043	0.021	0.011	0.005

If the typical WT chord size (c) is 1 m, the eddy-size is of the same order of the airfoil chord dimension for $f \approx 85$ Hz. Only below that frequency, i.e. in the infrasound portion of the audio range, the airfoil can be considered a compact source. In this case, $\Lambda/c \gg 1$, and the passage of the eddy by the blade will change the loading over the entire blade, giving rise to a compact dipole-type source, generating LFN as seen on Eqn. (2-3), where $I \propto M^6$.

On the other hand, if the eddy size is comparable to or smaller than the blade chord, $\Lambda/c < 1$, as will happen for higher frequencies, the blade cannot be considered acoustically compact. The eddy will not engulf the whole foil, and will be deformed close to the airfoil LE, changing the blade loading only locally. This will originate an edge-type source²³, generating HFN as seen on Eqn. (2-2), and $I \propto M^5$.

2.1.5 Airfoil Self-Noise

By referring to Table 2-1, there are six sources classified under *Airfoil Self-Noise*, which will be further discussed below.

2.1.5.1 The Trailing-Edge Noise

²³ Similar to a Trailing Edge source, except for the turbulence length scale, which is $\gg \delta^*$

This source of noise is typical of the outboard sections of the WT blade, when $Re_c > 1 \times 10^6$, the established flow is turbulent and the flow remains attached up to the TE. As highlighted before, this is considered the main source of high frequency noise (750 Hz $< f < 2$ kHz) for large, modern WT, in low Mach number, smooth inflow regime (Brooks, Pope, & Marcolini, *Airfoil Self-Noise and Prediction*, 1989); (Hubbard & Shepherd, 1990), (Wagner, Bareiß, & Guidati, *Wind Turbine Noise*, 1996).

More recently, acoustic field measurements accomplished within the European research project SIROCCO context, confirmed that the TBL-TE noise is the dominant noise mechanism for large wind turbines (Oerlemans, Sijtsma, & Méndez-López, *Location and Quantification of Noise Sources on a Wind Turbine*, 2007), (Kamruzzaman M. , Lutz, Nübler, & Krämer, 2011), (Oerlemans, *Wind Turbine Noise: Primary Noise Sources*, 2011). This information will be further confirmed by the typical WTN spectrum that will be shortly presented.

It was shown earlier that turbulence noise is of the quadrupole type, thus a poor noise radiator. The features that transform this otherwise poor radiator into the most relevant noise mechanism are the boundaries present in the flow. The boundaries may be represented by surface distributions of monopoles and of dipoles, which are more efficient noise radiators (see section B.9.2).

The seminal investigation on this type of source is the work of FW-Hall (Ffowcs-Williams & Hall, 1970). For the eddies to produce any sound amplification while convecting along the edge, they must be close enough to the edge so that $kr_0 \ll 1$, where, k is the wave number and r_0 is the distance between the center of the eddy and the edge. For the eddies that match this requirement, the noise output from the turbulence quadrupoles are amplified by a factor of $(kr_0)^{-3}$ and the far field noise intensity associated with these sources depends on the fifth power of the typical fluid velocity. The exact shape of the TE is of importance only for relatively high-frequencies (Wagner, Bareiß, & Guidati, *Wind Turbine Noise*, 1996), while the properties of the surface might influence the directivity function (Ffowcs-Williams & Hall, 1970).

2.1.5.2 The Tip Noise

Since the local flow velocity is largest at the tip of the rotating WT blades and all noise sources originated from the interaction between the boundary layer and the airfoil discussed so far display a fifth or sixth order dependence on the flow speed, it may be expected that the outboard portion of the blades, closest to the tips, will radiate most of the noise. Indeed, this fact may be fully confirmed in Figure 2-6.

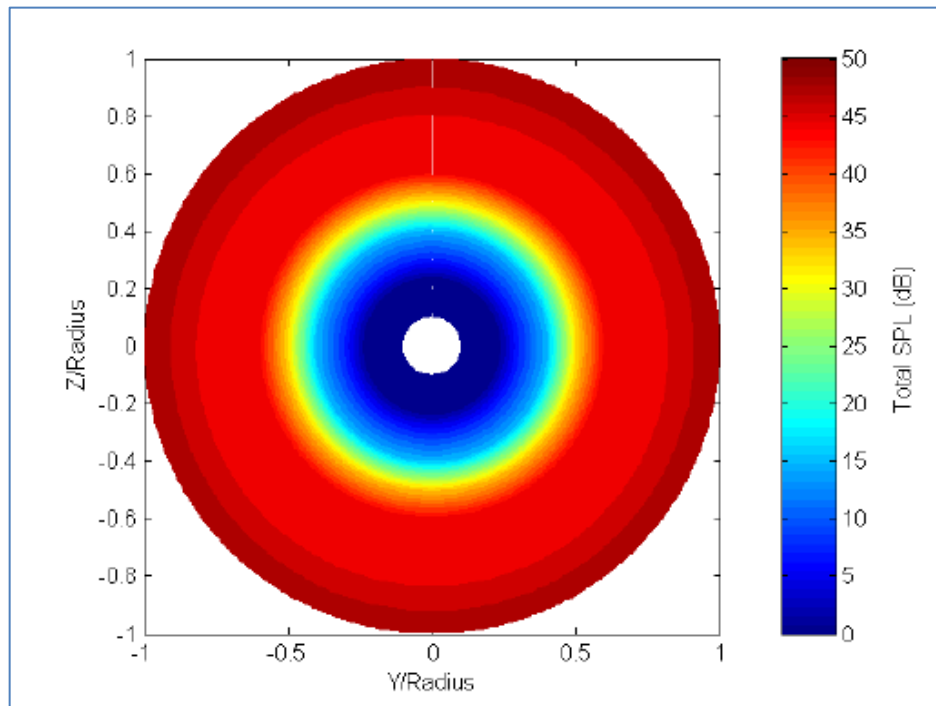


Figure 2-6 - Average distribution, over 5 minutes, of noise sources that contribute to total SPL, as observed 32.5 m upwind, at the height of the hub, for an AOC WT in steady 8 m/s wind with no turbulent inflow noise (Moriarty & Migliore, Semi-Empirical Aeroacoustic Noise Prediction Code for Wind Turbines, 2003).

In practice, when the difference in pressure level between two regions is larger than 15 dB, the contribution of the lower source may be neglected (see, for instance (Bistafa, 2011), page 39, Fig. 3.8). In the case of the AOC WT depicted in Figure 2-6, operating in 8 m/s wind with no inflow noise, this translates into practical terms as all relevant noise sources being in the outboard range of the rotor, or $r/R > 0.5$.

This is also confirmed by other field measurements by Oerlemans (Oerlemans, Wind Turbine Noise: Primary Noise Sources, 2011), as depicted in Figure 2-7.



Figure 2-7 - Average distribution, over many revolutions, of the noise source distribution in the azimuthal plane, for a typical, modern, large-size WT, projected over a picture of the WT, for illustration purposes only (Oerlemans, Wind Turbine Noise: Primary Noise Sources, 2011)

Apart from being a region of high flow velocity and noise radiation, there seems to be no remarkable contribution from the particular 3D-flow around the tip, for the overall noise radiated. Brooks et al. (Brooks, Pope, & Marcolini, Airfoil Self-Noise and Prediction, 1989) compared 2-D and 3-D airfoil noise data, for the same airfoil and flow conditions, and proposed a high frequency, broadband model for this source. A direct spectra comparison for the 2-D and 3-D cases (p. 72 of the reference) shows that only the 1/3 octave bands above 12 kHz were increased by 1-2 dB. It is important to add that the airfoil was at the significant angle of attack (AOA) of 10.8° , since the airfoil employed was the symmetrical (NACA 0012) and it is naturally necessary to produce lift for the induced-drag vortex to be present around the blade tip.

2.1.5.3 The Stall-Separation Noise

While for attached flow the TE Noise is the dominant mode, beyond stall the separation noise is the dominant Airfoil Self-noise mode. At stall, the noise may increase by more than 10 dB relative to TE Noise emitted by low-alpha, attached flows (Brooks, Pope, & Marcolini, Airfoil Self-Noise and Prediction, 1989). According to the same authors, there were no predictive models for Separation Noise then, and also the extensive bibliographic research accomplished since then did not unveil any such model.

According to Eisele et al. (Eisele, Pechlivanoglou, & Nayeri, 2013), a HAWT may induce very high AOAs under certain specific conditions like during the *cut-out*²⁴ phase or transient, low-rpm, high wind speeds which could make the stall separation a problem. On the other hand, there are no models for such a noise source. A direct discussion with one of the authors (Georgios Pechlivanoglou), led to the conclusion that a well-designed rotor is made up of blade sections stacked along the chord in such a way (geometry, chord and twist) as to result in the most efficient, attached flow possible for producing torque. The stalled condition may be real, but should be treated like a transient, non-frequent situation, far away from the design point.

According to Brooks et al. (Brooks, Pope, & Marcolini, Airfoil Self-Noise and Prediction, 1989), a successful noise prediction method for this source would have to consider the gradual increase of noise from separation, as the airfoil angle of attack is increased and becomes dominant at deep stall.

2.1.5.4 The Laminar Boundary Layer Noise

When the rotor blades, or a section, operate at or under the transition Reynolds number ($Re < 10^6$), the laminar flow region might extend up to the TE in certain conditions. In this case, a resonant interaction, of tonal nature, might occur as the TE noise waves travel upstream and couple with the Tollmien-Schlichting waves of the laminar BL,

²⁴ The *cut-out* speed is the wind speed that drives the WT to its operational upper limit in terms of rotational speed. It is chosen to protect the turbine from exceeding the design loads, and it is usually around 25 m/s (Burton, Sharpe, Jenkins, & Bossanyi, 2008). The *cut-in* speed is determined by the transmission losses and represents the wind speed at which the WT starts to generate net power.

producing vortex shedding. The noise tones produced are related to the vortex shedding frequency at the TE (Brooks, Pope, & Marcolini, Airfoil Self-Noise and Prediction, 1989). Also, in the case of the laminar flow described, a laminar separation bubble may occur.

Both phenomenae, the non-linear process of feedback of the noise on the instabilities of the laminar flow and the formation of the laminar bubble, may originate tonal noise, but these mechanisms are usually more relevant for small scale WT, where $Re < 10^6$ (Oerlemans, Wind Turbine Noise: Primary Noise Sources, 2011), and even then the tonal noise may be prevented by tripping the boundary layer far upstream of the TE.

2.1.5.5 The Blunt Trailing-Edge Noise

The frequency f_s of vortex shedding behind cylinders of diameter d is a simple function of the Strouhal number, which is a function of the Reynolds number only.

$$\frac{f_s d}{U_\infty} = F\left(\frac{U_\infty d}{\nu}\right) \quad (2 - 4)$$

On the other hand, the problem of vortex shedding from lifting surfaces is much more complex (Blake, Mechanics of Flow-Induced Sound and Vibration, 1986 I), involving viscous boundary regions on the surface and details of the geometry of the trailing edge. Blunt, i.e., non-sharp TE edges may be characterized by thickness, radius, or angle, depending upon the type of geometry. At table 11-3 of Blake (Blake, Mechanics of Flow-Induced Sound and Vibration, 1986 II), the Strouhal number for sharp and blunt TE airfoil geometries can be found as function of the flow regime and bluntness parameter, h/δ^* , where h is the TE thickness.

As the bluntness parameter increases above 0.25, $h/\delta^* > 1/4$, a secondary hump appears in the sound spectrum and it increases in energy and decreases in band-width (Blake, Mechanics of Flow-Induced Sound and Vibration, 1986 I), becoming eventually a tonal noise, frequently described in the bibliography as airfoil *singing* noise, for large enough h/δ^* ratio. The reason for this behavior is that fluctuating forces will prevail,

resulting in dipole noise of tonal character (Wagner, Bareiß, & Guidati, Wind Turbine Noise, 1996).

This tonal noise may be illustrated by looking at the spectrum depicted earlier at Figure 1-12, provided the data of 1/6 octave or higher resolution is considered. Also, Figure 2-8 shows the distinctive signature of blunt TE noise. For the tripped case, a secondary hump is formed and for the untripped case a quasi-tonal noise is characterized.

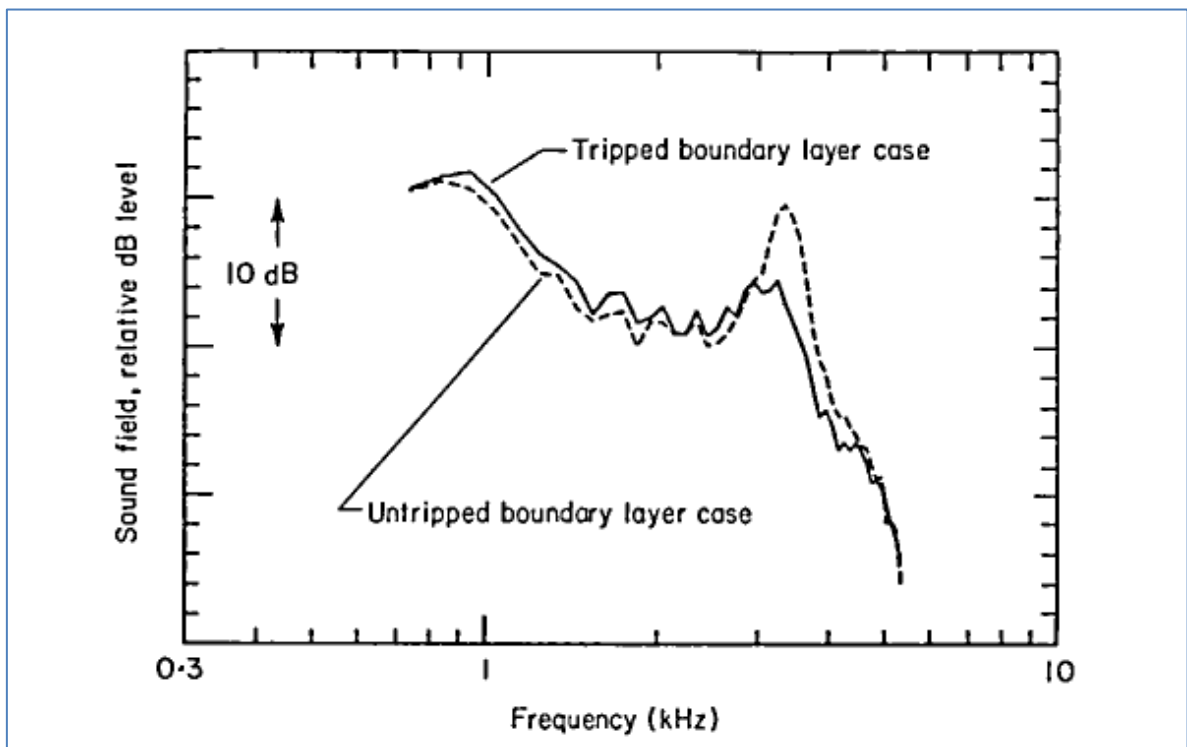


Figure 2-8 – The sound spectrum for a blunt TE NACA0012 airfoil, with spectral “hump” near 3 kHz (Brooks & Hodgson, 1981).

Figure 2-9 shows the effect of sharpening the TE on the noise spectrum.

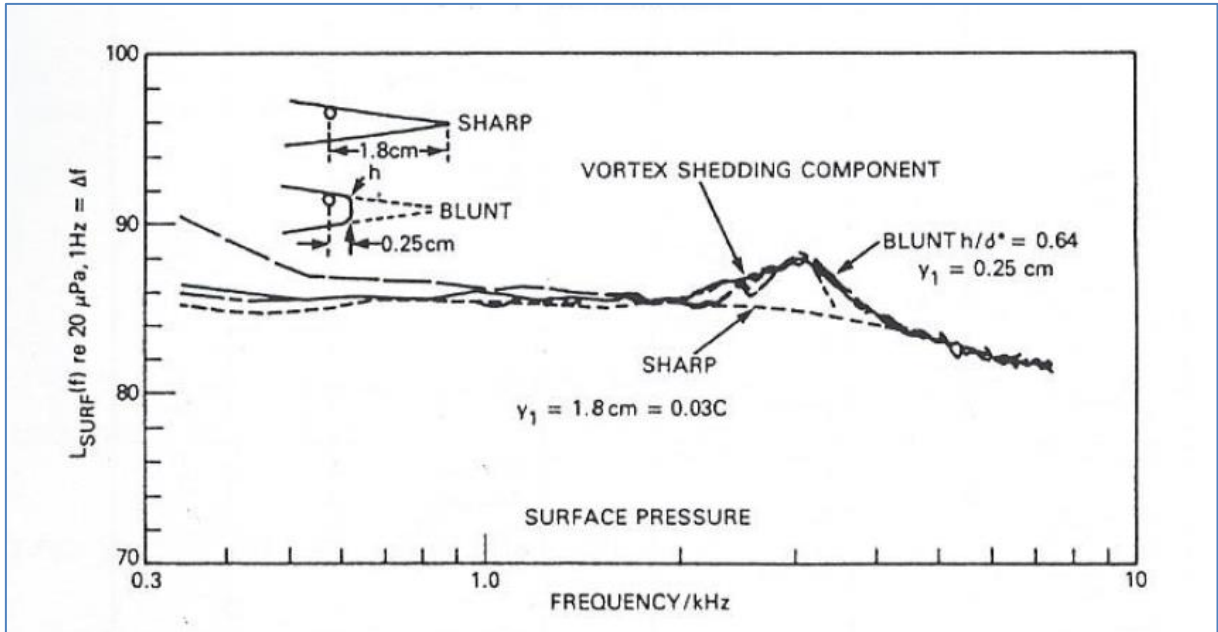


Figure 2-9 – Radiated sound for sharp and blunt TE NACA0012 airfoil, LE tripping (Brooks & Hodgson, 1981) data, adapted by (Blake, Mechanics of Flow-Induced Sound and Vibration, 1986 II).

Figure 2-10 shows a direct comparison of WT broadband spectra for sharp and blunt TE blades for a medium-sized 50 kW wind turbine.

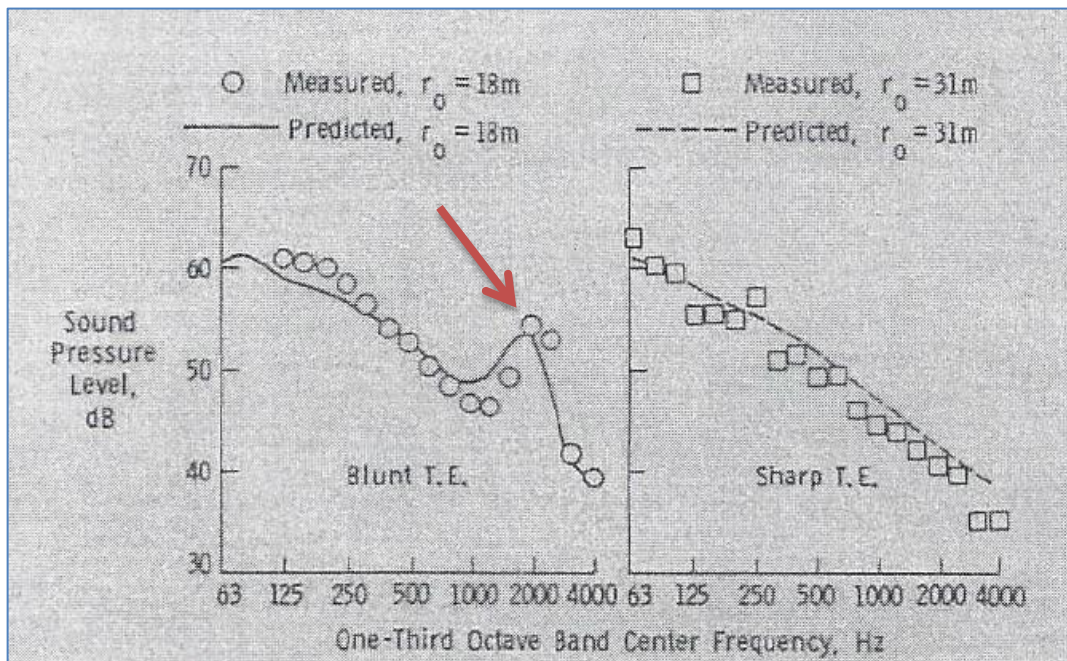


Figure 2-10 – Measured (continuous lines) broadband noise spectra for a U.S. Wind Power Inc. machine with blunt and sharp TE (Grosveld, 1985).

A broad comparison study of typical TE shapes and their relative amplitudes of tones (singing) may be found in Blake (Blake, Mechanics of Flow-Induced Sound and Vibration, 1986 II), p. 761. Figure 2-11 shows a summary of geometries and relative tone noise amplitudes. It is worth noticing that some simple TE geometries may reduce the singing to 1% or less, compared to the fully blunt TE configuration.

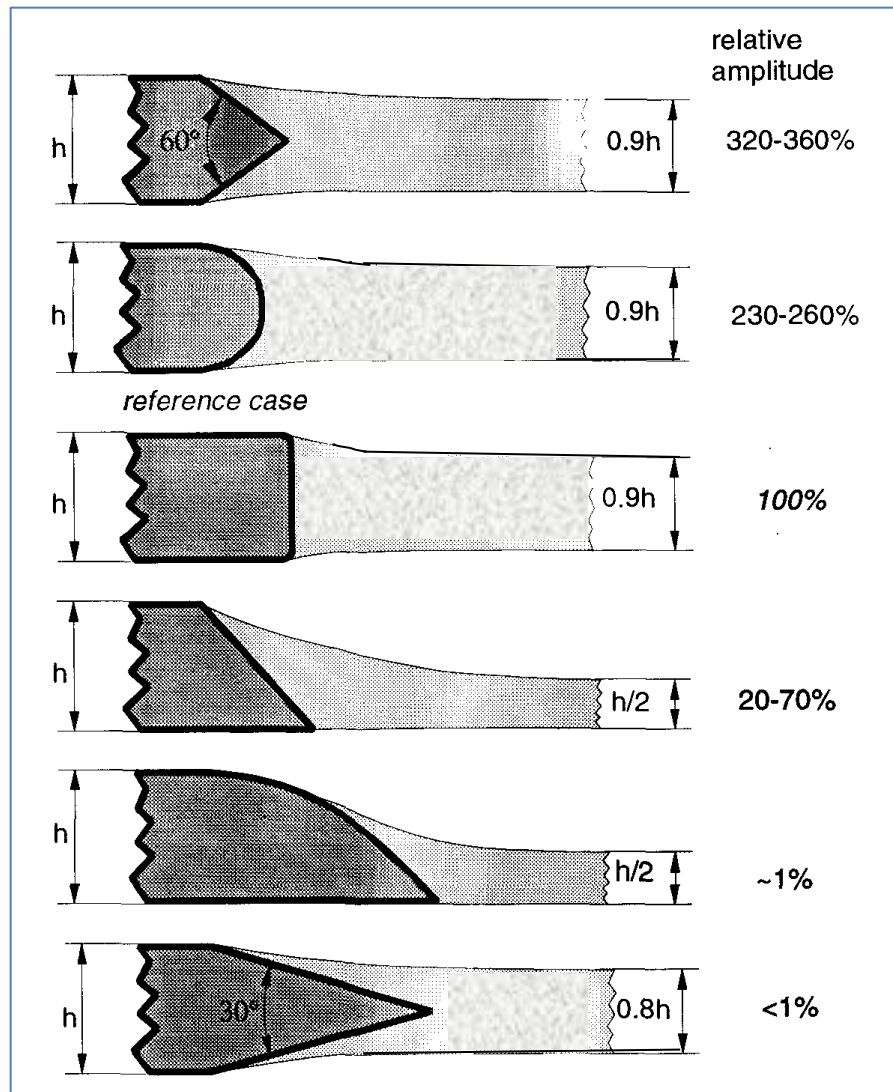


Figure 2-11 – A summary of airfoil TE shapes and relative tone noise amplitude, (Wagner, Bareiß, & Guidati, Wind Turbine Noise, 1996).

According to Grosveld (Grosveld, 1985), the smaller the TE thickness, the higher the peak frequency of shedding, so that sharpening the TE effectively shifts the peak away from the audio range, to the ultra-sound region of the spectrum. The practical limit of sharpening the TE is of major concern for construction and installation purposes and it is important to recognize, when modeling, that there exists no fully sharp TE in

practice. While Wagner et al. (Wagner, Bareiß, & Guidati, Wind Turbine Noise, 1996) consider the typical TE thickness to be in the 1-3 mm range, depending on the blade chord and operation condition, a consultation made directly with the industry (Sloth, 2011) revealed that, for current, large size WT, TE thicknesses are typically specified in the range of 2 to 5 mm for the 1/3 outboard part of the blade, but are often seen manufactured with thicknesses from 10 to 20 mm. Chord lengths in this blade range (50 m span) are typically 0.6 to 1 m - leading to a specified TE percentage of 0.2 to 0.8 % chord, and realized percentages of 1 to 3% of the chord.

The evaluation of the consequences of the TE thickness in the blade singing sensitivity will depend not only on the thickness dimension itself, but also in the geometry of the TE, as seen above, and also on the boundary layer displacement thickness at the TE.

2.1.5.6 Noise from Flow over Holes, Slits and Intrusions

Deviations from design geometry do not occur solely in the blade TE thickness. The overall blade shape may display geometric deviations due to manufacturing tolerances, but also imperfections may originate or aggravate during the WT assembly, erection and operation. The classic situations that will add to geometrical imperfections and surface roughness are hail storms, lightning strikes, bird impact, insect impact (which will stick to the surface), dust, oil, loose tapes and slits.

There seems to be some different points-of-view concerning the consequences of the described surface imperfections. While Wagner et al. (Wagner, Bareiß, & Guidati, Wind Turbine Noise, 1996) state that any unwanted disturbance to the flow around the blade may cause additional noise, Brooks and Hodgson (Brooks & Hodgson, 1981) showed that a tonal noise may be avoided by the tripping of the BL, which is triggered by the imperfections described.

While Oerlemans (Oerlemans, Wind Turbine Noise: Primary Noise Sources, 2011) expects the boundary layer on either side of the airfoil might remain laminar up to the trailing edge for chord-Reynolds number below 1×10^6 , the reality of the operating conditions seems to be very different, as Eisele et al. (Eisele, Pechlivanoglou, & Nayeri, 2013) report that WT field tests could not reproduce low turbulence wind tunnel

test data since the presence of even the small surface waviness and dust were enough to cause boundary layer transition. Since the cumulative presence of dust, dents, scratches and insects seems the rule rather than exception in the operating environment of such large equipment, Oerlemans' assertion in this matter seems to be applicable only to the realm of small scale WT or brand-new equipment.

Like in any other typical design, an engineering tradeoff has to be achieved between the noise sources, and it is important to remember that the main objective of the WT manufacturer is the energy conversion performance of the equipment. The more recent noise-constraint requirements are additive to those and do not replace or take priority over them.

2.1.5.7 Relative relevance of Wind Turbine noise sources

A typical noise spectrum measured for one HAWT by T.H. Pedersen was presented in Figure 1-11. It is not feasible, in the field, to obtain the experimental spectrum radiated from the individual self-noise sources. Nevertheless, the total noise spectra may be inferred from partial models, validated to some extent for each of the individual sources, against wind tunnel or jet-flow potential-core tests. These modeling tools, which will be further discussed in the following sections, make it possible to evaluate the relative importance of the individual noise sources.

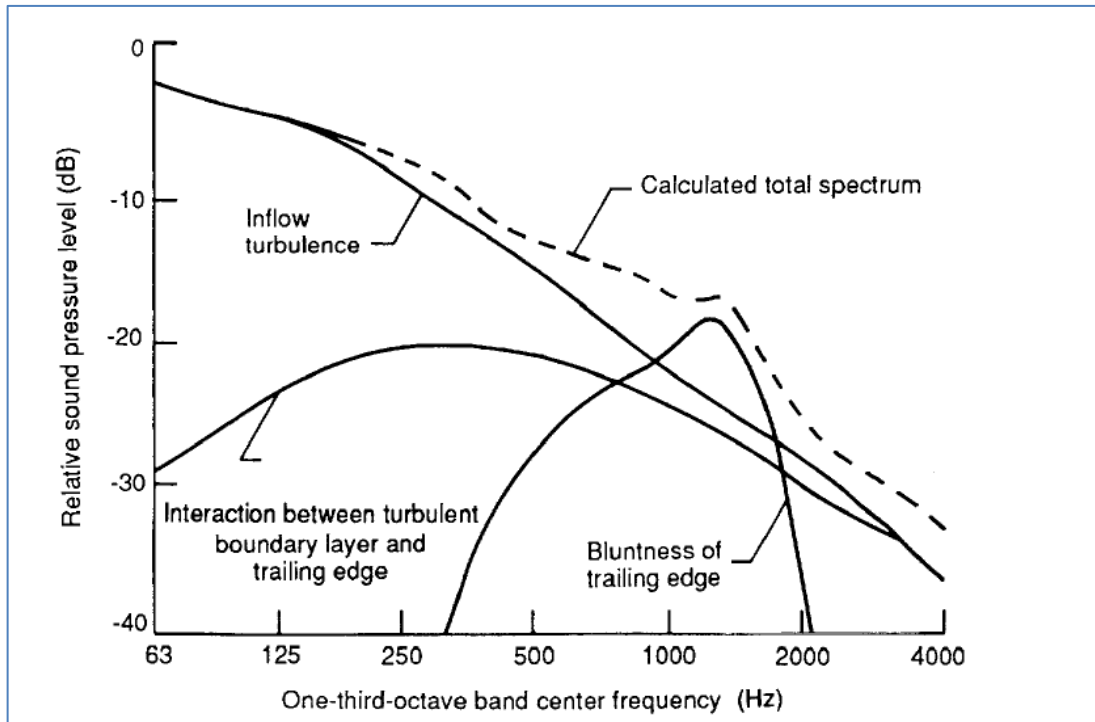


Figure 2-12 - Broadband noise prediction contributions, from different mechanism noise sources, at 100 m from a MOD-2 WT, operating in a 9.8 m/s wind and producing 1.5 MW (Grosveld, 1985).

First, by considering all aerodynamic noise sources, i.e. LFN, inflow turbulence and airfoil self-noise, Grosveld (Grosveld, 1985) shows the broadband noise prediction contributions at a distance of 100 m, calculated over the axis line of a MOD-2²⁵ HAWT.

Figure 2-12 shows that inflow turbulence is the dominant mechanism in the low frequency range, while the interaction noise, between the TBL and the TE edge, steadily grows and later decays after the peak (Strouhal dependent) reaching an SPL level equivalent to the inflow noise close to 1 kHz and higher. The TE bluntness also has a broadband nature but is marked by a tone between 1 kHz and 2 kHz. The total spectrum has close qualitative resemblance (provided the difference in abscissas range is observed) to the total measured spectrum in Figure 1-11, including the spike above 1 kHz, due to TE bluntness.

²⁵ The MOD-2 HAWT was the precursor of the modern HAWT in many aspects, having been designed by NASA and manufactured by Boeing from 1982 to 1988. The equipment had a 91 m diameter rotor in an upwind position, but the rotor had only two blades.
<http://www.boeing.com/history/products/mod-2-mod-5b-wind-turbine.page> accessed on June,2016.

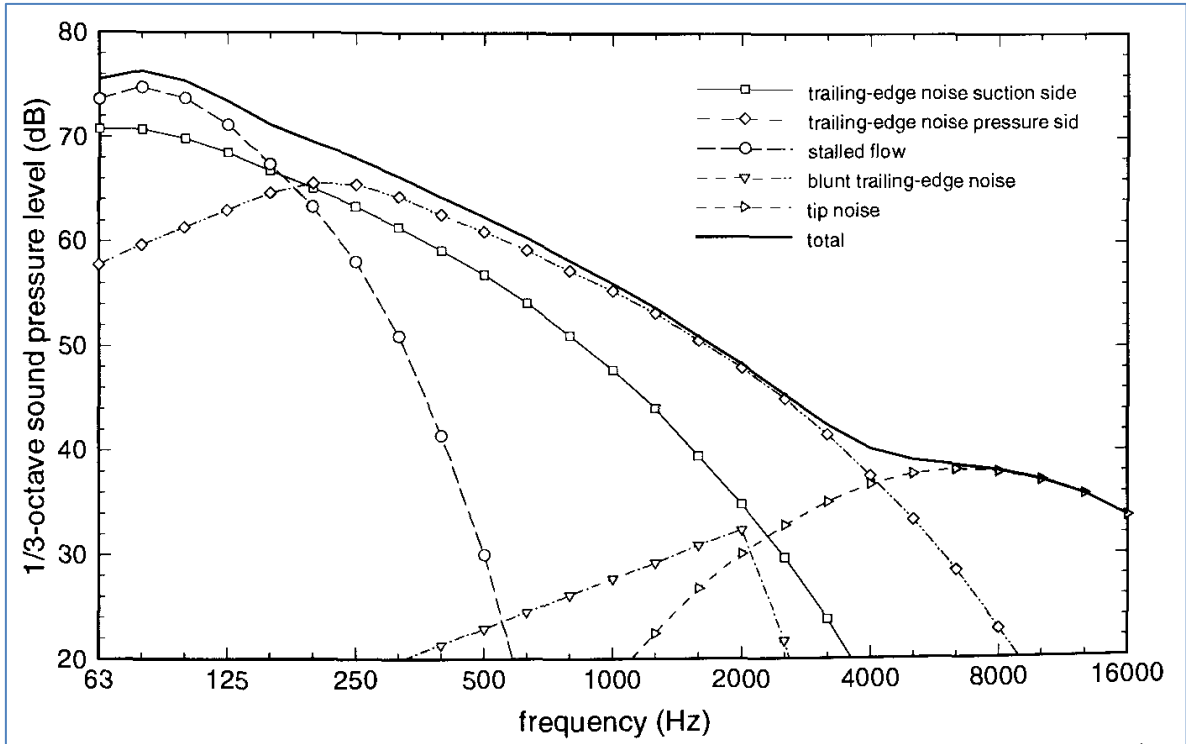


Figure 2-13 - Calculated contributions of airfoil self-noise individual sources, for a WT blade, and the total SPL spectrum, after (Bareiss, Guidati, & Wagner, 1994).

Figure 2-13 displays only airfoil self-noise spectra calculated for a blade, from models of individual contributions of the different mechanisms, plus the total noise spectrum. It is evident from the figure that the blade spectrum is dominated by the TE noise for most of the frequency range and then by the tip noise. While it seems that stalled flow contribution is sizeable, it is restricted to low frequencies and should become less important after A-weighting of the SPL, under the criterion of audio annoyance only. As a proof of this statement, Figure 2-14 shows an example of A-weighted, 1/3 octave band spectrum from a large, modern General Electric WT, with all the relative contributions from the flow-induced noise mechanisms (Petitjean, Drobietz, & Kinzie, 2011).

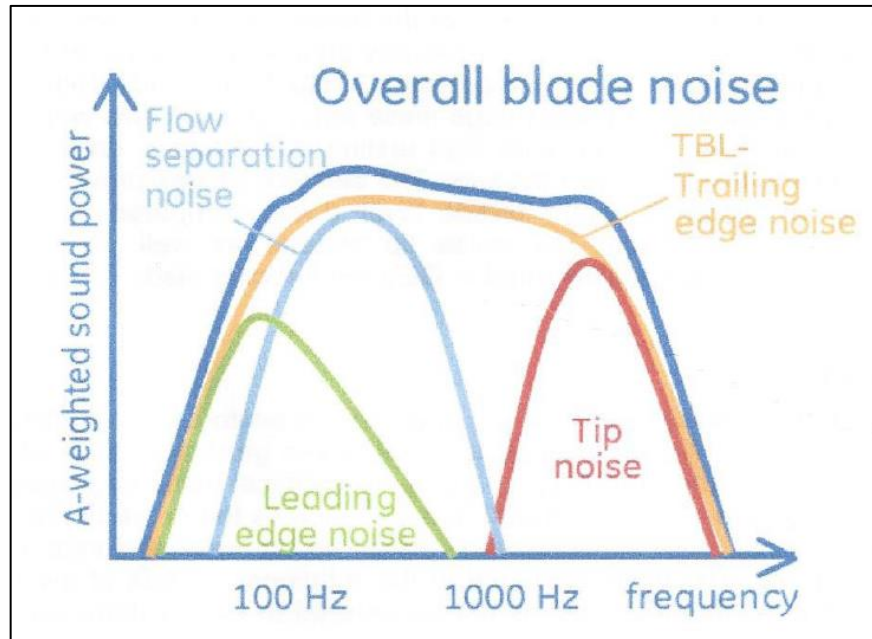


Figure 2-14 - A-weighted, 1/3 octave band spectrum from a large size, modern construction General Electric WT, with relative contributions from the most relevant flow-induced noise mechanisms (Petitjean, Drobiez, & Kinzie, 2011) for this kind of equipment.

All spectra discussed strongly suggest that the most relevant mechanism of aerodynamic noise generation in a modern, large size WT in nominal wind speed conditions, non-stalled operation, is the TE noise.

It is possible to conclude that the desired characteristics for a well-designed WT rotor, in respect to noise emission, would include a blade optimized for low TE noise and Tip noise, while being as much insensitive as possible with regards to inflow noise. Also, all those characteristics would have to subtract little from the blade capability to perform an efficient energy conversion.

For considerations on the wind speed distribution, the reader is referred to Appendix C.

At this point of the bibliographic review it is possible to foresee that a “quiet blade” concept would have to encompass several good manufacturing practices and probably a family of tailor-made airfoils, to be used in a blade with controlled chord and twist along the spanwise distribution.

2.2 CONSIDERATIONS ON INFLOW TURBULENCE

Inflow turbulence noise, although not a primary objective of this research, is a relevant source of noise, with strong dependence on the turbulence intensity of the inflow air. Inflow noise is essentially uncontrolled once the Wind Farm siting place has been chosen.

The turbulence intensity, Tu , for which a WT must be designed to meet, is specified in IEC 61400-1 standard (Burton, Sharpe, Jenkins, & Bossanyi, 2008) in two categories, A (higher turbulence area) and B (lower turbulence area), which are independent of the wind speed:

$$Tu = \frac{u'}{\bar{U}} = \frac{Tu_{15} \left(a + \frac{15}{\bar{U}} \right)}{a + 1} \quad (2 - 5)$$

where Tu_{15} is the turbulence intensity at mean wind speed of 15 m/s, defined as 18% for category A and 16% for category B type equipments. \bar{U} is the mean wind speed at hub height and $a = 2$, for category A and $a = 3$ for category B.

As an example, for $\bar{U} = 10$ m/s at hub height, the resultant turbulence for category A turbulence, would be $Tu_{10} = 0.21$ or 21%.

These conditions are very extreme and are probably defined in view of the structural sizing of the machines.

2.3 THE UTILITY-SIZE HORIZONTAL AXIS WIND TURBINE (HAWT)

The purpose of the Wind Turbine is to extract as much energy from the wind as possible and each component of the turbine has to be optimized accordingly. The blade design is influenced by the mode of operation of the turbine (Burton, Jenkins, Sharpe, & Bossanyi, 2011) i.e. fixed or variable rotational speed and, in an ideal situation, also by the local wind distribution at the site. Despite the always present engineering design tradeoffs, it is necessary to understand operational conditions so as to develop the best possible design.

The current, utility-size Wind Turbine is a large diameter, lift-type, variable speed, 3 bladed rotor, upwind, horizontal axis machine. According to Hahn et al. (Hahn, Durstewitz, & Rohrig, 2005), the average technical availability is high, around 98%.

While manufacturers tend to increase WT diameter, as discussed in section 1.1.2, there are some clear constraints to that trend: the material technology necessary to cope with tensile stress and bending moments at the root of the spinning blades, the erosion at the blade Leading Edge, the increasing cost of the blades with size and the need to keep the noise emission under control²⁶. For detailed discussions on current HAWT layout and design tradeoffs see Burton et al. (Burton, Jenkins, Sharpe, & Bossanyi, 2011), pp.325-346.

Figure 2-15 shows the general layout of a modern HAWT, with the two most important characteristic lengths, the hub height and the rotor diameter, while Table 2-3 shows an example of rotor-blade geometrical characteristics, including chord, thickness and twist as a function of the span position, for a small-size blade.

²⁶ These current limitations for the WT industry were learnt directly from a designer of large WT blades (Sloth, 2011).

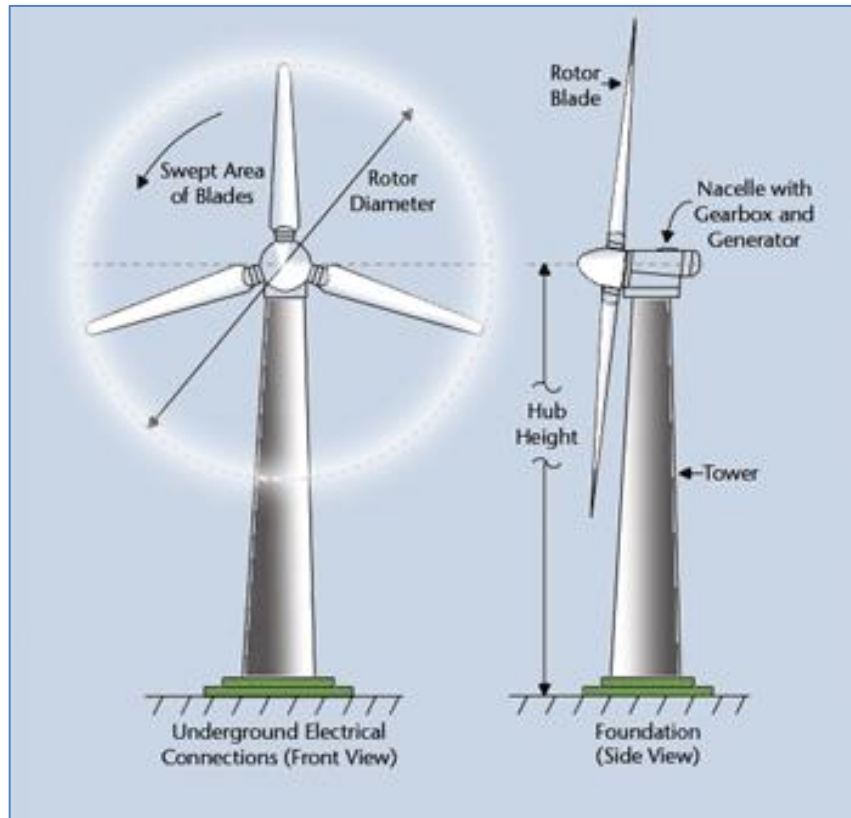


Figure 2-15 - A modern HAWT general layout with indication of the two most important linear dimensions: the hub height and the rotor diameter. Source: European Wind Energy Association.

Table 2-3 - Geometric characteristics of the rotor-blade for the SERI 7.9 m Airfoil Blade developed at Stanford University (Ong & Tsai, 2000).

SERI 7.9m Thin Airfoil Blade

Part	1	2	3	4	5	6	7	8	9	10	11	12	13
Station, in	12	36	60	84	108	132	156	180	204	228	252	276	300
Min, m	0.000	0.610	1.219	1.829	2.438	3.048	3.658	4.267	4.877	5.486	6.096	6.706	7.315
Mid, m	0.305	0.914	1.524	2.134	2.743	3.353	3.962	4.572	5.182	5.791	6.401	7.010	7.620
Max, m	0.610	1.219	1.829	2.438	3.048	3.658	4.267	4.877	5.486	6.096	6.706	7.315	7.925
Mass, lbm	184.09	67.05	62.64	49.13	36.38	31.10	28.72	25.75	27.75	38.41	53.85	27.18	10.35
Mass, kg	83.50	30.41	28.41	22.28	16.50	14.11	13.03	11.68	12.59	17.42	24.43	12.33	4.69
Chord, in	17.83	29.43	44.00	43.09	41.42	39.27	36.71	33.81	30.61	27.13	23.38	19.40	15.19
Chord, m	0.453	0.748	1.118	1.094	1.052	0.997	0.932	0.859	0.777	0.689	0.594	0.493	0.386
Thickness, m	0.453	0.369	0.235	0.203	0.183	0.165	0.146	0.129	0.111	0.094	0.076	0.060	0.044
Half Thick, m	0.226	0.185	0.117	0.101	0.091	0.082	0.073	0.064	0.056	0.047	0.038	0.030	0.022
Thick/Chord	1.000	0.494	0.210	0.185	0.174	0.165	0.157	0.150	0.143	0.136	0.129	0.121	0.115
Lead Edge, m	0.226	0.289	0.346	0.331	0.319	0.300	0.269	0.258	0.242	0.208	0.181	0.162	0.123
Trail Edge, m	0.226	0.459	0.772	0.763	0.733	0.697	0.663	0.601	0.535	0.481	0.413	0.331	0.263
Twist, deg	29.85	26.28	20.00	14.81	10.61	7.29	4.74	2.87	1.57	0.74	0.27	0.06	0.00
90-Twist	60.15	63.72	70.00	75.19	79.39	82.71	85.26	87.13	88.43	89.26	89.73	89.94	90.00
Top-TE-Yr	0.084	0.329	0.685	0.712	0.704	0.681	0.655	0.597	0.534	0.480	0.413	0.331	0.263
Top-TE-Zr	-0.309	-0.368	-0.374	-0.293	-0.225	-0.170	-0.128	-0.094	-0.070	-0.053	-0.040	-0.030	-0.022

The blade in Table 2-3 was divided into thirteen spanwise segments for design purposes. The chord and twist angle are variable along the span. Often a circular section is employed at the root segment which has a flange for attachment to the hub, while the neighboring segments make a transition to the root airfoil, usually located at station (part) 3 or 4. In some designs, not only the chord length, but also the airfoil shape is changed along the span, towards the tip.

In order to maintain each spanwise section at or close to the best aerodynamic efficiency condition, the blade is twisted along the span, as can be seen in Figure 2-16 and illustrated by Table 2-4.



Figure 2-16 - A large rotor blade from a point of view close to the azimuthal plane, which allows for clearly identification of the blade twist along the span. Source: General Electric.

Both the material technology problem and the self-noise problem described are dependent upon the tangential speed of the rotor, ωr , and this is one of the reasons why larger rotor diameter HAWTs have slower rotation compared to small scale wind turbines.

Another important reason that limits the tangential speed of the rotor is that the efficiency of the complete WT rotor, bounded by the theoretical Betz limit of 0.59, is close to its maximum at $TSR \approx 10$, as shown in Figure 2-17.

Table 2-4 - Twist and chord as a function of radius, for a Nordtank NTK 500/51 Wind Turbine.
Source: (Hansen, 2008), p. 58.

r [m]	twist [degrees]	chord [m]
4.5	20.0	1.63
5.5	16.3	1.597
6.5	13.0	1.540
7.5	10.05	1.481
8.5	7.45	1.420
9.5	5.85	1.356
10.5	4.85	1.294
11.5	4.00	1.229
12.5	3.15	1.163
13.5	2.60	1.095
14.5	2.02	1.026
15.5	1.36	0.955
16.5	0.77	0.881
17.5	0.33	0.806
18.5	0.14	0.705
19.5	0.05	0.545
20.3	0.02	0.265

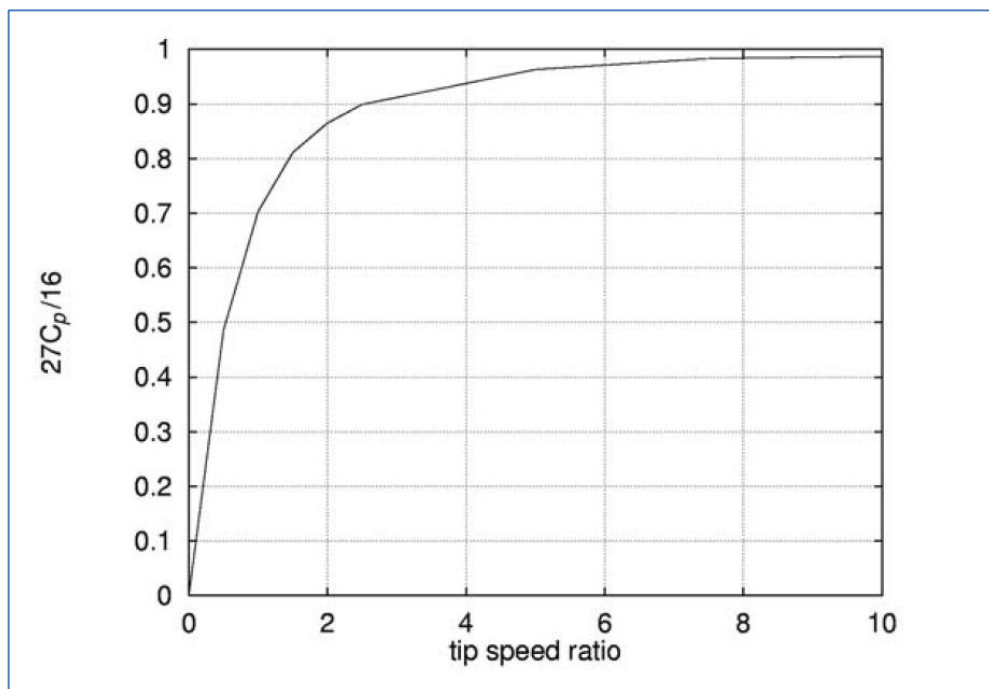


Figure 2-17 - The efficiency of the WT as a function of TSR (Hansen, 2008).

The inefficiency for TSRs under 6 are gradually steeper, due to the increasing loss induced by the rotating wake as the rotational speed decreases.

The aerodynamic models used to predict WT mechanical power and torque range from the simple 1-D Momentum Theory for an ideal turbine (Rankine's actuator theory), to the broadly used Blade Element Momentum (BEM²⁷) theory (Hansen, 2008) and the Vortex Wake methods (Gupta & Leishman, 2005), (Sanderse, 2009). More recently, CFD methods have been employed also for this purpose (Laursen, Enevoldsen, & Hjort, 2007), (Hartwanger & Horvat, 2008), (Lawson & Li, 2011), though not in the conceptual design phase, for they are time consuming and more suitable for the estimation of actuator-disk theory induction factors results for comparison with BEM methods and other studies.

Considering a generic radial position r along the WT blade span, represented in Figure 2-18, the local AOA, α , is a function of the local angle between the chord and the rotation plane, called local pitch angle θ , and the angle formed between the relative velocity, V_{rel} and the plane of rotation, ϕ .

$$\alpha = \phi - \theta \quad (2 - 6)$$

Where the local pitch angle θ is a combination of the pitch angle and the twist angle, $\theta = \theta_p + \beta$ and ϕ is the flow angle, found via

$$\tan\phi = \frac{V_a}{V_{rot}} \quad (2 - 7)$$

Because of the induced velocity field, however, the axial and radial velocities must be corrected by the axial (a) and tangential (a') induction factors:

$$V_a = (1 - a)V_0 \quad (2 - 8)$$

$$V_{rot} = (1 + a')\omega r \quad (2 - 9)$$

where V_0 is the undisturbed wind approach speed.

²⁷ Also designated "BET" method in some references, in order to avoid confusion with the Boundary Element Method.

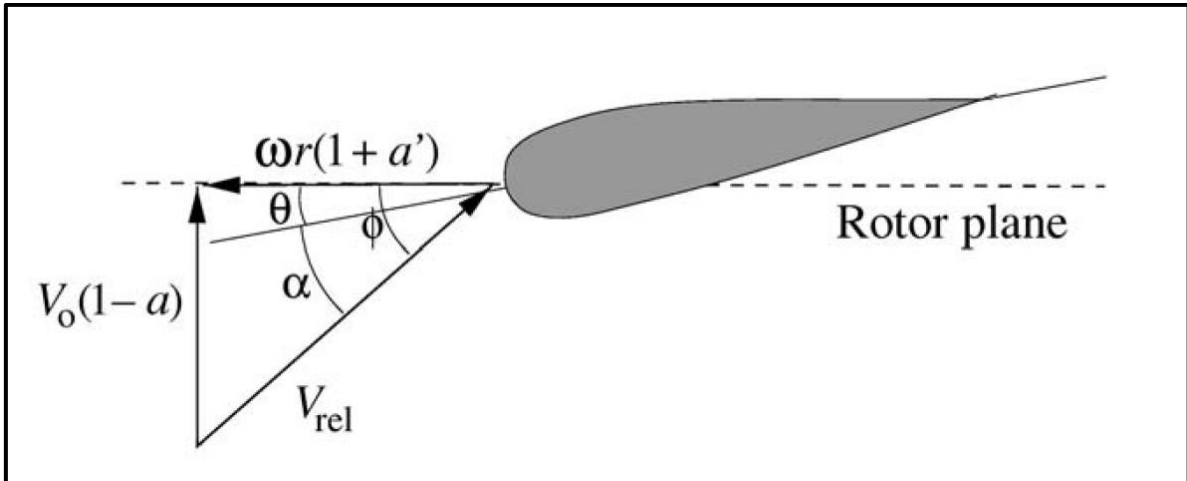


Figure 2-18 - Local flow velocities and angles for a blade section at radial distance r . (Hansen, 2008), p. 47.

The goal of the BEM method, described in section 2.8 is to estimate the axial and tangential induction factors, so that blade loading and performance may be acceptably evaluated during design. The simplifying assumptions of the BEM model along with the necessary corrections for the 3-D domain problem are further discussed in the Methodology section.

The operating regimes for WT blades is characterized by complex, unsteady flow fields (Eisele, Pechlivanoglou, & Nayeri, 2013), which, according to Imamura (Imamura, 1999) makes unsteadiness investigation crucial for understanding WT aerodynamics. Researches on WT unsteadiness can be found in Huyer et al. (Huyer, Simms, & Robinson, 1996), and Leishman (Leishman, 2002).

A detailed comparison between the different performance prediction methods for WT is beyond the scope of the present work and may be found in Imamura (Imamura, 1999) and Hansen (Hansen, 2008).

In Appendix C, it is shown that the wind speed frequency distribution is such that the wind is blowing in the average speed value for only a fraction of the total time. For this reason it is necessary to design the WT rotors with acceptable performance over a range of operating speeds. The minimum production wind speed is known as the cut-in speed, and it is determined by general system losses and generator limitations. The

structural integrity is kept by setting a cut-out²⁸ speed, after which a mechanical or aerodynamic brake comes into action to prevent the rotor from over speeding. In between these characteristic operating speeds, the rotor-blade angle is changed by the pitch control mechanism, in order to keep each section close to the optimum AOA. For an illustration on these characteristic operating points, see Figure 2-19. It is important to notice that the twist embodied in design and manufacturing imposes different AOA for each blade section along the span, while the pitch control alters that distribution by a fixed delta, for all sections, during the operation.

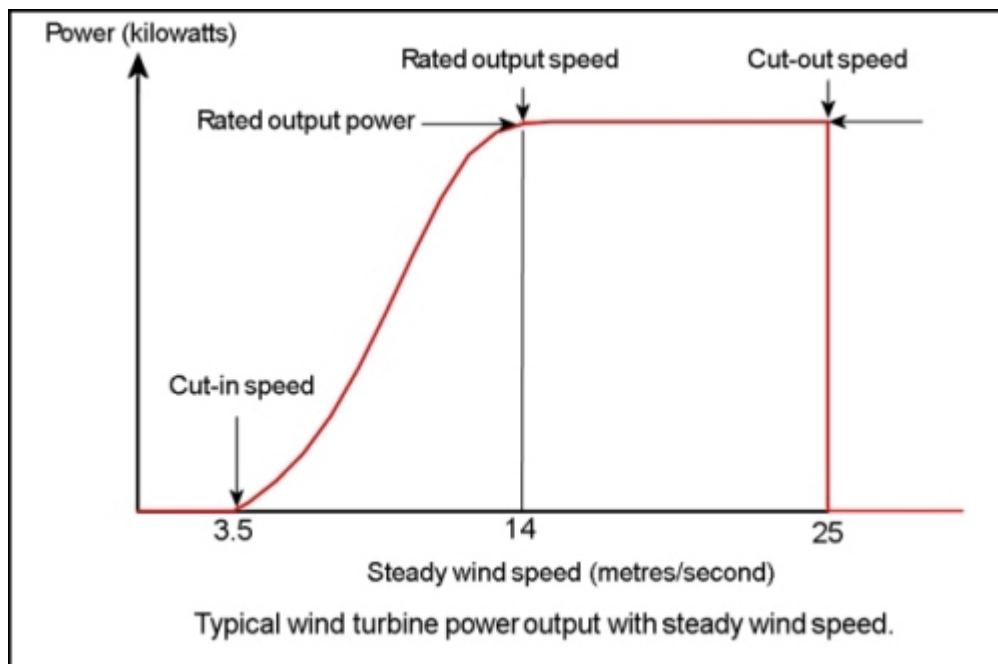


Figure 2-19 - The power production as a function of wind speed, with illustrations of typical cut-in and cut-out wind speeds for modern HAWTs. Source: AWEA.

A comparison between real power curves for a 70 m diameter 1.5 MW machine working in three different control modes (passive, stall-regulated, fixed speed; active, pitch-regulated, fixed speed; and active, pitch-regulated variable speed modes) is shown in Figure 2-20.

²⁸ Wind Turbines are normally programmed to shut down if the 10-minute mean wind speed exceeds 25 m/s (Siemens, 2013).

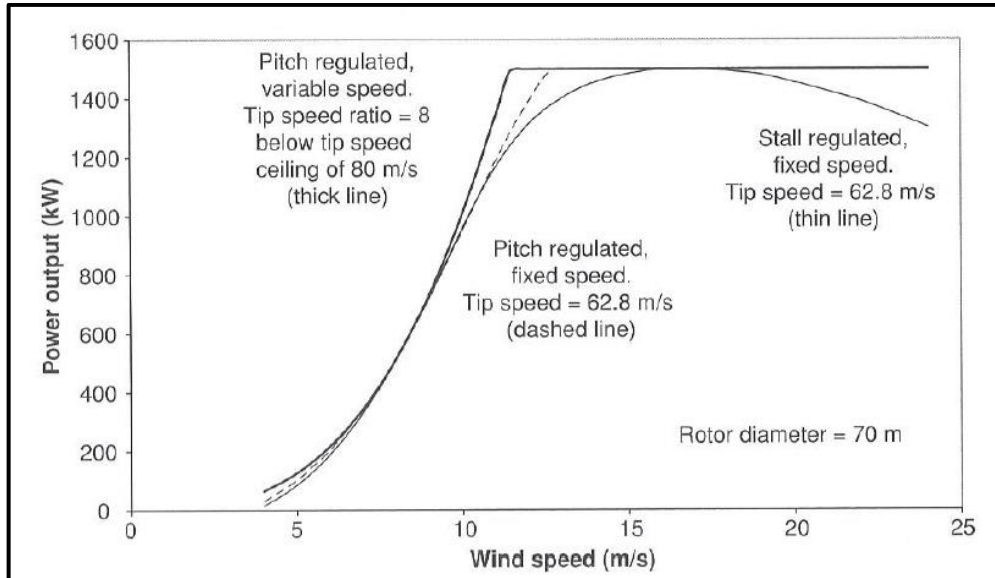


Figure 2-20 - Comparison of power curves for 70 m diameter machines with (i) passive, stall-regulated, fixed speed; (ii) active, pitch-regulated, fixed speed and (iii) active, pitch-regulated variable speed modes. Source: (Burton, Jenkins, Sharpe, & Bossanyi, 2011), p. 350.

From Figure 2-20 it is possible to estimate a 5% increase in power production in favor of the variable speed machine, when compared to the pitch-regulated fixed speed one.

Concerning *WTN* data, different manufacturers have different approaches but most provide essentially the OASPL at a fixed distance from the hub (see Table 2-5), so that the siting planner may use a propagation model to infer OASPL at a specific point, usually the closest dwelling from the tower.

Table 2-5 - The A-weighted OASPL for the Northern Power 100 *WT*, at 30 m from the tower, at hub height. (Northern_Power, 2013)

NOISE	DESCRIPTION
Apparent Noise Level	55 dBA at 30 meters (98 ft)

Due to the different approaches in distance, height and wind speed for reporting the noise among the manufacturers, the International Electromechanical Commission issued a standard, described in Section 1.1.6, the IEC61400 (IEC61400-11, 2012), that regulates the sound power level measurements under controlled conditions so that the sound emissions from different equipment may be compared on a consistent basis and provide input data for modeling analyses.

The measurements are made for wind speeds from 6 to 10 m/s (measured 10 m above the ground level). The results are expressed as the overall A-weighted sound power level at each of the mandatory wind speeds along the 1/3 octave band frequencies.

2.3.1 The Annual Energy Output

The chart displayed in Figure 2-21 is a numerical example of Figure 2-19, for a real equipment. This kind of chart is made available by the WT manufacturers so that the siting planner may be able to cross this information with site specific wind information and simulate annual production potential for equipment selection purposes.

The most employed method for the purpose of annual energy output estimation seems to be the Method of Bins (GIPE, 2004), (Burton, Sharpe, Jenkins, & Bossanyi, 2008). In this method, the wind speed is divided into 1 m/s increments, from the cut-in to the cut-out speed. For each speed bin, a chart like the one in Figure 2-21 or an equivalent table is searched for the instantaneous production capability [kW]. Next, the wind Weibull or Rayleigh distribution model at the specific site (see Appendix C) is determined and the frequency [% of occurrence] for that speed is obtained [h/yr]. The frequency of occurrence for each bin is then multiplied by the total hours per annum [h/yr] that the WT will be working at that speed. At this point the siting planner should also consider the history of availability from the same or similar type of equipment, which was stated as being around 98%²⁹ for a modern type HAWT, at the beginning of the present section. Finally, the total annual output of energy [kW] may be obtained by summing up the annual production of the WT for each wind speed bin, as shown in Table 2-6.

²⁹ 98% of 8,760 hours/year.

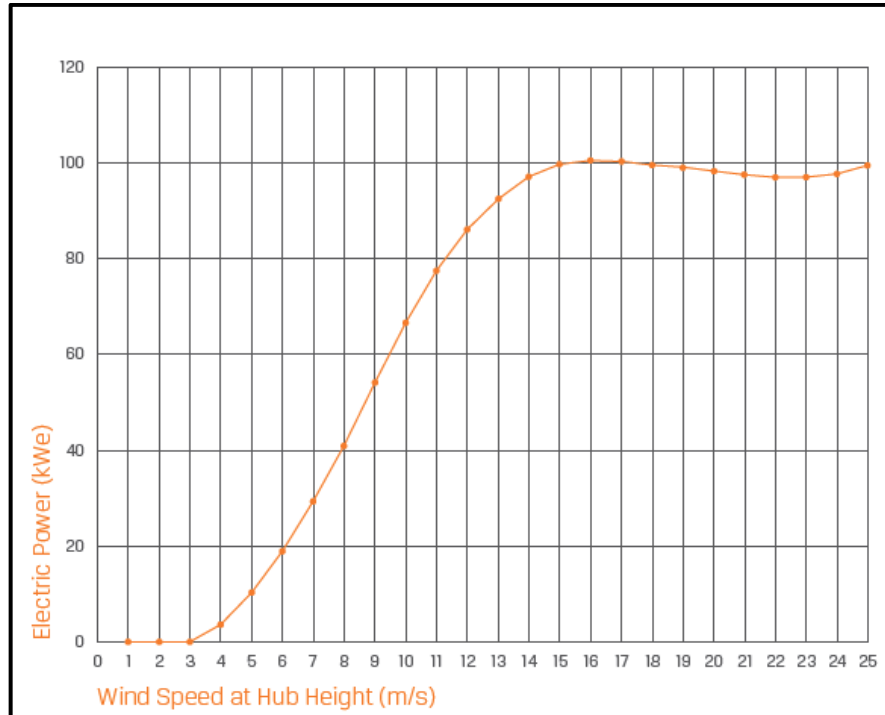


Figure 2-21 - The power production [kW] as a function of wind speed at hub height [m/s] for the Northern Power 100 WT, at sea level, 15 °C standard air density (Northern_Power, 2013).

Table 2-6 - Example of the bin method applied to the estimation of the total annual power output for a small size, 2.4 m diameter WT, with Rayleigh wind distribution and average annual wind speed of 12 m/s (GIPE, 2004).

Wind Speed Bin (mph)	Instantaneous Power (kW)	Rayleigh Frequency Distribution (% Occurrence)	(h/yr)	Energy (kWh/yr)
8	0.010	0.0616	539	5
9	0.030	0.0631	553	17
10	0.055	0.0632	554	30
11	0.082	0.0620	543	45
12	0.111	0.0597	523	58
13	0.142	0.0564	494	70
14	0.175	0.0524	459	80
15	0.210	0.0480	420	88
16	0.247	0.0432	378	93
17	0.286	0.0383	336	96
18	0.327	0.0335	294	96
19	0.370	0.0289	253	94
20	0.415	0.0246	216	90
33	1.055	0.0009	8	9
34	1.030	0.0007	6	6
35	0.400	0.0005	4	2
36	0.240	0.0003	3	1
37	0.250	0.0002	2	1
38	0.240	0.0002	1	0
39	0.250	0.0001	1	0
40	0.260	0.0001	1	0
Annual Energy Output (AEO)				1,416

Note: Sample small wind turbine 2.4 meters (8 ft) in diameter, Rayleigh distribution average annual wind speed = 12 mph

2.4 MODELS AND METHODS FOR TRAILING EDGE NOISE PREDICTION AND THEIR IMPLEMENTATION.

In this section it is important that an ad-hoc differentiation between TE noise prediction *models* and *methods* is made before proceeding. *Models* will be referred hereon to as the set of semi-empirical or theoretical equations, with their associated hypotheses and conditions, that will allow the prediction of one or more noise source mechanisms, while the combination of models plus the tools that provide the necessary flow data for its basic prediction or that allow extrapolation of the results (for instance, 3-D rotor noise prediction from 2-D airfoil predictions) will be collectively addressed to as *methods of noise prediction* (i.e. complete application tools).

In some cases (e.g. NAFNoise, IAGNoise), the method may employ more than one type of noise prediction model and in this situation it will be reviewed in the track where most of the research is dedicated to i.e., Semi-Empirical track for the NAFNoise and Simplified Theoretical track for the IAGNoise.

2.4.1 Semi-Empirical Models.

The Trailing Edge Noise models developed from 1959 to 1977 are summarized in Howe (Howe, 1978), the main motivation problem being aircraft wing noise (with and without flaps) over airfields, at flight Mach numbers corresponding to take-off and landing ($M < 0.3$), and the effects of forward aircraft flight. Also, at this time there was an increasing interest in helicopter rotor noise, which provided the basis for the Grosveld Model (Grosveld, 1985) discussed among others in Appendix D.

Due to the extensive text resultant from the review of the Semi-Empirical Models, which spans decades of research, the text may be found in Appendix D, except for the NASA BPM model, which is reviewed next.

2.4.1.1 BPM (NASA) Model

The BPM model (Brooks, Pope, & Marcolini, Airfoil Self-Noise and Prediction, 1989) is the cumulative result of preceding, comprehensive aerodynamic and acoustic wind tunnel tests described in Brooks and Hodgson (Brooks & Hodgson, 1981) and Brooks and Marcolini (Brooks & Marcolini, 1985). A semi empirical scaling effort over the extensive data resulted in a model with predictive capability for all the five self-noise mechanisms.

The scaling is based on aerodynamic and acoustic testing of six NACA 0012 2-D and six NACA 0012 3-D airfoil models of varying chord length (from 1 *in* to 2 *ft*), with Reynolds numbers up to 3×10^6 and Mach number up to 0.21. The measurements included relevant TBL integral parameters and sound pressure levels, for tripped and untripped conditions, at freestream velocities up to 71.3 *m/s* and angles of attack from 0° to 25.2° . All the 2-D airfoil models tested had 1.5 *ft* span and sharp trailing edges, without beveling, and with a slope at the surface close to the TE of 7° off the chord line. The models were tested in the low-turbulence potential core of a free jet, discharging inside an anechoic chamber. Five of the 3-D models also had sharp TE, 1 *ft* span, and rounded tips defined by rotating the NACA 0012 shape about the chord line. The last 3-D airfoil employed in the research had blunt TE and was tested previously by Brooks and Hodgson (Brooks & Hodgson, 1981). The test cases included untripped BL flows (surface smooth and clean) and heavily tripped BL flows, with random distribution of 60-grit in strips from LE to 20% of the chord.

In their preceding research, Brooks and Marcolini (Brooks & Marcolini, 1985) had demonstrated that, if sufficient information was known about the TBL convecting surface pressure field passing the TE, then TBL-TE noise could be accurately predicted. Also, they concluded that the TBL-TE noise normalized level, spectral shape and Strouhal number were all dependent on Reynolds number. The corrected measured spectra of the Brooks et al. (Brooks, Pope, & Marcolini, Airfoil Self-Noise and Prediction, 1989) research were used to establish the parametric dependences to account for these variations in spectral scaling.

Brooks et al. (Brooks, Pope, & Marcolini, Airfoil Self-Noise and Prediction, 1989) concluded that previous research developed at NASA-Langley proved disappointing to

predict TBL-TE noise because knowledge of mean, turbulent boundary layer characteristics alone were not enough to define the turbulence structure: the results indicated that a successful description of the surface pressure depended upon the history of development of the turbulence being incorporated into the mean TBL characteristics and that this would require a level of turbulence modeling not attempted at that time. The subject of TE noise prediction based on the pressure field beneath a TBL will be further discussed under the *Simplified Theoretical* models, in Section 2.4.2 and Appendix E.

Because of the reason explained above, the simpler approach of the scaling law based on the analysis of FW-Hall (Ffowcs-Williams & Hall, 1970) for the problem of turbulence convecting past the TE, was adopted. The paper does not explain in details the steps going from the FW-Hall analysis to the scaling law in the root of the BPM TE noise model, but an effort is made below to bridge the model construction.

According to FW-Hall (Ffowcs-Williams & Hall, 1970), p. 668, the eddies close to the edge of a half plane are much more powerful sources of sound than eddies far from the edges. The intensity at a far field point of the sound from an eddy near the edge (i.e., $2kr_0 \ll 1$, or much less than a wavelength from the edge) may be approximated by the following expression if directional factors are suppressed:

$$I \sim \rho U^3 \left(\frac{U^2}{c_0^2} \right) \frac{\delta^2}{r^2} \quad (2 - 10)$$

where r is the separation of the source point and the far field point considered.

Thus, the scattered intensity increases in proportion to the fifth power of the fluid velocity as opposed to the eighth power law from free turbulence or the sixth power law from the surface dipole term for acoustic compact surfaces.

The sound intensity is related to the *rms* pressure signal, \hat{p}^2 , by:

$$I = \frac{\hat{p}^2}{\rho c_0} [W/m^2] \quad (2 - 11)$$

Combining the two last expressions, a reference scaling law for TE noise is obtained:

$$\hat{p}^2 \sim \rho^2 U^3 \left(\frac{U^2}{c_0} \right) \frac{\delta^2}{r^2} \quad (2 - 12)$$

A very close scaling law is used as the departure point for the BPM TE noise model:

$$\hat{p}^2 \propto \rho^2 u'^2 \frac{U^3}{c_0} \left(\frac{Ll}{r^2} \right) \bar{D} \quad (2-13)$$

where u'^2 is the mean square turbulence velocity, L is the spanwise extent of the wetted edge by the flow, and l is a characteristic turbulence correlation scale. The directivity factor, \bar{D} , equals 1 for observers normal to the surface from the TE.

Since the usual scaling assumptions for boundary layer flows, are $u' \sim U$; $L \sim \delta$ or δ^* , the initial relation (2-13) becomes closer to the reference scaling law (2-12):

$$\hat{p}^2 \propto \rho^2 \frac{U^5}{c_0} \left(\frac{L\delta}{r^2} \right) \quad (2-14)$$

The relation of the *rms* pressure signal and the sound pressure level is given by:

$$SPL = 10. \log_{10} \left(\frac{\hat{p}^2}{\hat{p}_{ref.}^2} \right) [dB] \quad (2-15)$$

where $\hat{p}_{ref.} = 2.10^{-5}$ Pa is the standard reference pressure, corresponding to the weakest audible sound, at 1000 Hz, or 1dB.

Next, a universal spectrum shape $F(St)$ was assumed for self-noise dominated by TBL-TE, which is a function only of the ratio of the Strouhal number $St = f\delta/U$ to its peak value, St_{peak} . The resultant normalized form for the 1/3 octave SPL spectral shape is:

$$SPL_{1/3} - 10. \log \left[\left(\frac{U}{100} \right)^5 \frac{L\delta}{r^2} \right] = F(St) + K \quad (2-16)$$

with $SPL_{1/3} = OASPL + F(St)$ and where K is an empirical constant.

The next step in the development of the model was the use of extensive experimental spectra for the determination of the parametric dependencies and spectral scaling, resulting in the following initial scaling law for zero angle of attack:

$$Scaled SPL_{1/3} = SPL_{1/3} - 10. \log \left[M^5 \frac{L\delta_0^*}{r_e^2} \right] \quad (2-17)$$

where δ_0^* is the displacement thickness at the TE at zero AOA and r_e is the retarded observer distance, fixed at 1.22 m.

However, the (i) peak Strouhal number, (ii) scaled noise level and (iii) spectral shape varied significantly by comparing the scaled spectra for airfoils with different chords, suggesting that the right hand side of scaling (2-16), $F(St) + K$ was not an accurate representation of the phenomena.

Further study of the measured data provided the means to improve upon the model. First, it was found a dependence of the peak Strouhal number (i) on the Mach number of the experiment

$$St_{peak} \approx 0.02M^{-0.6} \quad (2 - 18)$$

Second, the sound pressure scaled level (ii) was found to depend on chord-based Reynolds number, Re_c , up to approximately 7×10^5 , above which it was forced to be constant in order to be compatible with other studies (see Figures 76 and 77, p. 53, of Brooks et al. (Brooks, Pope, & Marcolini, Airfoil Self-Noise and Prediction, 1989) for further details). A continuous function, designated K_1 was added in the scaling to account for this variation.

Finally, in order to cope with the spectral shape difference (iii) a shape function denoted by A was proposed as representative of the 1/3 octave spectral shape of the TBL-TE noise mechanism. This new proposed spectral shape is symmetrical about the peak Strouhal number ($St/St_{peak} = 1$) and its width or broadness depends on Re_c .

One of the key findings of a previous research by Brooks and Hodgson (Brooks & Hodgson, 1981) was that the noise produced by each side of an airfoil with well-developed BL is independent and, for consistency reasons, the scaling expression was further adjusted by a level of -3 dB in order to consider the noise from each side independently.

The final scaling expression for the i side ($i=p,s$ for pressure and suction sides), results:

$$Scaled SPL_{1/3,i} = SPL_{1/3,i} - 10 \cdot \log \left[M^5 \frac{L\delta_i^*}{r_e^2} \right] = A \left(\frac{St_i}{St_1} \right) + (K_1 - 3) \quad (2 - 19)$$

where $St_1 = St_{peak}$, $St_i = (f\delta_i^*/U)$ and K_1 is the function described before, that expresses the scaled sound pressure level variation with Re_c .

The total spectra for the TBL-TE noise, zero AOA, in 1/3 octave presentation, for both the pressure and the suction sides is then:

$$SPL_{TBL-TE} = 10 \cdot \log \left(10^{SPL_s/10} + 10^{SPL_p/10} \right) \quad (2 - 20)$$

In order to generalize the TE noise prediction model for AOA other than zero, the noise spectra for the same tripped flow airfoils was scaled³⁰ for varying AOA, at the constant free-stream velocity of 71.3 m/s. For increasing effective AOA, α_* , the peak Strouhal number and sound pressure level increased and the spectra became sharper at the peak, situations not predicted by the scaling law developed before. Also, beyond $\alpha_* \approx \alpha_{stall}$, substantial changes occurred to the scaled spectra, that required further modeling.

In order to model the new physical behavior, it was postulated that at non-zero AOA an additional contribution to the noise spectrum appeared, that controlled the spectral peak. The hypothesis behind this postulation was that the noise spectrum was formed by the total contributions from the attached TBL portion and from the separated TBL portion on the suction side, and this proved valid for high Reynolds numbers.

The trend of increasing the peak Strouhal number and level was explained mostly by velocity and AOA dependence. A new function, St_2 was hand-fitted to the data in order to model the peak Strouhal number variation as a function of α_* , whose value decays into St_1 (peak Strouhal) for $\alpha_* = 0$.

Concerning the new physical sound pressure levels attained at AOA, they were subtracted from the noise levels at zero AOA (Eqn. 2-20) and the difference was normalized by subtracting the function K_1 for zero AOA levels. This new function was designated $K_2 - K_1$, and it stemmed from partially observed, partially postulated dependence of level on velocity and AOA.

Finally the new spectral shape for this additive source was called function B , defined from data for non-zero AOA, in a manner analogue to the definition employed in

³⁰ In this case the flow is not symmetrical about the chord, and the displacement thickness of the suction side is employed as the TBL scaling length, δ_s^* .

function A for zero AOA, i.e. so that the width is dependent on chord Reynolds number. The resulting additional scaling model for angle of attack dependent noise, SPL_α was

$$Scaled\ SPL_\alpha = SPL_\alpha - 10 \cdot \log \left[M^5 \frac{L\delta_s^*}{r_e^2} \right] = B \left(\frac{St_s}{St_2} \right) + K_2 \quad (2 - 21)$$

where the expression above represents the noise contribution from the separated TBL to the total noise, which is given by:

$$SPL_{TOT} = 10 \cdot \log \left(10^{SPL_s/10} + 10^{SPL_p/10} + 10^{SPL_\alpha/10} \right) \quad (2 - 22)$$

Finally the substantial changes that occurred to the shape of the scaled spectra beyond $\alpha_* \approx \alpha_{stall}$, called *the switching angle*, were modelled by replacing the B function in Eqn. (2-21) for A' , which is the value for the A function when the R_c is three times the original value.

2.4.1.2 Original Model validation.

Since testing of the airfoil models occurred in an open wind tunnel, significant interference from the induced flow curvature and downwash occurs, that are not present in the free air flow. This phenomena reduces the geometric AOA, α_t , which must be then corrected into an effective AOA, α_* . The effective AOA is the angle in free air necessary to produce the same lift measured in the tunnel, at geometric angle, α_t .

The comparison of the semi-empirical BPM TE noise model with the measured spectra of the NACA 0012 airfoil (Brooks & Marcolini, 1985), (Brooks, Pope, & Marcolini, Airfoil Self-Noise and Prediction, 1989), from which the model was derived, is shown in Figures 2-22 through 2-25, for tripped and naturally developing TBL, for both zero and non-zero AOA, and for flow velocities from 31.7 to 71.3 m/s.

The noise prediction calculations employed displacement thickness correlation data from the NACA 0012 airfoil at AOA from zero to 25° , observer position simulated at $r_e = 1,22\ m$ and $\theta_e = \phi_e = 90^\circ$.

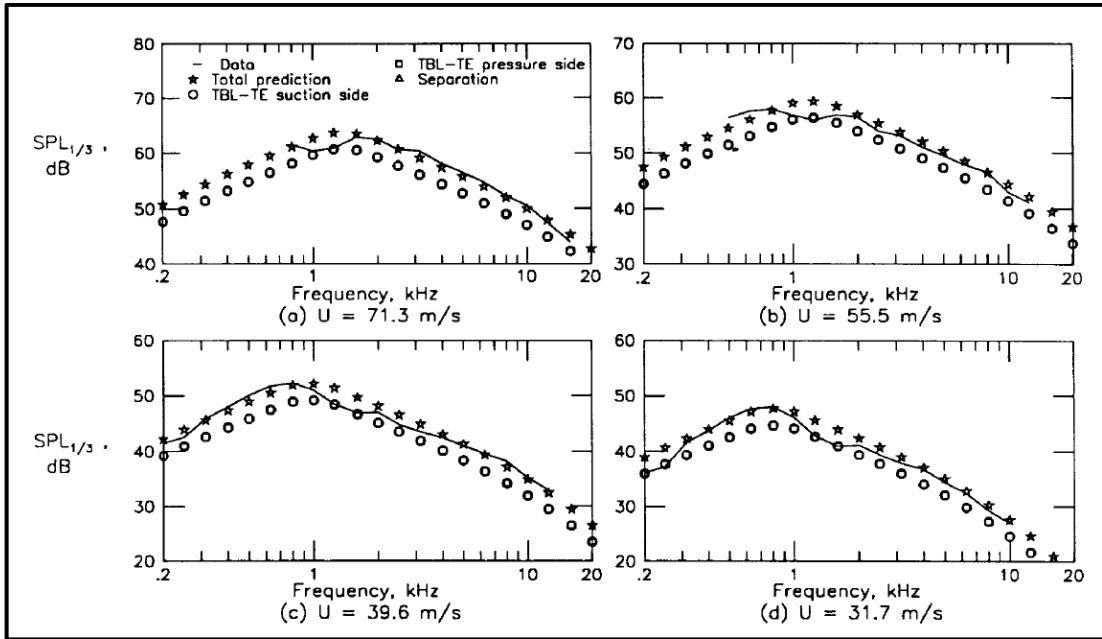


Figure 2-22 - Self-noise spectra for the 0.3048 m –chord, NACA 0012 airfoil at zero angle of attach, for tripped boundary layer and freestream velocities between 31.7 to 71.3 m/s. Source: (Brooks, Pope, & Marcolini, Airfoil Self-Noise and Prediction, 1989), p.18.

In all validation graphs shown, the measured spectra are represented by continuous lines. The measured spectra were edited by the authors to eliminate the upper and lower frequencies whenever extrinsic noise affected the spectra by 2 dB or more.

In Figure 2-22 it is possible to see that the BPM model predicts satisfactorily the $SPL_{1/3}$ level throughout the available measured spectrum, but has a tendency to overpredict the $SPL_{1/3}$ in the peak frequencies. For the case $U = 39.6$ m/s, a logarithmic sum of the $SPL_{1/3}$ levels was accomplished, with visual precision, through the measured and calculated available spectra (200 Hz to 12 KHz), resulting in OASPL of 71 dB for the measured and 72 dB for the calculated spectra, or a 1 dB overall conservative prediction, which gives a general measure of the accuracy of model for zero AOA, tripped BL cases, when TBL-TE noise is dominant.

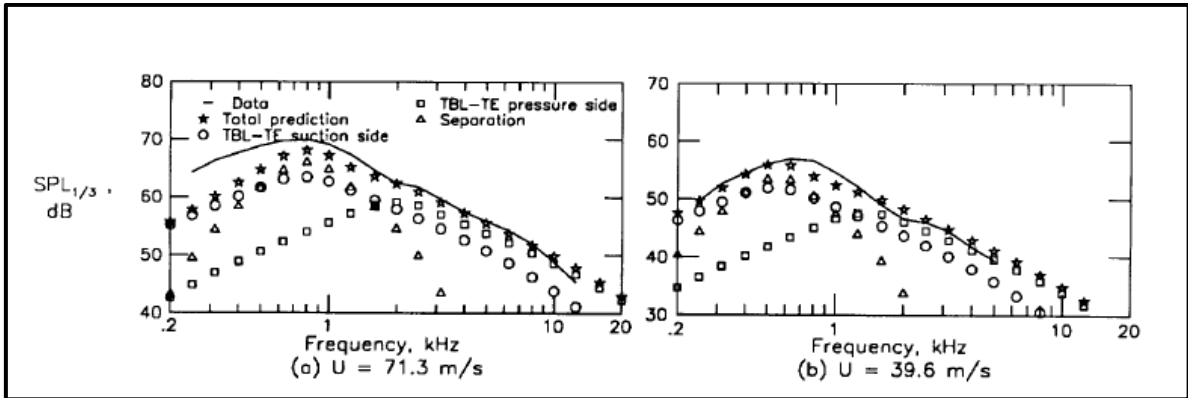


Figure 2-23 - Self-noise spectra for the 0.3048 m chord NACA 0012 airfoil, with tripped BL, at $\alpha_t = 14.4^\circ$, corrected $\alpha_* = 4.0^\circ$ and flow velocities of 39.6 and 71.3 m/s. Source: (Brooks, Pope, & Marcolini, Airfoil Self-Noise and Prediction, 1989), p. 19

In Figure 2-23 it is possible to see that for positive, moderate AOA, tripped BL, the adherence of prediction to measured data is still quite good at lower speeds, but there is now a slight tendency of underprediction for the peak levels. For higher speeds, when the separation is not mild, the adherence is very good at higher frequencies, with underprediction at lower frequencies.

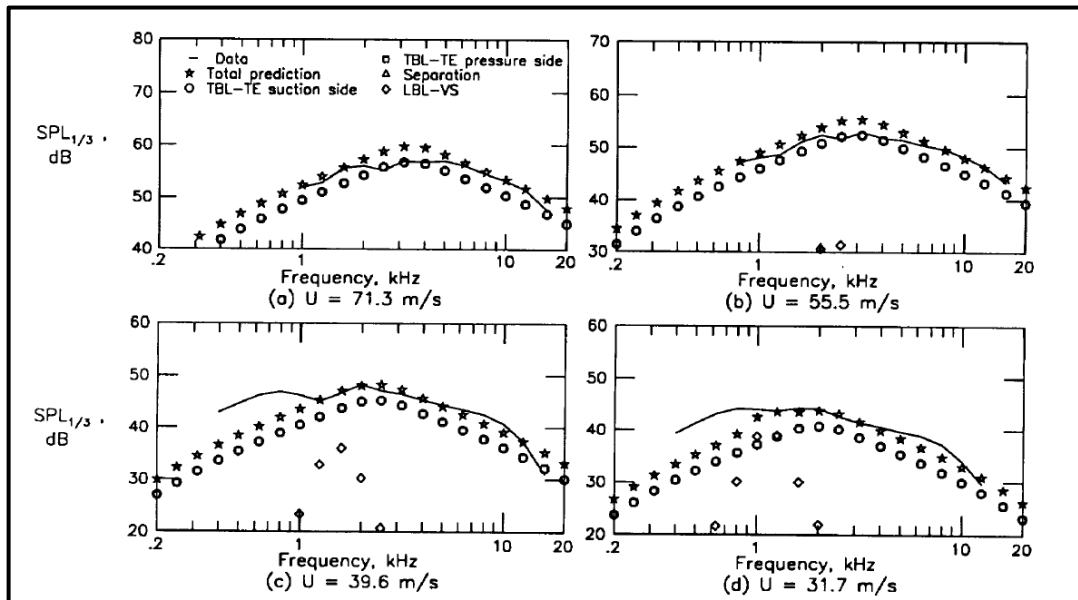


Figure 2-24 - Self-noise spectra for the 0.3048 m-chord, NACA 0012 airfoil at zero angle of attack, for the natural transition case and freestream velocities between 31.7 to 71.3 m/s. Source: (Brooks, Pope, & Marcolini, Airfoil Self-Noise and Prediction, 1989), p.35.

In Figure 2-24 it is possible to see that the model overpredicts the peak SPL_{1/3} levels for high speed, natural transition BL flow at zero AOA, but because of the development of laminar boundary layer vortex shedding (LBL-VS) phenomena at lower speeds,

which is not well modeled, the model underpredicts the lower frequencies, below 1 kHz. However, because of the upper shift produced by the LBL-VS in this part of the spectrum, the prediction of the peak frequencies is now more accurate.

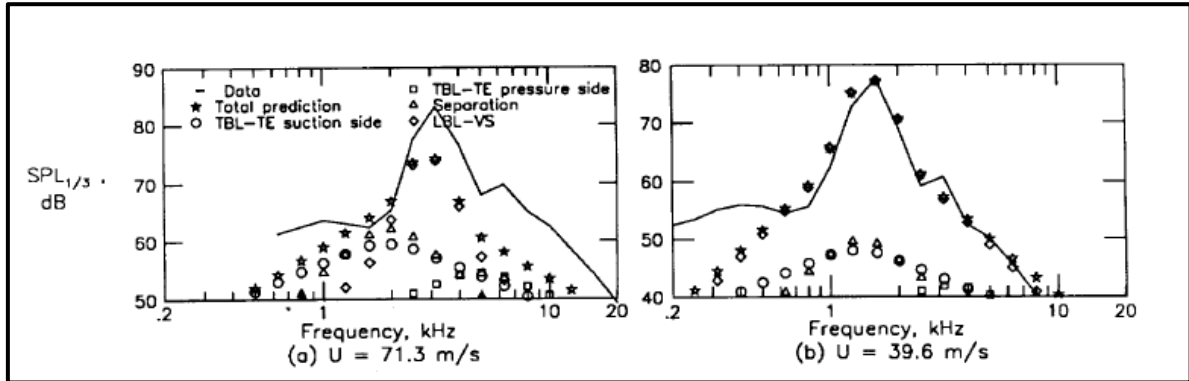


Figure 2-25 - Self-noise spectra for the 0.3048 m chord NACA 0012 airfoil, with natural transition BL, at $\alpha_t = 14.4^\circ$, corrected $\alpha_* = 4.0^\circ$ and flow velocities of 39.6 and 71.3 m/s. Source: (Brooks, Pope, & Marcolini, Airfoil Self-Noise and Prediction, 1989), p. 36

In Figure 2-25 it is possible to see that, in natural transition flow, when the airfoil is in lifting mode, the model does a very good prediction job for the lower speed, at frequencies above ≈ 600 Hz, including the peak level prediction. However, for higher speeds, highly separated flow, there is no good agreement, except around the 2 kHz band.

The final step of the original validation effort was to compare the prediction model results also with spectral measurements made by other authors. Schlinker and Amiet (Schlinker & Amiet, 1981) had conducted spectral TE noise measurements from a cambered helicopter blade section (Sikorsky rotor blade) of comparable blade chord and span (0.406×0.533 m), in 2-D flow, with Mach numbers ranging from 0.1 to 0.5 and angles of attack from -0.4° (the zero lift angle for the cambered airfoil) to 12° . Since in this work the tripping was very light, the original boundary layer thickness and displacement thickness ratios were multiplied by a correction factor (of 0.6) in order to correspond to the heavy tripping employed by Brooks et al. (Brooks, Pope, & Marcolini, Airfoil Self-Noise and Prediction, 1989). The results of the validation against third party data are shown in Figure 2-26 and Figure 2-27.

Brooks et al. deemed that the predicted and experimental data compared satisfactorily, especially considering different airfoil geometries and measurement methods employed by the research teams. They concluded to exist a mild, non-systemic,

overprediction tendency for the TE noise. Similar conclusions were drawn after comparing the noise predictions with further work conducted by Schlinker et al., that also employed the NACA 0012 airfoil but in a different wind tunnel facility and with alternative measurement methods.

The authors of the BPM model believed that it should be useful for the determination of broadband noise for helicopter rotors, wind turbines, airframe noise and other cases where airfoils encounter low or moderate speed flow.

At least six of the reviewed TBL-TE noise models (Appendix D), developed from 1989 through 2011 adopted the BPM TE noise model, suggesting wide acceptance in both academy and industry for the model. In most cases it seems that the model offers the best compromise between accuracy and computational efficiency for practical applications.

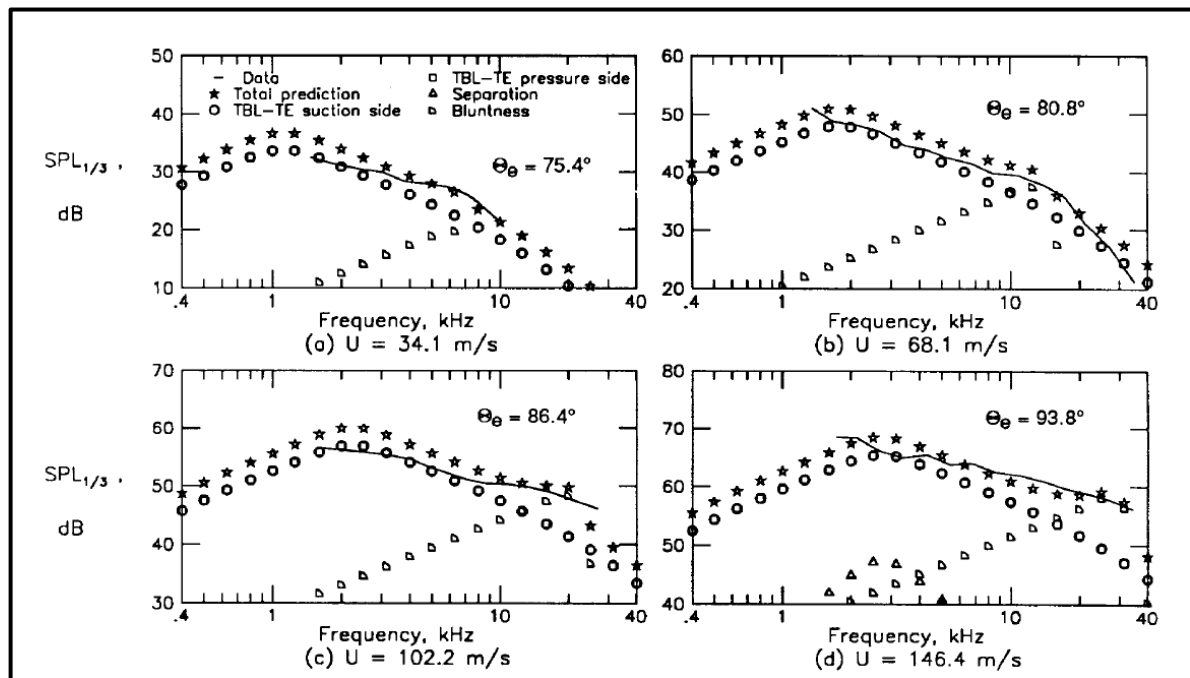


Figure 2-26 - Self-noise spectra for the Sikorsky airfoil at $\alpha_t = -0.4^\circ$ ($\alpha_* = 0^\circ$) from (Schlinker & Amiet, 1981), compared with prediction from the BPM model. Source: (Brooks, Pope, & Marcolini, Airfoil Self-Noise and Prediction, 1989), p.86.

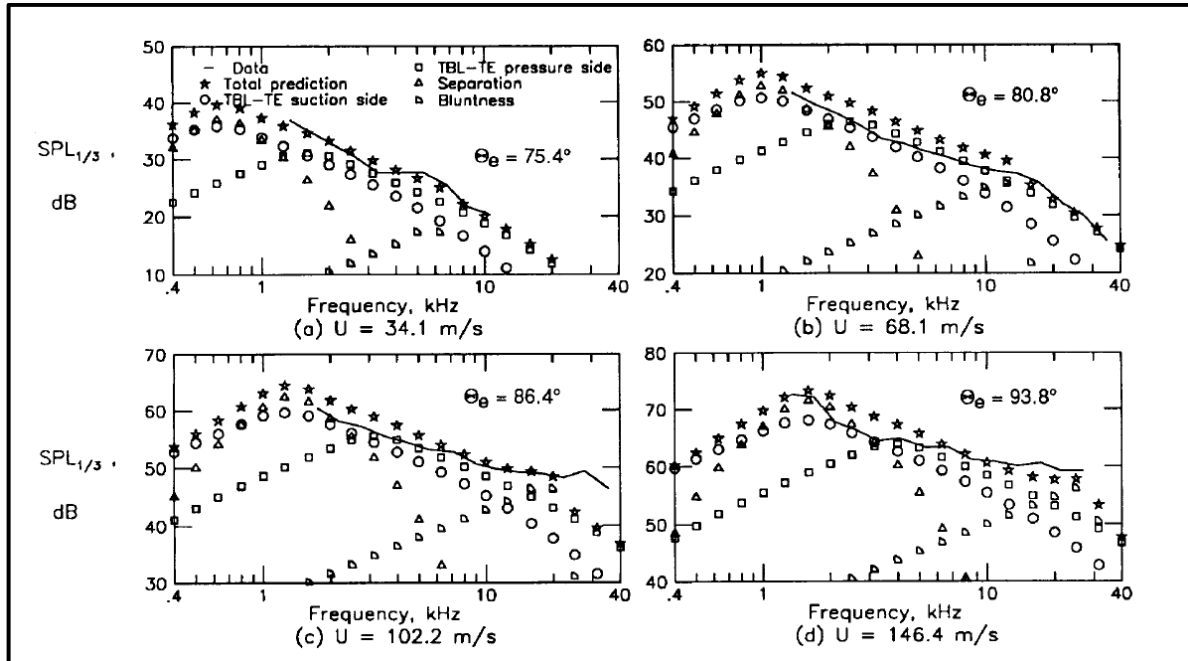


Figure 2-27 - Self-noise spectra for the Sikorsky airfoil at $\alpha_t = 7.6^\circ$ ($\alpha_x = 3.9^\circ$) from (Schlinker & Amiet, 1981), compared with prediction from the BPM model. Source: (Brooks, Pope, & Marcolini, Airfoil Self-Noise and Prediction, 1989), p.87.

2.4.1.3 Summary of Model Limitations

Summarizing the applicability and limitations of the model, the BPM model is an overall prediction approach for airfoil self-noise based on theoretical studies and experimental data of (mostly) 2-D airfoil.

The scaling is based on aerodynamic and acoustic testing of a set of NACA 0012 airfoil models with varying chord length (from 1 in to 2 ft), with Reynolds numbers up to 3×10^6 and Mach number up to 0.21.

The TBL-TE noise prediction capability and accuracy was demonstrated by the authors but TE-noise scaling peak Strouhal for different airfoil chords did not collapse well after scaling, for the smaller chord airfoils, where laminar BL is dominant and thus it may be concluded that the TBL-TE noise prediction model is more readily applicable to high Re number flows.

In the model review section (Appendix D), validations of the BPM model by different authors are also reported. In the case of NREL validations, which employed a different data set and, thus, is considered most relevant, Moriarty and Migliore (Moriarty &

Migliore, Semi-Empirical Aeroacoustic Noise Prediction Code for Wind Turbines, 2003) have found the overall BPM noise prediction performance to be within 2-3 dB from measurements.

The use of the symmetrical NACA 0012 airfoil and its boundary layer displacement thickness correlations for both the zero and non-zero AOA cases are among the most criticized aspects of the BPM method (Fuglsang & Madsen, Implementation and Verification of an Aeroacoustic Noise Prediction Model for Wind Turbines, 1996), (Wagner, Bareiß, & Guidati, Wind Turbine Noise, 1996), (Guidati & Wagner, 2000), (Moriarty, Guidati, & Migliore, Recent Improvement of a Semi-Empirical Aeroacoustic Prediction Code for Wind Turbines, 2004), (Lutz, Würz, Herrig, Braun, & Wagner, 2004).

A recent review of Turbulent TE noise data by Doolan and Moreau (Doolan & Moreau, 2013) explains that most of the understanding of the physics associated with TE noise derives from experiments that employed the NACA 0012 airfoil profiles in anechoic wind tunnel tests. The review compared data at zero AOA from different facilities and concluded that there is reasonable agreement across different data sets at moderate Reynolds numbers ($Re \approx 1 \times 10^6$), but limited agreement for Reynolds numbers high enough to represent flow on outboard sections of modern WT rotor blades, suggesting the need for further testing and updating of the noise prediction models. This review further concluded that the BPM model predictions compared well with most data sets for low Mach numbers, but the Mach number dependency of the BPM model did not seem appropriate when compared to experimental or numerical simulation data. The experimental data suggested that the noise spectrum should display only Reynolds number dependency, provided other variables were properly scaled. Also, no variation on the peak Strouhal number with Reynolds number was detected.

The detailed calculation procedure for the BPM TE noise on the pressure and suction side of the airfoil, and also from partially separated flow noise on the suction side will be described in detail in Section 3, Methodology.

2.4.2 Simplified-Theoretical Models.

Academic and research institutions have concurrently pursued development of more complex, flow and geometry intensive models like the simplified theoretical and Computational Aeroacoustics (CAA) approaches.

The simplified theoretical approach evolved from the model of Glegg (Glegg S. , Significance of Unsteady Thickness Noise Sources, 1987), (Glegg, Baxter, & Glendinning, The Prediction of Broadband Noise From Wind Turbines, 1987), described in Appendix D.

The simplified theoretical approach for TE noise prediction requires a much larger set of information, including turbulence information, than the semi-empirical models. Despite that, with the cumulative adoption of empirical constants, law of the wall, turbulence isotropy hypothesis and simple turbulence scale models for closure and simplification, the method will not necessarily lead to a noise prediction of superior accuracy. Also, the method is more time consuming and would probably lie between the semi-empirical and CAA methods in terms of turnaround time.

Often, steady-state CFD-RANS simulation codes with two equation turbulence models are employed for the purpose of estimating the turbulence parameters needed (Glegg & Reba, 2010), (Remmler, Christophe, & Anthoine, 2010), (Kamruzzaman M. , Lutz, Herrig, & Krämer, 2012a), (Eisele, Pechlivanoglou, & Nayeri, 2013).

According to Kamruzzaman (Kamruzzaman M. , Lutz, Nübler, & Krämer, 2011), the accuracy of the noise prediction schemes depend upon the accurate modelling of the turbulent noise source terms employed in the TNO-Blake or TNO-TPD noise prediction model. This statement can be safely generalized by saying that the accuracy of all noise prediction methods depends upon the quality of the data inputted to them, whether simplified theoretical or semi-empirical methods.

The most relevant Simplified-Theoretical models and methods found in the bibliography, including the TNO-Blake or TNO-TPD, are discussed in Appendix E.

2.4.3 The Computational Aeroacoustic Methods.

Concerning Computational Aeroacoustics (CAA) models, two approaches are possible, according to Orselli (Orselli, 2011), the direct and the hybrid approach. In the direct one, the use of compressible DNS (Direct Numerical Simulation) allows for accurate representation of the dynamic and acoustic phenomena, including propagation (Sandberg & Jones, 2010), while the hybrid methods employ CFD in order to determine the strength of the sources (for application in propagation models) or in order to calculate the propagation to the far-field via integral (FW-H, Kirchhoff) or advection (Acoustic Perturbation Propagation, Linearized Euler Equation) approaches.

Some authors will apparently reserve the CAA acronym solely for the direct computational approach (Tam, 2012). DNS simulation will avoid interfacing between solution methods, as required by the hybrid methods, and allows for the presence of acoustic feed-back loops (Sandberg & Jones, 2010). Also, according to Sandberg and Jones, DNS is the preferred investigation tool when identifying noise reduction mechanisms for different geometry and lends itself to fundamental studies because of the lack of modeling.

Despite that, DNS results are currently few and a possible reason is pointed out by (Eisele, Pechlivanoglou, & Nayeri, 2013):

“The high computational cost of high-order numerical methods have been a traditional barrier for the limited budget of the wind industry compared to aerospace applications. Therefore, low order numerical tools such as the Eppler code or the XFOIL code of M. Drela have been the “work-horses” of this industry.”

For a brief discussion on the wide ranges of frequencies and amplitudes covered in the broadband acoustic problem, see Appendix B.8. For a quick review on hybrid methods, the reader is referred to Da Silva (Da Silva, 2011) and Orselli (Orselli, 2011), and for a detailed treaty on the subject of CAA, the reader is referred to Tam (Tam, 2012).

2.4.4 Noise Prediction Methods - Existing Classification

It should be stressed at this point that the combination of a noise prediction model plus the accessory tools necessary to deploy it (e.g. flow field solver) is called a *noise prediction method* in this text.

Since noise emission is one of the major problems for further spread of onshore wind turbines and limits its public acceptance (Lutz, Herrig, Würz, Kamruzzaman, & Krämer, 2007), there is an increasing demand for the use of noise prediction codes (Wagner, Bareiß, & Guidati, Wind Turbine Noise, 1996).

Noise prediction codes may be used in different design phases of airfoils, blades and rotor development, and they help design noise-efficient equipment that will meet community acceptance and economic, legal and environmental restrictions. Their development requires a set of assumptions and simplifications and the main concerns are with the geometrical, flow and noise-source modelling.

The first classification for noise prediction methods aimed at WT was proposed by Lawson (Lawson, 1993), which divided the schemes in three classes:

Class I methods: Predictions resulting in estimation of the sound pressure level (SPL) or the sound power level (SPW) as a simple algebraic function of basic WT parameters. For an example of a Class I method, see van der Borg's one parameter model, employed in section 1.1.6 and reproduced below for convenience, where the only independent parameter is the WT rotor diameter, D .

$$SPW = 22 \cdot \log D + 65 \text{ dB(A)} \quad (1 - 3)$$

Many other class I methods are compiled by Wagner et al. (Wagner, Bareiß, & Guidati, Wind Turbine Noise, 1996), p. 95. Some of them employ the rated power of the WT instead of the diameter while others employ both the diameter and tip speed. Some of them will return the SPW, which does not depend upon directivity, and others will return the SPL at 1 m from the rotor shaft. Although some of the class I methods will demand more rotor information (area, number of blades) and some are equipped with a simple, spherical propagation model, no detailed information concerning the blade-geometry or the flow are employed in class I methods, by definition. According to Vér and Beranek (Vér & Beranek, 2006), p. 680, the real SPL of some WT will be larger than predicted by as much as 10 dB(A) with this class of methods.

Class II methods: Predictions are based on specific considerations for the different mechanisms causing WTN, but the use of WT and flow related parameters is limited. For examples of Class II methods, see the models from Grosveld (Grosveld, 1985), Glegg et al. (Glegg, Baxter, & Glendinning, The Prediction of Broadband Noise From Wind Turbines, 1987) and Brooks et al. (Brooks, Pope, & Marcolini, Airfoil Self-Noise and Prediction, 1989), among others.

Class III methods: Predictions using full information about the noise mechanisms, rotor geometry and flow properties. These methods, by definition, are not suitable for preliminary design of blades or rotors, because detailed geometric information is not available ex-ante at the preliminary design and naturally no experimental data will exist at this time of the product development cycle, for comparison. Nevertheless, the methods of this class are suitable for design optimization and provide the most accurate results short of experimentation. In theory, DNS computation would bear the potential for returning exact predictions.

For both Class II and Class III methods, there is limited experimental data for validating the results (Doolan & Moreau, 2013) since many crucial information about the geometry of the blades, like the airfoil shape, chord and twist distribution along the span, are treated as proprietary information (De Andrade, Milone, & Joaquim, 2013). Also, detailed experimental flow information like the local AOA and velocity at blade stations or turbulence parameters are seldom available.

According to Lawson (Lawson, 1993), Class II and III models may be further classified as complete or incomplete, depending upon the number or noise mechanisms considered and also whether the directivity function of the noise sources is considered or not.

A table of typical input necessary for Class II and Class III noise prediction codes is provided below.

Table 2-7 - Typical input required by Class II and Class III noise prediction models. Source: (Wagner, Bareiß, & Guidati, Wind Turbine Noise, 1996)

<i>Group</i>	<i>Parameter</i>	<i>Class II</i>	<i>Class III</i>
Turbine configuration	Hub height	x	x
	<i>Type of tower</i>		x
Blade/rotor	<i>up/downwind orientation</i>		x
	Number of blades	x	x
	Chord distribution	(x)	x
	Thickness of trailing edge	(x)	x
	Radius	x	x
	<i>Profile shape</i>	(x)	x
	<i>Shape of blade tip</i>	(x)	x
Atmosphere	<i>Twist distribution</i>	(x)	x
	Turbulence intensity	x	x
	Ground surface roughness	x	x
	<i>Turbulence intensity spectrum</i>		x
Turbine operation	<i>Atmospheric stability conditions</i>		x
	Rotational speed	x	x
	Wind speed, alternatively: rated power, rated wind speed, cut-in wind speed	x	x
	<i>Wind direction</i>		x

The work of Zhu (Zhu, 2004) discussed in the Appendix D, is an implementation of a noise prediction Class III method with extra details such as blade tip shape, tower geometry and wind direction, which was referred to, by the author, as a “Class III-plus” method.

A classification scheme of noise prediction methods that is more suitable for the newest numerical methods is employed by Kamruzzaman (Kamruzzaman M. , Lutz, Herrig, & Krämer, 2012a), based on the nature of the core noise prediction model employed:

- Semi-Empirical Methods, based on the semi-empirical models (e.g. (Brooks & Hodgson, 1981), (Brooks, Pope, & Marcolini, Airfoil Self-Noise and Prediction, 1989))
- Simplified Theoretical Methods, based on the simplified theoretical models (e.g. (Blake, Mechanics of Flow-Induced Sound and Vibration, 1986 II), (Lutz, Herrig, Würz, Kamruzzaman, & Krämer, 2007), (Kamruzzaman M. , Lutz, Nübler, & Krämer, 2011)).
- Computational Aeroacoustics Methods, based on CAA models (e.g. (Lockhard, 1999), (Morris, Long, & Brentner, 2004), (Sandberg & Jones, 2010))

2.4.5 Noise Prediction Methods Classification

All self-noise prediction methods employing the semi-empirical or simplified theoretical models discussed in the text and appendixes must rely on 2-D TBL flow information for noise prediction. The source of TBL flow data should be compatible with the noise model and will define the method accuracy and turnaround time (TAT).

Also, methods that predict blade and rotor-noise emission will demand additional induced-flow field information in order to evaluate local conditions (AOA and relative speed) for each spanwise section of the rotor blade.

Thus, at least one supplemental model for the induced-flow calculation, among those briefly described in section 2.3 (disk actuator model, BEM and Vortex Wake) should be also selected and it may be supplemented by other models like 3-D corrections, tip corrections, etc.

While combining noise prediction models with flow-field solver tools and other accessory models, the authors have generally one of two goals: (a) to identify methods that can return acceptable information in short turnaround times, or (b) to identify methods that can return very reliable results, regardless of the computational cost.

No broad classification was identified in the literature for *methods*, under the definition employed herein, i.e., for the different combinations of models, even though there are few self-noise and inflow turbulence prediction models available and much of the effort discussed in the literature describes the integration of these models, basic or improved, in tools that can provide noise spectra results with useful quality.

Although a two-dimensional classification system based solely in the turnaround time and accuracy would probably suffice to sort all methods in the future³¹, at this time it is possible and necessary, for differentiation purpose, to sort the noise prediction methods applicable to WTN according to many different relevant aspects:

- Modeled noise sources
- Type of theoretical base
- Type of noise field

³¹ Due to historically increasing computational speeds and decreasing costs.

- WT geometry description required as input data
- Flow Field data required as input
- Turnaround time for deployment
- Accuracy as measured against experimental data.
- Type of application domain (validation geometry)
- Location of the observer
- Availability
- User-Friendliness

Another important factor considered by industries and researchers alike is the economic cost of procuring (or assembling) and running noise prediction tools, especially in the recurring environment of airfoil, blade and rotor development design. Although this cost is not directly assessed by this proposed broad classification method, which is still essentially qualitative, it may be inferred through some proxy variables like the turnaround time, availability and user-friendliness.

The classification criteria and respective descriptions are all given below from Table 2-8 through Table 2-18.

Table 2-8 - Modeled noise sources.

Method Classification based on modeled sources	Description
Self-Noise	Modeling of Self-Noise (all sources).
Inflow Noise	Modeling of Turbulent inflow noise.
Stall noise	Modeling of Self-Noise and Inflow noise in the post-stall regime
Complete	Modeling of Self-Noise (all sources), Turbulent inflow noise and Stall noise.
Partial	Any incomplete combination of the above sources.

Table 2-9 - Type of theoretical base.

Method Classification based on theoretical base	Description
E	Empirical correlation
AA (Acoustic Analogy) - SE	Ffowcs Williams & Hall or Ffowcs Williams & Hawkings analogies based, Semi-Empirical.

AA - ST	Ffowcs Williams & Hall or Ffowcs Williams & Hawkings analogies based, Simplified Theoretical.
Hybrid	NS in the near field and AA or ray-tracing theory for the far field.
NS	High resolution Navier-Stokes solution (e.g., LES, DNS).

Table 2-10 - Type of noise field.

Method Classification based on the noise field	Description
NF	Near Field
FF	Far Field, without propagation models
FF +P	Far Field, with propagation models
Full Field	Full Field (CAA models only)

Table 2-11- WT geometry description required as input data

Method Classification based on WT geometry required	Description
DP	Data-plate information only (e.g.; diameter, rated power, etc.)
2D	Airfoil geometry only.
Q3D	Quasi-3D. Airfoil, chord and twist as a function of radius.
Q3D+T	Quasi-3D + Tower. Airfoil, chord and twist as a function of radius, tower geometry and position.
3D	Detailed rotor information.
3D+T	3D plus tower geometry and position information.

Table 2-12 - Flow field data required as input

Method Classification based on flow field data detail	Example	Description
None	None	Data-plate information only (e.g.; diameter, rated power, TSR, etc.)
Very Little	TBL-FP	Turbulent Boundary Layer correlations for Flat Plate
Little	XF(XFOIL-type)	Turbulent Boundary Layer Integral relations calculated over real airfoil geometry.
Some	RANS-2ISO	RANS calculated field, with 2-equation isotropic turbulence model.
Intensive	RANS-2ANISO	RANS calculated field, with 2-equation anisotropic turbulence model.

	RANS-RSM	RANS calculated field, with Reynolds Stresses Modeling (RSM)
	URANS-RSM	Unsteady RANS, RSM calculated flow field
Very Intensive	DES/LES	Detached Eddy Simulation / Large Eddy Simulation
	DNS	Direct Numerical Simulation
	EXP	Experimental

Table 2-13 - Turnaround time (TAT).

Method Classification based on comparative TAT	Description
S	Short
M	Medium
L	Long
VL	Very long

Turnaround time is judged comparatively, based in the full circle of (i) prediction tool availability, (ii) ease of use, (iii) information gathering, (iv) setup, (v) run and (vi) analysis of the results. For methods that involve codes that are not in public domain, the information analysis process and software coding time should be considered in the prediction tool availability time. Computational time should be considered in the run time.

The degree of freedom in airfoil design optimization allowed is inversely proportional to total TAT for each method, making this an important selection criteria.

Table 2-14 - Accuracy class against experimental data.

Method Classification based on accuracy.	Description
OM	Suitable for Order of Magnitude estimation, only (~ 10 dB).
PD	Suitable for Preliminary Design (3 – 5 dB).
OPT	Suitable for Optimization Design (< 3 dB).

Since the most popular semi empirical (SE) and simplified theoretical (ST) methods generate output in 1/3 octave bands (SE) or selected frequencies (ST), they are often tentatively validated by comparison of the predicted noise spectrum with an experimental spectrum. The prediction errors are not homogeneous throughout the frequency range and the authors usually do not provide an error variation as a function

of frequency, issuing instead qualitative evaluations (e.g. “satisfactory” or “unsatisfactory”). The OASPL might be employed as a measure of the overall method quality, when compared against measurements, but the bibliographic review showed that this data is seldom available³². Nevertheless, when available, it might be a good indicator of the accuracy of the method when only systemic errors are present in the formulation. In the case a method is affected by non-systemic errors though, the predicted OASPL could be very close to measured values while some frequencies might show unacceptably large deviations from band-measured SPL.

Table 2-15 - Type of application domain (geometry validation).

Method Classification based on application domain.	Description
Specific	One airfoil or family, limited AOA
Restricted	Some airfoils of families, unlimited AOA below stall.
Generic	Any airfoil, unlimited AOA below stall.

Table 2-16 – Location of the observer.

Method Classification based on location of the observer on the far field.	Description
AF	Fixed in relation to the airfoil section.
HF	Fixed in the WT hub shaft line.
VPF	Fixed in the vertical plane through the tower and hub.
ALUS	Any location, user specified.

Table 2-17 – Availability.

Method Classification based on the availability of the tool	Description
Text	Text description available only
Flow Chart	Flow Chart Description available
Code listing	Detailed Code Listing for programming
Online	Online access and use of the code
Download - Compiled	Available for download in compiled form
Download – Source	Available for download in source code form

³² One possible reason is that the experimental data often lacks some frequency bands, discarded because of signal-to-noise ratio and also because some noise prediction models, like the simplified theoretical TNO applies to TE noise only which, like any other isolated noise source, is difficult to isolate from the overall measured noise spectrum.

Table 2-18 – User-Friendliness.

Method Classification based	Description
UNK	Unknown
NO GUI	No Graphic User Interface
GUI	Graphic User Interface

2.4.6 TE Noise Prediction Methods: A New Classification

The qualitative noise prediction method classification procedure proposed in the previous sub-section was applied to the methods reviewed in section 2, plus Appendixes D and E, in order to highlight the differences, individual advantages and general opportunities, with results displayed in Table 2-19.

Table 2-19 - Classification of all reviewed Semi-Empirical and Simplified-Theoretical WT noise prediction methods, in accordance with the proposed criteria.

Wind Turbine Noise Prediction Method Classification Dimensions													
			1	2	3	4	5	6	7	8	9	10	11
	Method	Ref.	Noise Sources	Theor. Model base	Noise Field	Geometry data	Flow Field Data	TAT	Accuracy class	Validation Domain	Observer position	Availability	User-Friendliness
1	Grosveld	Grosveld, 1985	Partial (TE + Inflow)	SE	FF	2D/Q3D	very little	N/A	PD	Specific	ALUS	Text	Unk
2	Howe	Howe, 1978	Partial (TE)	SE	FF	2D	intensive	long	OM	Specific	ALUS	Text	Unk
3	Brooks-Hodgson	Brooks and Hodgson, 1981	Partial (TE)	SE	FF	2D	intensive	long	OPT	Specific	AF	Text	Unk
4	Brooks-Marcolini	Brooks and Marcolini, 1985	Partial (TE)	SE	FF	2D	little	medium	PD	Specific	AF	Text	Unk
5	Glegg	Glegg, 1987; Glegg et al., 1987	Partial (TE + Inflow, separated flow)	SE	FF	2D	intensive	long	N/A	Specific	ALUS	Text	Unk
6	BPM	Brooks, Pope and Marcolini, 1989	Self-Noise	SE	FF	2D	little	medium	OPT	Specific	AF	Code List - Fortran 5	No GUI
7	Lowson	Lowson, 1993	Partial (TE + Inflow)	SE	FF	2D/Q3D	very little	medium	PD	Specific	AF	Text	Unk
8	IAG-I	Bareiss, Guidati and Wagner, 1994	Self-Noise + inflow	SE	FF	2D	little	medium	OM	Specific	AF	Text	Unk
9	RISO	Fuglsang and Madsen, 1996	Self-Noise + inflow	SE	FF	2D/Q3D	little/some	short	PD	Specific	ALUS	Text	Unk
10	NREL	Moriarty and Migliori, 2003	Self-Noise + inflow	SE	FF	2D/Q3D	little/some	short	PD	Specific	AF	Download - Source (Embedded into the NREL Aeroacoustic code - FAST)	No GUI
11	Zhu	Zhu, 2004	Self-Noise + inflow	SE	FF + P	2D/Q3D+T	little/some	short	PD	Restricted	ALUS	Text	Unk
12	NREL-NAFNoise	Moriarty, 2005	Self-Noise + inflow	SE	FF	2D	little	short	PD	Restricted	AF	Download - Source	No GUI
13	Vargas	Vargas, 2008	Self-Noise + inflow	SE	FF	2D/Q3D	little	short	PD	Specific	ALUS	Flow Chart + Online	GUI
14	Moriarty-Guidati-Migliore	Moriarty, Guidati and Migliore, 2005	Partial (TE + Inflow)	ST	FF	2D	little	short	PD/OPT	Restricted	AF	Text	Unk
15	Glegg-Reba	Glegg and Reba, 2010	Partial (TE)	ST	FF	2D	intensive	long	OPT	Restricted	N/A	Y237 Pratt&Whitney RANS proprietary code	Unk
16	IAGNoise	Guidati and Wagner, 2000; Lutz, Wurz et al, 2004; Lutz, Herrig et al, 2007; Kamruzzaman, Meister et al., 2010; Kamruzzaman, Lutz et al. 2011; Kamruzzaman, Lutz et al.. 2012a; Kamruzzaman, Lutz et al.; 2012b.	Partial (TE)	ST	FF, probably NF in recent LES validation work.	2D/Q3D	little/some/detailed	short/medium/long	PD/OPT	Restricted	N/A, ALUS	Text - Flow Chart	Unk

N/A = Not Available.

Unk = Unknown.

By analyzing Table 2-19, it was possible to draw some preliminary conclusions and to identify some opportunities:

- No model was found for noise prediction in the stalled regime and there is no complete noise prediction method for all sources and regimes.
- From the point of view of the WT industry, there is no readily available TE noise prediction method with a short TAT, all-geometry capacity, downloadable source code with GUI capability. All these dimensions will heavily impact TAT and productivity at the industry.
- There is no broad validation result published for any method, involving a significant number of different airfoil geometries and AOA.

2.5 AIRFOIL SECTIONS FOR HORIZONTAL-AXIS WIND TURBINES

A detailed description of the airfoil geometric and design parameters may be found in Pechlivanoglou (Pechlivanoglou, *Passive and Active Flow Control Solutions for Wind Turbine Blades*, 2012), pp. 9-13, including a list of common design requirements for WT airfoils, among which are tolerance to roughness, high aerodynamic efficiency, smooth stall and *low noise emission*.

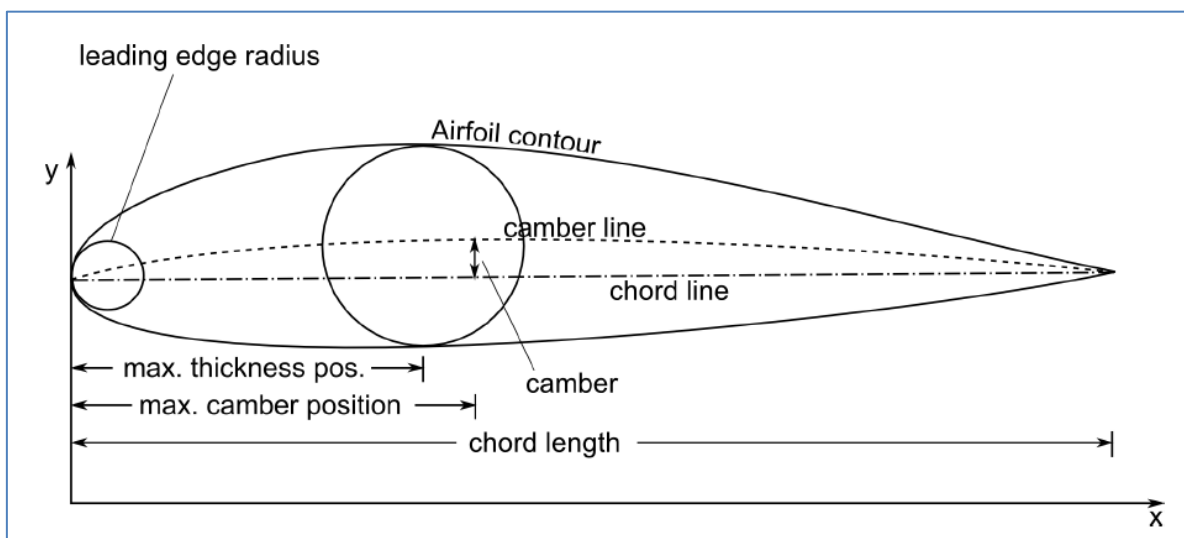


Figure 2-28 - The airfoil geometric parameters (Pechlivanoglou, *Passive and Active Flow Control Solutions for Wind Turbine Blades*, 2012).

After design, the contour (see Figure 2-28) or “profile” of an airfoil is stored in a set of coordinates describing discrete points of the upper and lower surfaces. This *thickness distribution along the chord* is generally represented by (x, y) coordinates, with $(0,0)$ frequently describing the LE and $(1,0)$ the TE. The surface is often reconstructed by the application of splines or other smooth curves through the given points.

The most commonly used performance curves for evaluating airfoils for WT blade applications are the classic lift, drag and moment coefficient curves plotted against the angle-of-attack (AOA), the drag polar diagram and the aerodynamic efficiency ratio (cl/cd) plotted against AOA.

The characteristics of the different airfoils designed for HAWTs are chosen by the designer based on his objectives (Pechlivanoglou, *Passive and Active Flow Control Solutions for Wind Turbine Blades*, 2012), with the most common requirements being:

- Surface roughness tolerance.
- Stall initiating distance from the trailing edge.
- Absence of laminar separation bubbles.
- Smooth stall (no rapid lift loss at stall).
- High structural stiffness.
- High aerodynamic efficiency at the design point.
- Clearly defined laminar-turbulent transition point.
- Low noise generation.

According to Timmer and van Hooji (Timmer & van Rooji, 2003), it was common practice in the last decades of the last century to use NACA 4 (44XX) and 6 digit (63 series) airfoils to design WT blades. Thicker airfoils for the inboard sections were obtained by scaling the coordinates from airfoils with smaller thickness. However, these scaled NACA airfoils suffered from severe degradation of performance due to premature transition forced by roughness and this motivated researches both in Europe and in the USA to develop alternative WT airfoils, especially for thicknesses of 21% of the chord or more. Also, the design was often not suitable for minimizing stall and post-stall loads frequently encountered by inboard blade sections during transient operation, which led to some early mechanical failures until further study of post-stall behavior was accomplished by Viterna and Janetzky (Viterna & Janetzky, 1982) and others.

Also, according to Burton et al. (Burton, Jenkins, Sharpe, & Bossanyi, 2011), NASA's 4 and 6 digit series airfoils were very popular due to the availability of high quality experimental data, in the form of NACA reports, from tests carried out from 1930 onwards, in its pressurized wind tunnel. A treaty on many of the airfoils developed and performance curves may be found in a classic text by Abbott and Von-Doenhoff (Abbott & Von-Doenhoff, 1959).

Five digit series were also employed in some of the first NASA large-size experimental HAWT models, like the 2 MW "MOD 2" (c. 1979), which employed the NACA 23014 airfoil. Around the turn of the century, NACA airfoils were still largely employed, as may

be seen from Guidatti and Wagner (Guidati & Wagner, 2000) which have justified the use of the NACA 64418 airfoil in an optimization study, by stating that the airfoil was commonly employed on, then current, WT designs. Also, Hansen (Hansen, 2008), employed the NACA 63415 airfoil in some optimization examples since, according to the author, it was proven to possess stall characteristics suitable for WT design and reasonably low sensitivity to roughness, two very important features for the application.

The NACA 0012 was employed in early machines and has been used as the standard airfoil in much of the fundamental experimental effort concerning WT noise measurements (Brooks & Hodgson, 1981), (Brooks & Marcolini, 1985), (Brooks, Pope, & Marcolini, Airfoil Self-Noise and Prediction, 1989). Although the use of this specific airfoil was eventually phased out in HAWT design and construction, most of the noise prediction tools developed to date still employ those experimental results for the purpose of validation.

The four-digit NACA 0012 airfoil is a zero-camber (symmetrical) airfoil, with a height of 12% of the chord, as shown in Figure 2-29.

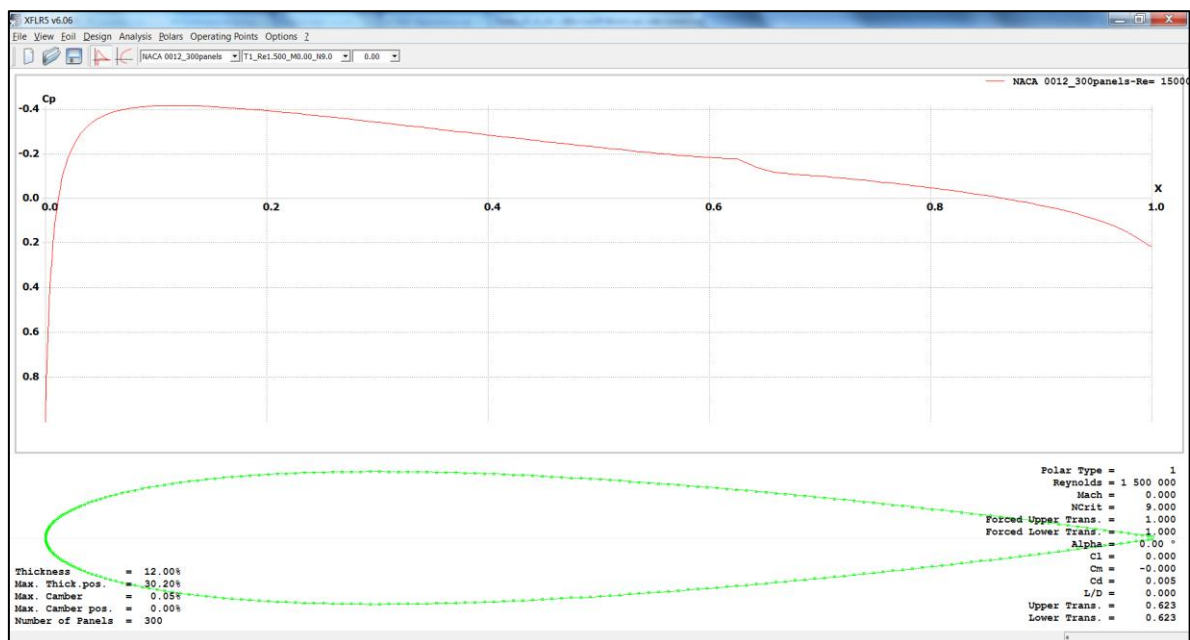


Figure 2-29 - The NACA 0012 airfoil (300 panels), plotted with the aid from XFOIL/XFLR5. Pressure Coefficient plotted over chord, for zero AOA and $Re = 1.5 \times 10^6$.

Some research was done in trying to understand the reason behind the selection of this simple airfoil as the workhorse of most of the early experimental tests. According to Hoerner and Borst (Hoerner & Borst, 1985), p.2-2, the most successful airfoil

sections developed in the first quarter of the twentieth century for use in cantilevered-wing monoplanes were the Gö-535, the Clark-Y, the USA-35B and the RAF-34, and all of them had 12% thickness. Also the first systematic series of sections named after Joukowski, who established the mathematical method of producing their shape and predicting their circulation, is similar in shape to those airfoils. But apart from having the “optimal” thickness for producing the least drag under moderate flow velocities, the ubiquitous NACA 0012 section has a very peculiar characteristic of displaying a good lift-slope curve in reverse flow direction (actually, it is slightly higher than under straight flow!). This makes the section especially suited for helicopter rotor design, since the inner part of the rotor may actually face reverse flow when the ship is in advancing flight. This findings allowed the understanding of the missing link: the first engineering studies on WT rotors were based on a proven helicopter rotor airfoil geometry (see Figure 2-30).



Figure 2-30 – Symmetrical airfoil sections similar to the NACA 0012 airfoil, employed in helicopter rotors (Bell UH-1 Iroquois helicopter rotor). Photo: author @ USS Intrepid Museum, NYC, 2014

Most of the airfoil shapes employed in current design by the leading manufacturers of large size HAWTs are considered proprietary design information and are not available to the general public. Government related agencies and laboratories worldwide, like

NREL (USA), RISO and DTU (Denmark) and Delft University-DU (Netherlands), have developed, sometimes under collaboration with private companies, dedicated airfoils for HAWT applications since 1984.

One partial exception to this situation is the availability of coordinates for the NREL family of WT airfoils, which may be currently found in the Laboratory web site (National Renewable Energy Laboratory - NREL 1, 2015). However the use of these airfoils in actual design is currently subjected to licensing fees.

2.5.1 AIRFOIL DEVELOPMENT AIMED MAINLY AT AERODYNAMIC EFFICIENCY

The clear trend of WT diameter increase over time, well-illustrated by Figure 1-8 (see also (European Wind Energy Association - EWEA, 2009) p.6), implies in a steady increase of local operating Reynolds and Mach numbers for blade sections in a fixed %-span position, at the same rotation rate. Therefore, “efficient airfoils” developed for 3 m – 50 m diameter WT in the past (see Table 2-24) are not necessarily efficient for current and future 100 m-plus diameter WT and, most often than not, their design and selection process did not address the acoustic emission problem.

This sub-section is a brief report on the development of some relevant WT airfoils, the primary design driver for which has been the aerodynamic efficiency. The reports are presented in chronological order, but that does not reflect necessarily the actual chronology of airfoil development, since some reports were published with large delays.

The development of WT airfoils at Delft University of Technology (DU) is reported by Timmer and van Rooji (Timmer & van Rooji, 2003). DU had to meet the requirement that the airfoils should be suitable for fixed and variable pitch blades, which required some compromise regarding the stall and post stall behavior. Although the airfoil design is always a tradeoff, a high lift-to-drag ratio and a low sensitivity³³ to airfoil surface contamination and contour imperfections have been generally primary design

³³ This low sensitivity to airfoil surface contamination means that, for WT design purpose it is important for the airfoil performance parameters not to decay abruptly or below requirements when the airfoil surface becomes rough due to dirt accumulation, impacts and roughness.

drivers at DU as far as WT airfoils are concerned. However, there are other specific design constraints that will depend upon the radial position the airfoil will assume along the span of the blade. Design features of the DU families of airfoils are shown in Table 2-20 and Table 2-21.

Airfoil sections close to the hub, for instance, are strongly affected by structural requirements and the 3D flow effects such as the centrifugal pumping, a phenomenon illustrated by Hansen (Hansen, 2008), p23. However, as confirmed by experiments from Moriarty and Migliore (Moriarty & Migliore, Semi-Empirical Aeroacoustic Noise Prediction Code for Wind Turbines, 2003) and Oerlemans (Oerlemans, Wind Turbine Noise: Primary Noise Sources, 2011), all significant self-noise sources are located at the *outboard* portion of the blade, for large size HAWTs, due to increased tangential speed and hence, high local Mach number.

For the outboard airfoils, the peak value of the c_l at the design point (maximum c_l/c_d) is relatively unimportant in a pitch controlled WT, from the performance perspective, according to Timmer and van Rooji (Timmer & van Rooji, 2003). Also a small (~ 0.2) difference between $c_{l,design}$ and $c_{l,max}$ is desirable to prevent excessive loads from gusts and also to prevent stalling due to slow control actuation. As far as $c_{l,max}$ is concerned, high values of this parameter associated with high AOA are not desirable, since the degradation of surface finish and corresponding increased roughness will reduce the $c_{l,max}$ corresponding angle by several degrees, resulting in large differences in lift between the clean and soiled airfoil surface conditions. Therefore, the authors (Timmer & van Rooji, 2003) recommend moderate values of $c_{l,max}$ (1.4~1.5). Less thick airfoils, like the DU 95-W-180 / DU 96-W-180 outboard airfoils, were designed with the aid of XFOIL, while thick ones, used inboard, where the 3D effects are more pronounced, used the RFOIL software, an XFOIL modified in-house for the 3D rotational flow effects. Table 2-22 shows design requirements and wind tunnel results for the DU 95-W-180 / DU 96-W-180 outboard airfoils. The DU airfoil coordinates are generally not available to the public.

Table 2-20 - Key design features for DU (Delft University) WT airfoils at Reynolds number of 3×10^6 . Source: (Timmer & van Rooji, 2003) p. 491.

Airfoil	Airfoil clean					Zigzag tape at $x/c=0.05$ u.s.	
	t/c	α_0	$C_{1,\alpha}$	$C_{1,max}$	$(C_1/C_d)_{max}$	$C_{1,max}$	$(C_1/C_d)_{max}$
DU 91-W2-250	0.25	-3.2	0.126	1.37	128	1.16	62
DU 93-W-210	0.21	-4.2	0.123	1.35	143	1.17	65
DU 95-W-180	0.18	-2.0	0.116	1.21	143	1.14	70
DU 96-W-180	0.18	-2.7	0.115	1.26	145	1.17	73
DU 97-W-300	0.30	-2.2	0.128	1.56	98	1.17	53

Table 2-21 - More design features of the DU (Delft University) airfoils for WT blades. Source: (Burton, Jenkins, Sharpe, & Bossanyi, 2011), p. 119.

Aerofoil	Max t/c %	x/c at max t/c	y/c at T.E.	Re $\times 10^{-6}$	α	c_1 Max	Design α	Design C_1	Max C_1/c_d
DU 96-W-180	18	0.3	0.0018	3.00	-2.7	1.26	6.59	1.07	145
DU 00-W-212	21.2	0.3	0.0023	3.00	-2.7	1.29	6.5	1.06	132
DU 91-W2-250	25	0.3	0.0054	3.00	-3.2	1.37	6.68	1.24	137
DU 97-W-300	30	0.3	0.0048	3.00	-2.2	1.56	9.3	1.39	98
DU 00-W-350	35	0.3	0.01	3.00	-2.0	1.39	7.0	1.13	81
DU 00-W-401	40.1	0.3	0.01	3.00	-3.0	1.04	5.0	0.82	54

Table 2-22 – Airfoil design requirements for DU 95-W-180 / DU 96-W-180 outboard airfoil and wind tunnel test results. Source: (Timmer & van Rooji, 2003), p. 492.

Design requirements for DU 95-W-180:

- 18% relative thickness
- cl_{max} of 1,25 @ 3×10^6
- $cl/cd > 140$ @ 3×10^6

Wind Tunnel test results for DU 95-W-180 (earlier version, year 1995):

- cl_{max} of 1,20 @ 3×10^6

Wind Tunnel test results for DU 96-W-180 (later version, year 1996):

- cl_{max} of 1,32 @ 3×10^6
- $cl/cd = 149$
- low sensitivity to le roughness (cl_{max} loss is 0.09)

Still in Europe, the researchers at RISO National Laboratory (Denmark) have also developed families of airfoils for WT applications as reported by Fuglsang and Bak (Fuglsang & Bak, Development of the Risø Wind Turbine Airfoils, 2004). The design targets were also high lift and limited sensitivity to roughness. The XFOIL, Ellipsis2-D (a CFD code) and wind tunnel tests were all employed as analysis tools in the effort and, according to the authors, the A series (see Figure 2-31 and Table 2-23) was later superseded by the P-series (Figure 2-31) for use in pitch controlled rotors.

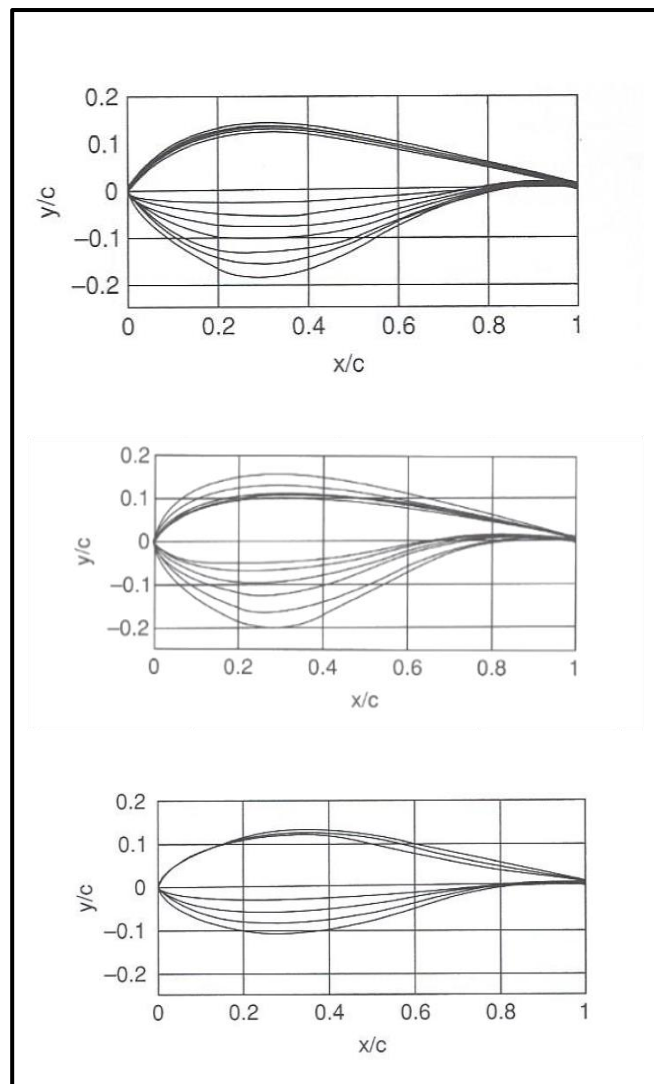


Figure 2-31 - The RISO A (upper plot), B (mid plot) and P (lower plot) series of airfoils. Source: adapted from (Burton, Jenkins, Sharpe, & Bossanyi, 2011), p. 117-118.

The main design features for the RISO airfoils may be found in Table 2-23.

Table 2-23 – Characteristics of the RISO A, B and P families of Airfoils for WT blades. Source: adapted from (Burton, Jenkins, Sharpe, & Bossanyi, 2011), p. 117-119.

Aerofoil	Max t/c %	x/c at max t/c	y/c at T.E.	Re × 10 ⁻⁶	α°	c _l Max	Design α	Design C _l *	Max C _l /c _d
Risø-A1- 15	15	0.325	0.0025	3.00	-4.0	1.50	6.0	1.13	168
Risø-A1- 18	18	0.336	0.0025	3.00	-3.6	1.53	6.0	1.15	167
Risø-A1- 21	21	0.298	0.005	3.00	-3.3	1.45	7.0	1.15	161
Risø-A1- 24	24	0.302	0.01	2.75	-3.4	1.48	7.0	1.19	157
Risø-A1- 27	27	0.303	0.01	2.75	-3.2	1.44	7.0	1.15	N/A
Risø-A1- 30	30	0.300	0.01	2.50	-2.7	1.35	7.0	1.05	N/A
Risø-A1- 33	30	0.304	0.01	2.50	-1.6	1.20	7.0	0.93	N/A

Aerofoil	Max t/c %	x/c at max t/c	y/c at T.E.	Re × 10 ⁻⁶	α	c _l Max	Design α	Design C _l	Max C _l /c _d
Risø-B1- 15	15	0.278	0.006	6.00	-4.1	1.92	6.0	1.21	157
Risø-B1- 18	18	0.279	0.004	6.00	-4.0	1.87	6.0	1.19	166
Risø-B1- 21	21	0.278	0.005	6.00	-3.6	1.83	6.0	1.16	139
Risø-B1- 24	24	0.270	0.007	6.00	-3.1	1.76	6.0	1.15	120
Risø-B1- 30	30	0.270	0.01	6.00	-2.1	1.61	5.0	0.90	N/A
Risø-B1- 36	36	0.270	0.012	6.00	-1.3	1.15	5.0	0.90	N/A

Aerofoil	Max t/c %	x/c at max t/c	y/c at T.E.	Re × 10 ⁻⁶	α	c _l Max	Design α	Design C _l	Max C _l /c _d
Risø-P- 15	15	0.328	0.0025	3.00	-3.5	1.49	6.0	1.12	173
Risø-P- 18	18	0.328	0.0025	3.00	-3.7	1.50	6.0	1.15	170
Risø-P- 21	21	0.323	0.005	3.00	-3.5	1.48	6.0	1.14	159
Risø-P- 24	24	0.320	0.01	2.75	-3.7	1.48	6.0	1.17	156

In USA, most of the published WT airfoil development work was accomplished under National Renewable Energy Laboratory (NREL) initiatives and was organized in the form of public reports released in 2005, although the research work had been ongoing for many years, and in some cases preceded the European researches reported before. Most airfoil families developed have been designed under development subcontract awarded to Airfoils Inc., e.g. (Somers & Tangler, 2005a), (Somers & Tangler, The Airfoils S830, S831 and S832, 2005b), (Somers & Tangler, The Airfoils S833, S834 and S835, 2005c), for rotor diameters ranging from 3 m to 50 m (see Table

2-24). Their development was carried out solely on theoretical grounds, based on results of simulations made with the Eppler airfoil code (Eppler, C.2000).

The need to boost efficiency and maintain it in the presence of LE debris was the primary design requirements for these families. The requirements translated into (i) high maximum lift; relative insensitivity to roughness and; (ii) low profile drag. They generally have thick sections with laminar flow development (retarded transition), as can be seen in Table 2-24, Figure 2-32 and Figure 2-33.

Despite the airfoil geometry optimized to delay transition, manufacturing tolerances and limited maintenance during operation contribute to WT blade surfaces to be inevitably far from optimal shape (see, for instance (Eisele, Pechlivanoglou, & Nayeri, 2013), page 7).

A list of Somers and Tangle's airfoil patents may be found in the NREL Web site (National Renewable Energy Laboratory - NREL 3, 2015). As mentioned before, the NREL WT sections coordinates are publicly available for research, but need licensing in case of actual use in a design.

Table 2-24 - Example of possible applications for the NREL Airfoil families. Source: (Burton, Jenkins, Sharpe, & Bossanyi, 2011), p. 115.

Diameter	Type	Aerofoil thickness	Primary	Tip	Root
3–10 m	Variable speed Variable pitch	Thick	—	S822	S823
10–20 m	Variable speed Variable pitch	Thin	S802	S802 S803	S804
10–20 m	Stall regulated	Thin	S805 S805A	S806 S806A	S807 S808
10–20 m	Stall regulated	Thick	S819	S820	S821
20–30 m	Stall regulated	Thick	S809	S810	S811
20–30 m	Stall regulated	Thick	S812	S813	S814 S815
20–40 m	Variable speed Variable pitch	—	S825	S826	S814 S815
30–50 m	Stall regulated	Thick	S816	S817	S818
40–50 m	Stall regulated	Thick	S827	S828	S818
40–50 m	Variable speed Variable pitch	Thick	S830	S831 S832	S818

Contrary to the DU and RISO wind turbine airfoil development reports, the NREL reports (Somers & Tangler, The Airfoils S830, S831 and S832, 2005b) show some concerns on noise emission but the requirements are unspecific towards frequency or level limitations. Because of profile availability, suitable thickness and low noise emission, the NREL S830 airfoil was selected, during the bibliography review, for use in the estimating process of the real, local flow conditions in a large-size HAWT, later in this research. The design requirements for the NREL S830 airfoil may be seen on the first data column of Table 2-25 and its profile is shown in the top of Figure 2-32.

Table 2-25 - Airfoil design specifications employed in the development of NREL S830 (first column), S831(middle column) and S832 airfoils. Source: (Somers & Tangler, The Airfoils S830, S831 and S832, 2005b), p.15.

Blade radial station	0.75	0.90	1.00
Parameter	Objective/Constraint		
Reynolds number R	4.0×10^6	3.5×10^6	2.5×10^6
Maximum lift coefficient $c_{l,max}$	1.60	1.50	1.40
Lower limit of low-drag, lift-coefficient range $c_{l,ll}$	0.80	0.70	0.60
Upper limit of low-drag, lift-coefficient range $c_{l,ul}$	1.40	1.30	1.20
Zero-lift pitching-moment coefficient $c_{m,0}$	≥ -0.15		
Airfoil thickness t/c	21%	18%	15%

Also, other families of airfoils were designed by NREL with other priorities in mind, according to Burton et al. (Burton, Jenkins, Sharpe, & Bossanyi, 2011), like improving the post-stall control (for stall-regulated rotors), high maximum lift coefficient (for variable-pitch, variable-speed rotors), etc. Some of them are depicted in Figure 2-33. According to Burton et al., one of the general tradeoffs faced in designing a WT airfoil is that low relative thickness results in lower drag but higher thickness allows for higher stiffness and strength with low weight due to the increased moment of inertia of the section.

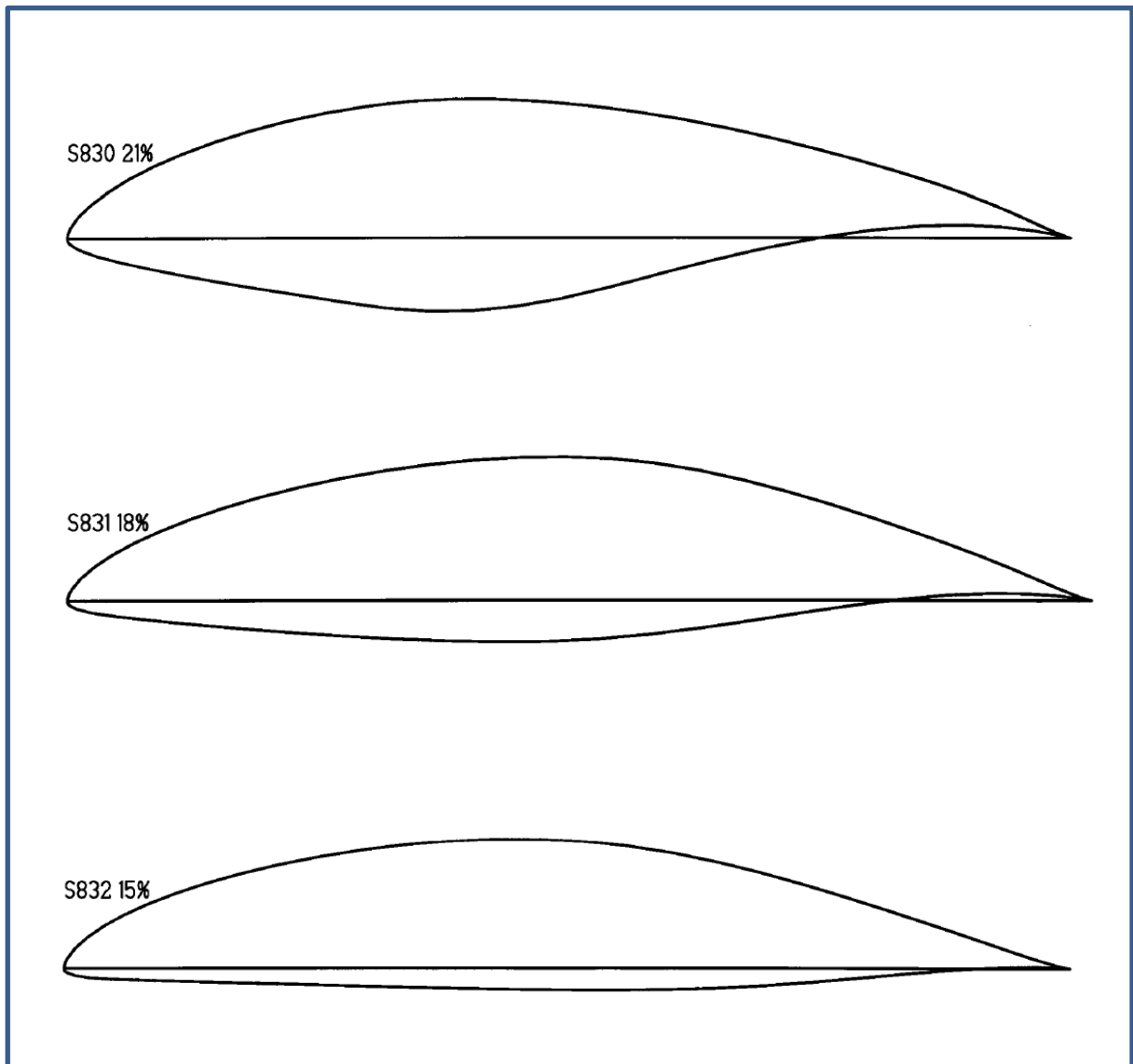


Figure 2-32 - The NREL S830, S831 and S832 airfoil profiles for WT application. Source: (Somers & Tangler, The Airfoils S830, S831 and S832, 2005b), p. 19.

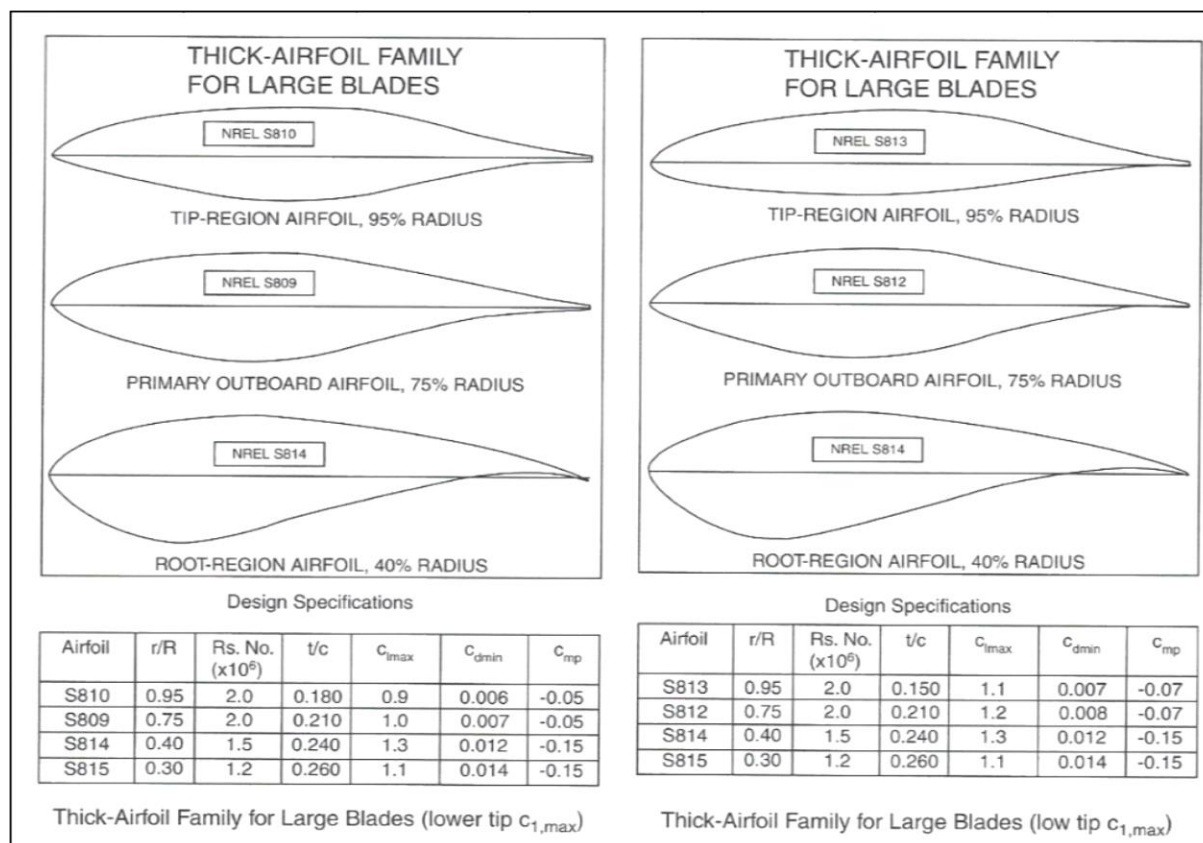


Figure 2-33 - Other profiles of the NREL family of airfoils for stall-regulated or smaller WT blades, typical radial position on the blade and some design characteristics. Source: (Burton, Jenkins, Sharpe, & Bossanyi, 2011), p. 116.

The theoretical performance of all WT developed by NREL were investigated with the aid of the Eppler airfoil code, according to Sommers and Tangle (Sommers & Tangle, 2005a). That code (Eppler, C.2000) employs a hybrid potential flow overlapped into an integral boundary layer formulation for calculating the viscous flow around a 2-D airfoil, but has a (i) weak potential/viscous flow interaction and requires additional models for separated flows as evidenced by Vargas et al. (Vargas, de Oliveira, Pinto, Bortoulus, & Souza, 2005). Also, another limitation of the Eppler code is (ii) the modelling of incompressible flow during all calculations. Some of the simulations accomplished for the current research, using the XFOIL (XFLR5 versions 6.06, 6.10, 6.11 and 6.12), showed a significant variation of the coefficient of lift with the compressibility model turned on and off. For instance, for the 50 m blade baseline configuration developed in this work and discussed later, the $(cl/cd)_{max}$ ratio calculated for the NREL S830 airfoil at 85% blade span, is 76.4 and corresponds to a 6° AOA for incompressible flow at $Re=3,1E+06$. However, when the $Mach=0.2$ (estimated via the BEM method) is

inputted into the XFOIL simulation the $(cl/cd)_{max}$ ratio falls to 72.7, corresponding to a 5° local AOA for the same Reynolds number. Also (iii) most NREL airfoils, including the selected baseline S830 were seemingly designed for lower ranges of Reynolds numbers. Finally, as evidenced by Devenport et al. (Devenport W. , et al., 2010), p. 43, the thick NREL WT airfoils, like the S831 depicted in the reference, (iv) do not necessarily have a large LE radius. As a consequence, as pointed out by Migliore and Oerlemans (Migliore & Oerlemans, Wind Tunnel Aerodynamic Tests of Six Airfoils for Use in Small Wind Turbines., 2003), sharp LE radius may lead to higher inflow noise, which could neutralize any efforts to reduce airfoil self-noise.

Attached flow through all operational AOA-envelope is a necessity from the point of view of both an aerodynamic efficient and a silent airfoil, strongly suggesting aerodynamic and aeroacoustic qualities are simultaneously present in an airfoil design. However, even by adopting highly developed WT airfoils like those from NREL this research will later investigate if there is some improvement to be made based on operating conditions closer to the ones prevailing at the outboard part of large size WT blades.

Airfoil	t/c		α (°)		Design Reynolds	Clean Airfoil		Tripped Airfoil			Blade size recomm.	Coordinates Available?	Public domain use?	Ref.
	max.	loc.	zero lift	design		cl, max.	(cl/cd)max.	trip loc.	cl, max.	(cl/cd) max.				
DU 91-W2-250	0.25	0.3	-3.2	6.6	3E+06	1.37	128	5% u.s.	1.16	62	N/A	No	No	a, b
DU 93-W-210	0.21	N/A	-4.2	N/A	3E+06	1.35	143	5% u.s.	1.17	65	N/A	No	No	a, b
DU 95-W-180	0.18	0.3	-2.0	N/A	3E+06	1.21	143	5% u.s.	1.14	70	N/A	No	No	a, b
DU 96-W-180	0.18	0.3	-2.7	6.6	3E+06	1.26	145	5% u.s.	1.17	73	N/A	No	No	a, b
DU 97-W-300	0.30	0.3	-2.2	9.3	3E+06	1.56	98	5% u.s.	1.17	53	N/A	No	No	a, b
DU 00-W-212	0.212	0.3	-2.7	6.5 @ cl=1.06	3E+06	1.29	132	N/A	N/A	N/A	N/A	No	No	a, b
DU 00-W-350	0.35	0.3	-2.0	7.0 @ cl=1.13	3E+06	1.39	81	N/A	N/A	N/A	N/A	No	No	a, b
DU 00-W-401	0.401	0.3	-3.0	5.0 @ cl=0.82	3E+06	1.04	54	N/A	N/A	N/A	N/A	No	No	a, b
Risø-B1-15	0.15	0.278	-4.1	6.0 @ cl=1.21	6E+06	1.92	157	N/A	N/A	N/A	N/A	No	No	b
Risø-B1-18	0.18	0.279	-4	6.0 @ cl=1.19	6E+06	1.87	166	N/A	N/A	N/A	N/A	No	No	b
Risø-B1-21	0.21	0.278	-3.6	6.0 @ cl=1.16	6E+06	1.83	139	N/A	N/A	N/A	N/A	No	No	b
Risø-B1-24	0.24	0.27	-3.1	6.0 @ cl=1.15	6E+06	1.76	120	N/A	N/A	N/A	N/A	No	No	b
Risø-B1-30	0.3	0.27	-2.1	5.0 @ cl=0.90	6E+06	1.61	N/A	N/A	N/A	N/A	N/A	No	No	b
Risø-B1-36	0.36	0.27	-1.3	5.0 @ cl=0.90	6E+06	1.15	N/A	N/A	N/A	N/A	N/A	No	No	b
Risø-P-15	0.15	0.328	-3.5	6.0 @ cl=1.12	3E+06	1.49	173	N/A	N/A	N/A	N/A	No	No	b
Risø-P-18	0.18	0.328	-3.7	6.0 @ cl=1.15	3E+06	1.50	170	N/A	N/A	N/A	N/A	No	No	b
Risø-P-21	0.21	0.323	-3.5	6.0 @ cl=1.14	3E+06	1.48	159	N/A	N/A	N/A	N/A	No	No	b
Risø-P-24	0.24	0.32	-3.7	6.0 @ cl=1.17	3E+06	1.48	156	N/A	N/A	N/A	N/A	No	No	b
NREL S825	0.17	0.3	≈-6	6.0 @ cl=1.31	2E+06	1.44	125	2% u.s.; 5% l.s.	1.37 (1.31 for fully rough)	81.4	20-40	Yes	No	a,c
NREL S830	0.21	0.3	≈-6.8	7.0 @ cl=1.45	4E+06	1.57	135.3	2% u.s.; 5% l.s.	1.47 (1.45 for fully rough)	70.0	40-50	Yes	No	a,d

Table 2-26 - A summary of major published airfoils developed for pitch-controlled horizontal axis wind turbines and their aerodynamic theoretical characteristics.

N/A Not Available
 a Timer & Van Rooji, 2003
 b Burton, Jenkins, Sharpe & Bossanyi, 2011
 c Somers & Tangler, 2005d
 d Somers & Tangler, 2005b

2.5.1.2 The Effect of Aerodynamic Devices

Active and passive aerodynamic devices like Gurney Flaps, Trailing Edge Wedges, Stall Strips, Vortex generators, Leading-Edge Slats, Flow Vanes, LE-Protuberances, Rigid and Flexible TE Flaps, Split Flaps, Spoilers, BL Blowing and BL Suction to the baseline WT airfoils have been introduced, simulated and tested as reported in texts from Timmer and van Rooji (Timmer & van Rooji, 2003) and Pechlivanoglou (Pechlivanoglou, Passive and Active Flow Control Solutions for Wind Turbine Blades, 2012), among others.

However, all of the devices listed above are proposed as means of increasing the aerodynamic performance of the WT blades, especially in off-design points, with no explicit considerations regarding noise emission effects. In fact, as many of the mentioned devices act to keep the flow attached, they may contribute to reduce laminar bubble noise and separated flow noise, two secondary sources of airfoil self-noise. However, they may also contribute to increase turbulence and pressure fluctuation intensity, which may boost the main airfoil noise source as the turbulent eddies are convected past the Trailing Edge.

2.5.2 Specific Studies Concerning Airfoil Aerodynamic-Noise

According to Wagner et al. (Wagner, Bareiß, & Guidati, Wind Turbine Noise, 1996), all tonal noise contributions from a WT can be avoided by proper blade design, so that the research in the field of noise reduction is concentrated in reducing TE noise, tip noise and inflow-turbulence noise. Some of the researches concerning TE noise control will be briefly presented in this section but, first, the scaling of the sound intensity I , resulting from the interaction of the TBL with the TE, will be reviewed below:

$$I \propto \rho_0 c_0^3 M^5 \alpha^2 \frac{Ll}{r^2} \cos^3(\bar{\theta}) \quad (2 - 23)$$

where $M = U/c_0$ is the eddy convection velocity Mach number, α is the normalized turbulence intensity, l is a length scale of the turbulent region, L is the span of the section, and $\bar{\theta}$ is the angle between the mean flow direction and the edge (see Figure 2-1). Equation (2-23) is the Eqn. (2-2) simplified for the situation when the observer is in a fixed position, perpendicular to the TE in both coordinates (ϕ, θ) . The intensity is then influenced by four main flow parameters:

- U - the eddy convection velocity.
- $\bar{\theta}$ - the angle between the eddy convective velocity and the edge.
- l - a length scale of the turbulent region.
- α - the normalized turbulence intensity.

Also, the intensity depends on the radiation efficiency of the edge, which can be minimized by rounding the edge (see Figure 2-34) or by changing the acoustic impedance ($\rho_0 c_0$) through the application of porous material.

The eddy convection velocity may be reduced either by reducing the freestream velocity, with negative effects on the power conversion of the equipment or by airfoil geometry manipulation. According to Lutz et al. (Lutz, Herrig, Würz, Kamruzzaman, & Krämer, 2007) the noise emission is influenced by the design of the airfoil because the state of the turbulence in the vicinity of the TE is determined by the development of the BL and, thus, by the shape of the pressure distribution along the blade section.

In fact, according to Wagner et al. (Wagner, Bareiß, & Guidati, Wind Turbine Noise, 1996), p. 167, except per the angle $\bar{\theta}$ all the remaining parameters listed above may be influenced by the design of the airfoil. However, at the time of their writing, it was not known which airfoil shape could result in reduced TE noise and they have prepared a table with different means for the reduction of TE noise and their potential effect, Table 2-27.

Table 2-27 - Different methods proposed for the reduction of TE noise. Adapted from (Wagner, Bareiß, & Guidati, Wind Turbine Noise, 1996), p. 168.

Possible Modification	Effect on main parameters	Comments
Reduced rotational speed	Reduces U	Reduces power conversion
Swept Blade	Increases $\bar{\theta}$	Impractical for long WT blades
Serrated TE	Reduces radiation efficiency of the TE	See text below.
Beveled TE	Reduces radiation efficiency of the TE	See Figure 2-34
Porous TE	Reduces radiation efficiency of the TE	See text below.
Modified Airfoil Shape	Affects U, l, α	Effect on noise is not clear

Figure 2-34 shows that by beveling the TE, the noise intensity decreases for increasing angle ψ . However, there is a practical limit of $\psi = 30^\circ$, above which separation occurs with additional turbulence and noise.

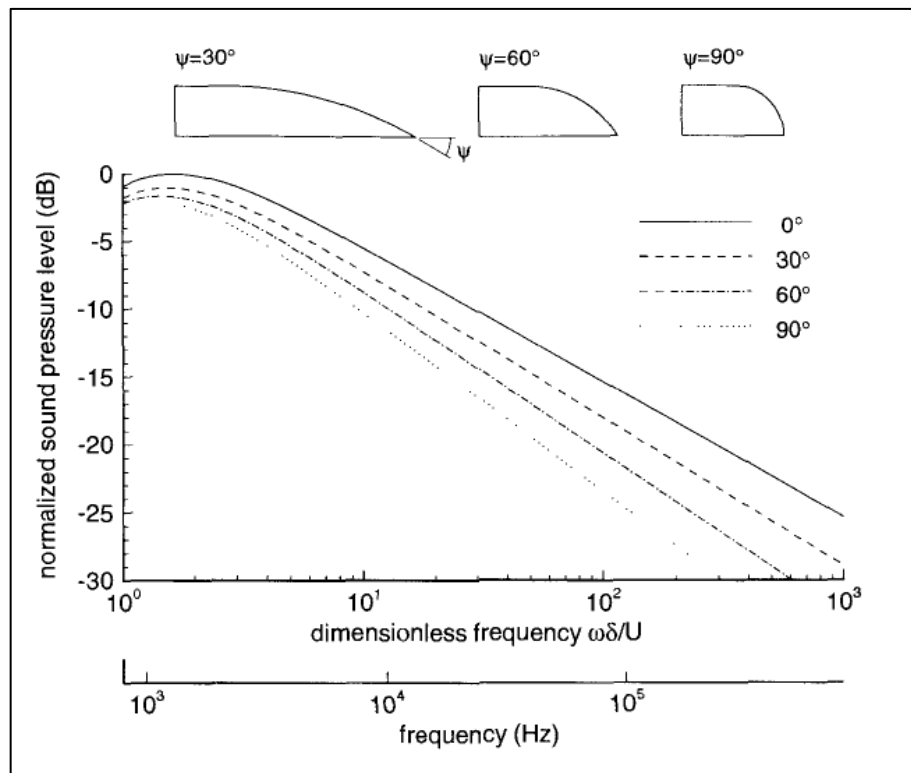


Figure 2-34 - TE noise resulting from different beveling of TEs, at $U=50$ m/s; $\delta=0.01$ m. (Wagner, Bareiß, & Guidati, Wind Turbine Noise, 1996).

Some experiments described by Wagner et al. (Wagner, Bareiß, & Guidati, Wind Turbine Noise, 1996) were also carried out with the concept of variable surface

impedance. A porous, triangular profile of open cell polyurethane foam was glued to the TE of a full scale WT, increasing its chord by 30 mm but a noise reduction of only 0.5 dB was obtained and found not-significant in relation to the solid, sharp TE noise.

Acoustic field measurements were accomplished on a three-bladed 2.3 MW, 94 m diameter WT by Oerlemans et al. (Oerlemans, Fisher, Maeder, & Kögler, 2009), in The Netherlands, who had modified two of the three original blades, one with serrated TE and one with an optimized airfoil shape (from the E.U. SIRROCO project (Schepers, et al., 2007)), in the outer 30% of the span. The third blade was left in standard condition (shape and roughness) as a reference for the experiment.

The overall serration setup is depicted in Figure 2-35, from another report of the same author (Oerlemans, Wind Turbine Noise: Primary Noise Sources, 2011). The TE Serrations were made from 2 mm thick aluminum foil, mounted to the outer 12.5 m of the blade, on the pressure side. The 2 mm step was smoothed with filler material spread over a few centimeters of the chord. The length of the serrations varied from 100 to 300 mm, approximately 20% of the local chord length. The plane of the serrations was aligned to the estimated flow direction at the blade TE.



Figure 2-35 – TE Serrations made from 2 mm thick aluminum foil, mounted to the outer 12.5 m of the blade, on the pressure side (Oerlemans, Wind Turbine Noise: Primary Noise Sources, 2011).

Details on the influence of the serration aspect ratio on the noise reduction may be found in Wagner et al. (Wagner, Bareiß, & Guidati, Wind Turbine Noise, 1996), p. 169.

Figure 2-36 below shows the average spectra measured for the three blades, with no BL tripping. The average overall noise reduction found by the authors was of 0.5 dB for the SIRROCO blade and 3.2 dB for the Serrated TE blade. These values were found as overall averages along all relevant wind speeds. For lower wind speeds and tripped³⁴ flow, the average noise reductions were between 0 and 0.2 dB for the SIROCCO blade and 1.2 to 1.6 dB for the Serrated TE blade.

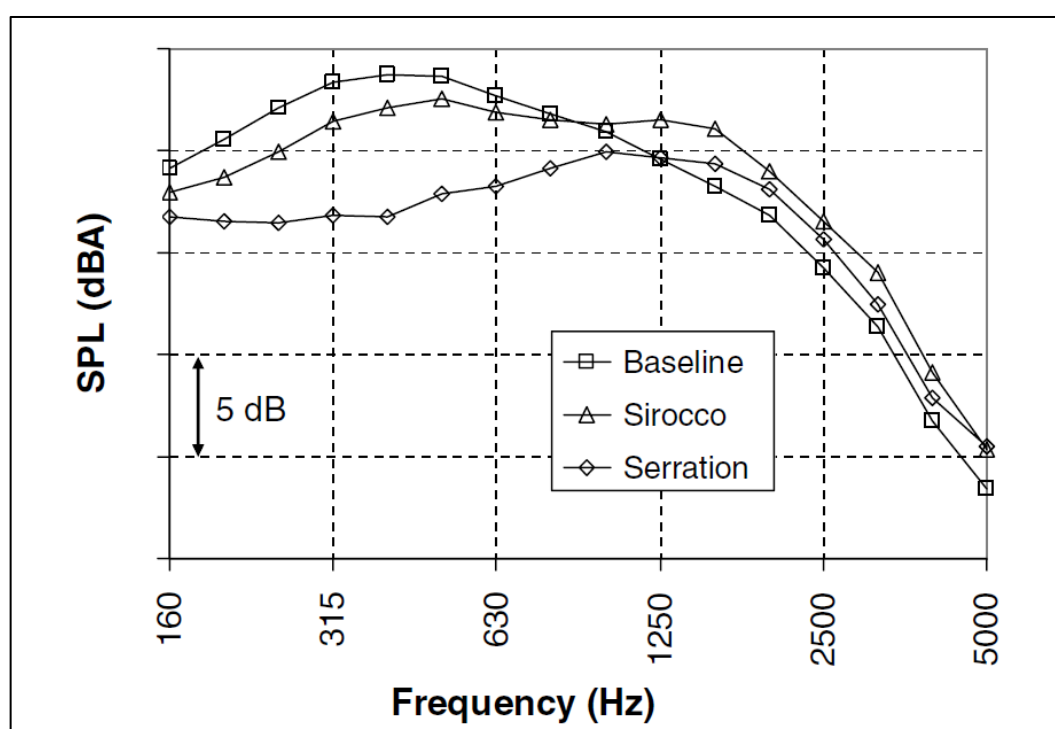


Figure 2-36 - Noise Spectra (average over all relevant wind speeds) for the baseline (unmodified), Sirocco (airfoil shape optimized) and serrated TE blades. Untripped, clean blades (Oerlemans, Fisher, Maeder, & Kögler, 2009).

Another important conclusion of the experiment by Oerlemans et al. (Oerlemans, Fisher, Maeder, & Kögler, 2009) was that the acoustic source maps for the baseline blade confirmed the TE noise of the outer 25% of the blade to be the dominant noise source.

³⁴ Tripping was employed in order to assess the result closer to the operating conditions with dirt and insects

General Electric later made a large measurement campaign with the DLR-IAG (Petitjean, Drobiez, & Kinzie, 2011) involving two proprietary airfoils (profiles “1” and “2”) modified to include TE serrations and materials of different porosities (metal foam and hollow sphere foam) in the TE. During acoustic wind tunnel measurements, all solutions showed similar trends, characterized by noise level decrease for lower frequencies (1-3 kHz) accompanied by noise level increase at higher frequencies. The preliminary conclusions based on tunnel measurements, were (i) that serrations provided more balanced benefits than porous TE, with limited noise increase at high frequencies (profile 1) and noise reduction over a wider frequency range (profile 2), and (ii) the noise reduction resulting from the serrations is strongly dependent upon the baseline airfoil configuration.

A full scale WT noise measurement was then accomplished in accordance with IEC 61400 (IEC61400-11, 2012), for blades with serrations, mounted on three GE wind turbines (1.5, 2.5 and 2.75 MW, with rotor diameters of 77, 110 and 103 m, respectively), with microphone recordings at 1.5D slant distance from the hubs, at wind speeds from 5 to 10 m/s. The results were presented for 500, 1.000 and 2000 Hz bands only and showed that TE serrations provided 4 to 6 dB(A) noise reduction on the lower frequency, 2 to 5 dB(A) for the intermediate frequency and a no-reduction to a slight noise increase at the 2000 Hz frequency. The OASPL decrease in noise found was in the range of 2 to 4 dB(A). Serrations were considered a “very efficient” way to reduce TE noise by the authors; however, the technology is apparently not currently mature³⁵.

A three-step noise prediction method was set up by Guidati and Wagner (Guidati & Wagner, 2000) in order to study the influence of the TBL structure on the TE noise and to investigate airfoil shape influence on noise emission. The first step of the method was to use XFOIL to compute the BL flow around the airfoil. The second step was to

³⁵ In a recent international Wind Turbine Noise conference, Arce et al. (Arce, Ragni, Pröbsting, & Madsen, 2015) compared the relative disturbance caused on the flow by solid and permeable serrations, by studying flow topology with particle image velocimetry (PIV) and RANS analysis. During the discussion that followed the paper presentation section, one of the authors was addressed with the question of the level of maturity of the technology for implementation and he replied to the audience that the deployment of serrations is still not mature for practical application and it still remains an active research and development subject.

reconstruct the TE velocity profile by using the Coles law (Schlichting & Gersten, 2003), p. 525. The last step was to obtain the far field noise employing the TNO TE noise model.

One important outcome of that research is that good validation results for the XFOIL and its embedded e^n transition model (Drela & Giles, Viscous-Inviscid Analysis of Transonic and Low Reynolds Number Airfoil, 1987) are provided against measurements accomplished at the IAG Laminar Wind Tunnel, concerning the drag-polars of different airfoils tested.

It was concluded by Guidati and Wagner (Guidati & Wagner, 2000) that a thin, attached BL is favorable for reducing TE noise and that a moderate noise reduction was achievable by airfoil shape manipulation. Also, since airfoils for reduced noise are designed for small δ^* at the TE, the thickness of the airfoil at the TE must be also carefully designed in order to avoid a tonal noise. The new airfoils developed showed a reduction from 2 to 4 dB(A) in the frequency range between 1 and 2 kHz, for the untripped flow only. However, under tripped flow the new airfoils produced more noise than the baseline NACA 64418 airfoil. No tradeoff study was reported regarding noise and performance for the newly developed airfoils, the profiles of which are not available in the research paper.

Apart from noise annoyance and visual pollution, birds and bat strikes are other important side effects of the operation of Wind Turbines described earlier in Section 1.1.5. On that matter, an interesting study on avian hearing is described by Dooling (Dooling, 2002), which suggests that, depending upon the signal-to-noise ratio (see Table 2-28), a tonal noise might help many types of birds to avoid collision with wind turbines. The concept is that noise, along with vision, is part of the multisensory process of object localization and the described tonal noise will, in biological terms, increase the perceptual contrast between the background and the object so that the latter can be more easily detected.

If this pure tone could be produced aero acoustically (for instance, by a vortex-shedding mechanism) and outside human hearing range, it would not give any contribution to the perceived (A-weighted) sound pressure level. However, according

to (Dooling, 2002), birds hear less well than most mammals, including humans³⁶, and their best hearing is essentially in the same frequency range as humans, preventing the use of infra or ultra sound pure tones for collision avoidance. For this purpose, the pure tone should be ideally produced between 2 and 4 kHz. Dooling considers that a single pure tone contribution to the overall SPL, even within hearing range and with a high signal-to-noise (S/N) might result in a small or negligible OASPL increase in a broadband noise, especially in cases where a large part of the energy lies in the low frequency range, like wind and WTN, for instance.

Table 2-28 – Signal/Noise (S/N) in dB to be exceeded for detection of tones over noise for an average bird (Dooling, 2002), p.12

Signal	1 kHz	2 kHz	3 kHz	4 kHz	Noise
S/N (dB)	24 dB	27 dB	28.5 dB	30 dB	1.5 dB

Table 2-28 also shows that the ratio between two noises must be at least 1.5 dB for a typical bird to distinguish between them. Thus, whenever the noise from the WT decreases to within 1.5 dB of the ambient noise (e.g. background, wind), the blade noise cannot be heard by an average bird. A human, on the other hand, can distinguish two different noises with a level difference of only 0.5 dB.

Also, an increasing whistle tone-to-ambient noise ratio is necessary for a bird to hear the whistle as the ambient noise increases. As shown in Figure 2-37, for an overall ambient noise of 70 dB, a blade whistle 28 dB above the spectrum level of the noise (the threshold of detection for the average bird) would be heard by the bird at 15 m or closer to the blade, only. For an overall ambient noise of 60 dB, the same blade whistle would be heard at 50 m or closer to the blade.

³⁶ A human can detect a sound in noise at twice the distance a typical bird can.

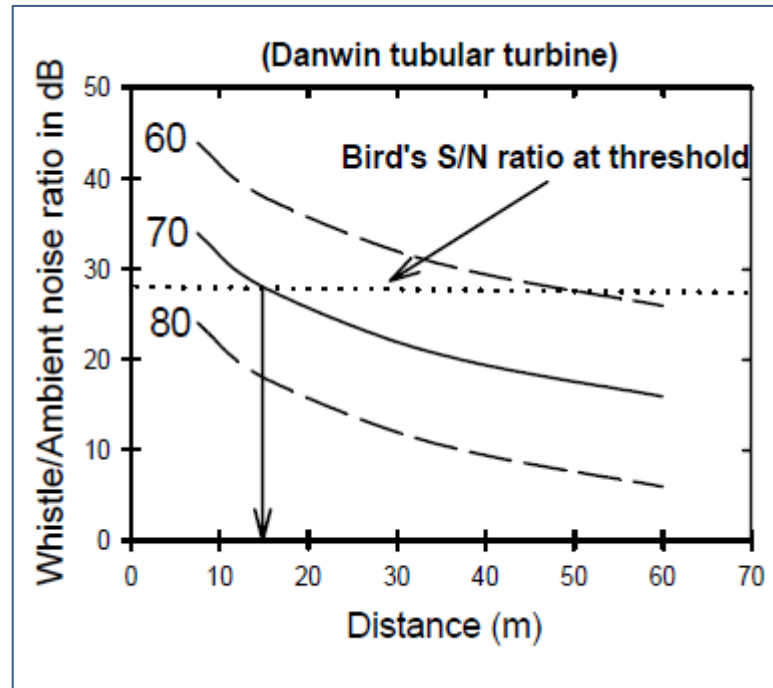


Figure 2-37 – Distance of Bird warning as a function of Whistle to ambient noise ratio and background noise level (Dooling, 2002).

In 2003, Migliore and Oerlemans (Migliore & Oerlemans, Wind Tunnel Acoustic Tests of Six Airfoils for Use in Small Wind Turbines., 2003) tested close to 500 flow combinations of 6 airfoils in wind tunnels, for aerodynamic and acoustic performance. All models had a 0.2286 m chord and 0.51 m span, with chord-based Reynolds numbers ranging from 200,000 to 1,000,000 and Mach numbers ranging from 0.12 to 0.18, with intended application to small WT. The airfoils tested were the FX 63-137, S822, S834, SD2030, SG6043, SH3055 and the results were compared against NACA 0012 benchmark data.

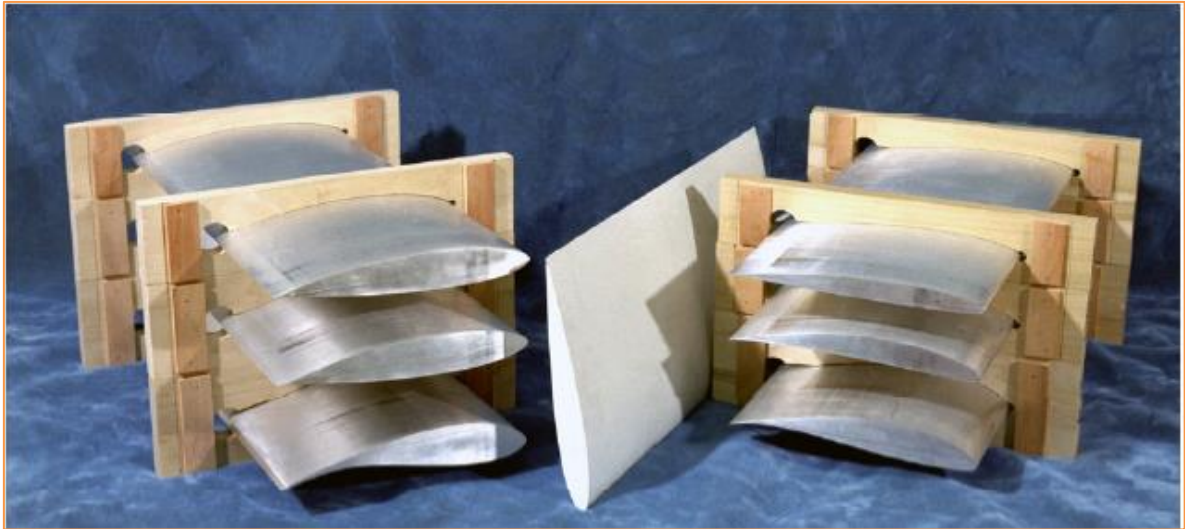


Figure 2-38 - Airfoils tested for aerodynamic and aeroacoustic performance: bare metal airfoils: (left hand, from top to bottom) S834, S822, FX 63-137, (right hand, from top to bottom) SD2030, SG6043, SH3055. The NACA 0012 is in white, in the middle. Source: (Migliore & Oerlemans, Wind Tunnel Aeroacoustic Tests of Six Airfoils for Use in Small Wind Turbines., 2003)

Measurements were made on the suction sides of the candidate airfoils, with and without tripping, and with and without turbulence grid, for 3 different angles of attack, 0° , 10° and 18° (or 0° , 5° and 10° in some cases).

The results for TE noise is exemplified in Figure 2-39, where the Sound Power Level spectra for the TE of the S822 airfoil (suction side only) is shown for tripped and untripped flow conditions.

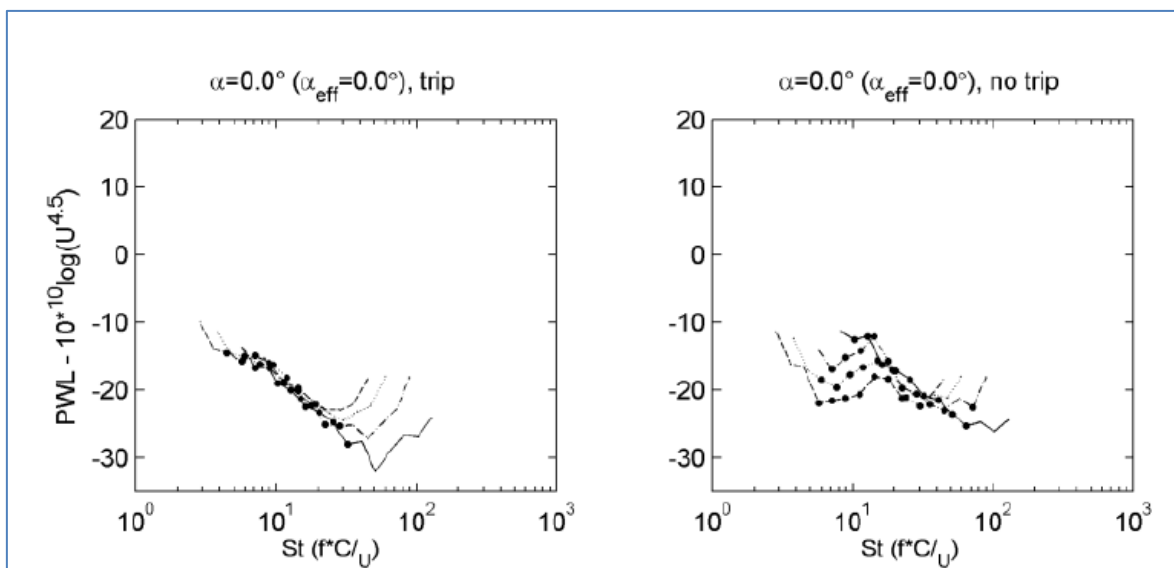


Figure 2-40 - Normalized TE Noise Spectra for the S822 Airfoil (suction side) as a function of the chord-based Strouhal number, for tripped (L) and untripped (R) conditions. Flow velocities: ___ 22,4 m/s; _ _ 32,0 m/s;47,9 m/s; __ 63,9 m/s. Source: (Migliore & Oerlemans, Wind Tunnel Aeoracoustic Tests of Six Airfoils for Use in Small Wind Turbines., 2003).

On the other hand, for untripped flow, a 30% variation was found in peak Strouhal numbers for different speeds. This result was considered a possible consequence of the use of a constant, chord-based Strouhal number, rather than the variable BL thickness Strouhal number, since the BL thickness at the TE decreases with increasing Reynolds number. The authors also conjectured that the normalization and plot had not been so successful for the untripped flow due to the complexity of the feed-back phenomena associated with laminar boundary layer vortex shedding noise.

The next step in the same study (Migliore & Oerlemans, Wind Tunnel Aeoracoustic Tests of Six Airfoils for Use in Small Wind Turbines., 2003) was for the authors to compare the NACA0012 results directly with NASA benchmark results, since the airfoil chords, tunnel setup and tested speeds had been the same. The comparison for effective AOA of 4° is shown in Figure 2-41.

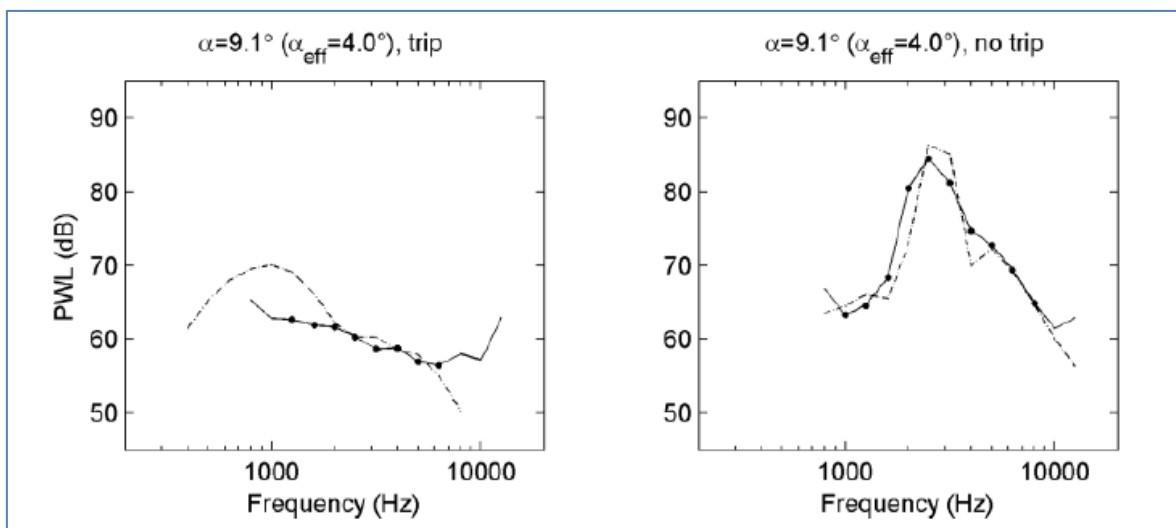


Figure 2-41 - TE Noise Spectra for the NACA0012 Airfoil at 55,5 m/s, for tripped (L) and untripped (R) conditions. Data sources: -- NLR data (suction side); - - NASA data. Source: (Migliore & Oerlemans, Wind Tunnel Aeracoustic Tests of Six Airfoils for Use in Small Wind Turbines., 2003)

Migliore and Oerlemans considered that the spectral characteristics agreed quite well, since broadband spectra and even tones were reproduced for some cases with untripped flow. However, NASA data consistently exhibited a hump close to 1 kHz for tripped flow, as may be clearly seen in Figure 2-41. The difference found was subject of correspondence among the parts, which have conjectured on differences on BL tripping and in measurement techniques as possible causes for the divergence.

In non-tripped experiments, a Laminar Boundary Layer Vortex Shedding noise (pure tone) was also observed consistently throughout the tests and appeared in the form of peaks in the spectra, between 1 kHz and 2 kHz. The frequencies, speeds and TE bluntness did not lead to a Strouhal number close do 0.2, ruling out a blunt TE as the cause of these peaks. The ranges of AOA for which the tones occurred at the most characteristic speed of 22,4 m/s were: $7.5^\circ < \alpha < 13^\circ$ for the S834, $-8^\circ < \alpha < 2^\circ$ for the SG6043 and $-10^\circ < \alpha < 4^\circ$ for the SD2030 airfoil.

Subsequent experiments by Migliore and Oerlemans (Migliore & Oerlemans, Wind Tunnel Aeracoustic Tests of Six Airfoils for Use in Small Wind Turbines., 2003) with BL tripping on selective sides of a S834 airfoil and with specific trip thickness showed that insufficient trip thickness (0.25 mm) may increase the frequency of the LBL-VS noise problem and sufficient trip thickness (0.30 mm) on the pressure side must be applied for the spectral level to decrease dramatically and the tone and its harmonics

to vanish completely. Also the broadband level decreased even further after the application of 0.30 mm tripping material to the suction side. This experiment suggested that the BL on the suction side dominates broadband noise production while the pressure side may generate tonal noises if not properly tripped. Another interesting observation made by the authors was that the tones vanished completely on the presence of upstream turbulence, indicating that the inflow turbulence interrupted the feedback mechanism associated with tones. However, in this situation the grid noise became dominant.

During the tripped-flow tests a “fully turbulent” BL was created with zigzag tape with 5%-chord-width, over the entire span. The LE of the tape was set at 2% of the chord at the suction and 5% of the chord at the pressure side, respectively.

The relative performance of all tested airfoils is shown in Figure 2-42. According to the authors (Migliore & Oerlemans, Wind Tunnel Acoustic Tests of Six Airfoils for Use in Small Wind Turbines., 2003) the values should be regarded as upper limits.

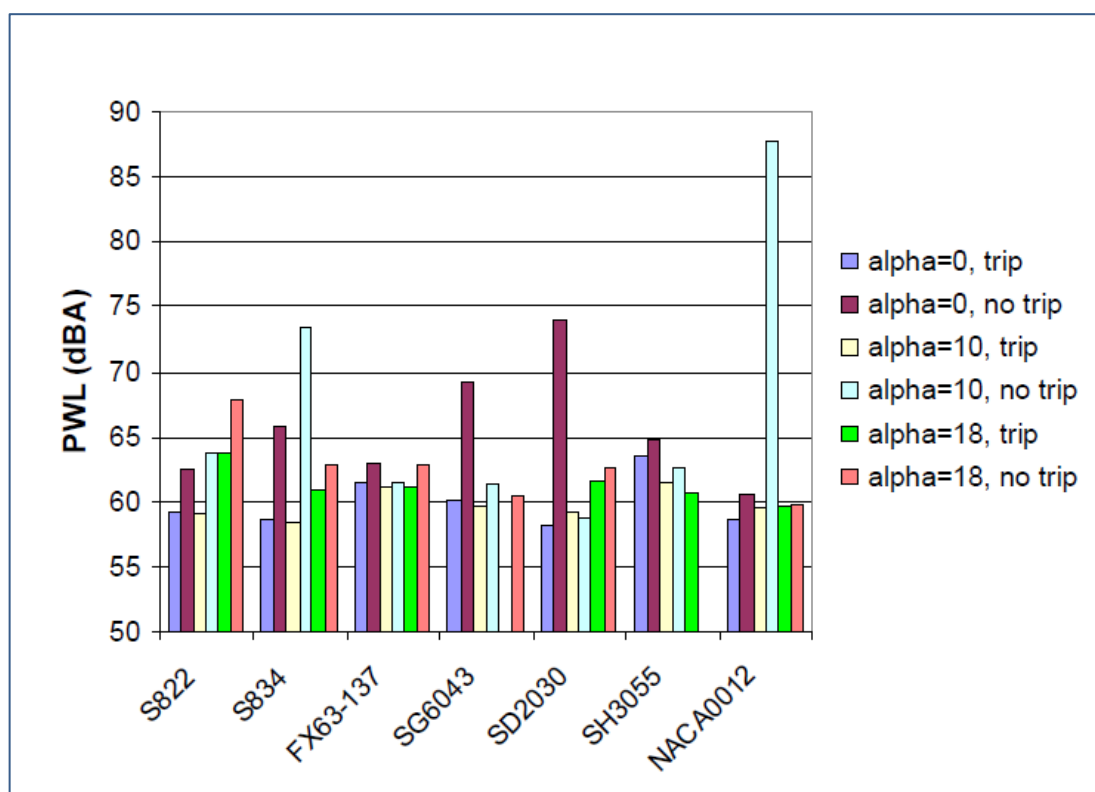


Figure 2-42 - A-Weighted Overall TE Sound Power Level (PWL) for some tested airfoils (upper limits). Source: (Migliore & Oerlemans, Wind Tunnel Acoustic Tests of Six Airfoils for Use in Small Wind Turbines., 2003).

Migliore and Oerlemans (Migliore & Oerlemans, Wind Tunnel Aeoracoustic Tests of Six Airfoils for Use in Small Wind Turbines., 2003) explain that comparing airfoil noise data at the same AOA can be misleading because different airfoils operate at different AOA. The maximum L/D for the FX63-137 occurs close to 4° while for the S822, it occurs close to 8° . Also, comparing data at the same Reynolds number is not enough because of eventual LBL-VS tones. The “character” of the BL, especially the extent of laminar flow, must also be simulated.

An interesting comparison between the FX63-137 and S822 airfoils is made. At first, by looking at Figure 2-42, it would seem that the FX63 would be quieter for the larger angles. However, when each one was measured at the operating angle and the BL was tripped to eliminate tones, the S822 turned out to radiate less noise.

Other relevant conclusions of this important research were:

- In quiescent inflow, the TE noise is dominant.
- The sharper the Airfoil LE radius, the higher the inflow turbulence noise.
- Even those airfoils that did not exhibit pure tones experienced reduction in SPL up to $3 \text{ dB}(A)$ when tripped.
- The tested airfoils exhibited clearly different Turbulent BL TE noise levels, a dominant source for typical WT, by as much as $8 \text{ dB}(A)$.
- It may not be appropriate to compare airfoils at the same AOA, but at the expected design condition.

From 2004 to 2008, NREL was engaged in a comprehensive research effort to improve the understanding of WT aeroacoustics. Wind Turbine airfoils were tested for acoustic characteristics under a broader Reynolds numbers range (1,500,000 to 3,800,000) at the Virginia Polytechnic Institute, as reported by NREL Subcontract Report 500-43471 of Devenport et al. (Devenport W. , et al., 2010).

The selected airfoils for the undertaking were the NACA0012, Delft DU96, Riso B1-18 and S831, some of which are shown in Figure 2-43, with data collected from zero lift to stall condition by an array³⁷ of 63 microphones, while previous NREL research

³⁷ Two different layout configurations for the microphone array, star and spiral, were used, one at a time, each with 63 microphones.

involved 48 microphones (Migliore & Oerlemans, Wind Tunnel Acoustic Tests of Six Airfoils for Use in Small Wind Turbines., 2003) and the research which led to the NASA BPM model involved 8 microphones (Brooks, Pope, & Marcolini, Airfoil Self-Noise and Prediction, 1989).

The turbulent flow over the airfoils was obtained with the tripping layout displayed in Figure 2-44.

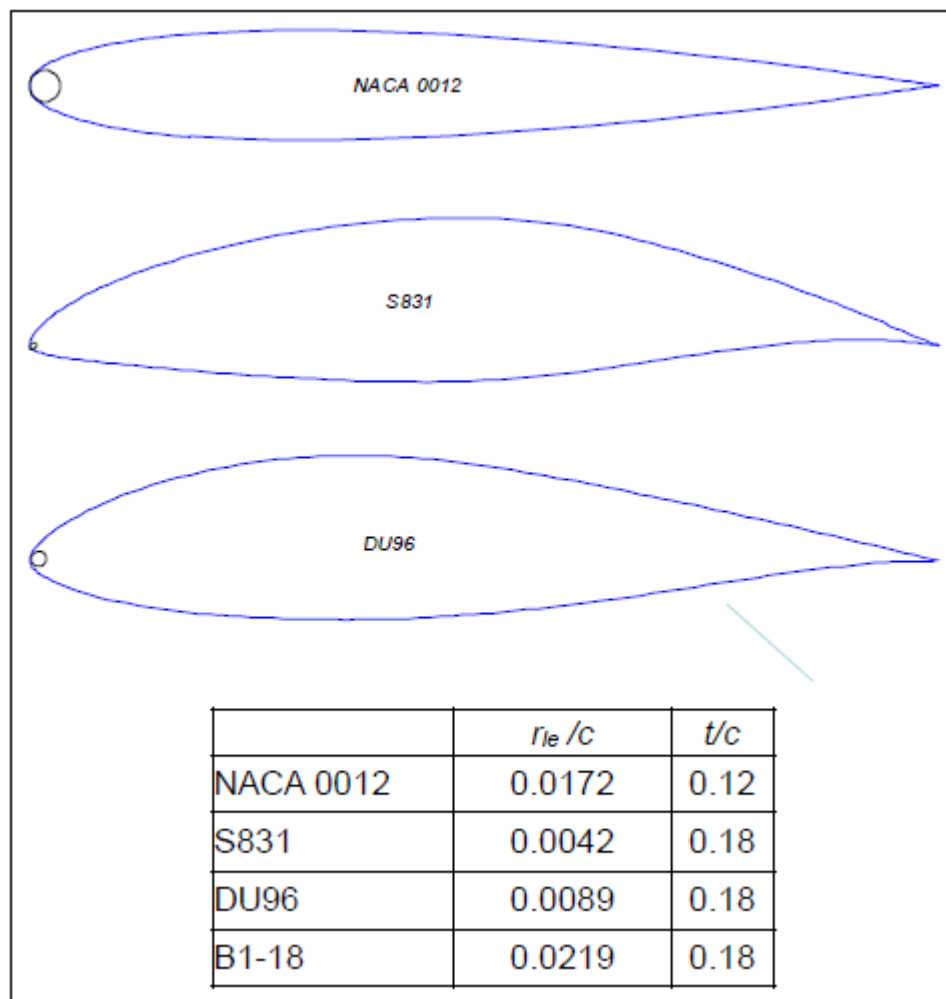


Figure 2-43 - Airfoil section profile and table for direct (to scale) comparison of thickness distribution, maximum thickness and LE radius. B1-18 is not shown due to proprietary image. Source: (Devenport W. , et al., 2010), p. 43.

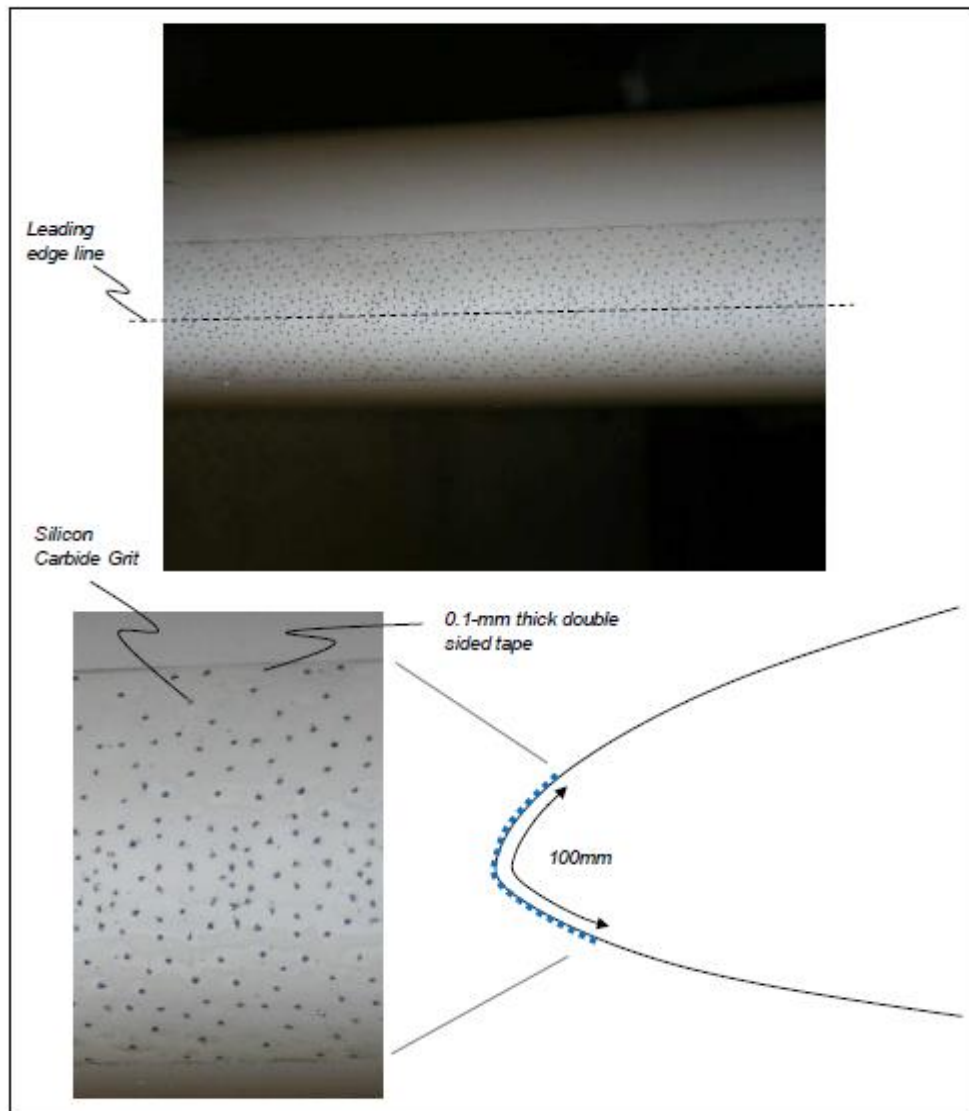


Figure 2-44 - Location and lay out of the “soiling trip” applied to the LE of the DU6 airfoil. Source: (Devenport W. , et al., 2010), p. 46.

At first, the spectral data provided by this broad experiment seemed an excellent reference against which to validate the suitability of the modified-BPM model implemented later in this research for TE noise prediction in Reynolds numbers above those over which the baseline BPM model was developed and also to verify its suitability to evaluate the noise for other types of airfoils, different than the symmetrical NACA0012. However, the spectra made available through the 2010 NREL Report include all airfoil self-noise sources, as exemplified in the spectra for the NACA 0012 at 4° AOA, shown in Figure 2-45.

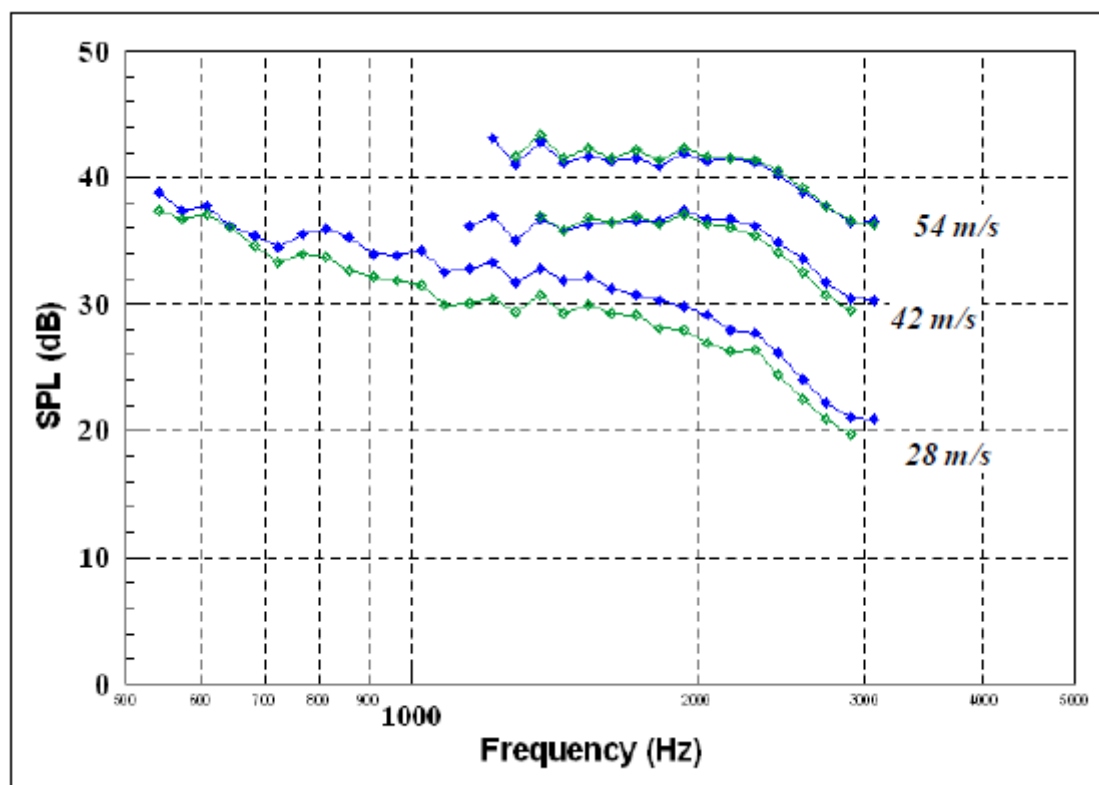


Figure 2-45 - One-twelfth octave bands spectrum derived from integration, for all NACA0012 airfoil self-noise sources, untripped flow at effective AOA of 4° (blue lines) and -4° (green lines). Source: (Devenport W. , et al., 2010).

In addition to that problem, the spectra available in this research (summed up in 38 1/12 octave bands) were not directly measured, but integrated from a beamforming algorithm throughout a volume enclosing the TE and the results ultimately held poor correlation with the original NASA wind tunnel data. Possibly some sort of significant noise attenuation feature was inadvertently built into the Virginia Tech wind tunnel acoustic set up, so that the all-source spectra measured showed systematically a lower sound pressure level than the TE noise alone, measured by the NASA experiments.

As highlighted by Herr and Kamruzzaman (Herr & Kamruzzaman, 2013), p.3, there are gaps in airfoil TBL-TE noise validation data and more future experimental programs attempting to fill the current gaps are needed and encouraged by guidance provided by the AIAA TE noise benchmarking conferences.

Active flow control was applied by Wolf et al. (Wolf, Lutz, Würz, Stalnov, & Seifert, 2011) in the form of constant suction on the upper surface of a NACA64-418 airfoil in order to try to reduce BL thickness, turbulence normal length scale and normal

Reynolds fluctuations, i.e., the TBL parameters employed by the TNO TE-noise prediction model. CFD and wind tunnel facilities were employed and a potential for noise reduction of up to 5 dB was found by the authors. No considerations on the energy budget were made in the research.

A more recent hybrid, 2D, numerical study on the influence of the airfoil shape in the TE noise was accomplished by Rautmann et al. (Rautmann, Ewert, & Dierke, 2015), which does not rely on semi-empirical noise prediction methods. The method employed hybrid approach with steady-state CFD simulation providing mean flow values for a subsequent CAA simulation, where the fluctuating turbulent noise sources were reconstructed from the RANS turbulence statistics by a stochastic method, thereby reducing the effort on the flow simulation compared to scale resolving methods. The baseline DU-96-W-180 airfoil was modified in camber and thickness resulting in nine different airfoil configurations, simulated at the (fixed) Reynolds number of 3×10^6 , for four different AOA and for both forced transition and (modeled) natural transition flows, resulting overall in 72 combined CFD/CAA simulations. The maximum resolvable frequency for the CAA mesh was around $f_{max} \approx 5 \text{ kHz}$, however most part of the TE noise spectra was within the resolvable range, according to the authors. The computational run time for each case was 16 hours in a 16-CPU cluster node. From previous validation work accomplished for this hybrid method in the German Aerospace Center (DLR - Braunschweig), the authors explained that, in order to compare the resultant spectra with measured values, a 2D to 3D correction had to be applied and also a negative constant off-set calibration of $- 4.5 \text{ dB}$ had to be used on all simulated CAA spectra to match experimental data in terms of absolute levels. Since both corrections were frequency-independent and yielded a constant shift in the spectra, they were not applied in the results shown, because the interest was centered in relative airfoil performance only.

The results obtained for forced and “natural” transition are shown in Figure 2-46.

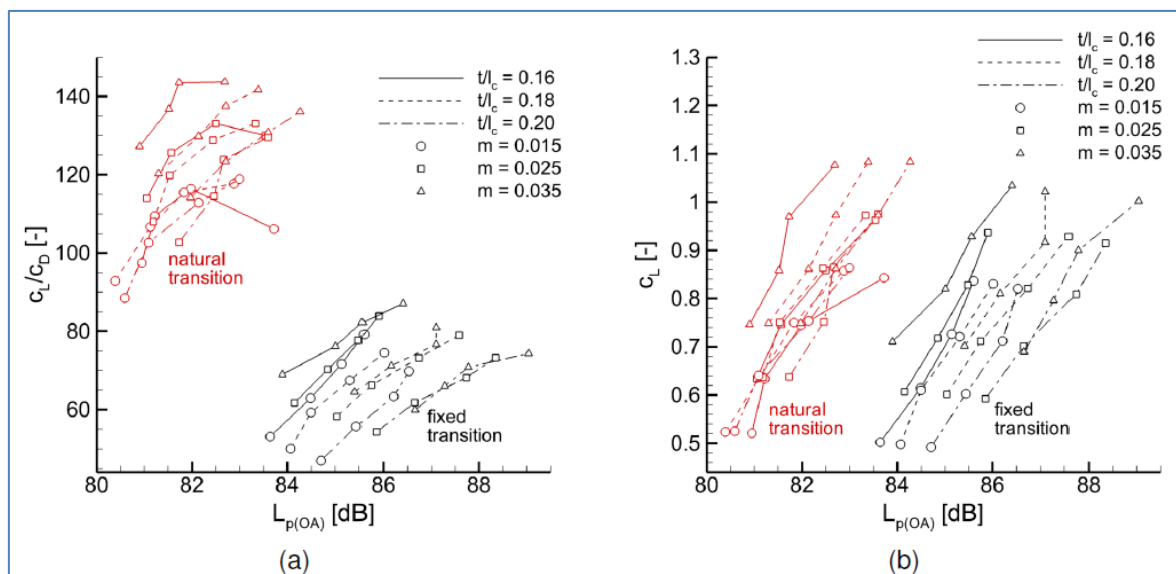


Figure 2-46 - Overall TE noise SPL as a function of aerodynamic parameters, for the tested geometrical variations of the DU-96 airfoil, at different AOA; (a) SPL as a function of cl/cd ; (b), SPL as a function of cl . m =camber; t/l_c =thickness. Source: (Rautmann, Ewert, & Dierke, 2015).

By observing the noise emission from the fixed transition cases, it was found that the airfoil thickness was the main driver for TE noise emission, with thin airfoils showing the smallest overall noise levels, 3 – 4 dB lower than thicker configurations. The best performance in terms of cl/cd and overall SPL was shown by the airfoil with minimum thickness and maximum camber. The same result may be seen for the best cl and overall SPL for fixed transition, since the transition affects little the coefficient of lift. For natural transition, on the other hand, a much higher aerodynamic performance (cl/cd) may be achieved with less noise emission, the reason being that the coefficient of drag may be halved by the longer laminar run of the boundary layer and its reduced thickness at the TE, which results in noise signal reduction of the order of 3 dB.

2.5.3 Airfoil Geometry Studies Involving Optimization

While developing new airfoil geometry for specific or multi-objective goal, some authors have applied optimization procedures, i.e. maximization and/or minimization of objective functions through variation of geometric parameters, while subjecting the airfoil to one or more constraints. This subsection describes such type of research.

In the Riso airfoil family development described earlier by Fuglsang and Bak (Fuglsang & Bak, Development of the Risø Wind Turbine Airfoils, 2004), the authors employed a direct design method detailed in Fuglsang et al. (Fuglsang, Bak, Gaunaa, & Antoniou, 2004), where a numerical model was coupled with the XFOIL. The design variables were the control points that described the airfoil shape. A traditional Simplex optimizer was used with a finite difference sensitivity analysis. The solution method was considered robust but computationally expensive. The optimization problem did not consider TE noise as an objective or constraint.

Later, the EU initiative called *SIROCCO*, reported by Schepers et al. (Schepers, et al., 2007), entailed developing silent rotors by acoustic optimization as a primary target. The idea was to modify the BL state at the TE, by adjusting the pressure recovery at the rear part of the airfoil. In this region, there is significant fluid acceleration - deceleration which violates the equilibrium boundary layer approach and, according to the authors, renders previous noise prediction schemes based on the TNO-TPD TE noise method unsuitable. A modified method was developed, taking into account the anisotropy effects via a Reynolds Stresses turbulence model. The combined aero-acoustic models were implemented in a numerical optimization environment that generated airfoil shapes with minimal noise production, in an automated way.

The airfoil shapes produced by the *SIROCCO* initiative are not available to the public and the 2D Wind Tunnel noise measurements reported indicated from 1 to 3 dB(A) less noise, at the design lift range. Field measurements, however, showed the noise reduction of these airfoils to be smaller, in the order of 0.5 dB(A), with reasons not fully understood but assigned to possible unsteady inflow conditions.

Bertanoglio et al, (Bertanoglio, Madsen, & Bak, 2009), concluded that the TNO model for TE noise displayed an offset of about 5 to 10 dB SPL underprediction (see Appendix E) when compared to NACA0012 noise data measured at NASA (Brooks & Hodgson, 1981) and at the Aeroacoustic Windtunnel Braunschweig (AWB). However, the authors considered the model still useful for relative airfoil performance comparison. They then implemented the model to extend an optimization code developed originally at RISO, in order to reduce a cost function (made up of aerodynamic plus TE noise components), subjected to many constraints. Basically, the code calculated the local gradient of the cost function associated with each parameter, adopting values that

would minimize the cost function. The treatment to avoid local minimal is not described. The RISO-B1-18 airfoil, which is of proprietary design, was subjected to optimization at the single AOA of 6° . The Reynolds number for the simulation is not mentioned, but previous validations attempt in the same research were accomplished at $Re = 1.6 \times 10^6$ and 2.9×10^6 . The geometry and boundary layer thickness of the modified airfoil were reportedly little different than the baseline values, however the authors concluded that the TKE had been reduced in the optimized design, particularly near the TE, with a resulting reduction in noise of $1 - 2 \text{ dB}$, which they considered relevant for the purpose of WT design.

Another optimization technique for two-dimensional wind turbine airfoils was presented by Li et al. (Li, Li, Gao, & Huang, 2010), where a combination of methods was used to optimize the lift-to-drag ratio of an airfoil at the design angle of attack. The upper and lower surfaces of a reference airfoil were replaced by two B-spline curves with four control points each. The optimization goal was to reach the maximum cl/cd ratio at the airfoil design AOA, but there was no concern with airfoil self-noise. Four examples of geometrical optimizations are shown with up to 24% improvement in $(cl/cd)_{max}$ at the airfoil design point. However the design requirements for real WT blades involve many more simultaneous requirements than this isolated aerodynamic efficiency at the design point.

In Petrone et al. (Petrone, de Nicola, Quagliarella, Witteveen, & Iaccarino, 2011), all aeroacoustic noise sources (airfoil self-noise plus inflow noise) were superimposed to calculate the acoustic signature of a complete, operating WT and a design optimization process based on a genetic algorithm was applied in order to seek for the reduction of noise, considering uncertainties involved in the process, e.g. insect contamination, geometrical imperfections, meteorological conditions. A simple WT baseline blade was assembled from 3 different airfoils (root, middle and tip), interpolated in between. The XFOIL (Drela, X-FOIL, 2000) was used for 2D flow calculation over each section and a finite-span effect was also integrated. The objective of the deterministic optimization, applied to an AOC 15/50 (15 m span, 50 kW rated power) WT, was to maximize the mean power coefficient while reducing the SPL at a microphone located 20 m downwind of the turbine, at the ground level. The authors claimed they were able to find a tradeoff blade geometry with significant reduced noise emission, and still with negligible Coefficient of Power reduction with respect to the baseline, factory optimized

geometry. However, no specific studies were made for the 2D sections of the optimized blade and no geometric data is provided for the final blade configuration. Petrone et al. also claimed to have demonstrated how the considered uncertainties mentioned resulted in a general decrease in performance with respect to the design scenario. This might work as a warning to the designers not to rely on hydraulic smooth and geometrically-perfect blade surfaces in order to reach the desired performance.

The XFOIL (Drela, X-FOIL, 2000) and the NAFNoise (Moriarty P. , NAFNoise User's Guide, 2005) tools were also employed in order to optimize some known airfoil profiles used in small scale WT by Göçmen and Özerdem (Göçmen & Özerdem, 2012). The authors supported the idea that existing optimization efforts were not computationally affordable for simultaneous calculation of many noise mechanisms, concluding that more practical methods were required. The research tried to reduce noise emission by changing the airfoil pressure side only, while trying to keep their aerodynamic efficiency unaltered. According to the authors, the results seemed promising, with less noise in the frequencies range up to 10 kHz and improved glide ratio for some cases. However, since the total TE noise comprises contributions from both sides of the airfoil and that maximum cl/cd ratio is usually attained at moderate positive AOA, the contribution of the pressure side will be generally small or negligible around this angle, which undermines the purpose of an optimization process involving the pressure side of the airfoil only. For examples of the predominance of the suction side TE noise emission, one may refer to Bertanoglio et al. (Bertanoglio, Madsen, & Bak, 2009), which considered the suction side as the only relevant contribution for their research, at $\alpha = 6^\circ$, or to Lutz et al (Lutz, Herrig, Würz, Kamruzzaman, & Krämer, 2007), who declared that: "For fully turbulent flow and high lift coefficients, the value of SPL is clearly dominated by the noise contribution of the thick suction side boundary layer". Despite this possible shortcoming, the research showed the potential of the XFOIL associated with the BPM model, in order to predict relative airfoil noise performance.

Xiaomim (Xiaomim, 2014) described the use of a genetic algorithm to optimize WT airfoils. The airfoil shapes were parameterized and the thickness was allowed to vary within 2% of the chord. For each parametric combination a CFD-RANS simulation was run in order to evaluate the cl and cd of the airfoil configuration. The quality of each variety was then assessed in order to breed another generation and so on,

successively, until a maximization goal was achieved. However, once again no acoustic restraints or objective functions were included in this research.

Also, in a recent review of state-of-the art of optimization techniques, as applied to wind turbines, Cherouri et al. (Cherouri, Younes, Llinca, & Perron, 2015), the reviewed cases were restricted to performance optimization only. The objective functions were, for instance, minimization of the cost of energy, maximization of annual production, minimization of blade mass, etc., all subjected to many design constraints (geometrical, aerodynamic and physical). However, no acoustic design objectives or constraints were considered, once more.

2.6 WIND TURBINE BLADES.

Based on the research by Rautmann et al. (Rautmann, Ewert, & Dierke, 2015), for fixed distance boundary layer transition cases, which may well represent the cases of in-service, soiled blades, the TE noise emission main driver is the airfoil thickness, with thin airfoils showing the smallest overall noise levels, 3 – 4 *dB* lower than thicker configurations. However, the minimum airfoil thickness at each span station, for given materials and processes, is determined primarily by structural requirements, rather than aerodynamics or aeroacoustics. A thick airfoil implies the possibility to embed deep spars and it has also a large shell moment of inertia, which makes it attractive for lightness and low production cost. With the advancement of the material science, it is possible to envision stronger materials with higher tensile and shear strengths, that will allow the design of thinner, quieter blades (for the same diameter and rotation).

Currently, the blades are basically made up of layers of composite material (mostly fiberglass) for the upper and lower panels, enclosing a single or double shear webs with upper and lower spar caps. There are also structural reinforcements and fittings at the leading and trailing-edge locations. A structural model of the blade section may be seen in Figure 2-47 and the “stacking” of different airfoils at different span stations to form a blade may be seen in Figure 2-48.

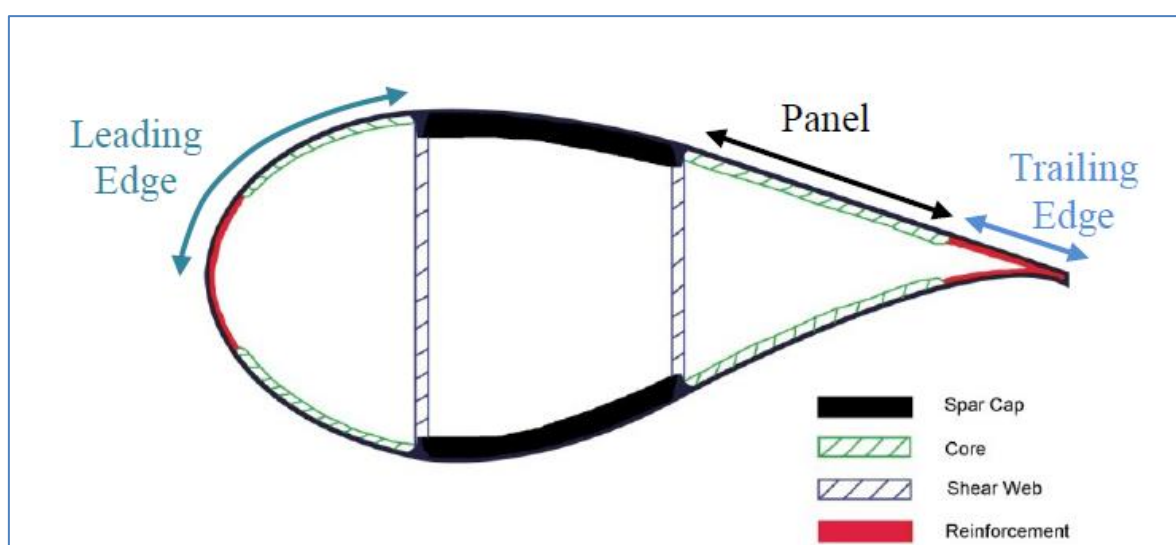


Figure 2-47 - Typical structural arrangement of a blade section. **Not to scale.** Source: (Griffith, Ashwill, & Resor, Large Offshore Rotor Development: Design and Analysis of the SANDIA 100 m Wind Turbine Blade, 2012)

The airfoils are defined for some of the span sections (blade stations) and a geometric interpolation is achieved between them. Usually, the root section is circular, as demanded by the pitch-regulating bearing and related drive mechanism. The root section blends gradually into a thick, large chord inboard section, called the *root airfoil*. The root airfoil proceeds towards mid span and transitions into a medium-thickness airfoil, called the *primary airfoil*, typically located at 75% span, acting where most of the torque is produced. The primary airfoil then transitions into a smaller thickness airfoil, called the *tip airfoil* at 90%+ span. Some blade arrangements may also have several different airfoils specified along the span, as shown in Figure 2-48.

The thicknesses of the root, primary and tip airfoils are determined by the class-size of the equipment, i.e. by its mass. By the turn of last century, the most common HAWTS had blade lengths between 20 m and 30 m and the family of NREL S818 / S825 / S826 airfoils (root, primary and tip, with relative thicknesses of 24%, 17% and 14% respectively) was considered suitable for this class-size. However, as explained by Griffin (Griffin, 2001), these airfoils had to be scaled up to 27%, 21% and 16% thicknesses respectively for the NREL blades with lengths from 40 m to 60 m, which still prevail currently.

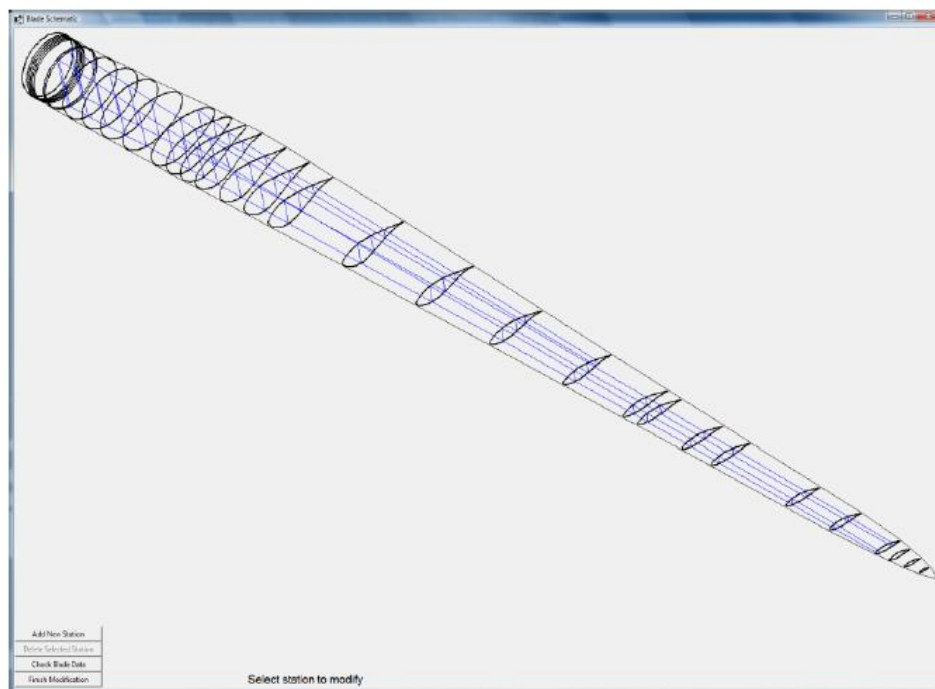


Figure 2-48 - Typical spanwise arrangement of airfoils in a blade: (Griffith & Ashwill, The Sandia 100-m All-glass Baseline Wind Turbine Blade: SNL100-00, 2011)

2.7 THE XFOIL / XFLR5.

The XFOIL is an efficient computational method, developed by Drela and Giles (Drela & Giles, Viscous-Inviscid Analysis of Transonic and Low Reynolds Number Airfoil, 1987) for the calculation of the flow field around 2-D airfoils. The method is currently most often deployed with the graphic user interface developed by Andre Deperrois, under the name XFLR5 (Drela, Youngren, & Deperrois, XFOIL/XFLR5, 2009), (Deperrois, 2011), however preserving the original algorithms. Since 2007, the XFLR5 software became an Open Source Development Project.

The names XFOIL and XFLR5 are used indistinctively along text, as reported by original authors; however, during this research only the XFLR5 was employed, albeit in different versions.

In the context of WT noise prediction methods, the XFOIL / XFLR5 may be used for providing TBL displacement thickness at the TE for airfoils of any geometry and flow conditions up to stall angles. Also, they may be used to provide drag-polar information for the application of the BEM method, explained in next sub-section.

The XFOIL / XFLR5 software has been extensively validated for low and high AOA regime (Drela & Giles, Viscous-Inviscid Analysis of Transonic and Low Reynolds Number Airfoil, 1987), (Fuglsang, Antoniou, Sorensen, & Madsen, 1998), (Guidati & Wagner, 2000) and it is currently quoted as “the standard tool for the calculations of airfoil drag-polars” by Marten (Marten D. , Extension of an Aerodynamic Simulator for Wind Turbine Blade Design and Performance Analysis, 2010) in the WT industry.

In the method, the steady Euler equations represent the inviscid flow and a compressible, integral method is used to represent the boundary layer and the wake. The viscous and inviscid flows are fully coupled through the displacement thickness (Drela & Giles, Viscous-Inviscid Analysis of Transonic and Low Reynolds Number Airfoil, 1987). The entire set of non-linear equations is solved simultaneously as a fully coupled system, by the use of a global Newton-Raphson method. Accurate representations of laminar and turbulent separations are modeled through the use of

a two-equation dissipation-type closure for laminar and turbulent flows, with a lag equation added to the turbulent formulation.

The XFLR5 code has a stronger coupling of the viscous/inviscid solutions (Vargas, de Oliveira, Pinto, Bortoulus, & Souza, 2005), when compared to the Eppler code originally used by NREL (Somers & Tangler, The Airfoils S830, S831 and S832, 2005b).

Since airfoil drag is affected by the momentum thickness jump during transition, the method employs the e^n transition model (White, 2006), which assumes, based on experimental evidence, that transition occurs when the Tollmien-Schlichting waves have grown by a factor of e^n , where usually $8 < n < 11$.

All the model equations and calculation procedure are described in detail by Drela and Giles (Drela & Giles, Viscous-Inviscid Analysis of Transonic and Low Reynolds Number Airfoil, 1987). The method is limited to predict lift and drag coefficients for angles where the flow is attached or mildly unattached, but not far over the stall angle.

In some operating regimes the WT blades may be subjected to large AOA and even backflow (see for instance the turbulent wake state or the vortex ring state in Hansen (Hansen, 2008), p. 33). According to Viterna and Janetzky (Viterna & Janetzky, 1982), this is especially true when high winds and low rotational speeds occur (low TSR). For large AOA operation, a region where the XFOIL do not converge, the drag-polar information may be approximated by considering that the airfoil behaves like a thin plate and using suitable extrapolations as proposed by Viterna and Janetzky (Viterna & Janetzky, 1982) among others. However, since there are no noise models available for the post-stall regime, this condition is not of special concern to this research.

2.8 THE BLADE ELEMENT MOMENTUM (BEM) METHOD.

The BEM (*Blade Element Momentum*) method, described by Hansen (Hansen, 2008) allows the calculation of the local flow speeds acting on the segments of the blade rotor, along with steady loads, thrust and power for different wind speeds, rotational speeds and pitch angles.

In the BEM method, the rotor is discretized into N annular elements of width dr as shown in Figure 2-49, the boundaries of which are streamlines.

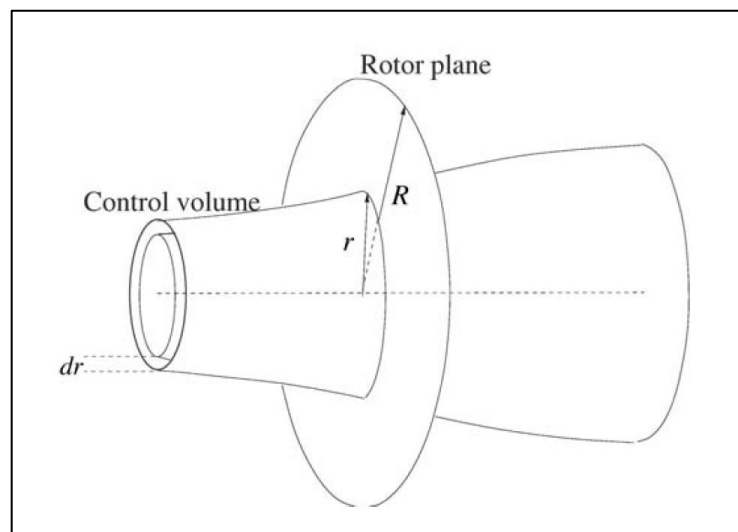


Figure 2-49 - Annular control volume employed in the BEM method. Source: (Hansen, 2008), p.45.

The model hypothesis for the control volumes are:

- No radial influence on neighbor control volumes. The control surface is a streamtube, as in Figure 2-50.
- The number of blades in the rotor is infinite. The force from the blades in the flow³⁸ is constant in each annular area. Later, a correction factor known as the Prandtl's tip loss factor will be introduced in order to compensate for this hypothesis.
- The pressure distribution along the curved streamlines enclosing the wake does not result in an axial force component.

³⁸ This statement gives a glimpse of the origin of the method: the BEM model was originally developed by Glauert in 1935, motivated by the study of aircraft propellers.

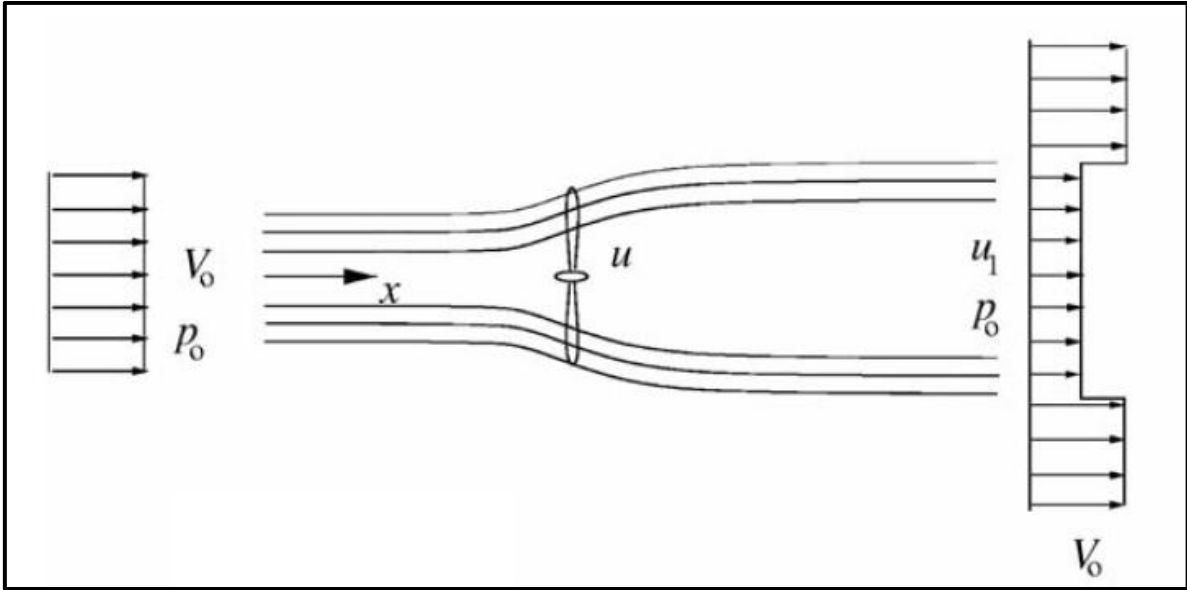


Figure 2-50 - Streamlines passing a rotor in the windmilling state, with axial pressures and velocities. Source: (Hansen, 2008), p.28.

With the velocity notation given by Figure 2-51, the thrust dT on the annular control volume with area $2\pi r dr$ can be found from the integral momentum equation:

$$dT = (V_0 - u_1)d\dot{m} = 2\pi r \rho u (V_0 - u_1) dr \quad (2 - 24)$$

Where V_0 is the undisturbed wind speed, the axial speed in the rotor plane is $u = (1 - a)V_0$, and the axial speed in the wake is given by $u_1 = (1 - 2a)V_0$, where a is the axial induction factor.

For the ideal rotor, there is no rotation in the wake and a' , which is the tangential induction factor, is zero. However, in the case of a modern WT, with a single rotor and no stator, the wake will have some rotation. Thus, the torque dM on the control volume, considering the rotational velocity upstream of the rotor as zero (it is non-zero only downstream of the rotor), is:

$$dM = r C_\theta d\dot{m} = 2\pi r^2 \rho u C_\theta dr \quad (2 - 25)$$

where $C_\theta = 2a'\omega r$ is the rotational velocity in the wake of the rotor and a' is the tangential induction factor.

The velocity triangles for a section of the rotor can be seen in Figure 2-51.

With the definitions of the axial and tangential induction factors, the expressions (2-24) and (2-25) may be rewritten as:

$$dT = 4\pi r \rho V_o^2 a(1-a)dr \quad (2-24a)$$

$$dM = 4\pi r^3 \rho V_o \omega(1-a)a'dr \quad (2-25a)$$

By resolving the local flow in the leading edge it is possible to calculate the thrust and torque, and to integrate them over the rotor area.

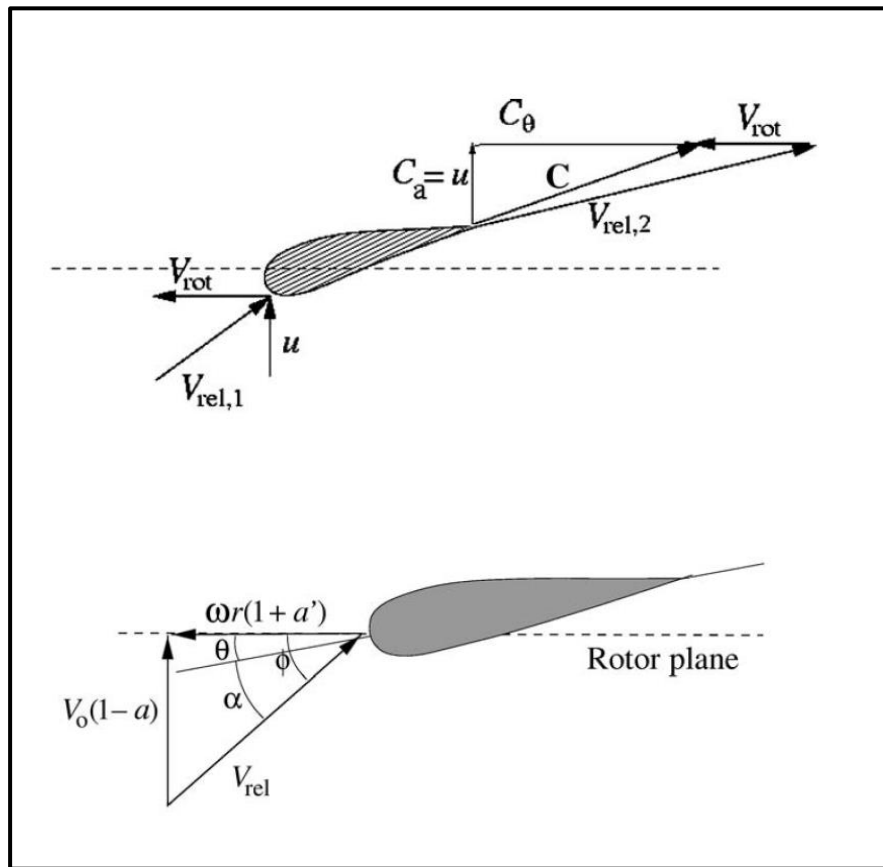


Figure 2-51 - Velocities triangles at the edges and relative velocity at the LE. Source: (Hansen, 2008), p.36 and 47.

As shown in lower diagram of Figure 2-51, the local angle of attack, α , is given by the angle between the plane of rotation and the relative velocity, ϕ , and the local pitch of the blade, θ :

$$\alpha = \phi - \theta \quad (2-26)$$

The local pitch angle of the section, θ , is the combination of the variable pitch angle, θ_p , and the twist of the blade, β :

$$\theta = \theta_p + \beta \quad (2 - 27)$$

From the lower diagram in Figure 2-51, the ϕ angle can be determined as:

$$\tan \phi = \frac{(1 - a)V_0}{(1 + a')\omega r} \quad (2 - 28)$$

With both axial and tangential local speeds determined, the relative velocity, V_{rel} , is also determined and the lift and drag components, which are by definition perpendicular and parallel to the relative velocity, may also be obtained by

$$\frac{L}{b} = \frac{1}{2} \rho V_{rel}^2 C_L c \quad (2 - 29)$$

$$\frac{D}{b} = \frac{1}{2} \rho V_{rel}^2 C_D c \quad (2 - 30)$$

where c is the local airfoil chord and b is the span of the airfoil segment in the considered section.

However, the designer is mostly interested in the forces acting on the rotor plane or perpendicular to it, i.e., the axial force for which the bearing will be sized and the torque on the shaft that will turn the generator. These loads may be found by projecting the aerodynamic resultant as shown in Figure 2-52.

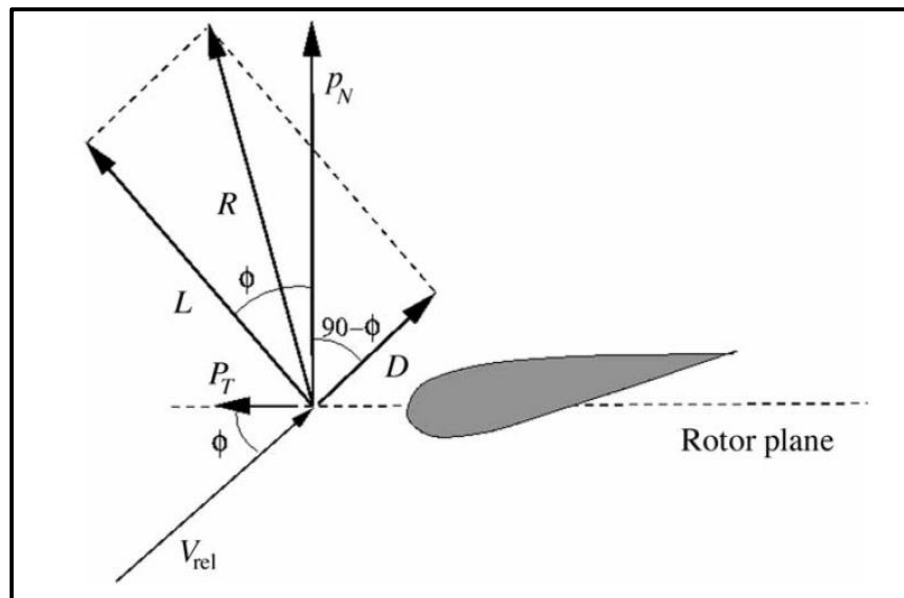


Figure 2-52 - Forces perpendicular and normal to the rotor plane. Source: (Hansen, 2008), p.48.

The resulting projected forces per unit span are shown below, along with their dimensionless (coefficient) forms:

$$p_N = L \cos \phi + D \sin \phi \quad (2 - 31)$$

$$C_n = C_L \cos \phi + C_D \sin \phi \quad (2 - 31a)$$

$$p_T = L \sin \phi - D \cos \phi \quad (2 - 32)$$

$$C_t = C_L \sin \phi - C_D \cos \phi \quad (2 - 32a)$$

The number of blades is finite and the fraction of the annular area covered by blades is a function of the rotor radius and is defined as the solidity ratio, σ :

$$\sigma(r) = \frac{c(r)B}{2\pi r} \quad (2 - 33)$$

where B is the number of blades in the rotor.

The axial (thrust) and tangential (torque) forces on the control volume of span dr are:

$$dT = B p_N dr = \frac{1}{2} \rho B \frac{V_0^2 (1 - a)^2}{\sin^2 \phi} c C_n dr \quad (2 - 34)$$

$$dM = r B p_T dr = \frac{1}{2} \rho B \frac{V_0 (1 - a) \omega r (1 - a')}{\sin \phi \cos \phi} c C_t r dr \quad (2 - 35)$$

By combining Eqns. (2-34) and (2-24a), and applying the definition of solidity, an expression for the axial induction factor is obtained:

$$a = \frac{1}{\frac{4 \cdot \sin^2 \phi}{\sigma \cdot C_n} + 1} \quad (2 - 36)$$

Similarly, by combining Eqns. (2-35) and (2-25a), an expression for the tangential induction factor is obtained:

$$a' = \frac{1}{\frac{4 \cdot \sin \phi \cdot \cos \phi}{\sigma \cdot C_t} - 1} \quad (2 - 37)$$

2.8.1 BEM Method Corrections

The assumption of an infinite number of blades does not apply to real equipment and the vortex system in the wake is different from the theory. This fact may be compensated for by the use of Prandtl's Tip Loss Factor, F , so that the thrust and torque may be corrected:

$$dT = 4\pi r \rho V_o^2 a(1-a)Fdr \quad (2-34b)$$

$$dM = 4\pi r^3 \rho V_o \omega (1-a)F a' dr \quad (2-35b)$$

where $F = \frac{2}{\pi} \frac{1}{\cos(e^{-f})}$, and $f = \frac{B(R-r)}{2s \sin \phi}$, B is the number of blades, R is the total rotor radius, r is the local radius and ϕ is the flow angle. With this correction, the axial and tangential induction factor expressions derived before assume the following new formulation:

$$a = \frac{1}{\frac{4F \sin^2 \phi}{\sigma \cdot C_n} + 1} \quad (2-36a)$$

$$a' = \frac{1}{\frac{4F \sin \phi \cdot \cos \phi}{\sigma \cdot C_t} - 1} \quad (2-37a)$$

Apart from the replacement of the expressions with correction factors, the BEM algorithm is otherwise unchanged.

Another type of correction is needed for flow conditions where the axial induction factor is larger than 0.4. Figure 2-53 shows that for $a > 0.4$ there is no adherence between the experimental data (triangles and circles in the Figure) and the predicted thrust coefficient, C_T .

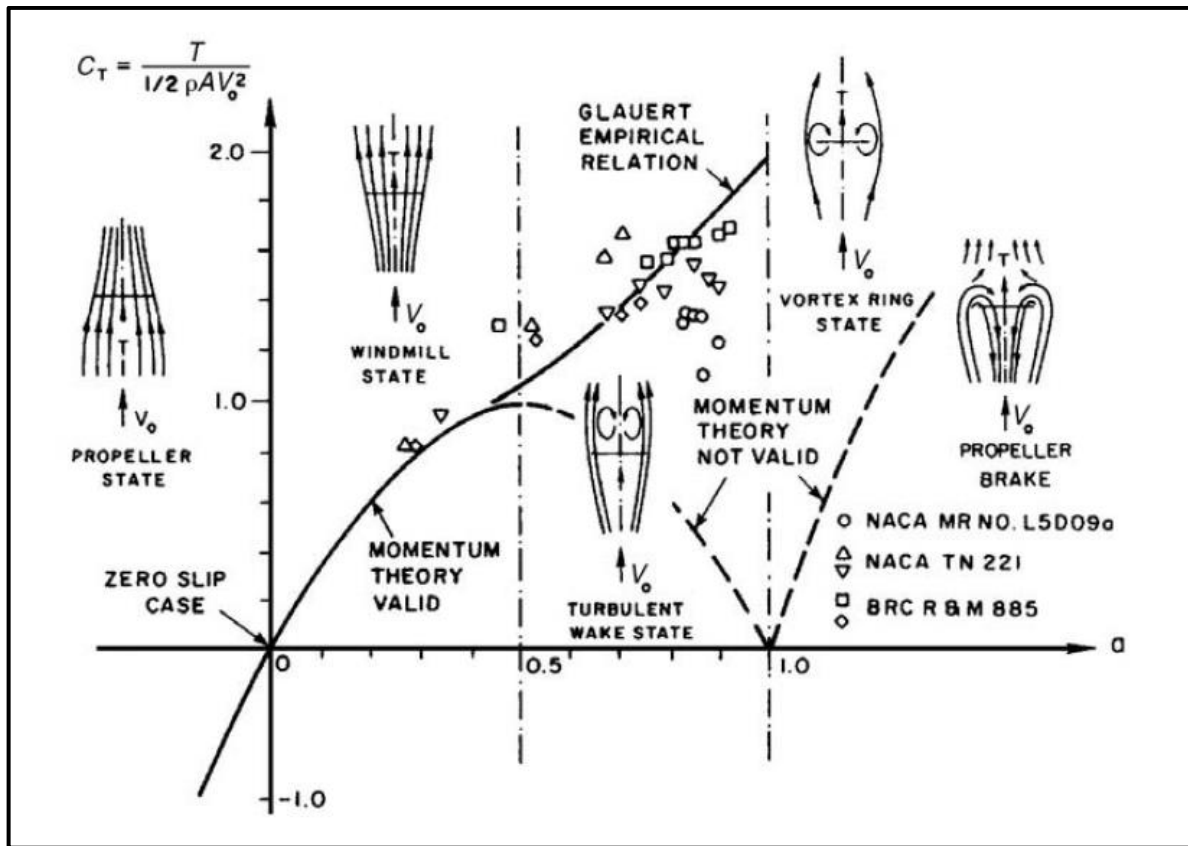


Figure 2-53 - Rotor thrust coefficient, C_T , as a function of axial induction factor. Source: (Hansen, 2008), p.33.

The operational regime for $a > 0.4$ is called *the turbulent wake state*, and the simple momentum theory over which the thrust and torque equations were developed for the rotor, are not valid anymore. According to Hansen (Hansen, 2008), empirical relations were proposed by Glauert (Eqn. (2-38)) and Wilson and Walker (Eqn. (2-39)), to adjust the thrust coefficient as a function of the axial induction factor in this regime, the result of which may be seen on Figure 2-54.

$$C_T = \begin{cases} 4a(1-a)F & a \leq \frac{1}{3} \\ 4a \left(1 - \frac{1}{4}(5-3a)a\right)F & a > \frac{1}{3} \end{cases} \quad (2-38)$$

or

$$C_T = \begin{cases} 4a(1-a)F & a \leq a_c \\ 4(a_c^2 + (1-2a_c)a)F & a > a_c \end{cases} \quad (2-39)$$

where $a_c \cong 0.2$.

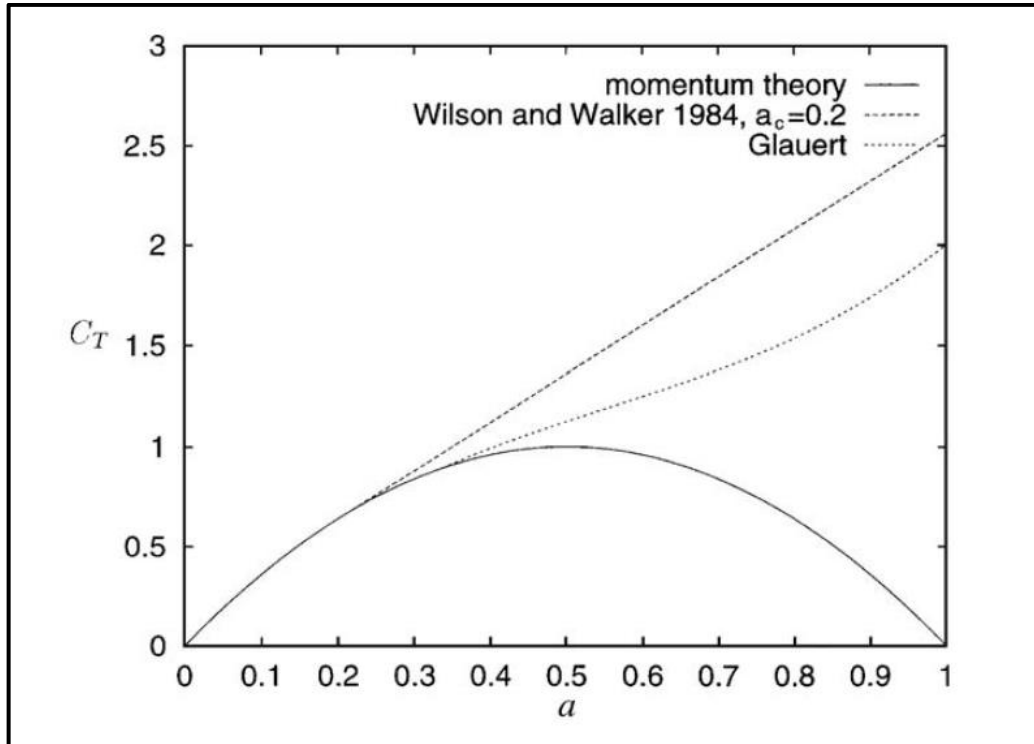


Figure 2-54 - Thrust coefficient as a function of axial induction factor for the momentum theory, continuous line; Glauert's correction Eqn. (3-16), dotted line; and Wilson and Walker correction Eqn. (3-17), dashed line. Source: (Hansen, 2008), p.54.

2.9 THE QBLADE

The QBlade code (Pechlivanoglou, Marten, G., N., & Wendler, 2009), (Marten D. , Extension of an Aerodynamic Simulator for Wind Turbine Blade Design and Performance Analysis, 2010), (Marten & Wendler, Qblade Guidelines v0.6, 2013), (Marten D. , Qblade Short Manual V0.8, 2014), (Marten D. , 2016), is an open source³⁹ wind turbine calculation software, distributed under the general public licensing (GPL) initiative.

The software provides design, simulation and performance analysis for HAWT and VAWT in an integrated environment with very intuitive graphical user interface (GUI).

Over the years since its inception, the code has been gradually boosted by the professional integration of existing open codes (XFLR5, Aerodyn/FAST⁴⁰) or by receiving purpose built powerful tools (Blade design module, BEM module, VAWT design capability, Viterna/Montgomery 360 polar extrapolation models, Structural Euler-Bernoulli beam model, Turbulent Wind Field Generator tool, Unsteady non-Linear Lifting Line method, Lifting-Line Free Vortex Wake method, etc.) by the TU-Berlin team.

The code is certainly the broadest and most capable GPL tool available for the WT industry, however it did not possess any aeroacoustic evaluation tool integrated into it up to v0.9.

As will be explained in further detail in Sections 3.5 and 3.6, the Modified-BPM TE noise model developed under this research and later named PNoise, was integrated into v0.95, released in June, 2016.

The reader is referred to the latest software manual for a full description of the models available and operating procedures (Marten D. , 2016).

³⁹ Written in Qt (GPL) (Rischpater, 2013).

⁴⁰ The Aeroelastic code from NREL.

3. METHODOLOGY

The general strategy followed in the course of this research is displayed in Figure 3-1

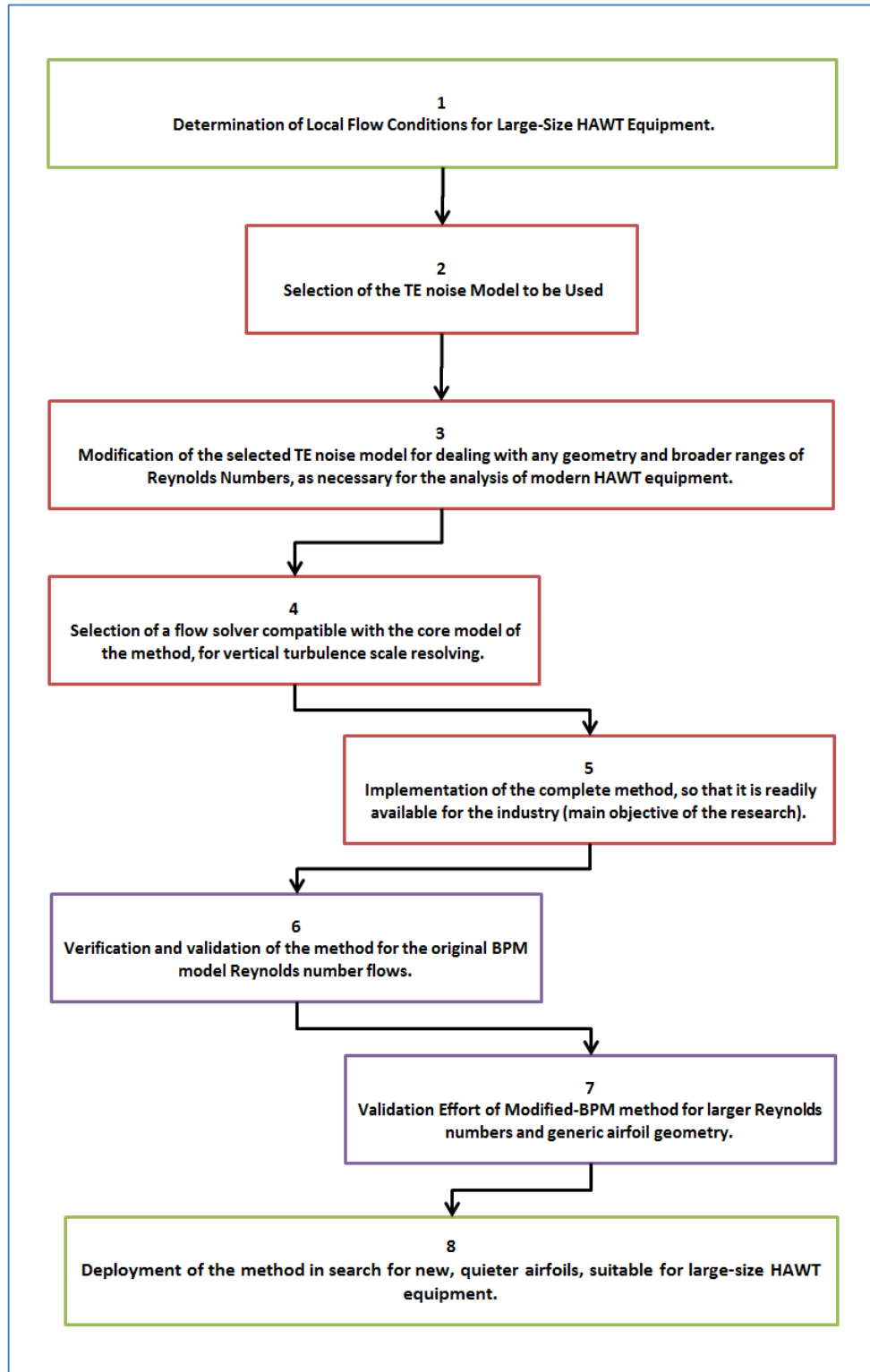


Figure 3-1 – General strategy pursued for the development of the TE noise code, its implementation, validation and later deployment in the search for quite airfoils.

In this section the methodologies and/or criteria will be described for:

- The calculating procedure for the BEM method implemented.
- The geometries for the large-size Horizontal Axis Wind Turbine.
- The modified-BPM TE-noise calculation method.
- The selection of the flow solver for the turbulence scale.
- The establishment of a partnership for efficient code implementation, considering the ultimate objective of making the method readily available for the WT Industry.
- Implementation of the method.
- Methodology for the investigation of quieter airfoils for WT.

Also, during the course of this research, the methodology was fully developed for an upcoming method for (full) blade and rotor TE noise prediction module, including the complete set of coordinate transformation matrixes for determining the observer position with relation to any blade segment of a rotating blade. However, this methodology will be presented in a follow-up paper along with the implementation details and results.

3.1 THE BEM METHOD IMPLEMENTATION.

For the task of determining the local flow at each WT blade section, the BEM method, described in detail in Section 2.8 was selected. Although Vortex-Wake methods (Gupta & Leishman, 2005) can include the effect of wake vortices, the BEM method has a much greater computational efficiency and is the primary tool adopted for performance analysis for HAWTs (Imamura, 1999). The reason for this is that the effect of wake rotation is negligible in the predictions of the power and aerodynamic loading on a WT (Gupta & Leishman, 2005), provided the rotor achieves high TSR. Hansen (Hansen, 2008), p. 36, confirms that the azimuthal velocity component in the wake decreases with increasing rotational speed.

The BEM algorithm described below is based on Hansen (Hansen, 2008), and was implemented in the course of this research, along with the necessary corrections described earlier in Section 2.8.1. It was implemented in order to allow reasonable prediction of the induced local speeds at each blade section of a spinning large-size HAWT, under high TSR conditions.

The method has been validated, with Glauert and Prandtl corrections, by Hansen (Hansen, 2008), p. 59, for wind speeds lower than approximately 20 m/s.

The implementation was accomplished both in *Wolfram Mathematica 8 for students* environment and in MS Excel.

With all the necessary equations derived in Section 2.8, the steps of the BEM algorithm may be summarized as follows:

- Initialize a and a' (usually $a = a' = 0$).
- Compute the flow angle by using Eqn. (2-28): $\tan \phi = \frac{(1-a).V_0}{(1+a').\omega.r}$
- Compute the local AOA using Eqn. (2-26) $\alpha = \phi - \theta$, with the known flow angle, ϕ , and the local pitch angle, θ .
- Obtain the lift and drag coefficients, as a function of local AOA, from a table, e.g. (Abbott & Von-Doenhoff, 1959), calculations or experiments.
- Compute the normal and tangential forces coefficients from Eqns. (2-31a) and (2-32a).
- Calculate the updated values for the axial and tangential induction factors from Eqns. (2-36) and (2-37).

- Set Prandtl and Glauert corrections on, if applicable.
- If the change in value for the induction factors among two subsequent calculation loops is above a certain acceptable tolerance, reiterate the process.
- When the final tolerance is reached, compute the local loads on the segment of the blades or the local flow components, as required.

The tolerance adopted for the induction factor between two subsequent calculation loops, which defines the convergence criteria, was smaller than 10^{-5} .

Usually, less than 20 iterations were required for convergence of the algorithm.

3.2 THE GEOMETRIES FOR THE LARGE-SIZE HORIZONTAL AXIS WIND TURBINES

For predicting the TE noise from an airfoil section, it is necessary to determine first its operating conditions, i.e. local AOA and Reynolds and Mach numbers. These conditions may be determined with the aid of the BEM method, provided a full blade aerodynamic description is known. However, this information is proprietary of each WT manufacturer. In the absence of complete sets of information for this purpose, it was decided that three representative Wind Turbines would be conceptually designed for this research.

A full blade aerodynamic description depends upon specification of airfoil, chord and twist distribution along the span, plus number of blades, incident wind speed (or field, for unsteady cases) and rotation information.

The WTs considered here are of the three-bladed, upwind, direct-drive, variable speed, pitch controlled type. The three-bladed rotor usually has a blade *solidity*⁴¹ range which yields a high Coefficient of Power, the main conversion performance driver, for a Tip Speed Ratio (TSR) between 6 and 10 (Burton, Jenkins, Sharpe, & Bossanyi, 2011), p. 175.

As seen in the bibliographic research Section 2.5.1, Table 2-26, the NREL family of “S” airfoils was designed for wind turbines with recommended diameters of up to 50 m, which is the typical blade length for the current technology (see Figure 1-8) and so this diameter was selected as the smallest of the three WT to be designed. The future designs in the medium term will have blades of 100 m or more (Griffith, Ashwill, & Resor, Design and Analysis of the SANDIA 100 m Wind Turbine Blade, 2012).

Scaling up a wind turbine blade is a complex, multidisciplinary task. According to Griffith et al. (Griffith, Ashwill, & Resor, Large Offshore Rotor Development: Design and Analysis of the SANDIA 100 m Wind Turbine Blade, 2012), root bending moments due to gravitational loads scale up at a faster rate with blade length ($\sim l^4$) than bending

⁴¹ Solidity, σ , is defined as the total blade area divided by the rotor disc area, and is relevant in determining rotor performance. The solidity ratio is generally specified between 2% and 5%.

moments associated with aerodynamic loads ($\sim l^3$). Thus, as blade length, l , increases, the bending moments will eventually exceed aerodynamic loads.

It is necessary, then, to choose the larger diameters from carefully scaled up options, which will insure that the length and chord distribution of the blades, over span, will lead to a valid weight range, close to the target-weight on Table 3-1. That will in turn allow the use of ordinary materials (mostly fiberglass FRP⁴²) and simple manufacturing processes (mostly manual lay-up followed by vacuum bagging cure) to be successfully employed in their construction, which will help keep the production costs down to a minimum.

Table 3-1 - Scaled up blade properties according to aerodynamic and gravitational scaling functions. The machine sizes of 10 MW and 15 MW were chosen as references for the larger blades designed in the context of the current research. Source: (Griffith, Ashwill, & Resor, Large Offshore Rotor Development: Design and Analysis of the SANDIA 100 m Wind Turbine Blade, 2012), SNL.

Machine Size	Rotor Diameter (m)	Blade Length (m)	Blade CG Location (m)	Blade Mass (kg)	Max Operating Speed (RPM)
5 MW	126	61.5	20.5	17740	12.1
* 10 MW	178.2	87.0	29.0	50184	8.56
13.2 MW	205	100.0	33.4	76402	7.44
* 15 MW	218.2	106.5	35.6	92131	6.99

Therefore, the two larger blade-lengths will be designed based on thoroughly scaled up blades by the Sandia National Laboratories (Griffith & Ashwill, The Sandia 100-m All-glass Baseline Wind Turbine Blade: SNL100-00, 2011), as indicated by asterisks in Table 3-1.

For design purposes the blades were discretized into 20 spanwise segments for the application of the BEM method and the calculation of local flow speeds and angles. The main interest lies in the outboard part of the span, since, according to the measurements⁴³ made by Oerlemans (Oerlemans, Wind Turbine Noise: Primary Noise Sources, 2011) p.26, “most of the noise is radiated from the outer part of the blades,

⁴² FPR- Fibre-Reinforced Plastic.

⁴³ These particular measurements were accomplished for a 94 m-diameter, 2,3 MW WT, without significant mechanical noise sources and in accordance with applicable IEC standards

but not the very tip”. The visual source intensity graph provided by the study above, shown in Figure 2-6, indicated the stronger sources to be located close to 85%-span of the blade, which was adopted as the main station of interest for this study.

Thus, three baseline wind turbines were designed with blade lengths of 50.0, 87.0 and 106.5 m, typical of 3.5, 10 and 15 MW nominal power-rating classes, respectively, with the purpose of obtaining a good insight into the local operating conditions, and associated TE noise emission, of the airfoils at 85% radial position of these large-size WTs.

The design criteria for the three wind turbines were the same: for a given chord distribution and selection of airfoil based on their availability and thicknesses, to identify the blade twist that will allow each blade section to be ideally positioned in relation to the local flow so that $(cl/cd)_{max}$ is achieved in each discretized section, allowing for efficient energy conversion while limiting aerodynamic loads acting on the large blades.

Also for the designs to be representative of a reasonably real operation, the Power Coefficient, was calculated for each case and assured to be $C_p > 0.45$. As explained in Section 1.1.2, according to Ragueb and Ragueb (Ragheb & Ragheb, 2011), a characteristic value for C_p is around 0.40 for a large size, modern WT.

3.2.2 The WT geometry and design point for the 50 m span, “Poli-100” WT blade.

For the reference 50 m blade, designated Poli-100, the NREL S818 / S830 / S832 airfoils with relative thicknesses of 24%, 21% and 15%, respectively, were selected based on the NREL tables of recommended use (Somers & Tangler, The Airfoils S830, S831 and S832, 2005b), on Table 2-24 and also on the public availability of the contours.

In planning for the later profile TE-noise study phase, the primary airfoil selected for the 85% radial station, was the 21% thickness S830 for the reasons already presented in Section 2.5.1 (the airfoil was designed to be both aerodynamically efficient and quiet from design requirements). Its design Reynolds number, according to the NREL airfoil website is of 4 million (National Renewable Energy Laboratory - NREL 4, 2016) but

during its development, the theoretical performance was investigated for a broad Reynolds number range from 1 to 9 million so that the S830 was expected to have good performance even above the original WT-diameter recommendation. Unfortunately, no experimental aerodynamic or aeroacoustic data is available for the airfoil to validate against its original design requirements or other flow conditions.

The operating conditions for the 50 m span blade were matched to those described by Medina et al. (Medina, Singh, Johansen, Jove, & Machefaux, 2011), corresponding to actual data for a Siemens SWT-2.3-101 WT (with the same general layout of the current machine), of 2.3 MW nominal power rating and three 49 m blades operating over a 80 m height tower:

- Cut in speed of 4 m/s
- Cut out speed of 25 m/s
- Nominal power of 2.3 MW reached at 12-13 m/s
- Rotor speed variation between 6-16 rpm.
- Design TSR=7.

These numbers are also compatible with those of Griffin (Griffin, 2001), p. 4, for a similar power-rating machine.

The basic geometry was defined as follows:

- 2.5 m spinner radius and 47.5 m length blade.
- S818/S830/S832 airfoils, as discussed.
- Typical chord distribution as recommended by Griffin (Griffin, 2001), p.6, reproduced in Figure 3-2.
- Solidity ratio between 3 and 5%.
- Initial twist distribution estimated with the aid of the BEM method.

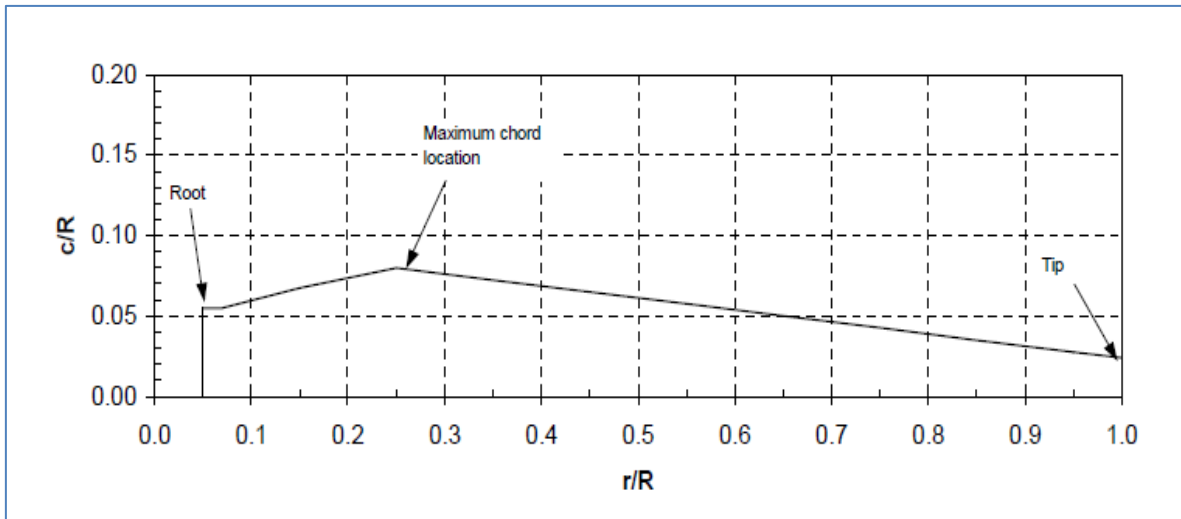


Figure 3-2 - Typical blade chord distribution (planform) for 40-m to 60-m span blades, after (Griffin, 2001), p.6.

After the determination of the airfoils, chord distribution and rotation range, the procedure devised for the determination of the twist along the span (with which the final conceptual design of the WT is complete), is described in the flow diagram of Figure 3-3.

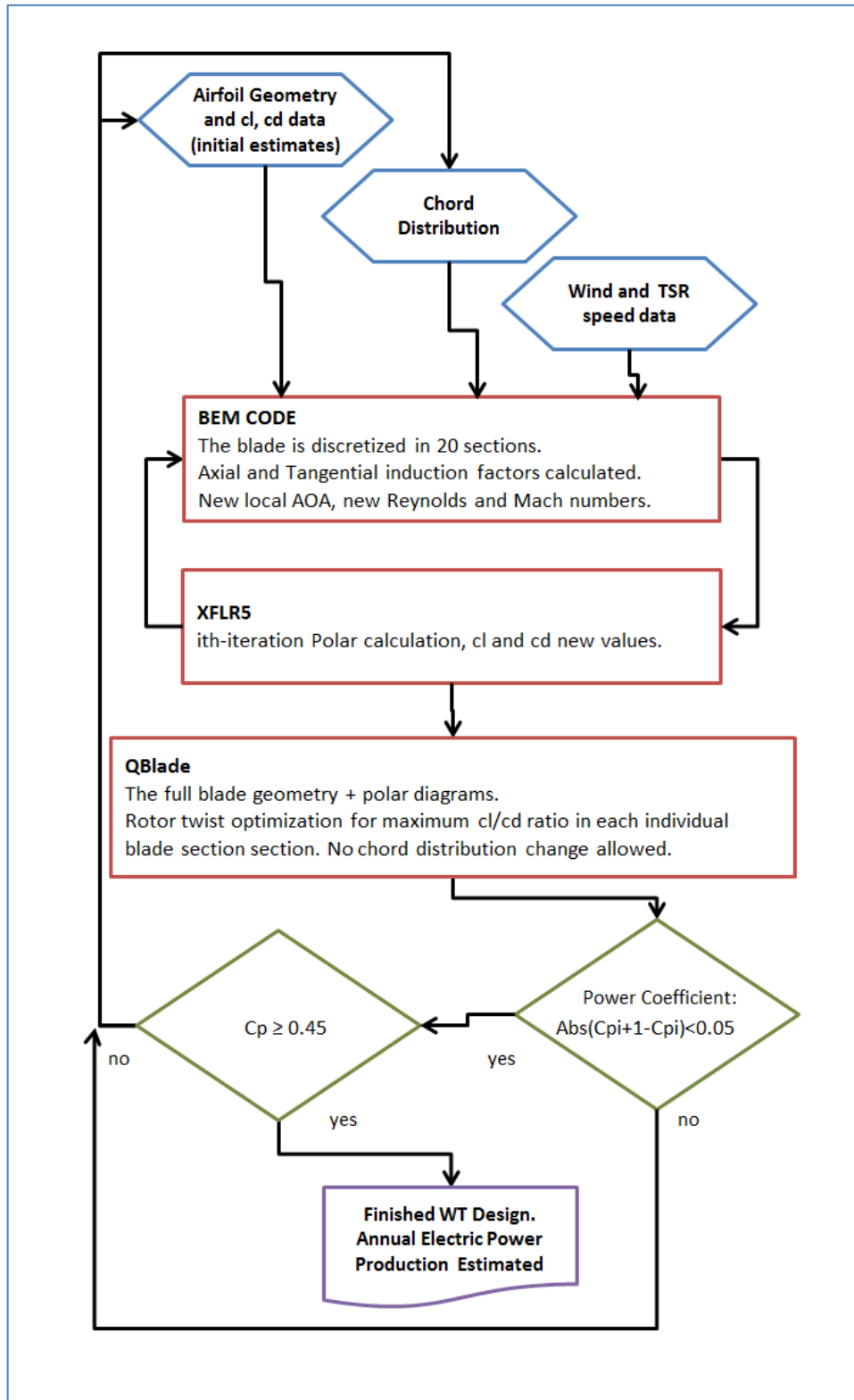


Figure 3-3 – Procedure devised for the geometric design of the WT under specified operating conditions.

3.2.3 The WT geometry and operating point for the 87 m (Poli-180) and 106.5 m (Poli-220) span blades.

For the larger machines, the operating conditions are shown in Table 3-2. They were defined as a compromise between the Griffith et al. (Griffith & Ashwill, The Sandia 100-m All-glass Baseline Wind Turbine Blade: SNL100-00, 2011) data and the rated rpm for the scaled up blades, so that the TSR would fall between 6 and 7⁴⁴ and the rotor speed would fall below maximum blade rpm, dictated by structural requirements (Table 3-1).

Table 3-2 - Operating conditions defined for the 87 m and 106.5-m-long blades.

	Poli-180	Poli-220	Ref.
Typical rating (MW)	10	15	Griffith et al., 2012, based on studies for the SNL 100-m blade.
Blade length (m)	87	106.5	
Hub radius (m)	2.4	2.9	
Rotor diameter	178.8	218.8	
Max Rotor speed (rpm)	8.56	6.99	
Cut in speed (m/s)	3	3	
Cut out speed (m/s)	25	25	
Rating wind speed (m/s)	11	11	
Rating rpm	8	6.4	Calculated from radius and wind speed to result in an acceptable TSR.
Design TSR	6.8	6.6	Above 6 for good efficiency (see Hansen, 2008, p.40).

The basic blade geometry was defined as follows:

- Typical, normalized, chord distribution adopted for the SANDIA 100 m blade is depicted in Figure 3-4.
- Airfoil distribution along span (stacking) followed the original Griffith et al, 2012, distribution, in Table 3-3 which is very close to the distribution adopted by NREL for the 5-MW Reference WT (Jonkman, Butterfield, Musial, & Scott, 2009).
- Although proprietary, the coordinates for the thick, DU airfoils employed in inboard stations were made available in appendix B of said reference and also in the NREL web forum (NWTC, 2016). They were, therefore, used in the same inboard positions of the current design, in order to allow a realistic assessment of the induced flow on the outboard sections, where accurate flow conditions are required.

⁴⁴ As discussed, this compromise will yield an efficient, yet light, blade.

- Initial twist distribution followed that of Jonkman et al. (Jonkman, Butterfield, Musial, & Scott, 2009) and was later refined with QBlade software optimization tool in order to yield the highest C_p possible, with tip and root corrections applied.

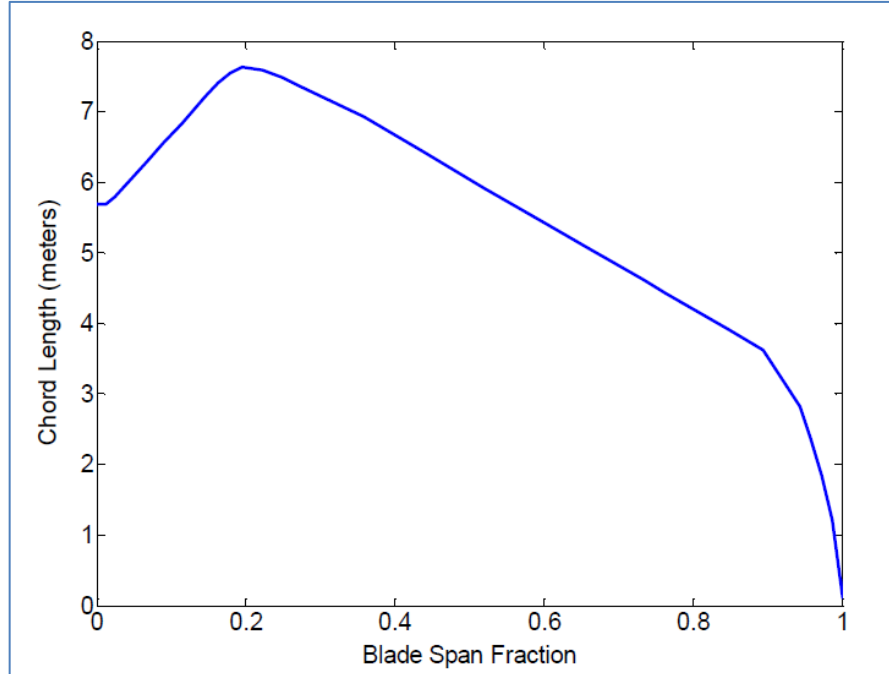


Figure 3-4 - Typical blade chord distribution (planform) adopted for the SNL-100, 100 m span blade (Griffith, Ashwill, & Resor, Large Offshore Rotor Development: Design and Analysis of the SANDIA 100 m Wind Turbine Blade, 2012).

Table 3-3 - Blade thickness distribution along the span and airfoil sections adopted for the SNL-100, 100 m span blade (Griffith, Ashwill, & Resor, Large Offshore Rotor Development: Design and Analysis of the SANDIA 100 m Wind Turbine Blade, 2012).

Airfoil	Thickness (% chord)	Position along Span (% span)
Cylinder 1	100.0	2.8 to 9.3
Cylinder 2	100.0	9.3+ to 15.7
DU-99-W-405 (mod.)	40.5	15.7+ to 23.3
DU-99-W-350 (mod.)	35.1	23.3+ to 31.8
DU-97-W-300	30.0	31.8+ to 41.5
DU-91-W2-250	25.0	41.5+ to 53.1
DU-93-W-21	21.0	53.1+ to 65.8
NACA 64-618	18.0	65.8+ to 100

The general design procedure for the rotors followed the same procedure described earlier for the 50 m span blade in Figure 3-3.

3.3 THE MODIFIED BPM TRAILING EDGE NOISE CALCULATION METHOD.

In this section, the selection of the BPM TE-noise model is explained along with the detailed calculation methodology for the original and the modified BPM TE-noise model.

3.3.1 The selection of the TE-noise prediction model and improvements.

For the TE noise source, many noise prediction models were developed after 1978 in the semi-empirical and simplified theoretical lines of research, as extensively discussed in Appendixes D and E, aimed at WTN application:

Simplified-theoretical models reviewed:

- Howe's model (Howe, 1978).
- The model of Brooks and Hodgson (Brooks & Hodgson, 1981).
- The model of Glegg et al. (Glegg, Baxter, & Glendinning, The Prediction of Broadband Noise From Wind Turbines, 1987).
- The TNO-Blake or TNO-TPD model (Kamruzzaman M. , Lutz, Nübler, & Krämer, 2011).
- The Glegg and Reba model (Glegg & Reba, 2010) .
- The modified TNO-TPD model of Kamruzzaman et al. (Kamruzzaman M. , Lutz, Herrig, & Krämer, 2012a).

Semi-empirical models:

- The Grosveld's model (Grosveld, 1985).
- The Brooks and Marcolini model (Brooks & Marcolini, 1985).
- The BPM model (Brooks, Pope, & Marcolini, Airfoil Self-Noise and Prediction, 1989).
- The Lowson's model (Lowson, 1993).

Some models in each group are only improvements over previous versions so that in the simplified theoretical group there are essentially the Glegg and Reba (Glegg & Reba, 2010) and the Modified TNO-TPD (Kamruzzaman M. , Lutz, Herrig, & Krämer,

2012a) models, while in the semi-empirical track there are, essentially, the BPM model (Brooks, Pope, & Marcolini, Airfoil Self-Noise and Prediction, 1989) and Lowson's model (Lowson, 1993).

In order to choose a suitable TE noise model, the first analysis was made concerning the accuracy of the model. Throughout the model and method review in Appendixes D and E, an effort was made to show the hypotheses, the equations underlying each method and also the validation process against experimental data, whenever available.

The simplified-theoretical model of Glegg and Reba (Glegg & Reba, 2010), tended to overestimate the noise for low frequencies and underestimate the noise for higher frequencies by 2 dB, with a prediction capability very close to the semi-empirical methods, but requiring a more intensive computational effort.

The semi-empirical model from Lowson (Lowson, 1993) was based on a natural developing boundary layer and fed with TBL-FP correlation displacement thickness data (multiplied by factors, as discussed in the Appendix D). The validation showed underprediction at lower frequencies and overprediction in the intermediate frequency range. The accuracy was found to be in the range 2 ± 4 dB.

While the simplified-theoretical model from Glegg and Reba (Glegg & Reba, 2010) is a more complex variation of the TNO-TPD model, the semi-empirical model from Lowson (Lowson, 1993) is a simplified precursor of the BPM model. However, in neither case a tangible advantage in accuracy or computation time was confirmed over the "main stream" models.

This analysis restricted our model options to the main stream models found in each line of research, i.e. the modified TNO-TPD model, by Kamruzzaman et al. (Kamruzzaman M. , Lutz, Herrig, & Krämer, 2012a) in the simplified-theoretical track, and the BPM model (Brooks, Pope, & Marcolini, Airfoil Self-Noise and Prediction, 1989) in the semi-empirical track.

By analyzing the column "accuracy class" of the new model/method classification criteria, in Table 2-19, it was noticed that there were methods employed for preliminary design and optimization, equipped with the simplified theoretical or the semi-empirical TE noise models described, suggesting some equivalence in this criterion. However, since a computationally-efficient tool was also needed, it was necessary to investigate

the relative accuracy of the methods in a suitable operating conditions range, when the methods are fed with the simplest possible solution to the flow field.

For this purpose it was considered useful to review the comments and conclusions of the extensive research from NREL that directly compared the performance of the TNO and the BPM methods when both were fed by XFOIL flow field data.

According to NREL (Moriarty, Guidati, & Migliore, Prediction of Turbulent Inflow and Trailing-Edge Noise for Wind Turbines, 2005), from the comparison of results for the NACA 0012 airfoil at AOA from 0° to 16.5° , they found that the TNO model “does a better job” of predicting the absolute values while the BPM model would tend to overpredict the measured values. However, according to the same authors,

“The true test of a prediction method is whether a designer can use it to design airfoils or choose among a set of airfoils with the lowest noise signatures. From the comparisons to measured trailing edge noise levels, it is not obvious that either the TNO model or the BPM can differentiate among airfoils under all conditions.”

This important statement reveals the neither the TNO model nor the BPM model can be always effective in differentiating design variations in airfoils, which is an important restriction of the resulting method, regardless of the chosen model. This also suggests that only experimental and high order CAA simulations might do the task in a suitable manner, options that are out of hands at the preliminary design phase of a blade or rotor, since the choice is bound by the initial purpose of this research.

The overprediction mentioned by Moriarty et al. (Moriarty, Guidati, & Migliore, Prediction of Turbulent Inflow and Trailing-Edge Noise for Wind Turbines, 2005) on the BPM method might be explained by Lawson (Lawson, 1993) who explains that the full freestream velocity is employed as the characteristic velocity of the eddies in the BPM model, when it is well established that this speed should be between 50% and 85% of the stream velocity, thus suggesting a way to improve the model.

The research from Glegg and Reba (Glegg & Reba, 2010) showed that the TNO noise prediction model suffered from overprediction in low frequencies and underprediction in high frequencies (see Appendix E) and Lutz et al. (Lutz, Herrig, Würz, Kamruzzaman, & Krämer, 2007) research showed underpredictions by 5-10 dB along all frequencies of the spectrum (see Appendix E) when compared to measured 2-D

airfoil spectra, even when the model was coupled with RANS flow solver and a turbulence model with anisotropy effect was employed.

Also, further development of the a noise prediction method based on the TNO model by Kamuzzaman et al. (Kamruzzaman M. , Lutz, Herrig, & Krämer, 2012a) ruled out the use of RANS with standard two equation turbulence models, because the predicted integral length scale was smaller than measurements (see Appendix E). The authors then suggested an “enhanced anisotropy model”, modifying the *SST k, ω* turbulence model to include a dissipation rate equation derived experimentally from turbulent flow over a flat plate and adjusted constants to the model. In this way the model was completely adjusted to reproduce the experimental data of the NACA 0012 airfoil at $Re = 1.5 \times 10^6$ and $M = 0.17$ and the generalization of the model applicability seemed impaired by so many adjustments. What was firmly established though, according to the authors, was that the accuracy and consistency of the TNO TE-noise prediction model was highly dependent upon an accurate modeling of the turbulent flow structure near the airfoil TE.

In light of these facts, the selection of the simplest model would seem the most suitable choice and thus the TE-noise model of the BPM model was chosen as the core of the noise prediction method to be put together.

Concerning the selection of the TE-noise sub model only, this decision was supported by the fact that this source is considered the dominant noise source in modern WT equipment and was also the only noise source modeled into the IAGNoise modules (Kamruzzaman, Meister, Lutz, Kühn, & Krämer, 2010).

It is important, however, to keep in mind the limitations of the applicability of the BPM model.

- The BPM model is an overall prediction method for airfoil self-noise based on theoretical studies and experimental data of (mostly) 2-D airfoil.
- The model was developed over experimental data on the NACA 0012 airfoil geometry for chord-based Reynolds numbers up to 3×10^6 and Mach numbers up to 0.21.
- The TBL-TE noise prediction capability and accuracy was demonstrated in Appendix D, but TE-noise scaling peak Strouhal for different airfoil chords did not collapse well after scaling, for the smaller chord airfoils, where laminar BL is dominant and thus it

may be concluded that the TBL-TE noise prediction model is more readily applicable to high Re number flows.

- Noise data from experiments that employed the NACA 0012 airfoils in anechoic wind tunnel tests, in different facilities, were compared with experimental data that originated the BPM model by Doolan and Moreau (Doolan & Moreau, 2013), which concluded that there is reasonable agreement across different data sets at moderate Reynolds numbers ($Re \approx 1 \times 10^6$), but limited agreement for Reynolds numbers high enough to represent flow on outboard sections of modern WT rotor blades, suggesting the need for further testing and updating of the noise prediction models. This review further concluded that the BPM model predictions compared well with most data sets for low Mach numbers, but the Mach number dependency of the BPM model did not seem appropriate when compared to experimental or numerical simulation data. The experimental data suggested that the noise spectrum should display only Reynolds number dependency, provided other variables were properly scaled. Also, no variation on the peak Strouhal number with Reynolds number was detected.
- According to NREL (Moriarty, Guidati, & Migliore, Prediction of Turbulent Inflow and Trailing-Edge Noise for Wind Turbines, 2005), neither the TNO model nor the BPM model can be always effective in differentiating design variations in airfoils.

The initial improvements envisioned for the BPM TE-noise model were the actual calculation of the displacement thickness, δ^* , at the TE for different airfoil geometries and flow conditions, and also the adoption of the eddy advective velocity of 80% of the freestream velocity, within the range suggested by Lawson (Lawson, 1993).

The original δ^* correlations were obtained for the NACA 0012 airfoil, from flow data with $Re_c < 3 \times 10^6$ for fully turbulent and transition flows. The current proposal is to integrate the BPM TE-noise algorithm to a flow solver, capable of solving the turbulent boundary layer flow around any airfoil geometry and at higher Reynolds numbers.

The newly-integrated method was initially referred to as the *Modified-BPM TE-noise prediction method*. Later, after implementation of the integrated algorithm in Qt/C++ language, the code was referred to as “*PNoise*”.

The methodology for the selection of the flow solver that was integrated with the BPM TE-noise model in the PNoise code is shown in Section 3.4.

3.3.2 Calculating procedures for the TBL-TE noise method

For angles of attack below the switching angle, $(\alpha_*)_0$, which is defined as the angle corresponding to the peak of the K_2 function or 12.5° , whichever is lower, the total TBL-TE and separation noise spectrum in 1/3 octave bands is predicted by:

$$SPL_{TOT} = 10. \log \left(10^{SPL_s/10} + 10^{SPL_p/10} + 10^{SPL_\alpha/10} \right) \quad (3-1)$$

where

$$SPL_{p,1/3} = 10. \log \left[M^5 \frac{L\delta_p^* \bar{D}_h}{r_e^2} \right] + A \left(\frac{St_p}{St_1} \right) + (K_1 - 3) + \Delta K_1 \quad (3-2)$$

$$SPL_{s,1/3} = 10. \log \left[M^5 \frac{L\delta_s^* \bar{D}_h}{r_e^2} \right] + A \left(\frac{St_s}{St_1} \right) + (K_1 - 3) \quad (3-3)$$

$$SPL_{\alpha,1/3} = 10. \log \left[M^5 \frac{L\delta_s^* \bar{D}_h}{r_e^2} \right] + B \left(\frac{St_s}{St_2} \right) + K_2 \quad (3-4)$$

In the pressure side SPL prediction, Eqn. (3-2), a ΔK_1 adjustment term was added, during the extensive development and validation of the model. Also, on the suction side SPL prediction, Eqn. (3-3), it was found that the Strouhal dependency on the suction side spectrum was better represented in relation to $\bar{St}_1 = (St_1 + St_2)/2$ than to St_1 (peak Strouhal). \bar{D}_h is the directivity function for the high-frequency (or large-chord airfoil) noise.

For angles of attack above the switching angle, $(\alpha_*)_0$:

$$SPL_p = -\infty \quad (3-5)$$

$$SPL_s = -\infty \quad (3-6)$$

$$SPL_\alpha = 10. \log \left[M^5 \frac{L\delta_s^* \bar{D}_l}{r_e^2} \right] + A' \left(\frac{St_s}{St_2} \right) + K_2 \quad (3-7)$$

where A' is the curve for A , but with a value of R_c three times the actual value. \bar{D}_l is the directivity function for the low-frequency noise. The directivity functions are given below, for an observer stationary in relation to the airfoil.

When the noise producing eddies are sufficiently small and the convection velocities, U_c , are sufficiently large so as to produce acoustic wavelengths much shorter than the chord length (non-compact behavior), the directivity of the resultant high frequency noise is given by:

$$\bar{D}_h(\theta_e, \phi_e) \approx \frac{2 \sin^2\left(\frac{\theta_e}{2}\right) \sin^2\phi_e}{(1 + M \cos\theta_e)[1 + (M - M_c)\cos\phi_e]^2} \quad (3 - 8)$$

where the convection Mach number is $M_c \approx 0.8M$.

The directivity function above is inaccurate for shallow angles ($\theta_e \rightarrow 180^\circ$), but suitable for all self-noise sources in the BPM model, with the exception of stalled airfoil noise.

When the AOA of the airfoil is increased sufficiently, the attached or mildly separated TBL flow on the suction side originates large scale eddies, comparable in size to the airfoil chord. The directivity for the resulting low-frequency noise is more properly defined as that of a translating dipole:

$$\bar{D}_l(\theta_e, \phi_e) \approx \frac{\sin^2\theta_e \sin^2\phi_e}{(1 + M \cos\theta_e)^4} \quad (3 - 9)$$

The angles and references for both directivity functions are shown in Figure 3-5.

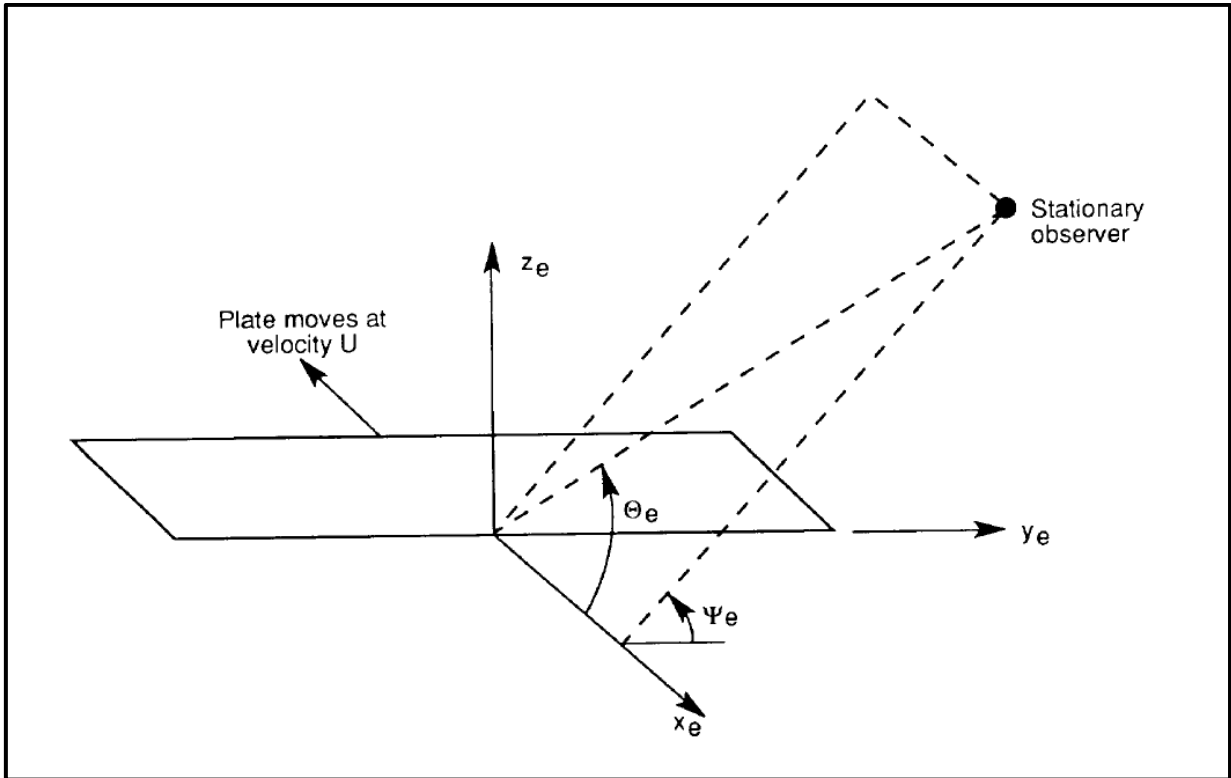


Figure 3-5 - The 3-D retarded coordinate system with origin at the TE of a thin plate representing the airfoil moving in rectilinear motion of velocity U in negative x_e axis direction. $\theta \rightarrow \theta$; $\Psi \rightarrow \phi$. Source: (Brooks, Pope, & Marcolini, Airfoil Self-Noise and Prediction, 1989), p. 107.

The Strouhal numbers definitions are:

$$St_p = \frac{f \delta_p^*}{U} \quad (3-10)$$

$$St_s = \frac{f \delta_s^*}{U} \quad (3-11)$$

$$St_1 = 0.02M^{-0.6} \quad (3-12)$$

$$\overline{St}_1 = \frac{St_1 + St_2}{2} \quad (3-13)$$

$$St_2 = St_1 \times \begin{cases} 1 & (\alpha_* < 1.33^\circ) \\ 10^{0.0054(\alpha_* - 1.33)^2} & (1.33 \leq \alpha_* \leq 12.5^\circ) \\ 4.72 & (\alpha_* > 12.5^\circ) \end{cases} \quad (3-14)$$

The dependencies of the peak Strouhal number on the chord Reynolds number and AOA are shown in Figure 3-6 and Figure 3-7, respectively.

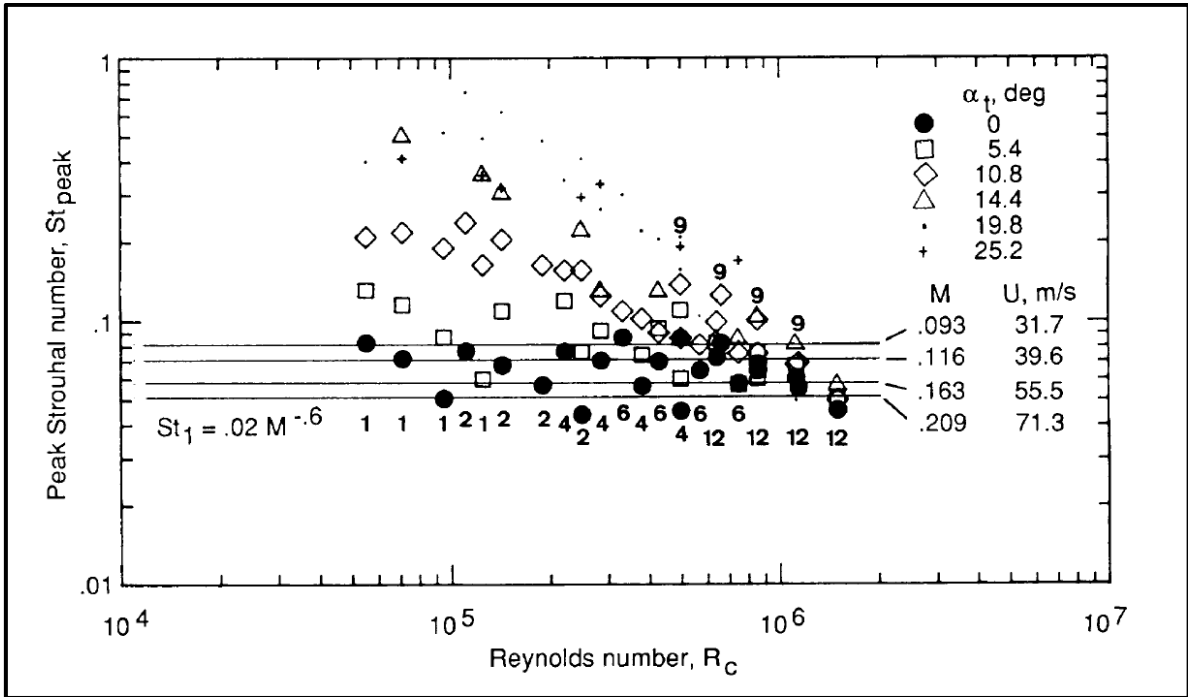


Figure 3-6 - Peak Strouhal number as a function of chord Reynolds number. Source: (Brooks, Pope, & Marcolini, Airfoil Self-Noise and Prediction, 1989), p. 53

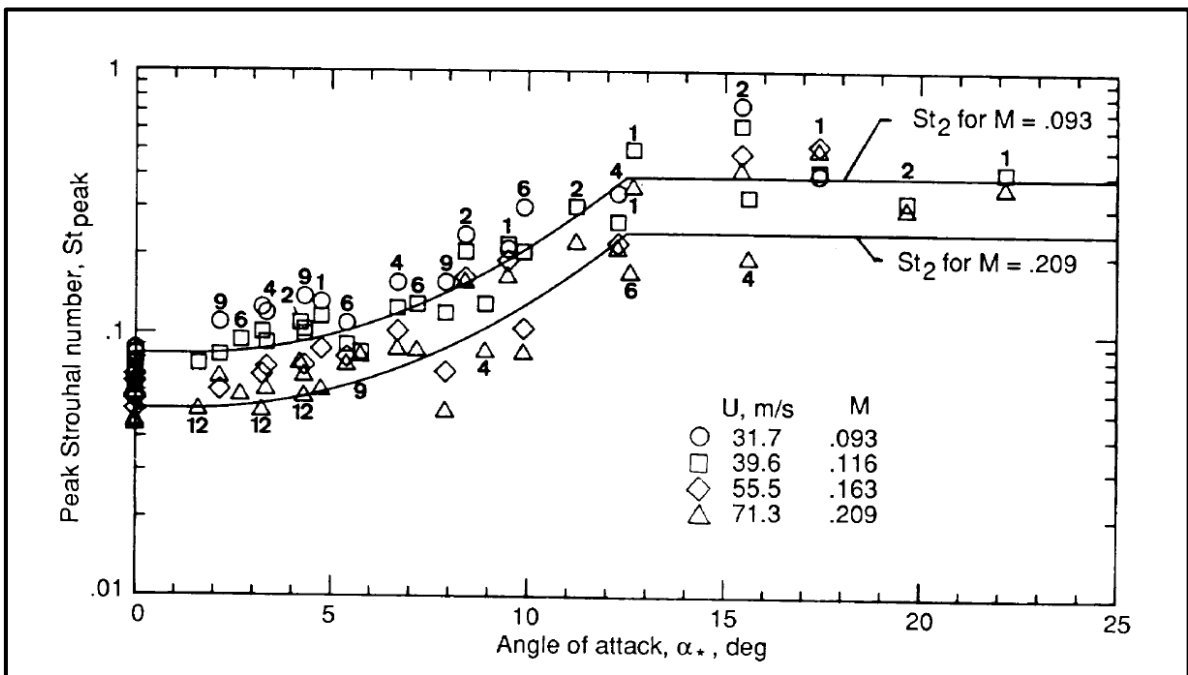


Figure 3-7 - Peak Strouhal number as a function of angle of attack. Source: (Brooks, Pope, & Marcolini, Airfoil Self-Noise and Prediction, 1989), p. 58

The spectral shape functions, A and B are shown in Figure 3-8 and Figure 3-9. The value of the functions for a particular chord Reynolds number is obtained by

interpolation between the curves A_{max} and A_{min} , corresponding to chosen values of $Re_{c,max}$ and $Re_{c,min}$.

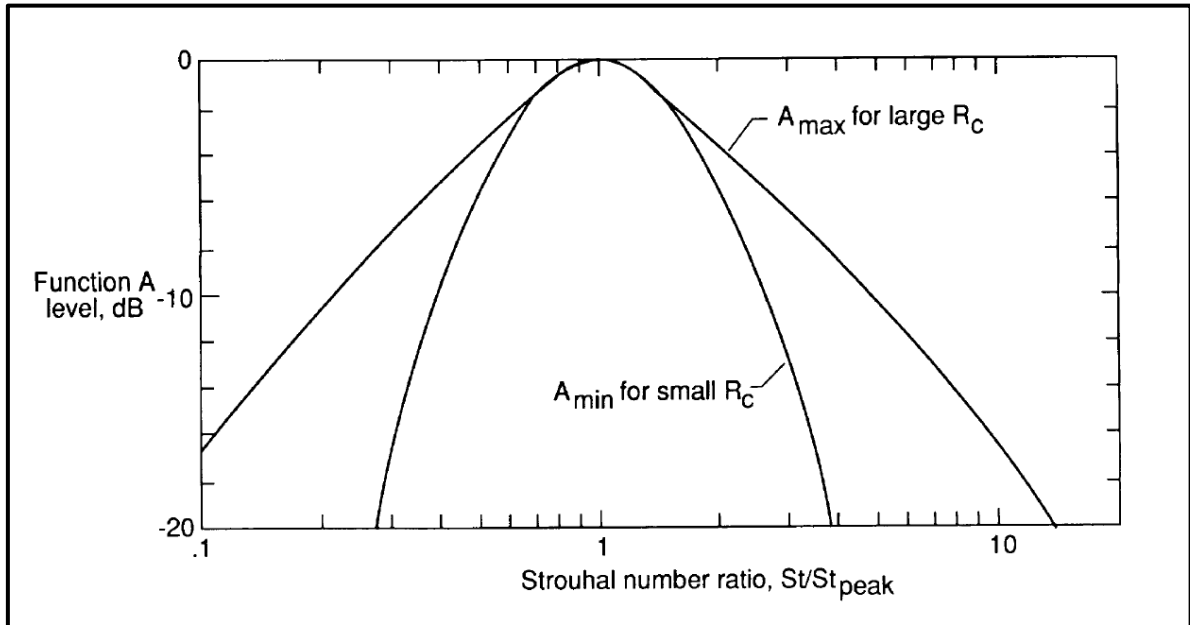


Figure 3-8 - One-third octave spectral shape function A , as a function of Strouhal and Reynolds numbers, for zero AOA. Source: (Brooks, Pope, & Marcolini, Airfoil Self-Noise and Prediction, 1989), p. 55.

The two curves are defined as:

$$A_{min}(a) = \begin{cases} \sqrt{67.552 - 886.788a^2} - 8.219 & (a < 0.204) \\ -32.665a + 3.981 & (0.204 \leq a \leq 0.244) \\ -142.795a^3 + 103.656a^2 - 57.757a + 6.006 & (a > 0.244) \end{cases} \quad (3-15)$$

and

$$A_{max}(a) = \begin{cases} \sqrt{67.552 - 886.788a^2} - 8.219 & (a < 0.13) \\ -15.901a + 1.098 & (0.13 \leq a \leq 0.321) \\ -4.669a^3 + 3.491a^2 - 16.699a + 1.149 & (a > 0.321) \end{cases} \quad (3-16)$$

where

$$a = |\log(St/St_{peak})| \quad (3-17)$$

And $St = St_p$ or St_s and $St_{peak} = St_1, \overline{St_1}$ or St_2

For interpolation procedure, a value $a_0(R_c)$ is defined at which the spectrum has a value of -20 dB. This point corresponds to a horizontal axis intercept in Figure 3-8 for an interpolated curve.

$$a_0(R_c) = \begin{cases} 0.57 & (R_c < 9.52 \times 10^4) \\ (-9.57 \times 10^{-13})(R_c - 8.57 \times 10^5)^2 + 1.13 & (9.52 \times 10^4 \leq R_c \leq 8.57 \times 10^5) \\ 1.13 & (R_c > 8.57 \times 10^5) \end{cases}$$

(3 – 18)

An interpolation factor $A_R(a_0)$ is determined from

$$A_R(a_0) = \frac{-20 - A_{min}(a_0)}{A_{max}(a_0) - A_{min}(a_0)} \quad (3 - 19)$$

where $A_{min}(a_0)$ and $A_{max}(a_0)$ are the A_{min} and A_{max} values determined at a_0 . The spectrum shape can now be evaluated for any frequency by computing the Strouhal number and the corresponding a , by using the interpolating factor. The result for direct use in the equations (3-2), (3-3) and (3-7) of the model is:

$$A(a) = A_{min}(a) + A_R(a_0)[A_{max}(a) - A_{min}(a)] \quad (3 - 20)$$

The shape function B for the equation of TE noise prediction in AOA other than zero is given by Figure 3-9, and may be calculated in an analogous manner.

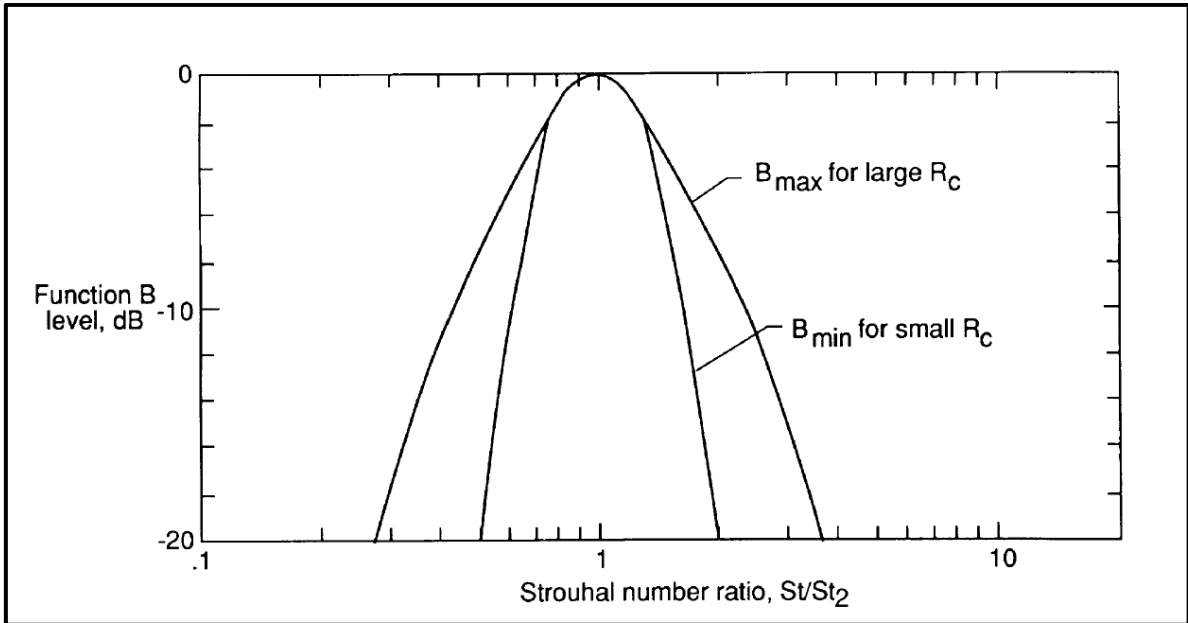


Figure 3-9 - One-third octave spectral shape function B , as a function of Strouhal and Reynolds numbers, for large AOA, separated flow noise. Source: (Brooks, Pope, & Marcolini, Airfoil Self-Noise and Prediction, 1989), p. 55

The two curves from which B is interpolated are:

$$B_{min}(b) = \begin{cases} \sqrt{16.888 - 886.788b^2} - 4.109 & (b < 0.13) \\ -83.607b + 8.138 & (0.13 \leq b \leq 0.145) \\ -817.810b^3 + 335.210b^2 - 135.024b + 10.619 & (b > 0.145) \end{cases} \quad (3 - 21)$$

and

$$B_{max}(b) = \begin{cases} \sqrt{16.888 - 886.788b^2} - 4.109 & (b < 0.10) \\ -31.330b + 1.854 & (0.10 \leq b \leq 0.187) \\ -80.541b^3 + 44.174b^2 - 39.381b + 2.344 & (b > 0.187) \end{cases} \quad (3 - 22)$$

where

$$b = |\log(St_s/St_2)| \quad (3 - 23)$$

The values of b for which the spectral shape B intercept the horizontal axis at -20 dB, for intermediate values of R_c are given by

$$b_0(R_c) = \begin{cases} 0.30 & (R_c < 9.52 \times 10^4) \\ (-4.48 \times 10^{-13})(R_c - 8.57 \times 10^5)^2 + 0.56 & (9.52 \times 10^4 \leq R_c \leq 8.57 \times 10^5) \\ 0.56 & (R_c > 8.57 \times 10^5) \end{cases}$$

$$(3 - 24)$$

And the interpolation factor $B_R(a_0)$ is determined from

$$B_R(a_0) = \frac{-20 - B_{min}(b_0)}{B_{max}(b_0) - B_{min}(b_0)} \quad (3 - 25)$$

The result for direct use in the Eqn. (3-4) is

$$B(b) = B_{min}(b) + B_R(b_0)[B_{max}(b) - B_{min}(b)] \quad (3 - 26)$$

The amplitude of the peak sound pressure level for each 1/3 octave band is given by the K_1 function for zero AOA and is plotted in Fig. 3.3.1-6 as a function of chord Reynolds number.

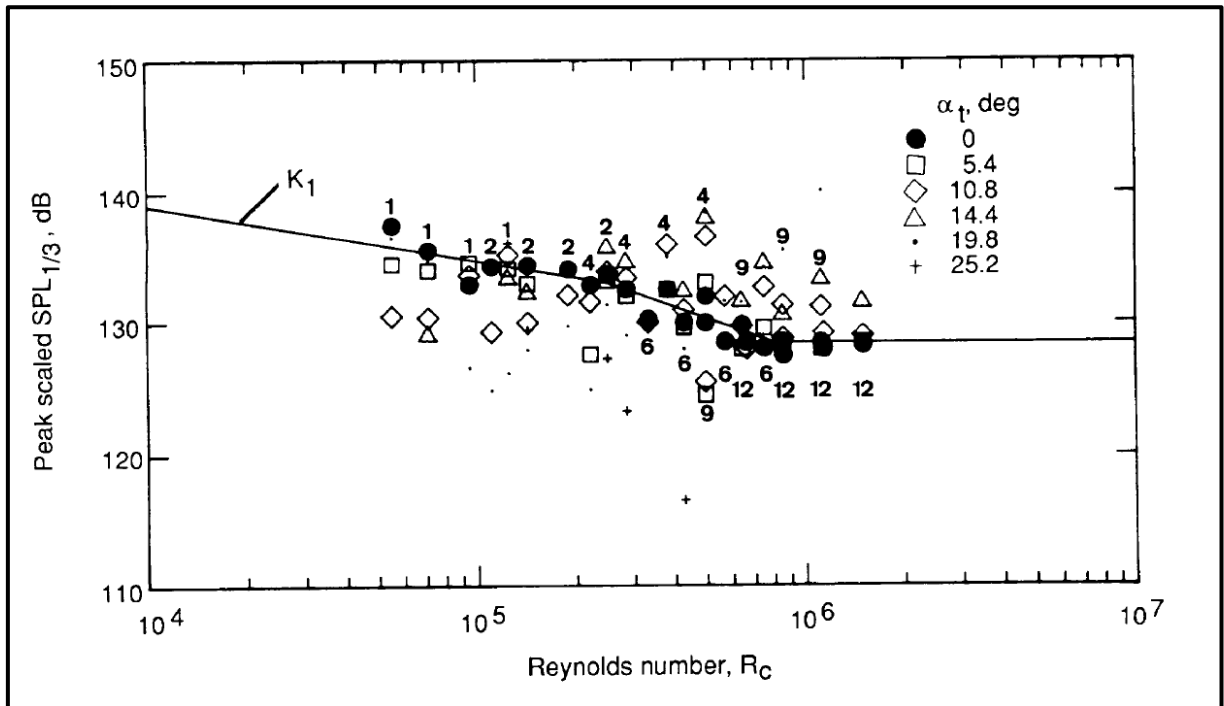


Figure 3-10 - Peak scaled level for TBL-TE noise versus chord Reynolds number. Source: (Brooks, Pope, & Marcolini, Airfoil Self-Noise and Prediction, 1989), p. 53

The K_1 function is also given by:

$$K_1 = \begin{cases} -4.31 \log(R_c) + 156.3 & (R_c < 2.47 \times 10^5) \\ -9.0 \log(R_c) + 181.6 & (2.47 \times 10^5 \leq R_c \leq 8.0 \times 10^5) \\ 128.5 & (R_c > 8.0 \times 10^5) \end{cases}$$

$$(3 - 27)$$

The level adjustment adopted for the pressure side SPL, Eqn. (3-2), ΔK_1 , is given by:

$$\Delta K_1 = \begin{cases} \alpha_* \left[1.43 (R_{\delta_p^*}) - 5.29 \right] & (R_{\delta_p^*} \leq 5000) \\ 0 & (R_{\delta_p^*} > 5000) \end{cases} \quad (3 - 28)$$

where $R_{\delta_p^*}$ is the Reynolds number based on the displacement thickness at the TE of the pressure side of the airfoil.

Finally, the amplitude of the peak sound pressure level for each 1/3 octave band is given by the K_2 function for AOA other than zero, which is plotted in Figure 3-11 as a function of AOA, for some Mach numbers.

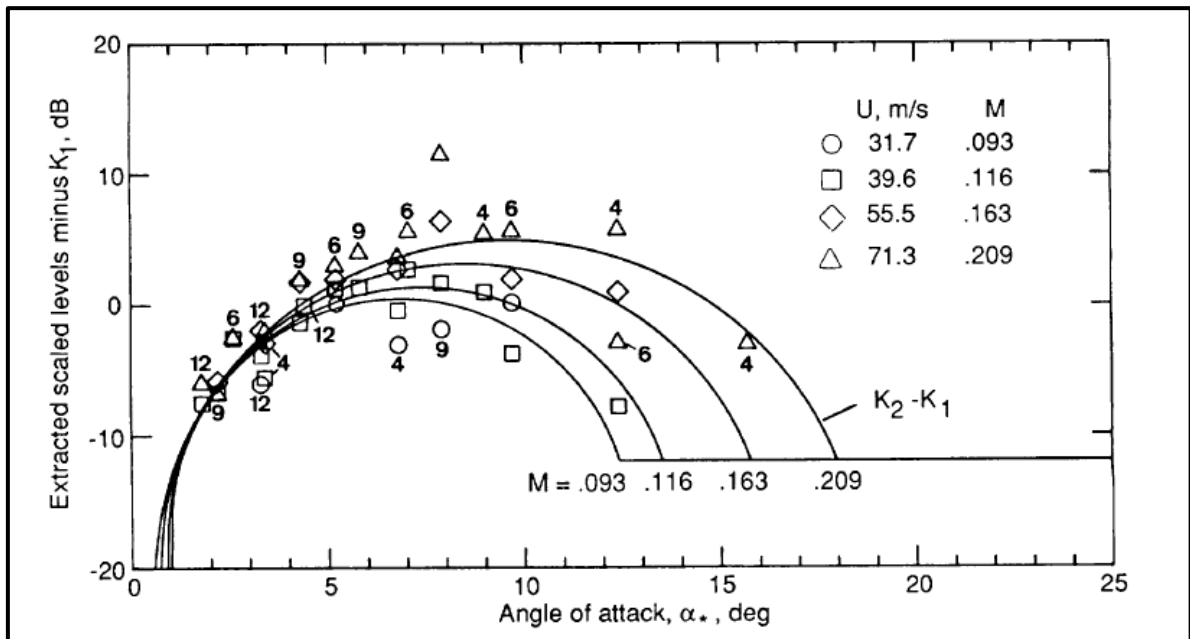


Figure 3-11 - Scaled TBL-TE noise level as a function of AOA, subtracted from the zero-AOA level. Source: (Brooks, Pope, & Marcolini, Airfoil Self-Noise and Prediction, 1989), p. 59

The K_2 function may be also computed from

$$K_2 = K_1 + \begin{cases} -1000 & (\alpha_* < \gamma_0 - \gamma) \\ \sqrt{\beta^2 - \left(\frac{\beta}{\gamma}\right)^2 (\alpha_* - \gamma_0)^2} & (\gamma_0 - \gamma \leq \alpha_* \leq \gamma_0 + \gamma) \\ -12 & (\alpha_* > \gamma_0 + \gamma) \end{cases}$$

(3 - 29)

where

$$\gamma = 27.094M + 3.32 \quad (3 - 30)$$

$$\gamma_0 = 23.43M + 4.651 \quad (3 - 31)$$

$$\beta = 72.65M + 10.74 \quad (3 - 32)$$

$$\beta_0 = -34.19M - 13.82 \quad (3 - 33)$$

All the angle definitions are in degrees.

3.3.3 Original Displacement Thickness Correlations of the BPM model.

For code calculation procedure verification and result validation purposes, the original BPM correlations for displacement thickness at the TE of the NACA 0012 airfoil were also added to the code, and remained as an additional option for the user.

In the original model (Brooks, Pope, & Marcolini, Airfoil Self-Noise and Prediction, 1989), the displacement thickness is calculated for zero alpha and for the type of flow regime (turbulent or transition) and for both the pressure and suction sides, as a function of chord-based Reynolds number (Re_C). When the alpha is other than zero, a scaling factor is calculated for each side of the airfoil (pressure and suction) and multiplies the original displacement thickness calculated for zero AOA.

For turbulent flows:

For $Re_C \leq 0,3 \times 10^6$

$$\delta_0^* = C * 0,0601 * Re_C^{-0,114} \quad (3 - 34)$$

For $Re_C > 0,3 \times 10^6$

$$\delta_0^* = C * 10^{[3,411 - 1,5397 \cdot \log(Re_C) + 0,1059(\log Re_C)^2]} \quad (3 - 35)$$

For zero AOA flow, $\delta_0^* = \delta^*$ (above results are final and the same for the pressure and suction sides)

For the transition flows:

For all chord-based Reynolds numbers:

$$\delta_0^* = C * 10^{[3,0187-1,5397.\log(Re_C)+0,1059(\log Re_C)^2]} \quad (3 - 36)$$

The correction for non-zero AOA, applicable for the pressure side only and for NT flows is made with the expression below, for all AOA:

$$\delta_p^* = \delta_0^* * 10^{[-0,0432.\alpha+0,00113.\alpha^2]} \quad (3 - 37)$$

The correction for non-zero AOA, applicable for the suction side depends upon the AOA and the flow regime:

For fully turbulent type of flows:

For $0^\circ \leq |\alpha| \leq 5^\circ$ (absolute value of alpha should be used, remembering that pressure and suction side definition depends upon the signal of α).

$$\delta_s^* = \delta_0^* * 10^{0,0679.\alpha} \quad (3 - 38)$$

For $5^\circ \leq |\alpha| \leq 12,5^\circ$

$$\delta_s^* = \delta_0^* * 0,381 (10^{0,1516.\alpha}) \quad (3 - 39)$$

For $12,5^\circ \leq |\alpha| \leq 25^\circ$

$$\delta_s^* = \delta_0^* * 14,296 (10^{0,0258.\alpha}) \quad (3 - 40)$$

For transition flows:

For $0^\circ \leq |\alpha| \leq 7,5^\circ$

$$\delta_s^* = \delta_0^* * 10^{0,0679.\alpha} \quad (3 - 41)$$

For $7,5^\circ \leq |\alpha| \leq 12,5^\circ$

$$\delta_s^* = \delta_0^* * 0,0162 (10^{0,3066.\alpha}) \quad (3 - 42)$$

For $12,5^\circ \leq |\alpha| \leq 25^\circ$

$$\delta_s^* = \delta_0^* * 52,42 (10^{0,0258.\alpha}) \quad (3 - 43)$$

3.4 THE SELECTION OF THE FLOW SOLVER.

The selection of the method for solving the flow around the airfoil and providing the vertical turbulence scale at the TE is key for delivering the main objective of providing the WT industry and researchers with a computationally efficient, high degree of freedom analysis tool that will support the preliminary design of quieter airfoil for WT equipment.

3.4.1 The selection of the method for solving the flow field.

Although the NACA 0012 correlations provided with the BPM model were fit to experimental data and should display experimental accuracy, they lack flexibility. It was shown in Section 2.5 that the airfoil profiles developed for modern HAWT equipment are different from the symmetrical NACA 0012.

In the detailed model review described in Appendixes D and E, it was shown that different authors adopted different approaches for providing their respective noise prediction methods with TBL flow field data. Apart from specific, proprietary CFD codes employed in some cases, the different approaches found are listed below in order of increasing geometric flexibility and decreasing computational efficiency.

- 1 Turbulent Boundary Layer Flat Plate (TBL-FP) correlation, (Lowson, 1993), (Glegg & Reba, 2010).
- 2 NACA 0012 correlations developed by BPM, (Fuglsang & Madsen, Implementation and Verification of an Aeroacoustic Noise Prediction Model for Wind Turbines, 1996), (Vargas L. d., 2008).
- 3 XFOIL/XFLR5 (Bareiss, Guidati, & Wagner, 1994), (Zhu, 2004), (Moriarty P. , NAFNoise User's Guide, 2005).
- 4 RANS, (Lockhard, 1999), (Glegg & Reba, 2010).

Because direct TBL measurement of characteristic lengths and fluctuations requires suitable experimental facilities and extensive analysis, no other case, other than the NASA-supported researches (Brooks & Marcolini, 1985) and (Brooks, Pope, & Marcolini, Airfoil Self-Noise and Prediction, 1989) were found where direct TBL

measurements were carried out for noise prediction purposes. However, experimental measurements should not be ruled out as the last, probably the most precise and the least flexible of all alternatives of the previous list.

Although all calculation approaches above were adopted for estimation of δ or δ^* in the TE of NACA 0012 and other specific airfoils, no study was found concerning the BPM model prediction sensitivity in respect to the quality of the method employed for the δ^* estimation. On the other hand, for simplified theoretical models, where more detailed information is required on the turbulence field, many authors have stressed the importance of the quality of the input data (Moriarty, Guidati, & Migliore, Prediction of Turbulent Inflow and Trailing-Edge Noise for Wind Turbines, 2005), (Lutz, Herrig, Würz, Kamruzzaman, & Krämer, 2007), (Kamruzzaman M. , Lutz, Nübler, & Krämer, 2011), (Kamruzzaman M. , Lutz, Herrig, & Krämer, 2012a), and CFD-RANS with turbulence anisotropy modeling seems to be currently the minimum acceptable standard for that kind of model.

The reason for the BPM TE-noise prediction method to be so complacent with flow field variable calculation method was not clear at this point, since a poor noise prediction method might lead to poorly designed equipment, which in turn might face siting problems in local communities. As shown in Section 1.1.5, a reaction study reported by (Bistafa, 2011) revealed that a 10 dB(A) increase in SPL could elicit strong community change in reaction, possibly going from periodic complaints to generalized complaints and threats of law suit.

For this reason, it seemed that an important step towards the assembly of a computationally-efficient, yet reliable, TE-noise prediction method based on the BPM model, would be the selection of the simplest flow field solver for the TBL that could preserve the original model order of accuracy.

3.4.1.1 Investigation of the Sensitivity of the BPM TE Noise Prediction Model in Relation to the TBL Displacement Thickness.

As mentioned before, no metrics were identified during the model review to evaluate the quality of the outcome of the different noise prediction models, when combined

with different flow field calculation tools. Generally the resultant spectrum from a method is compared with measurements and presented only graphically, showing variable deviations with frequency. The authors often refer to the deviations in a qualitative manner, as “good”, or “poor” adherence to measurements or “overprediction” or “underprediction” in certain frequency ranges. However, the noise is measured in logarithmic scale and a seemingly small 3 dB difference represents doubling the sound pressure level at the observer position.

In Section 3.3 the BPM TE noise model was presented, which is a semi-empirical relation scaled on acoustic and flow measurements and also on the edge-scatter theoretical formulation of Ffowcs-Williams and Hall (Ffowcs-Williams & Hall, 1970).

$$SPL = 10. \log \left[M^5 \frac{L \delta^* \bar{D}_h}{r_e^2} \right] + A \left(\frac{St}{St_1} \right) + (K_1 - 3) + \Delta K_1 \quad (3 - 44)$$

In the relation developed, Eqn. (3-44), the noise pressure level is proportional to the TBL displacement thickness, δ^* , which, for incompressible flow, is affected by Reynolds number and angle of attack⁴⁵, $\delta^* = \delta^*(\alpha, Re)$. The displacement thickness is employed as a record of the development history of the turbulence over the airfoil. The noise pressure level is also proportional to the fifth power of the Mach number, and inversely proportional to the square of the distance between the observer and the airfoil TE.

The relations $St_1 = 0.02M^{0.6}$, $K_1 = K_1(Re_c)$ and $\Delta K_1 = \Delta K_1(\alpha, Re_c)$, are three empirical expressions that determine the peak Strouhal number, the peak SPL and a correction factor for this level, all described in section 3.3. A is an empirical spectral shape function based on the Strouhal number, that essentially attenuates the $SPL_{1/3}$ spectrum on both sides, from 0 dB (at the Strouhal peak) to -20 dB at the extremes of the spectrum. The value for A is interpolated from composite curves based on Re_c . The subscript p of the original expression ($SPL_{p,1/3}$) referred to the *pressure* side of the airfoil, but was dropped since the sensitivity analysis will be made for a symmetrical airfoil in zero AOA condition. Also the subscript 1/3 was dropped for simplicity of notation.

⁴⁵ δ^* is also affected by the freestream turbulence level, which determines transition.

The intrinsic quality of the model was initially assessed by observing the typical plots of noise prediction spectra against measured spectra, as depicted in Figure 2-22, with the BPM model achieving a “very good” prediction of the SPL level throughout the available measured spectrum, but with tendency to overpredict the SPL in the peak frequencies. For the case $U = 39.6 \text{ m/s}$ of the mentioned figure, the OASPL was overpredicted by 1 dB only, providing a general measure of the intrinsic quality of the model for zero AOA, tripped BL, a condition dominated by TBL-TE noise. However, that was no coincidence, since Eqn. (3-44) had been modeled after that same data.

More important indications of the intrinsic quality of the BPM model were obtained from NREL (Moriarty & Migliore, Semi-Empirical Aeroacoustic Noise Prediction Code for Wind Turbines, 2003) which reported that the equations of the BPM model kept within 3 dB of measured levels for lightly tripped boundary cases, and also from (Kamruzzaman M. , et al., 2012b), p.47, which referred to this model as “quite popular” and its predictions being in good agreement with measurements “with a few decibel difference”.

Since the aim of this analysis was to preserve the intrinsic quality of the method by feeding a scaling parameter of suitable accuracy, it was assumed that the BPM method returned *exact* predictions of OASPL within the original model domain of applicability, for this sensitivity study purpose, only.

By analyzing individual terms in Eqn. (3-44) it seemed, at first, that the displacement thickness variation would affect the first and second terms of the model:

$$\partial SPL_p / \partial \delta^* = \partial / \partial \delta^* [10 \log(\delta_p^* M^5 L \bar{D}_h / r_e^2) + A(St_p / St_1)] \quad (3 - 45)$$

However, although A is an empirical spectral shape based on the Strouhal number, which in turn depends on δ^* , the ratio (St / St_1) should be independent of δ^* , its role in the empirical model being to identify the shift of the specific 1/3 octave band under analysis in respect to the peak frequency, and to apply the appropriate roll-off. Thus, for a reference geometry and flow, a fixed 1/3 octave frequency band and a fixed-position observer in relation to the airfoil TE, the expression was further simplified to

$$SPL = 10 \log \delta^* + C_1 \quad (3 - 46)$$

where constant C_1 included all the case, band and observer position (distance and angle for directivity function) fixed parameters.

Equation (3-36) is a statement that the sound pressure level will change arithmetically as the displacement thickness value changes geometrically, *ceteris paribus*. This translates into low SPL prediction sensitivity with displacement thickness variation and may possibly explain the tolerance or robustness of the model with regards to the type of flow solver employed. Also this might explain why no studies were found in the literature about the quality of the TBL length scale estimation for BPM-type models, while for the ST models, on the other hand, many authors have stressed the importance of the quality of the TBL parameters used in the models (Moriarty, Guidati, & Migliore, Prediction of Turbulent Inflow and Trailing-Edge Noise for Wind Turbines, 2005), (Lutz, Herrig, Würz, Kamruzzaman, & Krämer, 2007), (Kamruzzaman M. , Lutz, Nübler, & Krämer, 2011), (Kamruzzaman M. , Lutz, Herrig, & Krämer, 2012a).

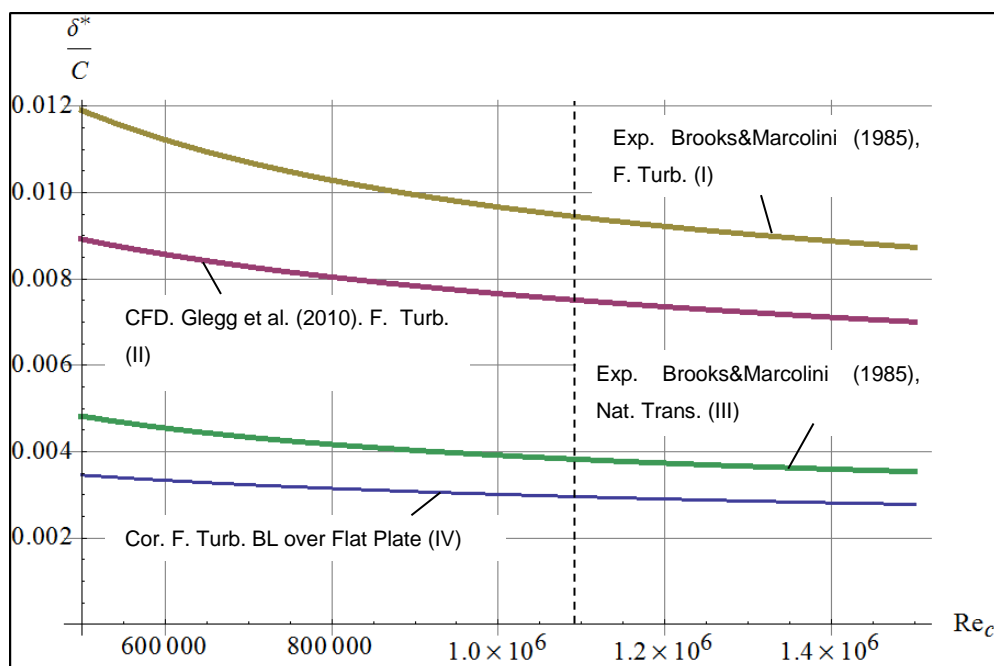


Figure 3-12 - Variation of δ^*/c values as a function of Reynolds number, close to the airfoil TE, for experimental I, III (Brooks & Marcolini, 1985), numerical II (Glegg & Reba, 2010) and correlation IV (Schlichting & Gersten, 2003) determination methods.

However, by comparing the values predicted for the normalized displacement thickness as a function of chord-based Reynolds number, by some of the different methods found, it was found that the displacement thickness may suffer from a broad

variation in value, depending upon the type of boundary layer development (natural or tripped) and method of assessment employed, as shown in Figure 3-12.

Table 3-4 - Displacement thickness data fit for experimental (I,III), CFD (II) and TBL correlation (IV).

Case	Reference	Data fit
I	Brooks et al., 1985, Fully Turbulent Experimental	$\frac{\delta^*}{c} = 10^{[3.411 - 1.5397 \log Rec + 0.1059(\log Rec)^2]}$
II	Glegg et al., 2010, Fully Turbulent CFD	$\frac{\delta^*}{c} = \frac{0.16}{Rec^{0.22}}$
III	Brooks et al., 1985, Natural Transition	$\frac{\delta^*}{c} = 10^{[3.0187 - 1.5397 \log Rec + 0.1059(\log Rec)^2]}$
IV	Turbulent Boundary Layer Model	$\frac{\delta}{x} = \frac{0,382}{Re_x^{1/5}} \quad \frac{u}{U} = \left(\frac{y}{\delta}\right)^{1/7} = \eta^{1/7} \quad \delta^* = \frac{\delta}{8}$

Table 3-4 and Figure 3-12 show best-fitted curves for experimental and numerical displacement thickness results measured at 1.3 mm downstream of the TE of a NACA0012, at zero angle of attack and incompressible flow regime (I, III) or calculated at 96% of the chord span (II). Prandtl's turbulent boundary layer model (IV) has been added for reference purposes, since it has been also employed in models of this kind (Lowson, 1993).

Table 3-5 shows the deviation of δ^* value in relation to the Brooks and Marcolini (Brooks & Marcolini, 1985) fully turbulent wind tunnel measurement (case I) as a function of the approach or regime considered, for $Re_c = 1.1 \times 10^6$, section indicated by a dashed line in Figure 3-12.

Table 3-5 - Impact of δ^* variation, in SPL noise prediction, for a fixed $Re_c \approx 1.1 \times 10^6$, using different estimation approaches.

Case	Reference	δ^* (central value) [m]	Var.	SPL 1/3 [dB] (minus constant)	Var. (abs) [dB]
I	Brooks et al., 1985, Fully Turbulent Experimental	0.00942	Ref.	-20	Ref.
II	Glegg et al., 2010, Fully Turbulent CFD	0.00750	-20%	-21	-1
III	Brooks et al., 1985, Natural Transition	0.00382	-59%	-24	-4
IV	Turbulent Boundary Layer Model	0.00296	-69%	-25	-5

3.4.1.2 The Proposal of a Criterion for the δ^* Evaluation Methods

Environmental certification of a WT siting operation requires a noise measurement procedure based on specific standards, e.g. IEC61400, (IEC61400-11, 2012), with suitable, calibrated equipment, followed by comparison of measured levels with levels allowed by local ordinance. However, it is reasonable to expect that during the preliminary design phase of an airfoil or WT blade, the design engineer would accept some trade-off between accuracy and process speed, since the industry is interested in how small modifications of a given blade geometry will influence noise generation (Wagner, Bareiß, & Guidati, Wind Turbine Noise, 1996) and, most of the times, large numbers of configurations must be tested for selection or optimization.

With an iterative design process in mind, it was proposed as a discriminating criterion for the evaluation of the δ^* calculation tools, that the resultant departure of the displacement thickness from its reference or “exact” value, should not lead to an OASPL deviation larger than ± 3 dB, estimated at a fixed (distance and angle) reference point, when applied to the BPM TE noise prediction method.

Although a 3 dB increase in SPL means doubling the source power, the criterion is proposed based on this SPL variation being “just perceptible” to the average human

auditory system, according to Bies and Hansen (Bies & Hansen, 2009), p.85, and generating only marginal increase in estimated public reaction to noise according to the same authors (Bies & Hansen, 2009) and also to Bistafa (Bistafa, 2011). Also, Stankovic et al. (Stankovic, Campbell, & Harries, 2009), p.90, claim that “a 5 dB sound pressure level change would probably be perceived by most people under normal listening conditions, although it would take ideal listening conditions to detect sound pressure level differences of 2 or 3 dB”. This metric proposal is then not based on equipment measurement capabilities, but rather on human psychoacoustic perception and is intended for use in the suitable selection of the elements of a TE noise prediction method that should be capable of determining comparative SPLs from different airfoils configurations, hopefully broadening the application of a method whose main limitations are geometric shape and flow speed restrictions.

Figure 3-13 is a plot of Eqn. (3-46) and displays SPL variation as a function of δ^* value fluctuation, for this type of TE noise prediction method. It translates the proposed noise criterion into practical limits of δ^* : an underprediction of up to 50% or overprediction of up to 100%, in respect to a reference value, would return SPL within acceptable limits to meet this criterion. Notice that, because the function is logarithmic, the upper and lower limits for $\delta^*\%$ variation are not symmetrical and each doubling of the displacement thickness will increase the SPL by 3 dB which makes the displacement thickness length analogous to the TE-noise source power.

The criterion may be tailored to suit specific needs, for instance, a blade designer working on the conservative side could choose to work only on the OASPL overprediction side; i.e., up to + 3 dB, for safe-design reasons. In this case, the designer should only employ a displacement thickness estimation method capable of reliably delivering values between *exact* and 100% overprediction.

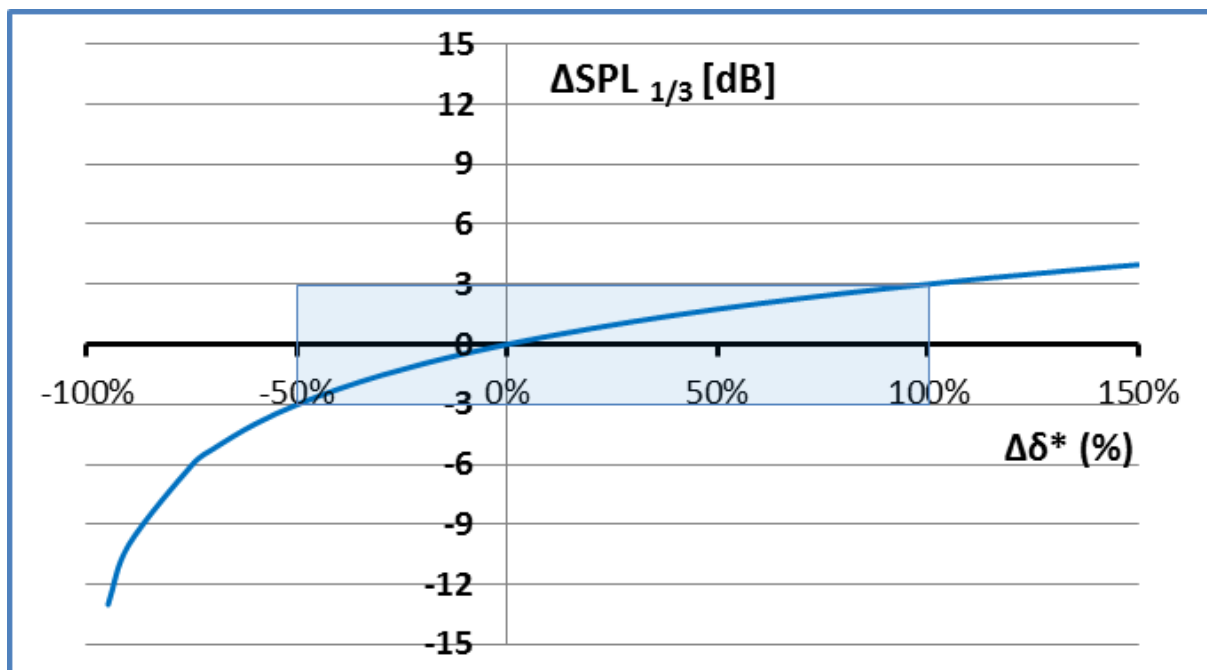


Figure 3-13 - SPL1/3-prediction variation with δ^* -prediction variation, in the BPM TE noise model.

3.4.1.3 Investigation of the compliance of the different methods.

In this sub-section the capability of the candidate methods for the displacement thickness calculation within the range specified in last sub-section is investigated.

Although the aim was to extend the BPM TE noise prediction model to generic airfoil geometry, the initial validation of each method was made against NACA 0012 data in zero AOA and chord based Reynolds numbers for which experimental data was available from Brooks and Marcolini (Brooks & Marcolini, 1985) and Brooks et al. (Brooks, Pope, & Marcolini, Airfoil Self-Noise and Prediction, 1989).

The pursued method had to be computationally efficient and geometrically flexible in order to supersede the experimental correlations for δ^* which are an integral part of the original BPM model, for both the fully turbulent and the natural transition regimes. The methods preselected to be tested were the XFOIL and the incompressible, steady state CFD-RANS, with one or two-equation turbulence models, plus transition equations when applicable.

3.4.1.3-1 XFOIL modeling details

Because of the efficient computational approach and high frequency of referral found during the noise prediction methods review, the XFOIL (Drela & Giles, Viscous-Inviscid Analysis of Transonic and Low Reynolds Number Airfoil, 1987) was tested first. Initially two variations of the NACA 0012 airfoil were modelled, the first one being the original profile, given by (Abbott & Von-Doenhoff, 1959):

$$\pm y_t = \frac{t}{0.20} (0.29690\sqrt{x} - 0.12600x - 0.35160x^2 + 0.28430x^3 - 0.10150x^4) \quad (3 - 47)$$

and
$$r_t = 1.1019t^2 \quad (3 - 48)$$

where $(\pm y_t, x)$ are the pressure and suction side coordinates of the airfoil surface, t is airfoil thickness relative to the chord (0.12 or 12% in the case of the NACA 0012 airfoil) and r_t is the leading edge radius of the airfoil. The TE of the original airfoil is blunt, with a thickness corresponding to 2.52% of the chord.

It was shown in Section 2.1.5, Figure 2-9, that for a bluntness parameter, $h/\delta^* > 0.25$, a secondary hump appears in the sound spectrum (Blake, Mechanics of Flow-Induced Sound and Vibration, 1986 I), becoming eventually a tonal noise, known as airfoil singing, which, while designing quieter airfoils, should be avoided.

For the NACA 0012 airfoil at zero AOA, at $Re_c = 1.1 \times 10^6$, with $\delta^* \approx 4$ mm at the TE (Brooks & Hodgson, 1981), p. 79, the maximum thickness allowed for a sharp, silent (in the audible range) TE would be close to one millimeter. This is a 0.1% thickness allowance in a typical 1 m chord airfoil and thus, 25 times smaller than the original 2.52% TE thickness designed into the airfoil TE.

The second geometry was then a modified, sharp TE NACA 0012. Both profiles were discretized with between 199 and 300 panels, with higher panel concentration towards the TE and the LE.

In the XFOIL integral method, the skin friction and velocity profile formulas of Swafford (Drela & Giles, Viscous-Inviscid Analysis of Transonic and Low Reynolds Number Airfoil, 1987) are employed in the turbulent regime. The cases tested are described in Table 3-6. The code version used was the XFLR5 v6.06. The convergence was generally achieved very quickly, in less than 10 iterations and with a few seconds for each operating point.

Table 3-6 – Cases tested in the XFOIL (XFLR5). Case A is based on Brooks and Hodgson, 1981. Cases B-H are based on Brooks and Marcolini, 1985. Case numbering is analog to (Glegg & Reba, 2010), p. 1297.

XFOIL Calculation - Tripped Condition – NACA 0012, zero AOA.							
(i) Brooks & Marcolini, 1985. Heavily Tripped (ii) Brooks & Hodgson, 1981, Tripped.					Sharp TE, Forced transition @ 0.2c		Ref.:
Case	Reynolds_c	Mach	δ^* @ 1.001c	δ^* @ 0.96c	δ^* @ 1.001c	δ^* @ 0.96c	
A	2.6E+06	0.11	N/A	4.0E-03	1.2E-02	4.0E-03	i
B	1.5E+06	0.06	8.7E-03	N/A	1.3E-02	4.5E-03	ii
C	1.2E+06	0.05	9.3E-03	N/A	1.3E-02	4.8E-03	ii
D	8.3E+05	0.04	1.0E-02	N/A	1.4E-02	5.2E-03	ii
E	6.6E+05	0.03	1.1E-02	N/A	1.5E-02	5.6E-03	ii
F	1.1E+06	0.05	9.4E-03	N/A	7.3E-03	4.9E-03	ii
G	7.5E+05	0.03	1.0E-02	N/A	7.9E-03	5.4E-03	ii
H	5.0E+05	0.02	1.2E-02	N/A	1.6E-02	6.0E-03	ii

Figure 3-14 displays the XFOIL results for the tripped, TBL displacement thickness prediction, for Reynolds numbers in the range $5 \times 10^5 \leq Re_c \leq 2.6 \times 10^6$, for both the original and sharp TE NACA 0012 airfoils. The parameter was evaluated in two different stations, at 100.1% and 96% of the airfoil chord, selected in accordance with the experimental work of Brooks and Marcolini (Brooks & Marcolini, 1985) and Brooks and Hodgson (Brooks & Hodgson, 1981), respectively.

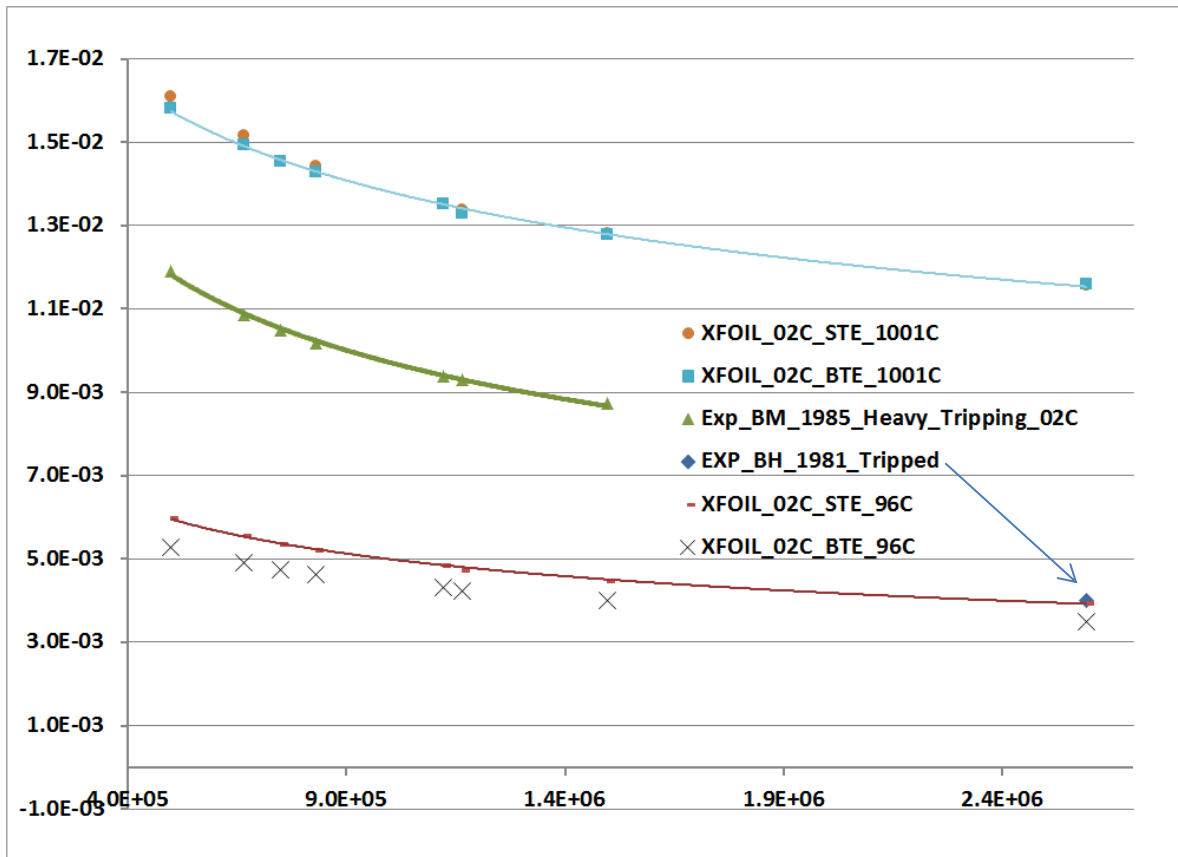


Figure 3-14 - XFOIL results for δ^* , calculated for tripped TBL in two different stations close to the NACA 0012 TE, at zero AOA, in the range $5 \times 10^5 \leq Re_c \leq 2.6 \times 10^6$, compared with experimental data.

The green (central) line in Figure 3-14 is from experimental data of Brooks and Marcolini (Brooks & Marcolini, 1985), heavily tripped, turbulent regime. The single diamond plot is from experimental data of (Brooks & Hodgson, 1981). The upper plots (almost overlapped) are XFLR5 calculations for both sharp and blunt TE airfoils, measured at 100,1% of the chord. The lower plots are XFLR5 calculations for both sharp and blunt TE airfoils, measured at 96% of the chord.

The calculated curves display physical behavior and there are some important conclusions to be considered:

- There is no apparent significant difference between the blunt and the sharp airfoils for reading in either station, when considered the larger difference between the calculations and the measurements of (Brooks & Marcolini, 1985). This relative insensitivity of the tool to the TE thickness should be useful to the Industry in order to compensate for manufacturing tolerances (see text below for caution).

- The accuracy of the XFLR5 calculation versus the single measurement point from (Brooks & Hodgson, 1981) is remarkable.
- It is not possible to say whether the calculation method is acceptable or not without an objective criterion.

Regretfully, due to the lack of additional data points measured at the experimental campaign of Brooks and Hodgson (Brooks & Hodgson, 1981) and the evident misalignment with data from Brooks and Marcolini (Brooks & Marcolini, 1985), the latter, larger data-set had to be selected as the reference for the upcoming analysis. Also the blunt NACA 0012 airfoil was dropped due to easier meshing operation on the sharp TE, for latter comparison with the CFD solution. However, in case a high resolution numerical method (DNS, CAA) is applied for acoustic analysis, it is important to hold true to the finite (production) thickness of the airfoil TE, since this might be an additional source of noise, as discussed earlier.

Figure 3-15 shows the calculation results of XFLR5 for δ^* on both tripped and transition flows, compared with (Brooks & Marcolini, 1985) data. All evaluations were accomplished at 100.1% chord.

In order to evaluate the XFLR5 predictions, an assessment was made based on the proposed criterion, as shown in Table 3-7.

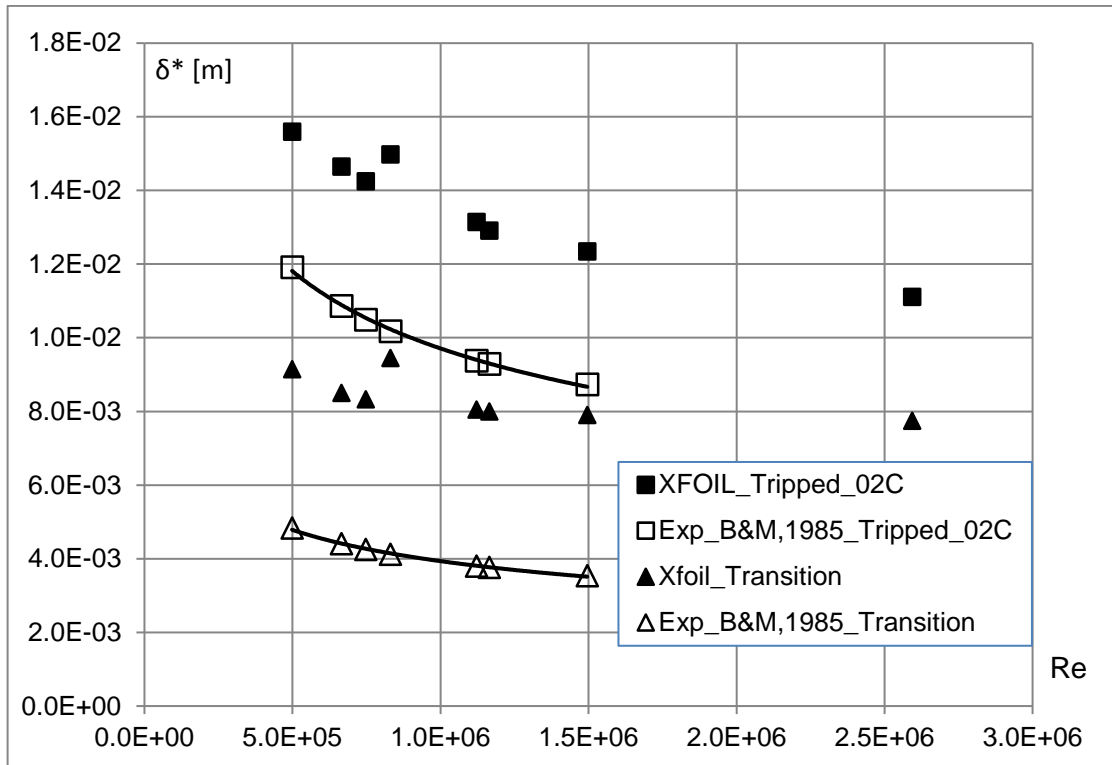


Figure 3-15 – XFLR5 results for δ^* , calculated for tripped and transition TBL, for the sharp TE NACA 0012, zero AOA, at station 1.0013C, in the range $5 \times 10^5 \leq Re_c \leq 2.6 \times 10^6$ (Saab Jr & Pimenta, 2016).

Table 3-7 - Relative error comparison for the XFOil results (tripped and transition TBL), for the sharp-TE NACA 0012 airfoil, in the range $5 \times 10^5 \leq Re_c \leq 1.5 \times 10^6$ (Saab Jr & Pimenta, 2016).

XFOIL Validation and Quality Assessment - Tripped and Transition Regimes									
Experimental				XFOIL		Quality Assessment			
Brooks & Marcolini, 1985.		Heavily Tripped	Natural Transition	Sharp TE, Tripped @ 0.2C	Sharp TE, e ⁹ transition	Heavy Tripping	e ⁹ transition	Heavy Tripping	e ⁹ transition
Case	Reynolds_C	δ^* @ 1.3 mm downstream of TE		δ^* @ 1.0013C		$\Delta\delta^*/\delta^*$ @ 1.0013C		$\Delta SPL = 10 \log(1 + \Delta\delta^*/\delta^*)$ [dB]	
B	1.5E+06	8.7E-03	3.5E-03	1.2E-02	7.9E-03	41%	123%	1.50	3.48
C	1.2E+06	9.3E-03	3.8E-03	1.3E-02	8.0E-03	39%	113%	1.43	3.27
D	8.3E+05	1.0E-02	4.1E-03	1.5E-02	9.5E-03	47%	129%	1.68	3.60
E	6.6E+05	1.1E-02	4.4E-03	1.5E-02	8.5E-03	35%	93%	1.30	2.86
F	1.1E+06	9.4E-03	3.8E-03	1.3E-02	8.1E-03	40%	112%	1.47	3.26
G	7.5E+05	1.0E-02	4.3E-03	1.4E-02	8.3E-03	36%	96%	1.33	2.92
H	5.0E+05	1.2E-02	4.8E-03	1.6E-02	9.1E-03	31%	89%	1.17	2.77

From Table 3-7 it is possible to see that the Xfoil results comply partially with the proposed criteria, when the calculation is done for station 1.0013C. The values for the heavy tripping situation are all acceptable in the Reynolds number range calculated, but those for transition TBL with relative deviations above 100% would induce artificial noise sources in excess of 3 dB per 1/3 octave band in a BPM-type TE noise model. Fortunately, the typical flow over large-size wind turbine blades is turbulent and it seems that early transition would be tripped by the rough surface condition found in in-service machines (Eisele, Pechlivanoglou, & Nayeri, 2013) .

3.4.1.3-2 CFD-RANS modeling details

The flow around the airfoil was modeled as a turbulent, incompressible, 2-D, steady flow, since the interest rests in integral TBL parameters (no CAA CFD simulation was attempted as of this time) and also a relatively quick method for deployment during the development phase of the airfoil is pursued. The chord was normalized to unitary length, and the resultant adjusted flow data is displayed in Table 3-8, for all simulation points.

Table 3-8 - Flow parameters for the cases tested in CFD-RANS simulations, after chord normalization.

CFD case	Airfoil Chord [m]	α [°]	U_∞ [m/s]	TU [%]	Reynolds_C	Mach	Ref.
B	1	0	21.74	0.05	1.5E+06	0.06	Brooks & Marcolini, 1985.
C	1	0	16.93	0.05	1.2E+06	0.05	
D	1	0	12.08	0.05	8.3E+05	0.04	
E	1	0	9.67	0.05	6.6E+05	0.03	
F	1	0	16.31	0.05	1.1E+06	0.05	
G	1	0	10.87	0.05	7.5E+05	0.03	
H	1	0	7.25	0.05	5.0E+05	0.02	

Finite-volume code ANSYS Fluent⁴⁶ was used throughout the simulations (ANSYS INC, 2013). Also, in order to test a consistent geometry (candidate for possible CAA simulation in the future), the same modified NACA 0012, with a sharp TE prepared for XFLR5 simulation was employed in the CFD simulations. The 2-D mesh architecture developed was an external D-grid with two internal stages of C-grids. The far field selected was 12.5 chords long, aft and forward of the airfoil, with no less than 10 chords on the sides.

A quad-elements-only mesh, initially structured⁴⁷, was created and refined using ANSYS ICEM software, as shown in Figure 3-16 and Figure 3-17, until the first element was set at $Y^+ < 1$ all over the airfoil surface, as may be seen on Figure 3-18. Around 80 elements were embedded within the BL, resulting in 272,000 cell elements for the basic mesh. The transition used was smooth and the distortion of the elements controlled.

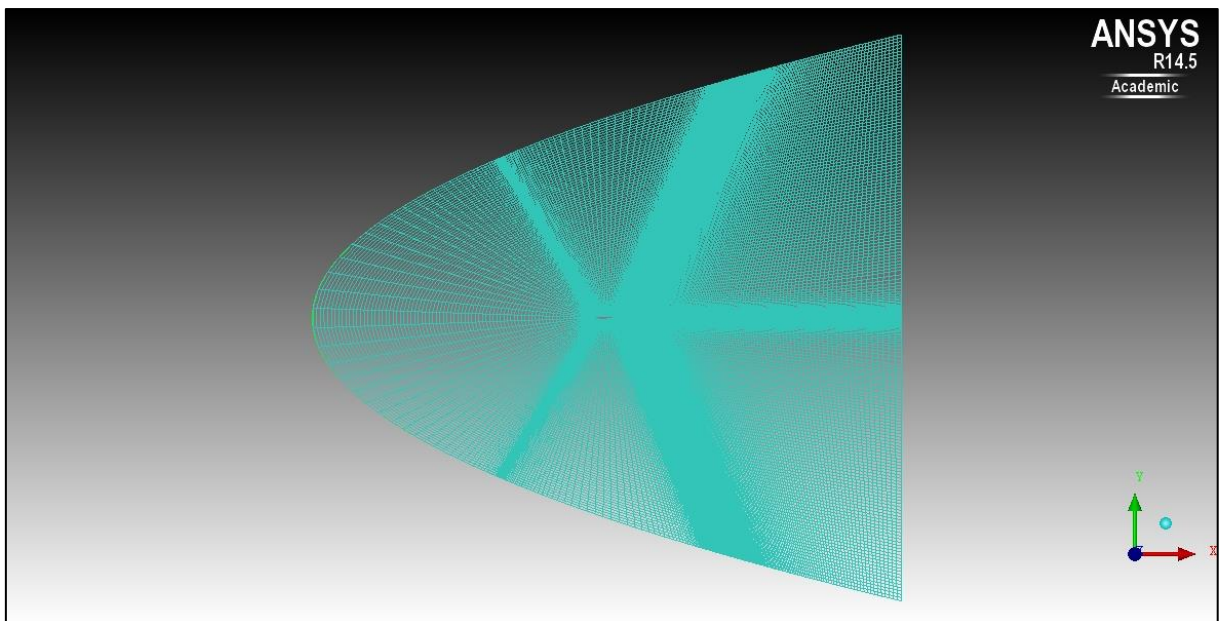


Figure 3-16 - “D”-mesh with all-quad elements developed for the domain calculation in the Ansys ICEM software.

⁴⁶Version 14.5.7.

⁴⁷ The mesh is not treated as structured by ANSYS FLUENT solver.

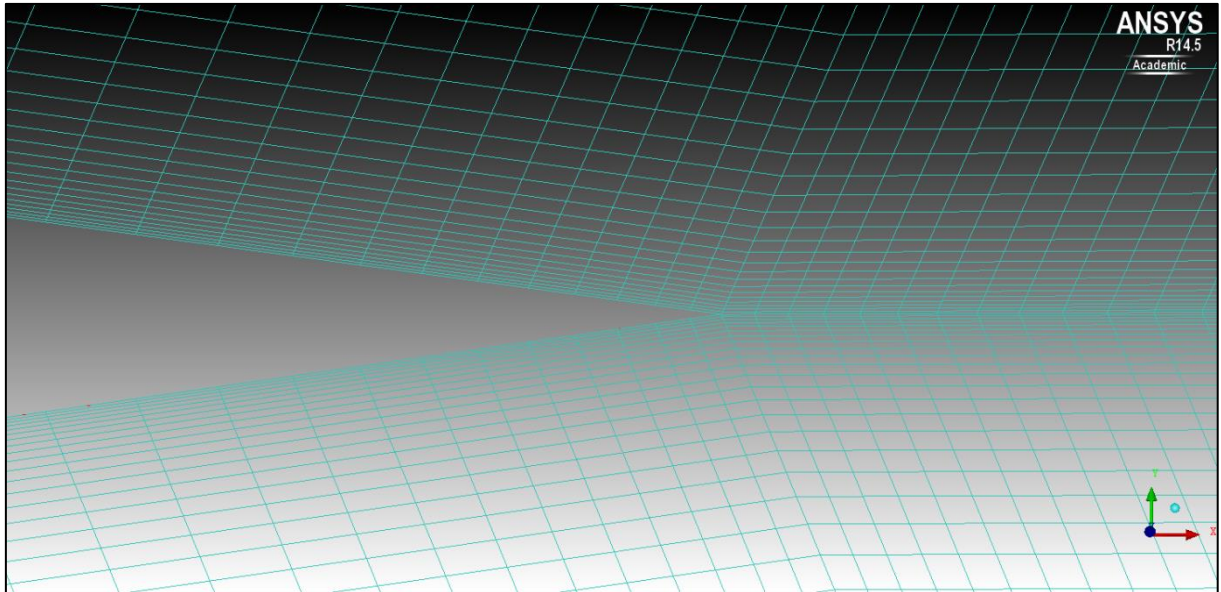


Figure 3-17 – TE mesh close up.

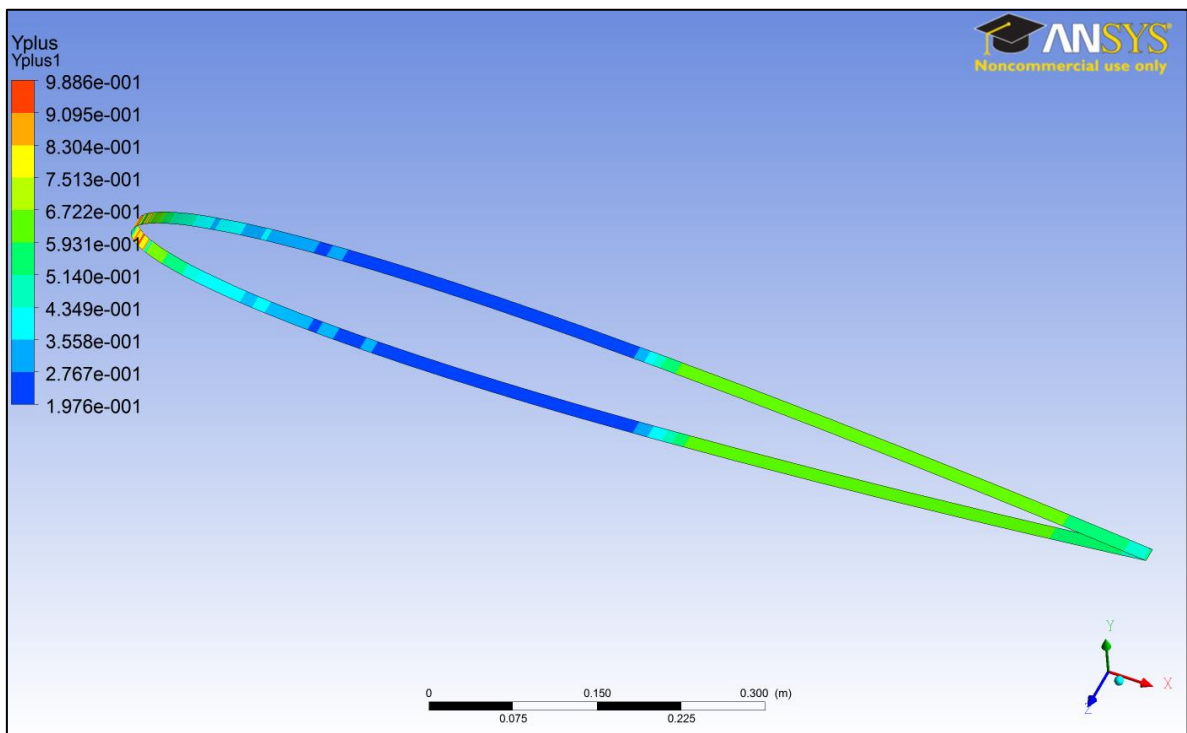


Figure 3-18 - The maximum distance from the wall to the first node inside the viscous sublayer was estimated with the flat plate theory and inserted as a restriction for the mesh generation, resulting in all first elements close to the surface to be within the sublayer, as verified later during post-processing.

The mesh development was time-consuming to prepare, but a procedure was written for the task in order to speed up the operation for future simulations with other airfoil geometries, in case this flow solver was selected. The procedure may be scripted into

the software for semi-automatic mesh development. The aspect ratio of some elements was beyond recommended values, but they were either inside the BL, aligned with the advection direction or quite far away from the areas of interest. The mesh was later refined in two progressive steps for application of the discretization error estimation.

In order to select a suitable turbulence model, a first run was organized with many one-and-two-equation models (Spallart-Almaras; κ, ε turbulence model modified from standard in order to cope with the wall presence and pressure gradient; κ, ω model; SST κ, ω model), for one selected case (F) only. The determination of the δ , employed as the upper integration limit in the determination of δ^* proved to be tricky in CFD solutions. Thus, an indirect method was devised through plotting and examination of the TKE energy profile for determination of BL thickness, which turned out to be a very consistent alternative. However, this procedure restricted the turbulence models usage to those that explicitly solved the TKE equation, eliminating the one-equation Spallart-Almaras model from the list of turbulence model candidates. After comparison of the results from all the turbulence models employed in the preliminary run with experimental data, the SST κ, ω model was selected for both fully turbulent and transition cases, because of the close proximity obtained with experimental results.

All cases were then run with this turbulence model, in coupled pressure and velocity fields and with pseudo-transient formulation. All transport equations were discretized in the domain via second order upwind schemes. Balance *rms* residues were set to a minimum of 10^{-6} for both momentum equations and a minimum of 10^{-5} for all other equations (continuity, TKE, ε , ω , γ , Re_{θ} , etc.).

The convergence was not always achieved for the transition cases with above targeted residues; however two sensitivity studies were carried out regarding convergence speed and accuracy. First it was observed that when velocity and pressure were prescribed simultaneously at the inlet section as boundary conditions with the SST κ, ω turbulence model, the convergence occurred sometimes in half the number of iterations. However, this approach does not work for the standard κ, ω model, which is very sensitive to boundary conditions. Second, a sensitivity study was carried out for 300, 600 and 900 iterations and the asymptotic behavior of the desired variables was

found to be stable after 100-300 iterations for fully turbulent and after from 300-400 iterations for transition cases, with subsequent selection of 600 iterations as the standard for fully turbulent and 900 iterations for transition cases. The pressure at the inlet section was found through the hypothesis of isentropic acceleration applied to a streamtube, going from rest to the inlet velocity.

The airfoil drag coefficient was monitored throughout each run for verification of the solution and although the behavior was physical for this parameter after just a few iterations, the value of the drag coefficient could only be verified for the A case, where $c_d \approx 0.0056$ for $Re_c = 2.6 \times 10^6$, against experimental data from (Abbott & VonDoenhoff, 1959), with $c_d \approx 0.006$ for $3 \times 10^6 \leq Re_c \leq 9 \times 10^6$. Also, the residues were visually monitored during the first run for each case, in order to investigate the behavior of the convergence. In general, monotonic convergence was attained for fully turbulent runs only, but asymptotic behavior of fluctuating residues was always attained, as shown in Figure 3-19, which is displayed for qualitative purposes, only.

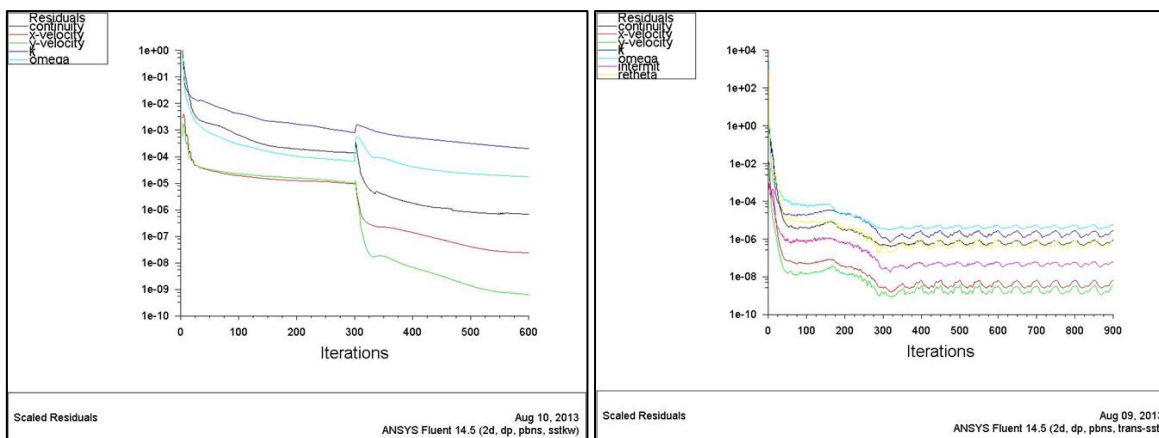


Figure 3-19 - Typical behavior of the residues (rms) of the balance equations during a fully turbulent simulation (left), and a transition simulation (right). Case F displayed (intended for qualitative evaluation only).

The direct assessment of the BL thickness with CFD was difficult because of the marked adjustment of pressure and velocity close to the TE, which is the result of viscosity in a real flow and equivalent to the Kutta condition imposed into an ideal flow. This fact rendered the BL thickness at the TE of the same order of magnitude of the airfoil chord, as displayed in Figure 3-20.

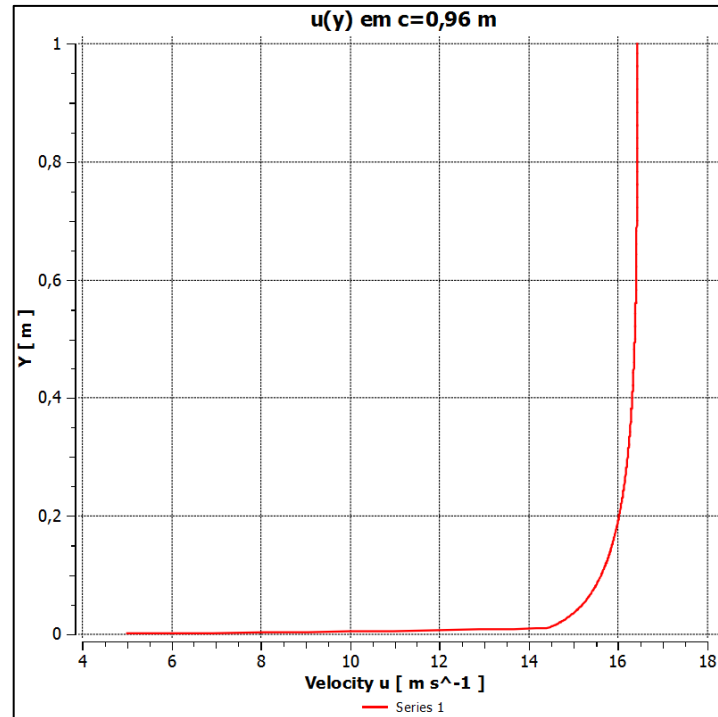


Figure 3-20 - Velocity plot at station $0.96c$ of the airfoil, showing that the BL thickness at the TE is typically of the order of the airfoil chord $\delta \approx 1 \text{ m}$, being unsuitable as an upper limit for the integration of the displacement thickness.

The following method was devised for the evaluation of the Boundary Layer thickness: for each calculation point, the TKE was plotted in a normal coordinate from the chord line, in order to obtain an acceptable measure of the BL thickness, as show in Figure 3-21.

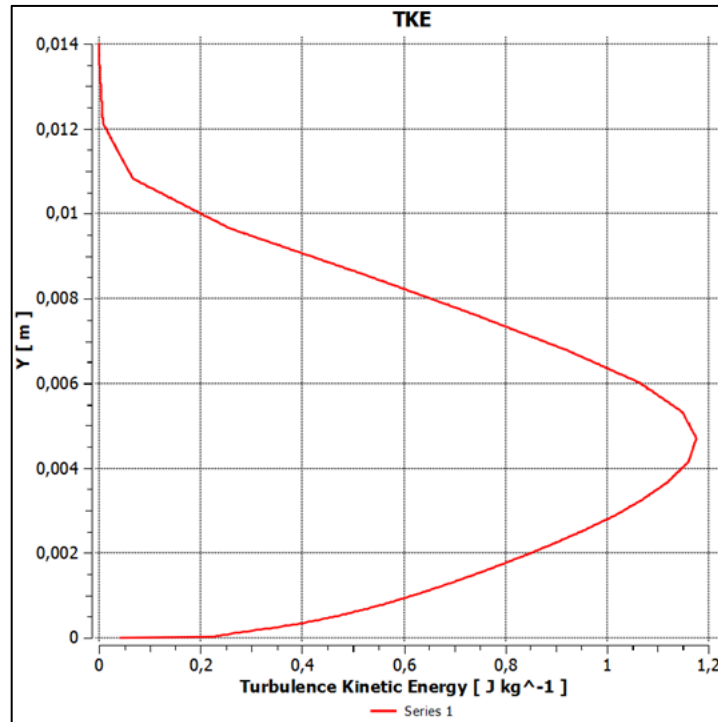


Figure 3-21 - TKE energy plot at station 1.001c, for the same simulation case of Fig. 4.3.2.3-6, showing the real TBL thickness at the TE to be of the order $\delta \cong 0.014 \text{ m}$. A thousand points were employed in the construction of the TKE profile.

A general overview of the CFD simulation results for $5 \times 10^5 \leq Re_c \leq 2.6 \times 10^6$ and XFLR5 (XFOIL) calculations is shown in Figure 3-22, along with the experimental results from Brooks and Marcolini (Brooks & Marcolini, 1985) and CFD results from Glegg and Reba (Glegg & Reba, 2010). Also, Prandtl's TBL over FP correlation model $\delta/c \approx 0.37/Re_c^{1/5}$ (White, 2006), was added for reference purposes, only.

Since Brooks and Marcolini (Brooks & Marcolini, 1985) measured the BL thickness in a fixed 1.3 mm position downstream of the airfoils with chords of different lengths for the different cases, and in the current CFD simulations the measurement point was fixed at 1.001c for all cases, this slight difference in measurement station might help explain the slight difference in curvature of the potential regressions adapted to the resulting points, when compared to the potential regressions of the measurements.

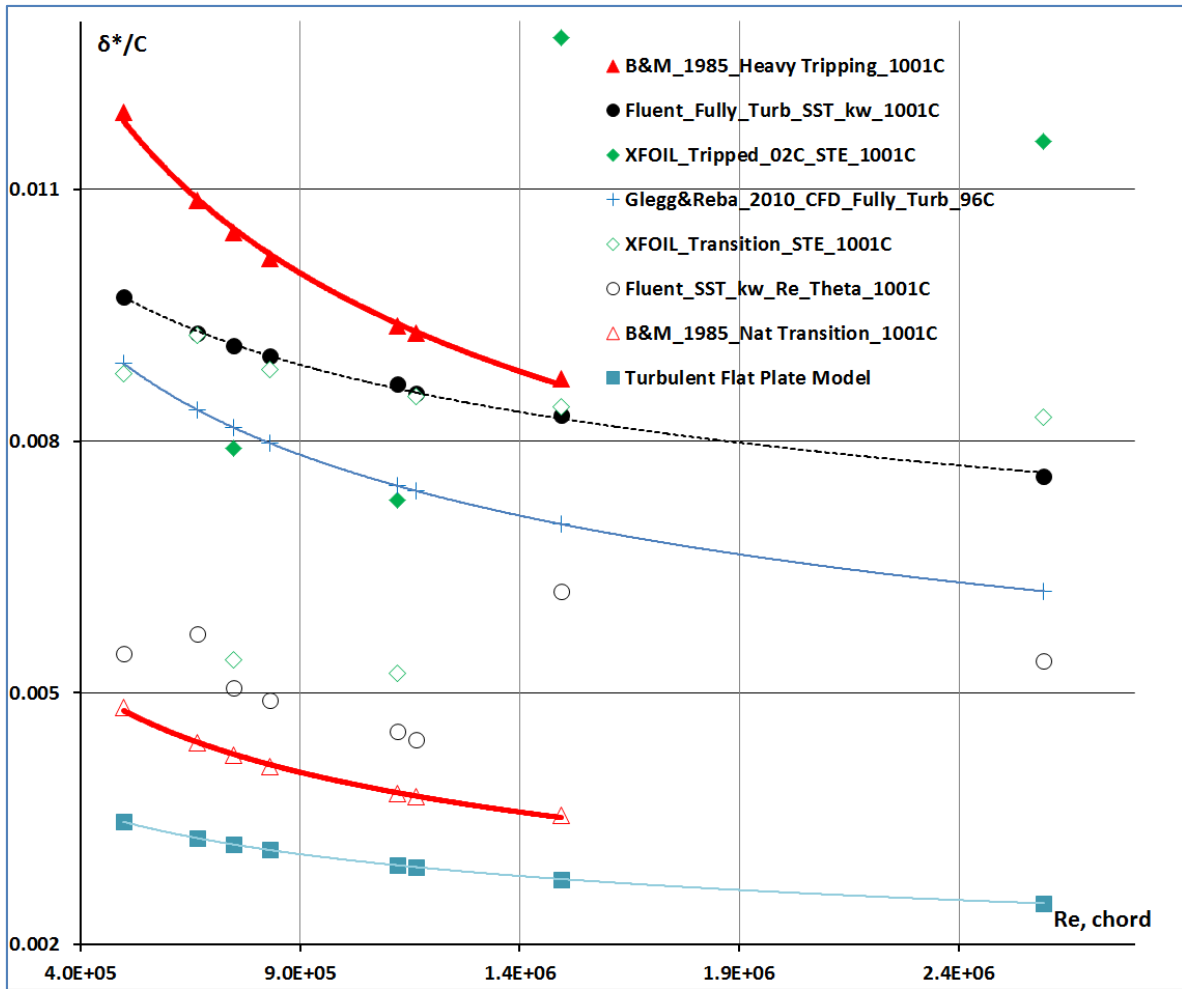


Figure 3-22 - CFD simulations results for fully turbulent and transition cases, compared to experimental data of Brooks, Marcolini, 1985, CFD data from Glegg, Reba, 2010, XFOIL simulations and Prandtl's turbulent flat plate model.

Concerning the quality assessment of the CFD results, Figure 3-23 and Table 3-9 show that all CFD results complied with the quality criteria proposed in this work, whether in the fully turbulent or transition models. However the run time necessary to solve all 16 plotted operating points and 4 error-study additional cases was close to 48 core-hours, or 2.4 core-hours per operating point⁴⁸.

⁴⁸ Average of 36 minutes per point in a 4 processor 3 GHz machine.

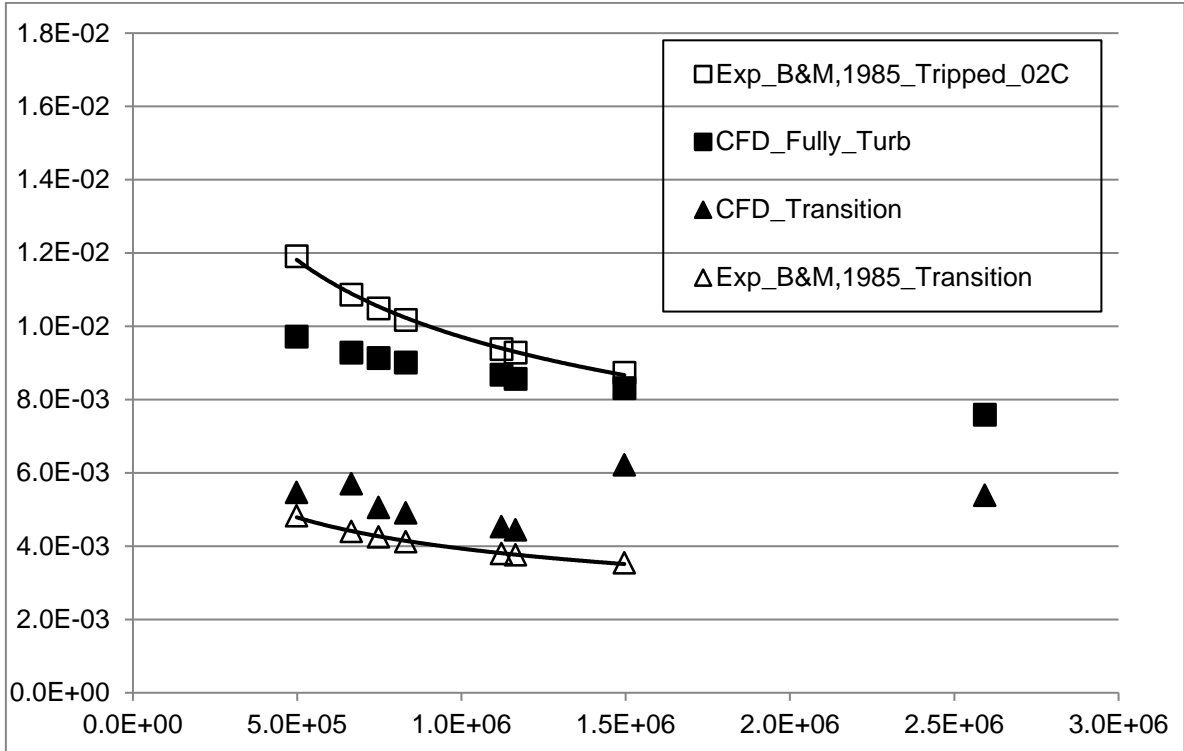


Figure 3-23 – CFD simulation results for fully turbulent and transition cases, compared with experimental data of Brooks and Marcolini, 1985 (Saab Jr & Pimenta, 2016).

Table 3-9 – Relative error estimation for the CFD results (turbulent and transition TBL), for the sharp-TE NACA 0012 airfoil (Saab Jr & Pimenta, 2016).

CFD Validation and Quality Assessment - Fully Turbulent and Transition Regimes - NACA 0012, 0° AOA									
Experimental				CFD		Quality Assessment			
Brooks & Marcolini, 1985.		Heavily Tripped	Natural Trans.	Sharp TE, Fully Turbulent	Sharp TE, Re-Theta transition	Turb.	Trans.	Turb.	Trans.
Case	Reynolds_C	δ^* @ 1.3 mm downstream of TE		δ^* @ 1.0013C		$\Delta\delta^*/\delta^*$ @ 1.0013C		$\Delta\text{SPL}=10\text{Log}(1+\Delta\delta^*/\delta^*)$ [dB]	
B	1.5E+06	8.7E-03	3.5E-03	8.3E-03	6.2E-03	-5%	76%	-0.22	2.44
C	1.2E+06	9.3E-03	3.8E-03	8.6E-03	4.4E-03	-8%	18%	-0.35	0.72
D	8.3E+05	1.0E-02	4.1E-03	9.0E-03	4.9E-03	-11%	19%	-0.53	0.76
E	6.6E+05	1.1E-02	4.4E-03	9.3E-03	5.7E-03	-15%	30%	-0.69	1.12
F	1.1E+06	9.4E-03	3.8E-03	8.7E-03	4.5E-03	-7%	19%	-0.33	0.77
G	7.5E+05	1.0E-02	4.3E-03	9.1E-03	5.1E-03	-13%	19%	-0.60	0.76
H	5.0E+05	1.2E-02	4.8E-03	9.7E-03	5.5E-03	-18%	13%	-0.88	0.54

The experimental data from Brooks and Marcolini (Brooks & Marcolini, 1985) have an associated uncertainty of less than $\pm 5\%$ for the tripped cases and less than $\pm 10\%$ for

the natural transition cases, while Glegg and Reba (Glegg & Reba, 2010) did not discuss the error estimate associated with their CFD results.

In order to formally compare the current CFD results with experimental data, the quantifiable uncertainties associated with each of the methods was taken in account. For this purpose, a subsequent discretization error evaluation proposed by ASME⁴⁹ (Celik, et al., 2008), based on the Richardson extrapolation (Ferziger & Peric, 2002) and called the *Grid Convergence Method*, was applied to the *SST k, ω* and *SST $k, \omega, transition$* solutions for one selected operating point only (case F; $Re_c = 1.1 \times 10^6$). Two progressively refined meshes, with grid refinement factors of 1.51 and 1.33 were generated for this evaluation, as shown in Figure 3-24.

After the CFD was run again for operating point F on the progressively refined meshes, the displacement thickness at 1.001c was re-evaluated and the discretization error computed for both cases (transition and fully turbulent), with results displayed in Table 3-10 and Table 3-11, below.

⁴⁹ The American Society of Mechanical Engineers.

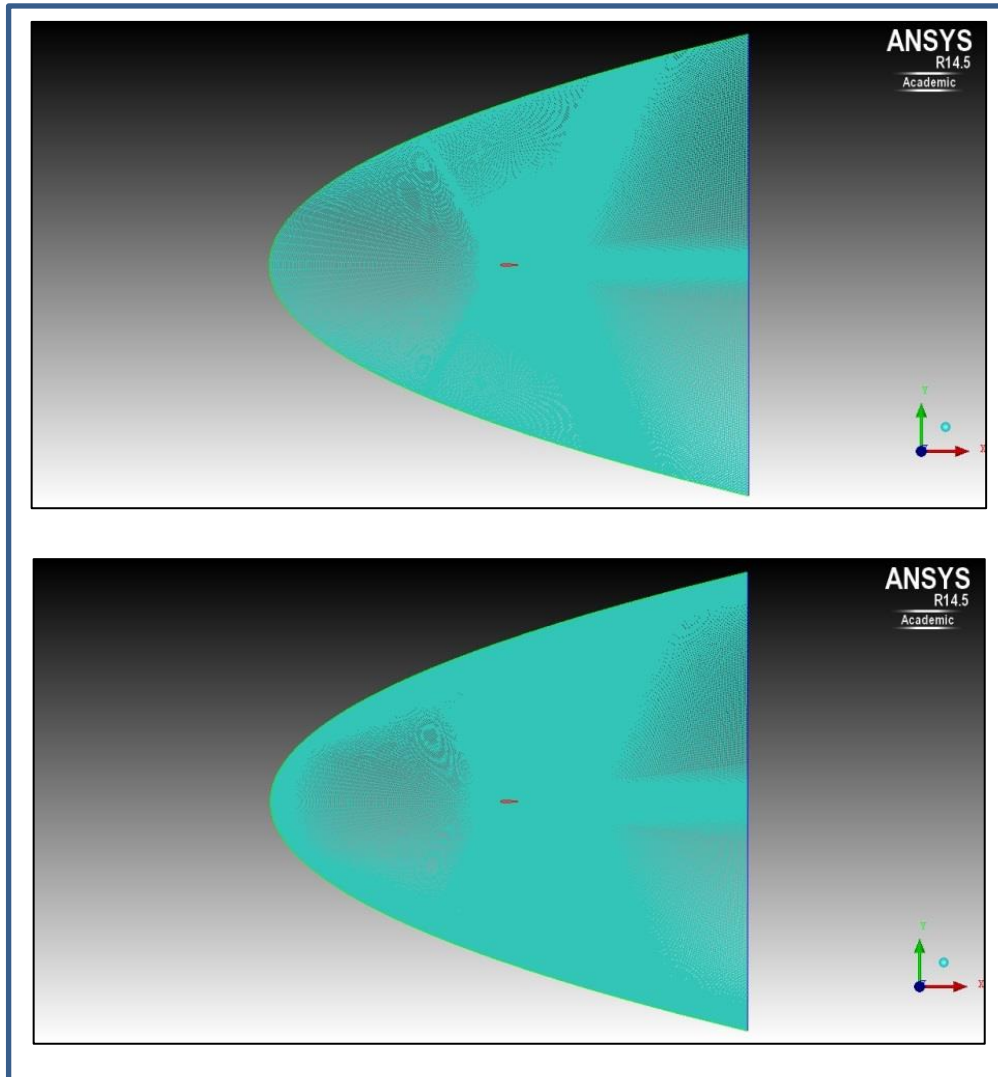


Figure 3-24 - Refined meshes for the discretization error study. Upper mesh has 51% more elements and the lower mesh has 100% more elements than the original mesh.

Table 3-10 - Discretization error associated with the CFD solution of the fully turbulent regime simulation, case F.

Fully Turbulent CFD Simulation:		"F" Case			
Control Parameter:		δ^* - displacement thickness @ 1.3 mm downstream of the TE.			
Type of convergence: Monotonic		Grid	Quad Cells #	Tot Area (m ²)	h
		N3	272,034	866	0.05642
		N2	308,847	433	0.03744
		N1	549,164	433	0.02808
Grid Refinement Factor	r_{21}	1.33	$p = \frac{1}{\ln(r_{21})} \left \ln \left \frac{\epsilon_{32}}{\epsilon_{21}} \right + q(p) \right $ $q(p) = \ln \left(\frac{r_{21}^p - s}{r_{32}^p - s} \right)$ $s = 1. \operatorname{sgn}(\epsilon_{32}/\epsilon_{21})$		
Grid Refinement Factor	r_{32}	1.51			
ϕ_3 (δ^* from Grid N3)	δ_{32}^*	8.68E-03			
ϕ_2 (δ^* from Grid N2)	δ_{21}^*	8.55E-03			
ϕ_1 (δ^* from Grid N1)	δ_{10}^*	8.48E-03			
	ϵ_{32}	1.35E-04			
	ϵ_{21}	6.78E-05			
	s	1			
Apparent Order of the Method	p	0.95			
Extrapolated value	δ_{ext}^{21}	8.26E-03			
	δ_{ext}^{32}	8.26E-03			
Approximate Relative Error	e_a^{21}	0.8%			
Extrapolated Relative Error	e_{ext}^{21}	2.6%			
Fine-Grid Convergence Index	CGI_{fine}^{21}	3.2%			

The relative discretization error for the fully turbulent case, based on the Richardson Extrapolation value, δ_{ext}^{21} , is 2.6%. However, the δ^* values employed in the evaluation table (Table 3-9) were not those from the finest grid, but from the courser one. The relative error based on grid N3 is actually 5.1%

Table 3-11 - Discretization error associated with the CFD solution of the transition regime simulation, case F.

Transition CFD Simulation:		"F" Case				
Control Parameter:		δ^* - displacement thickness @ 1.3 mm downstream of the TE.				
Type of convergence: Oscillatory		Grid	Quad Cells #	Tot Area (m ²)	h	
		N3	272,034	866	0.05642	h3
		N2	308,847	433	0.03744	h2
		N1	549,164	433	0.02808	h1
Grid Refinement Factor	r_{21}		1.33			
Grid Refinement Factor	r_{32}		1.51			
ϕ_3 (δ^* from Grid N3)	δ^*_3		4.53E-03			
ϕ_2 (δ^* from Grid N2)	δ^*_2		4.09E-03			
ϕ_1 (δ^* from Grid N1)	δ^*_1		4.16E-03			
	ϵ_{32}		4.45E-04			
	ϵ_{21}		-7.20E-05			
	s		-1			
Apparent Order of the Method	p		4.67			
Extrapolated value	δ_{ext}^{21}		4.19E-03			
	δ_{ext}^{32}		4.01E-03			
Approximate Relative Error	e_a^{21}		1.7%			
Extrapolated Relative Error	e_{ext}^{21}		0.6%			
Fine-Grid Convergence Index	CGI_{fine}^{21}		0.8%			

$$p = \frac{1}{\ln(r_{21})} \left| \ln \left| \frac{\epsilon_{32}}{\epsilon_{21}} \right| + q(p) \right|$$

$$q(p) = \ln \left(\frac{r_{21}^p - s}{r_{32}^p - s} \right)$$

$$s = 1. \operatorname{sgn}(\epsilon_{32}/\epsilon_{21})$$

For the transition case, the relative discretization error based on the Richardson Extrapolation value, δ_{ext}^{21} , is 0.6%. However, once more the δ^* values employed in the evaluation were not those from the finest grid, but from the courser one. The relative error based on grid N3 is actually 8.3%.

The errors from the discretization and from the experimental procedures are summarized in Table 3-12.

Table 3-12 – Experimental, discretizations and CFD versus Experimental relative errors.

	Fully Turbulent or Heavily Tripped	Transition
Experimental error	$\pm 5\%$	$\pm 10\%$
Discretization error	+ 5.1%	+ 8.3%
CFD (N3) X Experimental results	- 7%	+ 19%

Although the discretization error is usually the larger error associated with CFD simulation, there are other sources of potential errors (modelling, convergence, truncation, etc.). However, all recommended good practices were adopted throughout the operation in order to minimize those errors.

Since the discretization error associated with the CFD data is of the same order of the error for the experimental measurements, it was considered that the conclusions on the quality of the CFD method would not be adversely impacted by incorporating uncertainty.

Although no formal error study was accomplished for the XFOIL simulation, it is reasonable to assume that an integral method has a larger uncertainty associated with it than a second order finite volume method and also it became clear that the quality of the method was inconsistent and depended upon the chord station where the displacement thickness was selected to be measured, for a fixed tripping position. However, the computational efficiency and geometry flexibility advantages evidenced by the methodic simulations accomplished are so overwhelming that it was deemed worthwhile to give the XFOIL method a deeper analysis.

By observing the Figure 3-14, it was possible to see that the experimental values were always within the range of displacement thickness calculated by XFL5 at chord stations 0.96c and 1.001c. Also, the values calculated at station 0.96c were systematically underpredicted while the values calculated at station 1.001c were systematically over predicted. This suggested that the experimental displacement thickness value might be matched by reading the displacement thickness somewhere in between them.

By starting at the 100.1C station and gradually moving towards the LE, it was found that the XFLR5 values at 0.98c were closer to the experimental value and of better quality than either data at 0.96c or 1.001c, for both the tripped and the transition simulations, as shown in Table 3-13.

Table 3-13 - XFOIL results for δ^* , calculated for tripped and transition TBL, at station 0.98c of NACA 0012 TE, in the range $5 \times 10^5 \leq Re_c \leq 2.6 \times 10^6$ (Saab Jr & Pimenta, 2016).

XFOIL Validation and Quality Assessment - Tripped and Transition Conditions									
Experimental				XFOIL		Quality Assessment			
Brooks & Marcolini, 1985.		Heavily Tripped	Natural Transition	Sharp TE, Tripped @ 0.2C	Sharp TE, e ⁹ transition	Heavy Tripping	e ⁹ transition	Heavy Tripping	e ⁹ transition
Case	Reynolds_C	δ^* @ 1.3 mm downstream of TE		δ^* @ 0.98C		$\Delta\delta^*/\delta^*$ @ 0.98C		$\Delta\text{SPL}=10\text{Log}(1+\Delta\delta^*/\delta^*)$ [dB]	
B	1.5E+06	8.7E-03	3.5E-03	4.9E-03	2.7E-03	-44%	-23%	-2.53	-1.13
C	1.2E+06	9.3E-03	3.8E-03	5.1E-03	2.9E-03	-45%	-23%	-2.57	-1.12
D	8.3E+05	1.0E-02	4.1E-03	6.1E-03	3.5E-03	-40%	-14%	-2.24	-0.67
E	6.6E+05	1.1E-02	4.4E-03	5.9E-03	3.1E-03	-45%	-29%	-2.62	-1.47
F	1.1E+06	9.4E-03	3.8E-03	5.3E-03	2.9E-03	-44%	-23%	-2.52	-1.13
G	7.5E+05	1.0E-02	4.3E-03	5.8E-03	3.1E-03	-45%	-28%	-2.60	-1.43
H	5.0E+05	1.2E-02	4.8E-03	6.4E-03	3.4E-03	-46%	-29%	-2.71	-1.47

It was then concluded that, by calculating the displacement thickness with the XFLR5 at a station 0.03C upstream of the place of the experimental measurements (1.001C), the parameter value would consistently meet the quality criteria proposed. This procedure is analogue to correcting the SPL obtained at the original measuring station (1.001C) by a value between -0.67 dB and -2.71 dB.

Also, because the XFLR5 error calculated in this manner was of the same order of magnitude of the CFD error and the solution time was 3 orders of magnitude lower (2,160 seconds for CFD against <5 seconds for XFOIL, per point), the TBL layer solver method selected to feed the BPM TE model was the XFLR5.

3.5 IMPLEMENTATION OF THE METHOD.

At this point, the BEM method had been selected to calculate the local flow condition on the spinning blades of WT equipment; the BPM TE noise model basic equations had been selected for modification as the core of the new, more flexible method, and the XFLR5 had been selected as the 2D TBL flow solver, provided some care was taken on the selection of the chord station where the displacement thickness should be read.

Since the ultimate goal of the industry is to have efficient wind power conversion, it is necessary also to add a method for the estimation of the annual power conversion in a site with a known Weibull or Rayleigh wind distribution, for each blade geometry. This would assure the tradeoff between noise and performance to be acceptable for any noise-tailored equipment. For this purpose, the Method of Bins (GIPE, 2004), (Burton, Sharpe, Jenkins, & Bossanyi, 2008), described in Appendix C, was selected.

Because of the large reach and multidisciplinary character of the task of implementing a 2-D and “quasi 3-D” TE noise prediction method also capable of verifying Wind Turbine performance, it became evident that in order to fulfil the objective of this research within the existing time constraints, a collaboration effort would be necessary.

During the selection phase of the elements for the TE noise prediction method, contacts were considered with NREL (Moriarty P. , NAFNoise User’s Guide, 2005), and Vargas (Vargas L. d., 2008), for possible modification of their software platform, since these are essentially the only noise tools available in public domain, among all the methods reviewed. However, in the case of Vargas (Vargas L. d., 2008), the tool was available for use online only and extensive modification would be necessary to incorporate the XFLR5 tool, in order to obtain the desired geometry flexibility. In the case of NREL (Moriarty P. , NAFNoise User’s Guide, 2005), the software already incorporated the XFOIL, but was restricted to 2-D geometry and lacked the WT performance analysis tools, which would be necessary for the proposed method to be successful.

The QBlade software, described in Section 2.9, on the other hand, apart from a user-friendly graphic interface, is of the open source type and available to the researchers

and industries free of charge, under the GNU⁵⁰ General Public Licensing. The software is integrated with the XFLR5 and also employs the BEM method and has WT performance analysis tools. Since the QBlade dynamic analysis software was also developed with the same approach in mind, i.e., to provide WT industry with a quick and relatively accurate tool to be employed in the early assessment and comparative design of WT equipment, it is no surprise that it is assembled of many of the same computationally efficient tools selected for the implementation of the present noise prediction method.

However the software, at this point in time, had no noise prediction capabilities implemented or planned. The initial application focus was on performance analysis, but since release v0.8 (as of March, 2014), the software also offered good tools for sizing WT blades from the structural point of view.

The main software developer was contacted at TU-Berlin (Dr. David Marten) and along with the head of the chair of Fluid Dynamics in that University (Dr. George Pechlivanoglou), they welcomed the possible collaboration with Poli-USP for the development of the noise prediction module and three initial steps were planned:

- Modification of the XFLR5 module for saving displacement thickness information along chord for each airfoil operating point simulated (Re, M and AOA condition).
- Addition of the modified BPM 2D TE noise module, integrated with the XFLR5 output data, and with completely new input and output screens.
- Extension of the method in order to estimate the rotor noise with the Quasi-3D procedure.

The development of the noise modules (2D) and (3D) would be detailed, coded and integrated by Poli-USP into an earlier QBlade version and TU-Berlin would integrate the modules, after validation, to an upcoming software release.

The software capabilities then envisioned, with the eventual addition of the TE noise prediction modules, are depicted in Figure 3-25.

⁵⁰ The GNU General Public License is a free, "copyleft" license for software and other kinds of works. <http://www.gnu.org/copyleft/gpl.html>

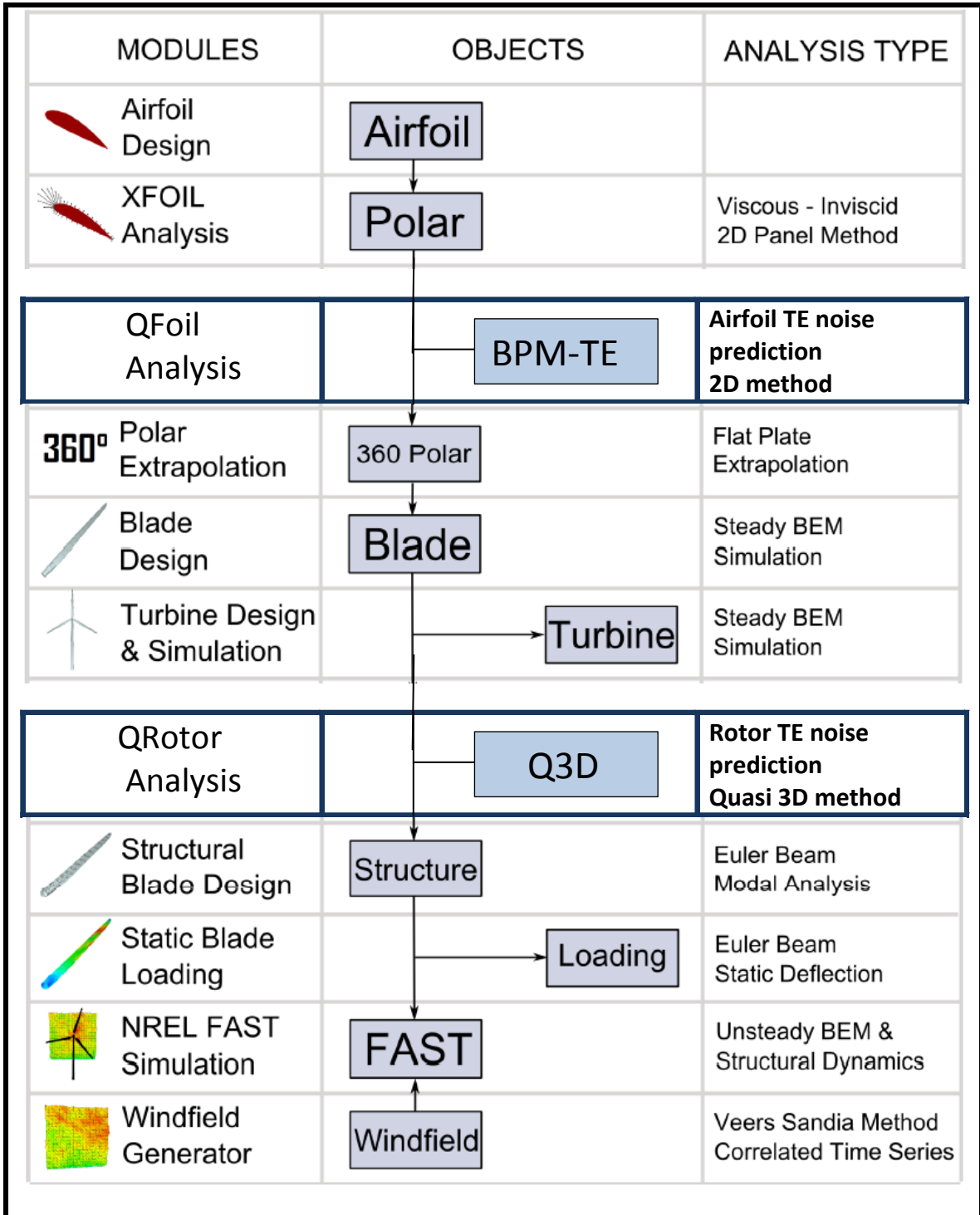


Figure 3-25 - Qblade V0.8 software original capabilities (Marten D. , Qblade Short Manual V0.8, 2014) and the proposed additional modules (blue frame) for 2-D and 3-D TE noise prediction capabilities.

For flexibility, it was decided that the TE noise module should be able to read integral flow parameters from any chord station specified along the flow, or receive imported data from experimental, CFD or other sources, via “.csv” files.

With the modular approach, many follow-on improvements could be made to the basic TE noise prediction module, such as the inclusion of the remaining BPM airfoil self-noise source models; the inclusion of other semi-empirical self-noise models; changing the position of the observer (microphone) to any designated point in the far field (for noise-standard compliance simulation) and also different terrain and atmospheric noise propagation models could be added.

Also, the release of the QBlade v0.8, with the unsteady BEM method and turbulent windfield generator, took the possibilities of collaboration to another level. It would be possible in the future to integrate the turbulence inflow noise source and to estimate the unsteady noise of the WT, making the QBlade potentially the only complete (not restricted to self-noise), flexible and quick-TAT airfoil and rotor noise prediction module available for the industry and researchers. Finally, the v0.8 release also incorporated aero elastic analysis, making possible the future analysis of the impact of the aero elastic effects in the TE and other sources of noise.

This integration was considered strategic for reaching the goal of providing the WT industry with the intended tool, due to the ongoing, long term dedication to this project from TU-Berlin personnel.

3.5.1 Comparison and improvements over other methods

The characteristics of the proposed TE noise prediction method integrated to Qblade are described in the revised method classification Table 3-14.

The proposed method is number 14 in the table and the main differences when compared to the most modern semi-empirical methods are highlighted in color.

The NREL method described in (Moriarty & Migliore, Semi-Empirical Aeroacoustic Noise Prediction Code for Wind Turbines, 2003) is not flexible in relation to geometry, employing the original correlations for the NACA 0012 airfoil and the observer position is fixed in relation to the airfoil TE.

The semi-empirical method from the University of Stuttgart (Zhu, 2004) is probably the closest method to the one proposed. However, the current method will be integrated

with the method of bins for determination of power generating capacity and will be available for industrial or academic use and modification. It is not known if the method from Zhu (Zhu, 2004) was made public, since the code is not listed in the research and there is no information concerning a download source or about its user friendliness.

The NREL-NAFNoise method (Moriarty P. , NAFNoise User's Guide, 2005) is a 2-D code with fixed observer position and no graphic user interface.

Finally, the method from Vargas (Vargas L. d., 2008) has no airfoil analysis capability, other than the NACA 0012 correlations embedded into the BPM model, and also has no downloadable source code.

Table 3-14 - The reviewed semi-empirical-based WT noise prediction methods (1-13), and the proposed method (14). N/A = Not Available.

Wind Turbine Noise Prediction Method Classification Dimensions													
			1	2	3	4	5	6	7	8	9	10	11
	Method	Ref.	Noise Sources	Theor. Model base	Noise Field	Geometry data	Flow Field Data	TAT	Accuracy class	Validation Domain	Observer position	Availability	User-Friendliness
1	Grosveld	Grosveld, 1985	Partial (TE + Inflow)	SE	FF	2D/Q3D	very little	N/A	PD	Specific	ALUS	Text	Unk
2	Howe	Howe, 1978	Partial (TE)	SE	FF	2D	intensive	long	OM	Specific	ALUS	Text	Unk
3	Brooks-Hodgson	Brooks and Hodgson, 1981	Partial (TE)	SE	FF	2D	intensive	long	OPT	Specific	AF	Text	Unk
4	Brooks-Marcolini	Brooks and Marcolini, 1985	Partial (TE)	SE	FF	2D	little	medium	PD	Specific	AF	Text	Unk
5	Glegg	Glegg, 1987; Glegg et al., 1987	Partial (TE + Inflow, separated flow)	SE	FF	2D	intensive	long	N/A	Specific	ALUS	Text	Unk
6	BPM	Brooks, Pope and Marcolini, 1989	Self-Noise	SE	FF	2D	little	medium	OPT	Specific	AF	Code List - Fortran 5	No GUI
7	Lowson	Lowson, 1993	Partial (TE + Inflow)	SE	FF	2D/Q3D	very little	medium	PD	Specific	AF	Text	Unk
8	IAG-I	Bareiss, Guidati and Wagner, 1994	Self-Noise + inflow	SE	FF	2D	little	medium	OM	Specific	AF	Text	Unk
9	RISO	Fuglsang and Madsen, 1996	Self-Noise + inflow	SE	FF	2D/Q3D	little/some	short	PD	Specific	ALUS	Text	Unk
10	NREL	Moriarty and Migliori, 2003	Self-Noise + inflow	SE	FF	2D/Q3D	little/some	short	PD	Specific	AF	Download - Source (Embedded into the NREL Aeroacoustic code - FAST)	No GUI
11	Zhu	Zhu, 2004	Self-Noise + inflow	SE	FF + P	2D/Q3D+T	little/some	short	PD	Restricted	ALUS	Text	Unk
12	NREL-NAFNoise	Moriarty, 2005	Self-Noise + inflow	SE	FF	2D	little	short	PD	Restricted	AF	Download - Source	No GUI
13	Vargas	Vargas, 2008	Self-Noise + inflow	SE	FF	2D/Q3D	little	short	PD	Specific	ALUS	Flow Chart + Online	GUI
14	POLI-TU Berlin		Partial (TE), scalable	SE	FF	2D/Q3D	little	short	PD	(Restricted)	ALUS	Download - Source	GUI

By incorporating directivity functions, it was made possible to estimate the SPL at any specified far field observer position in the current code. Also, the method was made more flexible with provisions for selection of the chord station where the displacement thickness should be read (or interpolated) and multiplication factors for the eddy convective velocities and displacement thickness when calculated by XFLR5 or imported from other sources.

The method was made downloadable, free of charge, under GNU and with the source code also available for download and customization.

Provisions were made for retrofitting with all BPM airfoil self-noise sources and inflow turbulence noise. Also, with the release V0.8, many more gradual expansion possibilities were open with the aero elastic analysis, transient-BEM and turbulent wind field capabilities.

The large-scale block diagram of the code implementation was shown in Figure 3-3.

3.6 METHODOLOGY FOR THE INVESTIGATION OF QUIETER AIRFOILS FOR WT.

Since the most important feature of the implemented method is the geometrical flexibility in the analysis, the sample application project selected was to investigate airfoil geometry impact on WTN. Since the investigation has led to some airfoil developments, it was considered necessary to establish some design requirements, although the requirements selected are of general nature, only.

3.6.1 Requirements for the development of airfoils with less overall and TE noise emission.

The list of general requirements laid out was based on the extensive bibliographical review and also on the need to develop quieter WT airfoils for large-size HAWTs with preserved aerodynamic performance. Most of the requirements aimed primarily at TE noise reduction and high aerodynamic performance, however, some secondary requirements, considered as “good practices” and aimed at avoiding other self-noise mechanisms and also inflow noise emission were added to the list. Finally, a provision for an airfoil variation with a purpose-built blunt-TE, aimed at producing an acoustic whistle for bird-warning was added in the hope of improving acoustic detection by the birds and improving chances of collision-avoidance with the WT rotor. If adopted by the designer, such an airfoil should be employed in a narrow section of the blade only, so that the tonal noise produced would not contribute to increase the overall sound pressure level signature of the full rotor. Since the warning effectivity of the tonal noise depends upon the signal-to-noise-ratio (SNL) (Dooling, 2002), the use of a quieter airfoil throughout most of the blade span would allow a moderate-level tone, produced in a limited span section, to be more easily heard by the migrating or local birds.

As explained by Somers & Tangler (Somers & Tangler, The Airfoils S830, S831 and S832, 2005b), p.3,

“Recent research suggests that the lift produced by the outboard portion of the blade should be constrained to alleviate noise. Accordingly, a decreasing, as opposed to

increasing outboard, maximum lift coefficient is specified for the outer quarter of the blade.”

This has led those authors to set the cl_{max} for large size HAWT at 1.6, which is not adopted here, since the objective is to design quieter airfoils without imposing penalties on aerodynamic characteristics.

Table 3-15 - Table of desirable requirements for a quiet airfoil aimed at 85% span of a large size HAWT, preserving aerodynamics performance.

#	Requirement	Reason	Reference
1	Airfoil suitable for a large size HAWT, outboard section @85% radius Reynolds and Mach numbers. Nominal radii to be used in the designs: 50, 87 and 106.5 m.	WT diameter increase trend displayed over time. Noise sources are concentrated on outer radius, but not at the very tip.	(Oerlemans, Wind Turbine Noise: Primary Noise Sources, 2011)
2	Suitable for pitch controlled WT.	Deep stall noise may be a dominant noise source and there is no noise prediction model for this regime. It must be avoided by a pitch control blade, which, except for the transient regime, will drive the blade to operate far from stall conditions. This is the current trend for machines with higher efficiency and power coefficients, C_p . Also, since a proposition is later made in this research to operate the blades of large size WT in a “quiet mode”, which does not correspond to the $(cl/cd)_{max}$ setting, a pitch control mechanism is necessary.	Ref. Current research.
3	The nose thickness (radius) should be significant.	To allow for smooth stall characteristics, to avoid deep stall in low angles and to reduce inflow noise.	(Timmer & van Rooji, 2003). (Somers & Tangler, The Airfoils S830, S831 and S832, 2005b). (Migliore & Oerlemans, Wind Tunnel Acoustic Tests of Six Airfoils for Use in Small Wind Turbines., 2003)
4	Relative insensitive to roughness.	According to (Somers & Tangler, 2005a), this is necessary in order to	(Somers & Tangler, 2005a)

		keep efficiency in the presence of LE soiling and debris accumulation.	
5	Early laminar to turbulent transition in a controlled point.	To reduce overall SPL; to eliminate tonal noise from the pressure side; to avoid laminar bubbles. This will be imposed by early tripping of the BL.	(Wagner, Bareiß, & Guidati, Wind Turbine Noise, 1996), p. 84
6	To have low profile drag, but to preserve airfoil thickness determined by structural requirements.	Compatible with the structural stiffness required at the radial position in which the airfoil will be implemented.	(Somers & Tangler, 2005a). (Somers & Tangler, The Airfoils S830, S831 and S832, 2005b).
7	The pitching moment coefficient about $\frac{1}{4}$ chord should be close to -0.145 of the S830 airfoil.	In order to limit aerodynamic torsion loads, which drive the weight of the blade up.	(Somers & Tangler, The Airfoils S830, S831 and S832, 2005b)
8	A TE with specified bluntness parameter may be added to the airfoil, for use in part span, in order to produce a 3 – 4 kHz tone.	In order to increase bird audibility and decrease bird killing ratio, without affecting significantly the OASPL.	(Dooling, 2002).

Also, the design should be robust enough for use in a reasonably wide range of flow conditions for simplicity of design and manufacturing. That range was defined to be the flow conditions prevailing from 55% to 90% of the span of the rotating blade.

3.6.2 Airfoil design methodology

Two important questions had to be addressed at the beginning of the design methodology section:

- 1) Did the semi-empirical modified-BPM TE noise model represent the aeroacoustic phenomena enough, from the physical point of view, so as to provide guidance for designing quieter and efficient airfoil geometries?
- 2) How should the new airfoil geometry be designed for reduced TE noise emission, based on the sources modelled by the model and their relative strength, obtained from preliminary and validation simulations, without disregard to other known noise sources?

As seen in Section 2.4.1.1, the BPM model is based (i) on a universal spectral shape, (ii) on a decade-worth of NASA wind and acoustic tunnel data, and also (iii) on the Ffowcs-William and Hall (Ffowcs-Williams & Hall, 1970) edge-scatter formulation, confirming its character of a mixed theoretical and empirical approach.

The architecture of the BPM model for TE noise prediction comprises the logarithmic sum of 3 uncoherent sources, (i) the suction side TE noise (SPL_s), (ii) the pressure side TE noise (SPL_p) and (iii) the angle-dependent noise (SPL_α), the need of which was experimentally determined and is intended to represent the partially separated boundary layer noise contribution over the suction side TE.

One of the main limitations of the BPM TE noise model, i.e., the single-geometry correlations for the turbulence vertical scale is, to a certain extent⁵¹, circumvented by the modified-BPM model implemented, which is now able to calculate and read the displacement thickness for any prescribed chord section, for any airfoil geometry of moderate camber, below deep-stall angles.

It is then assumed, as a hypothesis, that the physics underlying the model is sufficiently accurate for comparative purposes, and thus, “causality” relations between geometry and TE noise is assumed.

For the 50 m blade airfoil, a study was made by implementing modifications to the NREL S830 airfoil, already developed under requirements for low noise emission.

While it was recognized that a multi-disciplinary optimization (MDO) method might be a candidate approach for the development of airfoil geometry subjected to many structural, aerodynamic and acoustics requirements (objectives and constraints), a direct engineering design was selected for the task, the reason being to help establish a physical, causal relation between each airfoil geometry modification and the resulting polar and pressure coefficient diagram change that will eventually lead to the desired aerodynamic and/or aeroacoustics features.

⁵¹ The calculation of the TE displacement thickness for specific geometry will affect the theoretical portion of the model, only.

3.6.3 General design procedure developed for a quieter airfoil section.

For each case:

- Choose airfoil baseline geometry for 85% chord.
- Set up a WT blade and rotor geometry, plus operating conditions, as a reference.
- Using the BEM method, calculate the operating conditions at 85% length (Re , M).
- Test and save aerodynamic performance data of baseline airfoil geometry at required Re , M , numbers, using the XFLR5, for future reference. Since the blades operate in dirt (also noisier) condition most of the time, the primary focus is on performance under tripped flow.
- Test and save the ultimate aerodynamic performance data (the Power Coefficient), using the QBlade code.
- Test and save aeroacoustic performance data of the baseline airfoil geometry at required flow conditions, using the modified-BPM method implemented.
- Modify the selected baseline airfoil geometry, working on variations of the most relevant parameters (for a given, fixed maximum thickness):
 - LE radius.
 - Maximum camber and maximum camber position.
 - Maximum thickness position.
 - Shape of forward and aft regions of suction and pressure sides (convexity or concavity controlling the pressure gradient).
 - TE wedge angle.
 - TE gap.

Make a non-automated sensitivity analysis by comparing each modification with baseline data and establishing trends. Adopt modifications with improved aero and acoustic features or that represent acceptable tradeoffs.

- Identify an improved performance geometry that meets the requirements.
- Design a variant of the baseline WT blade, with the new airfoil in selected blade sections replacing the baseline airfoil. Verify the rotor Power Coefficient and energy conversion performance and compare to baseline data.
- Propose a Bird Saving (BS) variant for use in part-span.
- Make a final list of the developed airfoils, their geometric features and suggested operating conditions.

4. RESULTS AND DISCUSSION

4.1 TYPICAL OPERATING CONDITIONS CALCULATIONS FOR A LARGE SIZE HAWT

The typical power curve (operating envelope) for a pitch-regulated WT was illustrated in Figure 2-19 and Figure 2-21. Also the law of the diminishing returns applies to the efficiency as a function of increasing rotor speed, as illustrated by Figure 2-17.

It was possible, based on reference geometries and on the BEM method, to infer with reasonable accuracy the Reynolds and Mach numbers intervals that would be representative of the operational range for large-size WT blades.

4.1.1 Operating Conditions for Airfoils at 85% Span of Large-Size HAWTs.

The procedure followed for determining the rotor geometry and local Reynolds and Mach number for the blade sections was fully presented in Section 3.

Each individual 2-D airfoil aerodynamic characteristic curve (drag polar) for the process of determining the local actual operating conditions was calculated for specific Reynolds and Mach⁵² numbers prevailing at each spanwise station with the aid of XFLR5 (XFLR5 version V6.12, 64 bits). All section airfoil geometries were normalized, de-rotated and refined to around 300 panels, with TE/LE panels ratio improved to 20-30% from default values before simulation. Tripping was fixed at 5% chord at top and 10% chord at bottom in order to simulate a soiled airfoil condition, which should prevail

⁵² Contrary to NREL development of the 'S'-series Airfoils, which employed the Eppler code with incompressible simulation, some simulations with the XFOIL showed a significant difference in (cl/cd)_{max} and related AOA when calculated with compressible and incompressible flow, for a Mach number of 0.2, so all WT rotors designed in this research were simulated with the compressibility model of XFOIL turned on.

for most of the operating life of each blade and also to avoid the risk of laminar bubbles and tonal noises. The calculated AOA range, for most airfoils, was set from -8° to $+16^\circ$, with 0.5° increments. Maximum iterations per AOA calculation was set to 300. However, for most operating points the convergence was achieved in fewer than 10 iterations and for a few points the number of iterations exceeded 100. Some limiting high or low AOA points, depending upon Reynolds number, did not converge at all, indicating unattached flow or stall condition. These exceptions were considered irrelevant since the coefficient values sought after were those close to maximum aerodynamic efficiency points, $(cl/cd)_{max}$ which, in general, are achieved in moderate AOA. The elapsed time for a batch XFLR5 calculation of a large combination of operating Reynolds and Mach numbers, for one blade, was close to 90 minutes in a basic machine⁵³. However, the total iterative process for each Wind Turbine rotor design, when using the ad hoc BEM code implemented was quite iterative and laborious.

For this reason, the scratch-built BEM code was used for the first estimate (iteration 1) of the local Reynolds and Mach numbers at each spanwise station. Subsequent iterations were made using the BEM code embedded within QBlade software, after a blade twist optimization procedure. The axial and tangential induction factors were exported out of QBlade for local Reynolds and Mach number determination which allowed for more accurate polar curves to be prepared with the aid of XFLR5 and reassigned to each blade station inside QBlade for the next iteration.

4.1.2 Results for the 50 m length blade, and Poli-100 WT rotor.

The use of the ad hoc built BEM code for the initial determination of the blade Twist allowed the convergence of the method in 3 iterative steps only, i.e., the Power Coefficient changed less than the specified amount of 0.05 between step 1 and step 2 (see Figure 3-3).

⁵³ Intel i3-350M processor and 2 GB RAM memory.

The S818, S830 and S832 airfoils employed in the Poli-100 blade are shown in Figure 4-1.

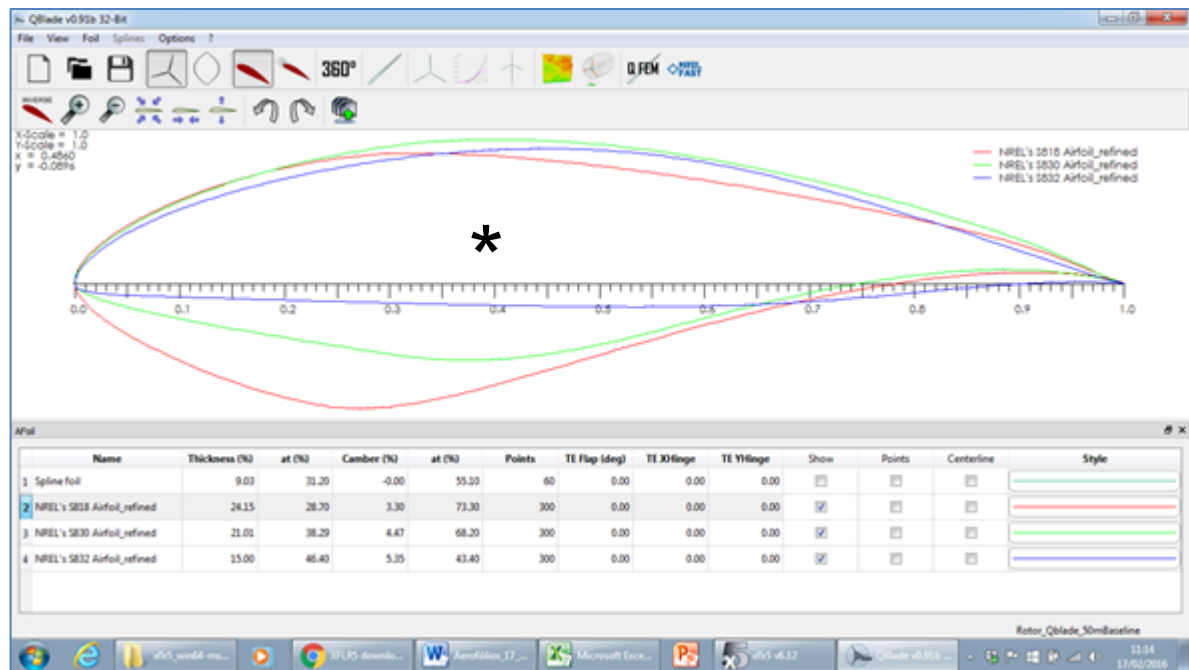


Figure 4-1- Airfoil geometries (*) for all NREL “S” Series Airfoils employed in the 50 m length blade (S818->red; S830->green; S832->blue).

Figure 4-2 shows the screen of the rotor design module from QBlade, with the geometry of Poli-100. The details of the geometry, as airfoil disposition, chord and twist are shown in Table 4-1, Table 4-2, Figure 4-3 and Figure 4-4.

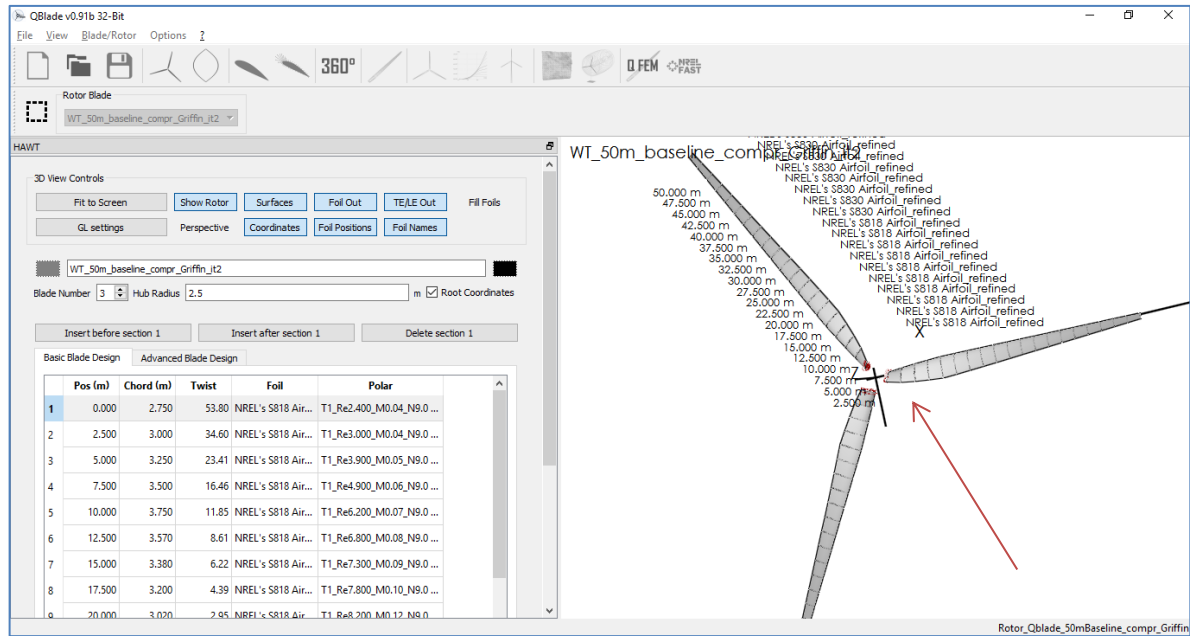


Figure 4-2 – Poli-100, general rotor geometry.

Table 4-1 – Geometry details of the 50-m length blade of Poli-100 rotor. Section at 85% radius is highlighted.

Sect	Radius[m]	r/R	Blade Section	Chord[m]
0	0	-	N/A	hub
1	2.50	0.05	S818	2.75
2	5.00	0.10	S818	3.00
3	7.50	0.15	S818	3.25
4	10.00	0.20	S818	3.50
5	12.50	0.25	S818	3.75
6	15.00	0.30	S818	3.57
7	17.50	0.35	S818	3.38
8	20.00	0.40	S818	3.20
9	22.50	0.45	S818	3.02
10	25.00	0.50	S818	2.83
11	27.50	0.55	S830	2.65
12	30.00	0.60	S830	2.47
13	32.50	0.65	S830	2.28
14	35.00	0.70	S830	2.10
15	37.50	0.75	S830	1.92
16	40.00	0.80	S830	1.73
17	42.50	0.85	S830	1.55
18	45.00	0.90	S830	1.37
19	47.50	0.95	S832	1.18
20	50.00	1.00	S832	1.00

Table 4-2 - Final operating conditions at each blade station for the 50-m length blade of Poli-100 WT, @ 12 m/s, TSR=7 and 16.4 rpm (typical output from the implemented BEM method). Section at 85% radius is highlighted.

Sect	Radius [m]	θ [°] (2)	Axial Induction Factor, a	Axial Velocity [m/s]	Tangential Induction Factor a'	Tangential Speed [m/s]	Resultant local speed [m/s]	Re, chord	Mach
0	0	0	-	12,00	-	-		0	0
1	2.50	53.81	0.0590	11.29	0.3292	5.58	12.60	2.4E+06	0.04
2	5.00	34.60	0.1056	10.73	0.1675	9.81	14.54	3.0E+06	0.04
3	7.50	23.41	0.1526	10.17	0.1073	13.95	17.26	3.9E+06	0.05
4	10.00	16.46	0.2052	9.54	0.0779	18.11	20.47	4.9E+06	0.06
5	12.50	11.85	0.2591	8.89	0.0597	22.25	23.96	6.2E+06	0.07
6	15.00	8.61	0.2941	8.47	0.0453	26.34	27.67	6.8E+06	0.08
7	17.50	6.22	0.3207	8.15	0.0353	30.44	31.51	7.3E+06	0.09
8	20.00	4.39	0.3464	7.84	0.0282	34.55	35.43	7.8E+06	0.10
9	22.50	2.95	0.3633	7.64	0.0230	38.67	39.42	8.2E+06	0.12
10	25.00	2.28	0.3513	8.18	0.0185	42.78	43.55	8.5E+06	0.13
11	27.50	3.82	0.3185	8.01	0.0145	46.87	47.55	8.7E+06	0.14
12	30.00	3.02	0.3325	8.00	0.0125	51.03	51.65	8.8E+06	0.15
13	32.50	2.34	0.3330	8.05	0.0106	55.18	55.76	8.8E+06	0.16
14	35.00	1.75	0.3293	8.13	0.0092	59.34	59.90	8.7E+06	0.18
15	37.50	1.24	0.3221	8.28	0.0079	63.50	64.04	8.4E+06	0.19
16	40.00	0.79	0.3101	8.47	0.0068	67.66	68.18	8.1E+06	0.20
17	42.50	0.89	0.2944	8.45	0.0059	71.82	72.32	7.7E+06	0.21
18	45.00	0.55	0.2955	8.65	0.0052	75.99	76.48	7.2E+06	0.22
19	47.50	1.22	0.2793	4.85	0.0045	80.16	80.31	6.5E+06	0.24
20	50.00	0.94	0.5957	12.00	0.0049	84.41	85.26	5.9E+06	0.25

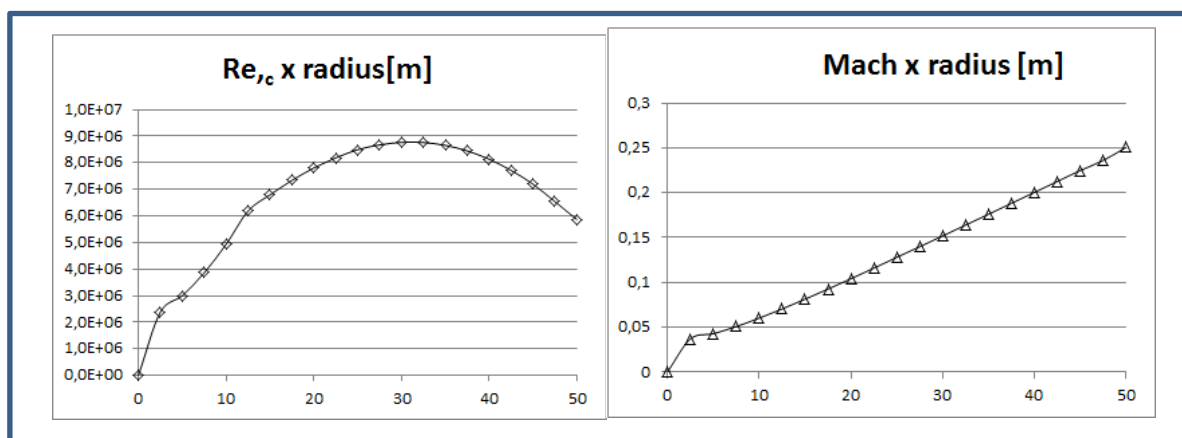


Figure 4-3 - Airfoil section local chord Reynolds and Mach numbers (vertical axis), as a function of radial position over blade span (horizontal axis).

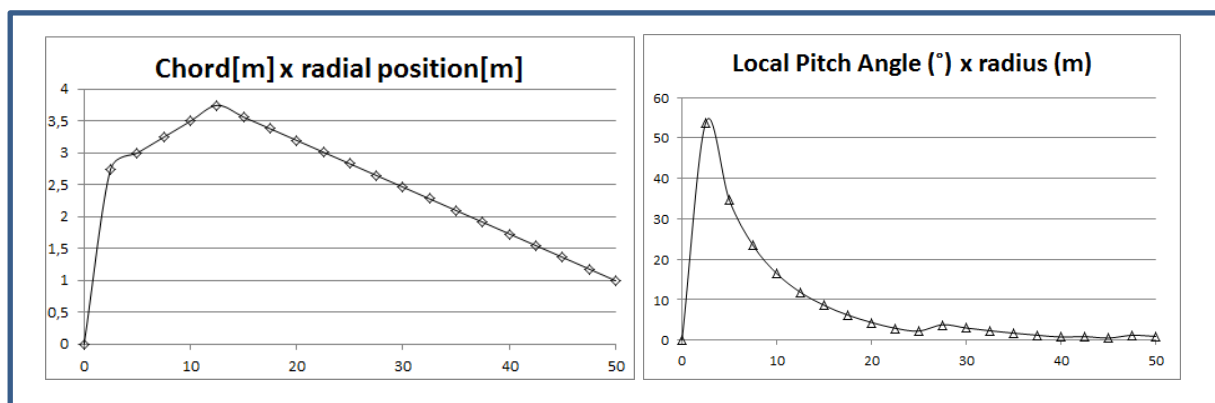


Figure 4-4 - Chord distribution and local pitch angle (vertical axis) for each section, calculated by the BEM method, for each airfoil section (horizontal axis) to work in ideal efficiency (maximum c_l/c_d ratio) throughout the blade span.

Some conclusions may be drawn from Figure 4-3 and Figure 4-4:

- The local flow speed and the Mach number increase monotonically from root to tip, and the Mach number stays under 0.3 at all times, confirming incompressible flow. However, the Reynolds number does not increase monotonically from root to tip.
- For the inner 40% of the blade, the portion closest to the hub, the Reynolds number increases monotonically with radius, from 2.5 to 8 Million.
- In the middle 1/3 portion of the blade, the Reynolds number displays relatively little variation, increasing a further 10% before decreasing by the same amount. The Reynolds number could be considered essentially constant in the middle 1/3 of the blade. In fact, if the chord variation is made inversely proportional to the radius, the Reynolds number may be designed to be constant along that portion of the blade.
- In the outer 20% portion of the blade, which includes the major TE-noise sources, the Reynolds number decreases monotonically with increasing radius, from 8 to 6 Million.

In trying to corroborate those findings, the following references are quoted:

“On the outer part of a large WT blade, $Re > 10^6$, and typically a turbulent boundary layer develops that remain attached up to the TE” (Bowdler & Leventhall, 2011).

“Most modern WT (>500 kW) operate at a local $Re > 3 \cdot 10^6$ ” (Wagner, Bareiß, & Guidati, Wind Turbine Noise, 1996).

“The boundary layer around the blade is usually turbulent for Reynolds number under consideration $Re \approx 1 - 6 \times 10^6$ ” (Wagner, Development of Design Tools for Reduced Aerodynamic Noise Wind Turbine (DRAW), 1997).

The final Power Coefficient achieved for the Poli-100 rotor was 0.495, which is 83% of the predicted theoretical Betz limit.

The theoretical power production prediction at a steady state wind field of 12 m/s and TSR=7 is 4.1 MW, quite above the 50 m WT usual average rating of 2.3 - 3.0 MW, however, no transmission and generator losses were accounted for.

The Power Coefficient, C_p , for the design point, may be obtained directly from the output graph generated by QBlade, or from:

$$P_{mech} = \frac{1}{2} C_p \rho_0 \pi R^2 U_\infty^3 \quad [W] \quad (1 - 1)$$

$$C_p = \frac{P_{mech}}{0.5 \rho_0 \pi R^2 U_\infty^3} \cong \frac{4,100,000}{0.5 * 1.225 * \pi * 50^2 * 12^3} \cong 0.493 \quad (4 - 1)$$

From the Table 4-2, it may be seen that the operating conditions at $r=0.85R$ are:

- Reynolds number of 7.7 million.
- Mach number of 0.21.

Since these figures depend upon the airfoil geometry, an assumption should be made at this point that any quieter airfoil developed for this station should have aerodynamic characteristics not very far from those of the NREL S830 airfoil, or else the operating conditions need to be recalculated for the new geometry. These conditions should be regarded as the initial condition of yet another iterative process for designing a quieter main airfoil and determining its particular operating conditions and aerodynamic performance.

Although Reynolds number value is quite above validation range of the original BPM TE noise model in order to forecast absolute values of SPL, the Mach number coincides with the upper extreme of the validation range.

Also, the main airfoil is not only employed in one specific blade station, but usually for quite a long length of the blade. In this particular design it was specified from 55% to

90% blade length, yielding a range of Reynolds and Mach numbers approximately as follows:

- Reynolds numbers from 7 to 9 million.
- Mach numbers from 0.14 to 0.22.

Any new main airfoil developed should perform quite well, from the acoustic as well as from the aerodynamic point of view, throughout this broad range of operating conditions.

The results for the operating conditions of the 87 m and 106.5 m blades for the Poli-180 and Poli-220 WT's, are shown in Appendix H.

4.2 THE IMPLEMENTED TE NOISE PREDICTION METHOD

The 2D TE noise prediction module was coded and coupled to the QBlade v 0.8 version, after the necessary boundary layer recording modifications had been accomplished to the embedded XFLR5 version. The results of the XFLR5 modification and the code implementation are displayed in this section.

Before the modification, the XFLR5 inside QBlade would save and export only displacement thickness calculated for the last value of a range of AOA values simulated, i.e. the last operating point of a polar object.

After the modification the code was able to save (for future work sessions) and export the displacement thickness for all operating point in any given polar object, as shown in Table 4-3.

Table 4-3 - Sample output file of XFLR5 v6.06 inside QBlade, after modification to store δ^* (D^*) for all AOA tested.

```

Modified XFLR5 v6.06 on QBlade v0.8
NACA 0012_refined_panels_STE

Alpha = 0.0, Re = 1500000, Ma= 0.2100, ACrit= 9.0

Top Side
  x      Hk      Ue/Vinf  Cf      Cd      A/A0      D*      Theta  CTq
0        2.22950  0.03314  0.00061  0.00001  0.00000  0.00006  0.00003  0.07170
0.968648 1.56618  0.92129  0.00182  0.00112  0.04140  0.00470  0.00297  0.04560
0.976198 1.58883  0.91131  0.00170  0.00109  0.04185  0.00496  0.00309  0.04674
0.983339 1.61857  0.89997  0.00156  0.00106  0.04239  0.00530  0.00324  0.04818
0.990029 1.65527  0.88783  0.00141  0.00103  0.04299  0.00570  0.00341  0.04989
0.99619  1.70353  0.87440  0.00124  0.00101  0.04370  0.00621  0.00361  0.05202
1        1.78578  0.85730  0.00102  0.00098  0.04463  0.00701  0.00389  0.05543
1.0001   1.78662  0.85730  0.00000  0.00166  0.04464  0.01405  0.00779  0.05563
1.00395  1.70000  0.87206  0.00000  0.00160  0.04392  0.01255  0.00731  0.05206

Bottom Side
  x      Hk      Ue/Vinf  Cf      Cd      A/A0      D*      Theta  CTq
0.968652 1.56730  0.92122  0.00181  0.00112  0.04143  0.00472  0.00298  0.04565
0.976201 1.59008  0.91122  0.00169  0.00109  0.04188  0.00499  0.00310  0.04680
0.983341 1.61996  0.89987  0.00155  0.00106  0.04242  0.00532  0.00325  0.04825
0.990031 1.65681  0.88773  0.00140  0.00103  0.04303  0.00573  0.00342  0.04996
0.99619  1.70522  0.87433  0.00124  0.00101  0.04374  0.00624  0.00362  0.05209
1        1.78747  0.85730  0.00101  0.00098  0.04466  0.00704  0.00390  0.05550
1.0001   1.78662  0.85730  0.00000  0.00166  0.04464  0.01405  0.00779  0.05563
1.00395  1.70000  0.87206  0.00000  0.00160  0.04392  0.01255  0.00731  0.05206
1.00813  1.65685  0.87992  0.00000  0.00156  0.04355  0.01184  0.00708  0.05017
1.01268  1.62027  0.88704  0.00000  0.00153  0.04321  0.01125  0.00687  0.04849

```

The 2D TE noise module, PNoise, input and output screens will be introduced below, along with the working procedure.

Step 1

- Open the QBlade with the 2D TE noise module.
- Open the working airfoil profile.
- Globally refine the airfoil from 160 to 300 panels and set the TE/LE panel density to 0.30. Normalize and de-rotate the airfoil, then save it.
- Define an XFLR5 analysis by the Reynolds and Mach numbers, plus transition details to simulate the experimental case the user wants to replicate, as seen in Figure 4-5.

Figure 4-5 – The XFOIL/XFLR5 flow analysis definition screen.

- Run the analysis along an AOA or angle range to meet the user specific needs, generating one or more Operational Points, as shown in Figure 4-6.

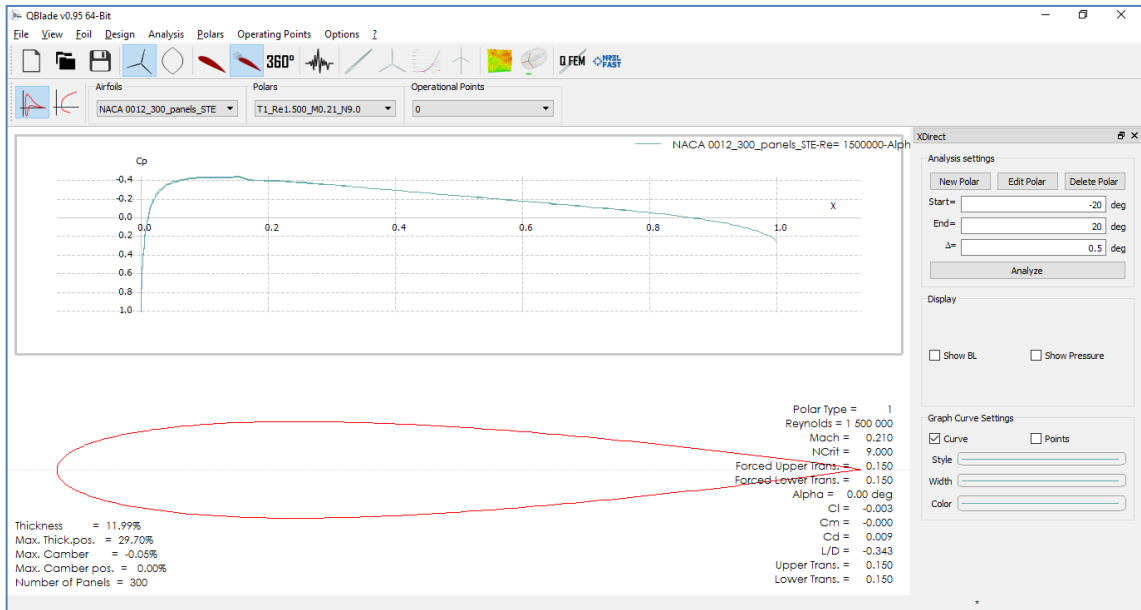


Figure 4-6 – Input/output screen for the flow analysis of XFOIL/XFLR5. The angles and steps are selected at the right hand upper screen windows and the Euler number is plotted over the airfoil chord at the upper screen. At the lower screen, the profile is visible.

Step 2

- Click in the NOISE module icon (indicated by the red arrow in Figure 4-7), to open the TE noise module:

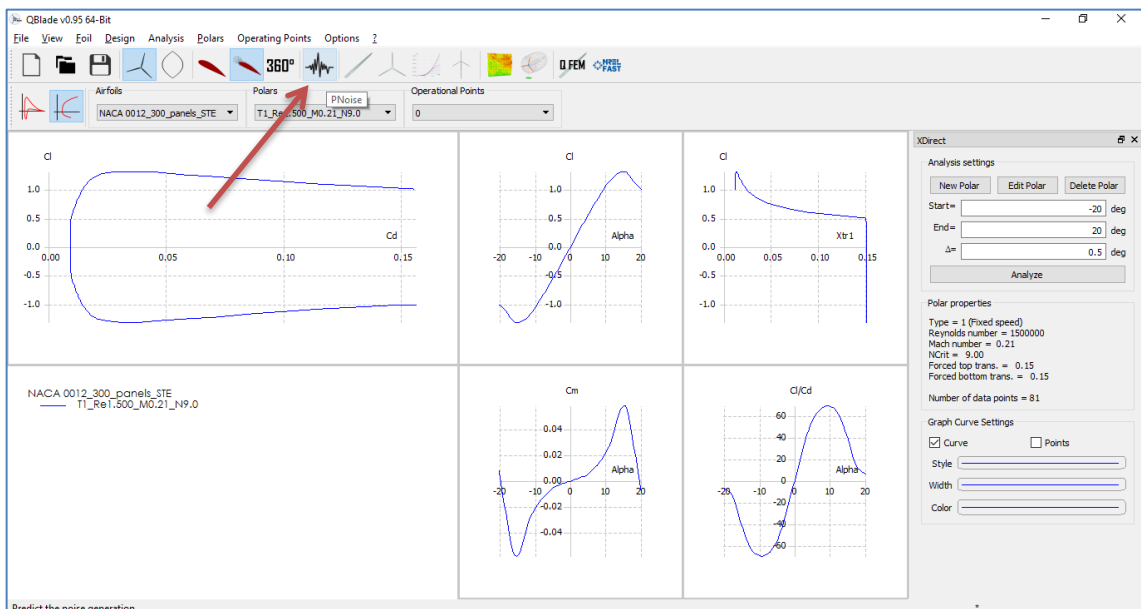


Figure 4-7 – This is the second output screen of the XFOIL/XFLR5 module, where the resulting polar diagram and other aerodynamic data may be verified. By selecting the indicated NOISE icon (red arrow), the code switches to the 2D TE noise module.

Step 3

- For important information on the model and the validity range, the user should check the “?” menu, option “About PNoise” and also “Noise Simulation” menu, option “Model Validity Hint” as shown in Figure 4-8 and Figure 4-9.

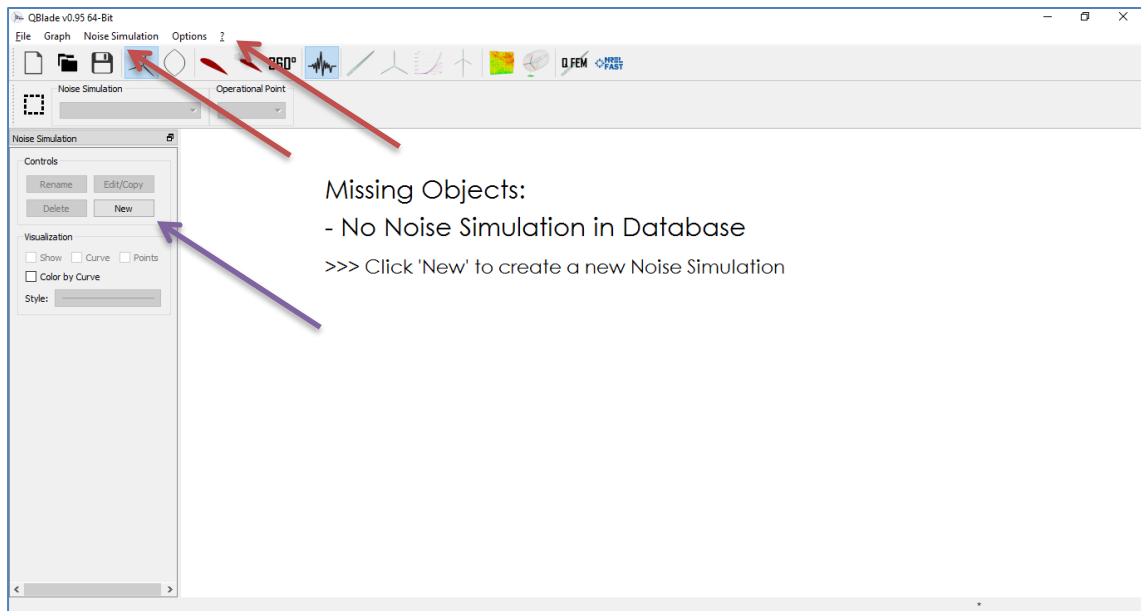


Figure 4-8 – Information resources for the user on the TE noise module are provided at the “?” menu, in “About Pnoise” option, and also in the “Noise Simulation” menu, option “Model Validity Hint”.

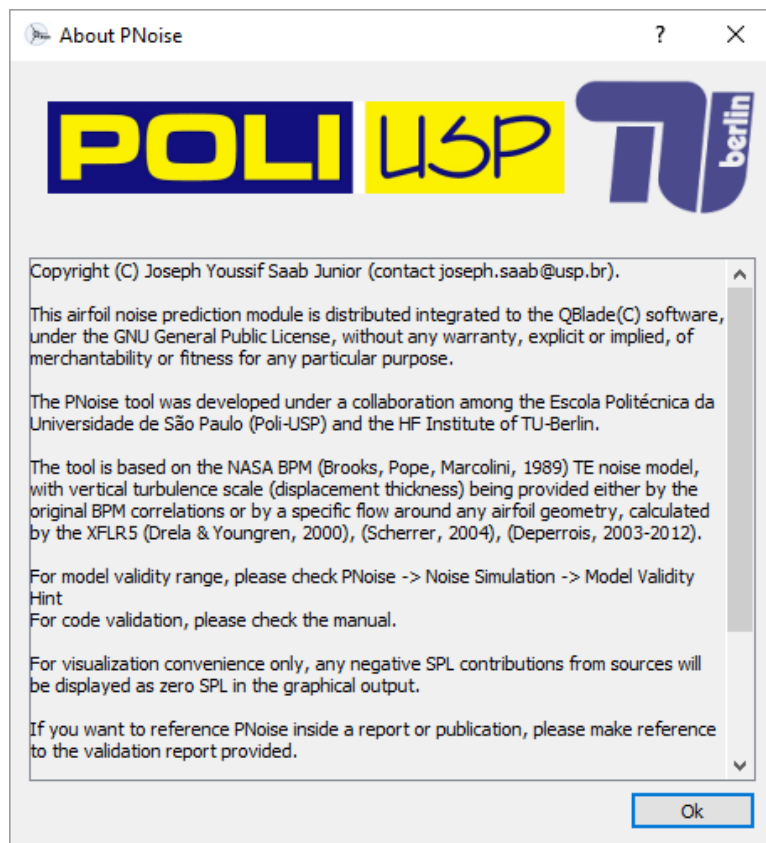


Figure 4-9 – Module copyright, General Public Licensing notices and references are available to the user.

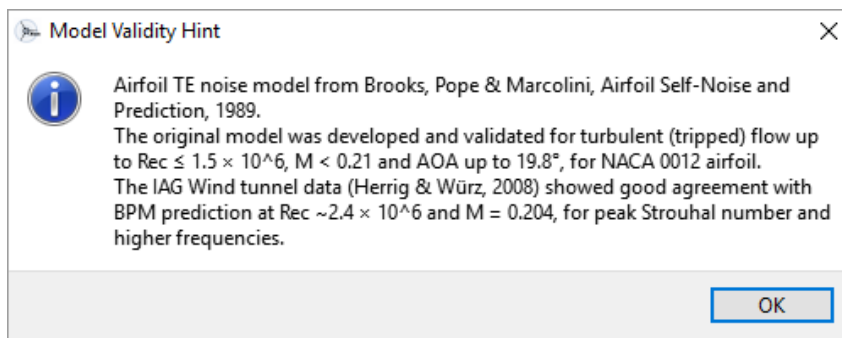


Figure 4-10 – Original (unmodified) Model validity is provided to the user.

- The user should read it carefully and review the definition of PREDICTION presented earlier. The result of any prediction should be declared alongside the limitations of the model employed.

Step 4

- Click the NEW simulation button shown by the blue arrow in Figure 4-8.

- The input screen, shown in Figure 4-11, will appear. The screen shows the input data that must be completed prior to any airfoil TE noise simulation.

2D Noise Simulation

Parameters Op. Points

Simulation Parameters

Name of Simulation:

Length of wetted Trailing-Edge (L) [m]:

Distance from observer to TE (re) [m]:

Original flow velocity (U) [m/s]:

Original airfoil Chord length (C) [m]:

Original flow Mach Number (M):

D* at chord station:

D* scaling factor:

Eddy Convection Mach number [%]:

Directivity angle θ_e [deg]:

Directivity angle ψ_e [deg]:

TE noise source contributions

Separated flow on the suction side (high Reynolds flow): enable

Suction side of airfoil (attached flow): enable

Pressure side of airfoil (attached flow): enable

Cancel Create

Figure 4-11 - The input screen has two tabs. In the first one (shown) the airfoil geometric and flow information is input. Also the noise sources are selected and the directivity angles informed.

- The next step is to open the second tab **Op.Points** and select the model (modified or original BPM TE noise models) and the angle of attack for the calculation as shown in Figure 4-12.
- Any combination of AOAs may be selected for any Polars available in the database.

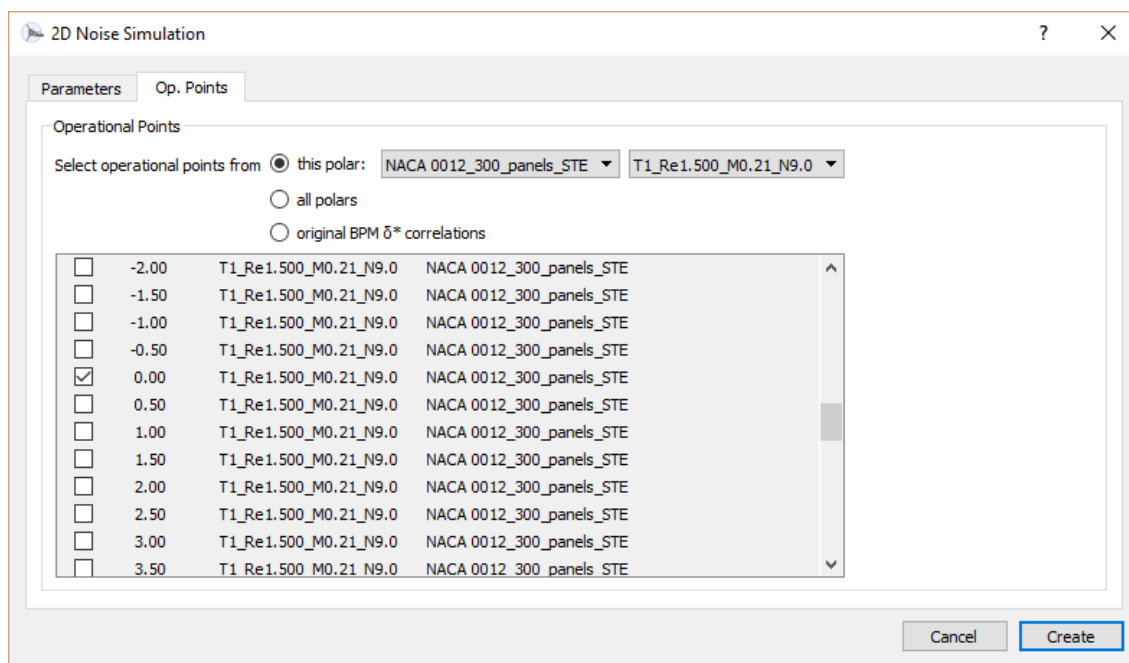


Figure 4-12 – In the second tab, any combination of AOAs may be selected for any Polars available in the database.

- The user may select more than one angle for direct comparison of results.
- Notice that the default option is to use boundary layer data (displacement thickness) calculated by the XFLR5, by selecting a specific airfoil + polar combination. The user should select the “**original BPM δ^* correlations**” option to run the unmodified BPM model.
- Click **Create**.

Step 5

- The individual contributions of each source and the total SPL are calculated and displayed in different quadrants of the screen, as seen in Figure 4-13.
- By right-mouse-clicking any of the graphs it is possible to choose the variables, scale, colors, etc, completely customizing the output screen.
- If many AOA are selected for the TE noise calculation, each different AOA is assigned automatically a different plot color.

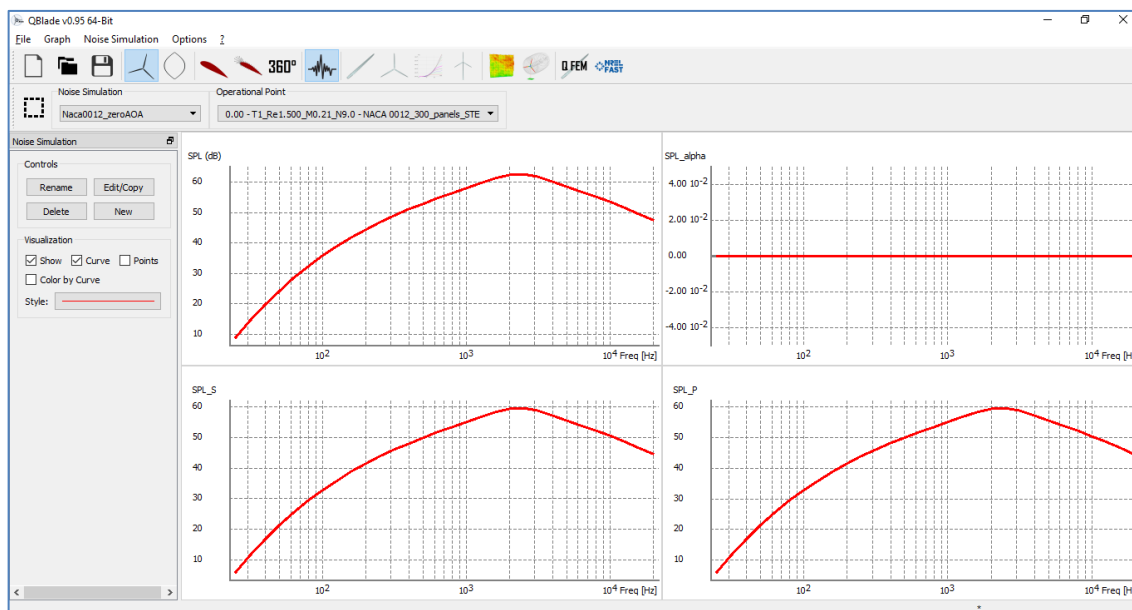


Figure 4-13 - individual contributions of each source and the total SPL are displayed in different quadrants of the screen. Upper LH: OASPL; Upper RH: SPL_alpha; Lower LH: SPL_S; Lower RH: SPL_P.

The original BPM model calculates the SPL_alpha contribution (unattached flow on the suction side) for zero AOA as a negative value. Since the negative values have no overall contribution to the OASPL and their absolute number is large, distorting the graph scale and making it difficult to read other curves (for other angles) in the same set of axis, it was decided that negative SPL contributions of the model would be plotted as zero values (see RH upper graph).

Also notice that, at zero AOA, the TE noise contributions should be the same for the pressure and the suction sides of the airfoil, which is confirmed above, and also, the logarithmic sum of two uncorrelated sources of the same strength should increase the total SPL by 3 dB, which can also be visually verified above and numerically confirmed in the “save to file” output option described next.

STEP 6

- The TE noise overall data may be saved to file by selecting the “Noise Simulation” menu, “Export Current Noise Simulation” option, as seen in Table 4-4.

Table 4-4 – Sample of file output for the NACA0012 at zero AOA, with overall noise levels (weighted and unweighted) plus one third octave spectra weighted and unweighted.

Noise prediction file export

Alpha: 0.00, Re = 1500000
 OASPL: 70.82949 dB
 OASPL (A): 71.35975 dB(A)
 OASPL (B): 70.30961 dB(B)
 OASPL (C): 70.26860 dB(C)
 SPL_a: -931.90020
 SPL_s: 67.80969
 SPL_p: 67.82868

Freq [Hz]	SPL (dB)	SPLa	SPLs	SPLp	SPL (dB(A))	SPL (dB(B))	SPL (dB(C))
25		8.81529	-1456.96154	5.74057	5.86847	-35.88471	-11.58471
31.5	14.32465	-1380.62597	11.25446	11.37343	-25.07535	-2.77535	11.32465
40	19.53943	-1310.34594	16.47362	16.58393	-15.06057	5.33943	17.53943
50	23.99696	-1252.14763	20.93499	21.03772	-6.20304	12.39696	22.69696
63	28.22047	-1198.97585	25.16220	25.25762	2.02047	18.92047	27.42047
80	32.19540	-1151.09917	29.14067	29.22908	9.69540	24.79540	31.69540
100	35.57681	-1112.41303	32.52512	32.60752	16.47681	29.97681	35.27681
125	38.66414	-1079.10545	35.61523	35.69210	22.56414	34.46414	38.46414
160	41.76772	-1047.99372	38.72160	38.79294	28.36772	38.76772	41.66772
200	44.31901	-1024.57624	41.27514	41.34202	33.41901	42.31901	44.31901
250	46.65542	-1005.17122	43.61354	43.67646	38.05542	45.35542	46.65542
315	48.87591	-988.83409	45.83584	45.89517	42.27591	48.07591	48.87591
400	50.98772	-975.45574	47.94923	48.00542	46.18772	50.48772	50.98772
500	52.81920	-965.70980	49.78193	49.83571	49.61920	52.51920	52.81920
630	54.60024	-957.93649	51.56396	51.61577	52.70024	54.50024	54.60024
800	56.34709	-951.87004	53.31155	53.36189	55.54709	56.34709	56.34709
1000	57.91968	-947.53966	54.88456	54.93405	57.91968	57.91968	57.91968
1250	59.46311	-944.04976	56.42812	56.47737	60.06311	59.46311	59.46311
1600	61.16785	-942.92492	58.13285	58.18210	62.16785	61.16785	61.06785
2000	62.42217	-937.87515	59.39535	59.42832	63.62217	62.32217	62.22217
2500	62.60944	-937.45596	59.59281	59.60545	63.90944	62.40944	62.30944
3150	61.67233	-940.11304	58.66764	58.65642	62.87233	61.27233	61.17233
4000	60.02262	-942.84396	57.01793	57.00671	61.02262	59.32262	59.22262
5000	58.48165	-946.12855	55.47698	55.46572	58.98165	57.28165	57.18165
6300	56.86691	-950.24452	53.86259	53.85061	56.76691	54.96691	54.86691
8000	55.14318	-955.77619	52.13951	52.12623	54.04318	52.24318	52.14318
10000	53.45559	-962.58736	50.45279	50.43778	50.95559	49.15559	49.05559
12500	51.66706	-971.43678	48.66537	48.64814	47.36706	45.56706	45.46706
16000	49.54008	-984.13200	46.53991	46.51963	42.94008	41.14008	41.04008
20000	47.45553	-998.71325	44.45700	44.43343	38.15553	36.35553	36.25553

- Also, any of the individual plots may be exported by pressing RMC, “Export Graph” option over the selected graph.

4.3 VERIFICATION AND VALIDATION OF THE IMPLEMENTED METHOD.

This verification and validation procedure was accomplished in the PNoise module originally implemented in QBlade v0.8.

The first aim of the verification process was to make sure the modification to the XFOIL/XFLR5 did not cause any abnormalities in the core flow calculation routine. For that matter, a table was prepared with displacement thickness data from three different sources: the XFLR5 v6.01.01 standalone version; the XFLR5 version inside the QBlade before modification and, finally, the XFLR5 version inside the QBlade after modification.

Table 4-5 – XFLR5/XFOIL module calculation procedure verification table before and after modification.

Step 0 calculation procedure verification table					
Version	AOA	# of data points	D* at 1C, Upper	D* at 1C, Lower	symmetry
XFLR5 V6.01.01	0	188	0.00702	0,00702	Ok
	10	213	0.02470	0.00305	N/A
	20	220	0.29521	0.00152	N/A
Qblade Baseline V0.8	0	188	0.00701	0.00704	acceptable
	10	213	0.02459	0.00305	N/A
	20	220	0.29403	0.00152	N/A
Qblade Modified	0	188	0.00701	0.00704	acceptable
	10	213	0.02459	0.00305	N/A
	20	220	0.29403	0.00152	N/A

N/A = non applicable

The results are shown in Table 4-5, where it is possible to see that the modification introduced to the code did not generate any abnormalities in the verified range.

The reference employed for the TE noise calculation was naturally Brooks et al. original BPM research (Brooks, Pope, & Marcolini, Airfoil Self-Noise and Prediction, 1989). The reference was used to provide baseline validation at different AOA and Reynolds number, for the NACA 0012 airfoil. However, the spectra measured are reported in graphical format, only, while the model returns SPL for each 1/3 octave frequency. So, the strategy adopted was to make the validation and verification

process of the coded modified-BPM model, in two phases. The first phase was the full implementation of the BPM TE noise model in a massive, controlled worksheet, in order to generate the graphical spectra necessary for validation against BPM graphs and also tabular spectra, for each 1/3 octave band, for each noise source, for further comparison with PNoise output.

The first phase included the validation of the code (Oberkampff & Roy, 2012) and consisted of comparing the worksheet graphical spectra against original BPM charts, which includes experimental spectra plus calculated spectra. For the first phase, the original BPM-model displacement thickness correlations were fed into the spreadsheet.

The second phase was considered a verification of the calculation procedure and consisted of comparing individual 1/3 octave frequency levels of the spreadsheet against the code output, plus overall sound pressure levels. For the second phase, the displacement thickness was evaluated by the XFLR5 at station 0.98C for all cases.

The validation spreadsheet SPL graphs were calculated and saved for the following three cases for phase 1 (validation):

- Zero AOA flow, tripped BL.
- Flow below the switching angle (4°), tripped BL.
- Flow above the switching angle (17.4°), tripped BL.

Notice: Switching angle calculated for the case was 9.56° .

4.3.1 – Validation of the spectral output.

The validation of the spectra generated by the auxiliary spreadsheet against original BPM output graphs and measured spectra is shown in Figure 4-14, Figure 4-15 and Figure 4-16. The spectral peak, frequency and roll-off rate may be directly compared for each case.

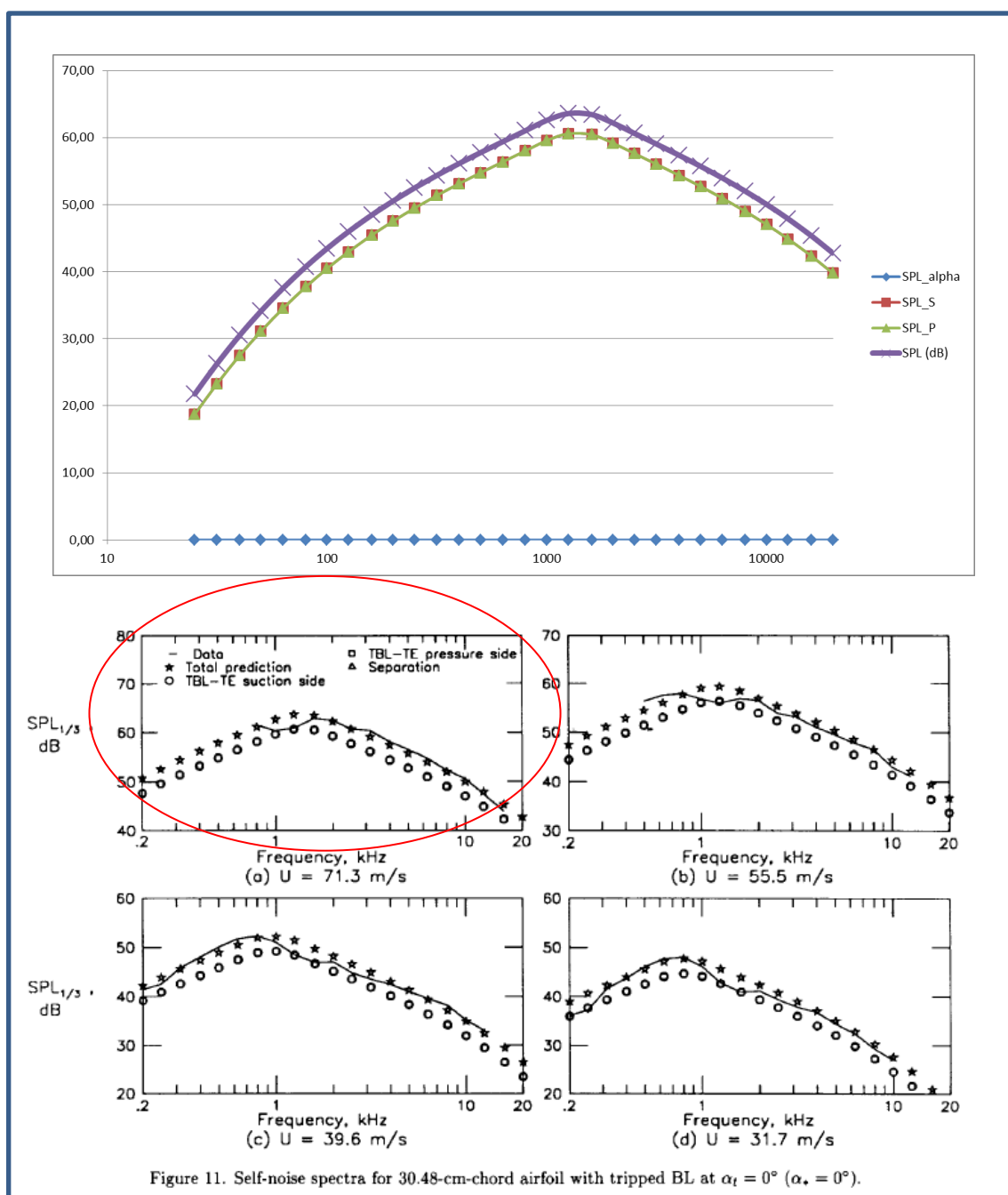


Figure 4-14 - For zero AOA flow and same conditions as in Fig. 11, item (a) of BPM paper: The upper graph is the spreadsheet output and it must be compared with the indicated calculated and measured spectra on the lower portion of the figure. Vertical axis=SPL (dB); Horizontal axis = Frequency (Hz), for all charts.

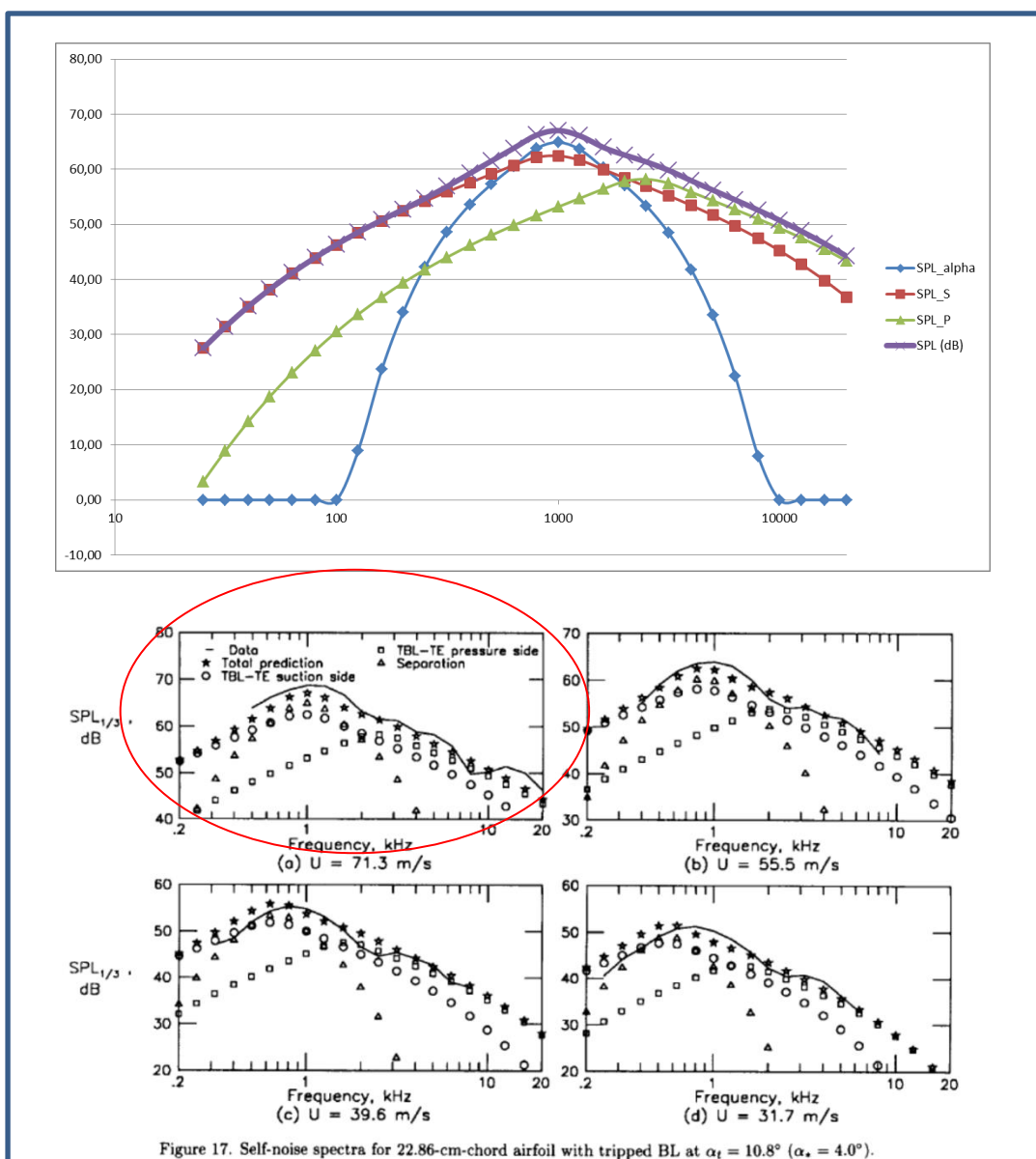


Figure 4-15 - For AOA=4° (below switching angle) flow and same conditions as in Fig. 17, item (a) of BPM paper. The upper graph is the spreadsheet output and it must be compared with the indicated calculated and measured spectra on the lower portion of the figure. Vertical axis=SPL(dB); Horizontal axis = Frequency (Hz), for all charts

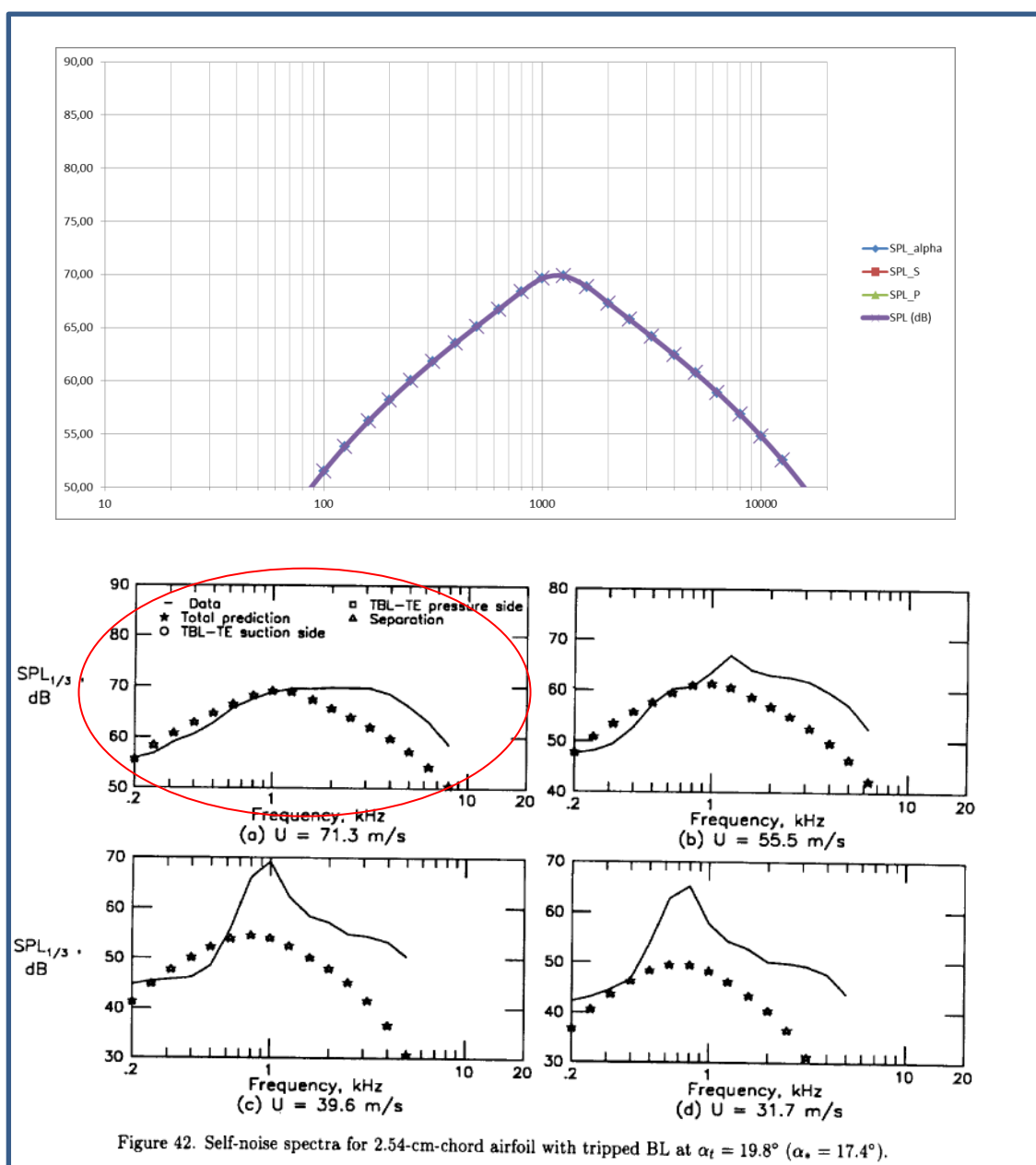


Figure 4-16 - For AOA=17,4° (above switching angle) flow and same conditions as in Fig. 42, item (a) of BPM paper. The upper graph is the spreadsheet output and it must be compared with the indicated calculated and measured spectra on the lower portion of the figure. Vertical axis=SPL (dB); Horizontal axis = Frequency (Hz), for all charts

4.3.2 – Verification of the calculation procedure.

After applying modifications to XFLR5 output, coding the new module and integrating all the structures of the code, the process of verifying the calculation procedure was initiated.

This phase turned out to be very extensive and the step-by-step procedure followed may be found in Appendix I, with summary tables only shown in this section.

4.3.2.1 – Verification of the calculation procedure for zero AOA, with flow data from XFLR5.

The first verification process was accomplished for the zero AOA and flow conditions found in Figure 11 of the original BPM paper:

- NACA 0012, Sharp Trailing Edge.
- Reynolds: 1,500,000
- Mach: 0.21
- Chord: 0.3048 m
- Wetted TE span: 0.4572 m

The verification tables were assembled with selected frequencies, including the peak frequency, for all considered sources and the displacement thickness for each flow was evaluated at 0.98C by the XFLR5.

Table 4-6 – Verification table for the TE noise predicted for the zero AOA flow over the NACA 0012 airfoil.

Frequency (Hz)	Source	SPL_alpha (dB)	SPL_S (dB)	SPL_P (dB)	SPL (dB)	Diff.(dB)
50	Spreadsheet	-1252.39	19.76	19.88	22.83	-0.07
	Code	-1251.97	19.84	19.95	22.90	
1,000	Spreadsheet	-948.72	53.66	53.72	56.70	-0.06
	Code	-948.65	53.72	53.77	56.76	
2,500	Spreadsheet	-938.72	58.34	58.35	61.35	-0.05
	Code	-938.68	58.38	58.39	61.40	

From Table 4-6, it may be seen that the result is acceptable, with differences between the code and the validated spreadsheet much less than 1 dB. Also, the difference improves (reduces) toward the peak frequency of 2,500 Hz.

These differences were attributed to numerical error accumulation due to different numerical precision used in the spreadsheet and in the C++ code.

Also the OASPL is 69.6 dB for the spreadsheet and 69.6 dB for the Code.

Thus the SPL and peak frequency for zero AOA is very good. The source selection combination was also tested (for zero and other AOA) and worked as expected.

The validation process will now be expanded to include AOA other than zero (both below and above the switching angle), and with displacement thicknesses provided by both the XFOIL embedded inside QBlade and by the original BPM correlations.

4.3.2.2 – Verification of the calculation procedure for AOA other than zero, with flow data from XFLR5.

Since the model has different calculation procedures for AOA below and above the “switching angle”, estimated for the Reynolds of 1,120 Million to be at 9.5°, one test was chosen to be made below the switching angle (4°) and the other above it (12.5°).

The 17.4° AOA condition employed earlier in the first phase (validation) could not be used in this case because there was no numerical convergence for the NACA 0012 airfoil at this high AOA, for this Reynolds number, with the XFLR5. In fact, this is above the stalled angle of the airfoil.

4.3.2.2.1 – Verification for AOA below the switching angle.

For AOA other than zero, the noise contributions for the pressure and suction sides are now different. The result is again good and improves toward the peak frequency of 2,000 Hz, as shown in Table 4-7.

Table 4-7 - Verification table for the TE noise predicted for the 4° AOA flow over the NACA 0012 airfoil.

Frequency (Hz)	Source	SPL_alpha (dB)	SPL_S (dB)	SPL_P (dB)	SPL (dB)	Diff.(dB)
50	Spreadsheet	-240.96	22.05	5.73	22.15	-0.07
	Code	-240.61	22.12	5.79	22.22	
1,000	Spreadsheet	52.09	54.88	47.16	57.17	-0.06
	Code	52.16	54.93	47.21	57.23	
2,000	Spreadsheet	61.10	58.95	52.13	63.55	-0.05
	Code	61.24	58.99	52.18	63.60	

Also the OASPL is 71.1 dB for the spreadsheet and 71.0 dB for the code or a 0.1 dB difference.

The next natural step was to verify whether the result was symmetric for a negative AOA angle (-4°).

In negative AOA, the upper surface, initially a suction side, becomes a pressure side and the lower surface, initially a pressure side, becomes a suction side. Since the output graphs of the code are named for the “pressure” and “suction” sides, not for “upper” and “lower” sides of the airfoil, the output does not change position in the output screen.

However, the reading of the displacement thickness calculated by the XFLR5 was correctly accomplished and the calculations have been done correctly, except per minor numerical asymmetry, as shown in Table 4-8.

Table 4-8 – Verification of SPL contributions for symmetrical AOA.

+4 AOA				
Freq [Hz]	SPL (dB)	SPLa	SPLs	SPLp
50	22.2248	-240.606	22.1248	5.7984
1000	57.2304	52.158	54.9347	47.2122
2000	63.5957	61.241	58.9912	52.1776
-4 AOA				
Freq [Hz]	SPL (dB)	SPLa	SPLs	SPLp
50	22.3387	-239.304	22.2442	5.6642
1000	57.2947	52.2691	54.9951	47.1504
2000	63.6285	61.2871	59.0207	52.1189

By comparing the OASPL for the symmetrical cases, the OASPL for + 4 AOA resulted in 71.0019 dB, while for -4 AOA, the result was 71.0171 dB.

4.3.2.2 – Verification for AOA above the switching angle.

For angles above the switching angle, like the current one ($12.5^\circ > 9.5^\circ$), the SPL_alpha should be the sole contributor for the TE NOISE, which is exactly the behavior displayed in Table 4-9.

Table 4-9 – Verification data for the 12.5° AOA calculation.

Frequency (Hz)	Source	SPL_alpha (dB)	SPL_S (dB)	SPL_P (dB)	SPL (dB)	Diff.(dB)
50	Spreadsheet	2.03	$-\infty$	$-\infty$	2.03	-0.11
	Code	2.14	0	0	2.14	
1,000	Spreadsheet	57.77	$-\infty$	$-\infty$	57.77	-0.09
	Code	57.86	0	0	57.86	
8,000	Spreadsheet	72.96	$-\infty$	$-\infty$	72.96	-0.07
	Code	73.03	0	0	73.03	

Once again, the numbers were very close and the accuracy improved towards the peak frequency.

4.3.2.3 – Verification of the calculation procedure for zero AOA, with the original BPM correlations.

The same three cases were analyzed in order to verify the calculation procedure for the cases when the original BPM-model displacement thickness correlations were employed: $AOA=0^\circ$, $AOA=4^\circ$, $AOA=12,5^\circ$, with further testing for negative AOA and any combination of source selection.

Table 4-10 - Verification data for the 0° AOA calculation, with original BPM correlations for the displacement thickness.

Frequency (Hz)	Source	SPL_alpha (dB)	SPL_S (dB)	SPL_P (dB)	SPL (dB)	Diff.(dB)
50	SpreadSheet	-1138.39	31.19	31.19	34.20	-0.07
	Code	-1138.14	31.26	31.26	34.27	
1,000	Spreadsheet	-938.72	59.63	59.63	62.64	-0.05
	Code	-939.47	59.68	59.68	62.69	
1,250	Spreadsheet	-936.48	60.61	60.61	63.62	-0.05
	Code	-936.43	60.65	60.65	63.67	

The results were in good agreement, as may be seen from Table 4-10, including the peak frequency of 1,250 Hz, which shifted in the fully turbulent flow, from the value previously calculated with the aid of XFLR5, for transition flow, when the peak was @ 1,500 Hz.

Also all the SPL values (weighted and unweighted) showed excellent agreement to the second decimal dB position. The OASPL was: 71.9 dB for the spreadsheet and 71.9 dB for the code calculation.

4.3.2.4 – Verification of the calculation procedure for AOA other than zero, with the original BPM correlations.

The comparison yielded good results, as may be seen from Table 4-11, for both SPL and for the peak frequency of 1,000 Hz.

Table 4-11 - Verification data for the 4° AOA calculation, with original BPM correlations for the displacement thickness

Frequency (Hz)	Source	SPL_alpha (dB)	SPL_S (dB)	SPL_P (dB)	SPL (dB)	Diff.(dB)
50	Spreadsheet	-85.55	38.20	18.76	38.25	-0.06
	Code	-85.33	38.26	18.83	38.31	
1,000	Spreadsheet	64.90	62.44	53.18	67.03	-0.05
	Code	64.94	62.49	53.23	67.08	
1,600	Spreadsheet	60.26	59.97	56.43	63.97	-0.04
	Code	60.29	60.01	56.48	64.01	

Also all the SPL values (weighted and unweighted) showed good agreement, usually to the first decimal dB position. The OASPL was: 74.4 dB for the spreadsheet and 74.5 dB for the code calculation.

Table 4-12 - Verification data for the 12.5° AOA calculation, with original BPM correlations for the displacement thickness

Frequency (Hz)	Source	SPL_alpha (dB)	SPL_S (dB)	SPL_P (dB)	SPL (dB)	Diff.(dB)
50	Spreadsheet	48.75	-∞	-∞	48.75	0.00
	Code	48.75	0	0	48.75	
1.000	Spreadsheet	78.41	-∞	-∞	78.41	-0.03
	Code	78.44	0	0	78.44	
1.600	Spreadsheet	80.42	-∞	-∞	80.42	-0.05
	Code	80.47	0	0	80.47	

The results for the AOA above the switching angle, as shown by Table 4-12 were also in good agreement, including the prediction of the peak frequency of 1,600 Hz.

The OASPL was also consistent: 88.6 dB for the spreadsheet and 88.6 dB for the code calculation.

4.4 ATTEMPT TO EXTEND THE VALIDATION OF THE MODIFIED-BPM TE NOISE MODEL FOR HIGHER REYNOLDS NUMBERS AND GENERIC AIRFOIL GEOMETRY.

From the results of Section 4.1, the Reynolds and Mach numbers of interest for the 50 m length blades WT should be, based on the POLI-100 Blade and operating conditions:

Specific conditions at the major TE noise source station (85% blade radius):

- Reynolds number of 7.7 million.
- Mach number of 0.21.

General conditions from 55% to 90% blade radius:

- Reynolds number range from 7 to 9 million.
- Mach number range from 0.14 to 0.22.

Although the Mach number range of interest is within BPM TE noise model original validation work, the range of Reynolds numbers of interest is beyond existing validation as well as the airfoil geometry.

If an extension of the validation process could be accomplished for the implemented modified-BPM method into the Reynolds number range needed and other geometries, the OASPL and TE noise spectra predicted from the model might be considered as an acceptable indication of the absolute value of the overall noise level and associated spectrum. However, as discussed in the bibliographical review, the model was developed after NACA 0012 airfoil aeroacoustic data for Reynolds numbers up to 3 Million (Brooks, Pope, & Marcolini, *Airfoil Self-Noise and Prediction*, 1989), p. 1, and the authors considered that the predictions compared successfully with published experimental data for NACA 0012 and a Sikorsky helicopter airfoil for Reynolds numbers up to 4.6 million (Brooks, Pope, & Marcolini, *Airfoil Self-Noise and Prediction*, 1989), p.83-98.

However, most of the original data over which the TE model was developed, were for flows with associated Reynolds numbers of up to 2.1 million and the Sikorsky helicopter

profile has a small camber and thickness when compared to the NREL “S” Series airfoils and other airfoils designed for wind turbines.

Since the report of Devenport et al. (Devenport W. , et al., 2010) had made public experimental airfoil self-noise measurements for both the NACA 0012 and other airfoils with significant camber, at higher Reynolds numbers, this was considered as a valuable opportunity from which to expand the modified-BPM model validation range.

The gradual steps for the planned validation extension were:

- NACA 0012 untripped flow, at higher Reynolds numbers at zero and moderate AOA.
- NACA 0012 tripped flow, at higher Reynolds numbers at zero and moderate AOA.
- Other airfoil geometry, at higher Reynolds numbers and zero to moderate AOA.

The experimental data from Devenport et at. (Devenport W. , et al., 2010), was obtained at the Virginia Tech (VT) Aeroacoustic Tunnel. Among the airfoil profiles tested (NACA 0012, RISO B1-18, DU-96 and S831), the NACA 0012 and the S831 were selected for “out of initial scope” validation study. Although the RISO B1-18 profile would be the preferred choice for validation, due to its design chord-Reynolds number of 6 million, only airfoils with known profiles could be used for the XFLR5 TBL simulation step that feeds the modified-BPM TE noise prediction model implemented.

Figure 4-17 shows a very limited data overlap among the BPM (Brooks, Pope, & Marcolini, Airfoil Self-Noise and Prediction, 1989) and the Virginia Tech wind tunnel data, for a Reynolds number (of 620,000) within the original validation scope of the BPM TE noise model. However, the authors (Devenport W. , et al., 2010) considered the results to be “*in good agreement in the 1,000 Hz to 4,000 Hz range*”, even though differences of approximately 10 dB may be seen in the figure close to 1,000 Hz.

Differences in measurements were attributed to the use of different wind tunnel test facilities and different methods to compute the airfoil self-noise, but were considered acceptable by the authors for a first validation of the facility.

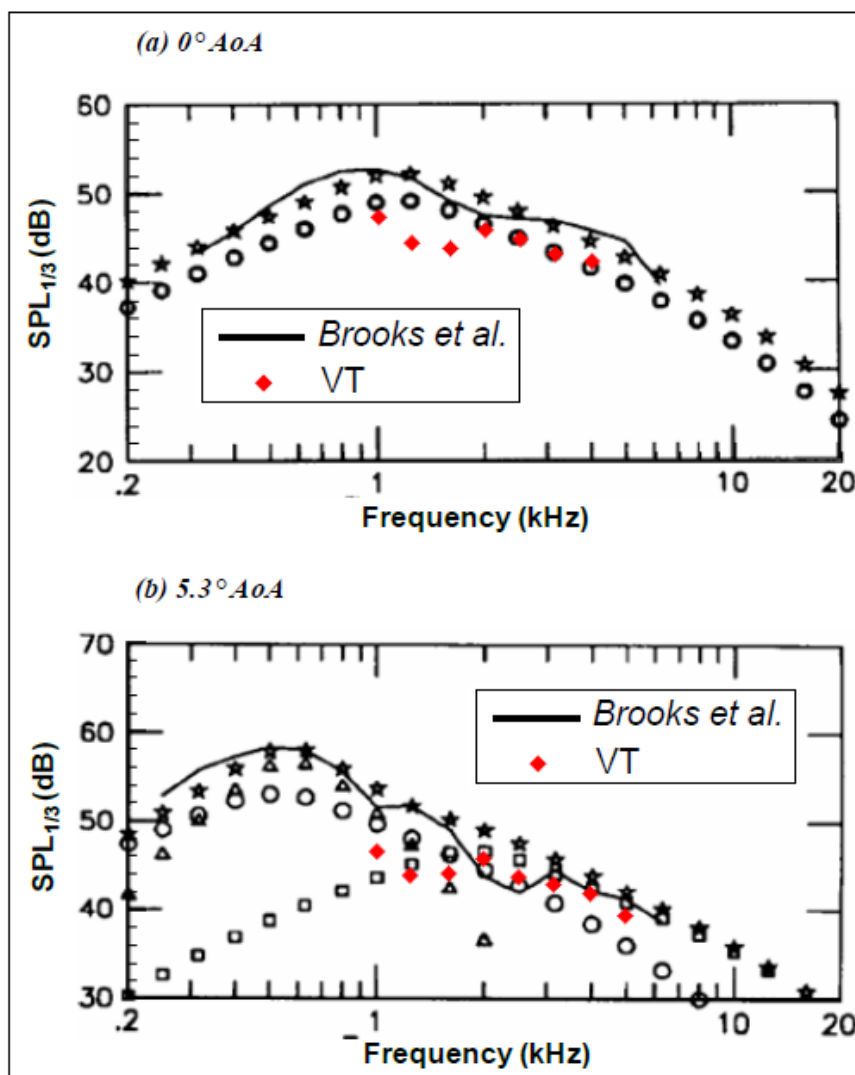


Figure 4-17 – Initial data validation for the Virginia Tech (red dots) measurements, against BPM measurements (black lines) and BPM model calculations (black stars). $Re_c \approx 620,000$. Upper plot: zero AOA. Lower plot: 5.3° AOA. Source: (Devenport W. , et al., 2010), p.180.

Unfortunately, this dataset was the only one available with aeroacoustic measurements for the NACA 0012 airfoils and other geometries, at Reynolds numbers closer to the real interest range. Concerning the need for further experimental data for self-noise model validation, see Doolan and Moreau (Doolan & Moreau, 2013).

In the next subsections, spectra derived from Virginia Tech (VT) measurements (Devenport W. , et al., 2010) were tentatively used as references against which TE noise spectra predicted by the modified-BPM TE model were compared to, for Reynolds number ranges and/or geometries beyond those employed in the original BPM method validation process.

Relevant to all calculations accomplished are the following parameters from the VT experimental research:

- All airfoils tested had a 0.914 m chord.
- All airfoils tested had a 1.8 m span, however, as described in the paragraph 4.3 of Devenport et al (Devenport W. , et al., 2010)., the TE noise of the tip sections of the model airfoils was removed from the integration area, leaving only the inner 2/3 of the span accountable at the microphone array positions (rendering an effective span of 1.2 m).
- The microphone array centers were always at 3.0 m perpendicular distance to the airfoil center of rotation as per drawing in figure 23, page 29 of the reference.
- All measured spectra are un-weighted.
- All measured spectra are for all airfoil self-noise sources, except per Figure 4-17, which is TE noise only.

4.4.1 Naca 0012 airfoil, untripped flow for higher Reynolds numbers at zero to moderate AOA.

The modified-BPM model TE calculations were accomplished with chord based Reynolds number of 3.2 million, untripped flow, and Mach number of 0.16⁵⁴, or 54 m/s. The same airfoil geometry definition file used in previous validation work was employed (NACA 0012, refined, with sharp trailing-edge).

A typical input screen of the PNoise in QBlade v0.8 is seen in figure Figure 4-18.

⁵⁴ Since many wind-tunnel entries were accomplished in the original experiment, each one with a different tunnel temperature, the Mach number employed in the simulations were approximated with sea-level, standard atmosphere conditions (i.e. 288,15 K).

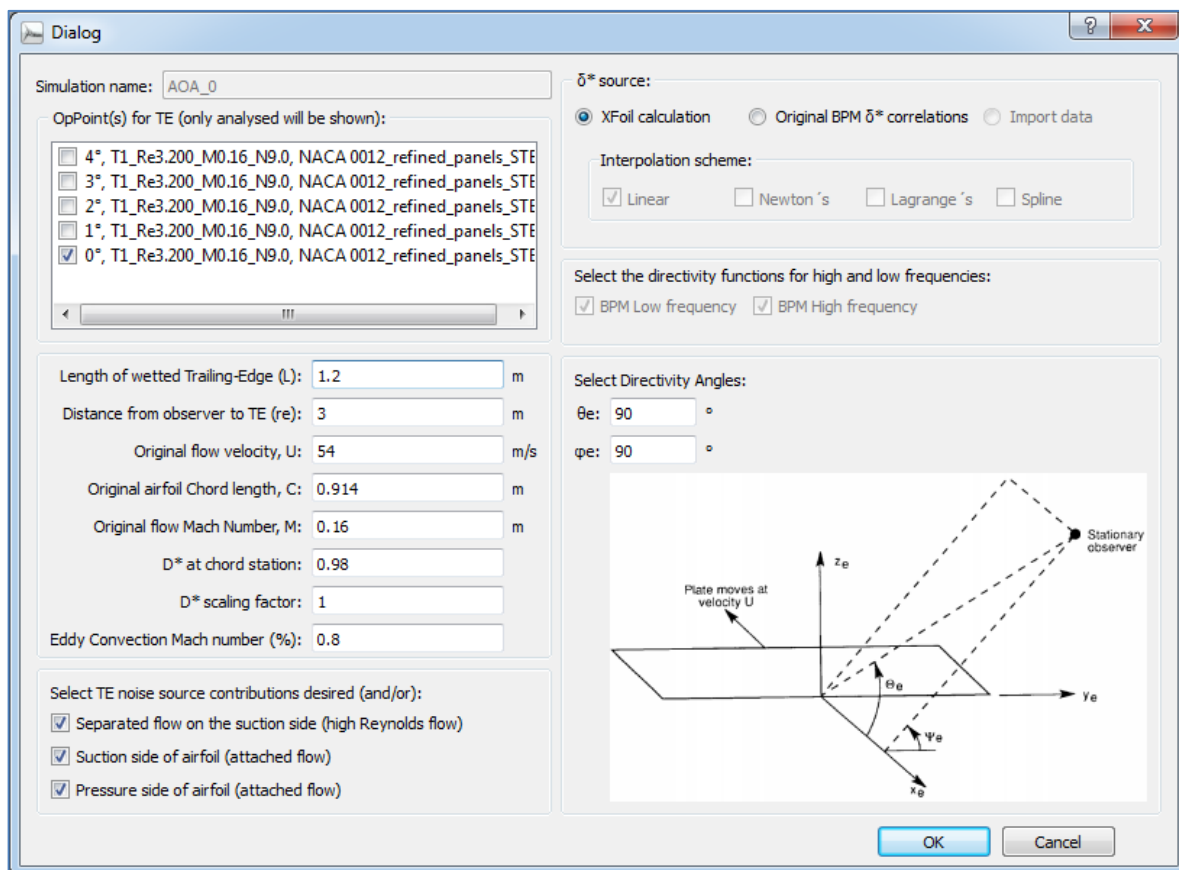


Figure 4-18 – PNoise inside Qblade v0.8, typical input screen for the validation attempt at higher Reynolds numbers and zero AOA.

The SPL at 1,000 Hz predicted by the BPM model is close to 55 dB, as seen in Figure 4-19, while the VT results show a value closer to 43 dB, as seen in Figure 4-20. This 12 dB overprediction of the modified-BPM model when compared to the VT data is about the same shown in Figure 4-17 among the original BPM WT data and the VT data.



Figure 4-19 - PNoise inside QBlade v0.8, typical output screen for the validation attempt at higher Reynolds numbers and zero AOA. Lower, RH plot highlight is the resultant Sound Pressure Level (from both sources) at the 1,000 Hz band region.

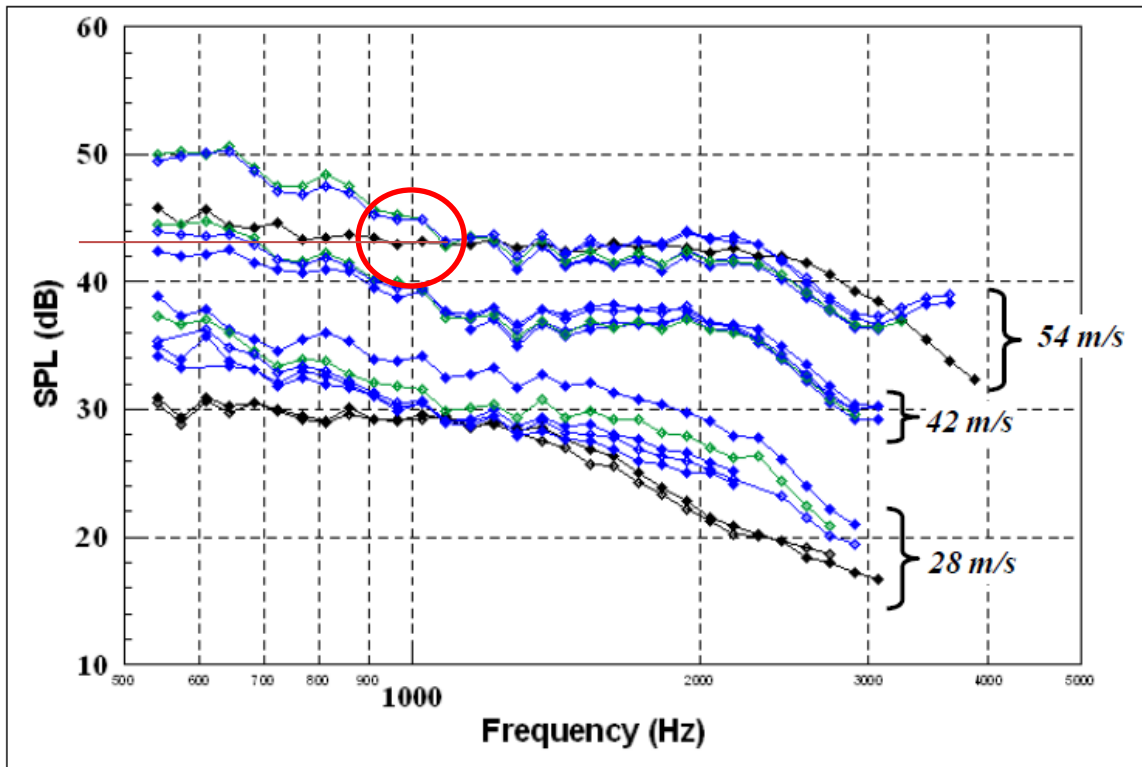


Figure 4-20 – Integrated spectrum for untripped NACA 0012 airfoil, at 0°, 2° and 4° for three different flow velocities for different wind tunnel data entries (different dates = different colors). (Devenport & Burdisso, Aeroacoustic Testing of Wind Turbine Airfoils, 2004), p. 189.

Figure 4-21 shows the calculated spectra in monolog scale for three different effective AOA, compared to a spectrum derived from measurements at VT. The experimental pressure levels for the three AOA tested are within the ± 2 dB thick line, plotted without access to tabular data, as a visual reference only. The differences in the 500 Hz to 5 kHz range from 6 dB to 12 dB excess noise prediction, showing poor numerical and geometrical validation. If the lowest frequency captured at VT also represented the peak of the full spectrum, then the peak frequency was suitably predicted by the modified BPM model. However, the level and the roll-off pattern are substantially different. Also, the VT noise data are for all self-noise sources together, while the Modified-BPM prediction is for TE noise only, which makes the difference in TE noise actually larger than shown and indicates that the relative disposition of the spectra to be unphysical in level terms.

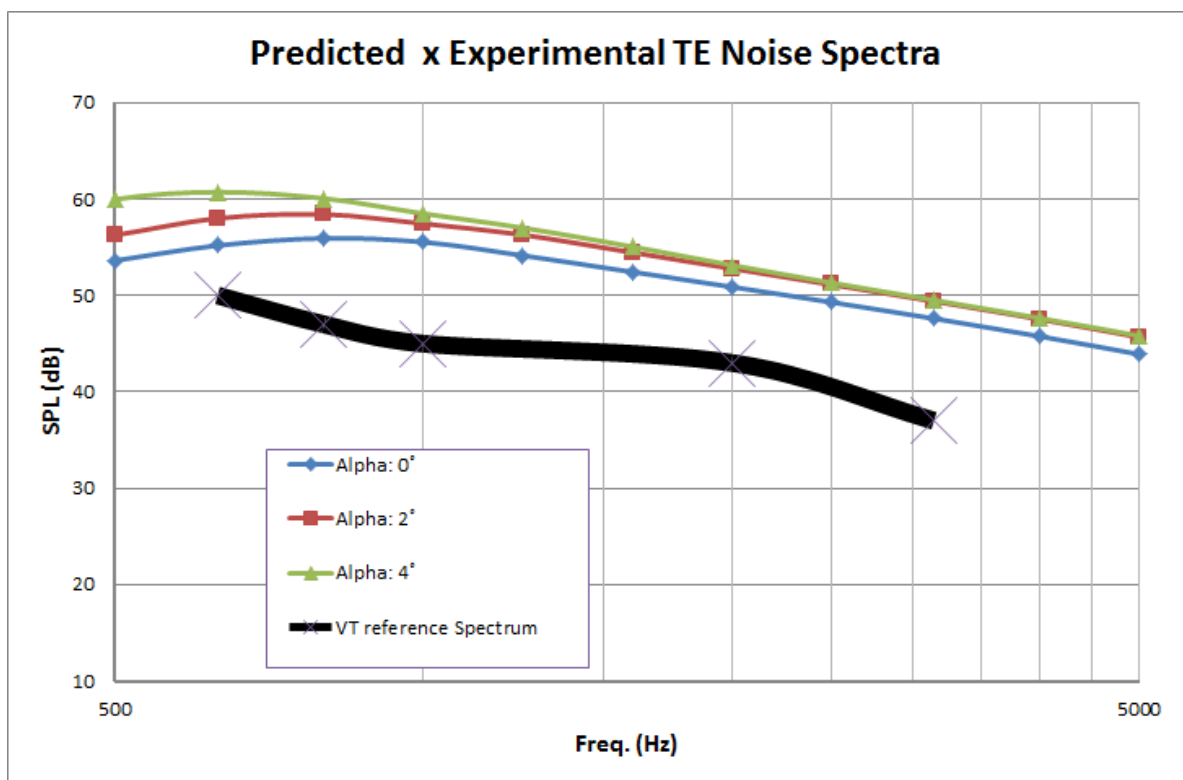


Figure 4-21 – Modified-BPM calculated spectra (color lines) for three different effective AOA, compared to VT data reference plot (thick, blackline).

4.4.1.1 Discussion on the differences found.

Differences in methodology of NASA and VT measurements were considered and some factors isolated, among which were the possible limitations on the VT data or report:

- i. Directivity function not properly considered, since the microphone array centerline was not located at 90° of the airfoil TE at mid span.
- ii. It was not clear from the report whether the measured spectrum was for one side only or both sides of the airfoil.

The geometry of the wind tunnel with the microphone array set up is depicted in Devenport et al. (Devenport W. , et al., 2010), p. 30, and allows the calculation of the θ_e directivity angle with relation to the center of the microphone array, which is 103.2° , instead of 90° used as default input in the previous modified-BPM model calculation. Also the corrected distance from the TE to the center of the array was found to be 3.08 m (as opposed to 3.00 m).

Recalculation process for the 0° AOA transition flow with these corrected conditions is illustrated in Figure 4-22.

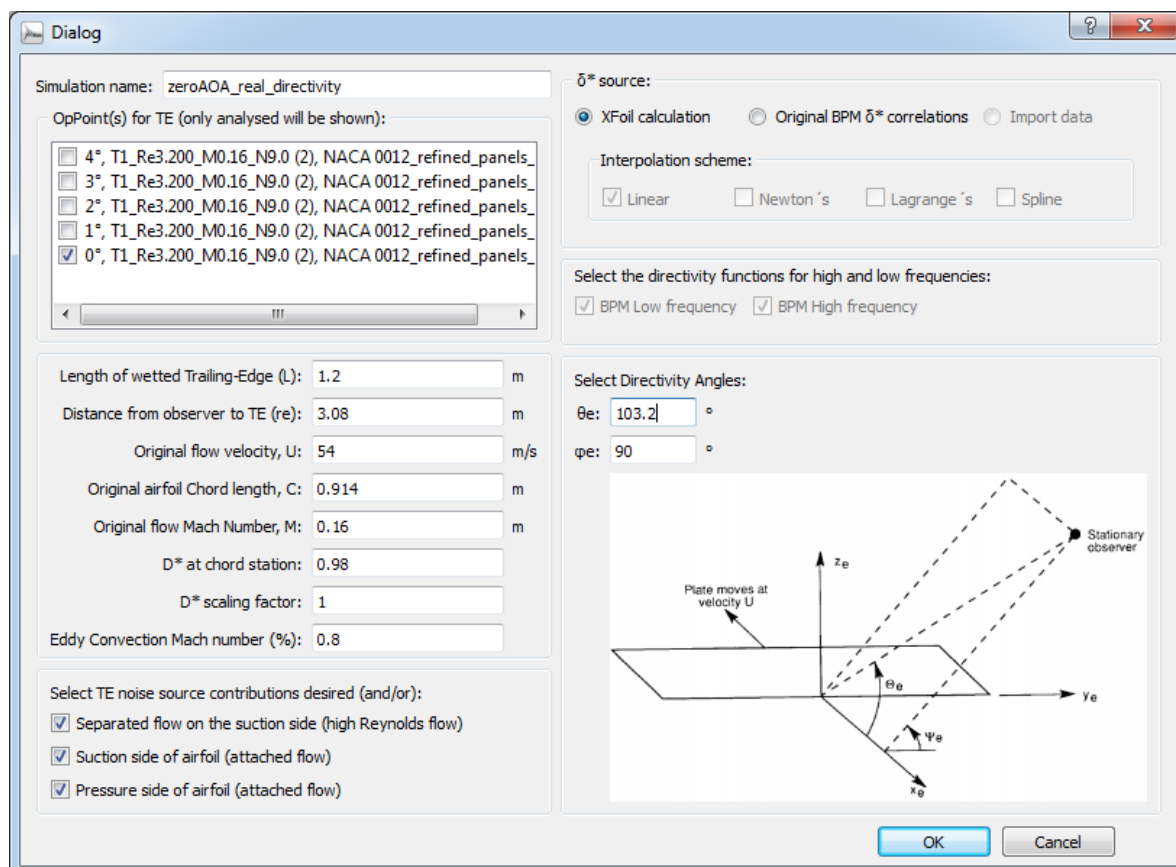


Figure 4-22 – Recalculation of the SPL for the transition flow at zero AOA, with corrected directivity and distance data.

Table 4-13 compares the 0° AOA results prior and after the directivity correction and shows that the OASP difference accounted for by the directivity angle and distance correction is less than 1 dB, for unweighted measurement.

Table 4-13 - Comparison of 0° AOA, transition flow results prior and after the directivity and distance adjustments.

Modified BPM TE Noise prediction file export		
Directivity Azimuthal Angle Θ_e :	Default (90°)	Corrected (103.2°)
Distance to central microphone (m)	3.0	3.08
Alpha and Reynolds	Alpha: 0, Re = $3.2e+06$	Alpha: 0, Re = $3.2e+06$
OASPL (dB)	64.115	64.941
OASPL (dB(A))	63.154	63.980
OASPL (dB(B))	63.782	64.609
OASPL (dB(C))	64.018	64.844

Considering the second possible source of error, if the microphone array measurement had been made for one side of the airfoil only (which is quite unlikely), for the zero AOA

case the result should have been increased by 3 dB, consistent with doubling the source level.

The evaluation attempt made above on these two possible (but not probable) sources of discrepancy between measured and calculated data could account for a maximum difference in OASPL of 4 dB and the same maximum amount on particular frequency bands and thus, would not explain the large excess noise prediction in the 500 Hz to 5 kHz bands displayed by the calculated values in Figure 4-21.

Additional explanations were sought after and considered for the differences:

- iii. The microphone matrix setup, where 63 electret microphones were arranged in a star or spiral pattern with 1.5 m external diameter, with individual microphones having distinct distances and directivity angles (azimuthal and elevation) to the source, and
- iv. There were microphone matrix resolution limitations combined with vortex shedding phenomena that prevented direct spectrum measurements in most cases:

“Data from the average spectrum proved useful only for the large chord NACA 0012 airfoil at an AOA greater than 4° and 28 m/s flow speed” (Deavenport W. , et al., 2010), p. 172. As a consequence, most 1/12 bands spectra displayed in the research, including those of higher Reynolds number selected for the attempted broadening of model validation in the present text, were numerically integrated from a volume enclosing part of the TE used for a beamforming integration process and not directly averaged from the microphone readings.

Also, for the cases of AOA other than 0° it was not clear how the differences had been measured and computed between the pressure and the suction side of the airfoil models, since the microphone matrix was always mounted to one side only of the discharge chamber at a time (spiral pattern used in the July, 2007 wind tunnel entries, mounted to the starboard side or left hand side when looking from the LE to the TE of the airfoil; star pattern used in the November-December, 2007 wind tunnel entries, mounted to the port side or right hand side when looking from the LE to the TE).

Based on (a) the described limitations of the experimental high Reynolds data obtained at Virginia Tech, (b) on the direct evidence provided by Figure 4-17, which showed levels of TE noise for the VT experiment to be much lower than the NASA data, and (c) on the capability demonstrated to identify the peak frequency, it was not possible to discard the hypothesis that the modified-BPM TE noise model might be suitable for

higher Reynolds numbers, although this hypothesis clearly needs further testing against one or more consistent data sets.

Before proceeding to compare the modified-BPM model predictions to other types of flows and geometries and based on the very limited success obtained this far, It was deemed useful⁵⁵ to determine what should be the fraction of the actual wetted TE length that would correspond to the calculations and would result in some overlap with the VT reference data.

After some trials with the model, the length of the wetted TE had to be severely reduced, from 1.2 m to 0.2 m, before the experimental and calculated spectra displayed some overlapping, as shown if Figure 4-23.

The reduction was found to be very severe and discarded as a possible additional source of significant discrepancy.

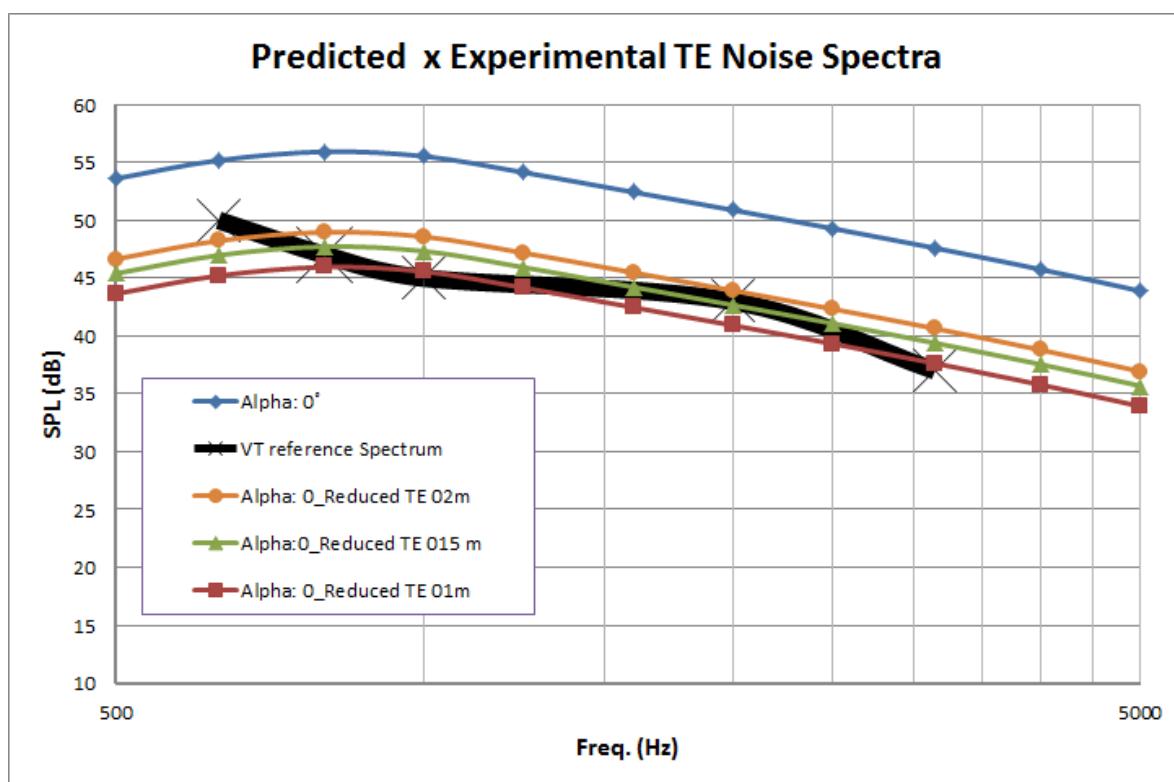


Figure 4-23 – VT data (black) versus predicted spectra. Overlap was forced by progressive reduction of the wetted TE length on the simulated blade segment.

⁵⁵ In order to confirm that the 1.2 m span was the correct fraction of the 1.8 m total span section to be considered as noise sources.

4.4.2 Naca 0012 tripped flow for higher Reynolds numbers at zero and moderate AOA.

In the VT wind tunnel, the BL tripping was accomplished with serrated (“*turbulator*”) adhesive tape in order to ensure a uniform transition station and a fully turbulent BL at the TE. The adhesive tape had a thickness of 0.5 mm and its width was 12 mm. The tape LE was applied at 5% chord at the suction side and 10% chord at the pressure side⁵⁶.

A second method employed was the spreading of silicon carbide particles (grit 60), applied randomly to a band extending to 50 mm beyond the LE, at both sides (total length of 100 mm), in order to simulate the soiling of the LE caused by insects and dirt during operation.

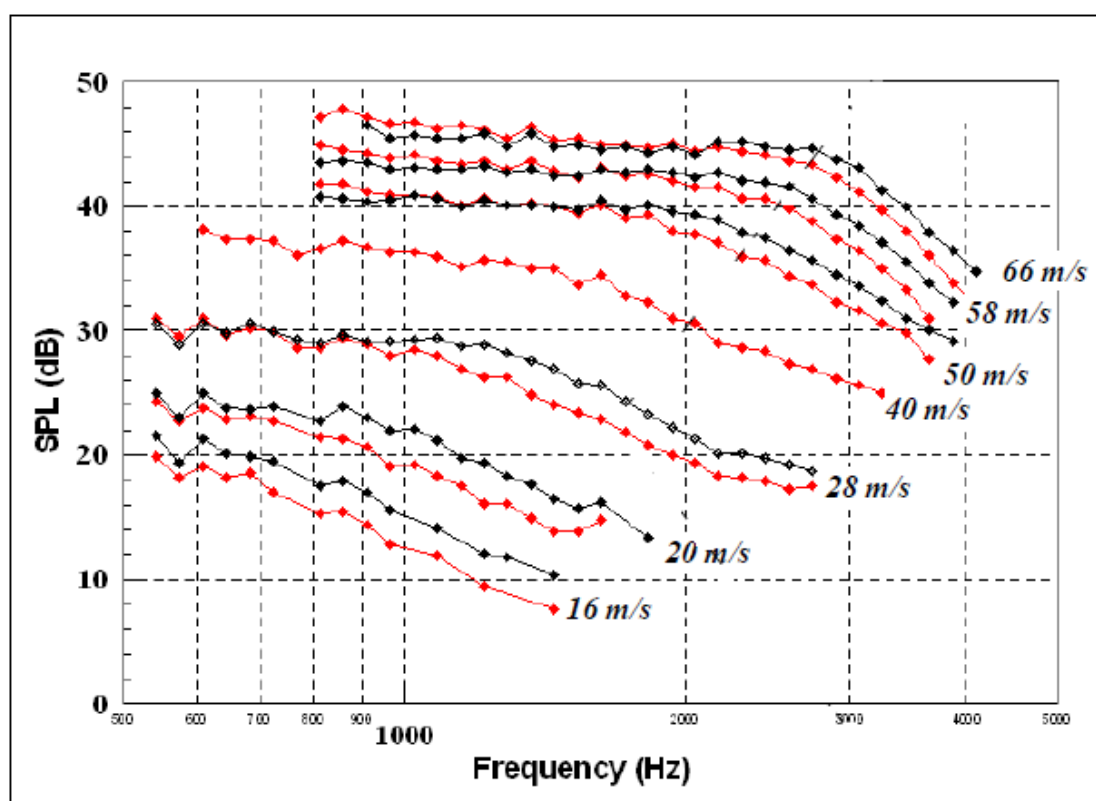


Figure 4-24 - Integrated Spectrum for NACA 0012 airfoil at 0° effective AOA. Untripped (black) and tripped (red) spectra shown for the July, 2007 tunnel entry. Source: (Devenport W. , et al., 2010), p. 197.

⁵⁶ This tripping position was used as a standard pattern for all later numerical simulations in the present research.

Figure 4-24 shows the VT integrated spectra for speeds from 16 m/s to 66 m/s, corresponding to chord-based Reynolds numbers from 800,000 to 3,800,000, respectively. It may be seen that BL tripping (red spectral lines) resulted in noise attenuation of 2-3 dB in relation to untripped flow (black spectral lines), especially in the roll off portion of the spectra, with better results for the lower Reynolds numbers.

The simulation using the modified-BPM TE noise prediction method was accomplished as shown in Figure 4-25 and Figure 4-26, at the moderate chord-based Reynolds number of 1,520,000, corresponding to 28 m/s ($M=0.11$). The reason was that this was the only tripped flow velocity of the VT data at 4° AOA, and also the modified-BPM method had been thoroughly validated at this Reynolds and flow angle.

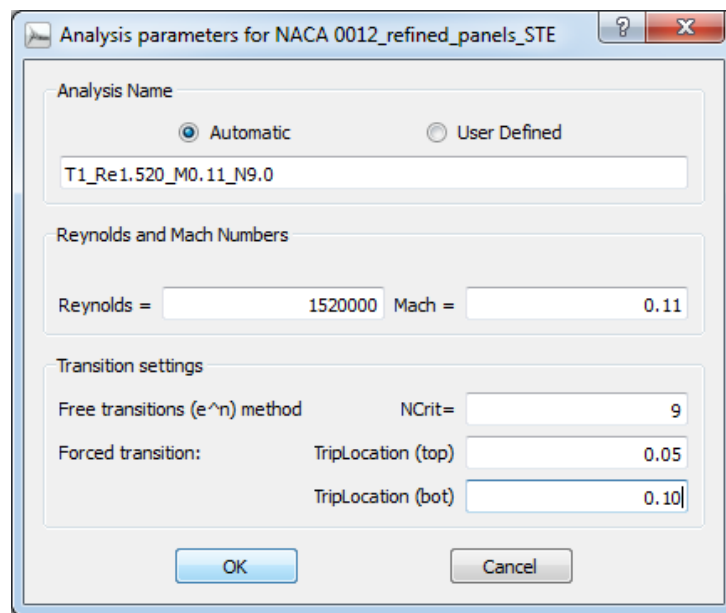


Figure 4-25 - XFLR5 simulation input for 28 m/s, zero AOA and tripping at 5% upper and 10% lower surfaces.

Dialog

Simulation name: A_NACA0012_Tripped_4AOA_uns_trip

OpPoint(s) for TE (only analysed will be shown):

- 4°, T1_Re1.520_M0.11_N9.0 (2), NACA 0012_refined_panels_
- 3°, T1_Re1.520_M0.11_N9.0 (2), NACA 0012_refined_panels_
- 2°, T1_Re1.520_M0.11_N9.0 (2), NACA 0012_refined_panels_
- 1°, T1_Re1.520_M0.11_N9.0 (2), NACA 0012_refined_panels_
- 0°, T1_Re1.520_M0.11_N9.0 (2), NACA 0012_refined_panels_

Length of wetted Trailing-Edge (L): 1.2 m

Distance from observer to TE (re): 3.08 m

Original flow velocity, U: 28 m/s

Original airfoil Chord length, C: 0.914 m

Original flow Mach Number, M: 0.11 m

D* at chord station: 0.98

D* scaling factor: 1

Eddy Convection Mach number (%): 0.8

Select TE noise source contributions desired (and/or):

- Separated flow on the suction side (high Reynolds flow)
- Suction side of airfoil (attached flow)
- Pressure side of airfoil (attached flow)

δ^* source:

Xfoil calculation Original BPM δ^* correlations Import data

Interpolation scheme:

Linear Newton's Lagrange's Spline

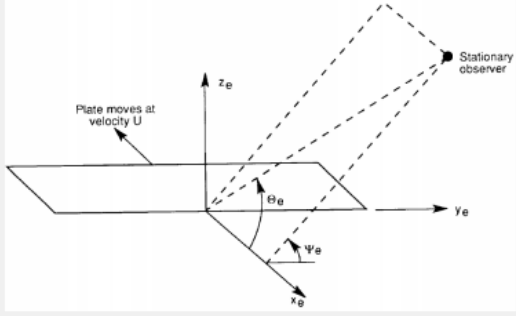
Select the directivity functions for high and low frequencies:

BPM Low frequency BPM High frequency

Select Directivity Angles:

θ_e : 103.2 °

ϕ_e : 90 °



OK Cancel

Figure 4-26 – PNoise input screen for the simulation.

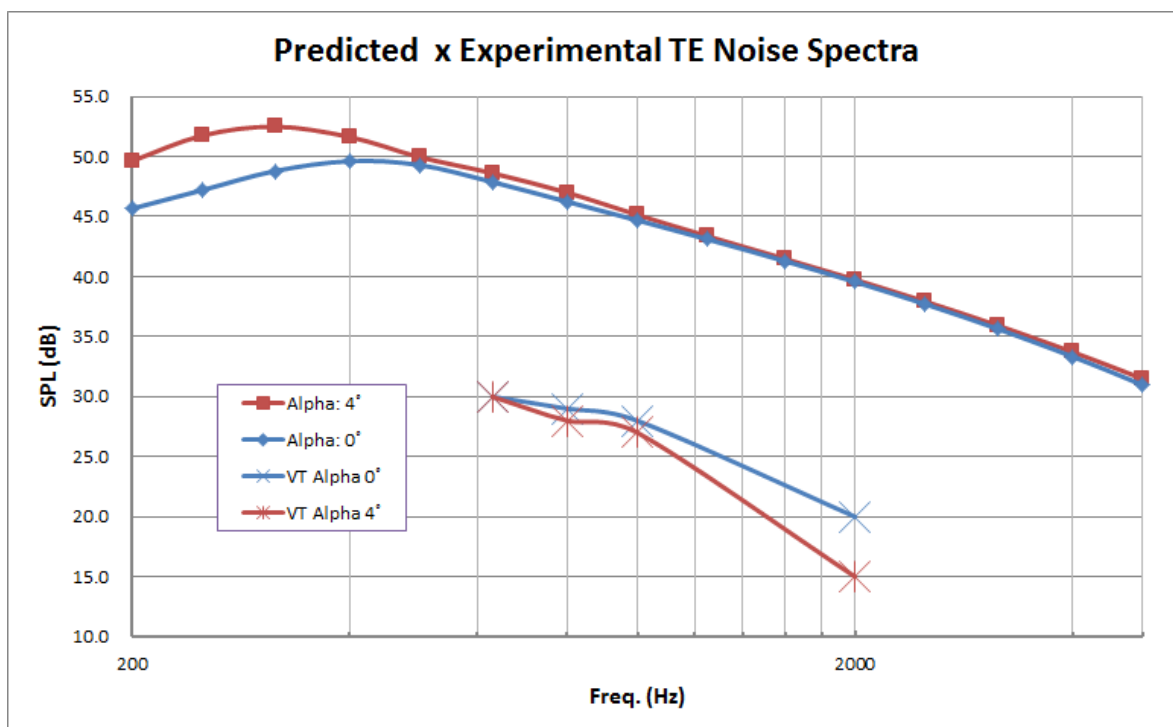


Figure 4-27 - Total TE-noise SPL calculated by the Modified-BPM method (upper plots), compared to VT measured spectrum (lower plots), for the NACA 0012 airfoil at 28 m/s, for 0° AOA with tripping at 5% chord, and 4° AOA with tripping at 5% chord for the suction side and 10% chord at the pressure side.

Figure 4-27 shows the comparison between predicted (modified-BPM) and VT spectra. The heavy shifts found, representing overprediction of the modified-BPM or under-evaluations of data measured at VT, were of 15-18 dB and larger than those previously found for transition flows. Also, there was still no physical sense in the relative spectra disposition, since the VT data included all self-noise sources but displayed lower noise levels throughout the available spectrum portion, when compared to the limited-source modified-BPM model.

For transition flow, the transition process and location are potential additional sources of discrepancy, to those already discussed in subsection 4.4.1.1.

In the calculation, the flow is considered to trip immediately at the tripping location, i.e., 5% chord. However, the actual transition phenomenon takes time and chordwise distance to happen, going through the steps of Tollmien-Schlichting waves, turbulent spots, vortex stretching mechanisms, etc., until a fully turbulent flow is established. Since the noise prediction model depends upon the turbulent BL scale at the TE, the

chordwise location of a realistic transition point might affect the results. However, the maximum noise level difference obtained from sensibility tests of the modified-BPM model later accomplished with the S830 airfoil was 6.7 dB at much higher speeds as may be seen from Table 4-14. Small variations of the transition position should result in a fraction of this value, especially in the case of the much lower Reynolds number of 1,520,000.

Table 4-14 – Sensitivity tests for the SPL as a function of tripped or transition flow, for the S830 airfoil, at two different Reynolds numbers.

Airfoil	S830	S830	S830	S830
Airfoil / case number	100	2	103	4
Aerodynamic/ Aero acoustic Characteristic	NREL design point	NREL design point	POLI_100 WT at 85% span	POLI_100 WT at 85% span
Reynolds number:	4,000,000	4,000,000	7,700,000	7,700,000
Mach number:	0.21	0.21	0.21	0.21
Tripping (%chord, upper and lower surfaces):	5%/10%	No tripping	5%/10%	No tripping
AOA test range:	-3 to +20	-6 to +25	-3 to +20	-3 to +20
Convergence range	-3 to +20	-5° to +18°	-3 to +20	-6° to +18°
OASPL (dB), @ (cl/cd)max.	94.02	89.80	94.30	87.60
Peak Frequency:	80 Hz (87,7 dB)	200 Hz (83,1 dB)	100 Hz (87,7 dB)	250 Hz (80,5 dB)

4.4.3 S831 airfoil tripped flow for higher Reynolds numbers at zero and moderate AOA.

For the sake of completeness, even though the results had been quite disappointing up to that point, a final simulation round was accomplished employing the modified-BPM method for the S831 geometry and compared to the VT integrated spectral data.

The pronounced geometric differences between the symmetric NACA 0012 and the cambered NREL S831 airfoils are highlighted in Figure 4-28.

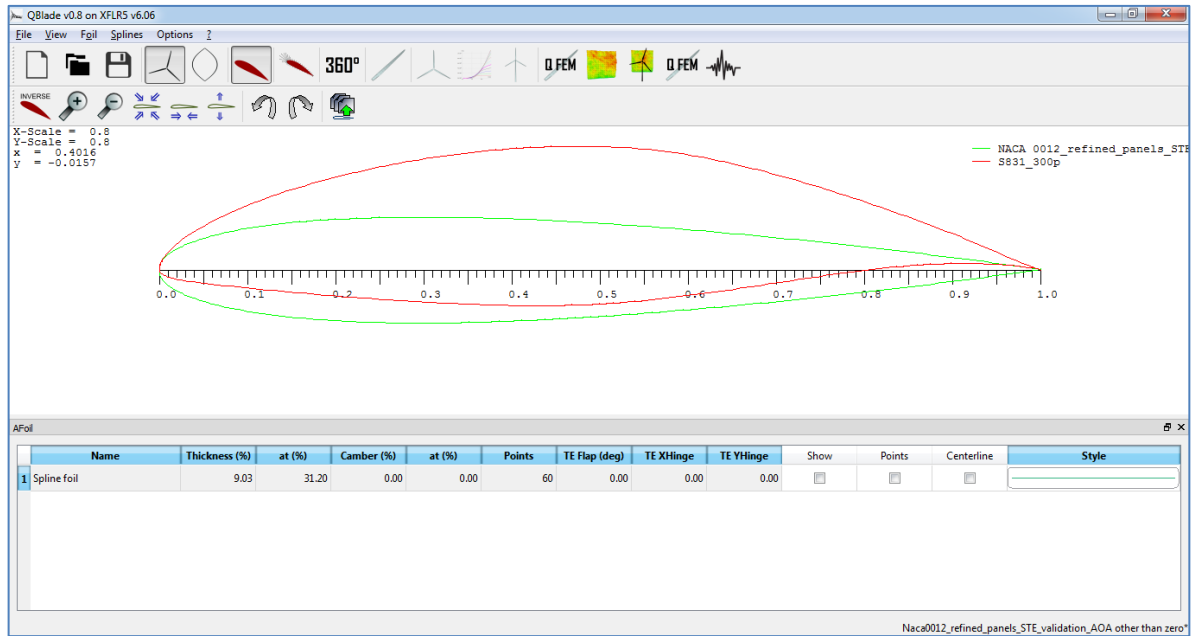


Figure 4-28 – The symmetric NACA 0012 airfoil profile (green) and the cambered NREL-Somers S831 airfoil profile (red).

The noise data derived from VT experiments were available for two Reynolds numbers for the S831 airfoil: 1,500,000 (28 m/s or Mach ≈ 0.08) and 3,200,000 (54 m/s or Mach ≈ 0.16). The modified BPM method was simulated for the lower value, since it was within NASA validation range and compared to some points of the spectrum from VT data for both -2° and 5° AOA and for tripped boundary layer (at 5% chord on the suction side and 10% chord at the pressure side). The result is shown in Figure 4-29.

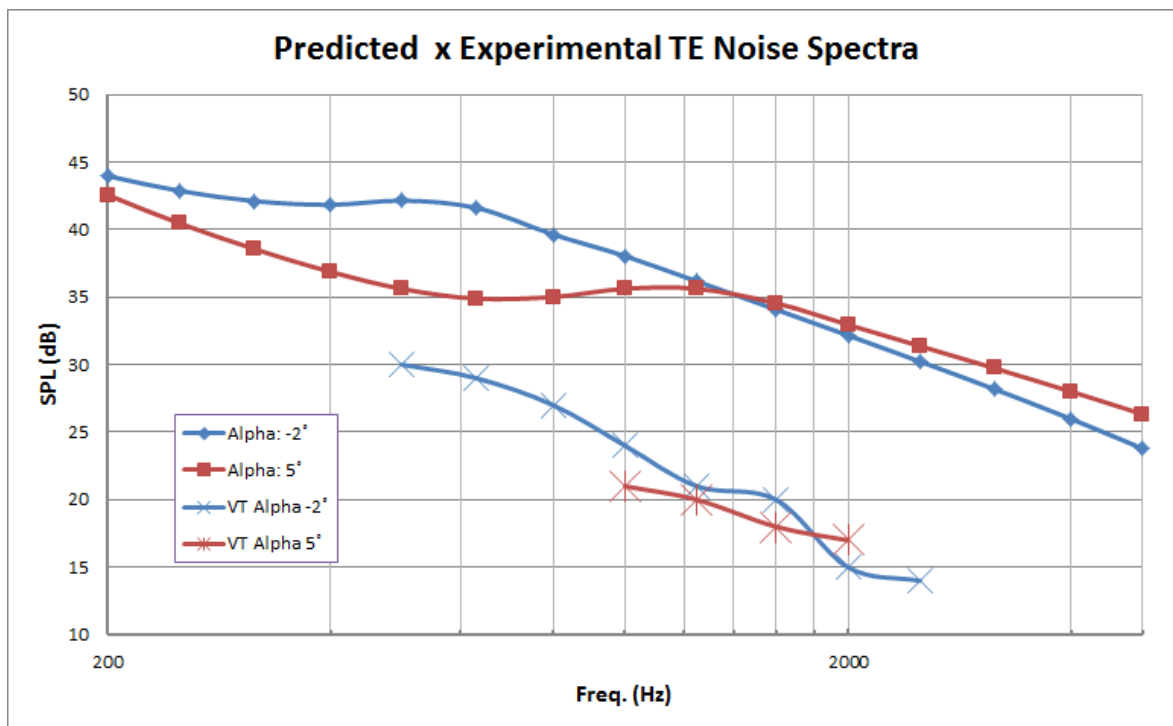


Figure 4-29 – Modified-BPM model TE noise calculations for the tripped, S831 airfoil, at -2° and $+5^\circ$ AOA (upper plots) compared to the VT derived spectra (lower plots), for the same nominal conditions.

Differences of 12-17 dB are noticeable between the predicted spectra (upper) and those derived indirectly from measured data, for -2° AOA and of the same order for the $+5^\circ$ AOA spectra.

All comparisons accomplished so far between predicted noise spectra and those derived indirectly from the NREL VT experiments for different AOA, Reynolds numbers and airfoil geometries, suggested that the modified-BPM model would not be suited to predictions at higher Reynolds numbers or geometries other than the NACA 0012 airfoil. However, Figure 4-17 showed significant discrepancies between the NASA experimental wind tunnel noise data and the Virginia Tech noise data for a Reynolds number close to 600,000, a lower range for which the original BPM model had been thoroughly validated by NASA. So, at this point it was considered necessary to compare these two experimental data sets also for a higher Reynolds number range for which the BPM model had been tested and verified. For this purpose, some frequencies of the VT spectra at Reynolds number of 1,500,000 were selected (based on graphical readability) for direct comparison, which is displayed in Figure 4-30.

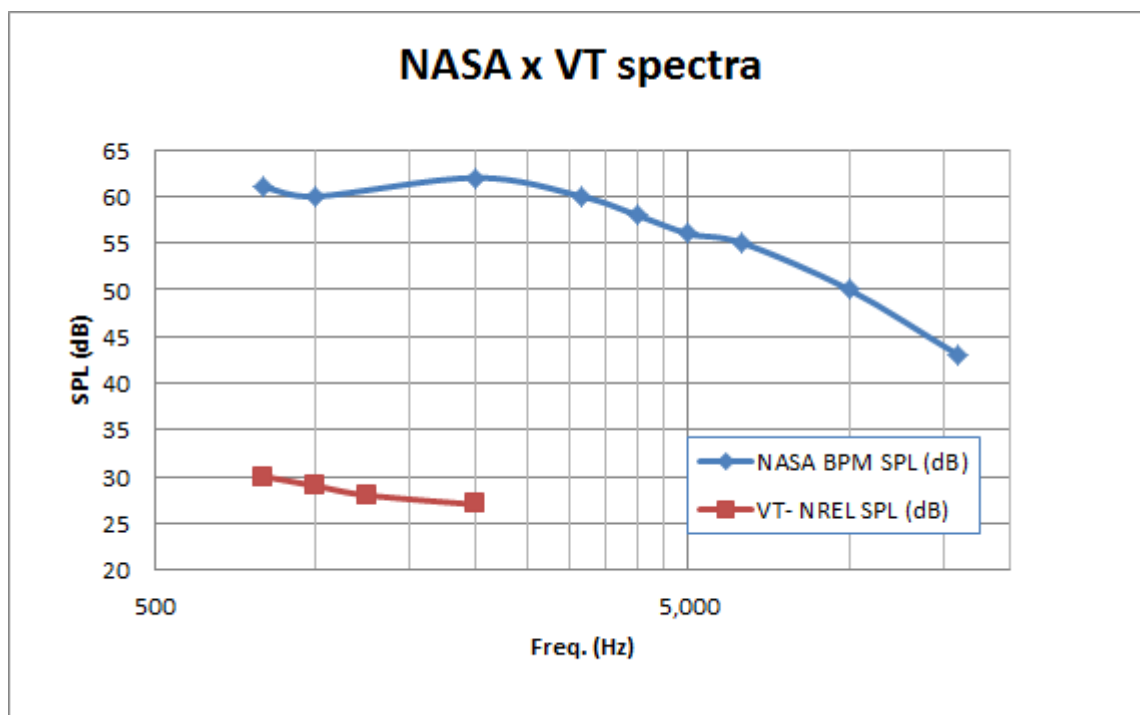


Figure 4-30 - Direct comparison of NASA wind tunnel acoustic data (Brooks, Pope, & Marcolini, Airfoil Self-Noise and Prediction, 1989), p.18, Fig. 11 (a), and Virginia Tech spectra derived from wind tunnel acoustic data (Devenport W. , et al., 2010), p.197 (red line, for 28 m/s), for a NACA 0012 airfoil at 0° AOA, tripped flow, and chord-based Reynolds number close to 1,500,000.

The differences among the spectra, for the same airfoil, AOA, Reynolds number and flow regimes were in the range of 30 to 35 dB along the 630 Hz to 2500 Hz spectral interval. This comparison supported the conclusion that differences between the NASA and VT/NREL datasets were not only significant at lower Reynolds numbers, but increased markedly for increasing Reynolds numbers.

This finding is confirmed by Doolan and Moreau (Doolan & Moreau, 2013):

“The BPM model agrees reasonably well with the NASA (Brooks & Hodgson, 1981) data and IAG (Herrig & Würz, 2008) data at $Re \approx 3 \times 10^6$, but does not compare well against the VT/NREL data (Devenport W. , et al., 2010)”.

According to Herr and Kamruzzaman (Herr & Kamruzzaman, 2013):

“even if quiet anechoic test facilities are used, the generally low signal-to-noise ratios require applications of focusing measurement techniques or specified correlations methods. As a consequence, extraction of TBL-TE noise from measured data is based on extensive system-inherent, facility dependent corrections which themselves have never been perfectly validated so far. Therefore, it will be instructive to both

experimentalists and numericists in academia and industry to elaborate comparisons of the various TBL-TE noise computational methods.”

The lack of acoustic data proximity among the simulated cases and the VT data, for the same geometry and similar flow conditions, did not endorse any extension of the validity range for the modified BPM model. However, due to the huge discrepancy found among VT data and NASA experimental data, both for low and high Reynolds numbers, and also to the fact that VT derived spectra showed inferior level, for all self-noise sources, than the NASA measurement for a single source, the VT/NREL data were considered not fit for the job.

One possible reason, as discussed elsewhere in the text is that VT/NREL spectra displayed were not direct microphone signal averages, like those from NASA, but were obtained by mathematical integration of rays in a beamforming region (that did not correspond to the full wetted TE length), through an algorithm. It is conjectured that this method possibly had some unintended attenuation built-in, for the self-noise sources in general or for the TE noise in particular. Other possible sources of discrepancies for these data were presented in this section and also in the bibliographic review sections.

As a measure of the enduring relevance and credibility of the BPM data and the semi-empirical BPM model, Herr and Kamruzzaman (Herr & Kamruzzaman, 2013) used the NREL NAFNOISE code (based on the BPM model) to calculate a reference TE noise spectrum against which to compare RANS-based TE noise simulations submitted to the 2012 BANC-II (Benchmark Problems for Airframe Noise Computations) conference. Also, XFOIL-calculated wall friction coefficients are used as benchmarks by AIAA for comparison with some of the RANS-calculated cases submitted.

From this point on, it was decided that the modified-BPM model and method would be employed, above the original Reynolds number range and with other geometries, for relative noise performance assessment only, until new, higher Reynolds numbers data bases are available for comparison.

4.5 DEVELOPMENT OF A NEW FAMILY OF AIRFOILS FOR WT WITH REDUCED TE NOISE EMISSION AND PRESERVED AERODYNAMIC PERFORMANCE.

Since the choosing of the NREL S830 airfoil as a starting geometry had been based on coordinate availability, high aerodynamic performance, low noise emission design and the thickness specified by structural requirements, it was decided early at the development phase to compare its noise performance against other 21% thickness NREL “S-series” airfoils. As it turned out, the S830 was the “S-series” airfoil with the least audible noise emission by a wide margin (from 1.1 to 11.8 dB(A)) and the third quietest airfoil (overall), as seen in Appendix K. Although defeated by the S819 and S823 in the overall low noise level, these alternative airfoils showed much higher audible range emissions and smaller c_l than the S830. Also, they were developed as root airfoils for smaller WT equipment. The conclusion was that the S830 is an excellent, low noise emission baseline geometry for the research, making any possible improvements over it difficult, but valuable.

4.5.1 The S830 baseline geometry performance under the defined 50-m blade operating conditions.

In Figure 4-31, the baseline S830 geometrical profile is shown.

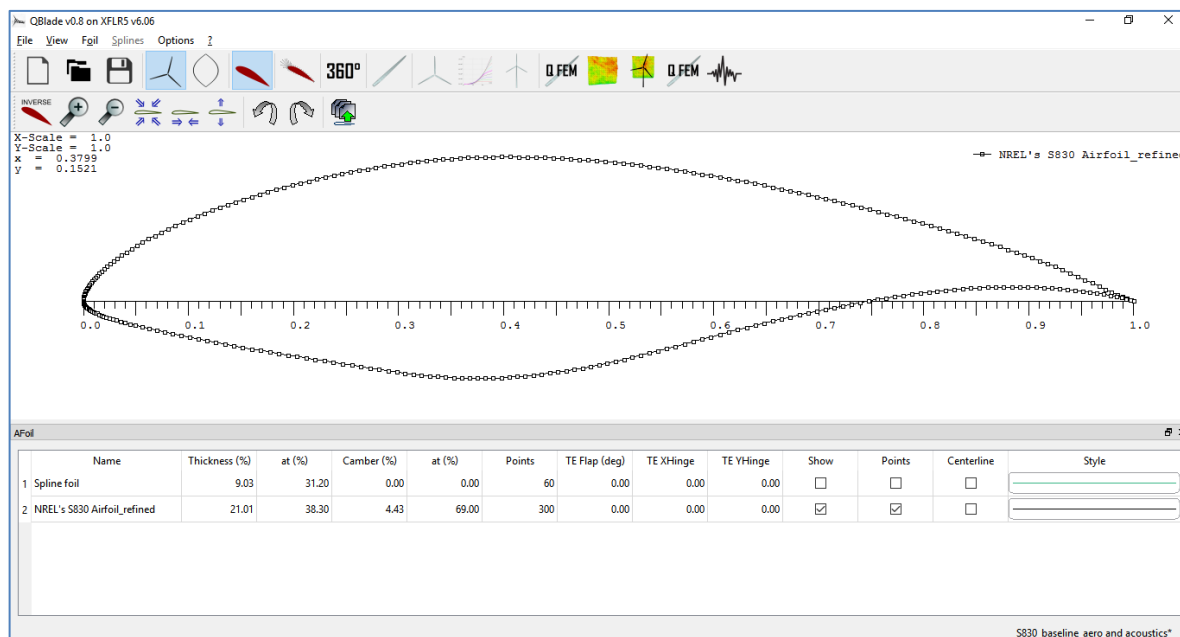


Figure 4-31 - The contour for the S830 airfoil (Copyright NREL-Somers).

In Table 4-15, the baseline S830 (21% thickness at 38% chord) aerodynamic and aeroacoustics characteristics obtained from simulation at both the original design Reynolds number (of 4 Million) and at the Poli-100 WT blade at 85% span operating Reynolds number (of 7.7 Million), are shown. All aerodynamic data resulted from the XFLR5 simulations and aeroacoustic data resulted from the new 2D TE noise module (PNoise) added to QBlade V0.8, at $M = 0.21$ and at the $(cl/cd)_{max}$ operating point.

Table 4-15 - Simulated aerodynamic and aeroacoustics characteristics for the S830 airfoil at the original design point ($Re = 4$ million) and for the POLI-100 WT blade at 85% span ($Re = 7.7$ million), for tripped condition (XFLR5 V6.06 and QBlade V0.8 with 2D noise module).

Airfoil	S830, original	S830, original
Airfoil / case number	#100	#103
Aerodynamic/ Aero acoustic Characteristic	NREL design point	Poli-100 WT @ 85% span
Reynolds number:	4,000,000	7,700,000
Mach number:	0.21	0.21
Polar object (file name)	T1_Re4,000_M0.21_N9.0	T1_Re7,700_M0.21_N9.0
cl max:	1.65	1.72

angle of cl max	18	18.4
Max cl/cd value:	77.1	91.7
Angle of max cl/cd	5.7	6.1
cl at max efficiency point:	1.16	1.20
cd at max efficiency point:	0.0150	0.0131
cm at max efficiency point:	-0.146	-0.144
Tripping (%chord), upper/lower surface:	5%/10%	5%/10%
AOA test range:	-3 to +20	-3 to +20
Convergence range	-3 to +20	-3 to +20
OASPL (dB), @ (cl/cd)max.	94.02	94.30
Peak Frequency:	80 Hz (87.7 dB)	100 Hz (87.7 dB)
OASPL (dB(A)):	80.30	81.00
OASPL (dB(B)):	88.20	89.30
OASPL (dB(C)):	93.40	93.60
SPL_α (dB)	92.10	92.80
SPL_s (dB)	89.20	88.80
SPL_p (dB)	77.60	77.00
Notices.	original geometry, original design point aerodynamic and noise performance.	original airfoil, new flow condition

By comparing the Coefficient of Pressure (c_p) diagram between both flow conditions, it was possible to see that the slightly larger cl at $AOA=6.1^\circ$ and Re of 7.7 million resulted in a slightly larger negative gauge pressure over the suction side, as seen on the c_p graph, Figure 4-32.

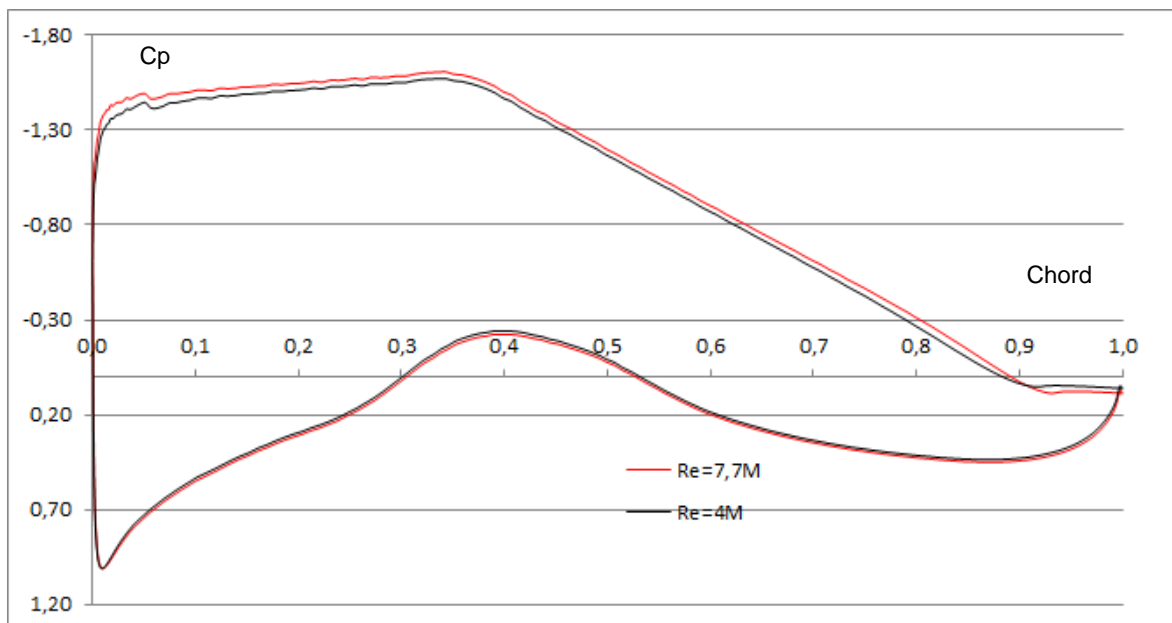


Figure 4-32 – Coefficient of Pressure (Euler number) over normalized chord, for the baseline S830 airfoil, for the original ($Re_c = 4,000,000$) and new operating conditions found at 85% radius of Poli-100 Wind Turbine ($Re_c = 7,700,000$).

The numbers shown for case #100 in Table 4-15 represent the aerodynamic and noise goals for the S830 airfoil at the original Somers & Tangle design conditions. When compared to case #103, which better represents the higher speed flow condition for the larger WT of the Poli-100 WT, it is possible to see that the aerodynamic performance increased with increasing flow speed (as expected), for both $(cl/cd)_{max}$ and cl_{max} . Also, the unweighted OASPL level increased by 0.28 dB in higher speed flow while the A-weighted SPL increased much more, by 0.70 dB.

By analyzing the three independent noise sources of case #103 that make up the TE noise, the contributions are 92.8 dB, 88.8 dB and 77.0 dB from the angle-of-attack, suction side and pressure side sources, respectively.

For this and consistently over the many simulations accomplished, the angle-of-attack dependent TE noise source has proven to be the dominant TE noise source.

The suction side contribution is 4.0 dB less than the largest source, adding only 1.4 dB to the total SPL. The pressure side contribution is 15.8 dB less than the largest source, adding approximately 0.2 dB (virtually no contribution) to the total SPL. The log sum of the three sources resulted in the displayed total SPL of 94.3 dB.

It is also possible to see that the C-weighted OASPL minus the A-weighted OASPL is significant (13.1 *dB* for case #100 and 12.6 *dB* for case #103), which implies that a significant amount of the noise energy is emitted in the low frequency range, which is supportive of Bowdler and Leventhall (Bowdler & Leventhall, 2011) findings.

Also, since the A-weighted SPL increment is larger than the total SPL increase, it is possible to say that, for AOAs close to 6° , some acoustic energy migrated from infrasound to audible frequencies with increasing Reynolds number.

Although audible frequencies are the most targeted for noise reduction due to direct human annoyance concerns, the impact of infrasound in human health may be also significant, with noise propagation occurring over large distances and the potential for high annoyance effects, which may include the induction of window and door panes vibration in audible frequencies or more significant physiological effects as discussed by Schomer et al. (Schomer, Erdreich, Boyle, & Pamidighatam, 2013).

The application of the aerodynamic and aeroacoustic tools at hand to the S830 airfoil in both the original design point and in the new operating point allowed reaching the important conclusions above but also raised some important questions whose answers helped define the strategy for the development of quieter airfoils, albeit with comparable or superior aerodynamic performance:

- Is it possible to reduce the intensity of the largest TE noise source, the one associated with the AOA?
- Is it possible to attenuate the suction side noise while transferring some of the airfoil loading (with opposite sign) to the pressure side, so that noise is reduced but overall aerodynamic efficiency is preserved?
- Is it possible to reduce at the same time the unweighted SPL and the A-weighted SPL, for the Poli-100 blade chord and flow conditions at 85% span?

The first question was considered the most fundamental and was addressed in the sequence, while the others were addressed during analysis of the sensitivity studies conducted later.

In order to reduce the strength of the angle of attack-dependent noise source, the first idea that would come to mind would be to reduce the AOA for a given lift coefficient, i.e. to increase the slope of the cl_α curve. However, according to the *Thin Airfoil Theory*

(Kuethe & Schetzer, 1961), p.86, the $cl\alpha$ curve slope is approximately constant and given by:

$$cl = 2\pi(\alpha - \alpha_{L0}) \rightarrow \frac{\partial cl}{\partial \alpha} = 2\pi \cong 6.28 \text{ per radian} \cong 0.11 \text{ per degree} \quad (4 - 2)$$

Where α_{L0} equals the zero-lift-angle for the cambered airfoil.

A theoretical correction may be applied to this value due to the S830 airfoil thickness of 21% (Kuethe & Schetzer, 1961), p. 356, fig.6, bringing the slope down to 0.102 per degree. This corrected value is in good agreement with the linear portion of the $cl\alpha$ slope simulated with the aid of XFLR5 for the S830 airfoil, as may be seen from Figure 4-33 and Table 4-16.

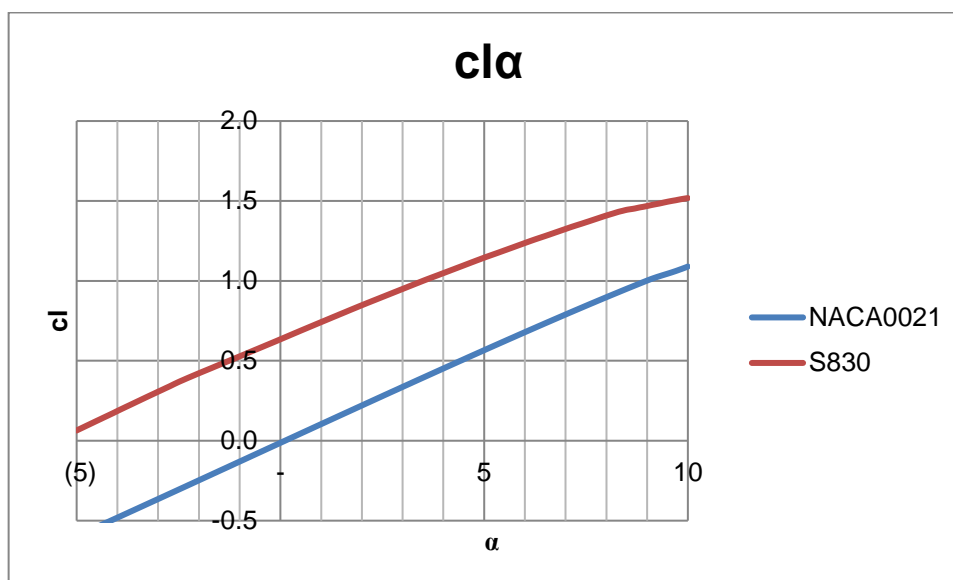


Figure 4-33 - S830 and NACA 0021 $cl\alpha$ curves at 7.7M Reynolds number.

Table 4-16 - $cl\alpha$ [1°] estimation based on XFLR5 output for the S830 and NACA 0021 airfoils at Reynolds number of 7.7M.

clα slope, approx.				
	NACA0021		S830	
	α	cl	α	cl
	- 0.00	- 0.013	- 5.00	0.064
	10.00	1.090	8.00	1.409
Δ	10.00	1.103	13.00	1.345
clα		0.110		0.103

Naturally, the final wing (blade) $cl\alpha$ curve slope will depend upon its aspect ratio, however, for aspect ratios larger than 7, the 2D curve slope will be a good representation of the final blade lift slope. For the Poli-100 rotor blade, the aspect ratio of the blade is close to 20, but there are also centrifugal effects not present on fixed-wing aircraft and effects from a strong induced vortex system, part of which is also not present in fixed-wing aircraft systems. However, both effects will affect mainly the blade portion near the hub and the portion very near the tip.

The cl_{max} value, on the other hand, will increase with Reynolds number “as a complicated function of the thickness, camber and leading-edge radius” (Kuethe & Schetzer, 1961), p. 368. In the present case (#103), the cl_{max} reached a predicted value of 1.72 at 18.4° , well in excess of the prescribed original coefficient of 1.6 for the S830 in original design condition. At the same time, the coefficient of drag decreased with increasing Reynolds number, when compared at the maximum efficiency point for both flows (#103 and #100), taking the $(cl/cd)_{max}$ up, to a value of 91.7 (with a corresponding angle of 6.1°) as compared to 77.1 (for a corresponding angle of 5.7°) for the reference design condition (case # 100).

The conclusions so far were that the $cl\alpha$ slope is not significantly changed by design (except by a weak dependency on thickness, which is fixed by requirement at the current case) and operating the airfoil consistently at the $(cl/cd)_{max}$ angle, due to increased Reynolds number, would also lead to an adverse increase of the strongest source of TE noise.

From the above discussion it was inferred that an airfoil designed for less angle-of-attack-dependent TE-noise should operate at a shallow AOA, below that corresponding to $(cl/cd)_{max}$, but with enough performance to produce a minimum $cl \sim 1.2$ (as in the original S830 requirements) and high aerodynamic efficiency (> 77). As a consequence, a good-candidate airfoil for low AOA-induced TE-noise should display a higher slope $\partial(c_l/c_d)/\partial\alpha$, provided this advantage was not offset by too large a negative zero-lift angle, α_{L0} (i.e., with limited camber).

There are many possible ways to obtain a high cl/cd value for limited camber airfoils in relatively small AOA, turbulent flow, including the application of high-lift devices (flaps, slats, slots, etc.) and active boundary layer control techniques. However, for a

very cost sensitive and dependable equipment, the ratio would be most simply controlled by a low coefficient of drag denominator imposed by design. One possible alternative, passive solution for turbulent drag reduction with benefits to noise abatement, would be the application of *riblets* of suitable aspect ratio to the airfoil surface, after flow tripping, as discussed in the context of transport aircraft in (Saab Jr. & Silveiras, 1993).

Since the airfoil surface becomes heavily soiled in a wind turbine, especially in the LE area, and the flow is modeled as tripped flow close to the LE, there would be no such drag savings through the use of laminar boundary layer airfoils where the transition is delayed in favor of a smaller coefficient of friction over a large portion of the airfoil surface. This also raises questions concerning the applicability of the delayed maximum thickness position of the S830 airfoil, set at 38% chord, for WT applications. Therefore, the geometric options to be explored should search for airfoils with decreased turbulent drag that can be obtained via minute geometric changes with implications on the pressure gradients and wall friction coefficients.

It is interesting to see the signs of a possible tradeoff in this matter: the lesser the skin friction coefficients, the larger cl/cd will be attained at a shallower angle; however, the turbulent boundary layer thickness and associated turbulence scale will also grow in this condition, resulting in increased suction and/or pressure side TE noises and at lower noise frequencies. This seemed to pose a delicate balance question, one that could explain the very modest achievements so far in noise reduction derived from airfoil geometry optimization.

The geometrical changes imposed to the original S830 geometry in order to observe the sensitivity of TE noise on many parameters and to help find answers for all three questions raised earlier, were discussed next.

4.5.2 Airfoil modification sensitivity analysis, for the 50 m blade under Poli-100 WT flow conditions.

As discussed in the methodology section, a several-step modification study was accomplished in order to investigate changes and rate of changes on aerodynamics and noise characteristics over the baseline airfoil characteristics.

The increased Reynolds number at 85% radius of the Poli-100 blade naturally enhanced the baseline airfoil (S830) aerodynamic characteristics as shown in the previous section, which also pointed possible strategies and tradeoffs for reducing TE noise emission.

The following limited-amplitude geometric changes were incorporated into the baseline configuration and were investigated independently, except as noted, in order to observe aerodynamic and aeroacoustic sensitivity for each alteration:

- LE radius variation.
- Upper surface forward side convexity variation “forward convexity-FC”.
- Camber variation.
- Flap angle variation.
- Maximum thickness position variation.
- Upper surface aft side convexity variation “aft convexity-AC”.
- Trailing Edge gap.

It should be restated at this point that all acoustic performance results obtained were evaluated in respect to a couple of reference geometrical configurations and flow conditions, since no formal validation of the acoustic method against experimental data had turned out to be possible. Thus, the results were always compared to the original geometry S830 airfoil at original design conditions (Reynolds number of 4 million) or to a splined S830 shape (very close geometry made up of splines, suitable for later modification), at the larger Reynolds number of 7.7 million, as noted.

Some of the *good practices* adopted throughout the XFLR5 and PNoise simulation processes were:

- Airfoil re-meshing to a minimum of 160 points after each modification, with enhanced TE mesh.
- Reduced AOA step for Polar Curve calculation: 0.1 degree

- Geometrical differences between the actual S830 geometry and the splined S830 foil drawn for use as the editable baseline configuration may impart evaluation errors of the following maximum magnitude during comparison:
 - $\Delta\left(\frac{cl}{cd}\right)_{max} \sim 1$; $\Delta cl \sim 0.03(@ cl_{max})$; $\Delta cl \sim 0.06(@ (cl/cd)_{max}) \rightarrow \Delta SPL \leq 0.1 dB; \leq 0.2 dB(A)$.
 - Original S830 references: 4.45% camber at 68.41% chord, 20.96% thick at 38.40% chord.
 - Splined S830 references: 4.41% camber at 69.6% chord and 21.13% thick at 39% chord.
- All airfoils were re-meshed, normalized and de-rotated before simulations.
- 300 steps were allowed for convergence.
- Convergence log verified after each run.
- The designs were not compared at the same AOA, but at the most aerodynamic efficient point for each configuration, as proposed by Migliore and Oerlemans (Migliore & Oerlemans, Wind Tunnel Aeoroacoustic Tests of Six Airfoils for Use in Small Wind Turbines., 2003).
- The wetted edge length (2.5 m), the local flow velocity (72.32 m/s; M=0.21) and the airfoil chord at 85% radius of the Poli-100 blade (1.55 m) were input and double-checked for all acoustic simulations.
- All input and output files were saved for later reference.

The typical input and output screens and files of the modified-BPM TE noise model inside QBlade v0.8 may be seen in Figures 4-34 through 4-37, while the general results for the sensitivity analysis are shown in Table 4-17.

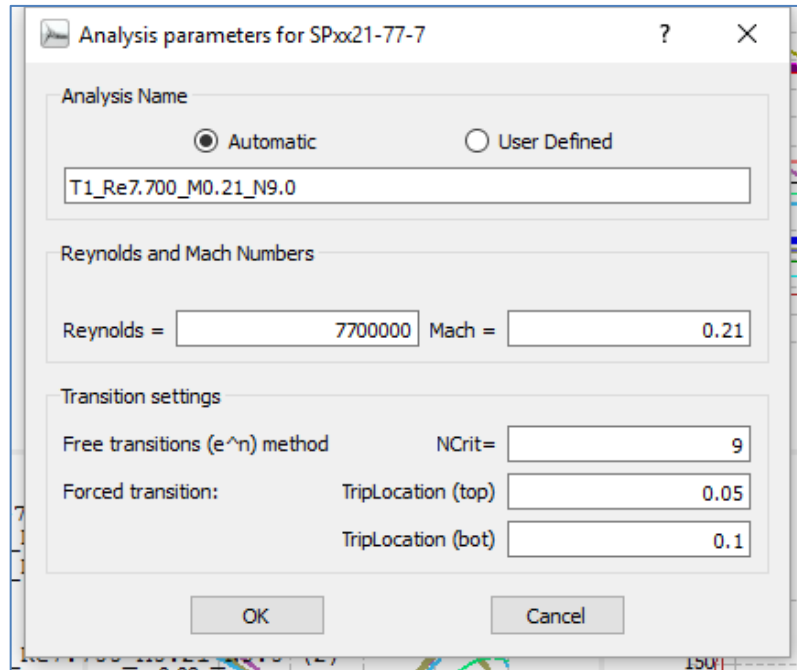


Figure 4-34 - Typical input data for Aerodynamic analysis (all cases) in XFLR5 V6.06, with tripping at 5% chord over the suction side and 10% chord upper chord over the pressure side.

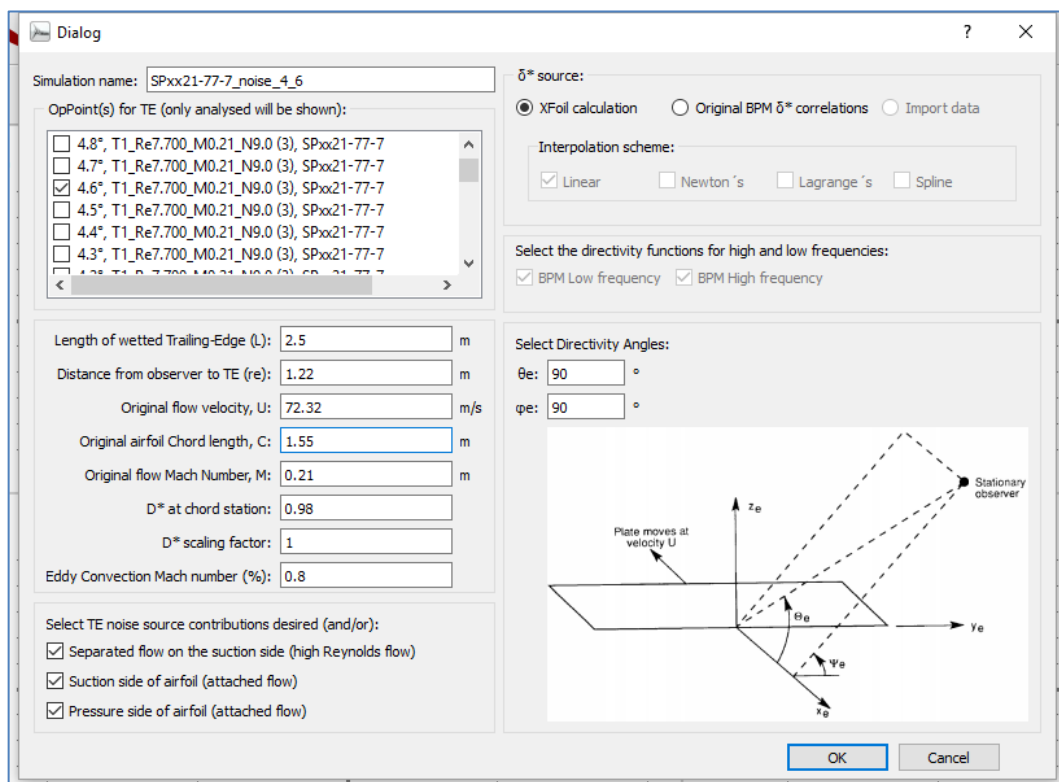


Figure 4-35 - Typical input data for Aeroacoustic analysis (different AOA and polar objects selected for each case) in the new 2D acoustic module of the QBlade software (PNoise).

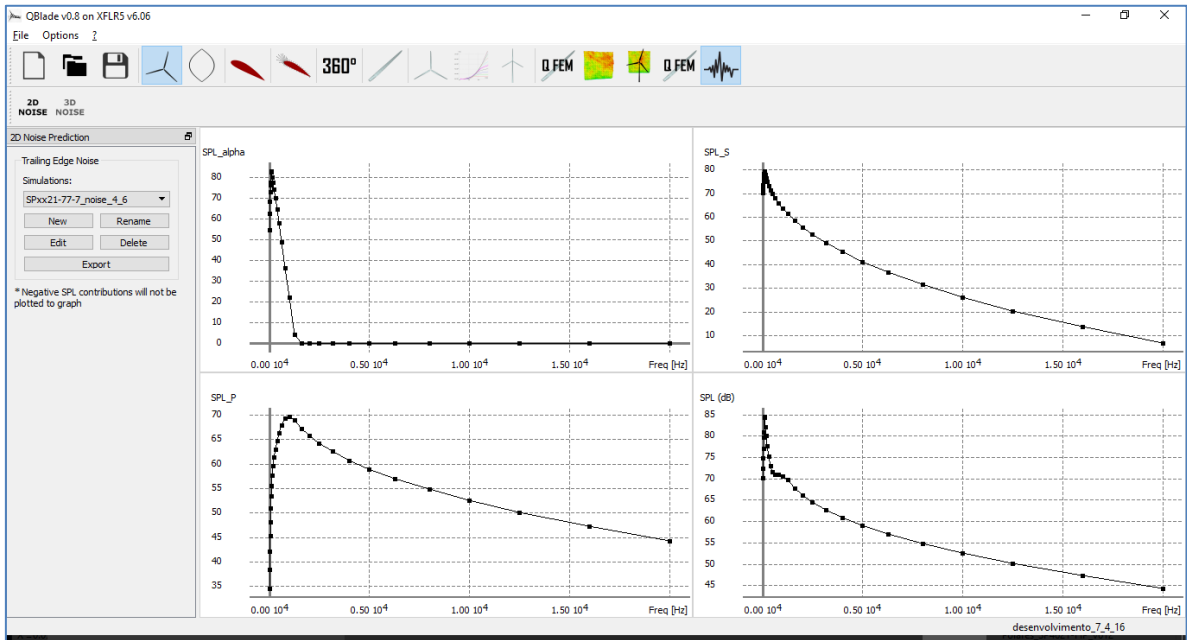


Figure 4-36 - Typical graphical output of the sound pressure level spectra with the 2D acoustic module coupled to the QBlade software.

SPxx21-77-7_noise_4_6 - Bloco de notas

Arquivo Editar Formatar Exibir Ajuda

Noise prediction file export

Alpha: 4.6, Re = 7.7e+06
 OASPL: 91.2382 dB
 OASPL (A): 80.7572 dB(A)
 OASPL (B): 87.2451 dB(B)
 OASPL (C): 90.8831 dB(C)
 SPL_a: 88.4981
 SPL_s: 87.488
 SPL_p: 77.8879

Freq [Hz]	SPL (dB)	SPLa	SPLs	SPLp	SPL (dB(A))	SPL (dB(B))	SPL (dB(C))
25	70.1819	54.6643	70.057	34.5367	25.4819	49.7819	65.7819
31.5	72.291	62.4603	71.8122	38.452	32.891	55.191	69.291
40	74.7368	68.5448	73.5399	42.1329	40.1368	60.5368	72.7368
50	77.1472	72.887	75.1017	45.2621	46.9472	65.5472	75.8472
63	79.6129	76.4986	76.698	48.2163	53.4129	70.3129	78.8129
80	80.9387	77.4545	78.3478	50.9929	58.4387	73.5387	80.4387
100	84.2672	82.5762	79.3419	53.3595	65.1672	78.6672	83.9672
125	84.5489	83.0203	79.2538	55.5329	68.4489	80.3489	84.3489
160	82.0328	79.8743	77.9203	57.743	68.6328	79.0328	81.9328
200	80.1155	77.6596	76.3794	59.593	69.2155	78.1155	80.1155
250	77.7255	74.38	74.8369	61.3289	69.1255	76.4255	77.7255
315	75.2649	70.2744	73.2116	63.0339	68.6649	74.4649	75.2649

Figure 4-37 - Typical file output of the overall and 1/3 octave sound pressure level spectra with the 2D acoustic module coupled to the QBlade software.

Airfoil / case number	S830_4M, Tripped	S830_7_M, Tr	S830_Rx2	S830_Rx0.5	Spline_SB30_RO	Spline_JFC	Spline_JFC	Spline_JPC	Spline_LC	Spline_PC	Spline_LFA	Spline_PFA	Spline_FWD_TCK	Spline_AFT_TCK	Spline_LAC	Spline_PAC	Spline_TEGS	Spline_TEGL
Aerodynamic/Aero acoustic Characteristic Reynolds number:	NREL design point 4,000,000	POLL_100 WT at 85% span 7,700,000	POLL_100 WT at 85% span 7,700,000	POLL_100 WT at 85% span 7,700,000	POLL_100 WT at 85% span 7,700,000	POLL_100 WT at 85% span 7,700,000	POLL_100 WT at 85% span 7,700,000	POLL_100 WT at 85% span 7,700,000	POLL_100 WT at 85% span 7,700,000	POLL_100 WT at 85% span 7,700,000	POLL_100 WT at 85% span 7,700,000	POLL_100 WT at 85% span 7,700,000	POLL_100 WT at 85% span 7,700,000	POLL_100 WT at 85% span 7,700,000	POLL_100 WT at 85% span 7,700,000			
Match number:	0.21	0.21	0.21	0.21	0.21	0.21	0.21	0.21	0.21	0.21	0.21	0.21	0.21	0.21	0.21	0.21	0.21	0.21
Polar object (file name)	TL_Re4.000_M0.21_NS0.0	TL_Re7.700_M0.21_NS0.0	TL_Re7.700_M0.21_NS0.0	TL_Re7.700_M0.21_NS0.0	TL_Re7.700_M0.21_NS0.0	TL_Re7.700_M0.21_NS0.0	TL_Re7.700_M0.21_NS0.0	TL_Re7.700_M0.21_NS0.0	TL_Re7.700_M0.21_NS0.0	TL_Re7.700_M0.21_NS0.0	TL_Re7.700_M0.21_NS0.0	TL_Re7.700_M0.21_NS0.0	TL_Re7.700_M0.21_NS0.0	TL_Re7.700_M0.21_NS0.0	TL_Re7.700_M0.21_NS0.0	TL_Re7.700_M0.21_NS0.0	TL_Re7.700_M0.21_NS0.0	TL_Re7.700_M0.21_NS0.0
cl max:	1.65	1.72	1.89	1.55	1.75	1.79	1.73	1.72	1.72	1.77	1.725	1.777	1.74	1.765	1.684	1.7	1.78	1.84
angle of cl max:	18	18.4	19.0	13.4	20	20	15.4	20	20	20	20	20	20	20	20	18.5	18	17
Max cl/cd value:	77.1	91.7	90.2	92.1	95.4	95.4	95.3	95.5	90.1	97.0	92.5	97.0	85.0	85.0	108.6	81.6	96.0	96.5
Angle of max cl/cd	5.7	6.1	5.7	5.5	6.2	5.8	6.1	6.1	6.2	5.4	6.2	6.0	5.7	5.4	7.2	7.1	5.2	4.4
cl at max efficiency point:	1.16	1.20	1.25	1.2	1.263	1.225	1.275	1.275	1.21	1.24	1.23	1.283	1.235	1.15	1.457	1.282	1.27	1.305
cd at max efficiency point:	0.0150	0.0131	0.0139	0.0130	0.0136	0.0128	0.0134	0.0134	0.0127	0.0137	0.0133	0.0139	0.0127	0.0135	0.0134	0.0157	0.0132	0.0135
cm at max efficiency point:	-0.146	-0.144	-0.146	-0.147	-0.154	-0.161	-0.149	-0.149	-0.139	-0.168	-0.142	-0.166	-0.157	-0.150	-0.150	-0.149	-0.177	-0.205
Tripping (%chord, upper and lower surfaces):	5%/10%	5%/10%	5%/10%	5%/10%	5%/10%	5%/10%	5%/10%	5%/10%	5%/10%	5%/10%	5%/10%	5%/10%	5%/10%	5%/10%	5%/10%	5%/10%	5%/10%	5%/10%
ADA test range:	-3 to +20	-3 to +20	-3 to +20	-3 to +20	-3 to +20	-3 to +20	-3 to +20	-3 to +20	-3 to +20	-3 to +20	-3 to +20	-3 to +20	-3 to +20	-3 to +20	-3 to +20	-3 to +20	-3 to +20	-3 to +20
Convergence range:	-3 to +20	-3 to +20	-3 to +20	-2.3 to 417.1	-3 to +20	-3 to +20	-3 to +20	-3 to +20	-3 to +20	-3 to +20	-3 to +20	-3 to +20	-3 to +20	-3 to +20	-3 to +20	-3 to +20	-3 to +20	-3 to +20
OASPL (dB), @ (c)/cdmax:	94.02	94.30	93.60	93.40	94.40	93.30	93.80	93.80	93.40	93.30	93.90	94.10	93.00	93.50	92.20	96.40	92.00	89.40
Peak Frequency:	80 Hz (87.7 dB)	100 Hz (87.7 dB)	100 Hz (87.8 dB)	100 Hz (86.7 dB)	100 Hz (87.8 dB)	100 Hz (86.9 dB)	100 Hz (87.5 dB)	100 Hz (87.5 dB)	125 Hz (87.1 dB)	100 Hz (86.9 dB)	100 Hz (87.6 dB)	100 Hz (87.7 dB)	100 Hz (86.6 dB)	80 Hz (87.1 dB)	200 Hz (85.9)	80 Hz (90.2 dB)	125 Hz (85.4 dB)	160 Hz (82.5 dB)
OASPL (dB(A)):	80.30	81.00	80.70	80.80	81.20	81.00	81.10	81.20	81.50	80.50	81.20	81.00	81.00	80.30	81.20	80.30	81.20	81.50
OASPL (dB(B)):	88.20	89.30	88.50	88.40	89.30	88.50	88.90	88.90	89.10	88.10	89.00	88.90	88.40	87.90	89.10	88.50	88.10	86.90
OASPL (dB(C)):	93.40	93.60	93.10	92.90	93.80	92.80	93.30	93.30	93.10	92.80	93.40	93.40	92.60	92.90	92.10	95.60	91.60	82.20
SPL α (dB)	92.10	92.80	91.80	91.60	92.90	91.40	92.10	92.10	92.20	91.30	92.20	92.30	91.10	91.40	90.70	95.10	89.70	85.80
SPL α (dB)	89.20	88.80	88.70	88.40	88.80	88.30	88.60	88.60	88.30	88.80	88.90	88.20	88.90	88.20	86.30	90.40	87.60	85.80
SPL_p (dB)	77.50	77.00	77.10	77.30	77.40	77.50	77.50	77.50	77.60	77.50	77.40	77.30	77.70	77.70	77.50	76.70	78.00	77.80
Obs	original geometry, reference aerodynamic and noise performance:	original airfoil, new flow condition	halved LE radius	halved LE radius	Spine for new airfoil, beam flow condition	Less Upper Forward Side Convexity	Less Upper Forward Side Convexity	Plus Upper Forward side Convexity	-0.5% camber (Total camber 3.91%)	-0.5% camber (Total camber 4.91%)	2 degress Less (up) Flap Angle, at 90% hinge at 50% thickness.	2 degress more (down) Flap Angle, at 90% chord, hinge at 50% thickness.	tck fwd 2% of chord (at 37% chord)	tck aft 2% of chord (at 41% chord)	Less Upper Aft Side Convexity	Plus Upper Aft side Convexity	TE Gap Small (-0.5% chord) - non-singing airfoil	TE Gap Large (2.1% chord) - singing airfoil

Table 4-17 - Aerodynamic and aeroacoustic performance for the S830 original geometry and the geometrical variations employed in the sensitivity study

All the modifications made to the baseline airfoil for the sensitivity study are depicted in Table 4-17, and are explained and discussed individually in the next sub-topics.

4.5.2.1 LE radius variation.

This step comprised testing cases #105 (with double the original LE radius) and # 108 (with half the original LE radius), against reference case #103.

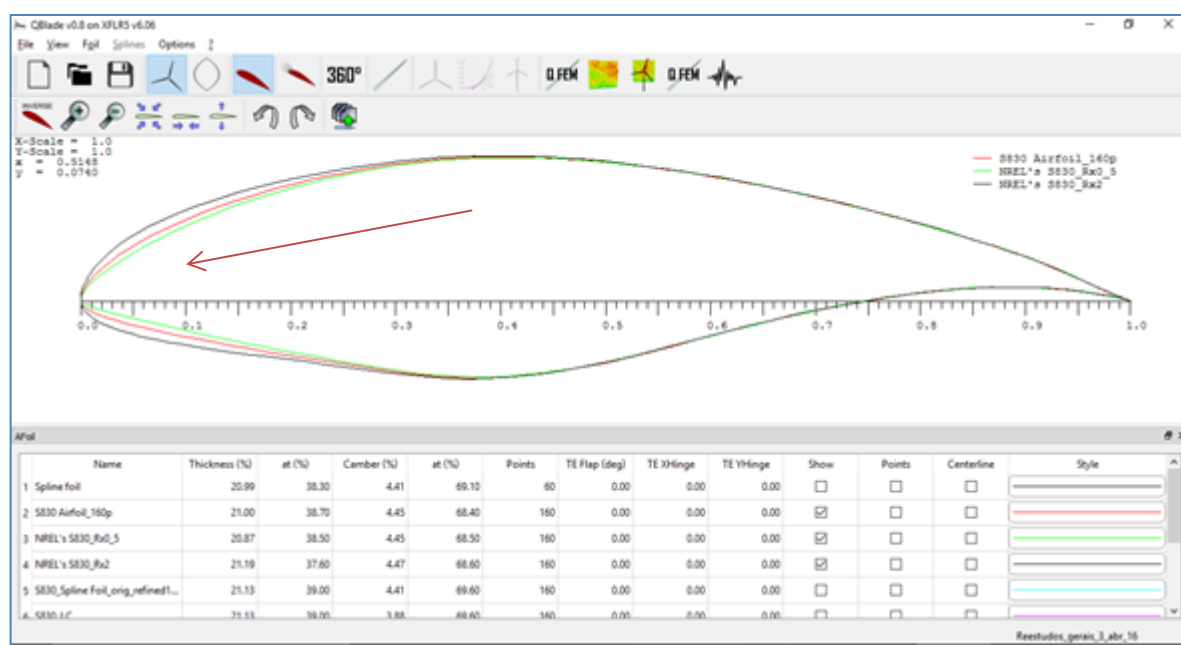


Figure 4-38 – Overview of the baseline geometry (red) and the variations with more (blue) and less (green) LE radius simulated.

Both cases produced variations with less OASPL noise, while matching or exceeding the aerodynamic features of the original airfoil. The version with halved LE radius displayed 1 dB less overall noise against 0.7 dB for the doubled LE radius version. However, convergence for the smaller LE radius is compromised in some AOA and the “flight envelope” is narrower. This is physically explained by the formation of a laminar bubble downstream of sharper LEs and more sudden stall characteristics. In the audible range there was less noticeable noise reduction, which reversed the advantage to the larger radius version, with a 0.3 dB (A) reduction.

The apparent overall advantage of the smaller radius version shown by the model was explained by a reduction in the corresponding AOA for the maximum aerodynamic efficiency point, from 6.1° to 5.5° , leading to a 1.5 dB smaller contribution from the angle-of-attack noise. However, most of the reduction happened in low frequencies (hence the smaller A-weighted reduction of 0.2 dB (A)).

Reducing the LE radius also detracted significantly from the airfoil performance at high AOA (both on cl,max and high-AOA range) and may lead to increased (unquantified by the current model) inflow noise problems that might easily offset this small reduction in emission.

4.5.2.2 Upper surface forward side convexity variation “forward convexity-FC”.

This step comprised testing cases #110 (less convexity) and # 111 (more convexity) at the suction side (upper surface) forward side, against reference case #109⁵⁷.

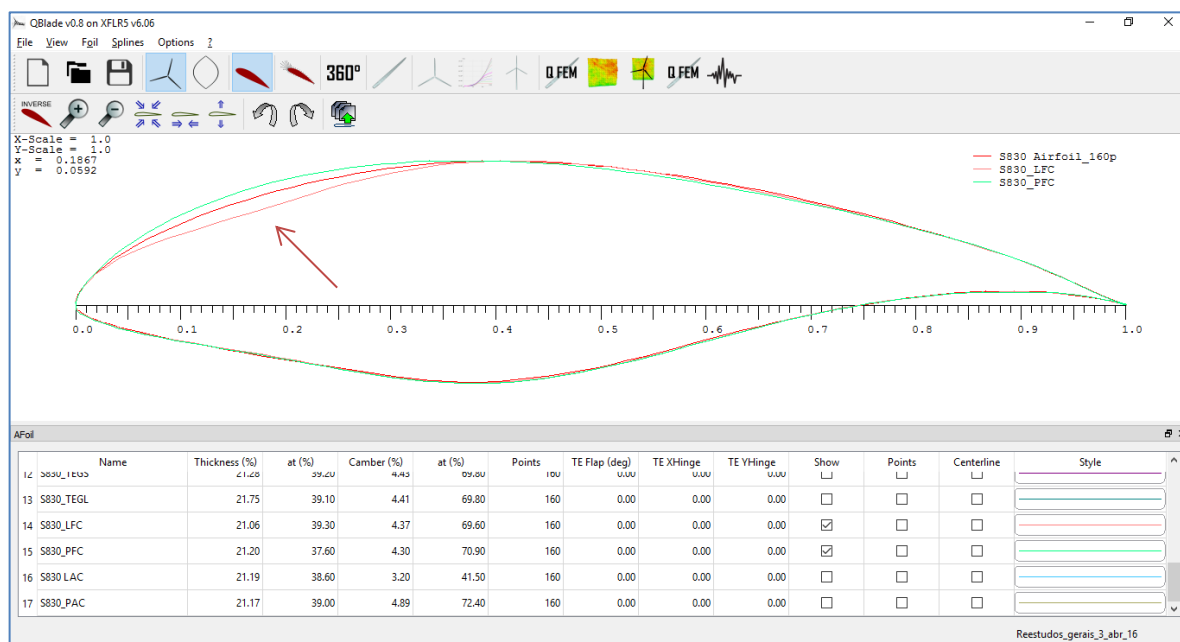


Figure 4-39 – Overview of the geometries with different suction side forward contour simulated.

⁵⁷ It is not possible to alter this geometry automatically from the original S830 geometry (case #103) using XFLR5 tools, so this and other larger modifications had to be accomplished by adjusting the splines on the splined version of the S830 airfoil, which corresponded to reference case #109.

The original suction side area convexity promoted a “transition ramp”, observable as a plateau on the C_p graph, for the design point condition. According to Somers and Tangler (Somers & Tangler, The Airfoils S830, S831 and S832, 2005b), this type of feature renders the transition imminent over the entire forward portion of the upper surface, resulting in a wide low-drag range and high lift coefficient. Also, the plateau causes the transition to migrate quickly towards the LE with increasing AOA, which gives roughness insensitivity to the profile close to the maximum lift coefficient.

The cl_{max} and $(cl/cd)_{max}$ values remained close to the reference #109 case (splined S830 airfoil) for both variations, but the decreased-convexity variant (#110) displayed a lower angle corresponding to the maximum aerodynamic efficiency, resulting in 1.1 dB less overall noise due to 1.5 dB less AOA-noise. The noise for #110 is also slightly smaller in the audible range (-0.2 dB (A)). Another case against the increased-convexity variant (#111) is that the stall angle was severely decreased in relation to the reference case.

It is important to register that increasing the splined airfoil convexity led to a slight shift in the maximum thickness location (advanced to 37.6% chord, from 39% original), decreased camber to 4.37% (from 4.41% original) and delayed maximum camber location to 70.9% chord (from 69.6% original).

Since a splined airfoil surface has tension in the curves linked by the control points, any geometrical modifications will result in changes to the neighboring points of the profile. Changes within $\pm 1\%$ of the original, reference values were controlled but were not reported.

4.5.2.3 Camber variation.

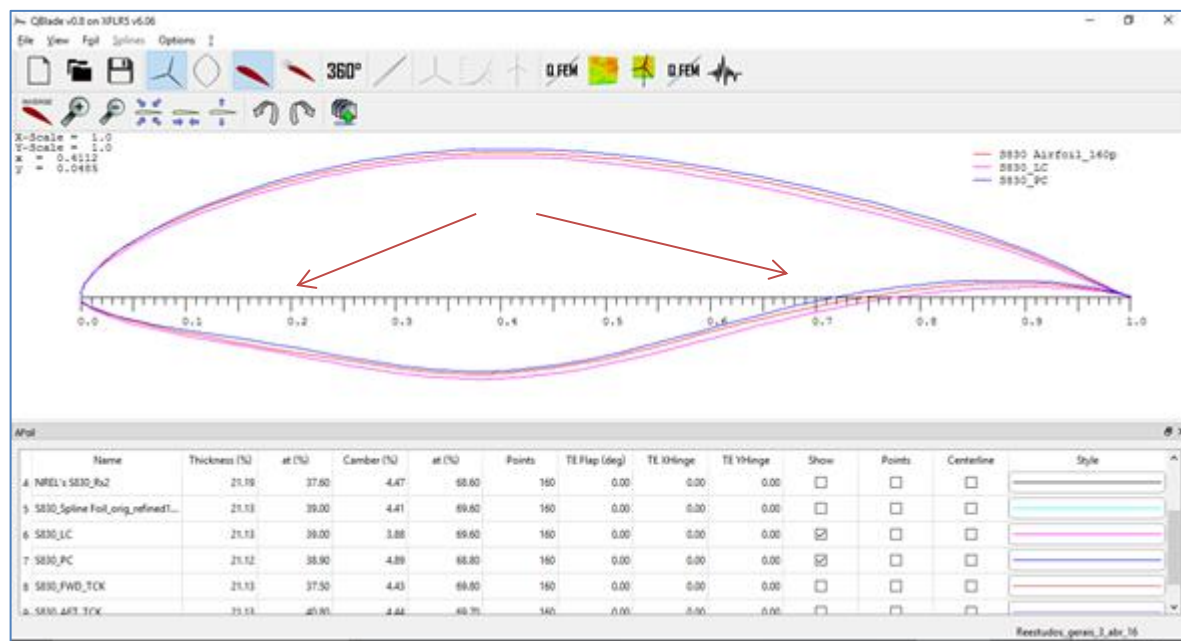


Figure 4-40 – Overview of the geometries with different camber percentages.

This step comprised testing cases #112 (less camber) and # 113 (additional camber) around the 69% chord position. The camber was changed ± 0.5 *pp*, or approximately 10% above and below the original value.

Decreased camber kept the main aerodynamic parameters very close to original (case #109) values, but decreased *cd* and the longitudinal (pitching) moment coefficient, *cm*, while the increased camber movement showed the opposite tendencies, with a significantly increased pitching moment coefficient. However, should the pitching moment not be of concern, the increased camber variant showed less overall noise (1.1 dB) and also a decrease in the level of the audible range SPL of 0.7 dB (A). Decreasing the camber also decreased the overall noise (-1 dB), but raised the audible noise by 0.3 dB (A). This shift in acoustic energy is confirmed by the spectrum peak shift, the frequency of which increased from 100 Hz to 125 Hz 1/3 octave band.

This result is consistent with the findings of Rautmann et al. (Rautmann, Ewert, & Dierke, 2015), which revealed the best performance in terms of *cl/cd* and overall SPL to be displayed by the airfoil with minimum thickness and maximum camber. However, in this development, the thickness is fixed due to structural requirements and camber variation only could be tested.

Since the modified BPM TE noise model preserved the original, geometrical AOA input instead of absolute AOA, more commonly employed for performance calculations of cambered airfoils (Kuethe & Schetzer, 1961) p. 87, this analysis should be seen with caution.

4.5.2.4 Flap angle (TE wedge angle) variation.

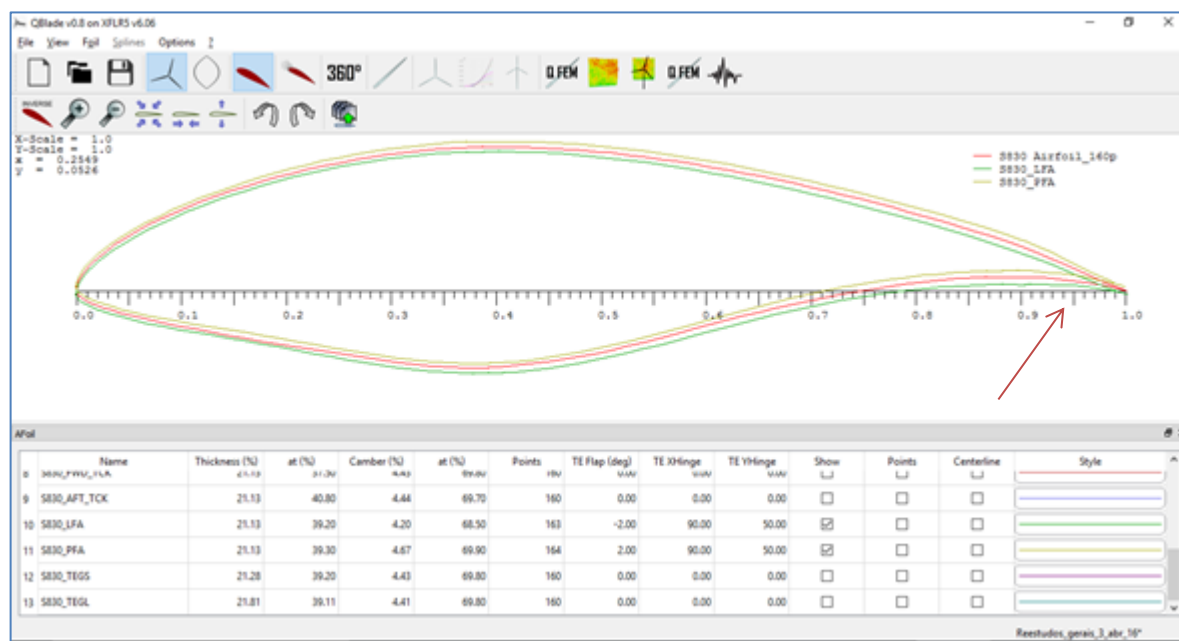


Figure 4-41 – Overview of the geometries with different flap angles, after de-rotation.

This step comprised testing cases #114 (with less flap angle) and # 115 (with more flap angle). The TE wedge angle or “flap angle” was changed $\pm 2^\circ$ from the original position. The “flap” was set at 90% chord length and 50% airfoil thickness.

The aerodynamic characteristics of the original, reference foil were hardly changed, except per the pitching moment of the section with increased flap angle (2° down flap), which once more exceeded the maximum requirement limit of -0.145. Increased pitching moment (#115) once again appears positively correlated with a reduction in the audible noise range (-0.4 dB(A)). Increased flap angle should increase the adverse (positive) pressure gradient over the aft suction side, increasing the TBL thickness (and hence the turbulence vertical scale), while reducing the associated turbulent eddies

frequency. However, the opposite is true for the pressure side, where the frequency of the turbulent eddies will increase. The final result will probably depend upon the relative strength of the TE noise sources on each side of the airfoil. The fact is that the C-weighted OASPL decreased by 0.4 dB (C) and this reduction in noise for the low frequencies is also reflected in a decrease in the overall SPL by 0.3 dB with respect to reference case #109.

The section with decreased flap angle (*2° up flap*), #114, showed a reduction in OASPL of 0.5 dB, but no reduction in the audible noise range SPL value. This variant should be of choice for less unweighted OSAPL but the variant with more flap angle should be preferable for less audible noise, should the pitching moment coefficient restriction be relaxed from the original requirements (≈ -0.145).

This case helps to clarify another of the questions raised before: as seen through the limited resolution lenses of this model, there seems to be a tradeoff among the unweighted and A-weighted noise levels, with little variation on the overall SPL. It is as if, for a certain circulation level around the airfoil, the flow energy converted into acoustic energy was approximately constant for a given Reynolds and Mach numbers, but the spectrum may oscillate among lower and higher frequencies depending upon details of the flow over the geometry and the resultant transversal turbulence length scales.

4.5.2.5 Maximum thickness position variation.

This step comprised testing cases #116 (with maximum thickness shifted forward, toward the LE) and # 117 (with maximum thickness shifted aft). The maximum thickness position was advanced and delayed 2% of the chord from the original position of 39% (reference case #109).

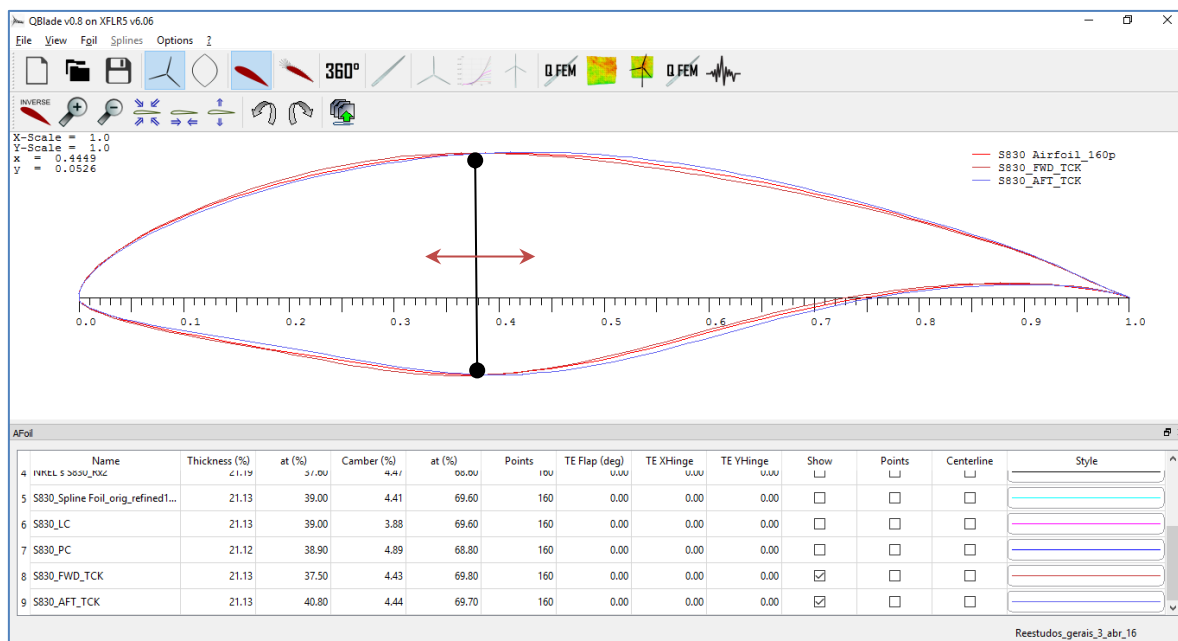


Figure 4-42 – Overview showing the geometries with different maximum thickness positions along the chord line.

Advancing the maximum thickness station towards the LE (#116) resulted in 1.4 dB less overall noise in relation to the reference case (# 109), but in the audible range the reduction was of 0.2 dB (A) only. The AOA corresponding to $(cl/cd)_{max}$ decreased significantly by half a degree, from 6.2° to 5.7°.

Most of the lift aerodynamic characteristics of the reference airfoil were preserved in this configuration (#116), but due to decreased drag it displayed an aerodynamic efficiency even larger than the reference airfoil under higher Reynolds flow.

According to Hoerner and Borst (Hoerner & Borst, 1985), p. 2-3, the maximum thickness of the high-speed airfoils was historically pushed back to between 40% and 50% of the chord in order to preserve laminar flow as much as possible and reduce drag in airplane wings. However, for the current WT application case, the operating environment lend the surface a permanent rough condition (hereby simulated by early BL tripping), and the flow speeds are of relatively low Mach numbers with less turbulent drag resulting from moving forward the maximum thickness section, as shown by the simulation.

By retarding the maximum thickness position (#117), the overall noise decreased by 0.9 dB and the same reduction was captured under A-weighted filter SPL, which

decreased by 0.9 dB (A). The AOA corresponding to $(cl/cd)_{max}$ decreased even more than the advanced thickness case, to 5.4° . However, the drag was increased for this section and the aerodynamic efficiency was lower in comparison with the reference case (#109).

In fact, it is possible to see that the noise energy is higher in the lower frequencies in the case of retarded maximum thickness position (#117), since the peak spectral frequency decreased from 100 Hz to 80 Hz and the C-weighted SPL is the only sound pressure level above the corresponding one from case #116.

4.5.2.6 Upper surface aft side convexity variation “aft convexity-AC”.

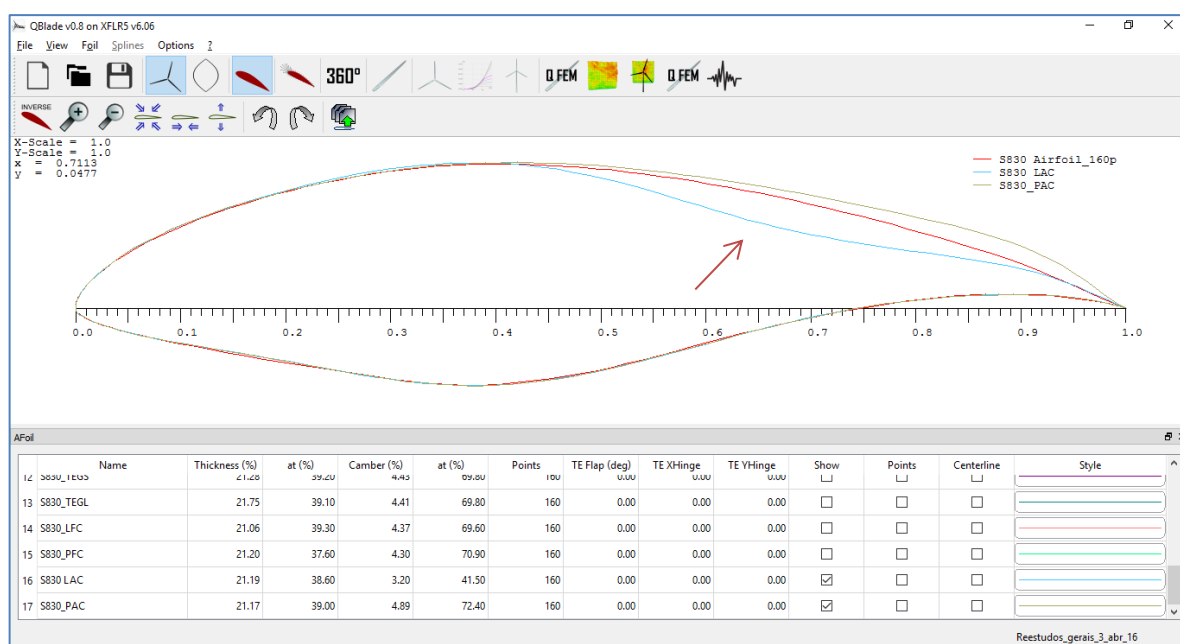


Figure 4-43 – Overview of the geometries with different suction (upper) side aft contour.

This step comprised testing cases #118 (with concave upper aft side) and # 119 (with more convex upper aft side).

These modifications interfered significantly with the camber and camber position, with both of them decreasing for case #118 and both of them increasing for case #119. Thus for analysis purpose it must be considered that the concave upper aft side variant

(#118) also has less camber (3,20%) at an early chord station (41,50%), while the more concave variant (#119) has more camber (4,89%) at a later chord station (72,40%).

The concave geometry (#118) displayed a significant -2.2 dB OASPL noise reduction over the baseline model. However, a significant part of the associated noise energy migrated to higher frequencies, bringing the spectral peak up to 200 Hz and increasing the A-weighted SPL by +2.9 dB(A). The section displayed very good aerodynamic performance, having reached a record $(cl/cd)_{max} = 108.6$ level among all the geometrical variations simulated and a higher cl at the maximum efficiency point.

The more convex (#119) displayed a significant increase in OASPL of +2 dB, but the noise energy migrated to lower frequencies, bringing the spectral peak down to 80 Hz and decreasing the audible noise level by 0.9 dB. At least part of this audible range noise reduction should be attributed to the increased camber associated with the more convex profile in the aft suction side. The # 119 geometry showed good aerodynamic characteristics but the convergence was limited for high AOA.

4.5.2.7 Trailing Edge gap.

This step comprised testing cases #120 (with small TE gap) and # 121 (with large TE gap).

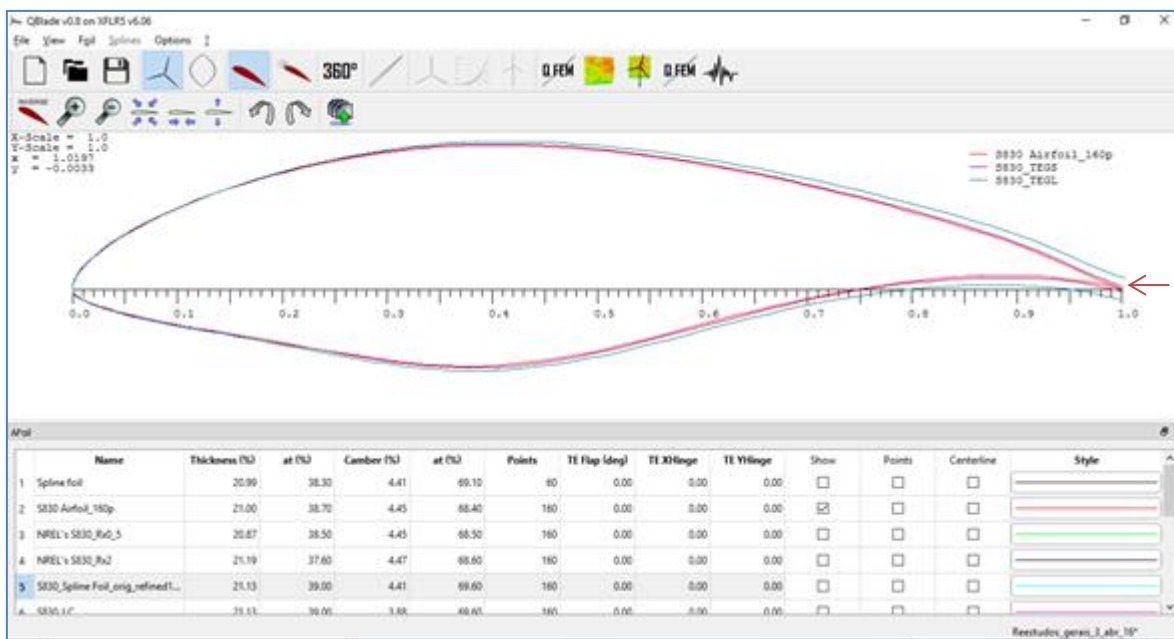


Figure 4-44 – Overview of the geometries with different LE gaps simulated.

The small and the large gaps were specifically designed for this simulation based on the general features of the sound spectrum for TE noise as discussed by Blake (Blake, *Mechanics of Flow-Induced Sound and Vibration*, 1986 II) p. 757. As discussed in the review foil section, if the airfoil thickness, h , is kept under $\delta^*/4$, the airfoil is considered “thin” and no additional hump is observed in the sound spectrum. However for thicknesses above that value (“blunt” TE) a distinct secondary hump is observed as a product of a vortex-induced tone. This condition is sometimes referred to as *airfoil singing*. The tone may become a noise with increasing bandwidth as h/δ^* , the *bluntness parameter*, is increased.

The #109 reference case displacement thickness at the TE was calculated for the reference flow and case #120 was prepared with a thin TE, with $h < \delta^*/4$, while case #121 was prepared with a blunt TE $h \sim \delta^*$. For the first case the thickness of the TE was set to $h < 0.5\%$ of the chord and for the second the TE thickness was set to $h \sim 2.1\%$ of the chord.

The modified BPM TE noise prediction method is not equipped, as programmed, to evaluate the blunt-TE vortex shedding noise. The interest at this point was on how the presence of finite TE thickness could influence the TE and AOA noises captured by the model.

This research is considered important because (i) there is no practical airfoil with an absolutely “sharp” TE, and (ii) the frequency of such a noise will be investigated later for eventual improved sound detectability of danger by nearby flying birds.

The small TE gap airfoil (case #120) showed a very significant reduction in overall SPL of 2.4 dB, however no variation was produced in the audible noise range. The cost of the reduced OASPL was an increased pitching moment, well above prescribed limits. The most significant noise reduction with this measure occurred at the lower frequencies, reflected in the C-weighted noise reduction of 2.3 dB (C). Also, the peak of the spectrum was now located at the 125 Hz band.

The large TE gap airfoil (case #121) displayed an even more impressive reduction in OASPL of 5 dB at the expense of a small increase of 0.2 dB (A) detected at the audible range. The spectral-peak frequency was raised to 160 Hz at a level 5.3 dB (A) lower than the level at the spectral-peak of the reference case (#109).

A large TE gap could be a suitable manner to control SPL in such a large size WT airfoil, except for the fact that it may be the source of blunt-TE vortex shedding noise, which can be significant and may offset completely this apparent advantage.

This might also remain an alternative worth investigating in case some flow might be ejected from the TE at a suitable jet coefficient, using TBL control techniques.

4.5.3 General Data Discussion.

While analyzing the overall modifications and performance at Table 4-17, it is important to remember that the returned numerical results are initial tendencies for the respective modifications applied over a baseline airfoil. The limits of the modifications acceptable were not tested at this point. Also, although the modifications were applied one at a time, the spline nature of the airfoil contour imparted secondary modifications to the geometry in some indicated cases, making the results not necessarily independent.

Figure 4-45 allows some overview of the simulation process and aids in the identification of dominant geometrical changes that might simultaneously improve

unweighted SPL, A-weighted SPL and the aerodynamic efficiency parameter $(cl/cd)_{max}$.

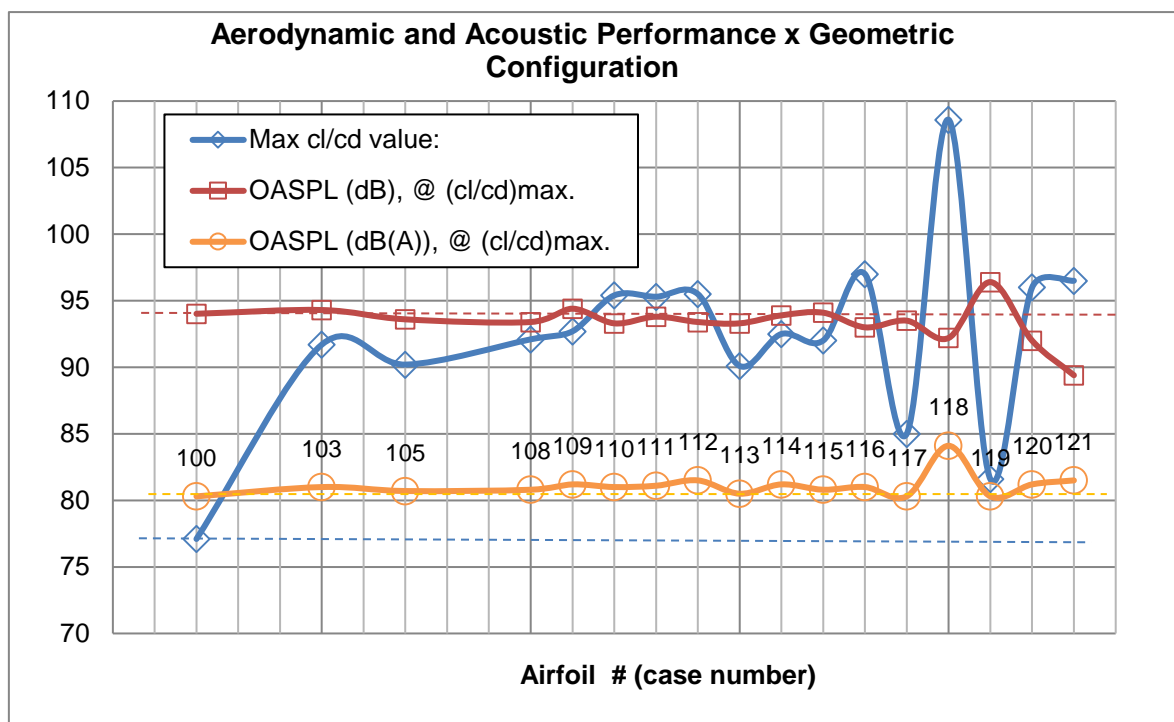


Figure 4-45 - Overall acoustic and aerodynamic performance for Airfoil #100 (S830 original geometry and design conditions), the reference spline foil #109 (S830 splined foil at Poli-100 blade operating conditions) and all geometrical variations studied. Red line = original S830 OASPL level (94 dB). Blue line = Original S830 cl/cd max level (77.1). Orange line = original S830 A-weighted OASPL (80.3 dB(A)).

Because of the increased Reynolds number, from design ($Re \sim 4,000,000$) to the Poli-100 85% span blade operating conditions ($Re \sim 7,700,000$), all simulated geometries show larger $(cl/cd)_{max}$ and most of them also display larger cl at the maximum efficiency point (see Table 4-17). While generally desirable, this excessive aerodynamic performance in relation to the requirements may subject the WT to excessive stresses, especially in the case of wind gusts, pitch control delay or malfunction. Also, it may be translated into additional, unwanted noise and additional costs for more sophisticated materials that would be necessary to bear higher stress loads.

As far as noise is concerned, many geometries displayed a tradeoff-type reduction involving unweighted and A-weighted noise sound pressure levels. Because of this situation, it was decided to classify the airfoil geometrical modifications in some categories:

- A. Dominant modifications (increased aerodynamic performance, decreased unweighted and A-weighted SPL) based on the # 100 reference case (original airfoil, original flow conditions).
- B. Dominant modifications (increased aerodynamic performance, decreased unweighted and A-weighted SPL) based on the #109 reference case (splined original airfoil, Poli-100 operating conditions).
- C. Geometrical modifications that have led to TE noise source strength reduction (reduction in OASPL and A, B and C-weighted SPL).
- D. Geometrical modifications that have led to frequency shift resulting in decreasing audible range noise.
- E. Geometrical modifications that have led to frequency shift resulting in increasing audible range noise.

Cases C,D,E are related to the following reference cases: for geometrical variations #105 and #108, the reference case is case # 103, the original airfoil at the new operating conditions; all other cases (#110 to #121) are referred to the #109 case, since they required the previous design of a spline-foil approximation before geometrical changes could be implemented to it. The result of the classification applied to the sensitivity study cases is shown in Table 4-18.

Table 4-18 - Classification of the geometrical modifications cases in relation to reference cases.

Case #	Description	Ref. Case for C,D,E	Classification
105	S830 original with doubled LE radius	103	C,D
108	S830 original with halved LE radius	103	C,D
110	S830 Spline Foil with less upper forward side convexity	109	B,C,D
111	S830 Spline Foil with more upper forward side convexity	109	B,C,D
112	S830 Spline Foil with less camber	109	E
113	S830 Spline Foil with more camber	109	C,D
114	S830 Spline Foil with less flap angle	109	C
115	S830 Spline Foil with more flap angle	109	C,D
116	S830 Spline Foil with thickness shifted towards LE	109	B,C,D
117	S830 Spline Foil with thickness shifted towards TE	109	A,C,D
118	S830 Spline Foil with less upper aft side convexity	109	E
119	S830 Spline Foil with more upper aft side convexity	109	D

120	S830 Spline Foil with small TE gap	109	B,C
121	S830 Spline Foil with large TE gap	109	E

The conclusions from Table 4-18, were:

- Case #117 airfoil, with thickness moved 2% aft of the original position, to 41% chord, was the only geometry dominant over the reference case #110 (original geometry, original Reynolds number). It displayed simultaneously a better aerodynamic efficiency and less noise in the new, higher velocity operating condition of $Re \sim 7,700,000$, when compared to the original S830 airfoil at $Re \sim 4,000,000$. The OASPL had been reduced by 0.5 dB, with no detectable variation at the audible range, while aerodynamic efficiency improved from 77.1 to 85.0.
- Cases #110, #111, #116 and #120 were dominant over the reference case #109 (original splined geometry, higher Reynolds number). The modifications in respect to the baseline geometry were variations in upper forward side convexity to both directions, thickness moved 2% forward of the original position and adoption of a small TE gap.
- The geometrical modifications that resulted in decreased TE-noise emission in all frequencies for the higher speed flow were (i) #105 and #108, LE radius change in both directions (see further discussion on the subject); (ii) #110 and #111, more and less upper forward side convexity; (iii) #113, increased camber; (iv) #114 and #115, flap angle variations in both directions; (v) #116 and #117, maximum thickness position in both directions and (vi) #120, the addition of a small TE gap. The general noise emission reduction tendency observed while so many variables change to any direction, suggests that these geometric features have been probably optimized to meet aerodynamic requirements, rather than aeroacoustic.
- The geometrical modifications that resulted in reduced audible range noise levels were (i) #105 and #108, LE radius change in both directions; (ii) #110 and #111, more and less upper forward side convexity; (iii) #113, added camber; (iv) #115, flap angle addition; (v) #116 and #117, maximum thickness position in both directions and (vi) #119, the addition of upper aft side convexity.

- The geometrical modifications that resulted in increased audible range noise levels were (i) #112 camber reduction; (ii) # 118, the reduction of upper aft side convexity and (iii) #121, the addition of a large TE gap.

This last observation poses another tradeoff, this time among the audible noise and the aerodynamic characteristics of the airfoil. While camber reduction could be the easiest way to decrease the airfoil aerodynamic efficiency (towards the S830 original design level), that could also imply in higher noise emission at the audible range.

The next step planned was to investigate the inception of new airfoils deriving from a combination and/or amplification of the geometrical variations that may eventually be successful at producing:

- Aerodynamic efficiency comparable to case #109 reference (higher flow velocities) but with reduced unweighted overall SPL.
- Aerodynamic efficiency comparable to case #109 reference (higher flow velocities) but with reduced audible SPL.
- Aerodynamic efficiency comparable to case #100 (original aerodynamic requirements) but emitting less noise than the S830 airfoil operating in the new, higher Reynolds regime (case #109).

It is acknowledged here that an increased aerodynamic performance airfoil employed to the full potential of the higher Reynolds number could induce higher aerodynamic stresses in the blade root and might require deployment of higher strength materials and result in increased blade cost and weight for the 100-m diameter rotor, for a fixed thickness schedule.

Before any design was attempted, the noise levels, by source type and filter, were plotted for the $Re \sim 7,700,000$ cases, along with one reference case (#109).

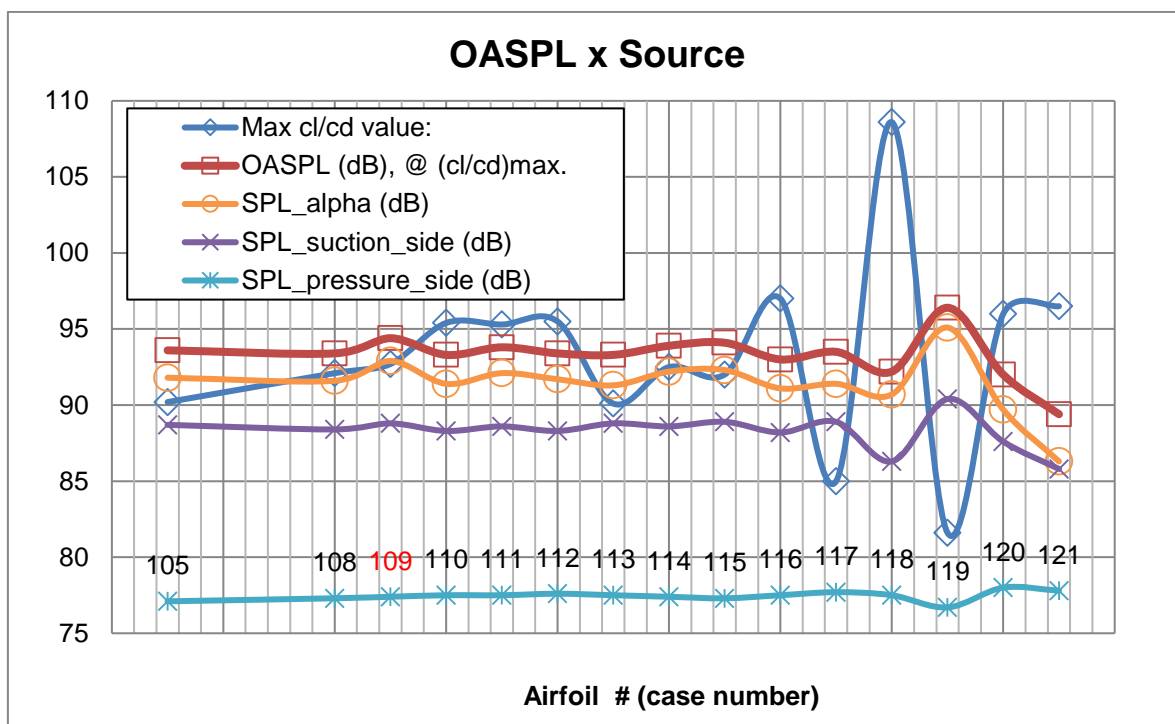


Figure 4-46 - Plot of OASPL x source graph for the higher velocity cases with the purpose of identifying priority sources.

Figure 4-46 above confirmed that the angle of attack dependent noise, SPL_α , also originally referred to by the BPM model authors as *the separated-boundary-layer*⁵⁸ *noise contribution*, is the main noise source for all cases, when the noise was evaluated at the $(cl/cd)_{max}$ angle for each case, which ranged from 4.4° to 7.2° .

Also it was possible to see some negatively correlated behavior between the aerodynamic efficiency and SPL_α and SPL_s . The SPL_p , on the other hand, displayed little variation throughout the 4.4 to 7.2 AOA range and seemed little correlated with the aerodynamic efficiency.

It was suggested by this plot that controlling SPL_α would be key for controlling OASPL, even when all the angles corresponding to $(cl/cd)_{max}$ were below the switching angle.

⁵⁸ The “separated-boundary-layer” terminology is employed in (Brooks, Pope, & Marcolini, Airfoil Self-Noise and Prediction, 1989), p. 57m to refer to the additional “angle-of-attack noise contribution” over the suction side, between zero AOA and stall, but not in a deep stall situation.

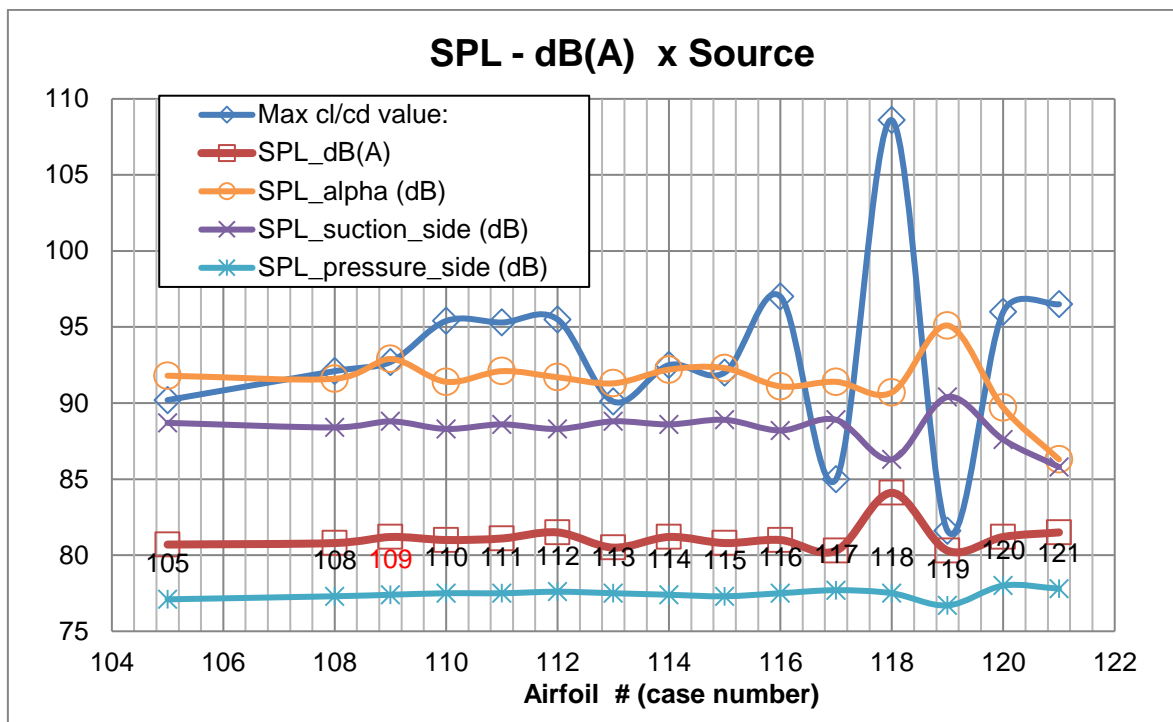


Figure 4-47 - Plot of SPL dB(A) x source graph for the higher velocity cases in order to investigate sources that contribute more to audible noise levels.

When graphically analyzing the audible overall SPL against the sources, Figure 4-47 revealed a strong visual, unbuffered, negative correlation among the SPL_s and audible overall SPL, suggesting that the mechanisms responsible for reducing SPL_s were also key for increasing audible frequency noise levels in this model and vice-versa.

It was also noticed that, throughout the range of cases simulated, no significant reduction in the audible SPL had been achieved.

Although larger reductions in the A-weighted SPL would be desirable, it turned out to be unlikely to happen according to these findings. The geometry size (chord, wetted edge size) and flow conditions (AOA, velocity, δ^*) of the cases presented have led to peak frequencies in or around the 100 Hz band, i. e., close to the lower end of the audible range. Since the A-weighted SPL scale is attenuated up to the 800 Hz band and it is strongly buffered at the 100 Hz band (-19.1 dB), even significant SPL reductions near the peak frequency will not translate into significant A-weighted SPL reductions.

As a confirmation of this hypothesis, the calculation of the peak frequency for an AOA below the switching angle was done explicitly. In the BPM model, the peak-frequency is determined by the peak-Strouhal number, St_1 , as a function of the Mach number:

$$St_1 = 0.02 \cdot M^{-0.6} \quad (3 - 12)$$

For a Mach number of 0.21, a local flow velocity of 72.32 m/s and a displacement thickness of 3.16×10^{-2} m, evaluated with the aid of XFLR5 at the suction side of the reference case #109, at 6° , the resulting peak-frequency was:

$$St_1 = 0.02 \cdot (0.21)^{-0.6} = 0.0510 = f \cdot \delta^* / U \quad (4 - 3)$$

$$f \sim 117 \text{ Hz} \quad (4 - 4)$$

This confirmed the previous argument that, for such airfoil scale and flow intensity, a “quiet airfoil”, as far as TE noise is concerned, is probably an airfoil with reduced sound pressure level emissions in the lower range of the audible range and possibly in the infrasound range, only.

Also, when the AOA is further increased towards the deep stall region, the turbulence scale is also increased, with more noise energy being emitted in the lower frequencies and infra-sound portion of the spectrum. This was compatible with another conclusion of the BPM experiments (Brooks, Pope, & Marcolini, Airfoil Self-Noise and Prediction, 1989), p. 3, that for mildly separated flows, the dominant noise was emitted from the TE area, while for deep stall flow, the noise was radiated from the whole chord. This finding was also consistent with the findings of Fink and Bailey (Fink & Bailey, 1980), whose concept of *universal noise spectrum* was borrowed by the BPM model (in the form of function A of Eqn (3-2) and Eqn (3-3)).

As a last observation on this point, the peak A-weighted SPL level occurs for case #118, with an increase of 4 dB (A) above the average level. This may only be achieved through a significant (~50%) BL thickness decrease, which decreases the turbulence vertical scale while increasing its frequency, explaining the spectrum peak shift up, towards the 200 Hz band in this particular case. This was most probably achieved due to a significantly decreased camber (to 3.2%) derived from the smoothed convexity on the upper aft side of the airfoil.

These preliminary results suggested that overall TE noise reduction was possible through geometry manipulation; however, TE noise reduction in the audible range for this scale of chord and flow (i.e. for this scale of vertical turbulence scale) would be very limited and would probably have to be traded for unweighted SPL.

A brief review of selected previous researches in this field is useful at this point to recall what level of SPL reduction might be expected from geometric manipulation and under which conditions. Unfortunately, all cases found involved smaller-chord airfoils at smaller Reynolds number flows:

- As discussed during the bibliographic review, it was concluded by Guidati and Wagner (Guidati & Wagner, 2000) that a theoretical reduction of OASPL of between 2 and 4 dB(A) is achievable by airfoil shape manipulation, but the authors managed to do so for untripped flow only, which is not a good representation of the flow around a large-size WT blade.
- During the EU *SIROCCO* Project (Schepers, et al., 2007), a modified TNO-TPD TE noise model considering turbulence anisotropy effects via a Reynolds Stresses turbulence model combined to a sophisticated aero-acoustic model was implemented in a numerical optimization environment that generated airfoil shapes with minimal noise production, in an automated way. The airfoil shapes would theoretically indicate from 1 to 3 dB(A) less noise, at the design lift range, but subsequent field measurements showed noise reduction in the order of 0.5 dB(A), only.
- The RISO-B1-18 airfoil optimization performed by Bertanoglio et al. (Bertanoglio, Madsen, & Bak, 2009), also used the sophisticated modified TNO-TPD TE noise model, at $AOA = 6^\circ$ only, and found the best OASPL reduction obtained in the 1 – 2 dB range, which they considered relevant for the purpose of WT design.
- OASPL reductions between 2 and 4 dB (A) were attained in particular conditions, with deployment of serrations by Petitjean et al. (Petitjean, Drobietz, & Kinzie, 2011), but noise was attenuated in frequencies below 2 kHz only.

Considering the small amplitude of the feasible gains, the family of “quieter” airfoils developed are discussed next.

4.5.4 Profiles of quieter airfoils for the POLI-100 m 85% radial blade station.

4.5.4.1 – A quiet airfoil aimed at high aerodynamic performance.

This analysis has led to the development of the SP4621HP airfoil, with high aerodynamic efficiency and reduced unweighted, overall SPL in relation to the S830 operating in its design condition and also in the new condition.

The airfoil coding is intended to represent:

SP – Silent Profile.

4 – The first digit stands for the nominal airfoil camber, as a % of the chord.

6 – The second digit stands for the nominal maximum camber position divided by 10, as a % of the chord.

21 – The maximum nominal airfoil thickness, expressed as a % of the chord.

HP – High Performance WT airfoil.

In principle, all configurations classified under at least one of the letters B, C, D and E of Table 4-18, would suggest geometrical modifications to be considered for this airfoil development. However, OASPL must be equal to or lower than the reference cases #100 (S830 in design condition) and #109 (splined S830 in the higher Reynolds operating condition). Also, the $(cl/cd)_{max}$ must be larger than that of the reference cases #109.

This limited the applicable modification choices to the following cases:

- #110 and #111
- #112
- #114
- #116
- #118
- #120 and # 121.

Before incremental modification was implemented during the iterative design process, the cases for which modification of the parameter to any direction showed improvement in noise emission had to be addressed.

Concerning configurations #110 and #111, the former (less upper forward side convexity) showed an increased rate of change, in the desired direction, for both noise reduction and aerodynamic efficiency and was thus considered dominant over the latter⁵⁹.

Concerning configurations #120 and #121, the smaller TE gap configuration was selected for implementation, even though the model employed suggested otherwise⁶⁰. The reason was that a large TE gap would induce vortex shedding noise, not captured or evaluated by the current model, which might create a tonal noise. If applied along all WT blade-span, this tonal noise would produce an audible tone of high SPL that would probably trigger a 5 dB measurement penalty prescribed by most noise control standards in the presence of a (more annoying) tonal noise.

Last but not least, although not specifically within the scope of the research, the increase of the LE radius had the potential to decrease the inflow noise significantly. Since by doubling the LE radius of the original airfoil the good aerodynamic characteristics had been preserved (including the roughness tolerance); the TE noise OASPL had decreased by 0.8 dB and the $(cl/cd)_{max}$ had decreased only very slightly (from 92.7 to 90.2), this modification was also adopted in the simulation and should be considered as a “good practice” rule when designing a quiet airfoil⁶¹.

After due considerations, the following modifications were additively and incrementally tried over the original airfoil shape:

1. LE radius increase (sample case #105).
2. Upper forward side convexity smoothing (sample case #110)
3. Less camber (sample case #112).
4. Less flap angle, or TE wedge angle (sample case #114).
5. Advancement of thickness toward the LE (sample case #116).
6. Upper aft side convexity smoothing (sample case #118).

⁵⁹ An automated optimization method would conclude the same way in this case.

⁶⁰ An automated optimization method would conclude otherwise in this case.

⁶¹ This is another aspect that could probably not be captured by an automated design optimization process.

7. Adoption of a small TE gap (sample case #120).

Many combinations were tried in this case, and the result proved sensitive to the order of application of the modifications, which would make an automated optimization process quite challenging, prone to finding many local minimums.

From 20 or so acceptable airfoil combinations produced, one revealed a very high aerodynamic performance standard $(cl/cd)_{max} \sim 110$; $cl_{max} \sim 2.0$ and almost 3 dB less unweighted OASPL over the baseline cases. This prototype (case #165), with development name *SP XX21-77-75163*, was later renamed *SP4621HP*, and its relative performance may be seen in Table 4-19, column three, as case #165:

Table 4-19 - Aerodynamic and aeroacoustic performance of the SP4621HP dedicated WT airfoil when compared to the S830 in design condition and higher Reynolds number condition. Only differences in SPL should be considered.

Airfoil	S830, 4M, Tripped	Spline_S830_RO	SP XX21-77- 75163 - thin TE gap	SP XX21-77- 75163 - thin TE gap - QMO
Airfoil / case number	#100	#109	#165	#166
Aerodynamic/ Aero acoustic Characteristic	NREL design point	POLI_100 WT at 85% span	POLI_100 WT at 85% span	POLI_100 WT at 85% span
Reynolds number:	4,000,000	7,700,000	7,700,000	7,700,000
Mach number:	0.21	0.21	0.21	0.21
Polar object (file name)	T1_Re4,000_ M0,21_N9,0	T1_Re7,700_ M0,21_N9,0	T1_Re7,700_ M0,21_N9,0	T1_Re7,700_ M0,21_N9,0
cl max:	1.65	1.75	2.0	2.0
angle of cl max	18	20	15	15
Max cl/cd value:	77.1	92.7	110.4	104
Angle of max cl/cd	5.7	6.2	6.2	4.0
cl at max efficiency point:	1.16	1.26	1.43	1.2
cd at max efficiency point:	0.0150	0.0136	0.0130	0.0115
cm at max efficiency point:	-0.146	-0.154	-0.174	-0.178
Tripping (%chord, upper and lower surfaces):	5%/10%	5%/10%	5%/10%	5%/10%
AOA test range:	-3 to +20	-3 to +20	-3 to +20	-3 to +20
Convergence range	-3 to +20	-3 to +20	-3 to +17.6	-3 to +17.6
OASPL (dB), @ (cl/cd)max.	94.02	94.40	91.56	88.10

Peak Frequency:	80 Hz (87.7 dB)	100 Hz (87.8 dB)	200 Hz (84.92 dB)	200 Hz (80.91 dB)
OASPL (dB(A)):	80.30	81.20	83.35	81.76
OASPL (dB(B)):	88.20	89.30	89.38	86.29
OASPL (dB(C)):	93.40	93.90	91.48	87.98
SPL _α (dB)	92.10	92.90	89.92	84.45
SPL _s (dB)	89.20	88.80	86.06	84.73
SPL _p (dB)	77.60	77.40	77.63	78.44

Other configurations were obtained with lower OASPL, but the coefficient of moment and the TE gap exceeded the specifications, or the aerodynamic efficiency or lift coefficient were poor. The SP4621HP airfoil profile is shown in Figure 4-48, along with the S830 profile. It is possible to see the preserved thickness of the original airfoil, considered a fixed requirement. The developed airfoil showed larger $(cl/cd)_{max}$, cl_{max} and less unweighted TE noise than the S830 in any of the reference flow conditions.

In spite of the fact that the SP4621HP also has an operating point $cl \sim 1.43$ higher than the regular S830 $cl \sim 1.2 - 1.3$ range, it emits lower unweighted overall TE noise than the original S830 in both flow conditions.

Also the new airfoil is expected to display superior performance concerning inflow-noise, although no advantages could be quantified with the current model, which is restricted to airfoil self-noise.

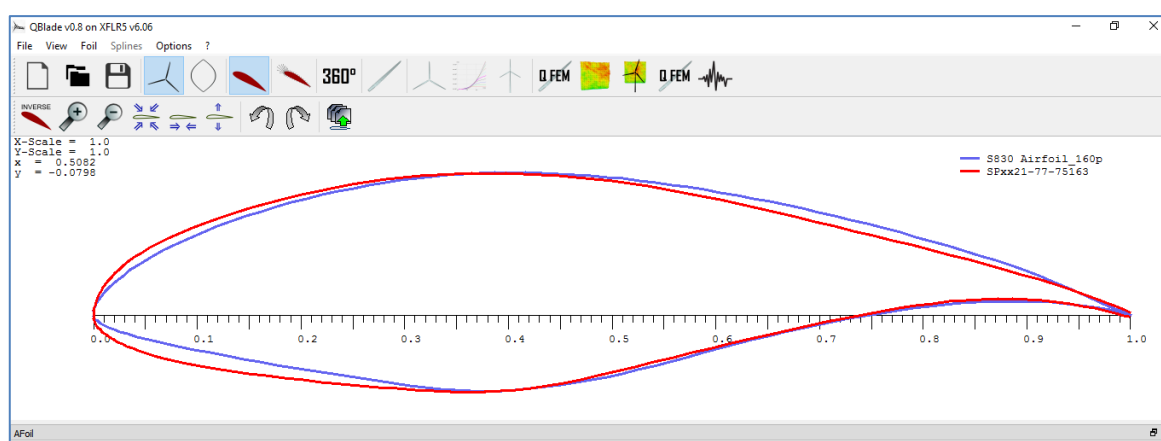


Figure 4-48 - The SP4621HP profile (red), with preserved original thickness in relation to the S830 airfoil (blue).

The TE gap is 0.235% of the chord at the design position of 0.85R span, or 3.65 mm, which is a very tight thickness to obtain from a 1.55 m chord airfoil. The $\frac{h}{\delta^*} < \frac{1}{4}$ must be verified for all spanwise stations where the airfoil is to be employed and this tight thickness tolerance might impose higher manufacturing costs to the design.

The clear advantages of the new design however, are in the reduction of SPL_α and SPL_s levels and correspondent sources. However, the reduced camber reduced also the BL thickness, which increased the TE noise frequency, as can be confirmed by the higher, 200 Hz peak in the spectrum. This resulted in increased A-weighted SPL which is from 0.8 to 2.4 dB (A) larger than the baseline cases. This fact also confirmed the main tradeoff revealed in the course of this research.

One opportunity that remains open to reduce TE noise even further is to find a way to transfer aerodynamic load from the suction side to the pressure side while alleviating the suction side noise contribution and increasing, in a controlled way, the noise from the pressure side, which is a much less relevant source of noise.

The key requirement for the design of this airfoil was the increased $(c_l/c_d) \times AOA$ slope (which proved higher than the slopes of the original airfoil for both Reynolds numbers), as revealed by the sensitivity analysis. This is show in Figure 4-49.

Also the polar diagram $(c_l \times c_d)$ reveals a very smooth behavior.

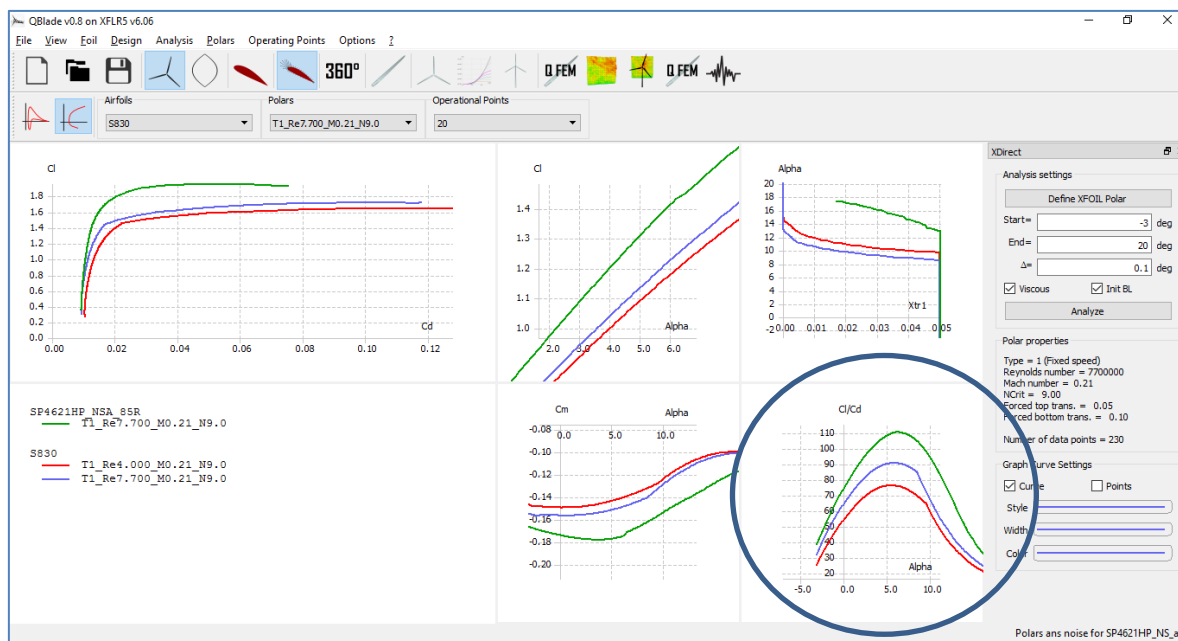


Figure 4-49 - The Polar diagrams for the S830 (red line = low Re; blue line = high Re) and the SP 4621HP (green line) airfoil. The $cl/cd \times AOA$ slope is slightly larger for the green curve in the circled graph.

Due to structural and production cost concerns, the SP4621HP airfoil may be operated below optimum conditions, hereby called a “*Quiet Mode Operation*”, QMO, defined as a the point of $(cl/cd) < (cl/cd)_{max}$, that corresponds to $cl \sim 1.2$.

This situation would not impose aerodynamic⁶² loads larger than expected at the original design condition of the S830 airfoil, provided the WT is operating close to a steady state.

By looking at the last column of Table 4-19, which represents this down-rated situation, it is possible to see that, at QMO, the SP4621HP airfoil operates in partial load and in AOA of 4.0° , as opposed to 6.2° in the maximum efficiency situation.

Apart from the large reduction in TE AOA dependent noise, the reduced AOA loads more evenly the suction and pressure sides of the airfoil for an exceptional overall combined unweighted-OASPL cut of 6.3 dB when compared to reference case #109.

The proposal of this “QMO”, or derated operation, was a direct consequence of the strategy envisioned earlier of unloading the suction side and loading the pressure side

⁶² For larger blades, the main structural concern may be the loading derived from gravitational and centrifugal stresses, not necessarily aerodynamic, as seen before.

for reducing the TE noise. However, this was not accomplished via geometric modification of the airfoil, but rather by working at an off-peak design point.

When the airfoil name is followed by the suffix QMO in the text, then, it does not refer to a different geometrical configuration but to a different pitch-angle setting. A flexible pitch control mechanism should be able to accommodate both operating programs⁶³, HP and QMO, the first one positioning the section at a pitch angle resulting in local AOA of 6.2° and the latter, 4.0° AOA.

4.5.4.2 – The SP4721LA.

The code name of the airfoil designed for less TE noise emission in the audible range is similar for the one seen before, except for the suffix “LA”, suggesting “A-Level” attenuation.

During this particular development, the objective was to investigate the feasibility of designing an airfoil geometry with flatter $\frac{cl}{cd} \times \alpha$ curve at the top. This would allow the airfoil to operate closer to the $(cl/cd)_{max}$ for a long range of AOA. Also, the plateau should start for a low AOA, which would allow the airfoil to operate at the QMO setting with little penalty in relation to the maximum efficiency AOA.

After many trials, it was found that the quick air acceleration over the suction side, with consequent formation of laminar bubble close to the LE, was one of the mechanisms capable of increasing the slope of the $\partial(cl/cd)/\partial\alpha$ curve. However, a “horn” appeared systematically at the polar diagram (and most aerodynamic diagrams) close to the angle of formation and bursting of the bubble, with corresponding flow reattachment. Unfortunately, while this bubble may help reduce one of the sources associated with the TE noise, it might also originate another, unmonitored source, which is the laminar boundary layer vortex-shedding, or LBL-VS, noise. However, as far as simple numerical simulation can analyze (which will be pending of experimental or more sophisticated CFD simulation validation), most of the benefit (the flat-top of the curve)

⁶³ Provided airfoils in other blade sections also have acceptable efficiencies when the design AOA is altered by the same amount.

can be preserved by advancing the tripping position to 1% of the chord, at the suction side. The resulting effect was a dedicated airfoil with a less-smooth polar behavior, but with good TE noise attenuation obtained for a $cl \sim 1.2$ at a low 4.5° AOA, which also corresponds to the $(cl/cd)_{max}$ angle. This is, so to describe, an airfoil for which the HP and the QMO modes of operations have merged together.

The main advantage of this airfoil is that it radiates less A-weighted SPL noise than the original S830 airfoil does at the same higher Reynolds number, and almost the same A-weighted SPL of the S830 airfoil operating at the original, lower Reynolds number.

The features of this airfoil, originally developed as the SPxx2177-751-Rx2 and later renamed as the SP4721LA (case #163), are shown in Figure 4-50, Figure 4-51 and Table 4-20.

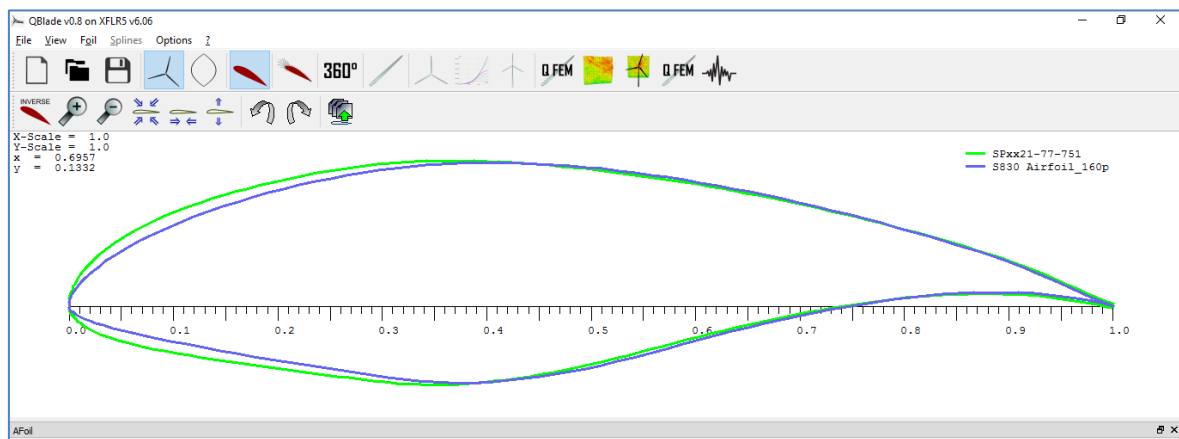


Figure 4-50 - The SP 4721LA profile, with preserved original thickness in relation to the S830 airfoil.

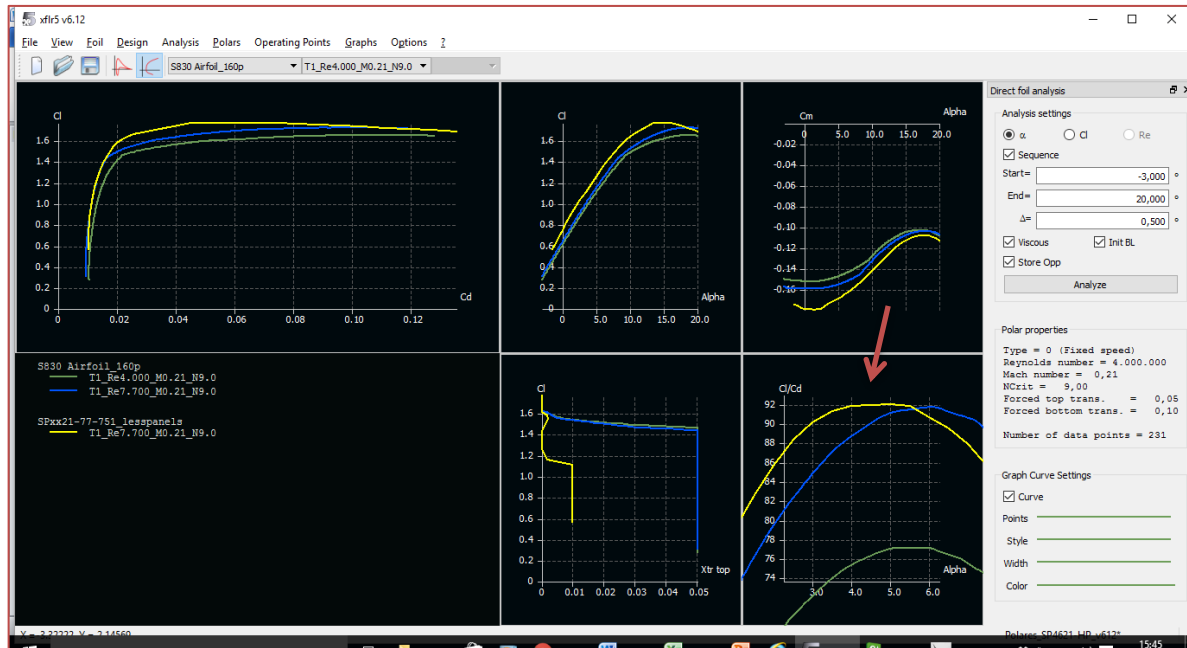


Figure 4-51 - The Polar diagrams for the S830 (green and blue) and the SP4621HP airfoil (yellow curve). Notice the flat-top curve of $(cl/cd) \times \alpha$ diagram indicated by the red arrow.

As may be seen on Table 4-20, the SP4721LA has values of $(cl/cd)_{max}$ and cl slightly below those of the reference case #109, however, in exchange for a significant 4.74 dB unweighted noise reduction and 0.5 dB (A) A-weighted noise reduction.

Table 4-20 - Aerodynamic and aeroacoustic performance of the SP4721LA (case #163) dedicated WT airfoil when compared to the S830 in design condition (case #100) and higher Reynolds number condition (case # 109).

Airfoil	S830, 4M, Tripped	Spline_S830_RO	SP xx21-77-751 Rx2, smoothed
Airfoil / case number	#100	#109	#163
Aerodynamic/ Aero acoustic Characteristic	NREL design point	POLI_100 WT at 85% span	POLI_100 WT at 85% span
Reynolds number:	4,000,000	7,700,000	7,700,000
Mach number:	0.21	0.21	0.21
Polar object (file name)	T1_Re4,000_M0,21_N9,0	T1_Re7,700_M0,21_N9,0	T1_Re7,700_M0,21_N9,0
cl max:	1.65	1.75	1.8
angle of cl max	18	20	14.9
Max cl/cd value:	77.1	92.7	91.5
Angle of max cl/cd	5.7	6.2	3.8
cl at max efficiency point:	1.16	1.26	1.14
cd at max efficiency point:	0.0150	0.0136	0.0125
cm at max efficiency point:	-0.146	-0.154	-0.172
Tripping (%chord, upper and lower surfaces):	5%/10%	5%/10%	1%/10%
AOA test range:	-3 to +20	-3 to +20	-3 to +20
Convergence range	-3 to +20	-3 to +20	-2.9 to +20
OASPL (dB), @ (cl/cd)max.	94.02	94.40	89.66
Peak Frequency:	80 Hz (87.7 dB)	100 Hz (87.8 dB)	125 Hz (82.6 dB)
OASPL (dB(A)):	80.30	81.20	80.70
OASPL (dB(B)):	88.20	89.30	86.32
OASPL (dB(C)):	93.40	93.90	89.38
SPL_α (dB)	92.10	92.90	85.96
SPL_s (dB)	89.20	88.80	86.68
SPL_p (dB)	77.60	77.40	78.16

4.5.4.3 – The SP4721BS.

As mentioned in Section 1.1.2, apart from noise disturbances and visual pollution, birds and bat strikes are other relevant side effects of the operation of Wind Turbines.

Although the current research is focused on a single airfoil self-noise mechanism, no opportunity was missed to add value to the design of quieter airfoils by including design practices that could contribute to the reduction of other noise sources, such as the inflow noise. This approach has been deemed necessary in order to avoid that, in the process of reducing TE noise, other noise sources could be strengthened or, in this particular case, bird awareness of the presence of the WT equipment could be reduced.

Due to this reason, it was decided to develop an airfoil derivative that could improve WT acoustic detectability by birds, and so, help to relieve another problem commonly attributed to wind turbine farms.

Even though a somewhat large set of restrictions must be met for aerodynamically generated noise to enhance WT detectability by birds, one important coincidence prompted the creation of this profile: for a specific TE gap size it seemed possible to generate a tone or a small hump, in the noise spectrum, near the 3 kHz band, as described by Brooks and Hodgson (Brooks & Hodgson, 1981) p. 79-81 and also Blake (Blake, *Mechanics of Flow-Induced Sound and Vibration*, 1986 II) p.758-763, at flow conditions similar to those present at the Poli-100 WT outboard radius. Also, the frequency of the tone thus generated would be in the range of the best audibility for many types of birds which is between 2 and 4 kHz (Dooling, 2002).

As seen in Section 2.5.2, Dooling (Dooling, 2002) considered that a single pure tone contribution to the overall SPL, even with a high signal-to-noise ratio against the background wind, might result in a small or negligible OASPL increase in a broadband noise, when the main noise contributions were in the low frequency range. Also, the ratio of two noises must be of at least 1.5 dB for a typical bird to distinguish between them. That means that if the noise from the WT is decreased to a very close level of the ambient noise (wind), the blade noise would not be heard by a bird, increasing the probability of strikes.

This led to the conclusion that the deployment of quieter WT airfoils might have also undesired side-effects over certain bird populations.

The problem of the frequency of vortex formation behind lifting surfaces is much more complex than the simple Strouhal number dependence found on cylinders, according

to Blake (Blake, Mechanics of Flow-Induced Sound and Vibration, 1986 II) p. 762-763, who assembled a table from several references showing the frequency dependence upon flow regime, trailing edge geometry and the Strouhal number based on the TE bluntness.

The general idea, then, is to deploy a short-span section of the WT blade with a special airfoil derivative whose TE thickness would be calibrated to correspond to $h \sim 0.64 \cdot \delta^*$ at the local flow conditions. Two hypotheses were adopted at this point:

- A tone or a small hump (narrowband noise) in the 2 – 4 kHz range can be produced by the calibrated TE gap.
- The tone or small hump produced in the spectrum of this specific blade section will not offset the overall SPL advantage of deploying quieter TE airfoils in large spans of the same blade.

A two-step design was adopted for this proposed *controlled singing blade*: first an estimation of the TE bluntness necessary to produce the tone close to 3 kHz was based on Brooks and Hodgson (Brooks & Hodgson, 1981) findings (A); and then it was verified against data correlations amassed by Blake (Blake, Mechanics of Flow-Induced Sound and Vibration, 1986 II) (B):

Since it is desirable to produce the warning tone in a section away from the section with the strongest noise sources (which in this case would be the $r \approx 85\%$ span), a radial position was selected at 35 m, corresponding to $r \approx 70\%$, where the same flow Mach number of the Brooks and Hodgson (Brooks & Hodgson, 1981) measurements was found for the Poli-100 WT equipped with the SP4621HP airfoil. The local flow conditions found there were $Re \approx 8,700,000$ and $M \approx 0.18$ (local velocity is 59.81 m/s and the local blade chord is 2.1 m). By simulating the SP4621HP airfoil at these local (2D) flow conditions, the displacement thickness calculated at the TE⁶⁴, for AOA=6,2° was:

$$\delta^*_{upper} \approx 0.01613 \text{ m}$$

$$\delta^*_{lower} \approx 0.00233 \text{ m}$$

⁶⁴ For coherence with previous findings in this research, the displacement thickness was evaluated at 98% of the chord.

$$\delta^*_{total} \approx 0.01846 \text{ m}$$

For the condition $h/\delta^* \sim 0.64$ to be obtained, based on the suction side displacement thickness (as defined by Blake), the TE thickness resulted in $h \sim 0.64 * \delta^* = 0.0103 \text{ m}$ for this specific design point.

Accordingly, the SP4621HP airfoil was modified in order to have a 0.0103 m gap at the TE, or $0.0103 \text{ m} / 2.1 \text{ m} = 0.5\% \times chord$, generating test case #161.

By simulating the flow conditions at $r = 70\%$, over the modified SP4621HP airfoil, the displacement thickness calculated at the TE, for $AOA=6,4^\circ$ (the new maximum efficiency point) is:

$$\delta^*_{upper} \approx 0.01465 \text{ m}$$

$$\delta^*_{lower} \approx 0.00224 \text{ m}$$

$$\delta^*_{total} \approx 0.01689 \text{ m}$$

According to Blake (Blake, Mechanics of Flow-Induced Sound and Vibration, 1986 II), the Strouhal number observed⁶⁵ for blunt TE in the range of Reynolds numbers from 1.5 million to 7.8 million, for a flow perpendicular to the TE, is given by:

$$\frac{f \cdot (h + (\delta^*_{upper} + \delta^*_{lower}))}{U_\infty} = 0.18 \quad (4 - 5)$$

With a local flow velocity at 70% blade span of 59.81 m/s calculated with the aid of the BEM method for the geometric and general flow conditions given, the resultant frequency would be:

$$f \approx 396 \text{ Hz} \quad (4 - 6)$$

This frequency is much lower than the recommended for bird warning purposes and does not confirm the expectations.

Verification for the modified airfoil: $h/\delta^* = 0.0103/0,01465 \cong 0.7 > 0.5$ (ok).

⁶⁵ According to Blake (Blake, Mechanics of Flow-Induced Sound and Vibration, 1986 II), the TE vortex shedding relations established of certain observed Reynolds range does not exclude the possible validity of the relations in untested ranges which, of course, needs further testing.

According to Blake (Blake, Mechanics of Flow-Induced Sound and Vibration, 1986 II) when the airfoils in the turbulent regime have the necessary degree of bluntness ($h/\delta^* > 0.5$) discrete shedding occurs above some threshold Reynolds number. The relationship employed above is derived from the observation of singing hydrofoils and do not apply to situations of beveled trailing edges, where turbulent flow separation occurs on one side somewhat upstream of the bevel. In the present simulation case, however, the TE is not beveled and the examination of the friction coefficient along both upper and lower surfaces (Figure 4-52) did not reveal unattached flow prior to the TE, except for the brief bubble formation at 45% of the lower surface, which reattaches and transitions the flow.

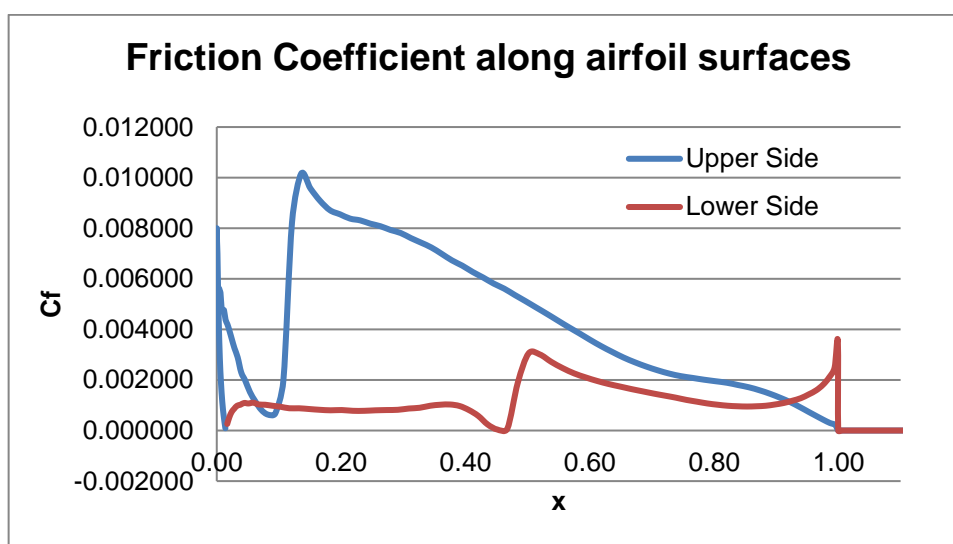


Figure 4-52 - Friction coefficient over upper and lower surfaces for the SP 4621 – HP airfoil for untripped flow at AOA=6.4, Reynolds = 8,7 Million and M=0.18.

The possible tonal noise feature measured by Brooks and Hodgson (Brooks & Hodgson, 1981), therefore, could not be initially correlated to other experiments reported by Blake (Blake, Mechanics of Flow-Induced Sound and Vibration, 1986 II).

One natural question that emerged was is if the same relation from Blake would be capable of predicting the 3 kHz tone found in the experiments by Brooks and Hodgson (Brooks & Hodgson, 1981), p. 78-79, at their original flow conditions:

- NACA 0012 airfoil (0.6096 m)
- Flow speed: 69.5 m/s
- Mach number = 0.18

- Reynolds number = 2,900,000
- AOA = 0°
- Tripped flow.
- TE thickness: 0.0025 m or 0.4% chord.

The TE bluntness parameter, calculated for the case with the aid of XFLR5 was in the singing airfoil range:

$$h/\delta^* \sim \frac{0.0025}{0.00403} \approx 0.62 \quad (4 - 7)$$

Actually, this proved to be a very good result from XFLR5 calculations, very close to the expected measured value of $h/\delta^* = 0.64$.

The blunt-TE vortex shedding frequency predicted by Eqn.(4-5) was

$$\frac{f \cdot (h + (\delta_{upper}^* + \delta_{lower}^*))}{U_\infty} = 0.18 \quad (4 - 5)$$

$$f = \frac{0.18 \cdot 69.5}{0.0025 + 2 \cdot (0.00403)} \approx 1,185 \text{ Hz} \quad (4 - 8)$$

The result is approximately 40% of the peak frequency found experimentally of 3 kHz, suggesting the model to be capable of indicating the order of magnitude of the frequency measured experimentally. Also, this result suggested that the noise emitted by the modified SP4721BS airfoil at AOA=6.4 to be probably closer to the 990 Hz frequency.

While still unsuitable for the intended warning effects over Passeriformes and Non-Passeriformes birds, as seen in Figure 4-53, the frequency of the tone is already enough to warn off Strigiformes⁶⁶ birds which have night-hunting habits and have a more developed aural system.

⁶⁶ Strigiformes are night-hunting birds, especially owls, which, not by coincidence, are known by their very silent flight.

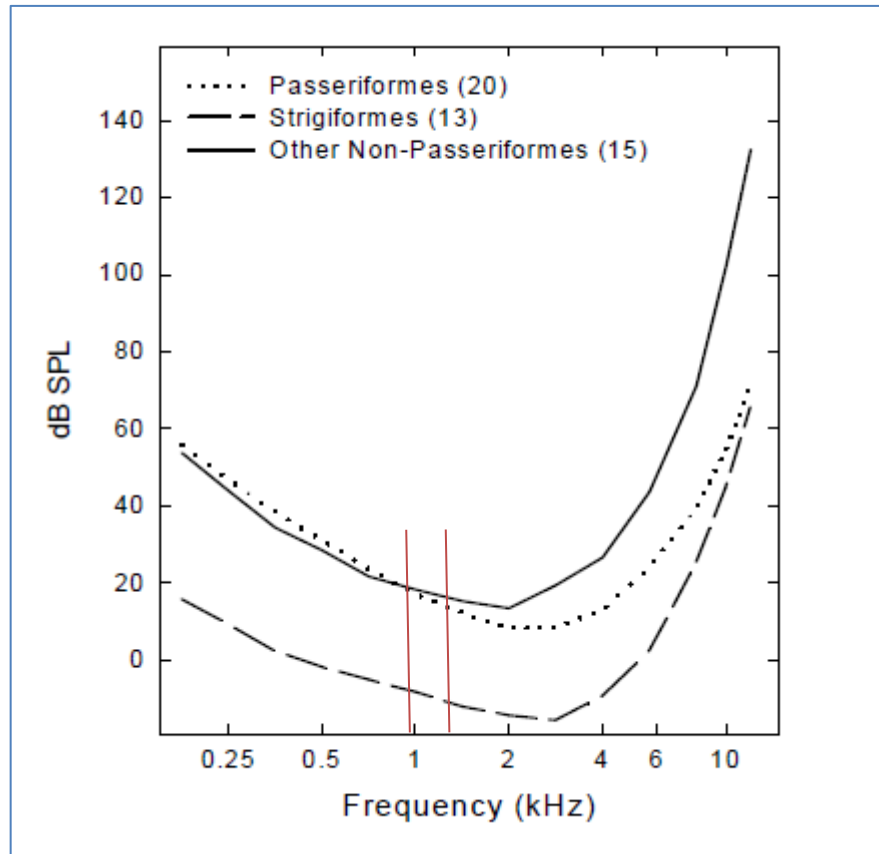


Figure 4-53 - Audiograms from birds assembled by Dooling (Dooling, 2002), based on other references.

The correlation represented by Eqn. (4-5) was then adjusted to represent Brooks and Hodgson (Brooks & Hodgson, 1981) particular experiment results, by making the Strouhal number based on the blunt TE to be:

$$\frac{f \cdot (h + (\delta_{upper}^* + \delta_{lower}^*))}{U_{\infty}} = 0.456 \quad (4 - 9)$$

The total transversal turbulence scale needed to produce the desired 3 kHz tone would be of $h + (\delta_{upper}^* + \delta_{lower}^*) = 0.009088 \text{ m}$ which, paradoxically, would lead to a bluntness parameter of a *non-signing* airfoil. Once again, due to the scale of the airfoil and the magnitude of the flow, high frequency noise seemed not to be a natural outcome.

How could this tradeoff between frequency and bluntness parameter be analyzed?

- (i) $h/\delta^* > 0,50$ for a singing airfoil.

- (ii) $(h + (\delta_{upper}^* + \delta_{lower}^*))$ must be minimum for the higher TE vortex-shedding frequency to be obtained.

If $h/\delta^* = 0.64$ was adopted and the displacement thickness for the pressure side (for $AOA \gg 0$) was momentarily disregarded, one expression of frequency as a function of airfoil thickness could be obtained:

$$f \cong \frac{0.456 \cdot 59.81}{1.64 \cdot h} = \frac{16.63}{h} \quad (4 - 10)$$

For the calculated airfoil TE thickness of 0.0103 m, it was predicted that the top TE vortex-shedding frequency attainable would be close to 1,615 Hz.

Although still lower than optimal, this peak frequency of the TE vortex-shedding would be enough to do the intended job for the groups of birds analyzed and is close to the most sensitive frequency for the non-Passeriformes⁶⁷ birds as may be seen from Figure 4-53.

The theoretical peak frequency at this radial position could only be attained if suitable means (whether passive or active) were found to minimize the total shear layer thickness. Some of the possibilities considered, were (i) positioning the airfoil under higher speed flows (further outboard) and (ii) reducing the AOA. The first option would bring the singing airfoil closer to the radial section where TE noise is close to maximum value and also away from the Mach number where the vortex-shedding noise was experimentally confirmed, which was deemed inappropriate; the second could be tested in the LA airfoil variant, which works well with a shallower AOA.

Testing conditions:

- Airfoil: SP4721LA modified to a larger TE gap of 0.5% chord.
- Flow conditions at 35 m, corresponding to $r = 70\% \text{ span}$
- $Re \approx 8,700,000$
- $M \approx 0,18$

⁶⁷ While in English the word “bird” is employed to designate individuals of any of the orders, in Portuguese, the Passeriformes are known as the “Pássaros” while the Non-Passeriformes, which are about 1/3 of the specimens and include the well-known Tucanos, Pica-Paus, Andorinhões, Beija-flores, periquitos, etc., are known as “Aves”. One of the key differences is the presence of three forward-pointing fingers and one aft-pointing finger in the Passeriformes, and two forward and two aft-pointing fingers in the Non-Passeriformes.

- $U_\infty = 59.81 \text{ m/s}$
- Local Blade chord: 2.1 m
- AOA=3.8°
- Tripped flow @ 1% upper and 10% lower surfaces.
- δ^* reading at 98% chord.
- TE height: $h = 0.0103 \text{ m}$ ($h/C = 0.0103/2.1 = 0.5\%$).

The resulting calculations from the XFLR5, were:

$$\delta^*_{upper} \approx 0.01797 \text{ m}$$

$$\delta^*_{lower} \approx 0.00259 \text{ m}$$

$$\delta^*_{total} \approx 0.02056 \text{ m}$$

This corresponded to a tonal frequency of TE vortex emission of:

$$f = \frac{0.456 \cdot 59.81}{0.0103 + 0.02056} \approx 1,327 \text{ Hz} \quad (4 - 11)$$

A last attempt was made to increase the frequency: the TE gap was increased to 0.6% of the chord ($h=0.0126 \text{ m}$), in the hope of decreasing the displacement thickness in a higher rate than the increase of TE thickness. The results were as follows:

Simulating conditions:

- Airfoil: SP4721BS with a 0.6% chord gap.
- Flow conditions at $r = 35 \text{ m}$, corresponding to $r = 70\%$ span.
- $Re \approx 8,700,000$
- $M \approx 0.18$
- $U_\infty = 59.81 \text{ m/s}$
- Local Blade chord: 2.1 m
- AOA=3.5°
- Tripped flow @ 1% upper and 10% lower surfaces.
- δ^* reading at 98% chord.
- TE height: $h = 0.0126 \text{ m}$ ($h/C = 0.0126/2.1 = 0.6\%$).

The resulting calculations from the XFLR5, were:

$$\delta^*_{upper} \approx 0.01591 \text{ m}$$

$$\delta^*_{lower} \approx 0.00268 \text{ m}$$

$$\delta^*_{total} \approx 0.01859 \text{ m}$$

and,

$$f = \frac{0.456 \cdot 59,81}{0.0126 + 0.01859} \approx 874 \text{ Hz} \quad (4 - 12)$$

From this point, it was considered unpractical to manually optimize this airfoil, which was left for the future, with the use of suitable optimization tools.

The Airfoil SP4721LA with TE gap of 0.5% of the chord was then designated the SP4721BS ($f_{BTE-VS} \approx 1,327 \text{ Hz}$).

Some tools are undergoing development in order to help evaluate a tonal emission frequency and level, under the Poli - TU-Berlin collaboration. These tools comprise the Blunt TE noise source model and the rotor 3D noise module, the development of which is completely specified and partially coded at this time. The complementary models will allow, in theory, calibrating the blade span over which the blunt TE noise airfoil derivative should be applied in order to result in the desired tone level. The desired tone level is defined as the one which is enough to provide the desired SNL for the tone to be detectable over the noise but not enough to increase significantly the OASPL emitted from the full rotor, at a given TSR.

4.5.4.4 – Spectral analysis for the baseline and proposed airfoils.

The spectra for the S830 airfoils, SP4621HP and SP4721LA were compared in this section.

Figure 4-54 shows that both developed airfoils, SP4621HP and SP4721LA have lower overall noise emissions than the S830. Also, most of the noise is emitted in the lower

frequency, with noise in the audible range displaying much smaller levels for this specific chord (1.55 m), Mach (0.18) and Reynolds number (7,700,00) flow. All airfoils were simulated at $(cl/cd)_{max}$.

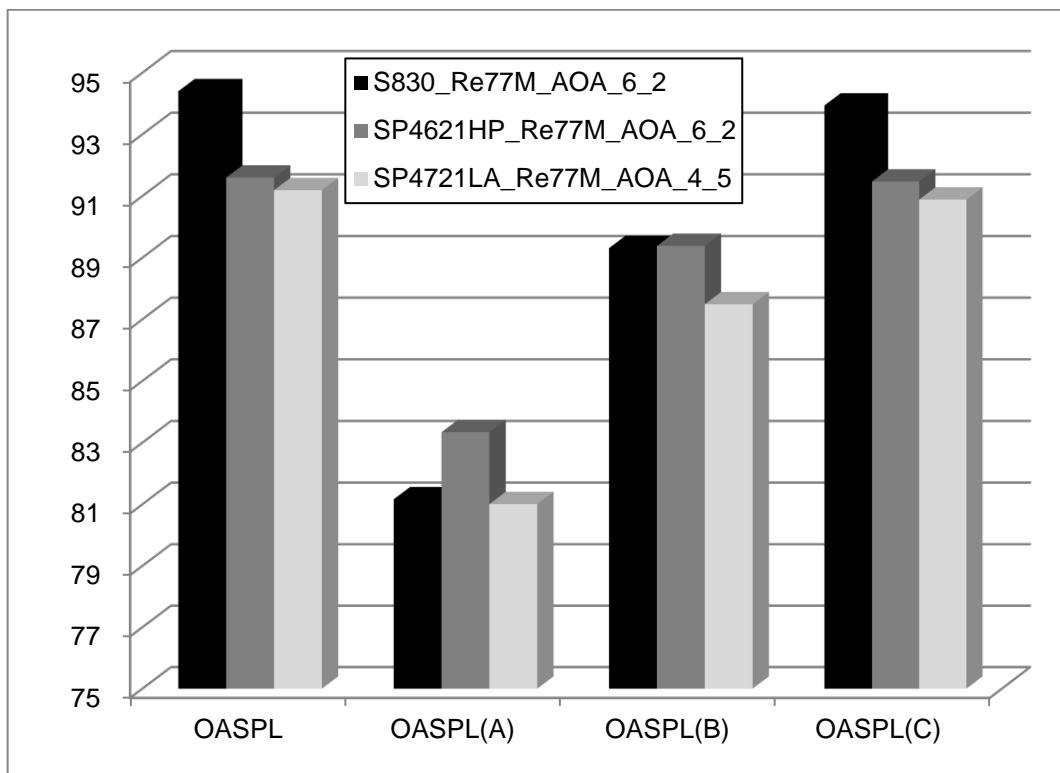


Figure 4-54 – Weighted and unweighted overall Sound Pressure Levels for the SP4621Hp and SP4721LA airfoils, compared with the baseline S830 airfoil.

Figure 4-55 shows that the baseline airfoil is dominated by the geometrical variations up to the frequency of 150 Hz. The SP4621HP has better aerodynamic characteristics than the S830 airfoil but higher noise in the 150 Hz to 1,000 Hz band while the SP4721LA has comparable noise emission in this range. All airfoils have close noise emission behavior above 1,000 Hz, when analyzed through the resolution of the PNoise method.

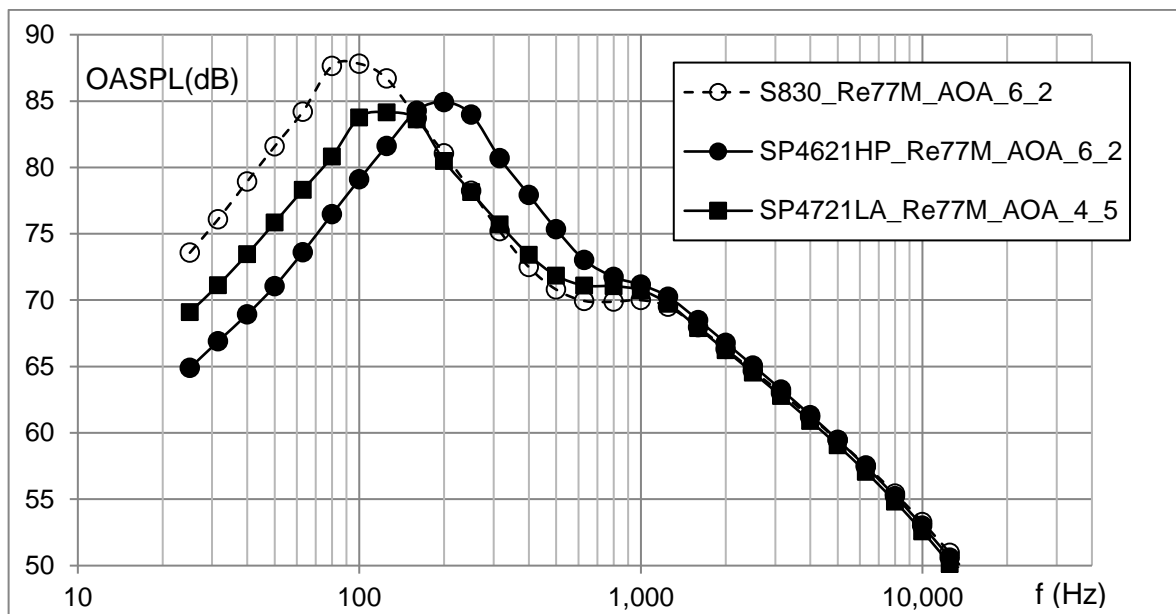


Figure 4-55 - OASPL spectra for the baseline airfoil (S830) and for two developed airfoils.

Figure 4-56 illustrates the higher audible noise levels from the SP4621HP airfoil and the noise performance of SP4721LA airfoil which is close to the S830 for mid and high frequencies, but better (lower emission) at the lower frequencies.

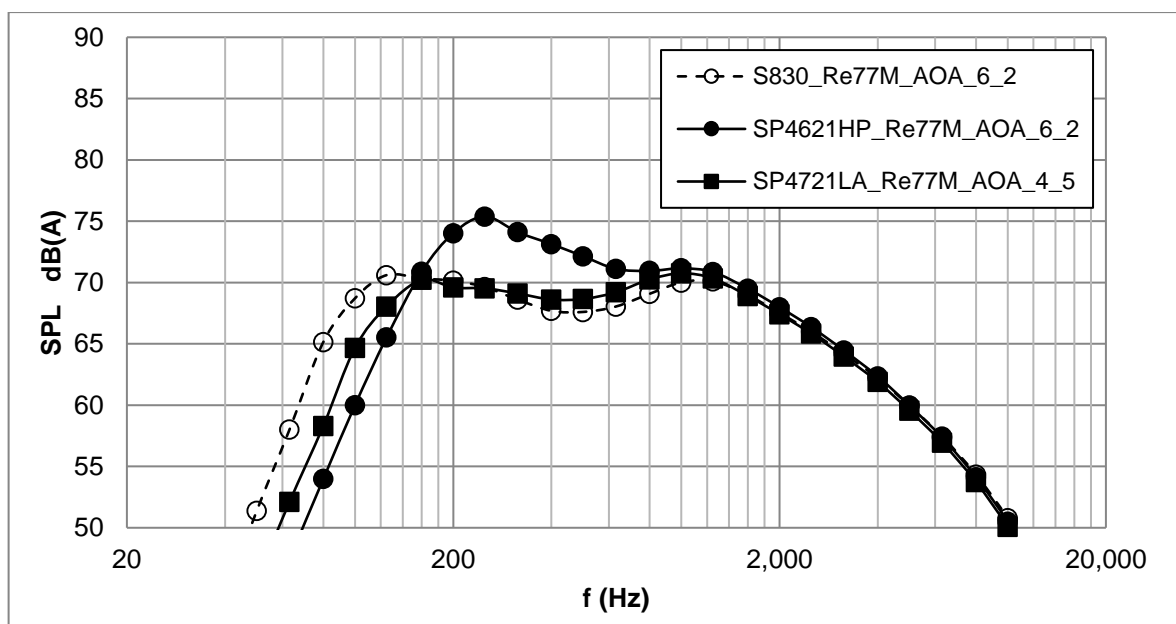


Figure 4-56 A-Weighted SPL spectra for the baseline airfoil (S830) and for two geometric variations. SP4621HP and SP4721LA.

Figure 4-57 illustrates the impact in SPL_α of two different strategies; geometric redesign (SP4621HP) which results in vertical and horizontal shifts of the spectrum and off-peak operation (SP4621-QMO), which results in mostly vertical shift of the spectrum.

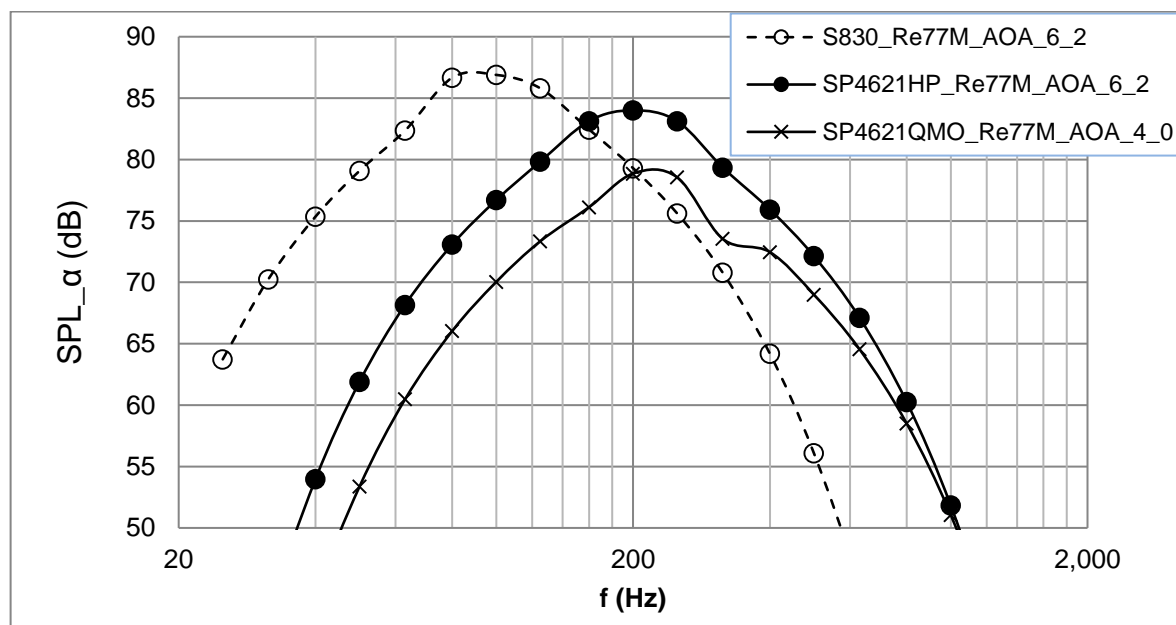


Figure 4-57 - Sound Pressure Level spectra for partially separated flow, SPL_α (dB).

4.5.5 – Aerodynamic Efficiency and Pressure Coefficient diagram (Euler number) comparison among the baseline and the SP4621HP and SP4721LA airfoils.

Figure 4-58 illustrates the superior SP4621HP aerodynamic performance, i.e., higher cl/cd ratio, when compared to the S830 airfoil, both of which reach the peak cl/cd at the same AOA of 6.2° .

Although the SP4721LA has only slightly higher aerodynamic efficiency when compared to the S830, the peak cl/cd is reached at a much lower AOA of 4.5° . The airfoil was designed in such a manner to display an essentially constant cl/cd over a wide range of angles-of-attack (3.8° - 5.0°).

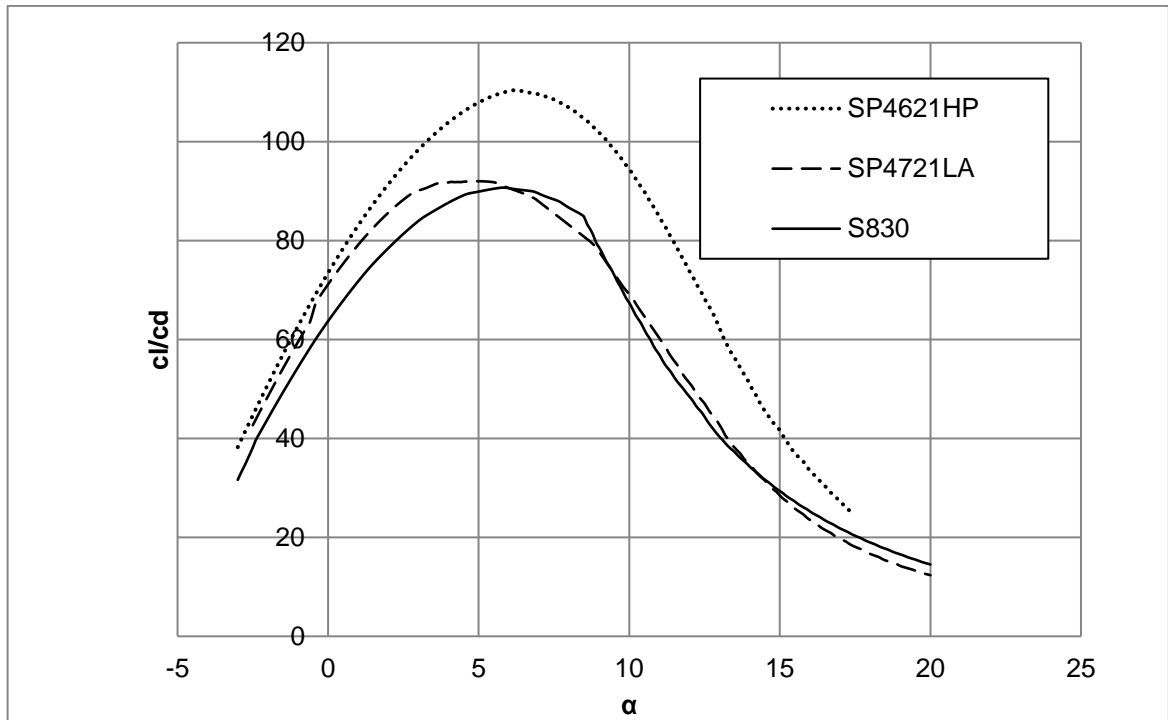


Figure 4-58 - Aerodynamic efficiency (c_l/c_d) versus AOA.

The Pressure Coefficient diagrams are compared in Figure 4-59, at the same lift coefficient value of 1.2. That corresponds to AOA=5.7° for the S830, AOA=4.5° for the SP4721LA and AOA=4.0° for the SP4621HP airfoils.

The pressure diagram shown in Figure 4-59 is an important tool in case of inverse design and the differences between the baseline airfoil and the quieter profiles are essentially:

- A more defined pressure peak deriving from a larger LE radius (1).
- More aft loading over the upper surface with the smoothing of the separation ramp (2).
- More aft loading over the lower surface (3).
- Less forward loading over the lower surface (4).

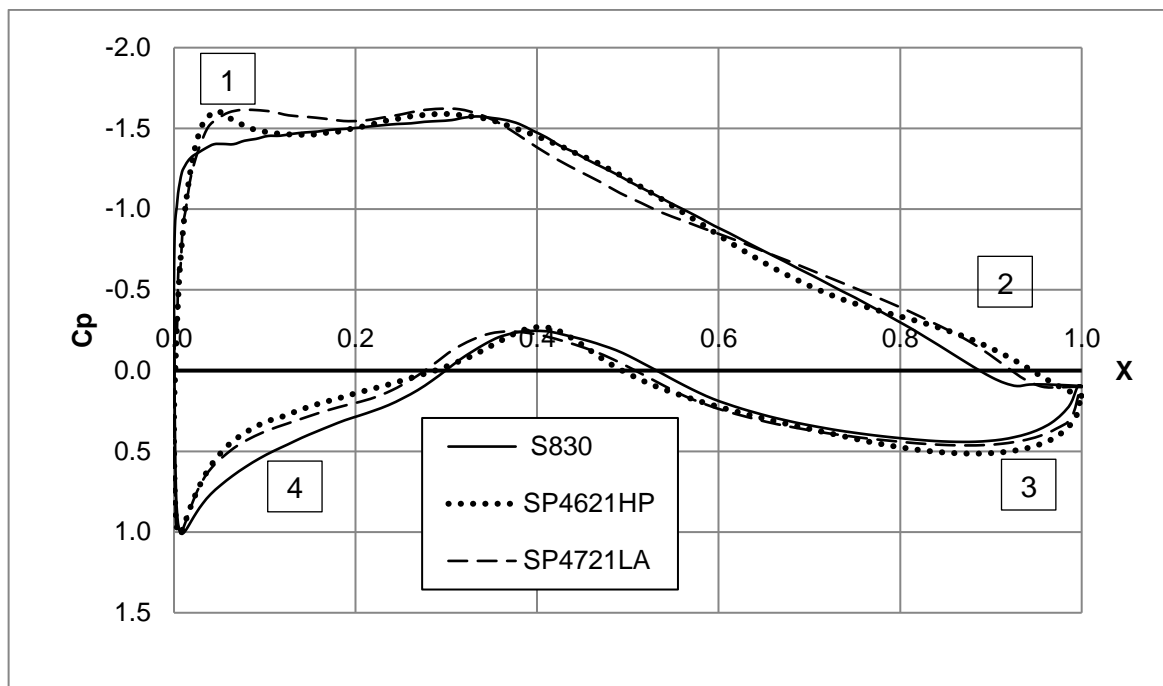


Figure 4-59 – The Euler number along the chord for the upper and lower airfoil surfaces.

The more heavily aft-loading of the new airfoils (Figure 4-59) would suggest increased pitching moment for the quieter airfoils, which is actually the case as may be seen from the data-tables of the previous sections (Table 4-19 and Table 4-20).

4.5.6 – Evaluation of proposed airfoil characteristics against the requirements.

Table 4-21 shows the result of the newly developed airfoils against the requirements set earlier in Section 3.6.1.

Table 4-21 - Comparison of airfoil characteristics with requirements.

#	Requirement	SP4621HP	SP4721LA	SP4721BS
1	Airfoil suitable for a large size HAWT, outboard section @85% radius Reynolds and Mach numbers. Nominal radii to be used in the designs: 50, 87 and 106.5 m.	Yes, for 85% radius of a 50 m-blade.	Yes, for 85% radius of a 50 m-blade.	For 70% spanwise position and limited TE length.
2	Suitable for pitch controlled WT.	Yes. May be employed in QMO mode by the pitch-control mechanism.	Yes. May be employed in QMO mode by the pitch-control mechanism.	Yes.
3	The nose thickness (radius) should be significant.	Double the original S830 LE radius.	Double the original S830 LE radius.	Double the original S830 LE radius.
4	Relative insensitive to roughness.	Ok. Little c_l variation on tripped and untripped flow.	Ok. Little c_l variation on tripped and untripped flow.	Ok. Little c_l variation on tripped and untripped flow.
5	Early laminar to turbulent transition in a controlled point.	Flow should be tripped at 5% upper side and 10% lower side.	Flow should be tripped at 1% upper side and 10% lower side.	Flow should be tripped at 1% upper side and 10% lower side.
6	To have low profile drag, but to preserve airfoil thickness determined by structural requirements.	Profile drag is similar to S830. Nominal thickness of 21%.	Profile drag is similar to S830. Nominal thickness of 21%.	Profile drag is similar to S830. Nominal thickness of 21%.
7	The pitching moment coefficient about $\frac{1}{4}$ chord should be close to -0.145 of the original S830 airfoil.	-0.155	-0.153	-0.158
8	A TE with specified bluntness parameter may be added to the airfoil, for use in part span, in order to produce a 3-4 kHz tone.	N/A	N/A	0.5%xC blunt TE added for a 1,327 Hz centered narrow band noise at design condition.

As may be seen from Figure 4-60, the polar diagrams are smooth for all airfoils, with c_l values approximately constant from minimum drag to maximum drag regions.

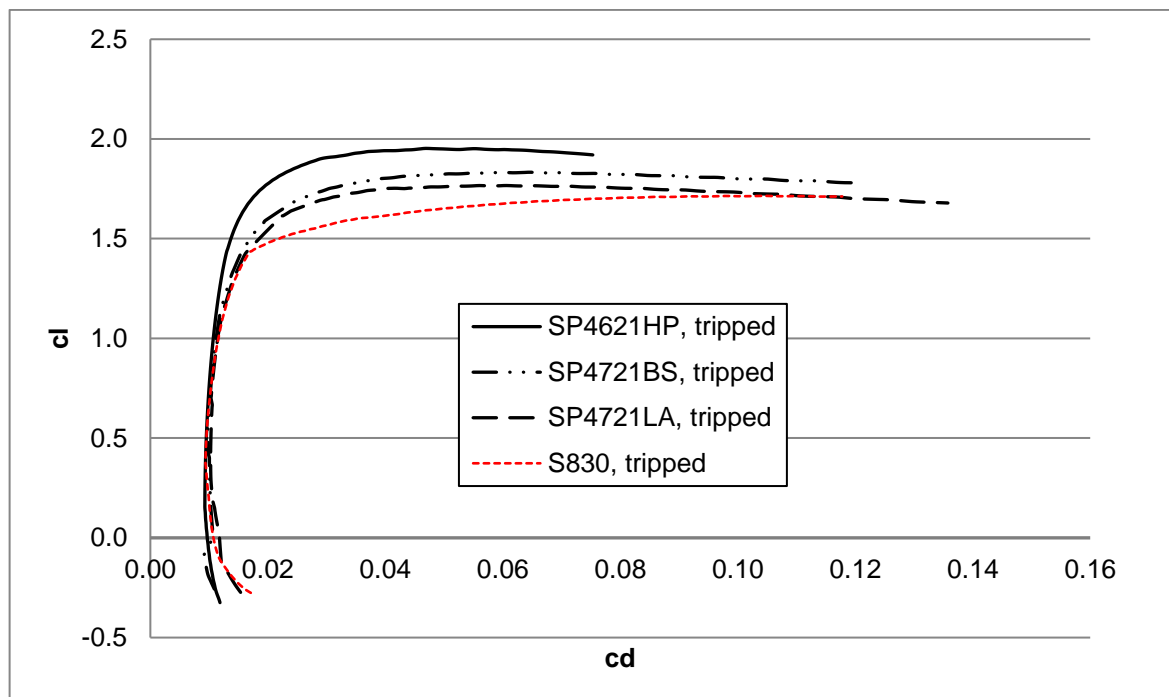


Figure 4-60 - Polar diagrams for the developed airfoils in tripped flow (black lines) and the polar diagram for the reference airfoil, S830 (in red).

When comparing untripped (e^9 transition model) with tripped flow conditions for the SP4621HP and SP4721LA airfoils, it is possible to see from Table 4-22 a very small difference in c_l for the maximum lift angle, between both flow conditions. This is indicative of good surface roughness tolerance of the airfoils. However, despite the fact that they closely resemble laminar-flow airfoils, in this application they are intended for tripped operation in order to avoid laminar flow detachment with bubble formation in transient operation, which are a potential source of additional noise. During steady operation at the recommended local-flow AOA, no bubble formation is predicted even for the untripped flow.

Table 4-22 - $c_{l_{max}}$ difference between tripped and untripped flow for the reference (S830) and the newly developed airfoils. The differences are quite low, indicating good roughness tolerance.

	S830	SP4621HP	SP4721LA	SP4721BS
$c_{l_{max}}$ tripped	1.715	1.953	1.765	1.830
$c_{l_{max}}$ untripped	1.725	1.964	1.770	1.840
$\Delta c_{l_{MAX}}$	0.010	0.011	0.005	0.010

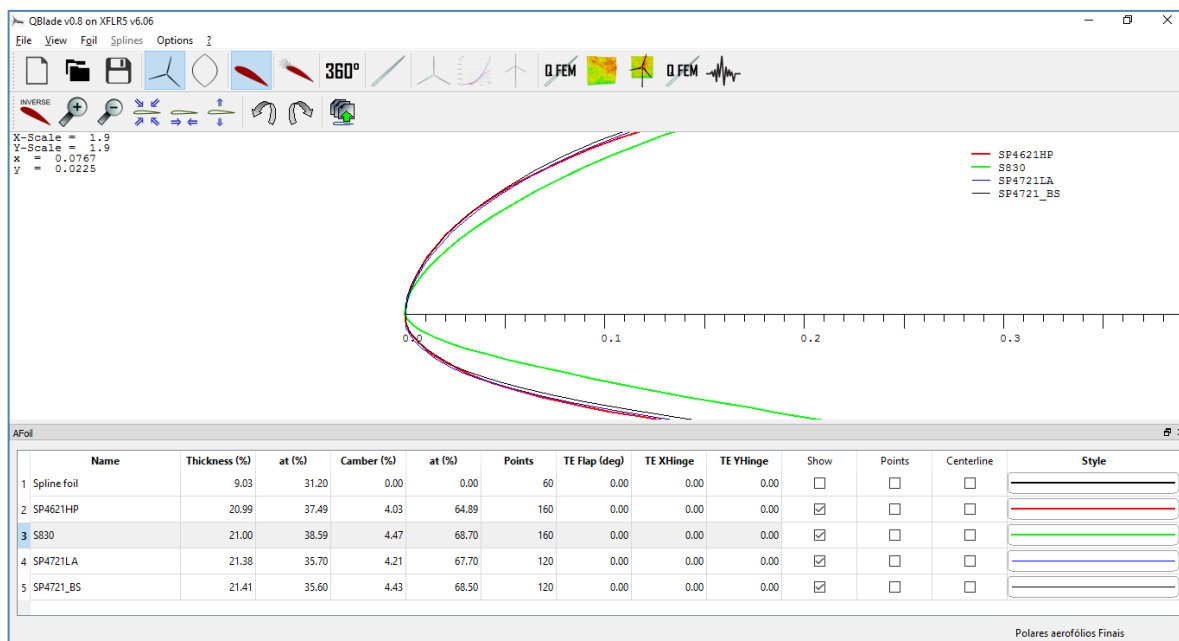


Figure 4-61 - Comparison among nose radii for the different airfoils. S830=green; SP4621HP=red; SP4721LA = blue.

Figure 4-61 shows that all developed airfoils have twice the LE radius of the S830 airfoil. The increased LE radius was incorporated as a matter of good practice for a silent airfoil, since its beneficial side-effect will be reducing inflow noise under turbulent inflow conditions.

4.5.6.1 – Verification of airfoil performance off-design point.

For practical and economical purposes, the SP4621HP airfoil should be able to perform aerodynamically well under all local flow conditions found from 55% radius to 90% radius of the POLI-100 WT blade.

The local flow conditions to be found in discretized 2.5 m span sections ranging between the 55% to 90% radial limits are shown in Table 4-23.

Table 4-23 - Local Reynolds and Mach numbers calculated from the BEM method for the blade stations ranging from 55% to 90% radial position in the POLI-100 WT blade.

Sect	Radius [m]	r/R	Airfoil Section	Chord [m]	θ [°]	Axial Induction Factor. a	Axial Velocity [m/s]	Tangential Induction Factor a'	Tangential Speed [m/s]	Resultant local speed [m/s]	Re.chord	Mach
11	27.50	0.55	SP4126HP	2.65	3.82	0.3185	7.32	0.0145	46.87	47.44	8.7E+06	0.14
12	30.00	0.60	SP4126HP	2.47	3.02	0.3900	7.20	0.0125	51.03	51.54	8.7E+06	0.15
13	32.50	0.65	SP4126HP	2.28	2.34	0.4000	7.32	0.0106	55.18	55.66	8.7E+06	0.16
14	35.00	0.70	SP4126HP	2.10	1.75	0.3900	7.44	0.0092	59.34	59.81	8.6E+06	0.18
15	37.50	0.75	SP4126HP	1.92	1.24	0.3800	7.80	0.0079	63.50	63.97	8.4E+06	0.19
16	40.00	0.80	SP4126HP	1.73	0.79	0.3500	8.16	0.0068	67.66	68.15	8.1E+06	0.20
17	42.50	0.85	SP4126HP	1.55	0.89	0.3200	8.16	0.0059	71.82	72.28	7.7E+06	0.21
18	45.00	0.90	SP4126HP	1.37	0.55	0.3200	8.65	0.0052	75.99	76.48	7.2E+06	0.22

A batch XFLR5 simulation for the SP4621HP airfoil was set up in order to calculate the local Reynolds and Mach numbers, corresponding to the last two columns of Table 4-23. Also, the polar diagrams for all flow conditions may be seen in Figure 4-62. The polar diagrams are smooth and almost overlapping, with little variation in the cl_{max} (ranging from 1.94 to 1.97, a 1.5% variation) and $(cl/cd)_{max}$ (ranging from 108 to 116, a 7% variation).

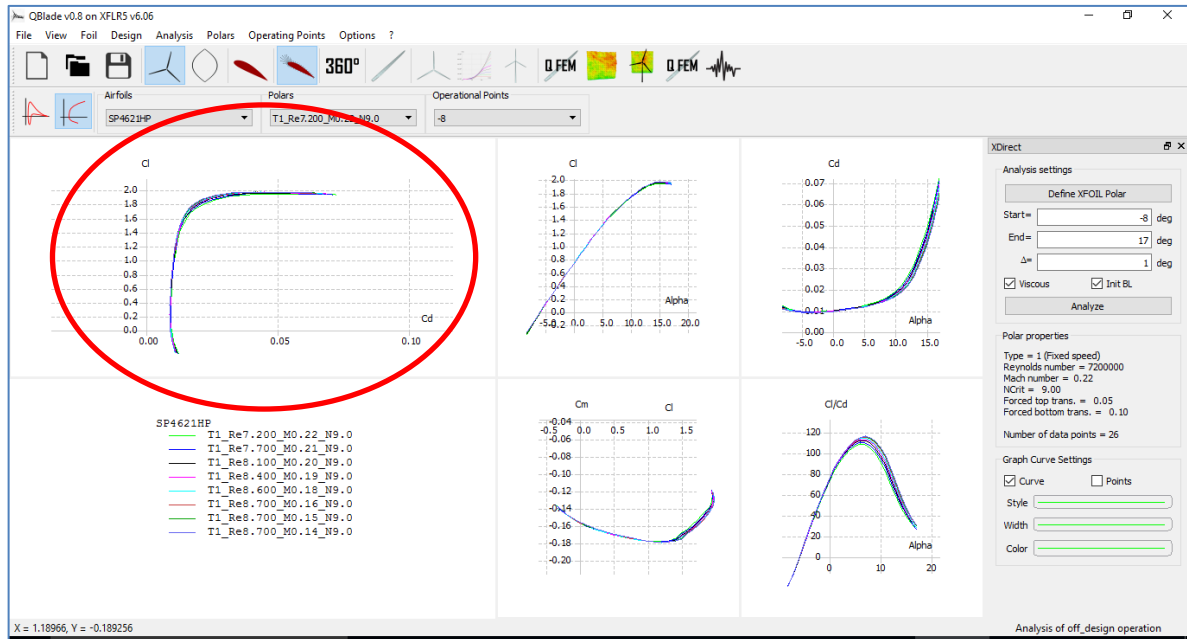


Figure 4-62 - Polar diagram (left) and other relevant diagrams for the SP4621HP airfoil for the local flow conditions on 8 discretized blade span sections 2.5 m wide, ranging from 55% to 90% of the POLI-100 WT blade.

The airfoil may be considered robust for the range of local flow conditions found in the 55% to 90% radial stations of the POLI-100 WT blade.

The TE thickness for quiet applications of the SP4621HP in spanwise sections other than the design point (85%R), should be calculated so as to obtain $h/\delta \leq 1/4$ at the TE.

4.5.6.2 – Power Coefficient and Energy Conversion rate of the Poli-100 WT equipped with the proposed airfoils.

The Poli-100 WT had been originally designed with the S830 as the prime airfoil. At this point the Poli-100 WT was upgraded with blade section where the SP4126HP airfoil was substituted for the S830, as shown in Figure 4-63.

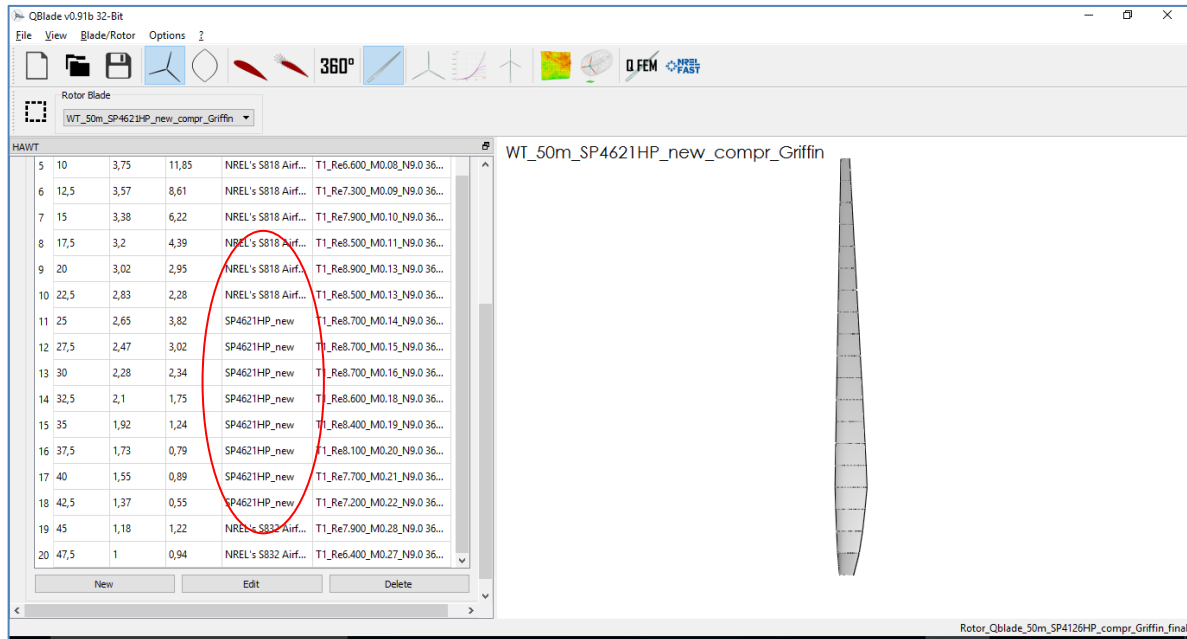


Figure 4-63 - Poli-100 WT upgraded with the SP4621HP airfoil for the radial stations from 55% to 90% radius, all other airfoils remaining unchanged from the baseline design.

A QBlade performance simulation was accomplished with the same parameters used in the original Poli-100 WT reference run:

- Cut in speed of 4 m/s
- Cut out speed of 25 m/s
- Wind speed of 12 m/s
- Rotor speed of 16 rpm
- TSR=7.

Figure 4-64 and Figure 4-65 show the Coefficient of Power for both configurations, with an increase in the C_p from 0.493 to 0.505 with the new blade configuration. The percentage of the Betz limit ($C_{p_{max}} = 0.5926$) has increased from 83.5% to 85.2% at the design rotational speed TSR=7.

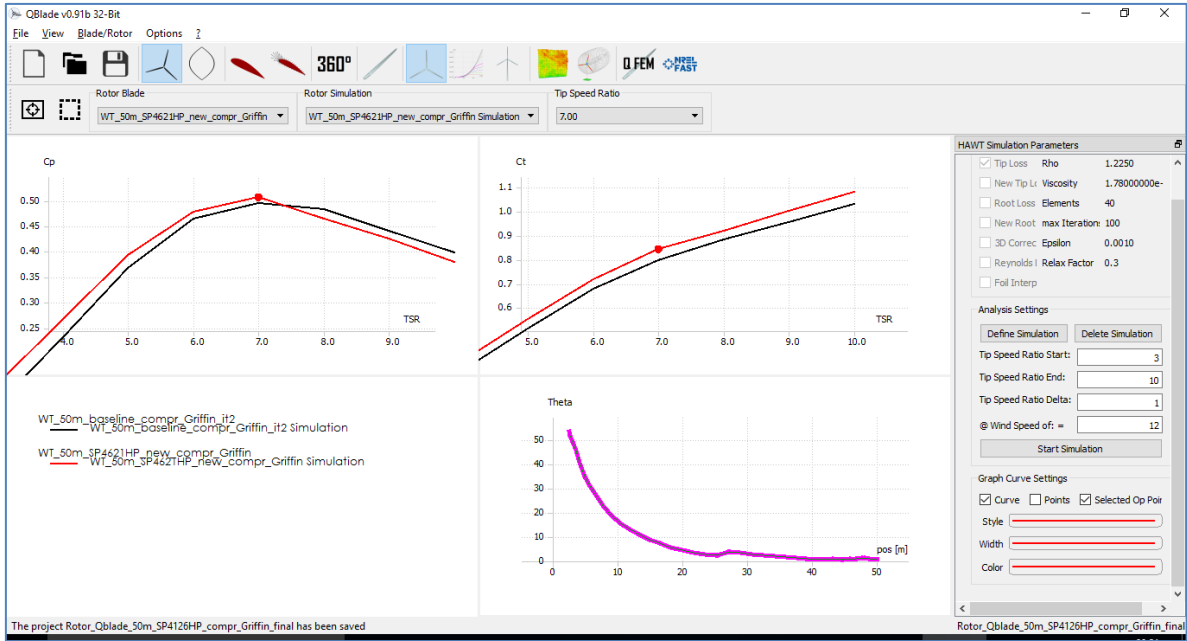


Figure 4-64 - Coefficients output screen for the Poli-100 WT upgraded with the SP4621HP airfoil in selected radial stations. Coefficient of Power (Cp) at the upper left; Coefficient of Torque (Ct) at the upper right. The upgraded blade is plotted in red.

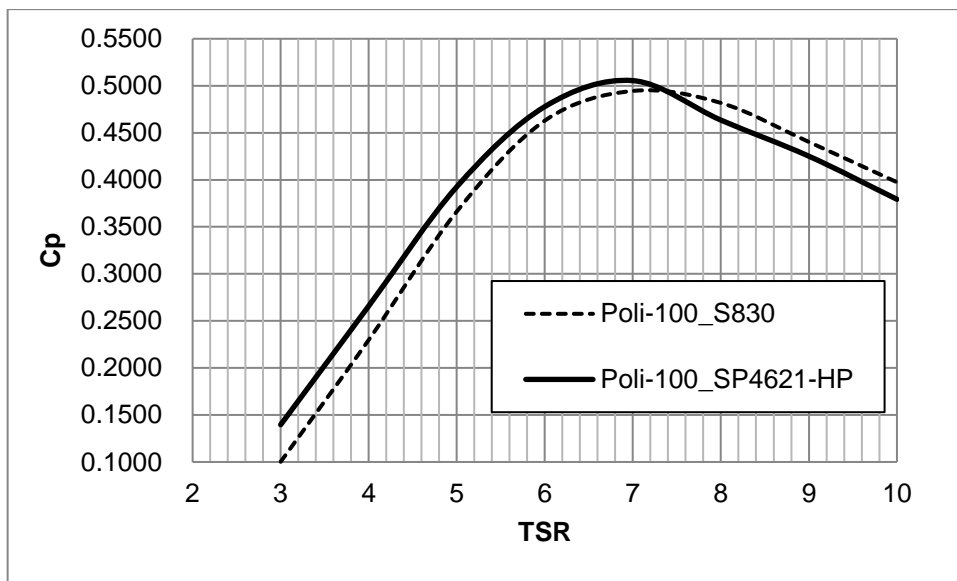


Figure 4-65 - Coefficient of Power versus TSR for the original and upgraded Poli-100 WT.

The shaft-power produced @ 12 m/s is of 4.2 MW (no transmission and generator losses accounted for), against 4.1 MW of the original configuration, a 2.4% increase in power generation at this specific design point as illustrated by Figure 4-66 and Figure 4-67.

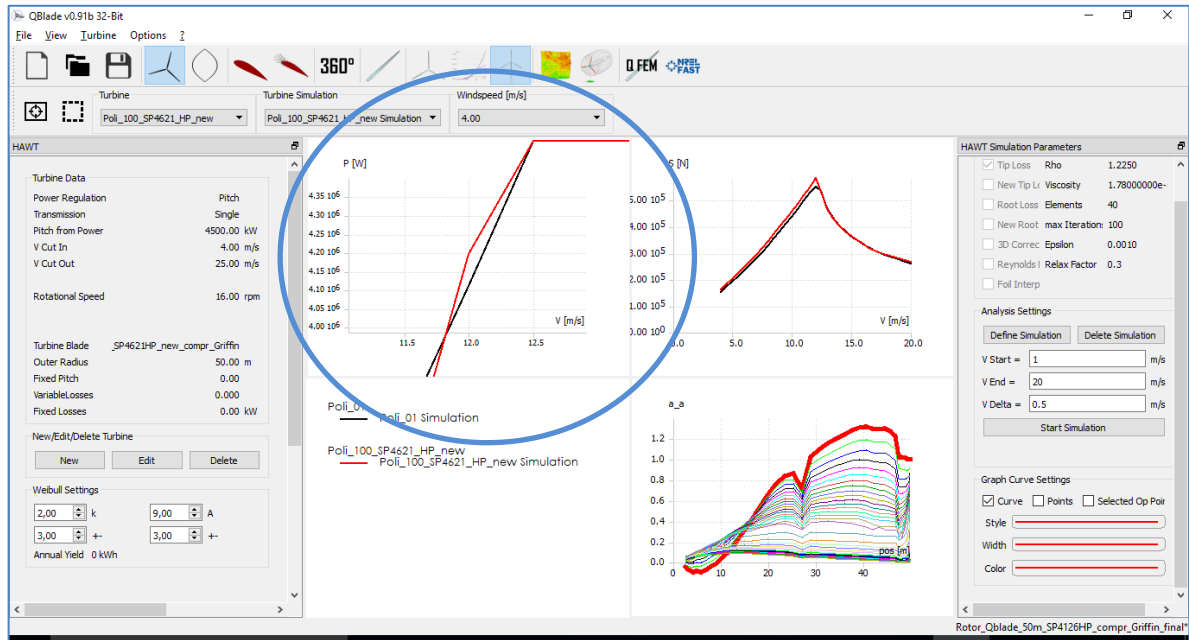


Figure 4-66 - Power output screen for the Poli-100 WT upgraded with the SP4621HP airfoil in selected radial stations. The upgraded blade is plotted in red.

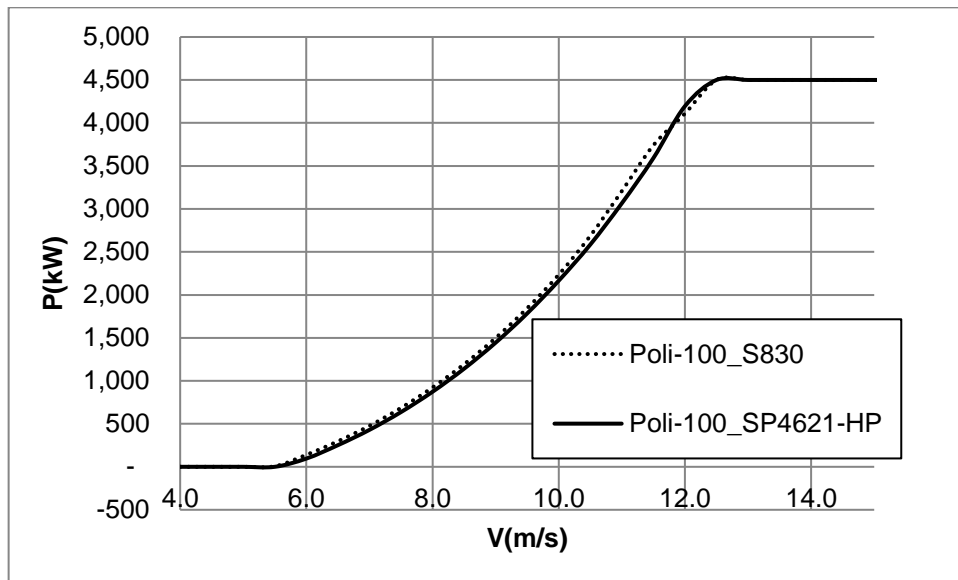


Figure 4-67 - Coefficients of Power versus TSR for the original and upgraded Poli-100 WT.

The annual power production comparison would depend upon the wind distribution found over the siting grounds.

5. CONCLUSIONS AND FURTHER DEVELOPMENT

The noise emitted from Wind Turbines imposes significant restrictions on the development of the Wind Energy. The subject was confirmed by the industry to be one of the main restrictions for the growth of WT equipment in size and also to limit penetration closer to populated areas. Also, the direct industry inquiry revealed the lack of a reliable and computationally efficient methodology for the early assessment and development of quiet airfoil and rotors, with open source and in public domain.

An extensive WT TE noise review covering the most relevant models and methods published in the last 30 years was accomplished, showing that the simplified-theoretical methods are still undergoing development and, at the current state of the art, they are very demanding (both in time and level of information from the TBL), also resort to empirical correction factors and do not delivered an indisputable superior or geometry-flexible TE-noise prediction. Hence, the less TBL-demanding semi-empirical BPM TE noise prediction model was selected as the core of the new methodology intended to fill in the gap indicated by the industry.

In order for the method to be flexible in terms of airfoil geometry, the original BPM displacement thickness correlations would have to be replaced by a generic flow solver. For that purpose, the XFLR5 and CFD solver were investigated in depth with regards to the capability of providing the BPM TE noise prediction model with the necessary balance between flexibility, accuracy and computational efficiency on the calculation of the flow field. While CFD-RANS showed the best accuracy and consistency, the XFLR5 displayed a marked advantage on flexibility and computational time, having been selected as most suited for the preliminary design phase of quieter airfoils, together with the particular noise prediction model selected.

The modified-BPM method was implemented as the “PNoise” module, a 2D TE-noise prediction tool embedded into the QBlade Wind Turbine design and analysis software from TU-Berlin. The calculation procedure was thoroughly verified and the PNoise has successfully gone public with the release of QBlade version 0.95, on May, 11th, 2016, logging 1,508 downloads in 28 days since the publication. The code is distributed with

a detailed validation and procedure calculation verification document, covering the original BPM model scope and range. It may be safely stated that the first main objective of the research has been completely met by public distribution of this flexible TE noise prediction tool. The major download destination Countries may be seen in Figure 5-1, the first four of which correspond to the locations of major wind turbine design and fabrication industries.

Country	Android	Linux	Macintosh	Unknown	Windows	Total
1. United States	1%	5%	3%	51%	41%	263
2. Spain	1%	0%	1%	87%	11%	230
3. Germany	0%	4%	0%	55%	41%	227
4. India	1%	7%	3%	3%	86%	69
5. Brazil	0%	6%	0%	0%	94%	54
6. Mexico	0%	6%	0%	0%	94%	49
7. Turkey	0%	0%	0%	0%	100%	47
8. Italy	5%	9%	2%	0%	84%	44
9. France	0%	25%	9%	9%	57%	44
10. United Kingdom	0%	5%	8%	0%	87%	39
11. Romania	0%	0%	0%	10%	90%	30
12. Japan	0%	0%	0%	7%	93%	29
13. Canada	0%	12%	4%	0%	83%	24
14. Iran	0%	0%	0%	0%	100%	24
15. Korea	0%	0%	0%	0%	100%	23
16. Morocco	0%	0%	0%	0%	100%	22

Figure 5-1 – QBlade v0.95 with PNoise: Partial list of download destination, by Country. Source: Sourceforge.net, accessed on July 7th, 2016.

In pursuing the second main objective, i.e. the quieter-airfoil development, a BEM method was scratch-built and allowed the calculation of realistic operating conditions for all the sections of large-size WT blades, in order to provide acceptable boundary conditions to support the development work. The BEM method also supported the complete aerodynamic design, mainly the twist distribution determination, of three, large-size WTs designed during the course of this work: the Poli-100, Poli-180 and Poli-220 wind turbines, described in Section 4.1.2 and Appendix H.

While trying to expand the validation limits of the PNoise method, the predictions were compared to data derived from high speed acoustic wind tunnel testing from Virginia Tech/NREL, with unfavorable results. However, the VT/NREL data were directly compared to original NASA experimental data at some overlapping Reynolds number region and were found not to reproduce satisfactorily the NASA measured spectra, suggesting some significant attenuation to have been inadvertently introduced into the

VT/NREL measurement or complex spectral derivation procedures. A decision was thus made to deploy the modified-BPM or PNoise method for relative performance simulations only, pending further validation against experimental data for evaluating its absolute prediction capability at very high Reynolds number flows.

In line with the findings, and due to the stringent aerodynamic and acoustic requirements it was designed to meet, the NREL/Somers S830 airfoil was selected as the benchmark airfoil from which a new generation of airfoils with improved relative performance would emerge, aimed at large scale HAWTs. The first step of the development was to undertake an extensive sensitivity study in order to assess how airfoil geometry influenced TE noise emission.

Some general guidelines for designing quieter airfoils, regarding TE noise, emerged as well as many types of tradeoffs between aerodynamic and aeroacoustic features were revealed by the sensitivity studies and laid out the strategy for the new designs.

Some of the important conclusions that emerged from the study were:

- The larger the WT blade, the more TE noise acoustic energy is shifted towards the lower frequencies.
- Achieving high (cl/cd) ratios at relatively shallow AOA and with moderate camber is a key factor for designing quieter (TE-noise) airfoils.

In order to fulfil the second large objective of the research, two new airfoils were proposed, namely the SP4621HP and the SP4721LA both of which provide a significant reduction in overall SPL close to 3 dB. The SP4621HP may be operated in a shallower AOA, with an overall SPL reduction in excess of 6 dB and with comparable aerodynamic performance to the S830 under original design requirements (“QMO mode”).

Due to the decreased detectability of quieter WT blades by birds, a third airfoil derivative, the SP4721BS, was also proposed, which produces a tonal noise around 1,327 Hz and could help warn nearby flying birds off the WT blades, mitigating this other negative aspect of wind energy proliferation. It is expected that the tonal noise emitted in a single, narrow blade section would not contribute significantly to the overall sound pressure level of the WT.

With all considerations given, the main objectives of this work, i.e., to provide the WT industry and researchers with a computationally efficient, high degree of freedom, user-friendly graphic interface analysis tool to allow early TE-noise assessment; and to design new, quieter airfoil for WT equipment, were completely and satisfactorily achieved.

It is hoped that this work will support the development of quieter WT equipment and help remove any pace-limiting factors for the continued, rapid advancement of this important renewable source in the world energy matrix.

Suggestions for improvements and future developments.

The PNoise method lacks validation for the NACA 0012 geometry above the original BPM scope and for other geometries in flows between $550,000 < Re_c < 10,000,000$.

All airfoils proposed are in prototype form and would benefit from an optimization process now that the number of variable is reduced and a fine tuning is desirable.

The 3D module, which will allow full blade and rotor TE-noise assessment was completely specified according to the collaboration schedule, and will be code next.

There are many collaboration opportunities for development and integration of other noise source models, both of self-noise and inflow nature, in the 2D and 3D modules.

The performance for the new airfoils under Poli-180 and Poli-220 WT flow conditions is still to be verified. Eventually, new airfoils will be also developed for these larger WT.

The method and tool developed will be also useful in developing airfoils aimed at smaller scale blades, since they radiate more acoustic energy at frequencies of higher audibility.

Restrictions.

All original BPM TE noise model limitations discussed in methodology, Section 3.3.1 applies when the code is used with original displacement thickness correlations.

The modified BPM TE noise model should be employed for relative airfoil acoustic performance comparison only, at this time.

REFERENCES

- Abbott, I., & Von-Doenhoff, A. (1959). *Theory of Wing Sections* (2nd ed.). New York: Dover.
- ABEEÓLICA. (2016). *Boletim de Dados - Maio 2016*. São Paulo: ABEEÓLICA.
- Amiet, R. (1975). Acoustic Radiation from an Airfoil in a Turbulent Stream. *Journal of Sound and Vibration* (41) 4, pp. 407-420.
- Amiet, R. (1978). Effect of Incident Surface Pressure Field on Noise due to Turbulent Flow past a Trailing Edge. *Journal of Sound and Vibration* (57), pp. 305-306.
- Ansys. (2013). *Advanced ANSYS CFD - Aeroacoustics Course*. ANSYS.
- ANSYS INC. (2013). *ANSYS Fluid Dynamics Verification Manual*. Canonsburg, PA: ANSYS.
- Arce, C., Ragni, D., Pröbsting, S., & Madsen, J. (2015). Impact on Flow Topology of Solid and Permeable Trailing Edge Serrations at Incidence on Cambered and Symmetric Airfoils. *6th International Meeting on Wind Turbine Noise* (pp. 1-16). Glasgow: INCE Europe.
- Ashwill, T. D. (C. 2008). *Developments in Large Blades for Lower Cost Wind Turbines*. Sandia National Laboratories, New Mexico.
- Bareiss, R., Guidati, G., & Wagner, S. (1994). An Approach Towards Refined Noise Prediction of Wind Turbines. *Proceedings of the European Wind Energy Association Conference & Exhibition.*, (pp. 785-790). Thessaloniki.
- Becker, S., Grabinger, J., Kaltenbacher, M., & Scheit, C. (2011). Computational Aeroacoustics for Rotating Systems. *4Th International Meeting on Wind Turbine Noise*, (pp. 1-10). Rome, It.
- Bertanoglio, F., Madsen, H. A., & Bak, C. (2009). *Experimental Validation of the TNO Trailing Edge Noise Model and Application to Airfoil Optimization*. RISO, Roskilde, Denmark.

- Bies, D. A., & Hansen, C. H. (2009). *Engineering Noise Control* (4th Ed. ed.). Abingdon, UK: Spon Press.
- Bistafa, S. R. (2011). *Acústica Aplicada ao Controle de Ruído* (Segunda ed.). São Paulo: Edgar Blücher.
- Blake, W. K. (1986 I). *Mechanics of Flow-Induced Sound and Vibration* (Vol. I). Orlando, FL.: Academic Press.
- Blake, W. K. (1986 II). *Mechanics of Flow-Induced Sound and Vibration* (1ed ed., Vol. II). Orlando: Academic Press.
- Bowdler, D., & Leventhall, G. (2011). *Wind Turbine Noise*. Brnetwood: Multi-Science Publishing Co Ltd.
- Brooks, T. F., & Marcolini, M. A. (1986, August 8). Airfoil Trailing-Edge Flow Measurements. *AIAA Journal*, pp. 1245-1251.
- Brooks, T. F., Pope, S., & Marcolini, M. A. (1989). *Airfoil Self-Noise and Prediction*. NASA. Langley: NASA.
- Brooks, T., & Hodgson, T. H. (1981). Trailing Edge Noise Prediction From Measured Surface Pressures. *Journal of Sound and Vibration* 78(1), pp. 69-117.
- Brooks, T., & Marcolini, M. (1985, February). Scaling of Airfoil Self-Noise Using Measured Flow Parameters. *AIAA Journal*, pp. 207-213.
- Burton, T., Jenkins, N., Sharpe, D., & Bossanyi, E. (2011). *Wind Energy Handbook* (2nd ed.). Chicester: J. Wiley & Sons.
- Burton, T., Sharpe, D., Jenkins, N., & Bossanyi, E. (2008). *Wind Energy Handbook*. Chichester: J. Wiley & Sons.
- Celik, I., Ghia, U., Roache, P., Freitas, C., Coleman, H., & Raad, P. (2008, July). Procedure for Estimation of Uncertainty Due to Discretization in CFD Applications. *Journal of Fluids Engineering*, pp. 1-4.
- Cherouri, A., Younes, R., Llinca, A., & Perron, J. (2015). Review of Performance Optimization Techniques Applied to Wind Turbine. *Applied Energy*, V. 142, pp. 361-388.

- Courant, R., & John, F. (2000). *Introduction to Calculus and Analysis II/2* (Reprint of the 1989 Edition ed., Vol. II/2). New York: Springer-Verlag.
- Couto, R. T. (2013, fev 02). Green's functions for the wave, Helmholtz and Poisson Equations on a 2D boundless domain. *Revista Brasileira de Ensino da Física*, V.35, n.1, pp. 1304-1 a 1304-8.
- Curle, N. (1955, September). The Influence of Solid Boundaries upon Aerodynamic Sound. *Proceedings of The Royal Society A*, Vol 231, n.1187, pp. 505-514.
- Da Silva, C. (2011). *Jet Noise Predictions For Complex Problems*. Escola Politécnica da USP, São Paulo.
- Davidson, P. (2009). *Turbulence. An Introduction for Scientists and Engineers*. Oxford: Oxford University Press.
- De Andrade, E., Milone, L., & Joaquim, P. (2013). *Geradores Eólicos - Metodologia de Análise e Seleção Baseada na Avaliação de Desempenho pelo Método BEM*. Escola de Engenharia Mauá - IMT, São Caetano do Sul.
- Deperrois, A. (2011). *Analysis of Foils and Wings Operating at Low Reynolds Numbers*.
- Devenport, W., & Burdisso, R. C. (2004). *Aeroacoustic Testing of Wind Turbine Airfoils*. NREL.
- Devenport, W., Burdisso, R., Camargo, H., Crede, E., Remilieux, M., Rasnick, M., & Van Seeters, P. (2010). *Aeroacoustic Testing of Wind Turbine Airfoils*. NREL/SR-500-43471.
- Domingos, J. (2013, janeiro). Atraso em linhas de transmissão piora cenário. *O Estado de São Paulo*.
- Doolan, C., & Moreau, D. (2013). Review of NACA 0012 Turbulence Trailing Edge Noise Data at Zero Angle of Attack. *5th International Meeting on Wind Turbine Noise* (pp. 1-10). Denver, Co.: INCE Europe.
- Dooling, R. (2002). *Avian Hearing and the Avoidance of Wind Turbines*. Golden, Co: NREL/TP-500-30844.

- Dowling, A., & Ffowcs Williams, J. (1983). *Sound and Sources of Sound*. Chichester, UK: Ellis Horwood Limited.
- Drela, M. (2000). X-FOIL. <http://web.mit.edu/drela/Public/web/xfoil/>: MIT.
- Drela, M., & Giles, M. B. (1987, October). Viscous-Inviscid Analysis of Transonic and Low Reynolds Number Airfoil. *AIAA Journal* V25 (10), pp. 1347-1355.
- Drela, M., Youngren, H., & Deperrois, A. (2009). *XFOIL/XFLR5*. MIT, Cambridge, Ma.
- Eisele, O., Pechlivanoglou, G., & Nayeri, C. . (2013). EXPERIMENTAL & NUMERICAL INVESTIGATION OF INFLOW TURBULENCE ON THE PERFORMANCE OF WIND TURBINE AIRFOILS. *Proceedings of ASME Turbo Expo 2013: Turbine Technical Conference and Exposition* (pp. 1-10). San Antonio, Tx: ASME.
- EPE, E. d. (2012). *Balanço Energético Nacional 2012: ano base 2011*. Ministério de Minas e Energia, Rio de Janeiro.
- Eppler, R. (C.2000). *EPPLER AIRFOIL DESIGN AND ANALYSIS CODE*. Airfoils, Inc., Stuttgart.
- European Wind Energy Association - EWEA. (2009). *Wind Energy - The Facts*. London: Earthscan.
- Everest, F. A., & Pohlmann, K. (2009). *Master Handbook of Acoustics* (5th ed.). New York: McGraw-Hill.
- Farassat, F. (1981, September). Linear Acoustic Formulas for Calculation of Rotating Blade Noise. *AIAA Journal*, V.19, n.9, pp. 1122-1130.
- Farassat, F. (1996). *Introduction to Generalized Functions With Applications in Aerodynamics and Aeroacoustics*. NASA Technical Paper 3428, Hampton, Va.
- Farassat, F. (2007). *Derivation of Formulations 1 and 1A of Farassat*. Nasa, Hampton, Va.
- Ferziger, J., & Peric, M. (2002). *Computational Methods for Fluid Dynamics*. Berlin: Springer-Verlag.

- Ffowcs Williams, J., & Hawkins, D. (1969, May). SOUND GENERATION BY TURBULENCE AND SURFACES IN ARBITRARY MOTION. *Phylosophical Transactions of the Royal Society of London*, V. 264, N. 1151, pp. 321-342.
- Ffowcs-Williams, J., & Hall, L. (1970, March). Aerodynamic Sound Generation by Turbulent Flow in the Vicinity of a Scattering Half Plane. *Journal of Fluid Mechanics*, V.40, pp. 657-670.
- Fink, M., & Bailey, D. (1980). *Airframe Noise Reduction Studies and Clean-Airframe Noise Investigation*. NASA Report CR-159311.
- França, V. (2011). *Challenges for the Optimal uses of Wind Power in Brazil*. The George Washington University, Institute of Brazilian Business and Public , Washington D.C.
- Fuglsang, P., & Bak, C. (2004). *Development of the Risø Wind Turbine Airfoils*. Risø, Roskilde.
- Fuglsang, P., & Madsen, H. A. (1996). *Implementation and Verification of an Aeroacoustic Noise Prediction Model for Wind Turbines*. RISO, Roskilde, Denmark.
- Fuglsang, P., Antoniou, I., Sorensen, N., & Madsen, A. (1998). *Validation of a Wind Tunnel Testing facility for Blade Surface Pressure Measurements*. Denmark: RISO.
- Fuglsang, P., Bak, C., Gaunaa, M., & Antoniou, I. (2004, November). Design and Verification of the Riso-B1 Airfoil Family for Wind Turbines. *Transactions of the ASME*, Vol. 126, pp. 1002-1010.
- GIPE, P. (2004). *Wind Power* (Revised and Expanded Edition ed.). Vermont: Chelsea Green Publishing Co.
- Glegg, S. (1987, June). Significance of Unsteady Thickness Noise Sources. *AIAA Journal* V. 25 (6), pp. 839-844.
- Glegg, S., & Reba, R. (2010, July 7). Using Reynolds-Averaged Navier-Stokes Calculations to Predict Trailing Edge Noise. *AIAA Journal* (48) 7, pp. 1290-1301.

- Glegg, S., Baxter, S., & Glendinning, A. (1987). The Prediction of Broadband Noise From Wind Turbines. *Journal of Sound and Vibration* v.118 (2), pp. 217-239.
- Göçmen, T., & Özerdem, B. (2012). Airfoil Optimization for Noise Emission Problem and Aerodynamic Performance Criterion on Small Scale Wind Turbine. *Journal of Energy* (04) 36.
- Griffin, D. A. (2001). *WindPACT Turbine Design Scaling Studies Technical Area 1 - Composite Blades for 80- to 120-meter Rotor*. Golden, Co.: NREL/SR-500-29492.
- Griffith, D., & Ashwill, T. (2011). *The Sandia 100-m All-glass Baseline Wind Turbine Blade: SNL 100-00*. Albuquerque, NM.: SANDIA/SAND2011-3779.
- Griffith, D., Ashwill, T., & Resor, B. (2012). Design and Analysis of the SANDIA 100 m Wind Turbine Blade. *53rd AIAA/ASME/ASCE/AHS/ASC Structures, Structural Dynamics and Materials Conference*, (pp. 1-18). Honolulu.
- Griffith, D., Ashwill, T., & Resor, B. (2012). Large Offshore Rotor Development: Design and Analysis of the SANDIA 100 m Wind Turbine Blade. *53rd AIAA/ASME/ASCE/AHS/ASC Structures, Structural Dynamics and Materials Conference*, (pp. 1-18). Honolulu.
- Grosveld, F. W. (1985, July-August). Prediction of Broadband Noise from Horizontal Axis Wind Turbines. *Journal of Propulsion*, Vol 1, No.4, pp. 292-299.
- Guidati, G., & Wagner, S. (2000). Design of Reduced Noise Airfoils for Wind Turbines. *ECCOMAS 2000: European Congress on Computational Methods in Applied Sciences and Engineering*. Barcelona.
- Gupta, S., & Leishman, J. (2005). Comparison of Momentum and Vortex Methods for the Aerodynamic Analysis of Wind Turbines. *43rd AIAA Aerospace Sciences Meeting and Exhibit*, (pp. 1-23). Reno, Ne.
- Hahn, B., Durstewitz, M., & Rohrig, K. (2005). *Reliability of Wind Turbines*. Institut für Solare Energieversorgungstechnik (ISET), Kassel, Germany.
- Hansen, M. (2008). *Aerodynamics of Wind Turbines* (Second Edition ed.). London: Earthscan.

- Hartwanger, D., & Horvat, A. (2008). 3D Modelling of a Wind Turbine Using CFD. *NAFEMS Conference*, (pp. 1-14). UK.
- Herr, M., & Kamruzzaman, M. (2013). Benchmarking of Trailing-Edge Noise Computations - Outcome of the BANC-II Workshop. *19th AIAA/CEAS Aeroacoustics Conference* (pp. 1-33). Berlin: AIAA.
- Herrig, A., & Würz, W. K. (2008). New CPV-Results of Naca 0012 Trailing-Edge Noise . *International Conference on methods of Aerophysical Research, ICMAR 2008*, (pp. 1-9).
- Herrig, T., Wurz, W., Kamruzzaman, M., & Kramer, E. (2007, april). Design and Wind-Tunnel Verification of Low-Noise Airfoils for Wind Turbines. *AIAA Journal*, 45, pp. 779-785.
- Hessler, G. (2011). A Note on the Debate about Health Effects from Low Frequency Noise (LFN) from Modern Large Wind Turbines. *Fourth International Meeting on Wind Turbine Noise* (p. 12). Rome: WTN2011.
- Hoerner, S. F., & Borst, H. (1985). *Fluid Dynamic Lift* (1 ed.). Bakersfield, Ca: Hoerner Fluid Dynamics.
- Howe, M. (1978). *Review of the Theory of Trailing Edge Noise*. NASA.
- Hubbard, H., & Shepherd, K. (1990). *Wind Turbine Acoustics*. NASA Tech. Paper 3057.
- Huyer, S., Simms, D., & Robinson, M. (1996, July). Unsteady Aerodynamics Associated with a Horizontal-Axis Wind Turbine. *AIAA Journal*, pp. 1410-1419.
- IEC61400-11. (2012). *Wind Turbine Generator Systems - Part 11: Acoustic Noise Measurement Techniques*. International Electrotechnical Commission - IEC.
- IEC61400-12-1. (2005). *IEC 61400-12-1 Power Performance Measurement of Electricity Producing WT*. International Electrotechnical Commission.
- Imamura, H. (1999). *Aerodynamics of Wind Turbines*. Yokohama National University, Yokohama, Japan.

- Instituto Chico Mendes de Conservação da Biodiversidade. (2014). *RELATÓRIO ANUAL DE ROTAS E ÁREAS DE CONCENTRAÇÃO DE AVES MIGRATÓRIAS NO BRASIL*. Cebedelo, PB: ICMBIO.
- Jonkman, J., Butterfield, S., Musial, W., & Scott, G. (2009). *Definition of a 5-MW Reference Wind Turbine of Offshore System Development*. Golden, Co.: NREI/TP-500-38060.
- Kamruzzaman, M., Lutz, T., Herrig, A., & Krämer, E. (2012a, January). Semi-Empirical Modeling of Turbulent Anisotropy for Airfoil Self-Noise Predictions. *AIAA Journal*, pp. 46-60.
- Kamruzzaman, M., Lutz, T., Nübler, K., & Krämer, E. (2011). Implementation and Verification of an Aeroacoustic Wind Turbine Blade Analysis Tool. *WTN 2011 Proceedings* (pp. 1-16). Rome: INCE Europe.
- Kamruzzaman, M., Lutz, T., Würz, W., She, W. Z., Hansen, M. B., & Madsen, H. (2012b). Validations and Improvements of Airfoil Trailing-Edge Noise Prediction Models Using Detailed Experimental Data. *Wind Energy* (15), pp. 45-61.
- Kamruzzaman, M., Meister, K., Lutz, T., Kühn, M., & Krämer, E. (2010). *Wind Turbine Aerodynamics and Aeroacoustics at University of Stuttgart - An Overview of Research and Development*. IAG, Stuttgart.
- Karim, S. M., & Rosenhead, L. (1952, april-june). The Second Coefficient of Viscosity of Liquids and Gases. *Reviews of Modern Physics*, pp. V.24 (108-116).
- Kerrebrock, J. L. (1992). *Aircraft Engines and Gas Turbines* (2nd ed.). Cambridge, Ma: The MIT Press.
- Krasnov, M., Kiselev, A., Makarenko, G., & Shikin, E. (1990). *Mathematical Analysis for Engineers* (Vol. 2). Moscow: Mir Publishers.
- Kuethe, A., & Schetzer, J.D. (1961). *Foundations of Aerodynamics, 2nd Ed.* New York: J Wiley & sons.
- Laursen, J., Enevoldsen, P., & Hjort, S. (2007, Jan). 3D CFD Quantification of the Performance of a Multi-Megawatt Wind Turbine. *Journal of Physics*, pp. 1-13.

- Lawson, M., & Li, Y. (2011). Development and Verification of a Computational Fluid Dynamics Model of a Horizontal Axis Tidal Current Turbine. *30th International Conference on Ocean, Offshore, and Arctic Engineering* (pp. 1-10). Rotterdam: NREL/CP-5000-50981.
- Lawton, D. (2015, October 30). Retrieved from San Jose Mercury News: http://www.mercurynews.com/ci_29048835/altamont-pass-controversial-wind-turbine-company-blamed-bird
- Lee, S., Lee, S., & Lee, S. (2011). Time Domain Modeling of Aerodynamic Noise from Wind Turbines. *4th International Meeting on Wind Turbine Noise*, (pp. 1-12). Rome, It.
- Lee, Y. T., Blake, W., & Farabee, T. (2005). Modelling of Wall Pressure Fluctuations Based on Time Mean Flow Field. *Journal of Fluids Engineering*, V. 127 (2), pp. 233-240.
- Leishman, J. (2002). Challenges in Modeling the Unsteady Aerodynamics of Wind Turbine. *AIAA Paper 2002-0037*, pp. 1-28.
- Leventhall, G. (2013). Infrasound and the Ear. *5th Int. Conf. on Wind Turbine Noise*. Denver: INCEUSA.
- Li, J.-Y., Li, R., Gao, Y., & Huang, J. (2010). Aerodynamic optimization of wind turbine. *Proc. IMechE Vol. 224 Part A: J. Power and Energy*, pp. 827-838.
- Lighthill, M. J. (1962). The Bakerian Lecture, 1961. Sound Generated Aerodynamically. *Proceeding of The Royal Society A* (pp. 147-183). London: Royal Society.
- LM Wind Power. (2012). *LM Wind Power Blades Catalogue*. LM Wind Power, Kolding.
- Lockhard, D. P. (1999). An Overview of Computational Aeroacoustic Modeling at Nasa Langley. *10th TFAWS - Nasa Thermal & Fluids Analysis Workshop*, (pp. 1-14). Hampton, Va.
- Lowson, M. (1993). *Assessment and Prediction of Wind Turbine Noise*. ETSU.

- Lutz, T., Herrig, A., Würz, W., Kamruzzaman, M., & Krämer, E. (2007, April). Design and Wind-Tunnel Verification of Low-Noise Airfoils for Wind Turbines. *AIAA Journal* V.45 N.4, pp. 779-785.
- Lutz, T., Würz, W., Herrig, A., Braun, K., & Wagner, S. (2004). Numerical Optimization of Silent Airfoil Sections. *DEWEK 2004: 7th German Wind Energy Conference*. Wilhemshaven: Deutsches Windenergie.
- Marten, D. (2010). *Extension of an Aerodynamic Simulator for Wind Turbine Blade Design and Performance Analysis*. Technischen Universität Berlin. Berlin: TU Berlin.
- Marten, D. (2014). *Qblade Short Manual V0.8*. Berlin: TU Berlin.
- Marten, D. (2016). *QBlade v0.95 - Guidelines for Lifting Line Free Vortex Wake Simulations*. Berlin: TU Berlin.
- Marten, D., & Wendler, J. (2013). *Qblade Guidelines v0.6*. Berlin: TU Berlin.
- Mase, G. E. (1970). *Continuum Mechanics*. Michigan: McGraw-Hill.
- Measnet. (2009). *Evaluation of Site-Specific Wind Condition*. Measuring Network of Wind Energy Institutes.
- Medina, P., Singh, M., Johansen, J., Jove, A., & Machefaux, E. (2011). *Aerodynamic and Performance Measurements on a SWT-2.3-101 Wind Turbine*. Golden, CO: NREL.
- Migliore, P., & Oerlemans, S. (2003). *Wind Tunnel Aeoracoustic Tests of Six Airfoils for Use in Small Wind Turbines*. NREL. Golden, CO.: NREL/CP-500-35090.
- Migliore, P., van Dam, J., & Huskey, A. (2003). *Acoustic Tests of Small Wind Turbines*. NREL - National Renewable Energy Laboratory, Golden, Co.
- Moriarty, P. (2005). *NAFNoise User's Guide*. NREL. Golden, CO: NREL.
- Moriarty, P. (2008). NAFNoise and FAST noise modules. *NREL Design Codes Workshop* (pp. 1-29). Golden: 080925_1430_nafnoise_moriarty.

- Moriarty, P., & Migliore, P. (2003). *Semi-Empirical Aeroacoustic Noise Prediction Code for Wind Turbines*. NREL, Golden, CO.
- Moriarty, P., Guidati, G., & Migliore, P. (2004). Recent Improvement of a Semi-Empirical Aeroacoustic Prediction Code for Wind Turbines. *10th AIAA/CEAS Aeroacoustics Conference*. UK: AIAA.
- Moriarty, P., Guidati, G., & Migliore, P. (2005). Prediction of Turbulent Inflow and Trailing-Edge Noise for Wind Turbines. *11th AIAA/CEAS Aeroacoustics Conference (26th AIAA Aeroacoustics Conference)* (pp. 1-16). Monterrey, Ca.: AIAA.
- Morris, P., Long, L., & Brentner, K. (2004). An Aeroacoustic Analysis of Wind Turbines. *42nd AIAA Aerospace Sciences Meeting and Exhibit* (pp. 1-11). Reno: AIAA.
- National Renewable Energy Laboratory - NREL 1. (2015, October 2). Retrieved from NWTC Information Portal: https://wind.nrel.gov/airfoils/Shapes/S823_Shape.html
- National Renewable Energy Laboratory - NREL 3. (2015, October 2). *Patent Report by Invention*. Retrieved from Patent Report by Invention: https://wind.nrel.gov/airfoils/Documents/AirfoilPatentReport_2009-03-18.pdf
- National Renewable Energy Laboratory - NREL 4. (2016, Feb. 02). *Wind Turbine Airfoil List*. Retrieved from NWTC Information Portal: <https://wind.nrel.gov/airfoils/AirfoilList.html>
- NBR10151. (2000). *Acústica - Avaliação do Ruído em Áreas Habitadas, Visando o Conforto da Comunidade - Procedimento*. ABNT.
- Northern_Power. (2013). *Northern Power 100-21 IEC Class II*. Retrieved 03 17, 2014, from Norther Power Systems: http://http://www.northernpower.com/wind-power-products/documents/NPS100-21_US_SpecSheet.pdf
- Norton, M., & Karczub, D. (2003). *Fundamentals of Noise and Vibration Analysis for Engineers* (Second ed., Vol. 1). Cambridge: Cambridge University Press.
- NREL. (2005). *Wind Energy Myths*. Retrieved may 7, 2013, from National Renewable Energy Laboratory, DOE: <http://www.nrel.gov/docs/fy05osti/37657.pdf>

- NWTC. (2016, may 25). *NWTC- NREL ´s National Wind Technology Center*. Retrieved from NREL 5MW Rotor Geometry: <https://wind.nrel.gov/forum/wind/viewtopic.php?f=2&t=440>
- Oberkampf, W., & Roy, C. (2012). *Verification and Validation in Scientific Computing*. Cambridge: Cambridge University Press.
- Oerlemans, S. (2003). *Wind Tunnel Aeroacoustic Tests of Six Airfoils for Use on Small Wind Turbines*. Golden, Co.: NREL SR-500-34470.
- Oerlemans, S. (2011). *Wind Turbine Noise: Primary Noise Sources*. National Aerospace laboratory NLR, Amsterdam.
- Oerlemans, S., Fisher, M., Maeder, T., & Kögler, K. (2009, June). Reduction of Wind Turbine Noise Using Optimized Airfoils and Trailing-Edge Serrations. *AIAA Journal* (47) 6, pp. 1470-1481.
- Oerlemans, S., Sijtsma, P., & Méndez-López, B. (2007, February 6). Location and Quantification of Noise Sources on a Wind Turbine. *Journal of Sound and Vibration*, pp. 869-883.
- Orselli, R. (2011). *Previsão Numérica de Escoamento e Ruído Gerado em Corpos Rombudos Prismáticos*. Escola Politécnica da USP, São Paulo.
- Panton, R. L. (2005). *Incompressible Flow* (3rd ed.). New Delhi: J. Wiley & Sons.
- Parchen, R. (1998). *A Prediction Scheme for Trailing-Edge Noise Based on Detailed Boundary Layer Characteristics*. Progress Report. TNO Applied Institute of Physics, The Netherlands.
- Pechlivanoglou, G. (2012). *Passive and Active Flow Control Solutions for Wind Turbine Blades*. Technischen Universität Berlin, Berlin.
- Pechlivanoglou, G., Marten, D., G., W., N., M., & Wendler, J. (2009). *QBlade*. Technische Universität Berlin, Berlin.
- Pereira, R. (19/June/2016). Acordava no Meio da Noise com o Ruído. *O Estado de São Paulo*, B9.

- Petitjean, B., Drobietz, R., & Kinzie, K. (2011). Wind Turbine Blade Noise Mitigation Technologies. *Fourth International Meeting on Wind Turbine Noise*, (pp. 1-14). Rome.
- Petrone, G., de Nicola, C., Quagliarella, D., Witteveen, J., & Iaccarino, J. (2011). Analysis and Optimization of Wind Turbine Noise Under Uncertainty. *4th International Meeting on Wind Turbine Noise* (pp. 1-16). Rome: Ince-Europe.
- Pinder, J. (1992). Mechanical Noise from Wind Turbines. *Wind Engineering, Vol. 16, No. 3*, pp. 158-168.
- Pope, S. B. (2011). *Turbulent Flows* (8th printing ed.). Cambridge: Cambridge University Press.
- Ragheb, M., & Ragheb, A. M. (2011). *Wind Turbines Theory - The Betz Equation Equation and Optimal Rotor Tip Speed Ratio*. UIUC, Urbana-Champaign, IL.
- Rautmann, C., Ewert, R., & Dierke, J. (2015). Simulation of Broadband Trailing-Edge Noise - Influence of Airfoil Shape and Flow Characteristics. *6th International Meeting on Wind Turbine Noise* (pp. 1-25). Glasgow: INCE/EUROPE.
- Raymer, D. (2006). *Aircraft Design: A Conceptual Approach, 4th ed.* (3rd ed.). Reston, VA: AIAA.
- Reichenbach, B., Vieira, F., Yoshimura, L., & Telles, M. (2012). *Potencial Eólico do Campus de São Caetano do Sul da Escola de Engenharia Mauá*. Escola de Engenharia Mauá, Sao Caetano do Sul, SP.
- Remmler, S., Christophe, J., & Anthoine, J. (2010, September 9). Computation of Wall-Pressure Spectra from Steady Flow Data for Noise Prediction. *AIAA Journal* (48) 9, pp. 1997-2007.
- Rischpater, R. (2013). *Application Development With Qt Creator*. Birmingham: PACKT Publishing.
- Rogers, A., Manwell, J., & Wright, S. (2006). *Wind Turbine Acoustic Noise*. University of Massachusetts, Amherst.

- Rooney, M. (2013). *Eco-Economy Indicators - Wind Power*. Retrieved APRIL 9, 2013, from Earth Policy Institute: http://www.earth-policy.org/indicators/C49/wind_power_2013
- Russell, D., Titlow, J., & Bemmen, Y. (1999, Aug). Acoustic monopoles, dipoles, and quadrupoles: An experiment revisited. *American Journal of Physics*, Vol 67, N.8, pp. 660-664.
- Saab Jr, J., & Pimenta, M. (2016, Feb). Displacement Thickness Evaluation for Semi-Empirical Airfoil Trailing-Edge Noise Prediction Model. *Journal of the Brazilian Society of Mechanical Sciences and Engineering*, V.38, N.2, pp. 385-394.
- Saab Jr., J. Y. (2012). *Relatório de Participação em Conferência Internacional sobre Energia Eólica AWEA 2012*. EPUSP, Sao Paulo.
- Saab Jr., J., & Silveira, O. (1993). *Redução do Atrito Viscoso em escoamento Turbulento Incompressível, pelo Uso de Superfície com Microranhuradas Longitudinais-Aplicação na Indústria Aeronáutica*. Sao Paulo: POLI BT-30 (Boletim Técnico).
- Sandberg, R., & Jones, L. (2010). Direct Numerical Simulations of Airfoil Self-Noise. *IUTAM Symposium on Computational Aero-Acoustics for Aircraft Noise Prediction* (pp. 274-282). Elsevier.
- Sanderse, B. (2009). *Aerodynamics of Wind Turbine Wakes*. Energy Research Centre of the Netherlands.
- Schepers, J., Curves, A., Oerlemans, S., Braun, K., Lutz, T., Herrig, A., . . . Kogler, K. M. (2007). SIRROCO: Silent Rotors By Acoustic Optimisation. *Second International Meeting on Wind Turbine Noise* (pp. 1-24). Lyon, Fr.: ECN.
- Schlichting, H., & Gersten, K. (2003). *Boundary Layer Theory* (8th ed.). Berlin: Springer.
- Schlinker, R., & Amiet, R. (1981). *Helicopter Rotor Trailing Edge Noise*. NASA.
- Schomer, P., Erdreich, J., Boyle, J., & Pamidighatam, P. (2013). A Proposed Theory to Explain Some Adverse Physiological Effects of the Infrasonic Emissions at Some Wind Farm Sites. *5th Int. Conf. on Wind Turbine Noise*. Denver.

- Siemens. (2013). *Siemens D3 Platform 3.0 MW Direct Drive Wind Turbines*. Siemens AG Wind Power, Hamburg.
- Sloth, E. (2011). [personal correspondence] received 28/sept/11. SUZLON BLADE TECHNOLOGIES, Aarhus V., Denmark.
- Somers, D., & Tangler, J. (2005a). *The S822 and S823 Airfoils*. NREL, Golden, Co.
- Somers, D., & Tangler, J. (2005b). *The Airfoils S830, S831 and S832*. NREL, Golden.
- Somers, D., & Tangler, J. (2005c). *The Airfoils S833, S834 and S835*. NREL, Golden, Co.
- Stankovic, S., Campbell, N., & Harries, A. (2009). *Urban Wind Energy* (1ed. ed.). London: Earthscan.
- Styles, P., Westwood, R., Toon, S., Buckingham, M., & Marmo, B. C. (2011). Monitoring and Mitigation of LFN from WT to Protect Seismic Monitoring Equipment. *Fourth International Meeting on Wind Turbine Noise*, (pp. 1-13). Rome.
- Tam, C. (2012). *Computational Aerocoustics, A Wavenumber Approach* (1st ed.). Cambridge: Cambridge University Press.
- Theodorsen, T., & Regier, A. (1946). *THE PROBLEM OF NOISE REDUCTION WITH RELATION TO LIGHT AIRPLANES*. NACA Technical Note 1145, Washington.
- Timmer, W., & van Rooji, R. (2003, Nov.). Summary of the Delft University Wind Turbine Dedicated Airfoils. *Transactions of the ASME*, Vol. 125, pp. 488-496.
- Vargas, L. d. (2008). *Wind Turbine Noise Prediction*. Instituto Superior Técnico, Lisboa.
- Vargas, L., de Oliveira, P., Pinto, R. L., Bortolus, M. V., & Souza, M. (2005). Comparison Between Modern Procedures for Aerodynamic Calculation of Subsonic Airfoils for Application in Light Aircraft Designs. *18th International Congress of Mechanical Engineering - Proceedings of COBEM* (pp. 1-8). Ouro Preto, MG: COBEM 2005.

- Vér, I. L., & Beranek, L. L. (2006). *Noise and Vibration Control Engineering: Principles and Applications* (2nd ed.). Hoboken, NJ: J. Wiley & Sons.
- Versteeg, H., & Malalasekera, W. (2006). *An Introduction to Computational Fluid Dynamics* (2nd ed.). Loughborough: Pearson.
- Viterna, L., & Janetzky, D. (1982). *Theoretical and Experimental Power from Larhe Horizontal Axis Wind Turbine*. NASA Lewis.
- Wagner, S. (1997). *Development of Design Tools for Reduced Aerodynamic Noise Wind Turbine (DRAW)*.
- Wagner, S., Bareiß, R., & Guidati, G. (1996). *Wind Turbine Noise*. Berlin: Springer.
- White, F. M. (2006). *Viscous Fluid Flow* (Third edition ed.). New York: McGraw-Hill.
- Wilcox, D. (2010). *Turbulence Modeling for CFD* (Third Ed, Second Printing ed.). DCW.
- Wind Energy Research Reaps Rewards*. (2006). Retrieved março 28, 2013, from NASA: http://www.nasa.gov/vision/earth/technologies/wind_turbines.html
- Wind Power - Special Report. (2012). *US Wind Market - Hoping for a Brighter Future*. Wind Power Montly.
- Wiser, R., & Bolinger, M. (2012). *2011 Wind Technologies Market Report*. US Department of Energy, Oak Ridge, TN.
- Wolf, A., Lutz, T., Würz, W., Stalnov, O., & Seifert, A. (2011). Trailing Edge Noise Reduction of Wind Turbine Airfoils by Active Flow Control. *Fourth International Meeting on Wind Turbine Noise*, (pp. 1-12). Rome.
- Xiaomim, C. (2014, Jan 20). Optimization of Wind Turbine Airfoils/Blades and. *PhD Thesis*. Saint Louis, Missouri, USA: Washington University in Saint Louis.
- Zhu, W. (2004). *Modelling of Noise From Wind Turbines*. DTU, Lyngby, DK.

APPENDIX A – FIELD RESEARCH RESULTS

The field research was carried out during the American Wind Energy Association annual Conference of 2012, in Atlanta, Ga. It entailed a survey designed to understand the importance of *WTN* to the Industry, the methods used for *WTN* prediction and also how soon in the product development cycle did the designers consider the noise problem.

Ten important *WT* industry players, including five large companies that altogether manufactured 55% of all U.S. installed wind power capacity (as of December, 2011) completed the survey.

The table below summarizes the findings among this representative cross-section of the *WT* industry.

Table A-1 - WT manufacturers and industry direct survey at AWEA 2012.

	Question	Answers (multiple answers or comments allowed for some questions).
Q1	Do you think aerodynamically generated Wind Turbine Noise is a relevant issue?	10/10 consider the issue relevant.
Q1.1	Why?	Due to legal restrictions (3); community acceptance (6); The rotor is de major cause for WTN (1); It is necessary to search for new methods to reduce WTN without compromising aero efficiency (1); The places where noisy WTN can be sited with no complaints are getting limited (1); WTN is an important factor for on-shore WT (2); It is a key barrier that limits the span of the blades, the tip speed and thus limits the energy capture (1);
Q2	When in the design cycle does your team deal with that problem?	We try to predict WTN in the early design phase (8); We predict WTN in a more advanced design phase, by testing the prototype or scale model testing (6); We measure WTN later, during test phase and compare with acceptable standards (6); We leave this aspect for the siting experts (2); The industry shall use all tools and the academics role is to develop new noise prediction models and new ideas (blade concepts) with little noise generation (1).
Q3	If you predict aero noise during the early design phase, which method do you use for modeling the noise sources?	BEM (5); Vortex Wake (3); CFD/Rans (4); Hybrid CFD (1); We use correlations such as Nasa's (BPM) for inferring the WTN (3); We use correlations developed in-house (3); We make measurements in our own wind tunnel (1).
Q4	If you deal with the problem during the prototype or model testing	We use various methods with different levels of accuracy, depending upon the phase of the project (1); We use BEM/BPM and CFD-RANS (1); We use IEC standard recommendations (1);

	phase, which method do you use to predict the aero noise?	We employ RANS and acoustic modeling (1); We use numerical predictions and measurements (1).
Q5	Do you feel you need a better, more reproducible method for aero noise prediction at the early stages of the design?	Yes (7/10). No (2/10). Comments: aerodynamic noise is a very complex issue and improved validated methods are always welcome. It would be desirable to have routines for estimating aero noise in the early phases that could be later optimized via CFD in more advanced design phases. The better we can predict WTN, the easier we can assure our customers of the quality of our product. The industry lacks better predictive methods and also better ideas to lessen WTN. Most current prediction tools requires calibration based on prototype performance parameters and thus any development that would make the design less dependent on model parameter calibration would be relevant.
Q6	Do you have acceptable guidelines for using the CFD/RANS approach on turbulence, law of the wall, grid spacing, etc?	Yes (5). No (1).

APPENDIX B – BASIC ACOUSTICS AND ACOUSTIC ANALOGY THEORIES, DISCUSSED AND COMMENTED.

B.1 SOUND POWER AND SOUND PRESSURE LEVELS

Noise control problems are systemic problems involving a source, a propagation path and a receiver. Sound energy is emitted by a noise source and transmitted to a receiver, where it is immitted (Vér & Beranek, 2006).

While the source strength is described by the sound power level and directivity function, the preferred descriptor for immission is the sound pressure level, since the human ear responds, in a non-linear way, to sound pressure. Both sound pressure and sound power levels are usually expressed in a logarithmic scale, because the range of the sound powers of practical interest covers more than 12 orders of magnitude.

The time signal of sound pressure (Eq. B-1) may have an arbitrary shape, but can always be characterized by a superposition of harmonic signals of different frequency and amplitude, the pure tones (Wagner, Bareiß, & Guidati, Wind Turbine Noise, 1996):

$$p(t) = A \cdot \cos(2\pi f \cdot t) = A \cdot \cos(2\pi \cdot \frac{1}{T}) = A \cdot \cos(\omega \cdot t) \quad [Pa] \quad (B - 1)$$

The definition of sound pressure level is:

$$SPL = 10 \cdot \log_{10} \left(\frac{\hat{p}^2}{\hat{p}_{ref.}^2} \right) = 20 \cdot \log_{10} \left(\frac{\hat{p}}{\hat{p}_{ref.}} \right) \quad [dB] \quad (B - 2)$$

where

$$\hat{p} = \sqrt{\lim_{T \rightarrow \infty} \left[\frac{1}{T} \int_0^T p^2(t) dt \right]} \quad [Pa] \quad (B - 3)$$

is the root mean square sound pressure level, and $\hat{p}_{ref.} = 2 \cdot 10^{-5} Pa$ is the standard reference pressure, corresponding to the weakest audible sound, or 1 dB at 1000 Hz. The definition of sound power level is:

$$SPW = 10 \cdot \log_{10} \left(\frac{P}{P_{ref.}} \right) [dB] \quad (B - 4)$$

where and $P_{ref.} = 10^{-12}$ W is the standard reference sound power.

The sound intensity is defined as the sound power transmitted per unit area. Far from the source it can be expressed as:

$$I = \frac{\hat{p}^2}{\rho_0 c_0} [W/m^2] \quad (B - 5)$$

where $\rho_0 c_0 = Z_0$ is the specific acoustic impedance with value $416 \text{ kg}/\text{m}^2\text{s}$ for the air.

The sound pressure level can also be expressed as a ratio between the intensity and a reference intensity, $I_{ref.} = 10^{-12} \text{ W}/\text{m}^2$:

$$SPL = 10 \cdot \log_{10} \left(\frac{I}{I_{ref.}} \right) [dB] \quad (B - 6)$$

The sound power transmitted through a surface S is:

$$P = \int_S I dS \quad [W] \quad (B - 7)$$

B.2 RADIATION FIELD OF A SOUND SOURCE

The pressure fluctuations radiating from solid vibrating surfaces or from turbulent eddies, propagate through the surrounding elastic medium to form a sound field. The sound field can be described as a perturbation of steady-state variables of the elastic medium which conveys the sound (Bies & Hansen, 2009). The pressure is the easiest variable to measure in a fluid flow and provide a scalar description of the sound field from which all other variables of interest may be derived.

In a fluid, the sound field expresses itself by very small amplitude variations in local pressure, associated with variations in density, displacement, particle velocity and temperature. Even though the motion associated with the passing of the acoustic

disturbance may be of the order of magnitude of the molecular motion, the particle velocity described refers to a macroscopic average motion superimposed upon molecular motion of the fluid (Bies & Hansen, 2009), allowing the problem to be approached with traditional continuum mechanics tools.

Although the pressure fluctuations trigger motions in the fluid, viscous effects are considered negligible in a sound field by many authors, (Dowling & Ffowcs Williams, 1983), (Bies & Hansen, 2009), since the pressure seems to induce far greater stress fields than viscosity, at frequencies of most practical interest. However, Panton (Panton, 2005) and White (White, 2006) discuss the case when a fluid is undergoing expansion or compression, a case for which Stokes⁶⁸ assumption is not valid, i.e., when the mechanical pressure, p_m , and the thermodynamic pressure, p_t , are not the same. According to Panton and White, if a compression or expansion of a fluid is very rapid, such as a shock or sound wave, and the molecules have internal degrees of freedom (vibration, rotation), thermodynamic equilibrium is not maintained and the energy appears first in the translation mode and only after several subsequent molecular collisions the energy is distributed to the rotation and later to the vibration models, in this order. In this case, the mechanical pressure, associated with the translation, is not the equilibrium thermodynamic value, i.e., the local ρ and e , nonequilibrium values, substituted in the equilibrium equation of state $p = p(\rho, e)$ would not return the mean value of the normal stresses. These nonequilibrium effects are important to be modeled when the relaxation time is long in comparison with the flow time and they can be modelled through the bulk viscosity coefficient, $\mathcal{K} = (\mathcal{L} + 2/3\mu)$:

$$p_m \equiv -\frac{1}{3}T_{ii} \quad (B - 8)$$

where T_{ii} are the normal stresses or diagonal elements of the stress tensor, \mathcal{L} is the Lamé or second coefficient of viscosity, and μ is the first coefficient of viscosity or coefficient of dynamic viscosity.

$$p_m - p_t = (\mathcal{L} + 2/3\mu)\partial_k v_k = -\frac{\mathcal{K}}{\rho} \frac{d\rho}{dt} \quad (B - 9)$$

⁶⁸ $\mathcal{L} \approx -2/3\mu$ is supported by the kinetic theory when the fluid is a monoatomic gas.

where the last term of above relation was obtained with the aid of the continuity equation, $\frac{d\rho}{dt} = -\rho \cdot \partial_i v_i$

One such situation is the process of absorption of sound waves in the air, and the nonzero value for \mathcal{K} strongly depends upon the water vapor content in the air, since it modifies heavily the relaxation times. In gases, both in the sonic and supersonic ranges, experimental values of absorption differ from the theoretical ones by a factor whose magnitude lies in the range of 4 to 100 (Karim & Rosenhead, 1952). More elaborate relaxation time modeling might require the use of non-Newtonian viscosity laws (Panton, 2005).

According to Dowling and Ffowcs Williams (Dowling & Ffowcs Williams, 1983) the ratio of the pressure to the viscous stresses is represented by the following Reynolds number:

$$Re = \frac{2\pi c_0 \lambda}{\nu} = \frac{\omega \lambda^2}{\nu} \quad (B - 10)$$

where c is the speed of sound, λ is the wavelength and ν is kinematic viscosity.

For sound in the air at 1,000 Hz frequency, the Reynolds number is large, approximately 4×10^7 and, for that reason Dowling and Ffowcs Williams believe the sound could be regarded essentially as a weak motion of an inviscid fluid, unless the problem of very long-distance propagation is of interest. Viscous effects may become relevant when the sound travels for millions of wavelengths. The viscous effects, thus, could be viewed as a small modifying influence on a sound field that is essentially established in an inviscid fluid.

The sound field radiated from a source may be divided into three regions: the hydrodynamic near field, the geometric (or Fresnel) near field and the far field (Bies & Hansen, 2009).

The hydrodynamic near field is less than one wavelength away from the source. It is characterized by fluid motion that is not directly associated with sound propagation. If the acoustic wavelength is much larger than the separating distance of adjacent parts of the vibrating surface, the source is considered compact (Lowson, 1993), (Wagner, Bareiß, & Guidati, Wind Turbine Noise, 1996). If the source is non-compact, the

acoustic pressure will be out of phase with local particle velocity. Since sound propagation to the far field is associated with in-phase components of pressure and particle velocity (Bies & Hansen, 2009), measurements of the acoustic pressure amplitude in the near field will provide inaccurate values of sound power radiated from the source.

The interference between waves from various parts of a non-compact source result in interference effects and sound pressure levels that do not necessarily decrease at the expected 6 dB per doubling of distance that characterizes the far field. This region is called the geometric near-field. It is possible to calculate the radiated sound power from the geometric near field (Bies & Hansen, 2009), but the problem is the determination of a sufficient number of sound pressure measurements such that further measurements would provide no improvement to the radiated sound power estimate.

If the source can be considered compact, difference in retarded time at different positions of the source region can be neglected and the evaluation of the sound field through volume integrals containing the source region can be considerably simplified (Wagner, Bareiß, & Guidati, Wind Turbine Noise, 1996).

Finally the region extending from the geometric near field to infinity is known as the far-field. As mentioned, the region is physically characterized by in-phase particle velocity and pressure of the waves and the sound pressure levels decrease monotonically at the rate of 6 dB per doubling of the distance from the source. Also, in the far field, the source directivity is well defined. Mathematically, the far field can be described by the sufficient but not always necessary⁶⁹ following conditions (Bies & Hansen, 2009):

$$r \gg \lambda/2\pi, \quad r \gg l, \quad r \gg \pi l^2/2\lambda \quad (B - 11)$$

where r is the distance from the source to the measurement position and l is the characteristic source dimension, the chord in the case of an airfoil. If the lengths involved are represented by dimensionless ratios $\gamma = 2r/l$ and $k = \pi l/\lambda$, where γ is a measure of how many source lengths away the measurement point is located at, and

⁶⁹ A large pulsating sphere, for instance, has only a far field.

k is a measure of how many wavelengths can be contained in the length of the source, the diagram Figure B-1 can be constructed (Bies & Hansen, 2009):

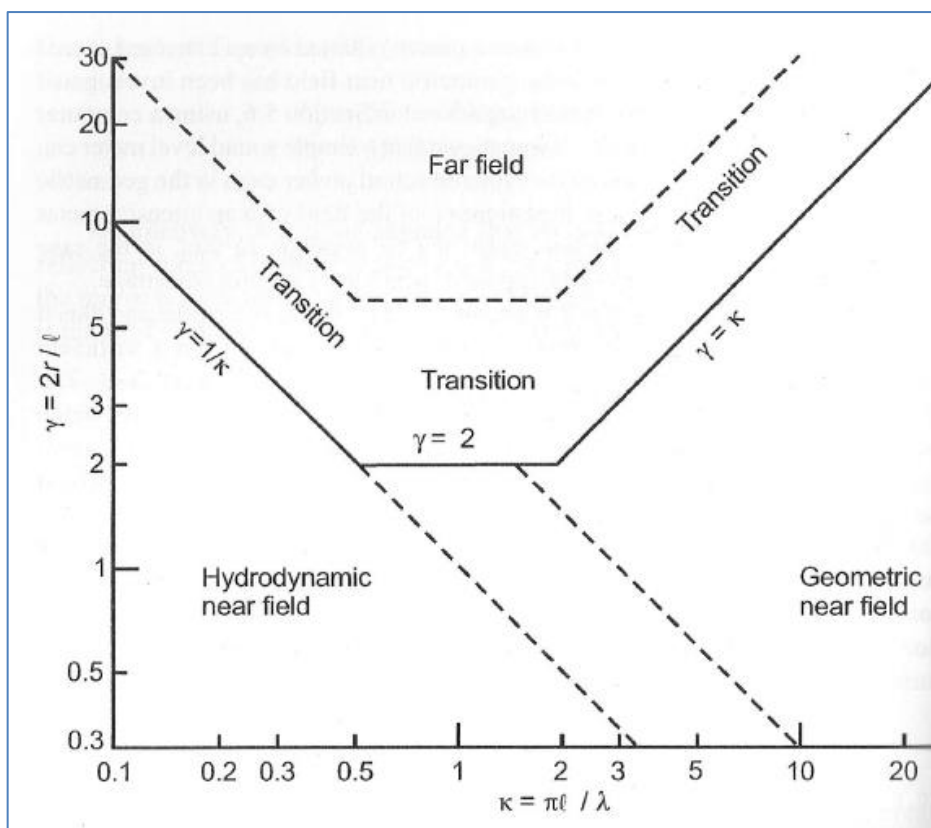


Figure B-1 – Hydrodynamic near field, geometric near field and the far field (Bies & Hansen, 2009).

In this research, there is no particular interested in the propagation phase of acoustic phenomena so that the Stokes assumption will be considered valid and the sound field will be treated like a perturbation to an inviscid medium.

For a typical airfoil chord of 1 m, and TE noise being of a broad-band nature, with peak frequency typically in the order of 500-1500 Hz (Wagner, Bareiß, & Guidati, Wind Turbine Noise, 1996), the dimensionless parameter would be $k \sim 9$ for an admitted peak frequency of 1000 Hz. For the calculation domain to achieve the ‘fully mature’ far field, a dimensionless distance of $\gamma \sim 30$ would have to be achieved, which translates into a surface approximately 15 m away from the 1 m airfoil source.

However, notice that for the calculation domain to achieve the transition between the geometric near field and the far field, a dimensionless distance of $\gamma \sim 10$ would be enough, which can be accomplished with a calculation domain with limits 5 m away

from the airfoil source. Working in the transition from the geometric near field to the far field should suffice if the source might be considered compact ($\lambda \gg chord$) which would not seem to apply to airfoil self-noise as a whole. However, since the focus here is in airfoil TE noise only, if the TE source could be characterized by a local TE length, instead of the full airfoil chord, this might be possible, since TE noise is produced by local turbulence convected past the airfoil TE.

B.3 HARMONIC FUNCTIONS

The harmonic function used to describe the sound pressure signal (B-12) of a pure tone or the motion of a harmonic wave can be represented using complex notation (Wagner, Bareiß, & Guidati, Wind Turbine Noise, 1996) :

$$p'(t) = A. e^{-i\left(2\pi\frac{t}{T}\right)} = A. e^{-i\omega t} \quad (B - 12)$$

$$p'(x, t) = A. e^{-i\left(2\pi\frac{x}{\lambda} - 2\pi\frac{t}{T}\right)} = A. e^{i(kx - \omega t)} \quad (B - 13)$$

where $i = \sqrt{-1}$ and $k = 2\pi/\lambda$ is the wavenumber.

If the wave is moving in two or three-dimensional space, in arbitrary direction, $p'(\vec{x}, t)$ can be expressed with the aid of the wave vector, where λ_i is the wavelength in the x_i direction:

$$\vec{k} = \frac{2\pi}{\lambda} \vec{n} = (k_1, k_2, k_3) = \left(\frac{2\pi}{\lambda_1}, \frac{2\pi}{\lambda_2}, \frac{2\pi}{\lambda_3} \right) \quad (B - 14)$$

$$p'(\vec{x}, t) = A. e^{i(\vec{k}\vec{x} - \omega t)} = A. e^{i(k_1x_1 + k_2x_2 + k_3x_3 - \omega t)} \quad (B - 15)$$

B.4 FOURIER TRANSFORMS IN TIME AND SPACE

A comprehensive summary of signal analysis and fundamentals of correlation analysis can be found in Blake (Blake, *Mechanics of Flow-Induced Sound and Vibration*, 1986 I). According to the author, Fourier analysis is the most used tool for analyzing random-data and theoretical formulations of steady-state vibration problems. In the present context it can be employed to relate statistical properties of sound (noise) signals to the frequency domain.

The importance of the harmonic functions previously discussed is that a non-harmonic function g of an independent variable t, x, \vec{x} can be expressed, through Fourier transform, as the sum of an infinite series of harmonic functions with different angular frequencies ω , wave numbers k , and wave vectors \vec{k} (Wagner, Bareiß, & Guidati, *Wind Turbine Noise*, 1996). The amplitudes of these harmonic functions are called the spectrum of the function g . According to Dowling and Ffowcs-Williams (Dowling & Ffowcs Williams, 1983), the Fourier theorem allows all linear fields to be regarded as a superposition of harmonic waves. This procedure is called “Harmonic Analysis” and it is particularly useful to describe the response of fan rotors to inflow distortions, as showed by Blake (Blake, *Mechanics of Flow-Induced Sound and Vibration*, 1986 I).

The Fourier transform of a function that depends on time only, $g(t)$, is given by the Fourier integral below and its dimension is equal to the original dimension of $g(t)$ multiplied by frequency (s^{-1}):

$$\tilde{g}(\omega) = \frac{1}{2\pi} \int_{-\infty}^{+\infty} g(t) \cdot e^{+i\omega t} dt \quad (B - 16)$$

The effect of the integral is to verify the agreement of the signal (function $g(t)$) with harmonic functions $e^{i\omega t}$ of different frequencies ω , returning large or small values of $\tilde{g}(\omega)$ when the agreement is high or low, respectively.

The inverse Fourier transform returns the original signal $g(t)$

$$g(t) = \int_{-\infty}^{+\infty} \tilde{g}(\omega) \cdot e^{-i\omega t} d\omega \quad (B - 17)$$

The Fourier series is the outcome of the Fourier transform applied to the particular case of a periodic signal. The Fourier transform can be likewise applied to functions of space variables and of both time and space variables as well. In those cases, the

kernel $e^{i\omega t}$ is to be replaced by e^{ikt} , where k is the wavenumber, or $e^{i(\vec{k}\vec{x}-\omega t)}$, respectively. In these cases, the Fourier transform compares the agreement of the function under investigation with plane waves of different ω and \vec{k} , returning the corresponding wave vector frequency $\vec{k}\omega$ spectrum. This spectrum for the pressure fluctuations over a surface finds use, for instance, in Howe's model (Howe, 1978) for TE noise, discussed in this work.

B.5 THE LINEAR WAVE EQUATION

In order to develop the linear wave equation, the hypothesis developed in the previous sections that the Stokes assumption (no distinction between mechanical and thermodynamic pressures) is applicable to aerodynamic sound waves and that the phenomenon can be viewed as a perturbation in an inviscid medium, will all be adopted, and they are all plausible in the far field.

In this way, the acoustic quantities ρ' , p' and u_i' , which are the acoustic density, pressure and particle velocity in the i^{th} direction respectively, are defined (Wagner, Bareiß, & Guidati, Wind Turbine Noise, 1996) as small departures from a quiescent state of a fluid of uniform density, ρ_0 , and uniform pressure, p_0 :

$$p = p_0 + p'; \quad \rho = \rho_0 + \rho'; \quad u_i = 0 + u_i' \quad (B - 18)$$

The homogenous wave equation for inviscid medium will first be derived and in the following sections the forcing terms responsible for the sources will be added. The first step is the application of the continuity equation and the inviscid momentum (Euler) equations for fluid flow, to a suitable control volume, free from mass sources, and from the effect of external body and contact forces:

$$\frac{\partial \rho}{\partial t} + \frac{\partial}{\partial x_i}(\rho u_i) = 0 \quad (B - 19)$$

$$\frac{\partial}{\partial t}(\rho u_i) + \frac{\partial}{\partial x_j}(\rho u_i u_j) = - \frac{\partial p}{\partial x_i} \quad (B - 20)$$

The time derivative of the continuity equation and the divergence of the Euler equations, yield:

$$\frac{\partial^2 \rho}{\partial t^2} + \frac{\partial^2}{\partial t \partial x_i} (\rho u_i) = 0 \quad (B - 21)$$

$$\frac{\partial^2}{\partial x_i \partial t} (\rho u_i) + \frac{\partial^2}{\partial x_i \partial x_j} (\rho u_i u_j) = - \frac{\partial^2 p}{\partial x_i^2} \quad (B - 22)$$

By subtracting Equation (B-22) from (B-21), the density momentum, ρu_i , can be eliminated:

$$\frac{\partial^2 \rho}{\partial t^2} - \frac{\partial^2}{\partial x_i \partial x_j} (\rho u_i u_j) - \frac{\partial^2 p}{\partial x_i^2} = 0 \quad (B - 23)$$

And by introducing the definition of the acoustic quantities (B-18):

$$\frac{\partial^2}{\partial t^2} (\rho_0 + \rho') - \frac{\partial^2}{\partial x_i \partial x_j} ((\rho_0 + \rho') u_i' u_j') - \frac{\partial^2}{\partial x_i^2} (p_0 + p') = 0 \quad (B - 24)$$

Finally, linearization of (B-24) is possible by neglecting the products of small quantities:

$$\frac{\partial^2 \rho'}{\partial t^2} - \frac{\partial^2 p'}{\partial x_i^2} = 0 \quad (B - 25)$$

Equation (B-25) has two independent variables, ρ' and p' , that can be related through an equation of state. The use of the ideal gas law ($p = \rho RT$) would introduce the temperature as a new variable. If the process may be considered adiabatic (according to Kerrebrock (Kerrebrock, 1992), this is acceptable when the fluid can be modelled as non-heat-conducting), the process will be also isentropic and barotropic, and the density will depend upon pressure only (Mase, 1970):

$$p - p_0 = c_0^2 (\rho - \rho_0)^\alpha \quad (B - 26)$$

where $\alpha = 1$ for ideal gases undergoing isothermal expansion (Blake, Mechanics of Flow-Induced Sound and Vibration, 1986 I), and c_0 is the velocity at which disturbances propagate through the medium, defined for a perfect gases as:

$$c_0^2 = \left. \frac{\partial p}{\partial \rho} \right|_{S=const} = kRT \quad (B - 27)$$

The barotropic equation of state (B.5.9) in (B.5.8), results in the homogeneous wave equation for the acoustic pressure or, alternatively, for the acoustic density (Wagner, Bareiß, & Guidati, Wind Turbine Noise, 1996):

$$\frac{1}{c_0^2} \frac{\partial^2 p'}{\partial t^2} - \frac{\partial^2 p'}{\partial x_i^2} = 0 \quad (B - 28)$$

$$\frac{\partial^2 \rho'}{\partial t^2} - c_0^2 \frac{\partial^2 \rho'}{\partial x_i^2} = 0 \quad (B - 29)$$

Sometimes in the bibliography (Blake, Mechanics of Flow-Induced Sound and Vibration, 1986 I), (Farassat, Introduction to Generalized Functions With Applications in Aerodynamics and Aeroacoustics, 1996), (Farassat, Derivation of Formulations 1 and 1A of Farassat, 2007), equations B-28 and B-29 are represented in the following short notation, where \square is called the *wave* or the *D'Alembertian* operator:

$$\square^2 p' = 0 \quad (B - 28a)$$

$$\square^2 \rho' = 0 \quad (B - 29a)$$

The general solution for a one dimensional wave equation of the type B-28, which describes the plane wave in the far field of an arbitrary source, is (Dowling & Ffowcs Williams, 1983), (Wagner, Bareiß, & Guidati, Wind Turbine Noise, 1996), (Courant & John, 2000):

$$p'(x, t) = f(x - c_0 t) + g(x + c_0 t) \quad (B - 30)$$

This general solution is called the D'Alembert solution (Krasnov, Kiselev, Makarenko, & Shikin, 1990) for the wave equation and each term of it is also a particular solution of the equation. The pressure perturbation maintains its form while traveling at the speed of sound, c_0 . Function f describes the forward wave traveling in the direction of increasing x , while function g describes a returning wave. When f and g are harmonic functions, the wave can be represented by:

$$p'(x_1, t) = A_1 \cdot e^{i(k_0 x_1 - \omega t)} + A_2 \cdot e^{i(k_0 x_1 + \omega t)} \quad (B - 31)$$

Where k_0 (the wave number) and ω (angular frequency) are related to c_0 via

$$c = \lambda/T = f \cdot \lambda = \omega/k \quad (B - 32)$$

Since the general solution is the sum of the forward and return waves, one term of the Eqn. B-30 or B-31 must be rejected when the problem represents a single wave, generated by a single source in a medium without reflections, like the propagation problem in a free field or anechoic room (Bies & Hansen, 2009) or in the case of a plane wave (Blake, *Mechanics of Flow-Induced Sound and Vibration*, 1986 I), where the general solution becomes the Eqn. B-15 discussed earlier.

B.5.1 The inhomogeneous linear wave equation

When dealing with a sound field that includes sound sources, it is necessary to use the inhomogeneous wave equation (Wagner, Bareiß, & Guidati, *Wind Turbine Noise*, 1996), which can be obtained from Eqn. B-28, by adding a right-hand side term, $\sigma(\vec{x}, t)$, that represents arbitrary sound sources, that may be distributed along the field:

$$\frac{1}{c_0^2} \frac{\partial^2 p'(\vec{x}, t)}{\partial t^2} - \frac{\partial^2 p'(\vec{x}, t)}{\partial x_i^2} = \sigma(\vec{x}, t) \quad (B - 33)$$

Equation B-33, may be also expressed in the frequency domain, with the aid of the Fourier Transform. Each dependent variable is then substituted by its Fourier Integral

$$p'(\vec{x}, t) = \int_{-\infty}^{+\infty} \tilde{p}'(\vec{x}, \omega) e^{-i\omega t} d\omega \quad (B - 34)$$

$$\sigma(\vec{x}, t) = \int_{-\infty}^{+\infty} \tilde{\sigma}(\vec{x}, \omega) e^{-i\omega t} d\omega \quad (B - 35)$$

into the inhomogeneous wave equation (B-33), resulting:

$$\begin{aligned} \frac{1}{c_0^2} \frac{\partial^2}{\partial t^2} \left(\int_{-\infty}^{+\infty} \tilde{p}'(\vec{x}, \omega) e^{-i\omega t} d\omega \right) - \frac{\partial^2}{\partial x_i^2} \left(\int_{-\infty}^{+\infty} \tilde{p}'(\vec{x}, \omega) e^{-i\omega t} d\omega \right) \\ = \int_{-\infty}^{+\infty} \tilde{\sigma}(\vec{x}, \omega) e^{-i\omega t} d\omega \quad (B - 36) \end{aligned}$$

After the evaluation of the double time derivative, the Helmholtz equation results, which is the inhomogeneous wave equation in the frequency domain:

$$\int_{-\infty}^{+\infty} \left(\frac{-\omega^2}{c_0^2} \tilde{p}'(\vec{x}, \omega) - \frac{\partial^2}{\partial x_i^2} \tilde{p}'(\vec{x}, \omega) - \tilde{\sigma}(\vec{x}, \omega) \right) \cdot e^{-i\omega t} d\omega = 0 \quad (B - 37)$$

For Eqn. B-37 to be true, the integrand must be zero, which leads to:

$$\frac{\partial^2}{\partial x_i^2} \tilde{p}'(\vec{x}, \omega) + k_0^2 \tilde{p}'(\vec{x}, \omega) = -\tilde{\sigma}(\vec{x}, \omega) \quad (B - 38)$$

or

$$\nabla^2 \tilde{p}' + k_0^2 \tilde{p}' = -\tilde{\sigma} \quad (B - 38a)$$

It is possible to find a solution function which satisfies Eqn. B-38a when the source term is modelled like an impulsive, harmonic point source, expressed as a delta function on the right-hand side (Couto, 2013):

$$\nabla^2 G + k_0^2 G = -\delta(\vec{x} - \vec{y}) \quad (B - 39)$$

where \vec{y} is the position vector of the point source and G is the Green's function, given by

$$G(\vec{x}, \vec{y}, \omega) = \frac{e^{\pm ik_0 |\vec{x} - \vec{y}|}}{4\pi |\vec{x} - \vec{y}|} \quad (B - 40)$$

According to Couto (Couto, 2013), Green's function describes the amplitude of the "stationary" motion ($t \gg t_0$) when the external force is concentrated at \vec{y} and oscillates with unit amplitude. Choosing the exponent signal will determine if G describes an outward travelling or collapsing wave. When the solution for the Helmholtz equation is obtained, i.e. the Green function that satisfies it is available, the solution to the inhomogeneous differential wave equation (B-331) can be obtained by the integration of the Green function over the region where the source term is not zero (Wagner, Bareiß, & Guidati, Wind Turbine Noise, 1996):

$$\tilde{p}'(\vec{x}, \omega) = \int_V \tilde{\sigma}(\vec{y}, \omega) \cdot G(\vec{x}, \vec{y}, \omega) dV(\vec{y}) \quad (B - 41)$$

This equation is valid for free, unbounded spaces only.

B.6 ELEMENTARY SOLUTIONS OF THE WAVE EQUATION

Since all sound fields in unbounded spaces are of three-dimensional nature, the 3D sound fields are used to exemplify the role of sound sources.

B.6.1 Monopoles

In the presence of a pulsating source of matter, the temporal and spatial variation of mass do not balance anymore and the continuity equation (B-19) must be restated as:

$$\frac{\partial \rho}{\partial t} + \frac{\partial}{\partial x_i} (\rho u_i) = Q(\vec{x}, t) \quad (B - 42)$$

where $Q(\vec{x}, t)$ is the flow rate intensity of the source, with dimensions, kg/m^3s . By performing the same path as for the deduction of the homogeneous equation, the source becomes, after linearization, the new term on the right hand side of the wave equation (see also Eqn. B-33):

$$\frac{\partial^2 p'}{\partial t^2} - c_0^2 \frac{\partial^2 p'}{\partial x_i^2} = \frac{\partial Q}{\partial t} = \dot{Q}(\vec{x}, t) \quad (B - 43)$$

where $\dot{Q}(\vec{x}, t)$ is known as the *forcing term* with dimensions, kg/m^3s^2 . It was shown that it is possible to find solutions for the wave equation when the source term can be modelled like an impulsive, harmonic point source. For a concentrated point source with mass flow rate $\dot{q}(t) \left(\frac{kg}{s^2}\right)$, located at \vec{y} , the Eqn. B-43 may be rewritten with the aid of the three dimensional (Dirac's) delta function⁷⁰, $\delta(x - x_0)$, which will restrain the mass flow rate injection to the point source itself

⁷⁰ Generalized Functions are useful in the solution of many differential equations, like the Cauchy problem for the heat equation (Krasnov, Kiselev, Makarenko, & Shikin, 1990), p. 639; or the problem of a beam with concentrated load (Courant & John, 2000), p.674. For a detailed review of generalized functions and their application to aerodynamics and aeroacoustics, see (Farassat, Introduction to Generalized Functions With Applications in Aerodynamics and Aeroacoustics, 1996).

$$\frac{\partial^2 p'}{\partial t^2} - c_0^2 \frac{\partial^2 p'}{\partial x_i^2} = \dot{q} \cdot \delta(\vec{x} - \vec{y}) \quad (B - 44)$$

The solution for this wave equation, can be found with the aid of a Green's function and is given by Wagner et al. (Wagner, Bareiß, & Guidati, Wind Turbine Noise, 1996), p.36; and Blake (Blake, Mechanics of Flow-Induced Sound and Vibration, 1986 I), p.53:

$$4\pi \cdot p'(\vec{x}, t) = \frac{\dot{q}(t - r/c_0)}{r} = \frac{\dot{q}(\tau)}{r} = \frac{[\dot{q}]}{r} \quad (B - 45)$$

where r is the distance between the point source and a field point located at \vec{x} , the observer or microphone position. For an interesting consideration, called *causality condition*, on the fact that the solution has only the term corresponding to the wave travelling outward, from the source to infinity, see Dowling and Ffowcs-Williams (Dowling & Ffowcs Williams, 1983), p. 45. The acoustic pressure p' depends on the value of \dot{q} emitted at a past time, called *the emission time* or *retarded time*, $\tau = t - r/c_0$, when the wave left the source in order to reach the observer position later, at time t . Terms taken at the retarded time are usually expressed within square brackets (Lighthill, 1962), (Wagner, Bareiß, & Guidati, Wind Turbine Noise, 1996)

$$\dot{q}(t - r/c_0) = \dot{q}(\tau) = [\dot{q}] \quad (B - 46)$$

The difference between the emission (or retarded) time, τ , and the observer time, t , is due to the finite speed of propagation in the medium, c_0 .

By applying the Fourier transform to Eqn. B-45 it is possible to obtain the analog solution in the frequency domain:

$$4\pi \cdot \tilde{p}'(\vec{x}, \omega) = \frac{\tilde{q}(\omega)}{r} \cdot e^{+ik_0 r} \quad (B - 47)$$

The solutions above (B-46) and (B-47) are approximations valid for point sources or sources whose diameters are small compared to the acoustic wavelength (see discussion on source compactness). The far field of a point volume source begins at a minimum distance r , where $2\pi r/\lambda \gg 1$ (Blake, Mechanics of Flow-Induced Sound and Vibration, 1986 I), which is equivalent to the first sufficient condition proposed by Bies and Hansen (Bies & Hansen, 2009) in B-11.

A point source displays a radial symmetry and depends on distance r from the source, only. It is called a monopole and is characterized by the monopole harmonically fluctuating strength, \dot{q} , or strength per unit volume, \dot{Q} . The monopole field displayed at Fig. B-2 was generated based on Eq. B-11 for a unitary strength source:

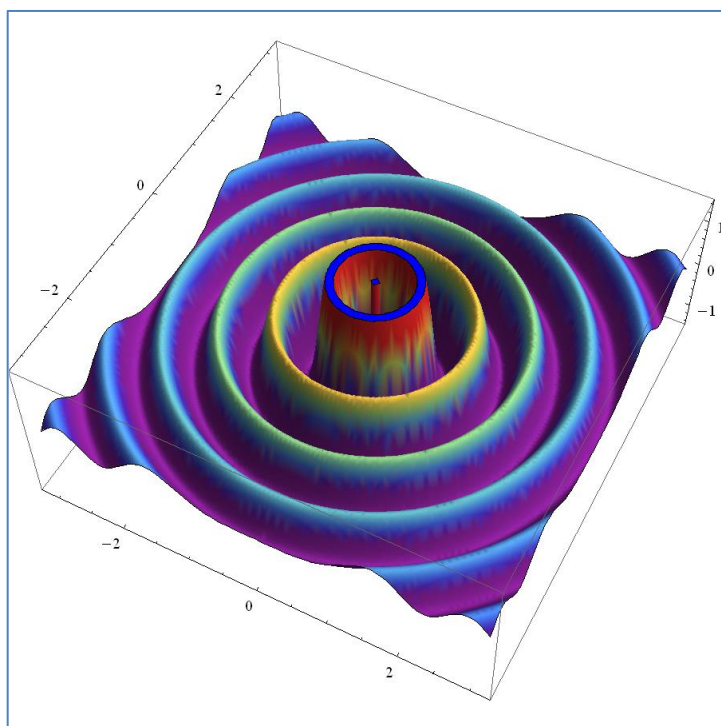


Figure B-2 – Graphical rendering of the acoustic field radiated by a monopole. Wolfram Mathematica Demonstration Program. Code author: Enrique Zeleny.

The small pulsating sphere (monopole) model is suitable for representing real sources that may be modelled by fluctuating sources of matter, like sirens and sound radiated by moving volumes like propellers and fan blades (Wagner, Bareiß, & Guidati, *Wind Turbine Noise*, 1996), or a pulsating jet (Kerrebrock, 1992).

B.6.2 Dipoles

If there is a force field distributed in part of the sound field instead of a source of matter, the momentum equation (B-20) must be reviewed in order to account for those forces:

$$\frac{\partial}{\partial t}(\rho u_i) + \frac{\partial}{\partial x_j}(\rho u_i u_j) + \frac{\partial p}{\partial x_i} = F_i(\vec{x}, t) \quad (B - 48)$$

where F_i (N/m^3) is the force density of the fluctuating force field. Once again, by performing the same path as for the deduction of the homogeneous equation, the source becomes, after linearization, the new term on the right hand side of the wave equation:

$$\frac{\partial^2 p'}{\partial t^2} - c_0^2 \frac{\partial^2 p'}{\partial x_i^2} = -\frac{\partial F_i(\vec{x}, t)}{\partial x_i} = -\frac{\partial F_1}{\partial x_1} - \frac{\partial F_2}{\partial x_2} - \frac{\partial F_3}{\partial x_3} \quad (B - 49)$$

The divergence of the force density, $\partial F_i / \partial x_i$, acts as the forcing term for the wave equation. Before evaluating the forcing term derivatives, the force density has to be expressed, in each direction, by using the three dimensional delta function:

$$F_1 = f_1 \cdot \delta(\vec{x} - \vec{y}) = \delta(x_1 - y_1) \delta(x_2 - y_2) \delta(x_3 - y_3) \quad (B - 50)$$

According to Wagner et al. (Wagner, Bareiß, & Guidati, Wind Turbine Noise, 1996), the delta function in any direction, x_1 for instance, can be replaced by two combined Heaviside functions. After performing the derivative of the force density in order to find the forcing term, the Heaviside functions derivatives will become once more delta functions, resulting in the following right hand term for the wave equation in the x_1 direction:

$$-\frac{\partial F_1}{\partial x_1} = \lim_{\varepsilon_1 \rightarrow 0} \left\{ -\frac{f_1}{\varepsilon_1} \cdot \delta(\vec{x} - \vec{y}_{-\varepsilon_1}) + \frac{f_1}{\varepsilon_1} \cdot \delta(\vec{x} - \vec{y}_{+\varepsilon_1}) \right\} \quad (B - 51)$$

where

$\vec{y}_{-\varepsilon_1} = \left(\left(y_1 - \frac{\varepsilon_1}{2} \right), y_2, y_3 \right)$; $\vec{y}_{+\varepsilon_1} = \left(y_1 + \frac{\varepsilon_1}{2}, y_2, y_3 \right)$ and ε_1 is some vanishing small distance in the vicinity of y_1 .

The forcing term represented by Eqn. B-51 comprises two point sources (see Eqn. B44 for comparison), with equal and opposite signal strengths, very close to each other. Although they have equal opposite strengths, $+f_1/\varepsilon_1$ located at $\vec{y}_{+\varepsilon_1}$ and $-f_1/\varepsilon_1$ located at $\vec{y}_{-\varepsilon_1}$, resulting in zero instantaneous strength for the dipole, the 180° out-of-phase situation is responsible for producing a net fluctuating force. The divergence can be seen as a tendency for the source elements within the fluid to cancel (Norton & Karczub, 2003). When the distance between the sources, ε_1 , is small compared to the distance from y_1 , the source, to any point of the sound field and also small compared

to the wavelength of the radiated sound, λ , the field will only depend upon the product between the monopole-strength f_1/ε_1 and the small separation distance, ε_1 . The system of two monopoles close together will form a dipole of strength (or moment) f_1 , with axis in the x_1 direction.

The same reasoning applied to the x_1 direction will also apply to other (x_2, x_3) directions, resulting in dipoles of strengths f_2 and f_3 , aligned to x_2 and x_3 directions, respectively. Altogether, they form a dipole of strength \vec{f} , aligned with the force vector.

The sound field radiated from a concentrated point force can be once more calculated with the aid of Green's function for the wave equation

$$4\pi \cdot p'(\vec{x}, t) = -\frac{\partial}{\partial x_i} \cdot \left(\frac{[f_i]}{r} \right) \quad (B - 52)$$

And, by evaluating the space derivative,

$$4\pi \cdot p'(\vec{x}, t) = \frac{x_i - y_i}{r} \left\{ \frac{1}{rc_0} \left[\frac{\partial f_i}{\partial t} \right] + \frac{1}{r^2} [f_i] \right\} \quad (B - 53)$$

The solution in the time domain (B-53) has the following corresponding solution in the frequency domain

$$4\pi \cdot \tilde{p}'(\vec{x}, \omega) = -\tilde{f}_i(\omega) \frac{\partial}{\partial x_i} \left(\frac{e^{ik_0 r}}{r} \right) \quad (B - 54)$$

Once more, evaluating the space derivative,

$$4\pi \cdot \tilde{p}'(\vec{x}, \omega) = \tilde{f}_i(\omega) \frac{x_i - y_i}{r} \left(-\frac{ik_0}{r} + \frac{1}{r^2} \right) e^{ik_0 r} \quad (B - 55)$$

By looking at Eqn. B-55, it becomes apparent that the dipole has specific behavior according to distance from the source. The near field is dominated by the pressure fluctuations falling off by $1/r^2$, while in the far field the pressure fluctuations fall off by $1/r$, making a marked difference between the stronger near field and the weaker far field, unlike the monopole. The pressure fluctuations in the near field are intense, but fluid can move back and forth between the two sources (Wagner, Bareiß, & Guidati, Wind Turbine Noise, 1996), avoiding some compression. For this reason, less energy

is radiated from the near field into the far field and the dipole is said to be less efficient than the monopole, as a radiator.

Another important characteristic of the dipole source is the directional dependence of the sound field radiated, illustrated in Fig. B-3 and B-4. In the far field of a point force, $k_0 \cdot r \gg 1$, and thus $1/r^2 \rightarrow 0$. In the far field, the dipole sound field can be expressed in the frequency domain as

$$4\pi \cdot \tilde{p}'(\vec{x}, \omega) = -\cos(\Phi) i k_0 \tilde{f}(\omega) \left(\frac{e^{i k_0 r}}{r} \right) \quad (B - 56)$$

where r is the distance and Φ is the angle to a field position. The directional dependence is introduced by the space derivative of the forcing term, with a maximum radiation in the direction of the dipole axis ($\Phi = 0, \pi$) and nil radiation perpendicular to the axis ($\Phi = \pi/2, 3\pi/2$). This is due to mutual cancellation of the two monopole fields whenever the geometric locus considered is equidistant from both sources.

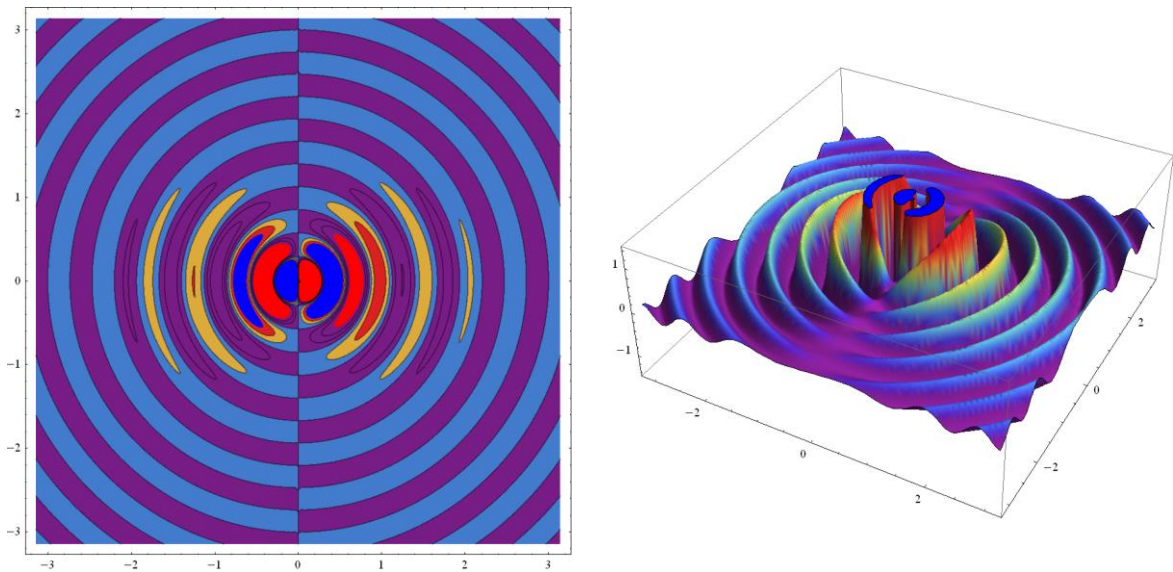


Figure B-3 – Graphical rendering of the acoustic field radiated by a dipole. Pressure fluctuation contour (left) and waves (right). Wolfram Demonstration Program. Code author: Enrique Zeleny.

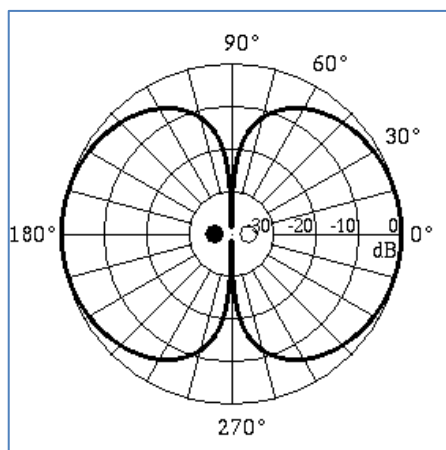


Figure B-4 – A dipole source does not radiate an isotropic field. The directivity pattern derived from Eqn. B-56 shows two opposed lobes or regions where sound is well radiated and two regions where sound cancels. Picture: courtesy of Dr. Dan Russell, Grad. Prog. Acoustics, Penn State.

Figure B-5 displays sound pressure levels as a function of distance and angle from a horizontal axis wind turbine operating in steady rotation and with no inflow noise.

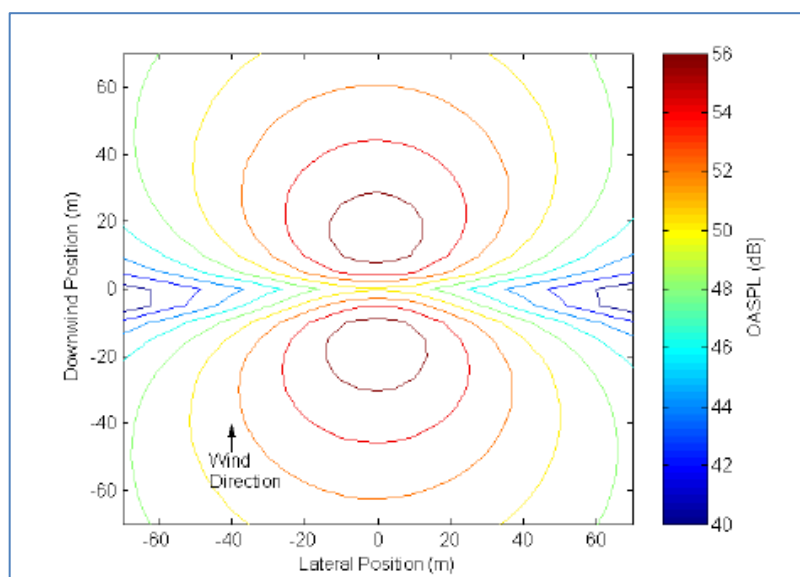


Figure B-5 – Constant sound pressure level (OASPL) contours for an AOC turbine, in steady 8 m/s operation. Source: (Moriarty & Migliore, Semi-Empirical Aeroacoustic Noise Prediction Code for Wind Turbines, 2003)

By looking along the “wind direction” axis in Fig. B-5 it is possible to see that the pattern of the pressure field is very close⁷¹ to that of a dipole, Fig. B-4., considering the wind

⁷¹ In fact there is a slight asymmetry in the directivity pattern of the WTN, caused both by the presence of the supporting tower on one side and also by the rotational movement of the blades.

approaching from 0^0 . This is the reason why airfoil self-noise is sometimes modelled as a dipole-type noise source.

B.7 ACOUSTIC ANALOGY OF Lighthill

The classical solutions to the linearized wave equations previously discussed describe sound radiation generated at points of singularity, both for the monopole, where the sound is originated as the variation of mass outflow, and for the dipole, where the sound is originated by injection of momentum. However, there is no doubt that the creation of mass outflow and induction of external forces would violate the underlying assumption of “weak perturbation” that allows for the linearization of the equation (Dowling & Ffowcs Williams, 1983). Despite the simplicity of the solutions, they are useful if the real source region can be modelled by a continuous distribution of such singularities (Lighthill, 1962), and the interest is only in the far field, for the reasons discussed.

In situations involving turbulence, however, the sound sources are convected and interact with the fluid flow (Norton & Karczub, 2003). In these situations, exemplified by unsteady duct flow, fan noise, jet noise, airfoil noise, cavity noise, and general shear and boundary layer flow, an inhomogeneous wave equation is of order, one that do not neglect the non-linear terms.

“The whole science of noise generated by unsteady turbulent flow, both underwater and in the air, rests on an adequate modeling of the source process” (Dowling & Ffowcs Williams, 1983).

According to Dowling and Ffowcs-Williams (Dowling & Ffowcs Williams, 1983), Lighthill characterized the sources of sound as the differences between the acoustical, simplified equations of the conservation of mass and momentum, and their natural, complete statements:

$$\frac{\partial \rho}{\partial t} + \frac{\partial}{\partial x_i}(\rho u_i) = 0 \quad (B - 19)$$

$$\frac{\partial}{\partial t}(\rho u_i) + \frac{\partial}{\partial x_j}(p_{ij} + \rho u_i u_j) = 0 \quad (B - 57)$$

where Eqns. B-57 are the Navier-Stokes Equations, and the stress field $p_{ij} = p'\delta_{ij} - \tau_{ij}$, where $p'\delta_{ij}$ are the diagonal, compressive elements of the stress tensor and τ_{ij} are the symmetrical viscous tensor elements.

Now proceeding again as in section B.6, the divergence of the NS equation is subtracted from the time derivative of the continuity equation, in order to eliminate the momentum density, ρu_i

$$\frac{\partial^2 \rho}{\partial t^2} = \frac{\partial^2}{\partial x_i \partial x_j}(p_{ij} + \rho u_i u_j) \quad (B - 58)$$

The final manipulation calls for subtraction of $c_0^2 \partial^2 \rho / \partial x_i^2$ and the inclusion of the reference (undisturbed) p_0, ρ_0 terms

$$\frac{\partial^2 \rho'}{\partial t^2} - c_0^2 \frac{\partial^2 \rho'}{\partial x_i^2} = \frac{\partial^2 T_{ij}}{\partial x_i \partial x_j} \quad (B - 59)$$

$$\text{And } T_{ij} = \rho u_i u_j + (p - p_0 - c_0^2(\rho - \rho_0))\delta_{ij} + \mu \left[-\frac{\partial u_i}{\partial x_j} - \frac{\partial u_j}{\partial x_i} + \frac{2}{3} \left(\frac{\partial u_k}{\partial x_k} \right) \right] \quad (B - 60)$$

T_{ij} is the ‘‘Lighthill tensor’’ (Dowling & Ffowcs Williams, 1983), with dimensions $kg/m.s^2$ and the following tensor terms:

$\rho u_i u_j$ - the stress derived from the convection of the momentum component ρu_i by the velocity component u_j ;

$(p - p_0 - c_0^2(\rho - \rho_0))$ - the stress derived from the heat-conduction which affects the speed of sound in the fluid (departure from a state of isentropic fluctuations);

and the last term, $\mu \left[-\frac{\partial u_i}{\partial x_j} - \frac{\partial u_j}{\partial x_i} + \frac{2}{3} \left(\frac{\partial u_k}{\partial x_k} \right) \right]$, is the transport of momentum due to viscous stresses.

For low Mach number flows, the $(p - p_0 - c_0^2(\rho - \rho_0))$ term represents a second-order effect (Norton & Karczub, 2003) and the fluctuations are close to isentropic. Also, at high-Reynolds number turbulent flow, the fluctuating Reynolds Stresses are much

larger than viscous shear stresses, and the Lighthill tensor is dominated by the first term, only:

$$T_{ij} = \rho u_i u_j = \rho \begin{bmatrix} u_1^2 & u_1 u_2 & u_1 u_3 \\ u_2 u_1 & u_2^2 & u_2 u_3 \\ u_3 u_1 & u_3 u_2 & u_3^2 \end{bmatrix} \quad (B - 60a)$$

Resulting in the alternative, simplified inhomogeneous wave equation

$$\frac{\partial^2 \rho'}{\partial t^2} - c_0^2 \frac{\partial^2 \rho'}{\partial x_i^2} = \frac{\partial^2}{\partial x_i \partial x_j} \rho u_i u_j \quad (B - 59a)$$

In Eqn. B-59a, the non-linear term of convection of momentum, $\rho u_i u_j$, now appears as a forcing term, which is driven by the turbulent motion of the fluid and acts as source for a fluid medium that responds linearly to it outside the region of turbulent flow (Wagner, Bareiß, & Guidati, Wind Turbine Noise, 1996). The Lighthill “acoustic analogy” name comes from the fact that his theory allows for the solution of the sound field radiated by a bounded region of turbulent flow, by solving the analogous problem of forced oscillation, provided that the flow is previously known. In Lighthill’s own words:

“Physically, [(B-59)] equations state that a fluctuating flow, in a limited part of an atmosphere otherwise practically at rest, generates the same fluctuations of density as would be produced in a classical stationary acoustic medium by a system of externally applied stresses T_{ij} ” (Lighthill, 1962).

B.7.1 Quadrupoles

The source term of the Lighthill wave Eqn. B-59 represents a double divergence and may be seen as a double tendency of the various source elements within the fluid to cancel mutually (Norton & Karczub, 2003). Once more, the cancellation is not complete due to the retardation time effects, i.e., the time delays between the various sound waves reaching the position of the observer. Since there is zero rate of mass flow ($\dot{q} = 0$), if the retardation times were neglected, there would be no sound produced.

The right hand side of Eqn B-59 presents a sum of nine elements $\frac{\partial^2 T_{ij}}{\partial x_i \partial x_j}$ acting as the forcing terms. For interpretation of the characteristics of a quadrupole, only one forcing term will be examined, $\frac{\partial^2 T_{12}}{\partial x_1 \partial x_2}$. T_{12} is non-zero only for a vanishingly small cube. The concentrated strength of the source integrated over this volume is t_{ij} ($kg \cdot m^2/s^2$). For such a small cube, T_{12} has a large number and this behavior may be expressed, as in the case of the dipole, by using the three dimensional delta function:

$$T_{12} = t_{12} \cdot \delta(\vec{x} - \vec{y}) = t_{12} \cdot \delta(x_1 - y_1) \delta(x_2 - y_2) \delta(x_3 - y_3) \quad (B - 61)$$

The delta function, in any direction, can be replaced by two Heaviside functions, $H(x)$:

$$T_{12} = t_{12} \cdot \lim_{\varepsilon_1 \rightarrow 0; \varepsilon_2 \rightarrow 0} \left\{ \frac{H\left(x_1 - \left\{y_1 - \frac{\varepsilon_1}{2}\right\}\right) - H\left(x_1 - \left\{y_1 + \frac{\varepsilon_1}{2}\right\}\right)}{\varepsilon_1} \cdot \frac{H\left(x_2 - \left\{y_2 - \frac{\varepsilon_2}{2}\right\}\right) - H\left(x_2 - \left\{y_2 + \frac{\varepsilon_2}{2}\right\}\right)}{\varepsilon_2} \right\} \cdot \delta(x_3 - y_3) \quad (B - 62)$$

Since the derivative of a Heaviside function is a delta function, after performing the derivatives in the x_1 and x_2 directions, the source term will be again expressed by delta functions

$$\frac{\partial^2 T_{12}}{\partial x_2 \partial x_1} = t_{12} \cdot \lim_{\varepsilon_1 \rightarrow 0; \varepsilon_2 \rightarrow 0} \left\{ \frac{\delta\left(x_1 - \left\{y_1 - \frac{\varepsilon_1}{2}\right\}\right) - \delta\left(x_1 - \left\{y_1 + \frac{\varepsilon_1}{2}\right\}\right)}{\varepsilon_1} \cdot \frac{\delta\left(x_2 - \left\{y_2 - \frac{\varepsilon_2}{2}\right\}\right) - \delta\left(x_2 - \left\{y_2 + \frac{\varepsilon_2}{2}\right\}\right)}{\varepsilon_2} \right\} \cdot \delta(x_3 - y_3) \quad (B - 63)$$

Combining the delta functions

$$\frac{\partial^2 T_{12}}{\partial x_2 \partial x_1} = \lim_{\varepsilon_1 \rightarrow 0; \varepsilon_2 \rightarrow 0} \left\{ \begin{aligned} & + \frac{t_{12}}{\varepsilon_1 \varepsilon_2} \delta(\vec{x} - \vec{y}_{-\varepsilon_1 - \varepsilon_2}) - \frac{t_{12}}{\varepsilon_1 \varepsilon_2} \delta(\vec{x} - \vec{y}_{-\varepsilon_1 + \varepsilon_2}) \\ & - \frac{t_{12}}{\varepsilon_1 \varepsilon_2} \delta(\vec{x} - \vec{y}_{+\varepsilon_1 - \varepsilon_2}) + \frac{t_{12}}{\varepsilon_1 \varepsilon_2} \delta(\vec{x} - \vec{y}_{+\varepsilon_1 + \varepsilon_2}) \end{aligned} \right\} \quad (B - 64)$$

where

$$\vec{y}_{-\varepsilon_1-\varepsilon_2} = \left(\left(y_1 - \frac{\varepsilon_1}{2} \right), \left(y_2 - \frac{\varepsilon_2}{2} \right), y_3 \right); \quad \vec{y}_{-\varepsilon_1+\varepsilon_2} = \left(\left(y_1 - \frac{\varepsilon_1}{2} \right), \left(y_2 + \frac{\varepsilon_2}{2} \right), y_3 \right);$$

$$\vec{y}_{+\varepsilon_1-\varepsilon_2} = \left(\left(y_1 + \frac{\varepsilon_1}{2} \right), \left(y_2 - \frac{\varepsilon_2}{2} \right), y_3 \right); \quad \vec{y}_{+\varepsilon_1+\varepsilon_2} = \left(\left(y_1 + \frac{\varepsilon_1}{2} \right), \left(y_2 + \frac{\varepsilon_2}{2} \right), y_3 \right)$$

and $\varepsilon_1, \varepsilon_2$ are vanishingly small distances in the vicinity of y_1 and y_2 , respectively.

In order to understand the physical meaning of Eqn. B-64, the concentrated strength of the source will be replaced by its definition, the fluctuating Reynolds Stress times the volume of the small cube, $t_{12} = T_{12}\varepsilon_1\varepsilon_2\varepsilon_3$:

$$\frac{\partial^2 T_{12}}{\partial x_2 \partial x_1} = \lim_{\varepsilon_1 \rightarrow 0; \varepsilon_2 \rightarrow 0} \left\{ \begin{array}{l} - \left\{ -\frac{T_{12}\varepsilon_1\varepsilon_3}{\varepsilon_1} \delta(\vec{x} - \vec{y}_{-\varepsilon_1-\varepsilon_2}) + \frac{T_{12}\varepsilon_1\varepsilon_3}{\varepsilon_1} \delta(\vec{x} - \vec{y}_{-\varepsilon_1+\varepsilon_2}) \right\} \\ + \left\{ -\frac{T_{12}\varepsilon_1\varepsilon_3}{\varepsilon_1} \delta(\vec{x} - \vec{y}_{+\varepsilon_1-\varepsilon_2}) + \frac{T_{12}\varepsilon_1\varepsilon_3}{\varepsilon_1} \delta(\vec{x} - \vec{y}_{+\varepsilon_1+\varepsilon_2}) \right\} \end{array} \right\}$$

(B - 64a)

By comparing Eqn. B-64a with the dipole forcing term of Eqn. B-51, it may be seen that the forcing term is now made up of two dipoles of strengths $T_{12}\varepsilon_1\varepsilon_3$, acting in opposed volume faces and opposite x_1 axis directions. Their separation is ε_2 , the dimension of the cube perpendicular to these faces (in the x_2 direction). Since $T_{12}\varepsilon_1\varepsilon_3$ represents the force acting on the surface $\varepsilon_1\varepsilon_3$ as a result of the tangential stress T_{12} , it is possible to see that a small fluid element subjected to Reynolds fluctuating stress radiates sound like two dipoles acting on opposite surfaces of the element, with strength identical to the force created by the stress at the surface.

Quadrupoles from tangential components of the Lighthill tensor, like T_{12} , when the space derivatives are performed in different directions, originate *lateral quadrupoles* while those from normal components of the Lighthill tensor, like T_{11} , when both space derivatives are performed in the same direction, originate *longitudinal quadrupoles* as in Fig. B-6. In this latter situation, the two dipoles are aligned and the four sources are arranged over one line. In all, there are 9 quadrupoles, corresponding to each component of the Lighthill tensor.

The sound field radiated from a point quadrupole of strength t_{12} , in an unbounded field can be also calculated with the aid of Green's function for the Lighthill wave equation

$$4\pi \cdot p'(\vec{x}, t) = \frac{\partial^2}{\partial x_i \partial x_j} \cdot \left(\frac{[t_{ij}]}{r} \right) \quad (B - 65)$$

with the corresponding solution in the frequency domain:

$$4\pi \cdot p'(\vec{x}, \omega) = \widetilde{t}_{ij}(\omega) \frac{\partial^2}{\partial x_i \partial x_j} \cdot \left(\frac{e^{ik_0 r}}{r} \right) \quad (B - 66)$$

And, by evaluating the space derivatives of the time and frequency domain solutions, it is revealed that the quadrupole field has three different regions:

$$4\pi \cdot p'(\vec{x}, t) = \frac{x_i - y_i}{r} \frac{x_j - y_j}{r} \left\{ \frac{1}{rc_0^2} \left[\frac{\partial^2 t_{ij}}{\partial t^2} \right] + \frac{3}{r^2 c_0} \left[\frac{\partial t_{ij}}{\partial t} \right] + \frac{3}{r^3} [t_{ij}] \right\} \quad (B - 67)$$

$$4\pi \cdot \tilde{p}'(\vec{x}, \omega) = \widetilde{t}_{ij}(\omega) \frac{x_i - y_i}{r} \frac{x_j - y_j}{r} \left(-\frac{k_0^2}{r} - \frac{3ik_0}{r^2} + \frac{3}{r^3} \right) e^{ik_0 r} \quad (B - 68)$$

In the near field, the pressure fluctuations are dominated by the $1/r^3$ terms. In the far field, the pressure fluctuations fall off by $1/r$ and there is a region in between where the pressure fluctuations fall off by $1/r^2$. In this case, the difference between the stronger near field and the far field is even more pronounced than in the case of the dipole.

We have seen that for the monopole, there is essentially only the far field and the pressure fluctuation falls slowly for growing observer distance, by $1/r$. For the dipole, the pressure fluctuation falls off by $1/r^2$ in the near field and $1/r$ in the far field. For the quadrupole, the fall off is by $1/r^3$ in the near field and $1/r$ in the far field. The relation between the fall off in the near field and in the far field is what determines the efficiency of the sound radiator:

- For the monopole: $\frac{1}{r} / \frac{1}{r} = 1$
- For the dipole: $\frac{1}{r^2} / \frac{1}{r} = \frac{1}{r}$
- For the quadrupole: $\frac{1}{r^3} / \frac{1}{r} = \frac{1}{r^2}$

This analysis allows for the arrangement of these fundamental sources in order of radiation efficiency, going from the monopole, the most efficient type of source, to the quadrupole, the least efficient sound radiator.

If the position in the sound field is described by polar coordinates r, Φ in the far field only (near and transition field terms neglected for $k_0 r \gg 1$), the sound radiated from a longitudinal and a lateral quadrupole are respectively given by (Wagner, Bareiß, & Guidati, Wind Turbine Noise, 1996):

$$4\pi \cdot p'(\vec{x}, \omega) = -\cos^2(\Phi) k_0^2 \widetilde{t}_{ij}(\omega) \frac{e^{ik_0 r}}{r} \quad (B - 69)$$

$$4\pi \cdot p'(\vec{x}, \omega) = -\sin^2(2\Phi) k_0^2 \widetilde{t}_{ij}(\omega) \frac{e^{ik_0 r}}{r} \quad (B - 70)$$

As may be seen in Fig. B-6 and B-7, the lateral quadrupole has a four-lobed directional dependence in the far field, while the far field for a longitudinal quadrupole resembles a dipole field, although the fluctuations in the two lobes are in phase for the former.

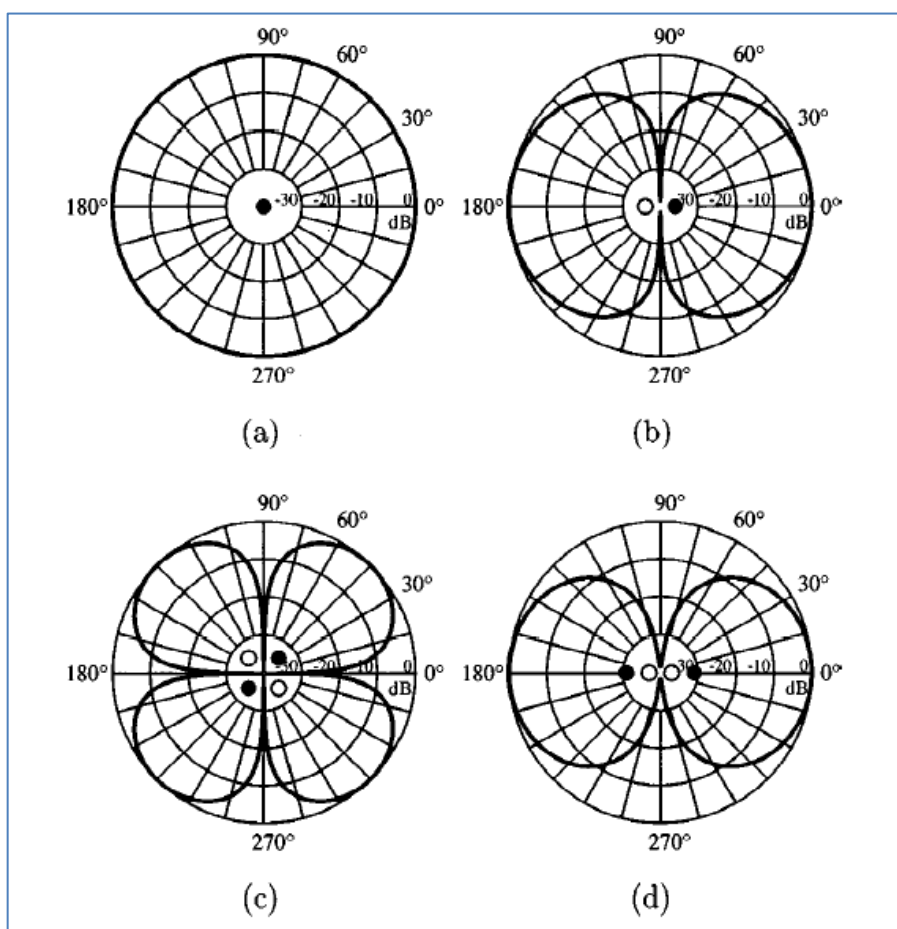


Figure B-6 – Comparative directivity pattern for the far field of a monopole (a), dipole (b), lateral quadrupole (c) and longitudinal quadrupole (d). Although (b) and (d) display similar shapes for the far field, the waves at the same (r, t) have opposite phases for each lobe in the case of the dipole, and same phase for the longitudinal quadrupole (Russell, Titlow, & Bemmen, 1999).

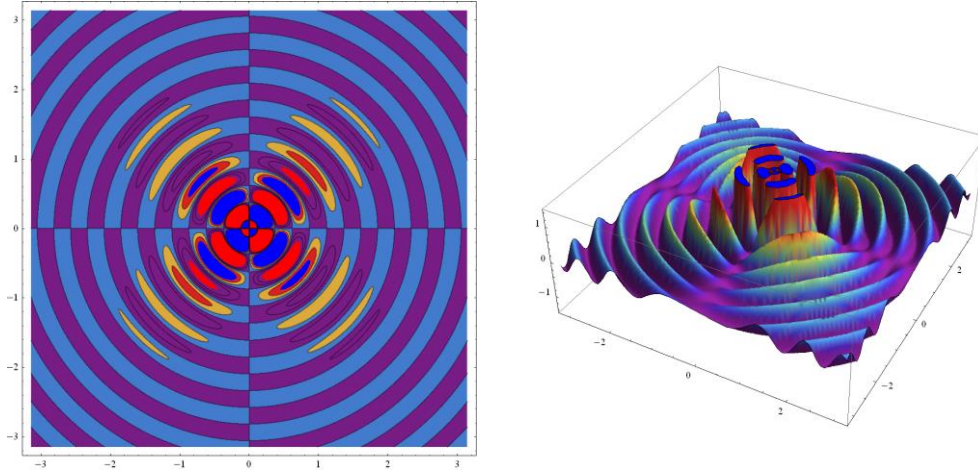


Figure B-7 – Graphical rendering of the acoustic far field radiated by a lateral quadrupole. Pressure fluctuation contour (left) and waves (right). Wolfram Demonstration Program. Code author: Enrique Zeleny.

B.7.2 The Powell-Howe theory of vortex sound

An alternative approach to that of Lighthill, who expressed the sound field radiated as the product of a turbulent fluid motion calculated by the volume integral of the Lighthill tensor, Powell proposed that the formation and motion of vorticity was the fundamental noise-producing mechanism (Wagner, Bareiß, & Guidati, *Wind Turbine Noise*, 1996), (Blake, *Mechanics of Flow-Induced Sound and Vibration*, 1986 I). In his analysis, the momentum equations are expressed in terms of the vorticity vector, $\vec{\omega}$

$$\rho \frac{\partial \vec{u}}{\partial t} + \rho(\vec{\omega} \times \vec{u}) + \nabla \left(\frac{\rho u^2}{2} \right) = -\nabla p \quad (B - 71)$$

The momentum equations are combined with the continuity equation (B-19) to provide the inhomogeneous wave equation for the density variation, in which the viscous stress tensor, τ'_{12} , is neglected and all terms of second order are also neglected for $|\vec{u}| \ll c_0$.

$$\frac{1}{c_0^2} \frac{\partial^2 p'}{\partial t^2} - \nabla^2 p' = \nabla \cdot \left\{ \rho(\vec{\omega} \times \vec{u}) + \nabla \left(p - c_0^2 \rho + \frac{\rho u^2}{2} \right) \right\} \quad (B - 72)$$

The right hand side of the equation is the Powell's source term. The $(\vec{\omega} \times \vec{u})$ term incorporates the sound due to the stretching of vortex filaments from an imposed velocity \vec{u} .

According to Blake (Blake, Mechanics of Flow-Induced Sound and Vibration, 1986 I), both statements of the inhomogeneous wave equation by Powell and Lighthill, are physically equivalent.

Howe (Blake, Mechanics of Flow-Induced Sound and Vibration, 1986 I) generalized Powell's inhomogeneous wave equation for the case when the sources are convected in non-isentropic flow and the first law of thermodynamic must be included in the analysis. The linearized result is

$$\frac{1}{c_0^2} \frac{\partial^2 B}{\partial t^2} - \nabla^2 B = \nabla \cdot \vec{\omega} \times \vec{u} \quad (B - 73)$$

where $B = \frac{p}{\rho} + \frac{1}{2}u^2$ is the stagnation enthalpy, employed as an acoustic variable.

Notice that only the vorticity is interpreted as a source term in this equation, however Blake (Blake, Mechanics of Flow-Induced Sound and Vibration, 1986 II), p. 730, concluded that the only component of the product $(\vec{\omega} \times \vec{u})$ that contributes to dipole sound radiation is the one normal to the plane of the lifting surface.

This finding became the base for the Blake TE noise model discussed in the model revision.

B.8 TIME, LENGTH, PRESSURE AND SOUND POWER SCALES

The audio range encompasses frequencies from 20 Hz to 20 kHz but, as explained in section 1.1.3, this work is particularly interested in the high-frequency trailing edge noise ($750 \text{ Hz} < f < 2 \text{ kHz}$), a broad band noise of a dipole nature, that has been considered the main source of high-frequency noise for an airfoil below stall angles. With periods in the range of 10^{-3} s to $5 \times 10^{-4} \text{ s}$, the temporal resolution needed for

acoustics modeling, which is a transient phenomenon, may be orders of magnitude larger than the time scales required by the dynamic of the mean flow.

Considering the Powell's theory described in the previous section, that incorporates the stretching of vortex filaments as sound sources, theoretically, coherent structures of all sizes would have to be resolved in the flow, from the integral scales to the Kolmogorov microscales (Davidson, 2009), in order to correctly predict the full spectrum of noise emitted from a turbulent flow. That kind of challenge can only be met by DNS solutions which seem unpractical, as of this writing, for solving high Reynolds number flows in large geometries, in the WT industry context (Marten D. , Extension of an Aerodynamic Simulator for Wind Turbine Blade Design and Performance Analysis, 2010), (Pechlivanoglou, Passive and Active Flow Control Solutions for Wind Turbine Blades, 2012). This is even more so for multiple-iteration process typical of conceptual design of a rotor blade. Alternative approaches currently employed in CFD solutions may be seen in Da Silva (Da Silva, 2011) and Orselli (Orselli, 2011). For now, it is important to say that the Courant Number (Versteeg & Malalasekera, 2006), which is the ratio between the spatial and the temporal resolution, may be expressed in aeroacoustic computations as

$$N. Courant = \frac{\lambda/\Delta x}{T/\Delta t} = \frac{c_0/f.\Delta x}{1/f.\Delta t} = \frac{c_0\Delta t}{\Delta x} \quad (B - 74)$$

For stability purposes and time resolution, the time steps required are so low that the dynamic flow becomes "frozen". According to (Tam, 2012), standard CFD second-order schemes require 18 to 25 mesh points per wavelength to ensure adequate accuracy, which is not practical, according to the author.

Regarding acoustic power, the reference value described in Eqn. B-4, $P_{ref.} = 10^{-12}$ W, or 1 picowatt, is the weakest sound power that the human ear drum can detect. On the other end of the scale, the human ear exposition to a power of more than 1W can inflict temporary hearing loss (Wagner, Bareiß, & Guidati, Wind Turbine Noise, 1996). Although the range of power sensitivity is very broad (which, as discussed, justifies the use of the log scale) even the acoustic pressures⁷² corresponding to the power peaks of the *acoustic range* are very small compared to hydrodynamic pressures. As a

⁷² From Eqns (B-5) and (B-7), the sound power level is proportional to the sound pressure level squared.

numerical example, admitting that the L_p measured at 1 m from an omnidirectional (monopole-type) source, away from any reflecting surface, is 95 dB, a number consistent with measurements close to the hub of medium-size HAWTs, the resultant Intensity from the application of Eqn. B-6 is $I = 0.0030 \text{ W/m}^2$ which, integrated over a 1 m radius, is a total transmitted acoustic power of 0.04 W. This is about 1/10 the power that can be provided by one AA-size alkaline battery⁷³. This numerical example is also useful to help understand why the total acoustic energy involved in very loud events, such as a large airplane take off, are generally very low⁷⁴.

In order to estimate and compare the radiated sound power for the different sources discussed earlier, it is important to review the equations for the sound intensity, I , (Eqn. B5) and for the sound power, P , (Eqn. B-7):

$$I = \frac{\hat{p}^2}{\rho_0 c_0} \quad [W/m^2] \quad (B - 5)$$

$$P = \int_S I dS \quad [W] \quad (B - 7)$$

By estimating the root mean square of the pressure fluctuation, \hat{p} , anywhere over a spherical surface of radius r in the free far field ($kr \gg 1$), with the aid of the expressions (B-45), (B-53) and (B-67), along some sampling time interval for the monopole, dipole and quadrupole types of sources, respectively, it is possible to evaluate the sound power radiated by each type of source using:

$$P = \frac{4\pi r^2 \hat{p}^2}{\rho_0 c_0} \quad [W] \quad (B - 75)$$

By using the scaling reasoning proposed by Norton and Karczub (Norton & Karczub, 2003), it is possible to relate the sound power to the mean flow variables

$$P \approx \frac{L^2 U^4 \rho_0}{4\pi c_0} \quad [W] \quad (B - 76) \quad \text{for an aerodynamically generated monopole,}$$

where L is a typical dimension of the region of fluid flow and U is the mean flow velocity. Also, the source dimension must be very smaller than L .

⁷³ 1.5 V x 0.25 A.

⁷⁴ It may sound like an anecdote the fact that the total acoustic energy emitted by a Boeing 747 during a take-off operation is not enough to boil an egg (Ansys, 2013).

$P \approx \frac{d^2 U^6 \rho_0}{3\pi c_0^3}$ [W] (B – 77) for an aerodynamically generated dipole, where d is half the separation between the two monopole sources and U is the mean flow velocity. This justifies the statement made at section 1.1.2, without proof, that $P \sim U^6$ for a dipole-type source.

Notice that for the monopole, the sound power scales with U^4 while for the dipole, it scales with U^6 . By comparing the radiation efficiencies of these two types of sources,

$$\frac{P_{Dipole}}{P_{monopole}} = \frac{4k^2 d^2}{3} \sim \left(\frac{d}{\lambda}\right)^2 \quad (B - 78)$$

It can be seen that the ratio depends on the wavelength. For long wavelengths (low frequency), the ratio is small, showing that the dipole is a very low efficiency radiator, compared to the monopole. At higher frequencies, however, the dipole efficiency is closer to that of a monopole.

It was mentioned at section 1.1.2, that the TE noise mechanism has been found to display a dipole nature (Brooks & Hodgson, 1981). Nevertheless, Oerlemans (Oerlemans, Wind Turbine Noise: Primary Noise Sources, 2011) has pointed out that experimental results for TE noise are best matched by a fifth power dependence of the power on the flow velocity: $P \sim U^5$. According to the author, the aerodynamic sound radiated from an airfoil TE depends upon the interaction between the turbulent length scale of the incident flow Λ , and the airfoil surface. If the airfoil can be considered a compact source ($\Lambda \gg \text{chord}$), the power will scale as $P \sim U^6$, characterizing a compact dipole. According to Lawson (Lawson, 1993), that is true for frequencies of 150 Hz and below, only. On the other hand, if the eddies are much smaller than the airfoil chord, they will induce only local pressure fluctuations, which do not affect the global aerodynamic force. In the case of TE noise, the turbulent eddies scale is taken to be δ^* at the trailing edge. The sound produced by the eddies will be scattered at the TE, resulting in high-frequency noise. In this case, the acoustic power will scale with the fifth power of the flow speed and the source behavior will change from a compact dipole to an *edge noise source*. This dependence characterizes a non-compact behavior:

$$P \approx \frac{U^5 \delta^* L}{r^2} \quad [W] \quad (B - 79)$$

Expression (B-79) is after Oerlemans (Oerlemans, Wind Turbine Noise: Primary Noise Sources, 2011) and the length scale L is the span of the blade segment considered. The dependence of the Power on the span and distance is reflected in the L/r^2 term: doubling the source (or in this case, the span), results in doubling the acoustic energy (+3 dB), while doubling the distance will decrease the acoustic energy by 75% (-6 dB).

The acoustic power radiated by aerodynamic quadrupoles, scales in the following way:

$$P \approx \frac{d^2 U^8 \rho_0}{n \pi c_0^5} \quad [W] \quad (B - 80), \text{ where } n \text{ is } 15 \text{ for a lateral quadrupole and } 5 \text{ for a longitudinal quadrupole.}$$

By comparing the radiation efficiencies of the quadrupole with the monopole, we can see that the Quadrupole is a radiator even less efficient than the dipole, when compared to the monopole:

$$\frac{P_{\text{Quadrupole}}}{P_{\text{monopole}}} = k^4 d^4 \sim \left(\frac{d}{\lambda}\right)^4 \quad (B - 81)$$

This also justifies the ranking of the sources made in section B.7.1 according to their radiating efficiencies.

B.9 THE INFLUENCES OF BOUNDARIES

While the Lighthill equation (B-59) allowed the inclusion of sources in the sound field, it is strictly valid for unbounded fluids only. When a boundary exists, its effect is to change the sound field physically by causing reflections, provided the surface impedance is different from that of the fluid, or by disturbing the flow locally, causing surface pressures that radiate as dipoles (Blake, Mechanics of Flow-Induced Sound and Vibration, 1986 I). This limitation makes the Lighthill equation applicable to problems like jet noise, the original motivation of the author, where solid surfaces do not play an important role, but hardly for the case of WT blade self-noise, where the influence of the boundaries cannot be neglected. For the specific case of TE Noise,

the noise generation mechanism is dominated by the presence of the airfoil surface in the flow.

Curle (Curle, 1955) made the first extension of the Lighthill theory to cope with surfaces in the field, although static ones. Ffowcs-Williams and Hawkins (Ffowcs Williams & Hawkins, 1969) added the influence of surfaces in arbitrary motion and Ffowcs-Williams and Hall, (Ffowcs-Williams & Hall, 1970) studied the influence of the presence of an edge (or half-plane) in the flow.

The application of the Ffowcs-Williams and Hall (Ffowcs-Williams & Hall, 1970) model to *WT* noise prediction requires assumptions to be made about the scale and effective velocity of the turbulent eddies passing by the *TE* of the rotor blade. According to Lawson (Lawson, 1993) it is well determined that the effective convection speed of the eddies is a function of the scale, and can vary in the range of 50% to 85% of U_∞ .

In his critical review of the Theory of Trailing Edge Noise, Howe (Howe, 1978) concluded that all theoretical models, when suitably viewed, lead to the $P \sim U^5$ scaling law for the radiated sound power from turbulent edge flows. As discussed in section B.8, this is valid for the case of high-frequency noise, when the airfoil is considered a non-compact source.

B.9.1 Ffowks Williams-Hawkings (FW-H) Equation and Farassat's solutions.

In the *FW-H* derivation both the surface shape and movement are simultaneously described by the implicit definition of the surface $f(\vec{x}, t) = 0$, with the unit normal vector satisfying $\vec{n} = \nabla f$, which implies that $f > 0$ outside de surface, and $f < 0$ inside it, as shown in Fig. B-8.

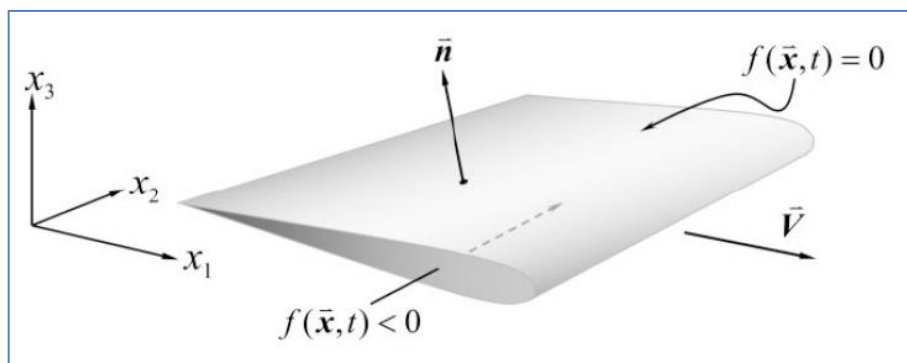


Figure B-8 – Definition of the coordinate system, of the moving surface implicitly defined ($f(\vec{x}, t) = 0$) and of the unit normal vector ($\vec{n} = \nabla f$) for the *FW-H* equation derivation. Illustration source: (Farassat, Derivation of Formulations 1 and 1A of Farassat, 2007).

Ffowcs-Williams and Hawkins (Ffowcs Williams & Hawkins, 1969) started their derivation from generalized conservation equations of mass and momentum, in order to account for sources of those extensive properties, which are isolated at the right hand side:

$$\frac{\partial \rho}{\partial t} + \frac{\partial}{\partial x_i}(\rho u_i) = \rho_0 u_i \delta(f) \frac{\partial f}{\partial x_i} \quad (B - 82)$$

$$\frac{\partial}{\partial t}(\rho u_i) + \frac{\partial}{\partial x_j}(\rho u_i u_j + p_{ij}) = p_{ij} \delta(f) \frac{\partial f}{\partial x_j} \quad (B - 83)$$

If there is only one mathematical region present, the flow field does not contain a solid surface and the generalized equations above decay into Eqns. B-19 and B-20.

As for the derivation cases of the inhomogeneous wave equation and of the Lighthill equation discussed before, the procedure for obtaining the *FW-H* equation is similar (the time derivative of the continuity equation combined with the divergence of the momentum equation in order to eliminate the density momentum). After due manipulation, the *FW-H* equation is

$$\frac{\partial^2 \rho'}{\partial t^2} - c_0^2 \frac{\partial^2 \rho'}{\partial x_i^2} = \frac{\partial^2 T_{ij}}{\partial x_i \partial x_j} - \frac{\partial}{\partial x_i} \left(p_{ij} \delta(f) \frac{\partial f}{\partial x_j} \right) + \frac{\partial}{\partial t} \left(\rho_0 u_i \delta(f) \frac{\partial f}{\partial x_i} \right) \quad (B - 84)$$

The *FW-H* equation,

“...shows that in general sound can be regarded as generated by three source distributions. The first of these is a distribution of acoustic quadrupoles of strength T_{ij}

distributed throughout the region exterior to the surfaces (Lighthill, 1952). This is supplemented by surface distributions of acoustic dipoles of strength $p_{ij}n_j$ (Curle, 1955), and if the surfaces are moving, by further surface distributions of sources essentially monopole in character, representing a volume displacement effect. It is to be emphasized that, although these may not be the physical origin of the sound, they do completely specify the field" (Ffowcs Williams & Hawkins, 1969).

According to Lockhart (Lockhart, 1999), the FW-H equation (B-84) is the most general form of the Lighthill acoustic analogy and is suitable for numerical computation of the acoustic field when provided with unsteady flow conditions as input.

Ffowcs Williams and Hawkins (Ffowcs Williams & Hawkins, 1969) provide many different, specific solutions for Eqn. B-84, while Farassat (Farassat, Linear Acoustic Formulas for Calculation of Rotating Blade Noise, 1981), (Farassat, Derivation of Formulations 1 and 1A of Farassat, 2007) provides a general solution for the monopole and for the dipole terms of the FW-H equation, as follows:

$$4\pi \cdot p'(\vec{x}, t) = \frac{\partial}{\partial t} \int_S \left[\frac{\rho_0 u_n}{r|1 - M_r|} \right] dS(\vec{y}) \quad (B - 85)$$

Equation B-85 is the solution for the monopole and is called the *thickness noise*, where u_n is the surface velocity normal to the surface, and M_r is the relative Mach number of the source region \vec{y} , i.e. the ratio between the component of the source velocity which is directed towards the observer at \vec{x} , and the speed of sound c_0 .

$$4\pi \cdot p'(\vec{x}, t) = -\frac{\partial}{\partial x_l} \int_S \left[\frac{p_{ij}n_j}{r|1 - M_r|} \right] dS(\vec{y}) \quad (B - 86)$$

Equation B-86 is the solution for the dipole and is called the *loading noise*, where p_{ij} is the force per unit area acting from the surface into the fluid.

For cases in which the acoustic compactness is acceptable, the solutions above may be further simplified. For a typical WT, this assumption is valid for frequencies below 50 Hz (Wagner, Bareiß, & Guidati, Wind Turbine Noise, 1996), i.e., for the infrasound range.

The FW-H equation is particularly useful for cases when the forces exerted by a moving body on the fluid are known by calculations or measurements and where the effects of

turbulence in the flow on noise are less important. Examples of application of the Farassat formulations for the FW-H equation, in the WTN field, can be found in Lee et al. (Lee, Lee, & Lee, 2011) and Becker et al. (Becker, Grabinger, Kaltenbacher, & Scheit, 2011).

B.9.2 The Influences of the Boundaries in the Frequency Domain

With the aid of the Green's function, the inhomogeneous Helmholtz equation (B-38a) can be transformed into a boundary integral equation, where the surface integrals are to be evaluated over all surfaces present in the flow

$$\tilde{p}'(\vec{x}, \omega) = \int_S \left\{ \frac{\partial \tilde{p}'(\vec{y}, \omega)}{\partial n} G - \tilde{p}'(\vec{y}, \omega) \frac{\partial G}{\partial n} \right\} dS(\vec{y}) + \tilde{p}'_i(\vec{x}, \omega) \quad (B-87)$$

Where $\tilde{p}'_i = \int_V \frac{\partial^2 \tilde{T}_{ij}(\vec{y}, \omega)}{\partial y_i \partial y_j} G(\vec{x}, \vec{y}, \omega) dV(\vec{y})$ (B-88) represents an incident wave resulting from a volume distribution of quadrupoles. Equation B-87 is the Helmholtz Integral Equation (Blake, Mechanics of Flow-Induced Sound and Vibration, 1986 I). The first surface integral is a source of monopole type and the second, which has a space derivative of the Green's function, is a dipole-type source. The conclusion is that the boundaries in the flow can be represented by surface distributions of monopoles (with strength proportional to the local normal acceleration of the surface) and of dipoles (with strength proportional to the forces acting on the fluid), just like in the time domain.

According to Wagner et al. (Wagner, Bareiß, & Guidati, Wind Turbine Noise, 1996), the formulations based on the Helmholtz equation are preferred due to the fact that they can be treated more easily mathematically than the time domain wave equation for problems involving vibrating surfaces, reflections, diffraction or scattering from bodies immersed in the fluid.

APPENDIX C - THE WIND

The wind speed distribution is asymmetrical, not Gaussian. This implies that the mean annual value is different from the mode. It has been found (Burton, Sharpe, Jenkins, & Bossanyi, 2008) that the wind hourly average over a year's period is well characterized by the two-parameter Weibull distribution in many sites.

$$f(v) = k/C * (v/C)^{k-1} e^{-(v/C)^k} \quad (C - 1)$$

where $f(v)$ is the frequency of occurrence of wind speed v , C (also designated A in some references) is the empirical scale factor [m/s] and k is the form factor for the Weibull Distribution (GIPE, 2004).

As an illustration of the value of this model in a real situation, Fig. C-1 shows the reasonable overlap of a histogram of wind speed versus frequency, measured at 45 m height, at Sao Caetano do Sul, SP, and the adjusted Weibull distribution. The site is subjected to orographic wind perturbations.

When $k = 2$ the Weibull distribution decays into the one-parameter Rayleigh distribution (GIPE, 2004), a special case when only the average wind speed is needed to define the shape of the distribution. According to Gipe, meteorologists use the Weibull and the Rayleigh distribution to describe mathematically the wind speed distribution whenever actual wind speed distribution over time is unavailable.

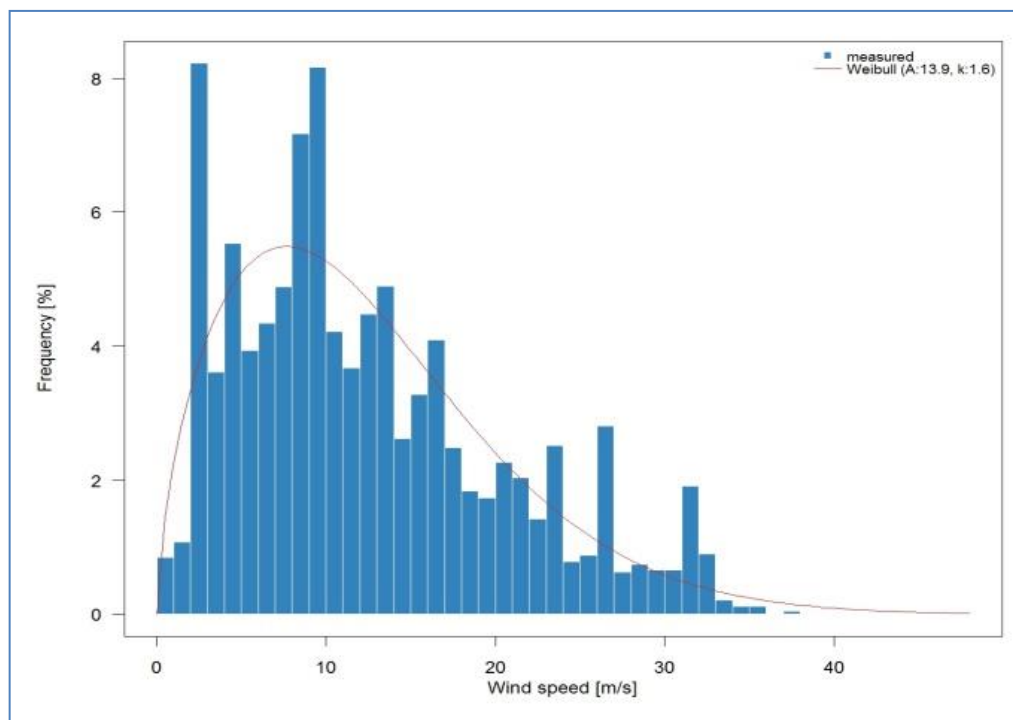


Figure C-1 – Histogram of Wind Speed versus frequency, 10-minute-averages, at 45 m height, at Sao Caetano do Sul, SP, overlapped with adjusted Weibull distribution (Reichenbach, Vieira, Yoshimura, & Telles, 2012).

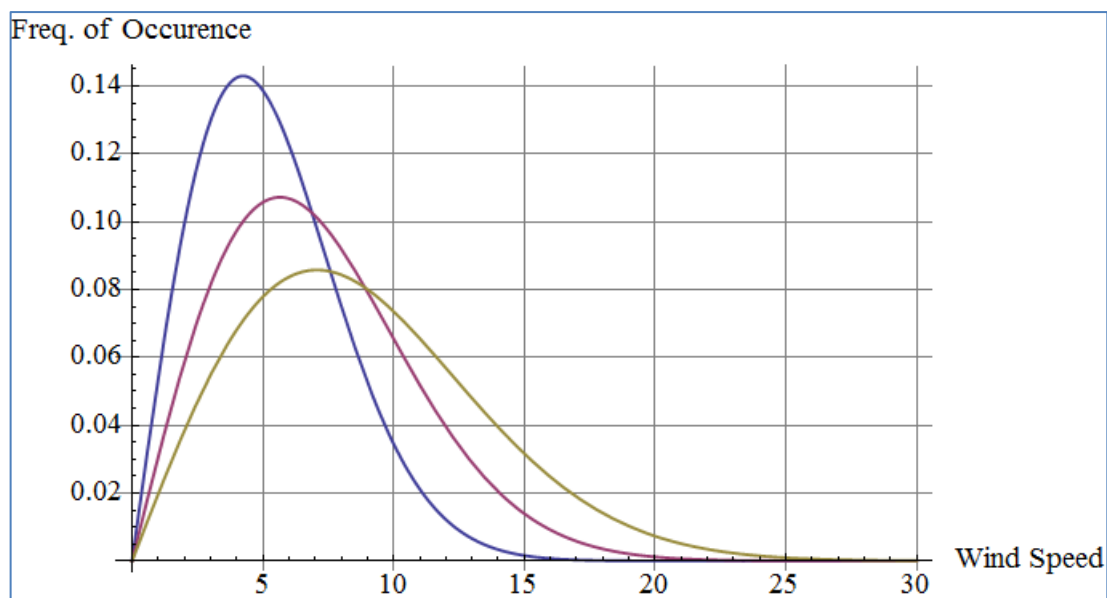


Figure C-2 – Rayleigh distribution plots of Eqn. (C-1), for wind averages of 6 m/s (blue line), 8 m/s (red line) and 10 m/s (golden line).

It is possible to see from Fig. C-2, that for a distribution characterized by a 10 m/s average Wind speed (blue curve), the wind is actually blowing at that speed less than 8% of the total time.

This helps explain the reason why many HAWTs are designed for variable speed, so that they can harvest wind energy more efficiently over a larger range of wind speeds.

APPENDIX D – SEMI-EMPIRICAL NOISE PREDICTION MODELS AND METHODS - A DISCUSSED REVIEW.

The high frequency Trailing-Edge Noise models selected for discussion in this section and in the next one are those more relevant in terms of bibliographical citations and directly applicable to the problem of wind turbine noise.

Because each different author employs different notation for angles and variable names, some standardization was attempted by adopting Blake (Blake, *Mechanics of Flow-Induced Sound and Vibration*, 1986 II) and Wagner et al. (Wagner, Bareiß, & Guidati, *Wind Turbine Noise*, 1996) notations whenever possible. However, in some cases the original notations were kept. For most cases, local definitions of the variables are provided in the text. For convenience, the flow and observer position in relation to the edge are reproduced at Figure D-1.

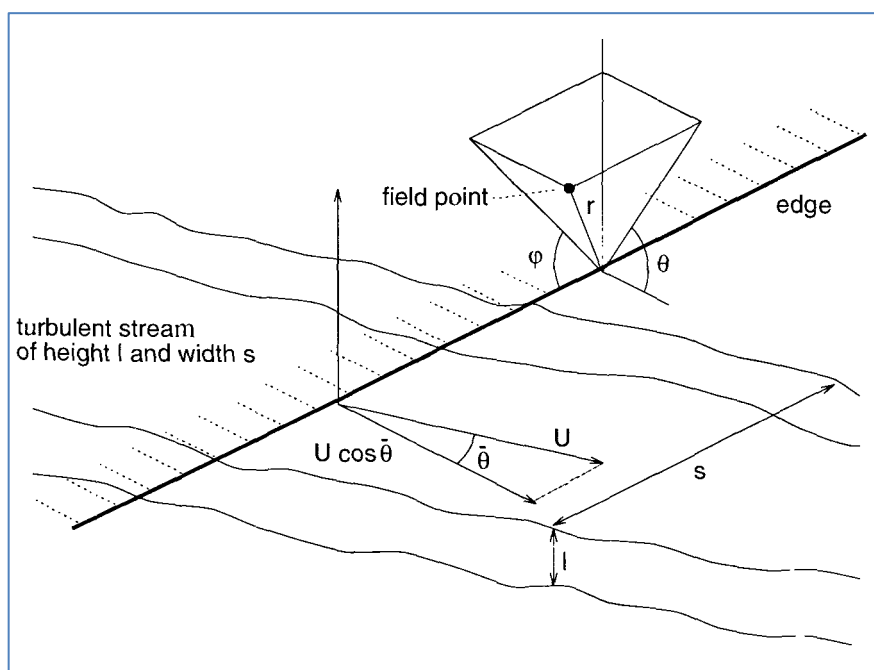


Figure D-1 – Basic geometry employed by BLAKE to study the wall jet incident on the TE of a semi-infinite plane (Blake, *Mechanics of Flow-Induced Sound and Vibration*, 1986 II), p. 726, adapted by (Wagner, Bareiß, & Guidati, *Wind Turbine Noise*, 1996).

The model and method review sequence proceed chronologically in this section regardless of the approach adopted by the authors, up to the review of Glegg et al.

(Glegg, Baxter, & Glendinning, The Prediction of Broadband Noise From Wind Turbines, 1987). After that point, the introduction of the BPM model marked a clear distinction between semi empirical models and simplified theoretical models, which also follow distinct review tracks in this work. Because of this organization method, the reader interested in the simplified theoretical approach should read this section up to Glegg's model (1987) and then continue from Appendix E. This would give the reader a chronological review of the simplified theoretical models.

D.1 Grosveld's Model

The WT TE noise model of Grosveld (Grosveld, 1985) is based on results aimed at helicopter noise prediction by Schlinker and Amiet (Schlinker & Amiet, 1981) and deals with the problem of noise generated when a semi-infinite plate-attached turbulent boundary layer convects over the TE, towards the wake. The Taylor hypothesis⁷⁵ approximation is employed and the Kutta condition is forced at the TE. The TE noise radiated from a local blade segment is a function of the local Mach number, boundary layer thickness, length of blade segment and observer position:

$$SPL_{1/3} = 10 \log \left\{ K_2 U^5 B \bar{D} \frac{\delta \cdot s}{r^2} \left(\frac{St}{St_{max}} \right)^5 \times \left[\left(\frac{St}{St_{max}} \right)^{1.5} + 0.5 \right]^{-4} \right\} \quad (D - 1)$$

where $K_2 = 3.5$ (for S.I. units); B is the number of blades; s is the airfoil span; r is the distance between the source and the observer and $St = f\delta/U$ is the Strouhal number.

\bar{D} is the directivity function for a dipole from Schlinker and Amiet (Schlinker & Amiet, 1981), p. 18, is employed, but corrected for directivity outside the vertical axis plane:

$$\bar{D}(\theta, \phi) = \sin^2(\phi) \cdot \frac{\sin^2(\theta/2)}{(1 + M \cos\theta)[1 + (M - M_c) \cos\theta]^2} \quad (D - 2)$$

⁷⁵ The Taylor approximation or "Frozen Turbulence hypothesis" entails replacing the spatial turbulent correlations by temporal correlations. It allows for the extraction of data with one single, stationary probe and may be quite accurate for some grid turbulence problems ($u' \ll U$) and inaccurate for free shear flows (Pope, 2011), p. 224.

where M_c is the eddy convection Mach number, $M_c \approx 0.8M$. The peak Strouhal number associated with TE noise is $St_{max} = 0.1$.

In the original text, the turbulent boundary layer thickness at the TE is simply estimated in the text by using the TBL over a flat plate correlation model, the adequacy of which will be the object of our later investigation.

According to the author, Eqn. (D-1) is essentially the TE noise prediction for a 2-D lifting airfoil in a uniform flow. In order to predict the TE noise from a rotating blade, the blade must be divided into segments of length L , each undergoing a different local flow velocity and each contributing to the noise at the receiver location. The resulting spectrum is then averaged around the azimuth because of the rotor rotation.

Apart from TE noise, Grosveld also modeled the inflow turbulence noise and TE bluntness noise. The result from his total noise prediction against measurements accomplished at some specified distance from a U.S. Windpower machine was already displayed in Figure 2-10, which was used to illustrate the spike added in the spectrum due to TE bluntness.

Although the model seems to return quite good prediction for the spectra in the range displayed, up to 4 kHz, the inflow turbulence noise part of the model only applies to low frequencies, when the length scale of incoming turbulence is large compared to the blade chord (compact source model).

The necessary improvements on the model seem to be the scaling parameter for the turbulence at the TE (boundary layer thickness), and the limitations of the inflow turbulence noise.

D.2 The Models from Howe, Brooks-Hodgson and Brooks-Marcolini.

A review and attempt of unification of the TE noise theory was accomplished by Howe (Howe, 1978), which proposed a relation between surface pressure fluctuations and the far field sound.

Howe showed that a relation exists between the far field acoustic spectrum and the measurable hydrodynamic surface pressure spectrum close to the TE (obtained from correlation measurements with respect to time and spatial separation parallel to the edge of the plate), but the prediction only applies to constant eddy convection velocity of the incident boundary layer. The acoustic spectrum is:

$$S_K(\omega) \cong \frac{2M_{\bar{v}}L \sin\phi \sin^2(\theta/2) \cos\beta \int_{-\infty}^{\infty} \mathbf{P}_{TE} \left(k_1, \frac{\omega \cos\phi}{c_0}, \omega \right) dk_1}{\pi r^2 (1 + M_{Or})^2 (1 - M_{\bar{v}r})^2 (1 - M_{Or})^2 (1 - M_{\bar{v}1} \sin\phi)} \quad (D - 3)$$

where L is the wetted length of TE, \mathbf{P}_{TE} , is the wavenumber-frequency spectrum of the pressure fluctuations that occur in the wake and on the plate or airfoil, very close to the TE, and k_1 is the wavenumber in direction x_1 (see Fig. D-2). The Mach numbers are defined as:

$$M_{\bar{v}} = \frac{\text{mean eddy convection velocity}}{c_0}$$

$$M_{Or} = \frac{\text{mean stream velocity at } r}{c_0}$$

$$M_{\bar{v}r} = \frac{\text{component of } \bar{V} \text{ in the observer direction}}{c_0}$$

$$M_{\bar{v}1} = \frac{\text{component of } \bar{V} \text{ normal to edge plane}}{c_0}$$

The denominator factors are called Doppler factors and account for the relative motion between the edge position (O), the incident turbulence velocity and the observer position (r).

β is the angle of incidence of the convecting turbulence and the edge plane, as shown in Fig. D-2

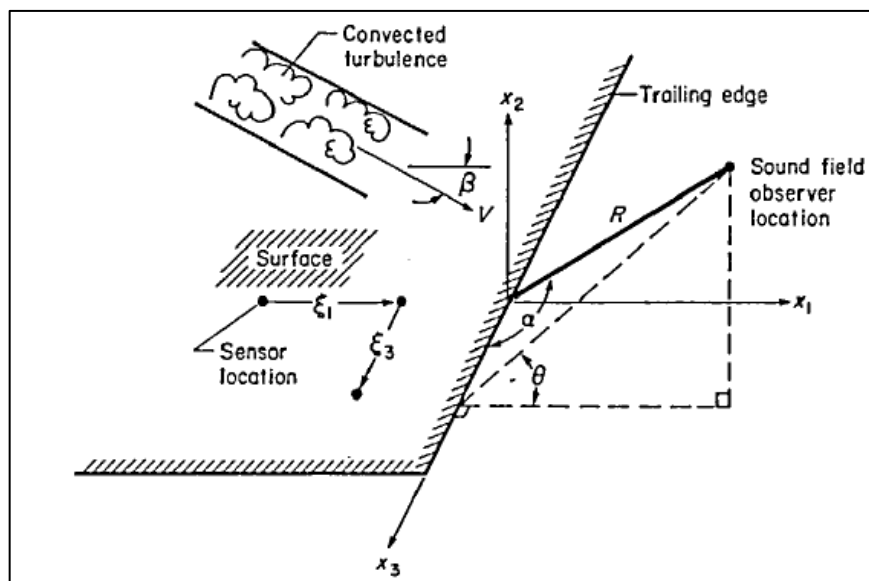


Figure D-2 – Basic geometry employed by (Howe, 1978) and (Brooks & Hodgson, 1981), for identification of the convected turbulence incidence angle, β , in Eqn. (2.5.2-1). Source: (Brooks & Hodgson, 1981).

The theory is expected to be valid also for high subsonic Mach numbers provided it is acceptable to neglect compressible effects in the specification of the aeroacoustic sources.

The author also deals inconclusively with the question of applying or not the Kutta condition to the model, where he obtained differences of 10 dB or more in the predictions with and without forcing the condition, i.e. forcing the flow to leave the edge tangentially or not.

“Such large overall differences are an indication of the weakness of the present state of the theory” (Howe, 1978).

The author concludes in the report, with a generalization of his own previous 2-D research results, that no edge noise is generated in the particular case in which the incident and shed vorticities convect at the same mean velocity.

The author does not display a comparison of the model against experimental data, since he considered the one set of data available (from Hayden et. al., 1976) not ideal.

Brooks and Hodgson (Brooks & Hodgson, 1981) developed the necessary experimental data for testing Howe’s model and improved upon it. They accomplished extensive experimental investigation of TE noise for the case of a 2-D airfoil embedded

in a uniform, low Mach number flow. Their experiment was later expanded in subsequent researches (Brooks & Marcolini, 1985), (Brooks, Pope, & Marcolini, Airfoil Self-Noise and Prediction, 1989), and has laid out the foundations for the broadly used BPM model, to be discussed in the upcoming sections.

In their work, Brooks and Hodgson (Brooks & Hodgson, 1981) defined in detail the statistics of the pressure field beneath the TBL. They have found the measured pressure field very close to the TE to be consistently predictable by the evanescent wave theory (see, for instance (Dowling & Ffowcs Williams, 1983), p. 90). The evanescent wave model is based on the premise that the turbulent flow which induces the surface pressure is constrained to move above the surface, past the edge and into the wake without altering the character of the edge and without “spilling over”, i.e. the flow perturbations causing the pressure do not touch the surface or edge, avoiding concerns about possible flow “singularities” at the edge. These singularities in velocity and pressure fields are avoided in potential flow by the imposition of the Kutta condition and in real flow by the viscous effects. The transition from the bounded pressure field to that unbounded occurs in the vicinity of the edge, by the pressure scatter process, when the convecting eddies give up half of their pressure amplitude while passing by the edge (Brooks & Hodgson, 1981). This renders the pressure continuous in the vicinity of the edge, where the scattered pressure field superimposes on the incident pressure field.

The authors noted that Howe’s model would converge to identical noise predictions, for both the Kutta and no-Kutta conditions, if the wake convection velocity W was taken to be vanishingly small in comparison to the TBL convection velocity V . They accordingly modified Howe’s model by making Howe’s edge parameter $W \rightarrow 0$. Equation (D-3) for the sound field spectrum was then simplified to represent the specific geometry and conditions of the experiment of Brooks and Hodgson (Brooks & Hodgson, 1981), i.e., non-skewed incident turbulence ($\beta = 0$), microphone position perpendicular to the edge line ($\alpha = 90^\circ$) and perpendicular to the edge plane ($\theta = 90^\circ$), and $k_1 = k$ due to the non-skewed flow.

Thus, the sound field spectrum for the symmetrical NACA0012 airfoil at 2-D, zero angle-of-attack flow and Reynolds number of 1.2 Million was predicted by the following model:

$$S(\omega) = \frac{1}{2\pi r^2} \left(\frac{\omega L}{c_0} \right) \int_{-\infty}^{\infty} \frac{\mathbf{P}(k_1, 0, \omega)}{|k_1|(1 - \omega/c_0 k_1)} dk_1 \quad (D - 4)$$

The Eqn. (D-4) was evaluated numerically for two of the free streams employed ($U_0 = 38.6 \text{ m/s}$ and 69.5 m/s) in the experiments and the resultant spectra were compared to the measured data for the sharp TE models, at those free stream velocities, in Figure D-3.

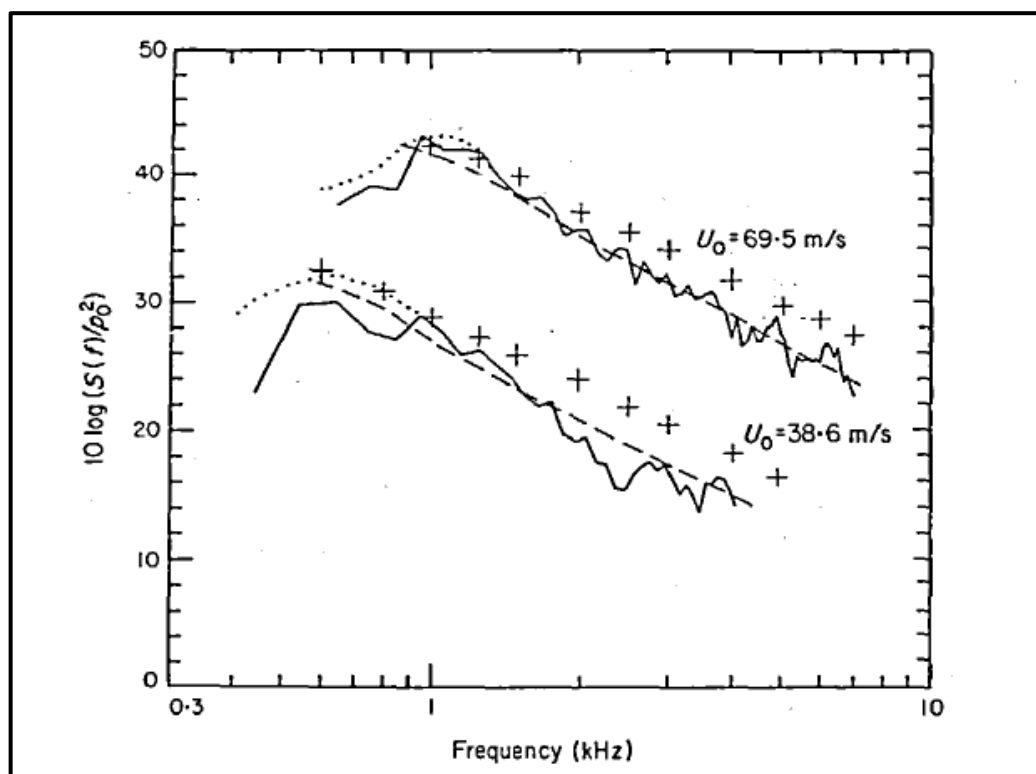


Figure D-3 – TE noise spectra predicted based on measured surface pressure, compared to the theoretical prediction of Eqn. (2.5.2-2), for free stream velocities of 38.6 and 69.5 m/s. Experimental _____; prediction - - - -; approximate prediction for low frequencies; and approximate prediction for turbulence convecting at 60% of U_0 + + + +. Source: (Brooks & Hodgson, 1981).

The surface pressure PSD employed was from a pressure sensor 29 mm upstream of the TE. For sensors in other positions, little variation was observed on the result. The agreement in amplitude and spectral shape was considered excellent by the authors, provided allowance was made for experimental variance for frequencies above 1 kHz, due to the limitations of some empirical equations employed.

The authors did not attempt to evaluate the more general equations by Howe (Howe, 1978), relating the amplitude and spectral shape of TE noise to turbulence statistics close to the TE, but instead, tried to avoid the complexities of the flow field by

concentrating on the surface pressure field, which is easier to measure and derive from the turbulent flow itself. They concluded that theories employing surface pressure measurements are applicable in the quantitative prediction of TE noise. The hypothesis that the TBL existing in both sides of the airfoil, close to the TE, are non-interactive and statistically independent is central to the analysis. Also, no hydrodynamic wake shedding predicted by Howe was confirmed, suggesting that there is no distinction between the Kutta and no-Kutta condition solutions for the noise spectrum and that flow singularities are avoided in the real case due to the natural action of viscosity in defining the TBL (independent of the distance from the edge), and not by rapid edge adjustments in the form of shedding activity. According to the authors, the scatter phenomenon provides the pressure adjustments needed in the TBL and wake without significantly affecting flow structure.

Later, Brooks and Marcolini (Brooks & Marcolini, 1985) reported more experimental work with the NACA 0012 airfoil, in 2-D flow and zero alpha aimed at normalizing TE self-noise data and assessing the capability of the scaling law based on the analysis of FW-H (Ffowcs-Williams & Hall, 1970) for the problem of turbulence convection above a large plate an past the TE into the wake, at low subsonic velocity U :

$$\langle p^2 \rangle \sim \rho_0^2 v'^2 \frac{U^3}{c_0} \left(\frac{Ll}{r^2} \right) \bar{D} \quad (D - 5)$$

where $\langle p^2 \rangle$ is the overall mean-square sound pressure at the observer location r , v'^2 is the mean-square turbulence velocity, l is a characteristic turbulence correlation scale and L is the spanwise extent of the wetted edge. The directivity factor \bar{D} is 1 for observer (microphone position) perpendicular to the surface TE.

The normalization form found for the one-third octave SPL bands was:

$$SPL_{1/3} = 10 \log \left[\left(\frac{U}{100} \right)^5 \frac{\delta L}{r^2} \right] + F_1(St) + K_1 \quad (D - 6)$$

where $F_1(St)$ is a universal spectrum shape for the noise based in the work of Fink (1977), that depends only on the ratio of $St = f\delta/U$ to its peak value St_{peak} . K_1 is an empirical constant found when the velocity is in knots.

The authors found that the TE self-noise data for tripped airfoils of different chord sizes, based on Eqn. (D-6) coalesced well for higher values of St , only (Fig. D-4). They argued that the effects of the smaller chord airfoils (Reynolds number) on the spectra could be partially responsible for the lack of coalescence at the lower Strouhal numbers. The boundary layers are largely laminar in these cases, whose instabilities result in vortex shedding.

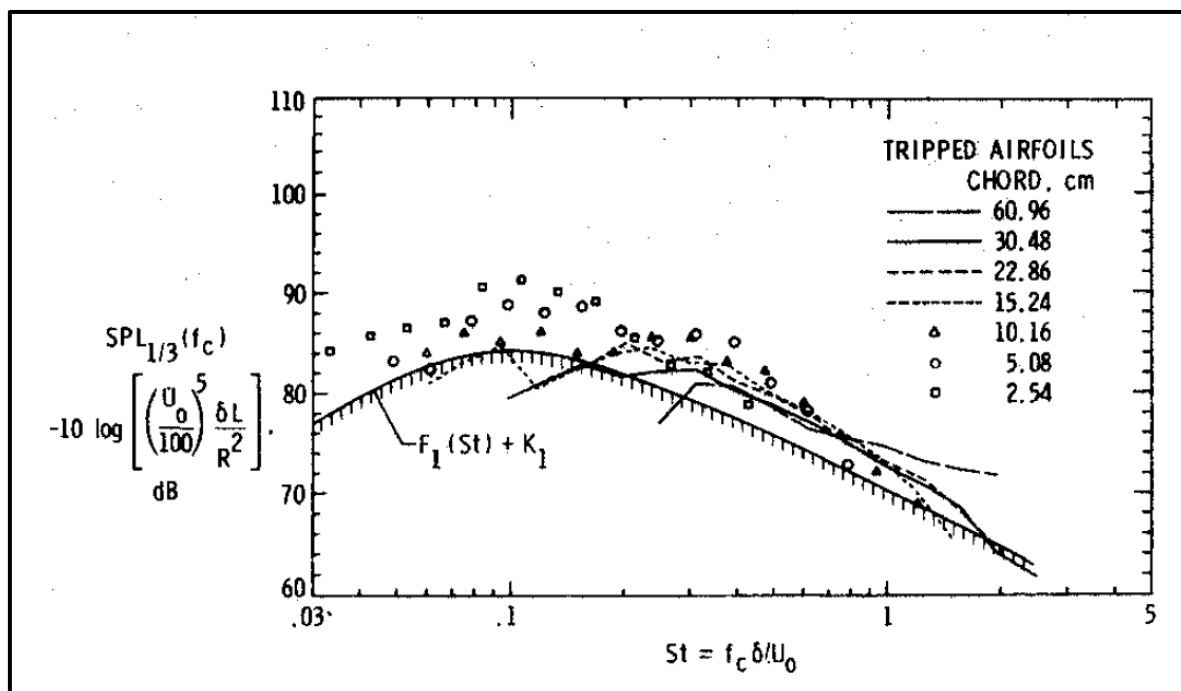


Figure D-4 – Normalized one-third octave spectra. All airfoils with tripped BL and $U = 71.3 \text{ m/s}$. Source: (Brooks & Marcolini, 1985).

The spectral peak Strouhal numbers based on δ were in the 0.25 – 0.3 range, but were found to be dependent on both chord size and velocity, i.e., Reynolds number. They concluded that the TBL-TE noise is dependent upon Reynolds number, as opposed to previous studies. The levels were found to increase with Reynolds number but not in a way to approach a single curve, suggesting that other factors, such as the method of BL tripping might affect the accuracy of scaling.

D.3 Glegg's Model

Glegg's researches at this time (Glegg S. , Significance of Unsteady Thickness Noise Sources, 1987), (Glegg, Baxter, & Glendinning, The Prediction of Broadband Noise From Wind Turbines, 1987), were centered in inflow turbulence noise, which he believed to be more relevant than self-noise. In his paper, he argues that the turbulence length scale generally employed to model the atmospheric BL is of very large scale, sometimes larger than the rotor diameter. Since the high frequency broadband noise is generated by turbulent gusts with wavelength of the order of 0.1 m, the relevance of the atmospheric turbulence, as it was, should be questionable. He developed a more detailed model of atmospheric boundary layer, specifying the length scale as a function of height above ground, wind speed and surface roughness; however he still got predictions 10 dB below measurements. The best fit to the data was attained for a turbulence length scale of one chord for machines with an advance ratio⁷⁶ of $C_j \approx 0.15$.

In terms of airfoil self-noise, Glegg modeled noises from separated flow and TE. For the latter, which is of main concern here, he employed a noise model based on the results by Amiet (Amiet, Effect of Incident Surface Pressure Field on Noise due to Turbulent Flow past a Trailing Edge, 1978), who specifies the acoustic pressure as a function of the surface pressure spectrum of the blade BL:

$$S(x, \omega) = \left(\frac{\omega}{4\pi c_0 r} \right)^2 (\rho_0^2 c_0^4 U^3 L) \left\{ \frac{l |\chi_T|^2 \mathbf{P}(\omega(1 - M_r))}{\rho_0^2 c_0^2 U^3} \right\} \quad (D - 7)$$

where S is the power spectral density of the acoustic pressure fluctuations, x is the position in the sound field, L is the span of the airfoil section, l is the correlation length scale, χ_T is a function of the Fresnel integrals which depend upon observer position (see (Glegg, Baxter, & Glendinning, The Prediction of Broadband Noise From Wind Turbines, 1987), p. 223 for details), wavenumber and flow speed, and \mathbf{P} is the surface pressure spectrum of the blade BL. This relation allows the calculation of individual upper and lower side contributions of the airfoil. In this case, the surface pressure distribution was obtained from empirical fit to experimental results. The results obtained highlighted inflow noise and are not relevant for future discussion, however, the model above was described for being an important step for other models.

⁷⁶ Advance ratio or advance coefficient, $C_j = U/n.D$, where U =wind speed, n =rotation and D =WT diameter.

Up to this point in time the TE noise prediction models were evolving in one single line of research, but after the BPM model (to be presented next), when a simpler semi-empirical perspective was adopted instead of a detailed description of the turbulent flow field, the research markedly evolved into two separate tracks, one for the semi-empirical and other for the simplified theoretical line. For this reason, the remaining of this section will be dedicated to the semi-empirical track, in chronological sequence, while the simplified theoretical line will be resumed in Appendix E, also in chronological order, from this point in time on, except as noted.

D.4 Lawson's Model and Method.

Lowson (Lowson, 1993) tried to develop a noise prediction method that would be straightforward and would depend only on basic WT data. For this reason he excluded or adapted any source prediction method that would require detailed calculation of boundary layer properties along the span and did not consider tip noise. His model included inflow-turbulence noise and TE noise only, which are considered the main sources of WTN since, according to the author, TE bluntness noise and laminar boundary layer vortex shedding noise could be avoided by the designer of the equipment.

The procedure employed for extending Lawson's 2-D noise prediction method to the WT blade was to integrate the prediction formulae over the whole blade length, based on the procedure proposed by Grosveld (Grosveld, 1985), but with some important differences:

- Use of BPM (Brooks, Pope, & Marcolini, Airfoil Self-Noise and Prediction, 1989) data instead of those from Brooks and Hodgson (Brooks & Hodgson, 1981).
- Employment of a new empirical spectrum shape.
- Wind speed was used directly in the computation, not inferred from the power curve, but it was factored by $2/3$ to account for flow deceleration at the turbine azimuthal plane and combined with blade tangential velocity in each section.
- Also, predictions are made for all one third octave bands (10 Hz to 20 kHz).

Lowson also points out that in the BPM model the boundary layer thickness at the TE of the airfoil is used as the length scale of the turbulent eddies, but the full freestream velocity is employed as the characteristic velocity of the eddies, when it is well established that this speed should be between 50% and 85% of the freestream velocity. He also explains that this physical mismatch is compensated for in the empirical fits to the spectra used to provide final prediction and so his prediction model is also based on the empirical models of BPM (Brooks, Pope, & Marcolini, Airfoil Self-Noise and Prediction, 1989):

The TE noise prediction model of Lowson (Lowson, 1993) is derived from BPM (Brooks, Pope, & Marcolini, Airfoil Self-Noise and Prediction, 1989) data, but changes were made in order to derive a model understood by the author to be more appropriate to the WT noise problem. The reason is that the BPM analysis was restricted to lower Reynolds number (typically from 10^5 to 1.5×10^6), where the BL had to be heavily tripped in order to represent the turbulent flow on the outboard sections of the WT blade. But Lowson believed that naturally developing TBL was more typical of the WT blade outboard section, a vision not quite parallel to that from more recent research (Eisele, Pechlivanoglou, & Nayeri, 2013), and also argued that the extrapolation of the BPM noise trends towards higher Reynolds and larger airfoil thicknesses could show significant errors.

According to Lowson (Lowson, 1993), there are three dominant issues for the prediction of the TE noise level:

- The prediction of the TBL thickness.
- The prediction of the scaled overall level.
- The prediction of the spectral shape.

In his model, Lowson (Lowson, 1993) determines the BL displacement thickness at the Trailing edge by using the TBL over a flat plate correlation: $\delta/c = 0.37 Re^{-0.2} \rightarrow \delta^* = \delta/8$, just like Grosveld (Grosveld, 1985). The displacement thickness thus estimated was then further multiplied by a factor between 2 and 4 in order to account for thicker boundary layers on airfoils, for later comparison to real WT machines.

It is worth noticing noticeable that, despite criticism on the lack of physical adherence of previous researches, Lowson (Lowson, 1993) allowed himself to some objectionable

representation of the BL thickness at the TE, although he conceded that explicit BL parameter calculation for specific airfoils, other than NACA 0012, would be an improvement over his model and had become practical with computer models.

For the prediction of the sound pressure level and spectral shape for the TBL-TE, Lowson proposed:

$$SPL_{p,TBL-TE} = 10 \log \left(\frac{\delta^* M^5 L}{r^2} \cdot G(f) \right) + 128.5 \quad (D - 8)$$

where $G(f)$ is the spectral shape function,

$$G(f) = \frac{4 \left(\frac{f}{f_{peak}} \right)^{2.5}}{\left[1 + \left(\frac{f}{f_{peak}} \right)^{2.5} \right]^2} \quad (D - 9)$$

and the peak frequency is given by

$$f_{peak} = \frac{0.02 U M^{-0.6}}{\delta^*} \quad (D - 10)$$

In the result section of his report, Lowson (Lowson, 1993) compares predictions to some real WT noise cases. One of them is a comparison among TE-noise prediction against data from NASA/BOEING MOD-2 WT, available at Hubbard and Shepherd (Hubbard & Shepherd, 1990).

The OASPL predicted was of 57.3 dB against real measurement of 57.1 dB, a very good agreement, but spectral analysis shows areas where the agreement is not so good, especially under 300 Hz and above 8 kHz (Figures D-5 and D-6).

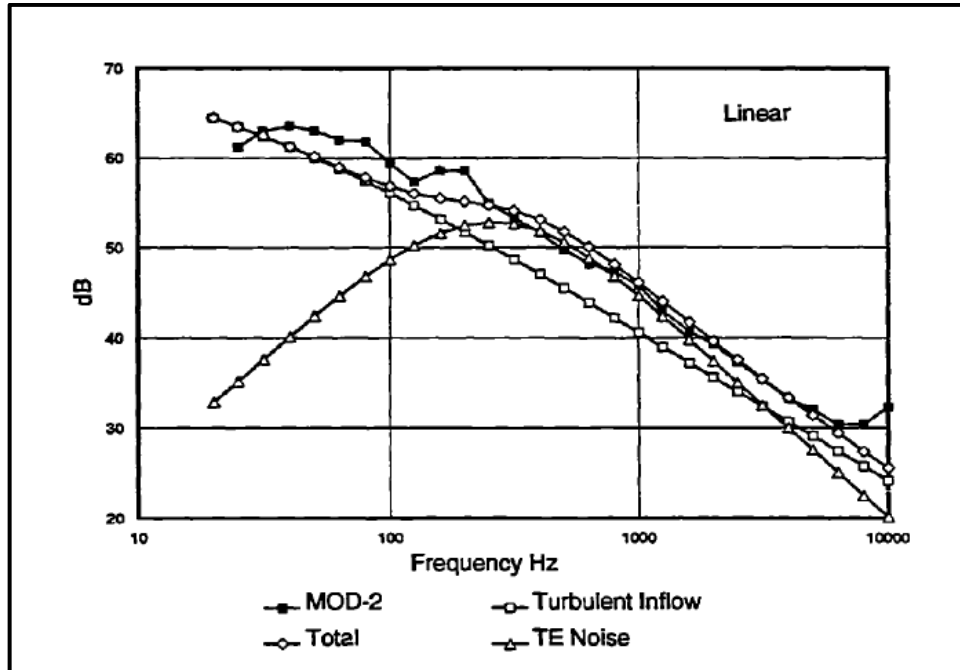


Figure D-5 – WT Noise spectra for the MOD-2 WT, against prediction for inflow noise and TE noise. Source: (Lowson, 1993) Fig. 12a.

The underprediction at lower frequencies was attributed to mechanical noise close to the 100 Hz range. The slight overprediction in the intermediate frequency range is attributed to the TE noise that crucially depends on the BL displacement thickness determination method employed.

The analysis of the A-weighted spectra allows for a clearer conclusion of the relative importance of the TE noise for the total predicted spectrum.

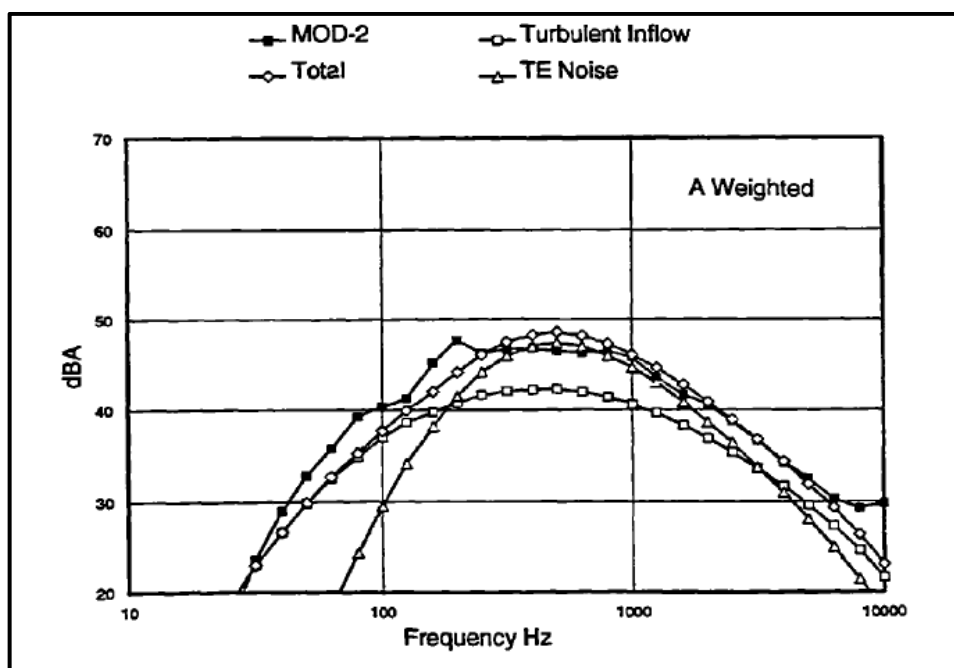


Figure D-6 – WT Noise A-weighted spectra for the MOD-2 WT, against prediction for inflow noise and TE noise. Source: (Lowson, 1993) Fig. 12b.

The results were also compared directly to calculations made with Grosveld (Grosveld, 1985) model and it was detected that the Grosveld model underpredicted TE noise by 6 dB because of a problem on measured data over which it was developed. Lowson concludes for the relative importance of the TBL TE noise and about the opportunity for designers to reduce noise at the source, particularly at lower wind speeds.

Further comparison was made against a Vestas WT noise data, with predicted OASPL of 56.6 dB, compared with a 59.0 ± 4 dB measurement. Same shift trends were observed in the spectrum.

D.5 The IAG Method (I)

The IAG model, from Bareiss et al. (Bareiss, Guidati, & Wagner, 1994), also known as XNOISE, is also a semi-empirical method for high-frequency noise. The bases for modeling the noise sources are from Grosveld (Grosveld, 1985), BPM (Brooks, Pope, & Marcolini, Airfoil Self-Noise and Prediction, 1989) and Lowson (Lowson, 1993), no

new source modeling is included. All basic five airfoil self-noise mechanisms are modeled and also inflow noise.

The induced velocities and AOA for different blade sections are calculated via the vortex lattice method (see, for instance (Gupta & Leishman, 2005)) and applied to the noise prediction model.

The prediction results for NACA 0012 airfoil, compared to experimental data for the FX-79W151A airfoil showed deviations up to 10 dB. This was considered a major drawback common to most noise prediction codes that were based on the BPM, NACA 0012 data. A sensitivity analysis revealed the TBL characteristics at the TE to be the most sensitive parameters of the noise model. The authors then decided to employ the XFOIL code (Drela, Youngren, & Deperrois, XFOIL/XFLR5, 2009) in order to calculate the TBL parameters at the TE of the FX-79W151A airfoil, which returned more acceptable results. Even then, better prediction was shown below 1 kHz, but not in the important region above it, although the OASPL was recovered to certain degree. Also, the sensitivity study revealed that the aerodynamic model employed for solving the TBL (correlations, XFOIL, vortex wake code, etc.) influences the spectrum mainly in the region above 1 kHz. The geometric AOA for different blade segments were then replaced by induced AOA from a free wake code, leading to better agreement in the range between the 1 kHz – 4 kHz.

Figure 2-13 shown before is a result of the research from Bareiss et al. (Bareiss, Guidati, & Wagner, 1994) and illustrates that the total spectrum is dominated by TE noise and Tip noise.

The IAG model did not generalize the capability of calculating the TBL TE thickness for any airfoil. The parameters at the TE were calculated for three real airfoils (NACA 0012, NACA 4412 and Wortmann FX-79W151A), while for other airfoils the TBL over a flat plate model was still assumed to be applicable.

D.6 The RISO Method

The work developed at RISO (Fuglsang & Madsen, Implementation and Verification of an Aeroacoustic Noise Prediction Model for Wind Turbines, 1996) was not a new WT prediction model per se, but the software implementation of the BPM model for self-noise and Lawson's model for inflow noise, in a way to result in the total aerodynamic noise prediction for a WT rotor, much in the same way intended by Grosveld, Lawson himself and the IAG model, described previously. The intention was to use the resultant tool in the optimization step of the blade design process a goal shared by the current research.

The aerodynamic input parameters for the noise prediction module came from a WT dynamics software developed at RISO, that employs the BEM method in blade strips. The total noise for a blade is the logarithmic sum of the contributions from all sources, but the tip noise is included for the last blade segment, only.

The total noise for the rotor is estimated by the use of the "quasi 3-D method" also employed in the BPM method (see Appendix F for details) where the noise from one blade is calculated at a number of different positions in the azimuthal plane and an averaged OASPL is obtained for these positions, and for the total number of blades in the rotor. In order to consider the directivity, the total SPL contribution of each blade segment is calculated at the observer retarded position, r_e , through a set of five coordinate systems, and also the directivity angles θ, ϕ , as shown in Figure D-7.

After the code implementation, the results were compared with measurements carried out for the Vestas V27 225 kW and the Bonus Combi 300 kW machines, according to IEC 88/48 standards and at wind speed of 8 m/s.

Calculations were made for tripped and untripped flow since the authors believed that neither the laminar nor the fully turbulent regime was completely dominant in a WT flow. The turbulence length scale employed for inflow calculation was 100 m and the distance from the observer to the rotor was 40 m downstream of the tower center. The resulting SPL was converted to the equivalent SPL for a single source at rotor center.

For the Vestas V27 machine (see Fig. D-8) the authors found the OASPL and spectral agreement to be sufficiently accurate and also found that the untripped case shifted the spectrum towards higher frequencies.

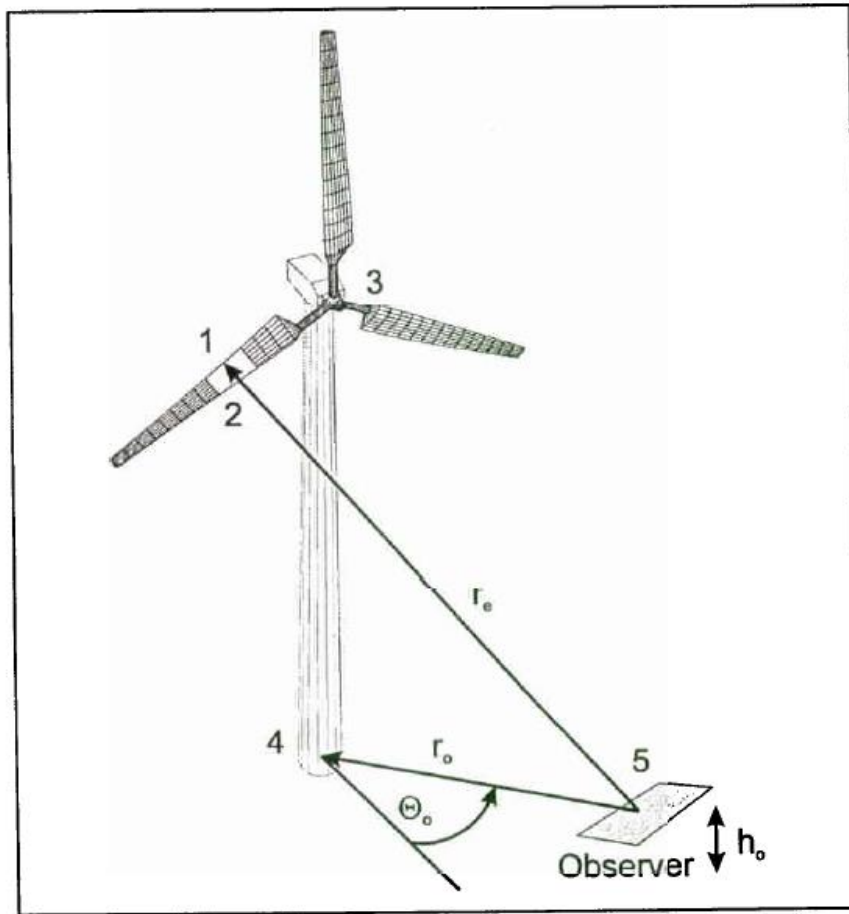


Figure D-7 – Relative position between the observer and the blade segment for consideration of directivity function. Numbers from 1 to 5 indicate the following coordinate systems applied: 1- at the plate TE, as shown in the previous figure; 2- at the lifting line; 3- at the rotor shaft; 4- at the tower base, and 5- at the observer position. Source: (Fuglsang & Madsen, Implementation and Verification of an Aeroacoustic Noise Prediction Model for Wind Turbines, 1996), p.18.

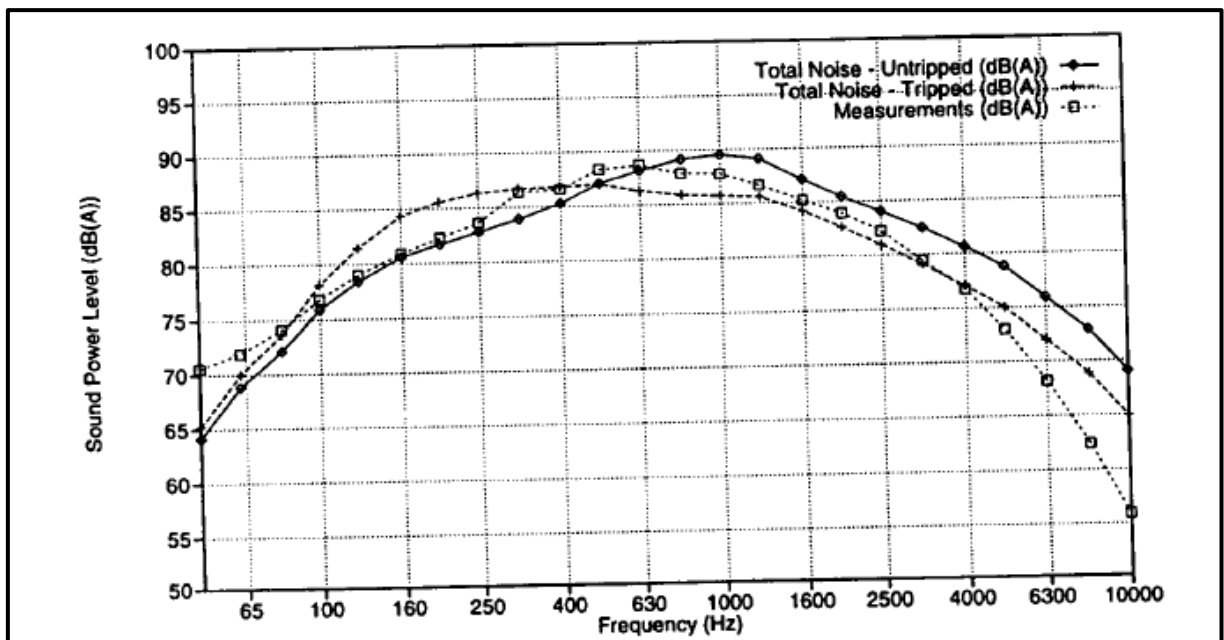


Figure D-8 – Experimental versus predicted A-weighted SPL [dB] for the Vestas V27 WT, at 8 m/s wind speed and 0.5° tip pitch. Source: (Fuglsang & Madsen, Implementation and Verification of an Aeroacoustic Noise Prediction Model for Wind Turbines, 1996), p.27.

While the OASPL measurement related to the experimental spectrum depicted in Fig. D-8 resulted 97.5 dB(A), the calculated OASPL amounted to 98.1 dB(A) for the untripped condition and 97.1 dB(A) for the tripped condition. The 1.5 dB(A) deviation was within the experimental uncertainty of the experimental data.

Similar trends were observed for the Bonus Combi machine, but that one also displayed tonal noise in the measurements due to the presence of mechanical sources.

By performing a sensitivity analysis on the validated model, the authors found that noise from inflow turbulence dominated the total noise at low wind speeds and, in that situation, changes in the airfoil self-noise would have little effect on total noise, a situation deserving further clarification. The importance of airfoil self-noise grows for intermediate and higher frequencies.

The authors believed that airfoil shape in the vicinity of the TE influenced the radiated noise and that future work ought to involve more detail on the airfoil contour.

The BPM directivity models were implemented for both low and high frequencies and compared to contour plots of sound measurements around the Vestas V27 machine and found to be in good agreement.

The BPM and Lawson models implementation was evaluated and found useful for absolute determination of SPL and also for relative comparison with parameter variation in the design phase of rotors concerning noise. Nevertheless, the authors warned that the accuracy of these models should not be overestimated and some of the self-noise sources needed better approaches, a key point being the lack of sensibility to the airfoil employed, since the self-noise model had been fully developed based on the NACA 0012 airfoil. Another point brought up was the need for additional controlled noise measurements of different airfoils in conditions closer to larger WT operational situation.

D.7 The NREL Method (I)

The next relevant class II WTN study was undertaken at NREL (Moriarty & Migliore, Semi-Empirical Aeroacoustic Noise Prediction Code for Wind Turbines, 2003), and it is also an implementation of the BPM and Lawson's models, with improvements.

Subroutines for the calculation of the five airfoil self-noise mechanisms from the BPM model and the inflow turbulence model from Lawson (Lawson, 1993) were superimposed and coupled to the in-house developed performance code "FAST", in order to predict total acoustic signature of WT under operation.

Also, the same directivity functions proposed in the BPM model for lower and higher frequencies were employed.

Parts of the code output were validated against acoustic data from Migliore and Oerlemans (Migliore & Oerlemans, Wind Tunnel Aeroacoustic Tests of Six Airfoils for Use in Small Wind Turbines., 2003), which tested six 2-D airfoil, including the NACA 0012 (see Fig. D-9), providing a data base other than the extensive one employed in the development of the BPM model.

In Fig. D-10, the comparison between predictions and test data for the NACA 0012 airfoil is presented for a range of AOA. The assumptions for the prediction code were that the TBL-TE noise was dominant source and the BL is "lightly tripped"⁷⁷, so that no noise from laminar vortex shedding results. Also there is no noise from TE bluntness or from turbulent inflow, since the test section turbulence intensity was ~0.5%.

⁷⁷ The heavily tripped BL thicknesses reported in this NREL paper are based on the same definition employed in the BPM data, i.e., grit applied from the LE of the airfoil to 0.2c. Nevertheless, the authors argue that this situation is unlikely to occur naturally and the dirt and bugs over the WT airfoils are more likely to produce a light tripping, closer to natural transition. For this purpose, the BL thickness is calculated as for the heavily tripped case and then multiplied by a 0.6 correction factor. They also highlight that for newly installed WTs, the behavior would be closer to the untripped situation.

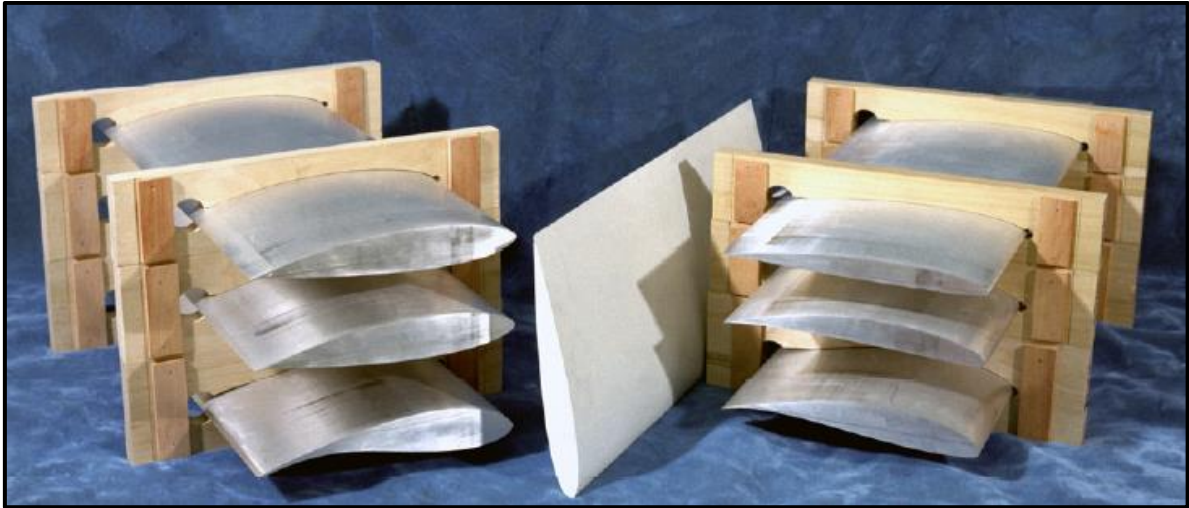


Figure D-9 – The six aluminum airfoil models employed by Migliore and Oerlemans (Migliore & Oerlemans, *Wind Tunnel Aeracoustic Tests of Six Airfoils for Use in Small Wind Turbines.*, 2003) in aeroacoustic tests: the Wortmann FX63-137, Selig S822 and S834, Selig-Donovan SD2030, Selig-Giguere SG6043 and Selig-Hanley SH3055. The white, composite-made NACA 0012, used as a benchmark, is at the center of the photograph.

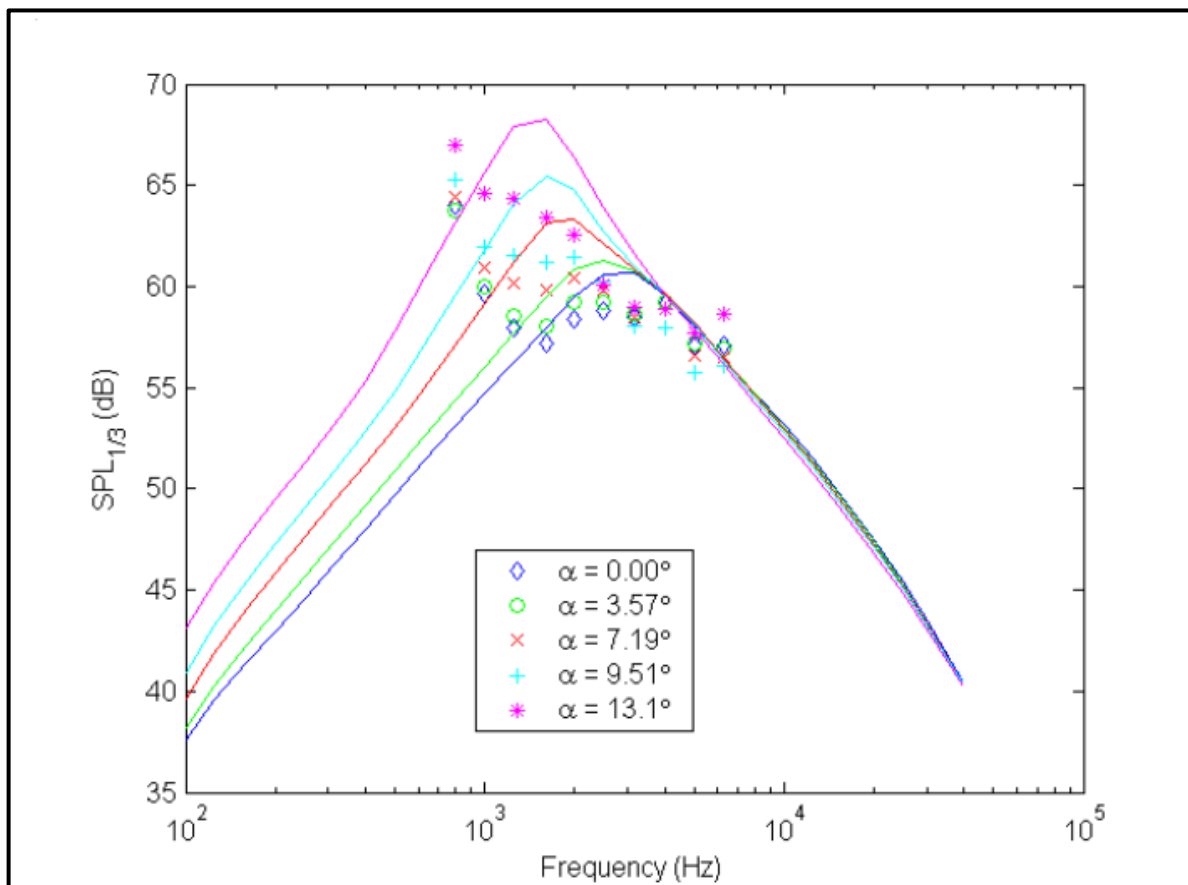


Figure D-10 – The points with symbols represent measured wind tunnel test data and continuous lines represent the predicted spectra for similar flow conditions. Boundary layer “lightly tripped”. Source: (Moriarty & Migliore, *Semi-Empirical Aeroacoustic Noise Prediction Code for Wind Turbines*, 2003), p.8.

The measurements and predictions collapse fairly close only near 3 kHz, but not for lower frequencies, where differences up to 6 dB are found. Despite the overprediction at frequencies below 3 kHz, the differences in level as a function of AOA are similar to the data, but the agreement worsens with increasing AOA.

Another experiment was set up with the NACA 0012 airfoil at a fixed 7.18° AOA and with a Mach number range that would allow direct comparison of the results with the BPM data. The results are displayed in Fig. D-11.

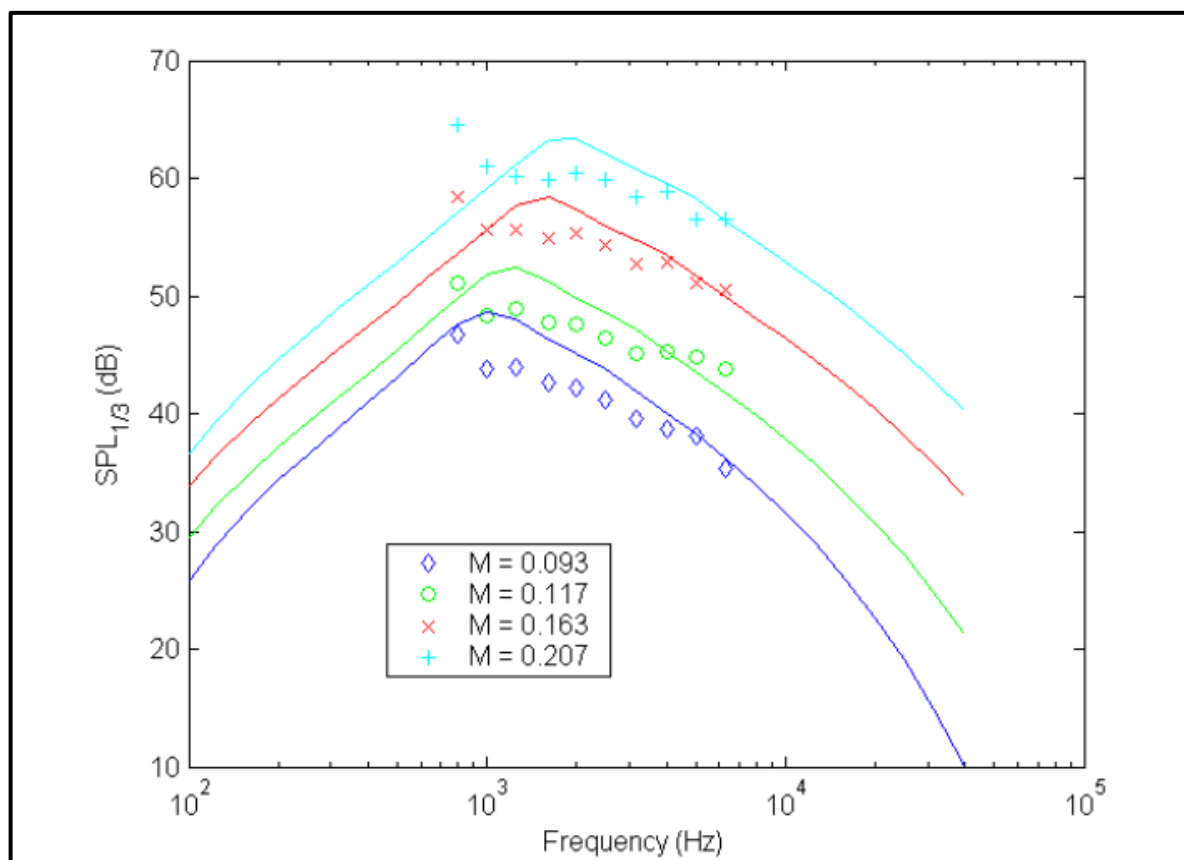


Figure D-11 – Comparison of measured and predicted noise for the NACA 0012 airfoil at fixed 7.18° AOA along a range of Mach numbers. Source: (Moriarty & Migliore, Semi-Empirical Aeroacoustic Noise Prediction Code for Wind Turbines, 2003), p.8.

From Fig. D-11 the authors concluded that agreement between data and predictions was reasonable and fell within 3 dB for all Mach numbers, with best agreement occurring for a Mach number of 0.163.

Regarding the prediction capability for airfoil other than the NACA 0012, Fig. D-12 shows the results for the Selig S822 airfoil at fixed Mach number of 0.038, for various AOA. For this case, TBL TE noise was again assumed to be de dominant noise source.

Even though the S822 is a significantly cambered airfoil, the authors found the noise pressure levels predicted from the BPM model to be rather reasonable for frequencies of 3 kHz and below, with agreement decreasing above that frequency. However the relative differences between AOAs were not well captured by the prediction method for the particular situation.

One possible explanation for this discrepancy, according to the authors, is the BL thickness empirically modeled in the BPM model from NACA 0012 data only, which represents an improvement opportunity for the model, i.e., more accurate prediction method for BL thickness that would allow for incorporation of different airfoil shapes.

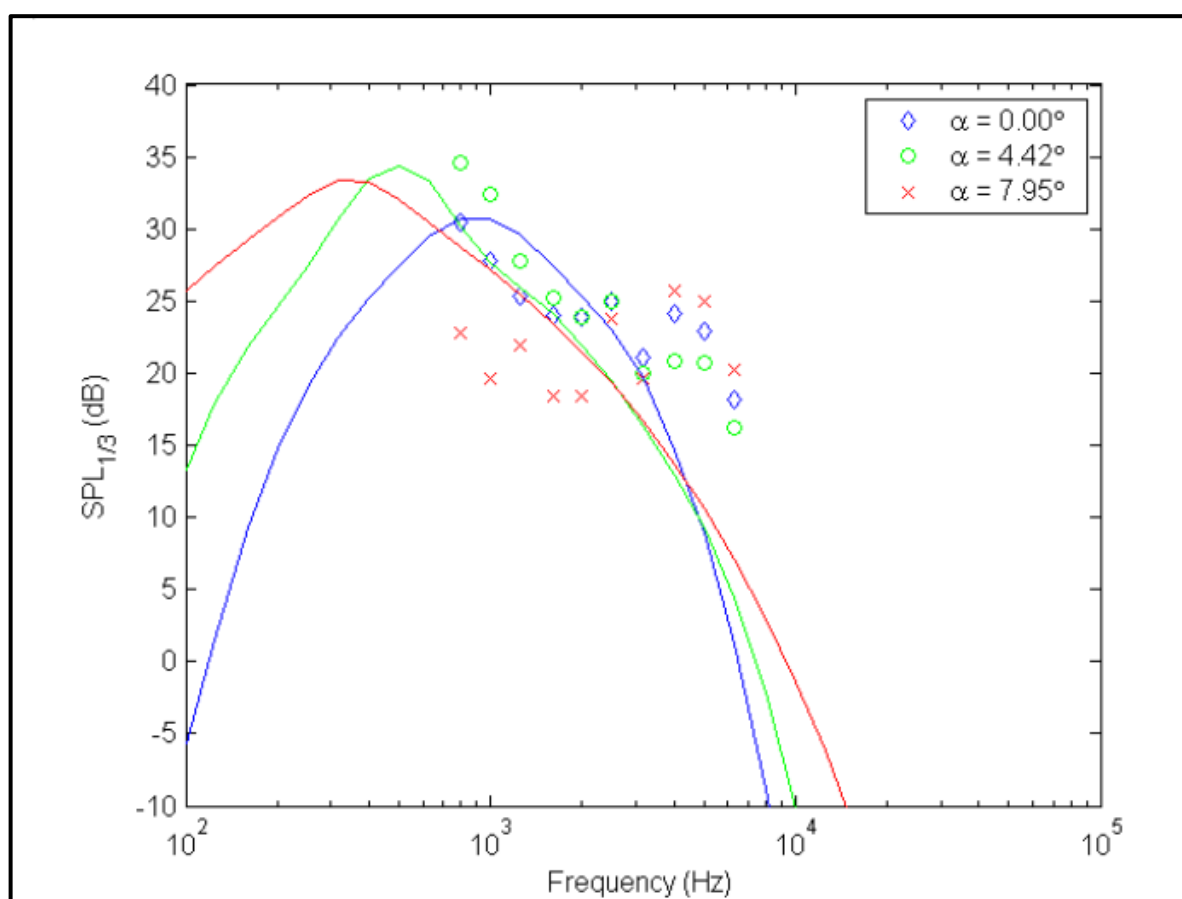


Figure D-12 – Comparison of measured and predicted noise for the S822 airfoil at fixed Mach number of 0.038, as a function of AOA. The BL is “lightly tripped”. Source: (Moriarty & Migliore, Semi-Empirical Aeroacoustic Noise Prediction Code for Wind Turbines, 2003), p.10.

A code validation was also tried against an operating WT, but a small, 15 m diameter, downwind model (AOC 15/50), without nacelle (which makes the gearbox noise a potential contributor to farfield noise) was employed for that purpose. The turbulence

intensity used to produce model prediction in order to compare to measurements made at 8 m/s and carried out in accordance with IEC 61-400-11 (IEC61400-11, 2012) requirements, was 22%, corresponding to IEC level A equipment. The turbulence length scale for the prediction was 61.25 m, as specified by the IEC for the hub height of 25 m. The BL was untripped so that vortex shedding noise was modelled. The result (Fig. D-13) showed that turbulent inflow noise dominated the whole spectrum, with tonal components appearing due to vortex shedding and TE bluntness contributions.

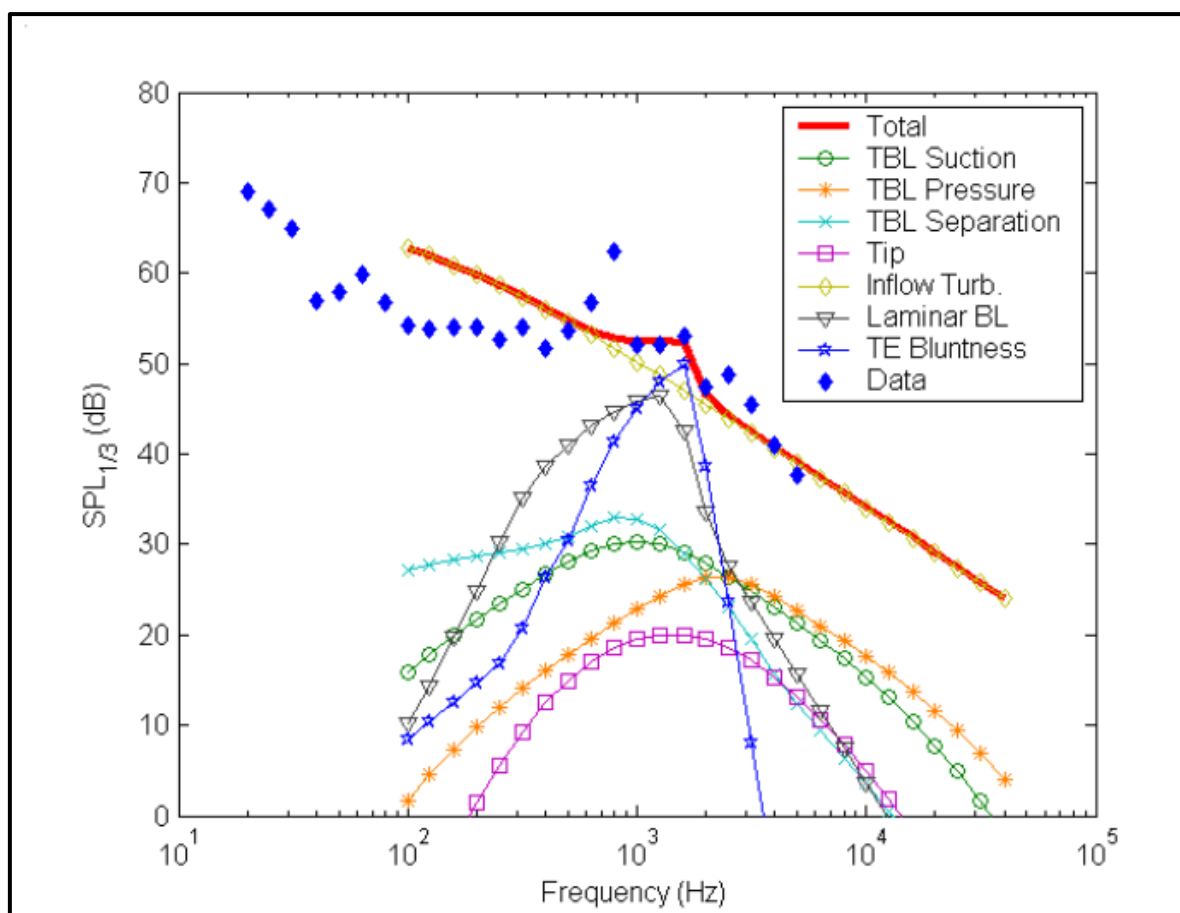


Figure D-13 – Comparison of measured and predicted noise for the AOC 15/50 WT in 8 m/s high turbulence wind. The BL is untripped. Source: (Moriarty & Migliore, Semi-Empirical Aeroacoustic Noise Prediction Code for Wind Turbines, 2003), p.13.

The work of Fuglsang and Madsen (Fuglsang & Madsen, Implementation and Verification of an Aeroacoustic Noise Prediction Model for Wind Turbines, 1996) discussed previously as the RISO model, employed the same turbulent inflow noise model from Lawson (Lawson, 1993), and showed that turbulent inflow noise tended to dominate only at lower frequencies, with decreasing influence at higher frequencies, where self-noise was increasingly important. According to the paper, private

correspondence between the authors revealed that further studies at RISO had showed that turbulent inflow noise was in fact secondary to airfoil self-noise for larger-size equipment, like the Vestas V27 and Bonus Combi. Nevertheless, Moriarty and Migliore (Moriarty & Migliore, Semi-Empirical Aeroacoustic Noise Prediction Code for Wind Turbines, 2003) concluded for this specific case, where a smaller diameter AOC WT was employed, that turbulent inflow noise dominated the full spectrum. In light of this situation, Moriarty and Migliore (Moriarty & Migliore, Semi-Empirical Aeroacoustic Noise Prediction Code for Wind Turbines, 2003) questioned the validity of the Lawson turbulent inflow noise and suggested that further research in the area was needed.

The authors also found inflow turbulence noise to be very sensitive to the length scale attributed to the turbulence in the model. While Fuglsang and Madsen (Fuglsang & Madsen, Implementation and Verification of an Aeroacoustic Noise Prediction Model for Wind Turbines, 1996) employed a 100 m length, (Moriarty & Migliore, Semi-Empirical Aeroacoustic Noise Prediction Code for Wind Turbines, 2003) employed 61.25 m, and other authors had employed different scales such as 0.01 m and 1m (this one based on the tower diameter for downwind type WT). A sensitivity study followed, showing that for lower frequencies, the total predicted SPL would agree more closely to measured data if the characteristic length of turbulence was taken to be 6.125 m, suggesting the radius of the rotor to be a more appropriate length scale for the turbulence at lower frequencies.

Later on Oerlemans et al. (Oerlemans, Sijtsma, & Méndez-López, Location and Quantification of Noise Sources on a Wind Turbine, 2007) executed more than 100 acoustic field measurements at wind speeds between 6 and 10 m/s, carried out within the European research project SIROCCO on a 58 m diameter WT (small by current standards but comparatively larger than equipment that had been measured in detail). The results revealed that most of the noise measured at the ground is produced during the downward movement of the blades, forming strongly asymmetric source pattern that can be explained by convective amplification and TE noise directivity. Also, it was confirmed that the noise is mainly produced at the outboard part of the blades, but not at the very tip, and that the SPL scales with the fifth power of local flow velocity. The experiment involved a three-bladed rotor with different surface finish qualities in each blade: one was clean, one was tripped and the remaining one was untreated. The results have shown that the tripped blade was significantly noisier than the others. A

narrowband analysis showed the TE bluntness to be unimportant. The final conclusion of the study was that the TE noise was the dominant source for that WT, which has been adopted as a rule for large-size WT since then (e.g. (Kamruzzaman M. , Lutz, Nübler, & Krämer, 2011)).

Some aspects of a more recent report from Oerlemans on WT noise primary sources (Oerlemans, Wind Turbine Noise: Primary Noise Sources, 2011) were discussed in Section 2.1, where Figure 2-7 shows, in a dramatic way, the location and concentration of noise sources during the downward movement of the blades.

D.8 Zhu's (DTU) Method

It may be easily noticed that after the release of the BPM model (Brooks, Pope, & Marcolini, Airfoil Self-Noise and Prediction, 1989), based on extensive experimental data, all relevant noise prediction semi-empirical codes implemented from 1989 onwards were based on that model, for self-noise sources, and also on Lawson's model (Lawson, 1993) for turbulent inflow noise. These became standards in terms of semi-empirical models and evolved little since then. From 2004 on, there seems to be a tendency for the academia to concentrate on more complex theoretical and numerical models while the industry practice (Sloth, 2011), (Saab Jr. J. Y., 2012), (Eisele, Pechlivanoglou, & Nayeri, 2013) seems to find more value in practical implementations of semi-empirical methods of much quicker turn-around times.

This finding is parallel with the opening statement of Zhu (Zhu, 2004), where he declares that numerical simulation of far-field sound on large computational domains is expensive and very difficult to perform even for simple flow conditions. The author consider his method as a *Class III* method (see Section 2.4.4) because of the detailed information required for its implementation, but it is once again based on the semi-empirical BPM model for self-noise and Lawson's model for turbulent inflow noise, representing another incrementally improved semi empirical model.

The major advantage of the implementation from Zhu (Zhu, 2004) is the use of XFOIL (Drela, Youngren, & Deperrois, XFOIL/XFLR5, 2009) in order to circumvent the NACA 0012 limitations embedded in the BPM model, an improvement suggested as necessary by most authors that implemented BPM-based models and tried by some to a certain extent.

Since a WT blade employs different airfoil types along the span, it is necessary to implement a flexible method for estimating the displacement thickness for each significantly different section. However, Zhu's model perform the BL calculation for three or four sections only along the blade span, applying linear interpolation between the calculated points.

In this specific implementation, the aerodynamic data is provided by a BEM code module locally developed at DTU (Technical University of Denmark). The sound directivity for both high and low frequencies are also the same employed in the BPM model.

Zhu compared predictions for the Bonus Combi 300 kW WT, which originally employs NACA 632XX airfoils, simulated in turns with NACA 0012, NACA 634xx series and NACA 632xx series (original) airfoils, as shown in Figures D-14, D-15 and D-16, for both tripped and untripped conditions, with experimental data at 8 m/s wind speed at hub height.

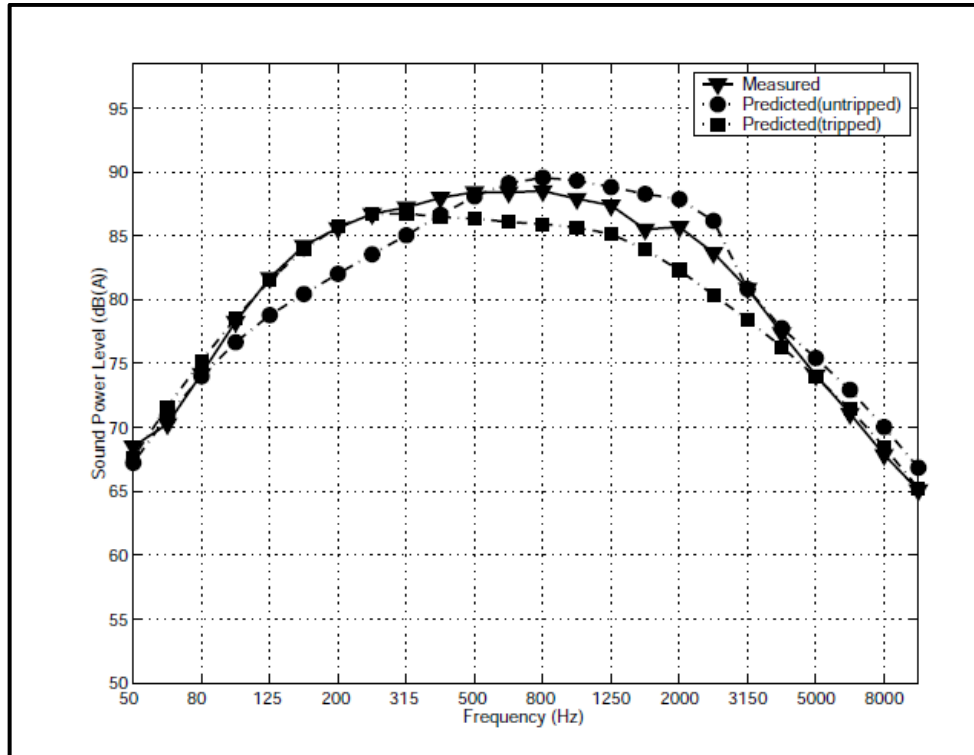


Figure D-14 – Comparison of measured spectrum for the Bonus Combi 300 kW WT, at 8 m/s wind speed at hub height, with calculations for the same WT, but employing the NACA 0012 airfoil instead, for tripped and untripped BL. Source: (Zhu, 2004), p. 52

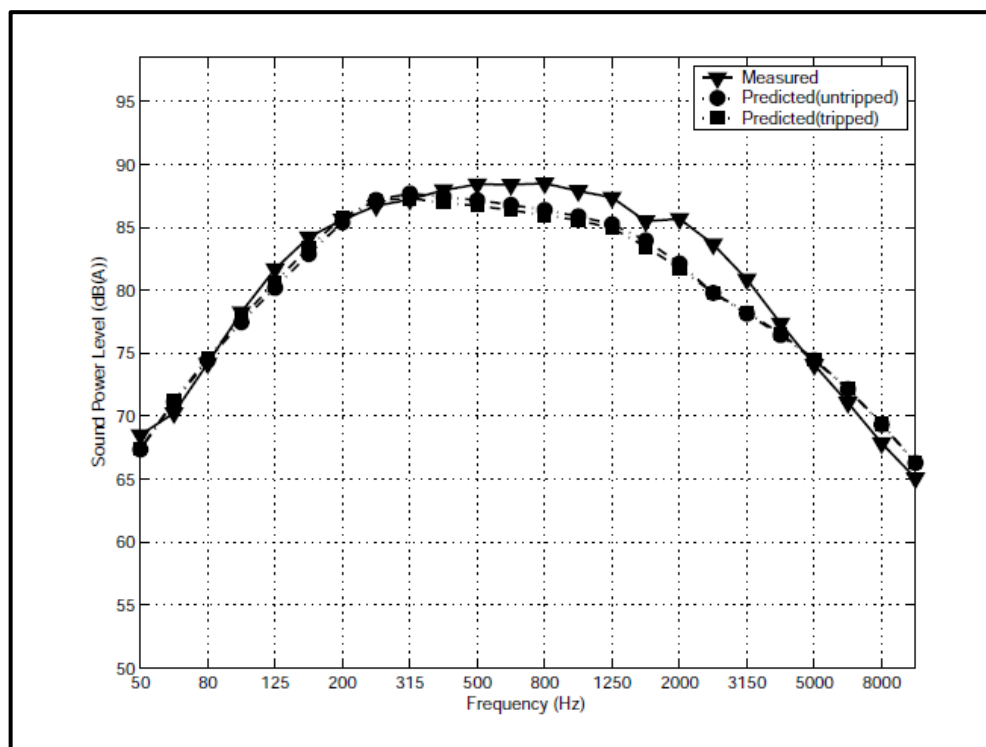


Figure D-15 – Comparison of measured spectrum for the Bonus Combi 300 kW WT, at 8 m/s wind speed at hub height, with calculations for the same WT employing the NACA 634XX airfoil instead, for tripped and untripped BL. Source: (Zhu, 2004), p. 53

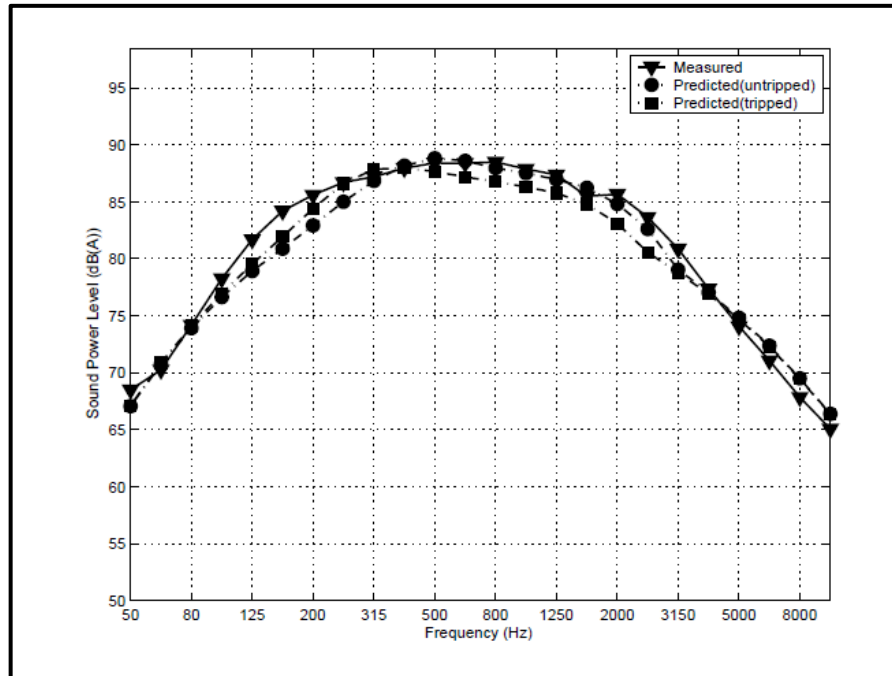


Figure D-16 – Comparison of measured spectrum for the Bonus Combi 300 kW WT, at 8 m/s wind speed at hub height, with calculations for the original NACA 632XX, for tripped and untripped BL. Source: (Zhu, 2004), p. 53

With the BL displacement thickness calculated with XFOIL for each specific profile above, Zhu managed to obtain OASPL results within 2 dB(A) from measured. However, the quality of the result is not equally distributed throughout the spectrum. It is possible to observe the same tendency described by other authors of spectrum shift according to the tripping condition. In general the prediction for the untripped results shows better agreement at high frequency range and the prediction for the tripped results shows better agreement at low frequency range.

Also, the author makes some wind speed profile corrections for the hub height that seems objectionable since he is comparing predicted 2-D spectrum against 2-D wind tunnel test data and not to a WT operating inside the atmospheric boundary layer.

D.9 The NAFNoise Method (NREL II)

The NAFNoise (NREL Airfoil Noise) is a tool that predicts 2-D airfoil noise for TBL TE, separated flow, LBL vortex-shedding, TE bluntness and turbulent inflow (Moriarty P. , NAFNoise User's Guide, 2005). Like the method from Zhu (Zhu, 2004) reviewed earlier, the tool is fed by XFOIL data and is capable of predicting noise for any airfoil shape. The models used for airfoil self-noise prediction are those of the BPM model while the model used for inflow turbulence noise is a model derived from the work of Amiet (Amiet, Acoustic Radiation from an Airfoil in a Turbulent Stream, 1975), modified to include inflow noise correction developed by Moriarty et al. (Moriarty, Guidati, & Migliore, Recent Improvement of a Semi-Empirical Aeroacoustic Prediction Code for Wind Turbines, 2004).

One interesting feature of NAFNoise is that the XFOIL TBL data can also be inputted into a simplified theoretical TBL TE noise model (TNO), that will be described in the next review track.

NAFNoise was not coupled to the FAST module and allowed for prediction of 2-D airfoil noise sections only. The validations for the NACA 0012 and FX-63137 airfoils are the same reviewed for the NREL method (Moriarty & Migliore, Semi-Empirical Aeroacoustic Noise Prediction Code for Wind Turbines, 2003). A summary of the conclusions of the authors after development and application of the tool for some time may be found in Moriarty (Moriarty P. , NAFNoise and FAST noise modules, 2008):

- Use of XFOIL to calculate BL thickness improves TBL noise prediction for BPM model.
- Use of XFOIL to calculate BL thickness does not improve not improve LBL Vortex Shedding noise prediction.
- Measurement and calculation of noise are sensitive to transition.
- TNO model is a suitable replacement for BPM, since it is as accurate as BPM but has more physical detail and may improve with more sophisticated boundary layer information.
- The predictions for full WT using the FAST module did not estimate absolute values accurately (~6 dB difference), but captured the trends.

Despite the statement that the TNO model is a suitable replacement for the BPM model, the two models seem to result in similar spectra, as show in the figures below.

Even for the S822 airfoil, not the original airfoil over which the BPM model was based, the results are very similar to the TNO model, once the BPM model has been fed with specific TBL information calculated with XFOIL (Figures D-17 and D-18).

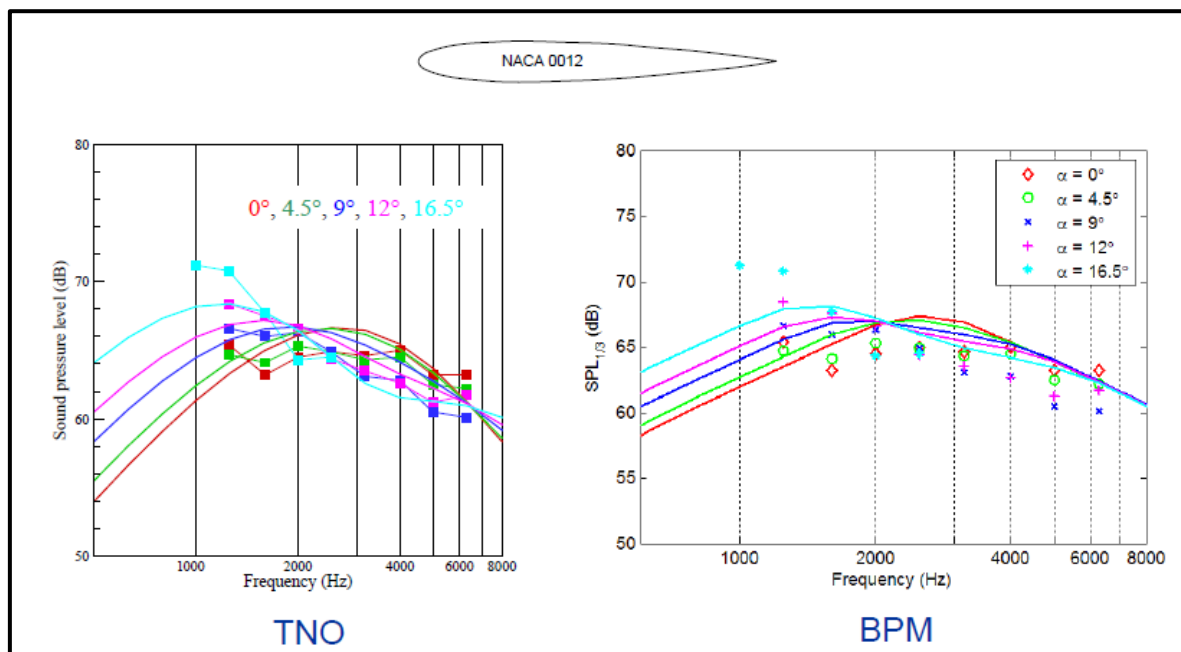


Figure D-17 – Comparison of measured NACA 0012 airfoil data with predicted noise spectra for different AOA, and Reynolds number of 1.1×10^6 . Source: (Moriarty P. , NAFNoise and FAST noise modules, 2008), p.21

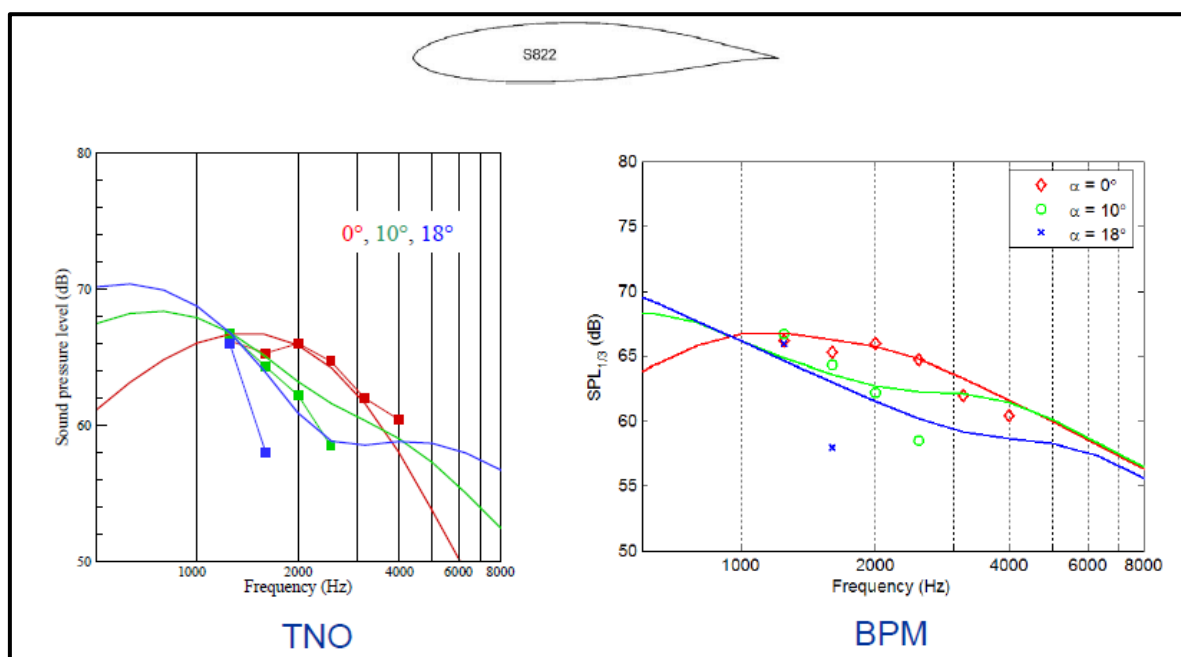


Figure D-18 – Comparison of measured of S822 airfoil data with predicted noise spectra for different AOA, and Reynolds number of 1.1×10^6 . Source: (Moriarty P. , NAFNoise and FAST noise modules, 2008), p.22

The second phase involved the comparison of the total predicted noise spectra against measured data of the Bonus 300 kW WT, already used in other validation studies described earlier in the text.

Finally, sensitivity studies were accomplished for BL tripping, local AOA, TE BL structure, turbulence scale and observer position, for the Total SPL and the directivity of the SPL around the WT is mapped.

D.10 The Vargas' Method (LVNP)

Vargas (Vargas L. d., 2008) implemented yet another prediction tool (called LVNP) based on the BPM model for all airfoil self-noise (and directivity for high and low frequency noise), and in the model of inflow turbulence noise as used by Zhu (Zhu, 2004) based on the proposal of Amiet (Amiet, Acoustic Radiation from an Airfoil in a Turbulent Stream, 1975) as modified by Lawson (Lawson, 1993).

While describing his prediction tool, Vargas (Vargas L. d., 2008) highlights that previous tools based on the same models lacked user friendliness in their interfaces, which was one of his goals. After validation of the code against BPM experimental data (Fig. D-19), the LVNP tool was applied to the Bonus 300 WT (input data in Table D-1) and compared to prediction data of Zhu (Zhu, 2004), for the same equipment, for verification purposes.

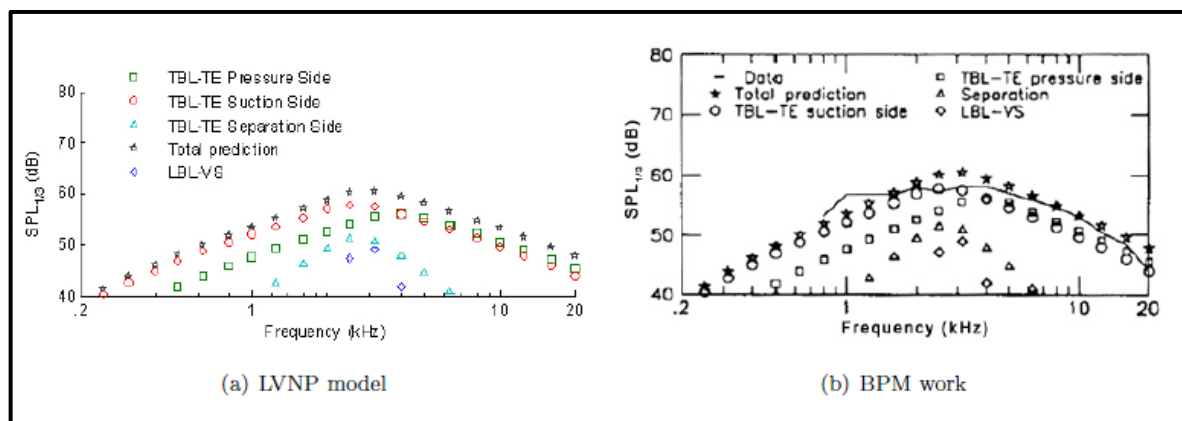


Figure D-19 – Comparison of spectra predicted by Vargas' tool (LVNP) against experimental and theoretical prediction from (Brooks, Pope, & Marcolini, Airfoil Self-Noise and Prediction, 1989). Source: (Vargas L. d., 2008), p.46.

Table D-1 – Input data for the Bonus Combi 300 kW WT, used as input to (Vargas L. d., 2008) and (Zhu, 2004) methods. Sources: (Vargas L. d., 2008), p.48; (Zhu, 2004), p.51.

rotor radius:	15.5 m
rotor style:	3-bladed, upwind, stall regulated
rotor angular speed	35.2 RPM
tower height:	31 m
airfoil:	profile series NACA632xx
tip pitch:	-1.0°
bluntness:	0.5% × chord
wind speed:	8 m/s, measured at 10 m height
wind direction:	upwind, perpendicular to rotor plane
observer position:	40 meters in the downwind direction, at ground level
ground surface roughness:	30 mm

The OASPL level predicted by both methods are not presented for comparison by Vargas, and the figure with the spectra for all noise sources (Figure D-20) is quite cluttered. The tendencies for all sources are well predicted, except for bluntness noise (modelled by Vargas but not by Zhu) and the “hump” imprinted in the total SPL spectrum by this mechanism, near 2 kHz, which is pronounced in Vargas' results.

By focusing in our main source of interest, it is possible to see that the spectra of the TBL-TE noise for the pressure and suction sides were much closer (to each other) in Vargas tool than in Zhu's tool, since the airfoil employed was not the NACA 0012 and Zhu's tool was capable of estimating the displacement thickness at the TE of the asymmetric NACA 632xx series airfoil in a more realistic way (by using XFOIL). For a given frequency, e.g. 250 Hz, the LVNP tool over predicts the SPL by close to 10 dB on the pressure side and under predicts the SPL by close to the same amount on the suction side, in relation to the method from Zhu. On the high frequency range, e.g. 4 kHz, the LVNP tool display once again an overprediction of the noise of around 10 dB for the pressure side, but a value close to Zhu (72-75 dB) for the suction side.

While reviewing the BPM-based method from Zhu (Zhu, 2004), we have seen that it displayed very good performance in the prediction of the Bonus 300 WT total noise spectrum (and OAPSL) with results improving as the displacement thickness was calculated at the TE for airfoils closer to the real ones employed in the real equipment.

Vargas did not expand the original BPM model in his method so as to deal with other types of airfoils. Also, he stated that if another airfoil type was employed in the equipment rather than the NACA0012, the resulting prediction (spectrum or AOSPL) would not be accurate. However, we have seen that to be the opposite in the works of Zhu (Zhu, 2004) and Moriarty (Moriarty P. , NAFNoise and FAST noise modules, 2008), i.e., the BPM model may have its use extended as a result of dedicated calculation of boundary layer displacement thickness for the specific airfoil under consideration.

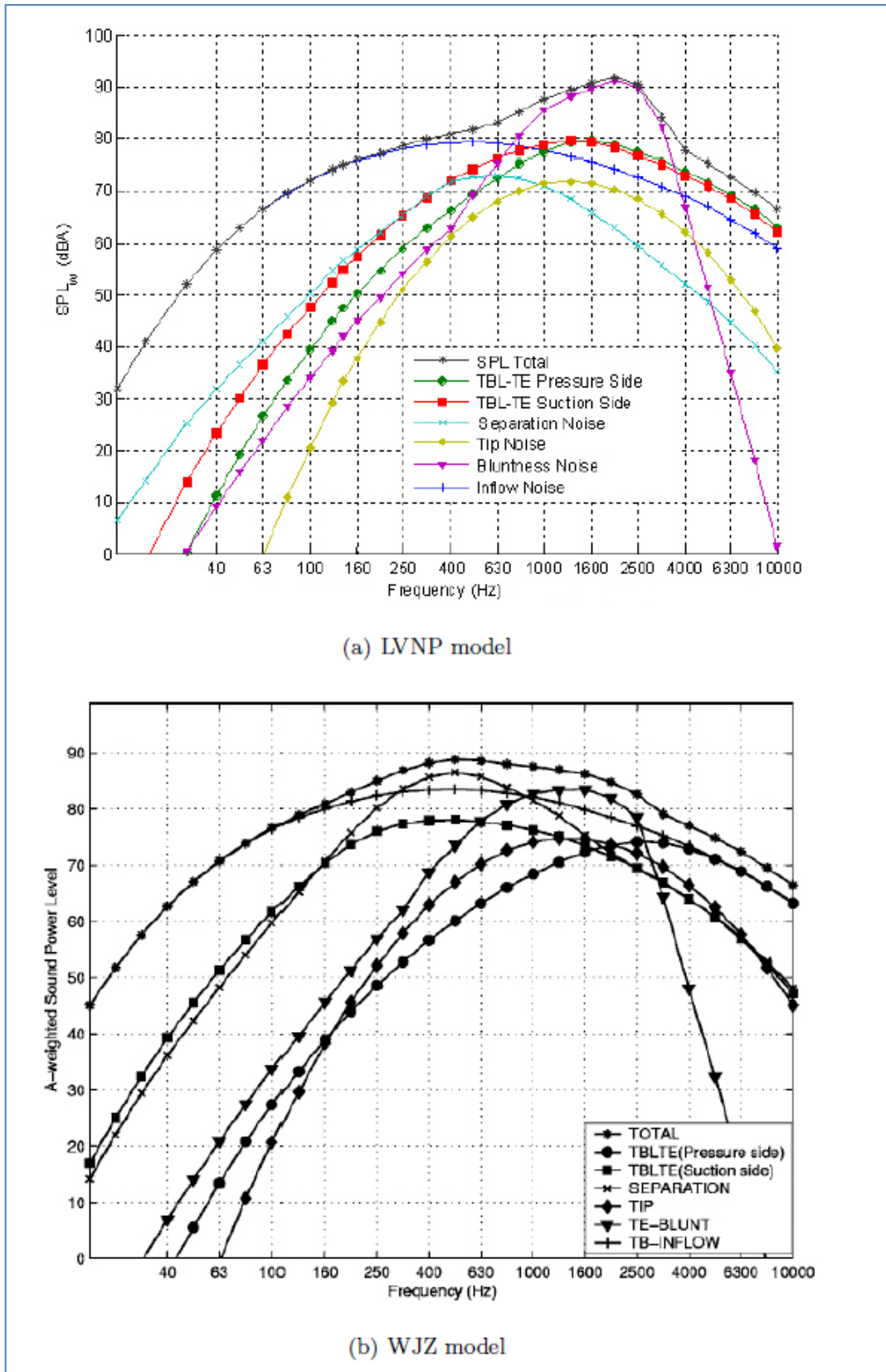


Figure D-20 – Comparison of total and partial noise spectra predicted by Vargas’ tool (LVNP) for the Bonus 300 WT (upper graph), against theoretical prediction from (Zhu, 2004) (lower graph), for the same equipment. Source: (Vargas L. d., 2008), p.50.

APPENDIX E – SIMPLIFIED-THEORETICAL NOISE PREDICTION MODELS AND METHODS - A DICUSSED REVIEW.

E.1 The TNO-Blake Model for Airfoil TE noise

As discussed in the preceding Appendix, the initial theoretical effort toward noise prediction was reviewed and tentatively unified by Howe (Howe, 1978), which proposed a relation between surface pressure fluctuations and the far field sound. After further development and test of his theory by Brooks and Hodgson (Brooks & Hodgson, 1981), Brooks and Marcolini (Brooks & Marcolini, 1985) diverted to simpler, scaled approaches that paved the way for the semi-empirical models.

However, simplified-theoretical models evolved in a track of their own, generating a central model, the TNO-Blake model, by Kamruzzaman et al. (Kamruzzaman M. , Lutz, Nübler, & Krämer, 2011), which evolved from the TNO-TPD⁷⁸ model from Lutz et al. (Lutz, Herrig, Würz, Kamruzzaman, & Krämer, 2007) and from the TNO model from Bertanoglio et al. (Bertanoglio, Madsen, & Bak, 2009).

The model is based on the work of Parchen (Parchen, 1998) at TNO-TPD for TE noise prediction, which expanded on the work of Brooks and Hodgson (Brooks & Hodgson, 1981), Blake (Blake, Mechanics of Flow-Induced Sound and Vibration, 1986 II) and others. The basic concept is that the convecting turbulent eddies induce unsteady wall pressure fluctuations (WPF), described by a wavenumber-frequency $k - \omega$ spectrum. A methodology was developed by (Parchen, 1998) to derive the $k - \omega$ spectrum from the BL mean velocity profile in the vicinity of the TE and the (time-averaged) distribution of turbulence data across the BL.

The $k - \omega$ spectrum of the WPF underneath a TBL is also given by Blake (Blake, Mechanics of Flow-Induced Sound and Vibration, 1986 II), in the form of a solution of the simplified Poisson equation (Lutz, Herrig, Würz, Kamruzzaman, & Krämer, 2007):

⁷⁸ Department of Flow and Structural Dynamics (TPD) of the Institute of Applied Physics (TNO) at Netherlands Organization for Applied Scientific Research, where (Parchen, 1998) first developed the model.

$$\mathbf{P}(k_1, k_3, \omega) = 4\rho^2 \left(\frac{k_1^2}{k_1^2 + k_3^2} \right) \int_0^\infty \Lambda_2(y_2) \left[\frac{dU_1(y_2)}{dy_2} \right]^2 \cdot \tilde{\phi}_{22}(y_2, k_1, k_3) \cdot \phi_m(\omega - k_1 U_c) \cdot \langle u_2^2(y_2) \rangle \cdot e^{-2|K|y_2} dy_2 \quad (E - 1)$$

where $\mathbf{P}(k_1, k_3, \omega)$ is the wavenumber-frequency $(k - \omega)$ WPF spectrum; $\tilde{\phi}_{22}(y_2, k_1, k_3) = \phi_{22}(y_2, k_1, k_3) / \langle u_2^2(y_2) \rangle$ is the normalized wavenumber spectrum of the vertical velocity fluctuations squared or vertical Reynolds Stress, $\langle u_2^2(y_2) \rangle$; Λ_2 is the integral length scale of the eddy field; ϕ_m is the moving axis spectrum (describes the energy distribution away from the convective ridge, for the energy in the vertical velocity as explained by Wolf et al (Wolf, Lutz, Würz, Stalnov, & Seifert, 2011), p. 2); $U_1(y_2)$ is the streamwise mean velocity; $U_c \cong 0.8U$ is the mean convective velocity of wall pressure fluctuations and y_2 is the normal wall coordinate.

After the WPF is obtained, the noise emission associated with the surface pressure fluctuations may be evaluated at the far field (see Fig. E-1) through the following diffraction integral for a semi-infinite flat plate:

$$S(\omega) = \frac{L}{2\pi r^2} \int_0^\infty \frac{\omega}{c_0 k_1} \mathbf{P}(k_1, 0, \omega) dk_1 \quad (E - 2)$$

where $S(\omega)$ is the far field spectrum (power spectral density) of the scattering pressure; L is the airfoil span; r is the distance between the noise source and the receiver (with no considerations regarding directivity); k_1 is the wavenumber in the y_1 (streamwise) coordinate direction and $\mathbf{P}(k_1, 0, \omega)$ is the wavenumber-frequency $(k - \omega)$ WPF spectrum.

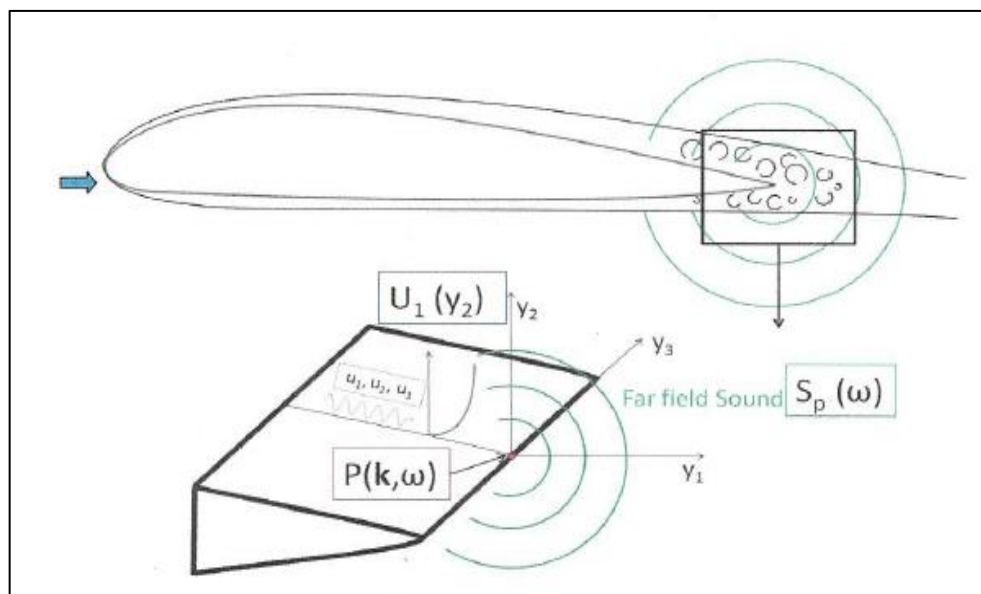


Figure E-1 – Illustration of the production of TE noise. Source: (Wolf, Lutz, Würz, Stalnov, & Seifert, 2011).

According to Bertanoglio et al. (Bertanoglio, Madsen, & Bak, 2009), the required TBL quantities near the airfoil TE for the TNO method may be calculated, for instance, by a panel method coupled to an integral BL formulation like XFOIL (Drela, Youngren, & Deperrois, XFOIL/XFLR5, 2009) or any CFD code with a suitable (non-algebraic) turbulence model. In their research for experimental validation of the TNO TE noise model, both methods were employed, however, for airfoil optimization purposes, only XFOIL was employed for being less computationally intensive.

The two components of the model, namely the WPF spectrum on the airfoil surface and the far-field noise SPL, were considered by Bertanoglio et al. (Bertanoglio, Madsen, & Bak, 2009) for evaluation purposes against a dedicated wind energy wind tunnel⁷⁹ experimental data with turbulence intensity of $\sim 0.1\%$ in the incoming flow and microphone positioned flush with the surface at $x/C = 0.567$.

⁷⁹ A dedicated wind tunnel from LM Windpower, a Danish-Dutch company was employed for the purpose.

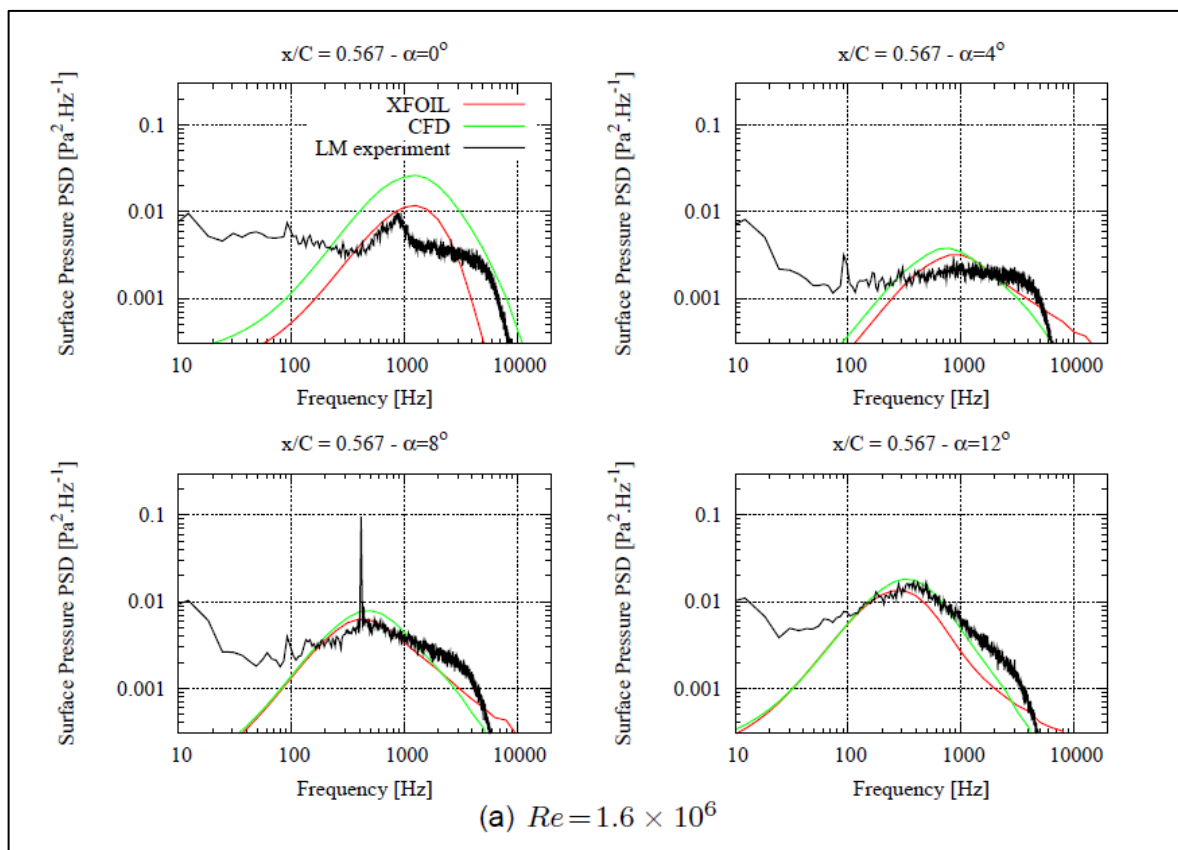


Figure E-2 – Comparison of Surface Pressure Spectra measured over a NACA 0015 Airfoil ($x/C = 0.567$), against calculation using the TNO model, with both XFOIL and CFD code EllipSys2-D, as a function of AOA. Source: (Bertanoglio, Madsen, & Bak, 2009). Data also available for higher Reynolds number in the reference, with similar conclusions.

Since the transition point for the NACA 0015 airfoil at $Re \approx 1.6 \times 10^6$ is close to the microphone position ($x/C = 0.567$) for $\alpha = 0^\circ$, there is little coincidence between the measured and calculated spectra for that angle (no fully-developed BL assumption acceptable for this condition), as seen in Fig. E-2. However, Bertanoglio et al. (Bertanoglio, Madsen, & Bak, 2009) consider that, for higher AOAs, when the transition takes place closer to the LE, with less impact over the measuring point, the numerical results reproduce quite well the increase in PSD for the range $300 < f < 9000 \text{ Hz}$ with increasing AOA, but the TNO model does not capture well the lower frequency part of the measured spectra. As it was shown in section 2.1, the inflow turbulence noise dominates at lower frequencies, which is the probable cause suggested by the authors for explaining the mismatch at lower frequencies, since the TNO model is a TE noise model only. In addition to that, the spectrum shape used in the TNO model was also considered to be a poor estimator at low frequencies. Concerning the relative performance of the numerical methods employed for dynamic

field variables fed into the TNO model, the predictions are similar for XFOIL and CFD, except at $\alpha = 0^\circ$, with CFD showing some advantage in the final high-frequency portion of the spectrum for all AOA.

In a second comparison against data measured by Brooks and Hodgson (Brooks & Hodgson, 1981), however, the results were not as reassuring, as shown in Fig. E-3.

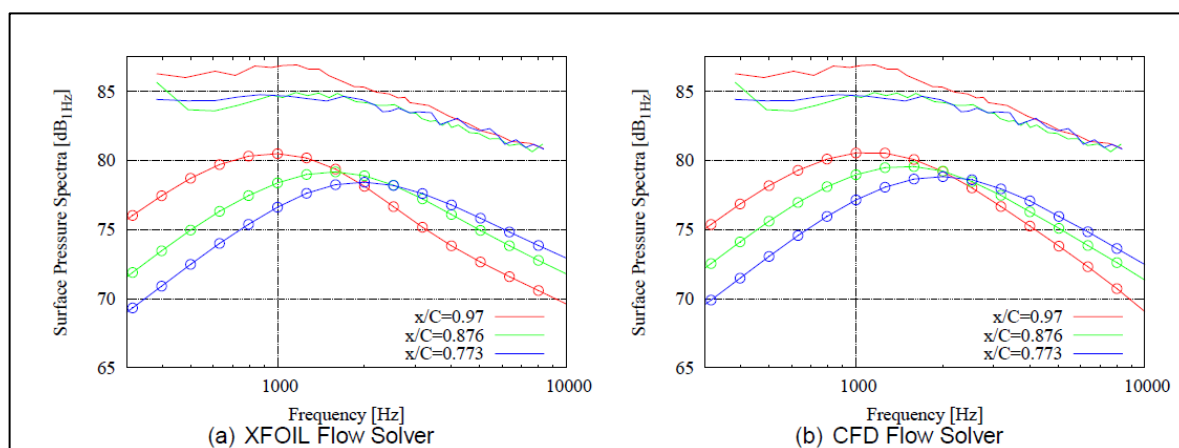


Figure E-3 – Comparison of Surface Pressure Spectra measured (continuous lines) over a NACA 0012 Airfoil (Brooks & Hodgson, 1981) in three different sensor positions, against calculation using the TNO model, with both XFOIL and CFD code EllipSys2-D (lines with points). $Re = 2.9 \times 10^6$ and $\alpha = 0^\circ$. Source: (Bertanoglio, Madsen, & Bak, 2009).

A 5 to 10 + dB offset is seen along the whole spectrum, although the tendencies are correctly captured for frequencies above 1 kHz, i.e. the PSD increases as the measurement point approaches the TE and the peak frequency decreases concurrently. Bertanoglio et al. (Bertanoglio, Madsen, & Bak, 2009) conjectured that there might be a difference in formulation for the TNO model used by them and that used by Brooks and Hodgson (Brooks & Hodgson, 1981), which presented very good agreement to measured data as depicted earlier in Fig. D-3. However, the good agreement obtained with their own measured data as shown in Fig. E-2 led them to believe that the difference could be attributable to inconsistencies in conventions.

New measurements for the NACA 0012 airfoil were accomplished, this time at the Aeroacoustic Wind Tunnel at Braunschweig (AWB) but a similar offset in SPL was observed.

Also, measurements accomplished by Lutz et al. (Lutz, Herrig, Würz, Kamruzzaman, & Krämer, 2007) at the IAG laminar wind tunnel (LWT) and compared to the predictions

of the TNO-TPD model, while designing new types of airfoil for WT, presented the same type of offset, as seen in Fig. E-4.

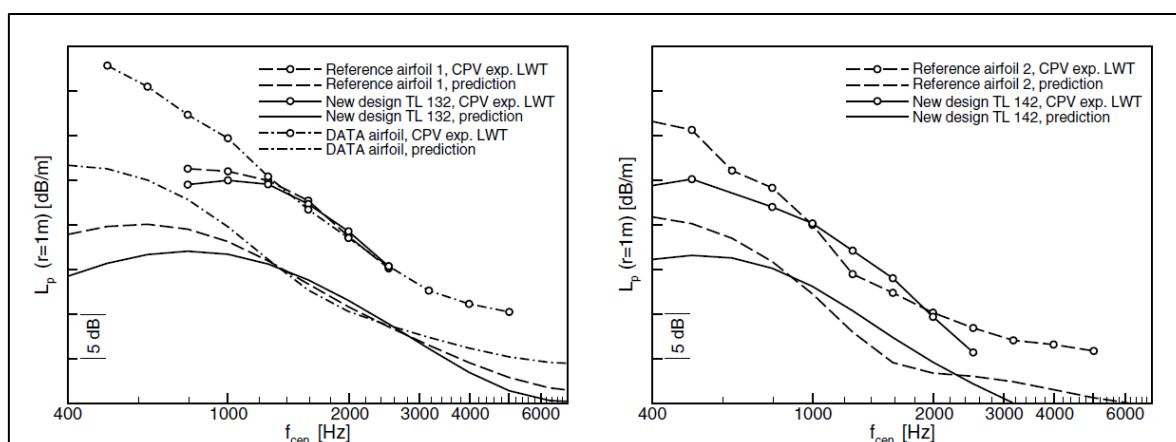


Figure E-4 – Comparison of Sound Pressure Level measured at LWT against prediction by the TNO model, at $Re = 1.6 \times 10^6$ and $c_l = 1$, for a reference airfoil (a design employed in a WT), a new airfoil design and an airfoil that resulted from the DATA⁸⁰ project. Source: (Lutz, Herrig, Würz, Kamruzzaman, & Krämer, 2007).

The result showed once more Sound Pressure Level underprediction throughout the spectrum. The research at the IAG concerning TE noise has spanned many years and will be covered in more detail later in this Appendix.

E.2 The Moriarty-Guidati-Migliore Model and Method (2005)

The paper from Moriarty et al. (Moriarty, Guidati, & Migliore, Prediction of Turbulent Inflow and Trailing-Edge Noise for Wind Turbines, 2005) describes the continued effort of the US Department of Energy's National Renewable Energy Laboratory (NREL) in order to develop a set of design tools that might be used to predict WT noise. The main motivating argument was that tip speed of many WT designs is limited by the amount of noise created by the blades in operation, which limits energy capture and restrain the cost of energy.

⁸⁰ Airfoil designed during the European Design And Test of Acoustically-Optimized (DATA) airfoil project.

The NREL method was previously described, with airfoil self-noise prediction based on the BPM model and the inflow turbulence noise model is derived from the work of Amiet (Amiet, Acoustic Radiation from an Airfoil in a Turbulent Stream, 1975), modified and improved by Moriarty et al. (Moriarty, Guidati, & Migliore, Recent Improvement of a Semi-Empirical Aeroacoustic Prediction Code for Wind Turbines, 2004).

In this research, Moriarty et al. (Moriarty, Guidati, & Migliore, Prediction of Turbulent Inflow and Trailing-Edge Noise for Wind Turbines, 2005) proposed a simplified model for the inflow turbulence noise, since the previous model was considered computationally intensive⁸¹ and thus, prohibitive for the wind turbine design industry. However, they simultaneously proposed a more complex model for TE noise prediction, aimed at modeling more closely the physical process of noise generation from the interaction with a TBL and at estimating the TE noise on both sides of an airfoil.

The new simplified inflow turbulence noise showed good agreement with the original model but only below 4 kHz for a 0.2 m chord airfoil and below 800 Hz for a 1 m chord airfoil.

The more complex modeling of the TE noise was attempted by using the TNO model, with TBL properties being fed by the XFOIL. The flow properties are used to model the surface pressure fluctuations on the airfoil and the resultant far-field noise. Despite the replacement of the semi-empirical BPM model by simplified theoretical TNO model, the authors (Moriarty, Guidati, & Migliore, Prediction of Turbulent Inflow and Trailing-Edge Noise for Wind Turbines, 2005) stressed in the paper that the new model still had empiricism present in the modeling of the BL properties, such as the length scale, whose role in noise prediction will become clearer in the next review of the IAGNoise method and of the anisotropy problem, Section E.4. In the present model of Moriarty et al. (Moriarty, Guidati, & Migliore, Prediction of Turbulent Inflow and Trailing-Edge Noise for Wind Turbines, 2005) the integral normal length scale, Λ_2 (see Eqn. E-1), is based on Prandtl's mixing length model (Schlichting & Gersten, 2003), p.539, and on a dissipation length. Such empiricism, which is always present also in all the simplified theoretical approaches reviewed, limits the potential accuracy of the method, which

⁸¹ Five minutes per calculated frequency in a 1.7 GHz machine.

ends up displaying similar accuracy to the semi-empirical BPM model, for the 2-D airfoils tested.

The BL parameters directly derived from XFOIL and the other necessary quantities “reconstructed” from the limited available dynamic field, e.g. the mean velocity in the BL, U_1 , are described in the paper by Moriarty et al. (Moriarty, Guidati, & Migliore, Prediction of Turbulent Inflow and Trailing-Edge Noise for Wind Turbines, 2005) along with the parameters used to “fine tune” the TNO model to the experimental data.

Another disadvantage of the method is that the Coles law of the wall (Schlichting & Gersten, 2003), p. 525, is employed for U_1 reconstruction, which do not allow for negative friction coefficient, typical of separated BL with a laminar recirculation bubble.

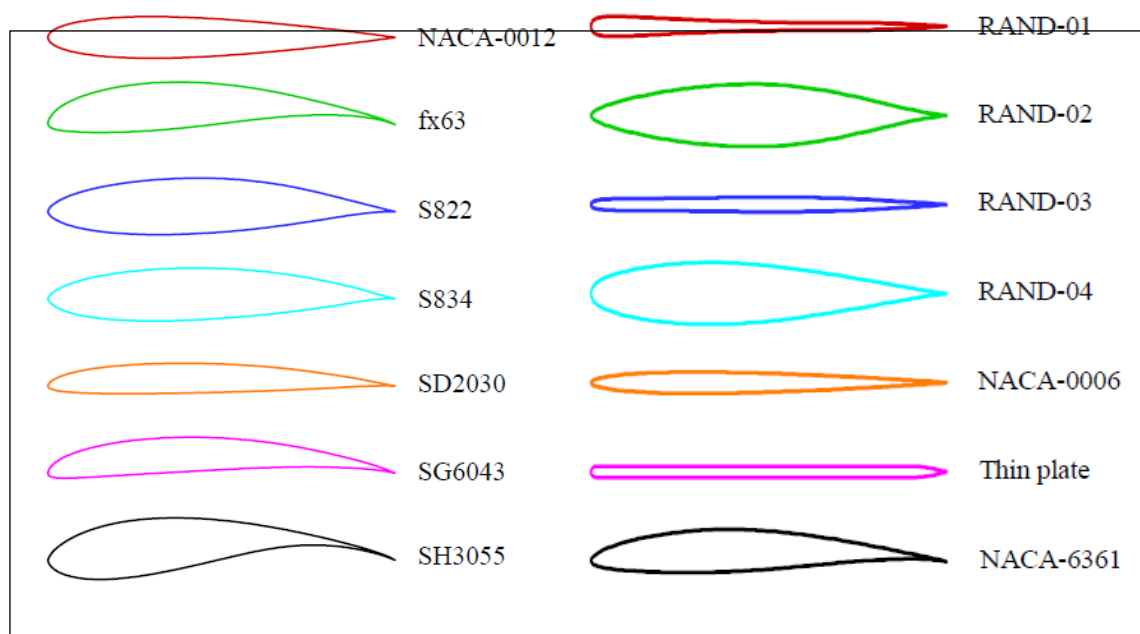


Figure E-5 — Airfoils used for noise prediction and validation in (Moriarty, Guidati, & Migliore, Recent Improvement of a Semi-Empirical Aeroacoustic Prediction Code for Wind Turbines, 2004).

From all the airfoils employed (see Fig. E-5), the SPL spectra predicted for one symmetrical airfoil (NACA 0012) and one heavily cambered airfoil (SH3055) were selected for reproduction here, against noise measurements, as an assessment of the quality of the TNO model, when implemented with XFOIL and many empiric parameters.

Few measured points are available in some comparisons since unidentified noise sources at the midspan edges of the models contaminated the measurements and

were discarded. The authors consider that there is reasonable agreement between measurements and TNO prediction in trends, but discrepancy in the absolute values.

The results are shown below (Figures E-6 and E-7) for both selected airfoils, comparing the measurements, the TNO model prediction and the BPM prediction, with both models fed by XFOIL data for direct performance comparison. However, while pre-testing the BPM/XFOIL results, the authors found that above 5° AOA the BPM model separation noise would dominate the spectrum, increasing SPL at all frequencies. On the other hand, for the measured data, the SPL increased with AOA at low frequencies only, decreasing at high frequencies and resulting in a crossover frequency where the SPL was independent of the AOA, around 2.5 kHz. By neglecting the separation noise module on the BPM model and leaving just the TBL noise from both sides of the airfoil, this crossover phenomenon could be reproduced so that this was the BPM model configuration chosen for the comparison in the following figures.

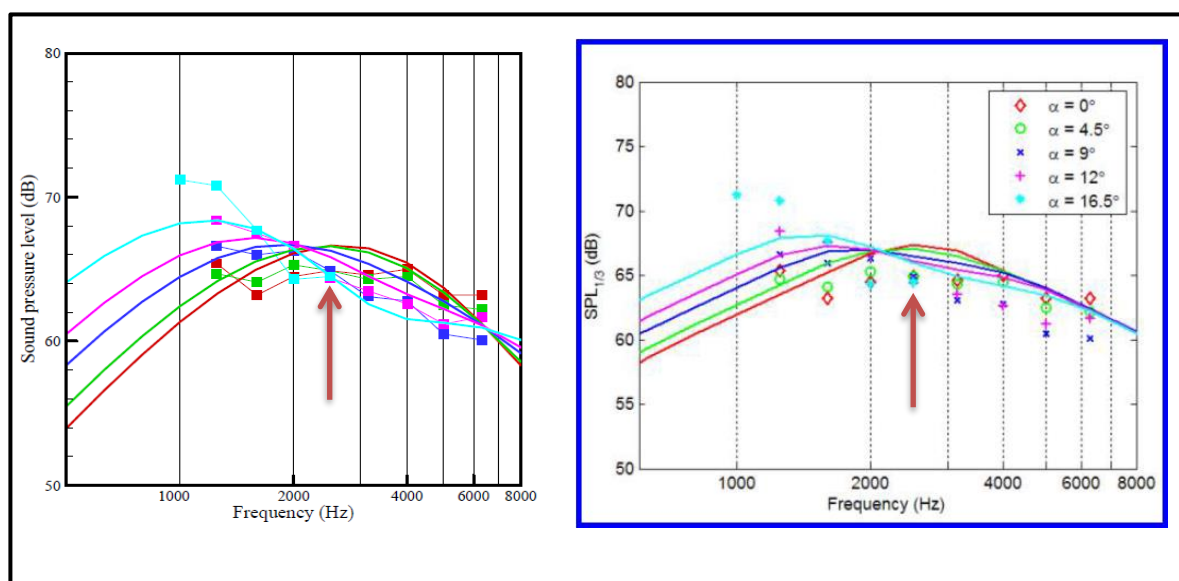


Figure E-6 – Measured (symbols) and predicted (lines) TE noise spectra for the NACA 0012 symmetrical airfoil at various AOA. Left: measurements plotted against TNO model prediction. Right, blue edge figure: measurements plotted against BPM model. See text for detail on models. $Re = 1.1 \times 10^6$. Source: (Moriarty, Guidati, & Migliore, Prediction of Turbulent Inflow and Trailing-Edge Noise for Wind Turbines, 2005), pages 11 and 14.

From this comparison for the NACA 0012 airfoil at AOA from 0° to 16.5° the authors found that the TNO model does a better job of predicting the absolute values while the BPM model would tend to overpredict the measured values.

However, by judging the output of the models by the graphs above it would appear that the prediction are equivalent for both of them, with underprediction at lower and very high frequencies and overprediction in the 1.5 to 5 kHz frequencies. Also the crossover frequency (see red arrow in Fig. E-6), the point for the same airfoil at which the low AOA becomes noisier than the higher AOA, seems to be the same for both TNO and BPM, at around 2.5 kHz (for $Re = 1.1 \times 10^6$).

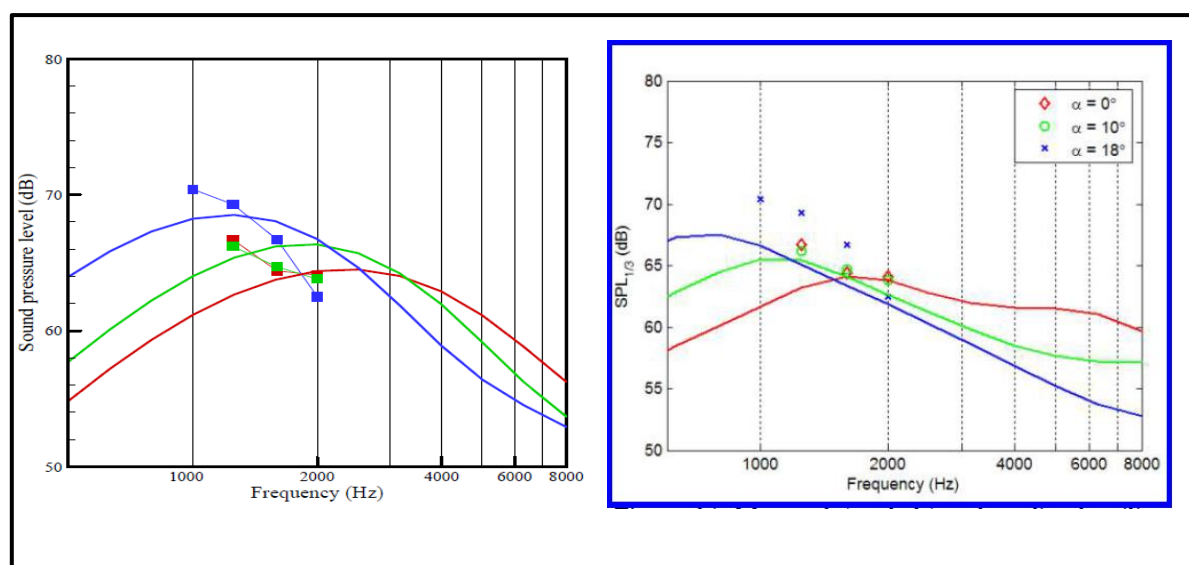


Figure E-7 – Measured (symbols) and predicted (lines) TE noise spectra for the SH3055 cambered airfoil at various AOA. Left: measurements plotted against TNO model prediction. Right, blue edge figure: measurements plotted against BPM model. See text for detail on models. $Re = 1.0 \times 10^6$. Source: (Moriarty, Guidati, & Migliore, Prediction of Turbulent Inflow and Trailing-Edge Noise for Wind Turbines, 2005), pages 12 and 15.

As for the cambered SH3055 airfoil, few experimental points were available. The authors concluded it was difficult to draw conclusions about the relative effectiveness of the prediction models.

One might notice that, at 18° AOA, the BPM model underpredicts significantly the noise spectra. However we should remember that at such large AOA the separation is inevitable without BL control and probably the BPM noise prediction module should not have been kept on.

This important NREL research allowed us to see the first direct performance comparison among the semi-empirical BPM noise prediction model and the simplified theoretical TNO noise prediction model. Although the authors believe that the TNO

model is more accurate, it is reasonable to assume, in light of the data published that the output of the models are qualitatively equivalent, as long as they are both fed by the XFOIL and many empirical correlations are embedded into the potentially more accurate TNO model. Also it seems that because of the difficulty presented by both models in order to predict the behavior along the full spectrum, the accuracy of the models with this implementation method would render both of them more suitable for relative performance comparison among airfoils than to predict absolute SPL value as a function of frequency. Unfortunately no measured and predicted OASPL data were made available by the authors so that the reader could have had a quantitative insight of the relative overall capability of each model when fed by the XFOIL.

E.3 The Glegg-Reba Model

An alternate procedure for estimating the far field sound radiated from a TBL over a sharp TE was proposed by Glegg and Reba (Glegg & Reba, 2010). The concept involves the use of an analytical model of turbulent velocity fluctuations to obtain a description of the two-point statistics of the flow. They showed how the spatial distribution of the turbulent kinetic energy (TKE) can be related to an integral of the local turbulence spectrum multiplied by a function of the mean flow velocity distribution. This relationship leads to the turbulence spectrum required for the calculations of the pressure on the surface beneath the TBL which in turn allows for the calculation of sound radiated to the far field, by using the model of (Howe, 1978).

According to the authors, some previous attempts to pursue this same objective had shown poor agreement with measurements (Lutz, Herrig, Würz, Kamruzzaman, & Krämer, 2007)⁸², while others, employing anisotropic turbulence models showed good agreement (Lee, Blake, & Farabee, 2005).

⁸² Discussed in section 2.6.4

The mathematical derivation of the model proposed by Glegg and Reba (Glegg & Reba, 2010) is very extensive and the resultant model is either fed by measured or estimated TBL parameters via CFD-RANS, which limits its computational efficiency.

The model depends upon TKE profile in the TBL, so that CFD-RANS tools are necessary for providing the flow field data. For validation purposes, the model prediction was fed by parameters derived from RANS calculations around a 2-D NACA 0012 airfoil, so that the resultant TE noise prediction could be directly compared with measured data. The code employed was the Y237 RANS/URANS developed at Pratt & Whitney, used in simulation of turbo-machinery flows, with k, ω turbulence model. Details of the calculation domain, mesh and boundary conditions are described in the original paper with the aim to replicate the measurement conditions as tested by Brooks and Hodgson (Brooks & Hodgson, 1981) and Brooks et al. (Brooks, Pope, & Marcolini, Airfoil Self-Noise and Prediction, 1989), except that the BL was considered fully turbulent from the LE of the airfoil for numerical simulation purposes, while the test data from Brooks and Hodgson (Brooks & Hodgson, 1981) was acquired with tripping at $x/c = 0.15$ and the test data from Brooks et al. (Brooks, Pope, & Marcolini, Airfoil Self-Noise and Prediction, 1989) was acquired for both naturally developing BL and heavy tripped BL. The RANS measurements were done at $x/c = 0.996$, just like Brooks and Hodgson (Brooks & Hodgson, 1981), but unlike Brooks et al. (Brooks, Pope, & Marcolini, Airfoil Self-Noise and Prediction, 1989), who report measurements 1.3 mm downstream from the TE.

The displacement thickness calculated at the NACA 0012 TE, compared to experimental data described is shown in Fig. E-8. It is evident from the figure that there is a broad variation of displacement thickness estimation values, depending upon the method of acquisition (measurement or calculation) and on the regime of the flow (naturally developing, tripped, heavily tripped or fully turbulent), which leads to a natural question concerning the sensitivity of noise prediction methods, both semi-empirical and simplified theoretical, that employ this parameter as a BL turbulence scale parameter. This important question is duly addressed in Section 3.4 of the present work.

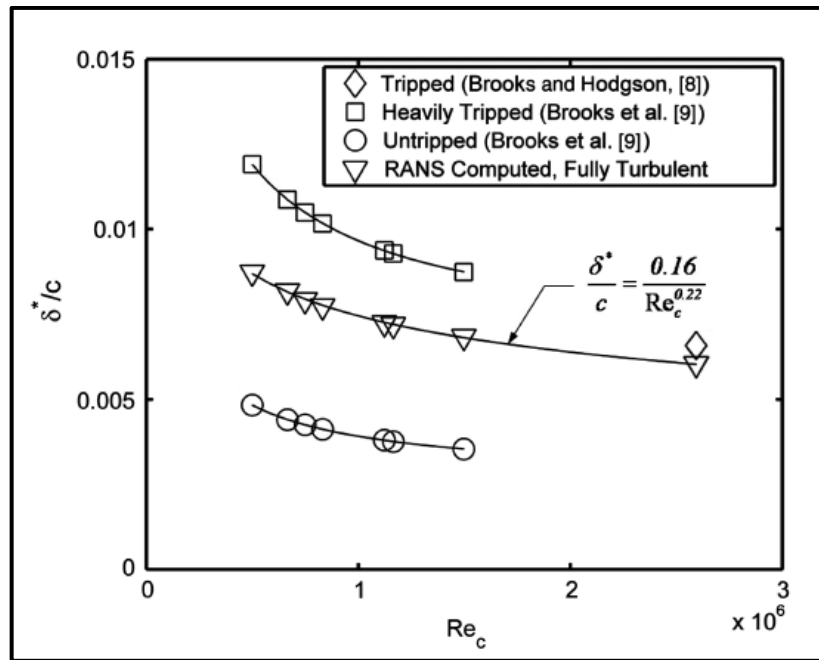


Figure E-8 – Comparison of $\delta^*/chord$ calculated with RANS, with experimental data from (Brooks & Hodgson, 1981) and (Brooks, Pope, & Marcolini, Airfoil Self-Noise and Prediction, 1989). $Re_c = chord \text{ based Reynolds number}$. Source: (Glegg & Reba, 2010), p. 1297.

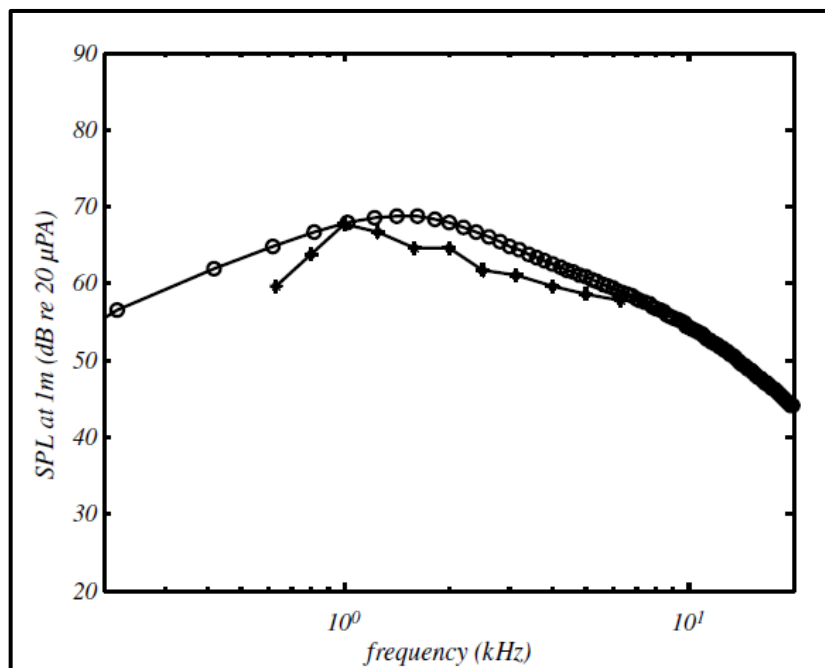


Figure E-9 – Comparison of SPL predicted spectrum (\circ) of the TE noise from a NACA 0012 airfoil (observer at 90° to the airfoil chord) against measurements from (Brooks & Hodgson, 1981) ($+$). Airfoil chord is 0.6096 m and flow speed is 69.5 m/s . Source: (Glegg & Reba, 2010), p. 1.298.

Glegg and Reba (Glegg & Reba, 2010) considered the agreement good between the predicted spectrum and the ones measured by Brooks and Hodgson (Brooks &

Hodgson, 1981) for the higher tested flow speeds (e.g. Fig. E-9). However, at lower flow speeds (see Fig. E-10) the model tended to overestimate the noise for low frequencies and underestimate the noise for higher frequencies by 2 dB, a shift attributed by them possibly to the RANS modelling of the BL tripping.

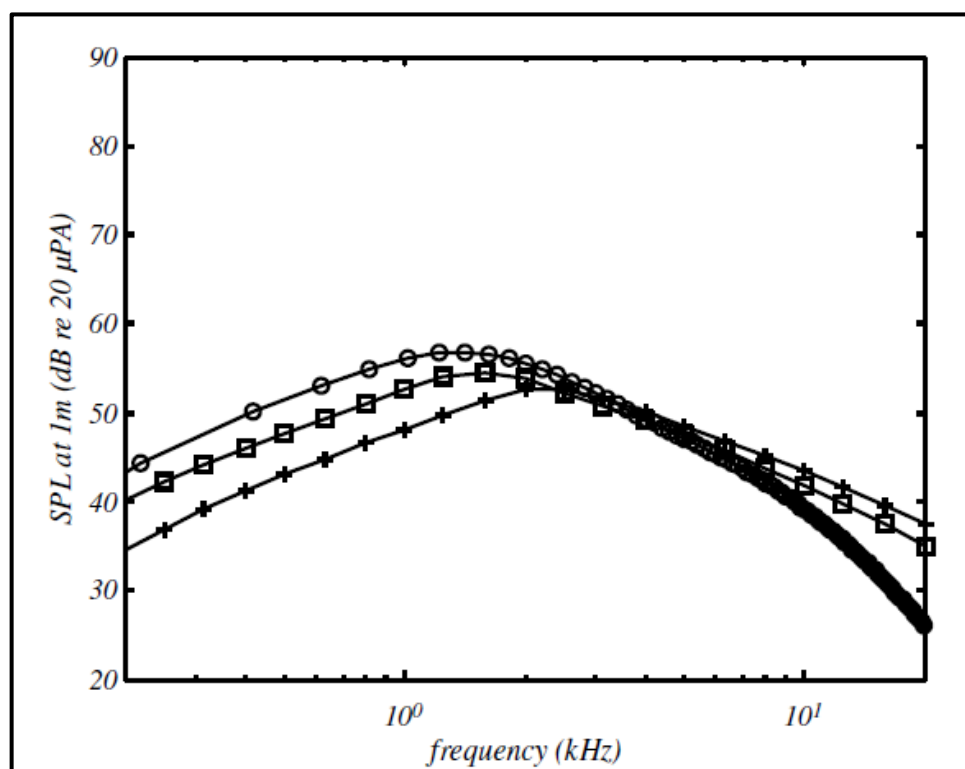


Figure E-10 – Comparison of SPL predicted spectrum (\circ) of the TE noise from a NACA 0012 airfoil (at 90° to the airfoil chord) against the empirical prediction of the BPM method (Brooks, Pope, & Marcolini, Airfoil Self-Noise and Prediction, 1989). Airfoil chord is 0.3028 m and flow speed is 39.6 m/s.; untripped (+); lightly tripped (\square); Re_c = chord based Reynolds number. Source: (Glegg & Reba, 2010), p. 1298.

Finally, a prediction was made for the TE noise of a small, 1.2 m diameter aircraft engine rotor and compared to aeroacoustic wind tunnel data measurements. The resultant data suffered from interference from the blade cascade disposition in the rotor and is of less relevance for the current investigation, but was considered consistent by the authors.

The overall prediction capability of the Glegg-Reba model seems very close to the semi-empirical methods discussed earlier, but rather more intensive in computational effort. For comparison purposes see the work of Zhu (Zhu, 2004), in Section D.8.

E.4 The IAGNoise Method (IAG II)

Concerning the simplified theoretical approach for TE noise prediction, the group from IAG (Stuttgart) reported by Guidati and Wagner (Guidati & Wagner, 2000) the effort to develop new, quieter airfoils for WT application, theoretically designed with the TNO prediction model in mind. The TNO model was fed with XFOIL dynamic field data⁸³ and the results concerning the new airfoil proposals were not completely satisfactory.

The group continued to develop the XFOIL-TNO method (Lutz, Würz, Herrig, Braun, & Wagner, 2004), improving the boundary layer profile available in the XFOIL code. However, because of limitations intrinsic to the XFOIL method (Drela & Giles, Viscous-Inviscid Analysis of Transonic and Low Reynolds Number Airfoil, 1987), i.e. the BL history of development is not directly calculated and also the lack of modeling of the anisotropic behavior of the turbulent fluctuations, the method was expected to be applicable solely to equilibrium boundary layers and not so well to situations of strong pressure gradients and extended laminar flows, which proved to be the case, according to the authors.

Later, the TNO model was coupled with a more detailed calculation method of the BL turbulence properties and a new semi-empirical scaling law for the vertical integral length scale aimed at increasing the consistency of the airfoil noise prediction (Lutz, Herrig, Würz, Kamruzzaman, & Krämer, 2007). The main goal was to develop new airfoil profiles for the outer part of large size HAWTs (1 – 2 MW) with potential for noise reduction but without loss in aerodynamic performance, under the European SIROCCO project. In this effort, the TNO model was coupled to the finite-difference EDDYBL code developed by Wilcox (Wilcox, 2010), which was capable of discretizing the BL both in streamwise and normal directions, leading to the mean velocity profile and time-averaged turbulence data distribution as a direct result of the calculations. Also the Wilcox *stress* – ω turbulence model allowed for anisotropy effect accounting

⁸³ This was probably the first attempt to do so for the TNO model. Please notice that this research was accomplished prior to the Moriarty et al. (Moriarty, Guidati, & Migliore, Recent Improvement of a Semi-Empirical Aeroacoustic Prediction Code for Wind Turbines, 2004) paper described at section 2.15.2 and it is presented in this section, out of chronological order, so as to join the other researches of the IAG on the WTN subject, which spanned more than a decade.

and provided the complete Reynolds Stress tensor. In this new method, the XFOIL was employed only in order to provide initial and boundary conditions.

As required by the TNO model, the problem was solved in two steps, (a) the description of the spectrum of the surface pressure fluctuations induced by the turbulent eddies at the TE was obtained and, (b) a diffraction problem was solved for the determination of the noise emitted by the TE due to the fluctuating pressure.

In the course of their investigations, Lutz et al. (Lutz, Herrig, Würz, Kamruzzaman, & Krämer, 2007) found that the determination of the vertical integral length scale Λ_2 was the most relevant aspect concerning consistency of the noise prediction method, however it was not derived from any established turbulence model or boundary layer calculation. It was then developed and proposed a method for calculating the integral length scale directly from the turbulence kinetic energy k_T and the turbulent dissipation rate ε provided by the Wilcox (Wilcox, 2010) *stress, ω* turbulence model:

$$\Lambda_2 \approx 0.387 \cdot \frac{(k_T)^{\frac{3}{2}}}{\varepsilon} \quad (E - 3)$$

This approach improved Λ_2 predictions against measurement, but additional scaling had to be made by the authors (an empirical multiplier to Λ_2 as a function of the pressure gradient, or “loading parameter” as referred to in the paper) to match experimental results for Λ_2 measurements. The discrepancies were again attributed to the anisotropic behavior of the turbulence length scales.

The effect of this new scaling method for Λ_2 , with and without the scaling law (empirical multiplier), on the SPL spectrum may be seen in Fig. E-11.

However, it would seem that the shift caused by the Λ_2 with the scaling law reinforces the characteristics of the TNO noise prediction model of overprediction in low frequencies and underprediction in high frequencies, as discussed before in the review of Glegg and Reba (Glegg & Reba, 2010)⁸⁴.

⁸⁴ The (Glegg & Reba, 2010) paper was exceptionally reviewed out of chronological order so that the many papers by the group from IAG, spanning 2007-2012, could be reviewed in sequence, under the same section number.

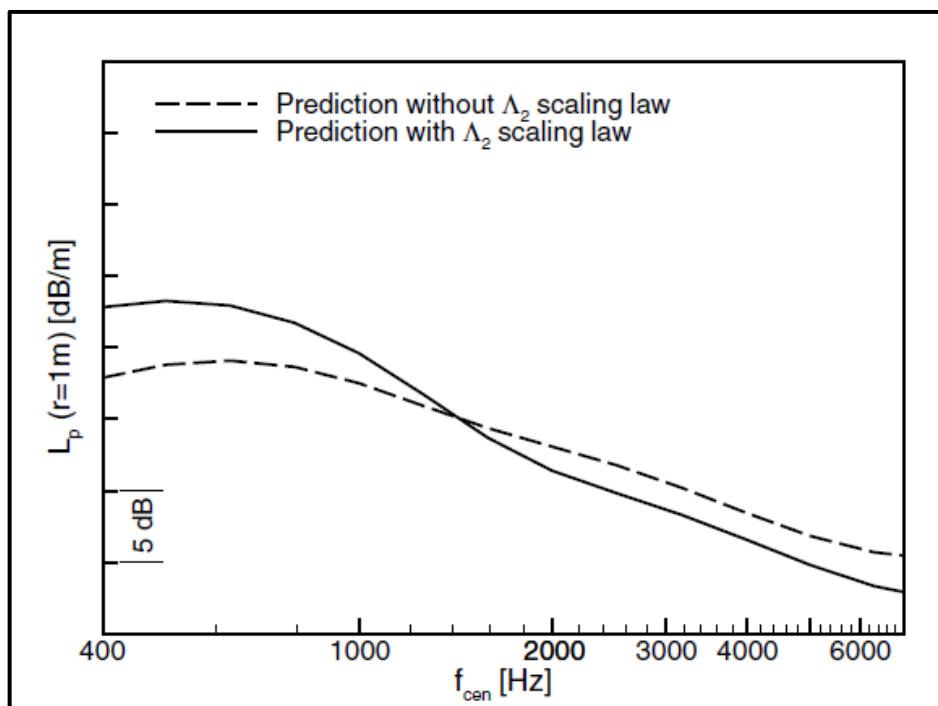


Figure E-11 – The effect on the SPL spectrum, of the proposed empirical scaling law (a multiplier as a function of pressure gradient) over Λ_2 . Source: (Lutz, Herrig, Würz, Kamruzzaman, & Krämer, 2007), p. 782.

Further results of the research by Lutz et al. (Lutz, Herrig, Würz, Kamruzzaman, & Krämer, 2007) were discussed in Section E-1 (Fig. E-4), where it was found a significant shift in prediction (underprediction by 5 – 10 dB) along all frequencies of the spectrum, when compared to measured data, for a series of 2-D airfoils.

The method developed at the IAG evolved towards the IAGNoise method (Kamruzzaman, Meister, Lutz, Kühn, & Krämer, 2010), (Kamruzzaman M. , Lutz, Nübler, & Krämer, 2011), (Kamruzzaman M. , et al., 2012b). The IAGNoise is a quasi 3-D WT rotor aeroacoustic simulation tool developed at the University of Stuttgart - Institute of Aerodynamics and Gas Dynamics, IAG.

The tool is also based on the TNO-Blake model for TE noise prediction, and the authors stress that the accuracy of the noise prediction via Eqn. (2.6.1-1) is a reflection of the accuracy in modelling the turbulent noise source terms $\phi_{22}(y_2, k_1, k_3)$, Λ_2 , $\langle u_2^2(y_2) \rangle$, and so, three aerodynamic analysis methods were coupled to the TNO-Blake model in order to investigate their relative performance: the panel integral BL code XFOIL⁸⁵

⁸⁵ It is interesting to note that, despite warnings from many authors concerning the relevance of detailed description of turbulent field variables for TE predictions with simplified theoretical models, the XFOIL

(Drela & Giles, Viscous-Inviscid Analysis of Transonic and Low Reynolds Number Airfoil, 1987), (Drela, Youngren, & Deperrois, XFOIL/XFLR5, 2009), the finite-difference BL code developed by Wilcox (EDDYBL) and a RANS flow solver developed at the IAG (FLOWer). Each combination of the TNO-Blake model with an aerodynamics code was given a specific name, for identification purpose, Xnoise for the XFOIL based code, XEnoise for the EDDYBL code and Rnoise for the Rans flow solver FLOWer. Latter, the NREL NAFNoise code, based on the semi-empirical BPM model was also incorporated for comparison purposes and the control module, with graphical user interface, that integrated all the modules was called the "IAGNoise", and is illustrated in Fig. E-4.

Because field measurements had conclusively indicated at this time (Oerlemans, Wind Turbine Noise: Primary Noise Sources, 2011) that the TE noise was the dominant noise source for large WT, this was the only noise source modelled into the IAGNoise modules.

The validation was accomplished in phases, starting with the 2-D airfoil TE noise spectra for checking the accuracy of the different BL calculations approaches. The wall normal distributions for the predicted turbulence noise source parameters ($\langle u_2^2 \rangle$, Λ_2 and $U_1(y_2)$), were obtained at $0.99c$, for the three calculation methods employing NACA 0012 airfoil at $Re = 1.5 \times 10^6$, $M = 0.166$ and $AOA = 0^\circ$, and were compared with wind tunnel measurement data.

integral method is often considered as the prime candidate for feeding the TE noise prediction model variables. This is probably due to its very efficient computational procedure and broad adoption in academia and industry.

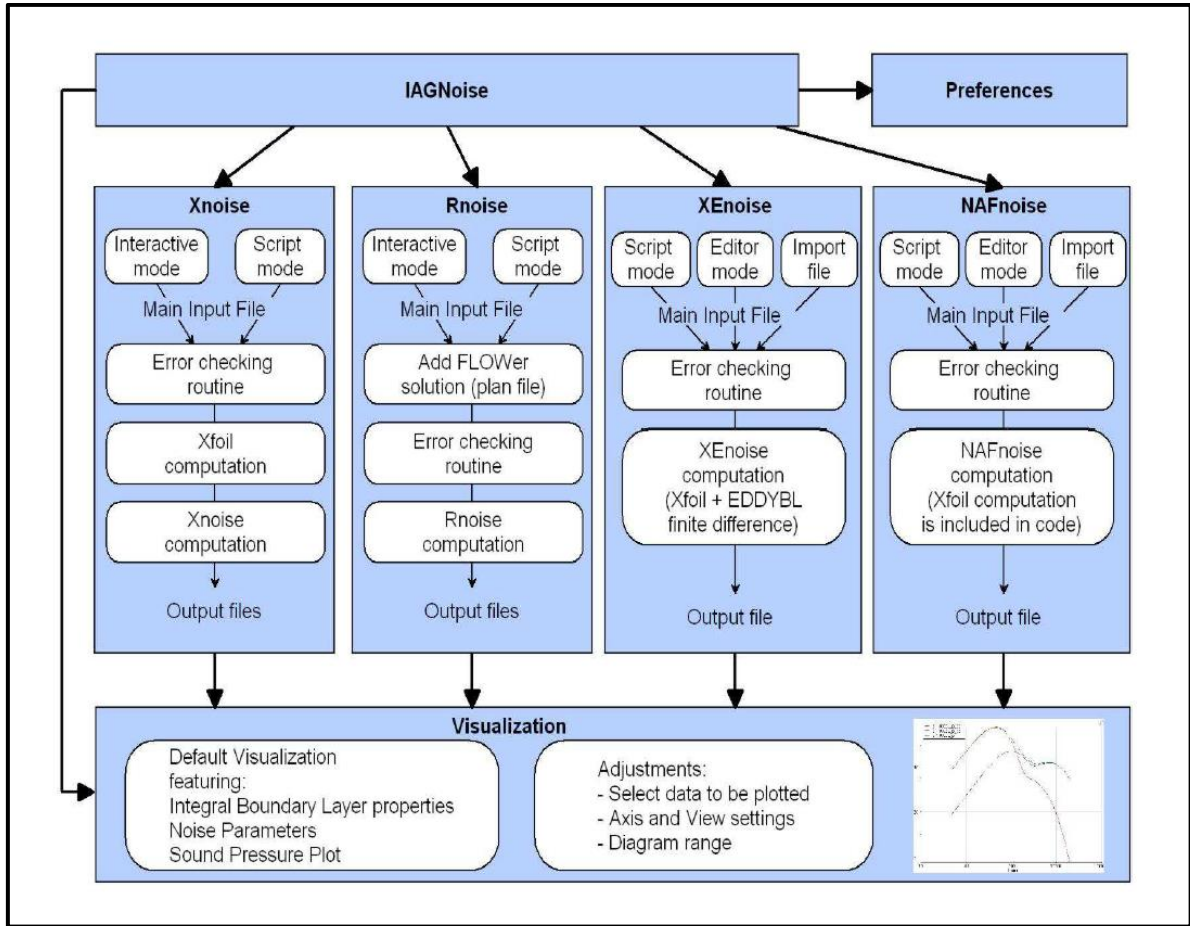


Figure E-12 – The IAGNoise controlling interface flow diagram and its internal modules. Source: (Kamruzzaman, Meister, Lutz, Kühn, & Krämer, 2010)

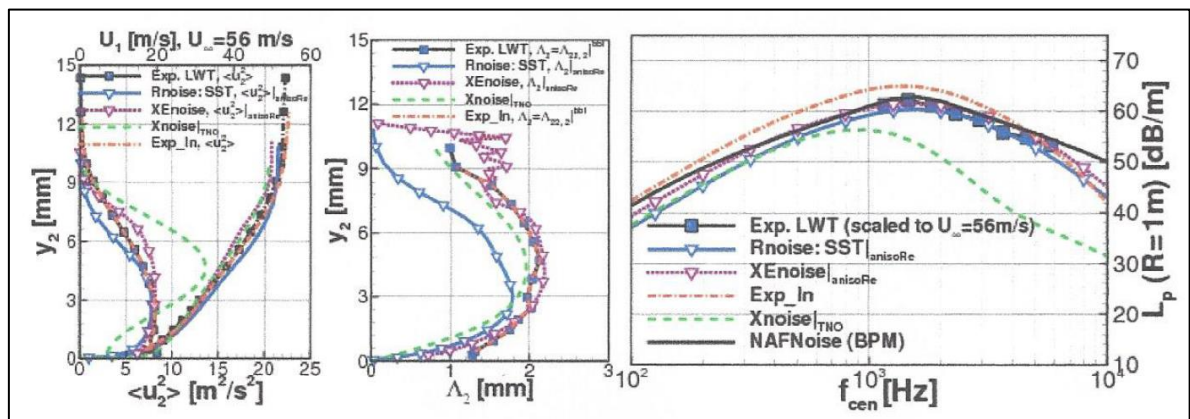


Figure E-13 – Noise sources parameters calculated by Xnoise (green dotted line), XEnoise (magenta dotted line), Rnoise (blue line with triangles), experimental data fed into the TNO-Blake model (orange dotted line) and experimental measurement (black line with squares). Source (Kamruzzaman M. , Lutz, Nübler, & Krämer, 2011).

The examination of Fig. E-13 yields many important conclusions:

- The velocity profile ($U_1(y_2)$) is reasonably good for all methods.
- The vertical velocity fluctuations ($\langle u_2^2(y_2) \rangle$) are well predicted by XNoise and Rnoise but a large disagreement is found for Xnoise (XFOIL based prediction). The difference in prediction capability for this parameter is attributed by the authors to the turbulence anisotropy modelling developed at the IAG, explained in more detail by Kamruzzaman et al. (Kamruzzaman M. , Lutz, Herrig, & Krämer, 2012a) and implemented into the XNoise and Rnoise tools, but not in Xnoise. The anisotropy modeling is important and will be discussed in further detail in this section.
- However, for the integral turbulent length scale Λ_2 distribution, the Xnoise prediction was better than that of Rnoise and a fluctuation of values from the XNoise model is visible at $y_2 > 9 \text{ mm}$.
- The impact of the input of all noise source parameters into the total predicted far-field noise levels at $r = 1 \text{ m}$ distance shows that the Xnoise underpredicts the measured spectra in a strong manner for frequencies above 1 kHz.
- The authors considered that the results from Xnoise had to be shifted by + 8 dB in order to be employed for further TE noise predictions.

It is also worth noticing that the inclusion of results from the NAFnoise (NREL, BPM based) shows that the BPM model, which is not fed with detailed turbulence field information, is capable of predicting the full spectrum with comparable or better accuracy and much simpler approach than Rnoise and XNoise, for the NACA 0012 airfoil at $Re = 1.5 \times 10^6$. However, this is the exact airfoil and Reynolds number range of the experimental data from which the BPM model was developed.

All further validation steps would employ the quasi 3-D method calculations using either the BPM TE model embedded inside IAGNoise (NAFNoise), or Xnoise method (XFOIL + TNO-Blake model) corrected by 8 dB, compared to calculated noise spectra for the Bonus 300 WT obtained by Zhu (Zhu, 2004) and also employed by Vargas (Vargas L. d., 2008), both previously discussed. The results generally showed underprediction along all spectra, but the shift was attributed to the inflow noise, not computed in the method but nevertheless deemed a dominant contribution for the specific case. These validations were little relevant for this quest concerning the understanding of the prediction capability of the modified TNO-Blake model, except for the fact that it does not seem appropriate, ex-ante, to feed a complex TE noise model, which depends upon many turbulent flow variables, with a simple, integral BL method

like XFOIL. It seems that a basic coherence of model order should be maintained in all methods employed throughout the noise prediction effort.

The IAG group continued to pursue improvement of the TE noise prediction method based on the modified TNO-Blake model, under the European Wind Energy Project (UpWind). After ruling out the XFOIL as a suitable dynamic field data provider for TNO-based noise prediction models, Kamruzzaman et al. (Kamruzzaman M. , Lutz, Herrig, & Krämer, 2012a) focused on steady CFD-RANS for the parameter evaluation of the turbulent field, due to reliability in performance. However, because the flow at the TE and in the near wake of an airfoil TE has inhomogeneous and anisotropic turbulence characteristics, most standard two-variable turbulence models, which are based on homogeneous and isotropic theory, would suffer from accuracy problems as well. The authors thus considered the modeling of the real anisotropic turbulent velocity field from mean flow properties as a crucial step for RANS-fed, TNO-based methods of noise prediction. The anisotropy modeling method, which was at least partially applied in Kamruzzaman et al. (Kamruzzaman M. , Lutz, Nübler, & Krämer, 2011), is described in detail in Kamruzzaman (Kamruzzaman M. , Lutz, Herrig, & Krämer, 2012a) and is the result of a search for an alternative, enhanced anisotropy scaling method, compared to the method proposed previously in Lutz et al. (Lutz, Herrig, Würz, Kamruzzaman, & Krämer, 2007), which resulted in a 5 – 10 dB noise underprediction throughout the spectrum as shown in Fig. E-4.

The enhanced anisotropy scaling method is based on the multiplication of the vertical velocity fluctuations $\langle u_2^2(y_2) \rangle$ and the integral length scale of the eddy field Λ_2 , by a proposed semi-empirical anisotropy scaling factor, as a function of Reynolds number based on the Taylor's microscale, $f_{22}^{aniso}(Re_\lambda)$:

$$\langle u_2^2 \rangle|_{aniso} = \frac{2}{3} k_T \cdot f_{22}^{aniso}(Re_\lambda) \quad (E - 4)$$

$$\Lambda_2(y_2)|_{aniso} = \Lambda_2|_{iso} \cdot \left(f_{22}^{aniso}(y_2) \right)^{\frac{3}{2}} \quad (E - 5)$$

The semi-empirical anisotropy scaling function can be derived from the relation below, from experimental data (Fig. E-14) or full RSM⁸⁶-based RANS simulation:

$$f_{22}^{aniso} = \frac{\langle u_2^2 \rangle}{\frac{2}{3} k_T} \quad (E - 6)$$

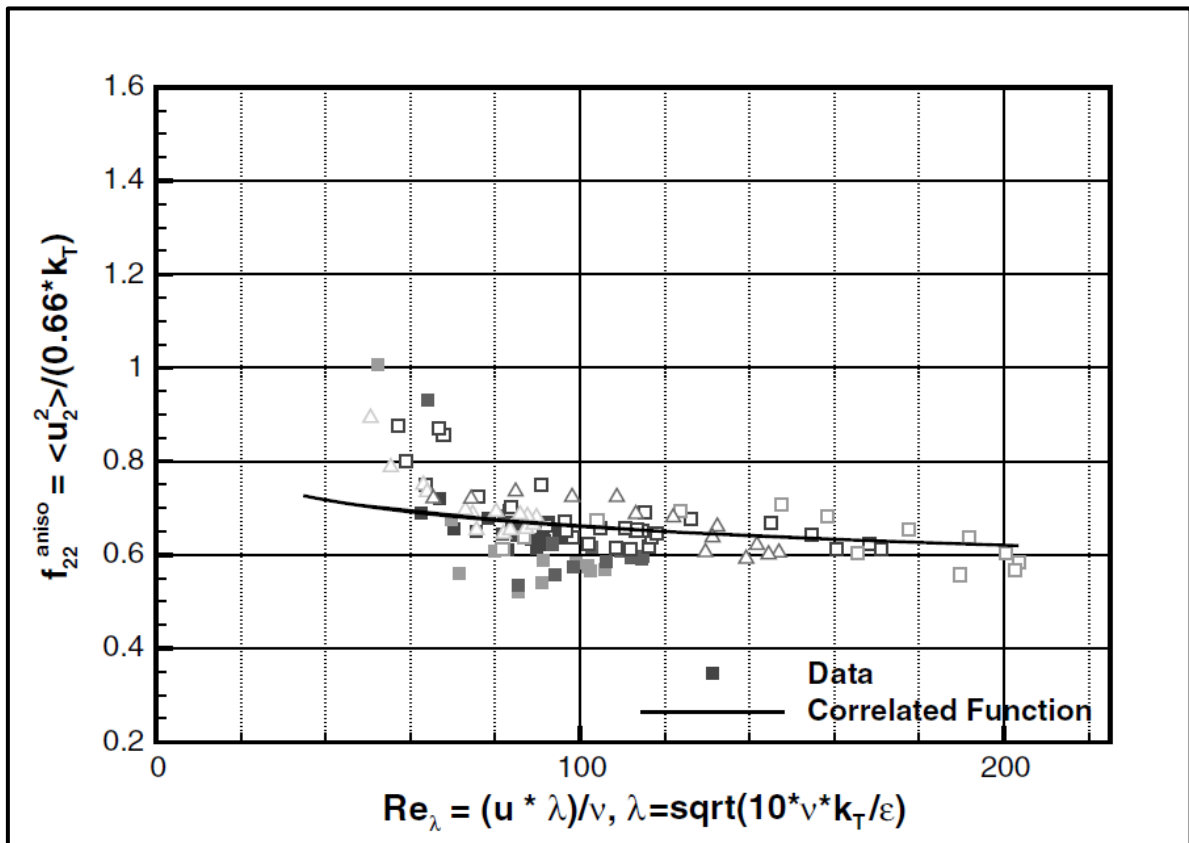


Figure E-14 – Correlated anisotropy scale function f_{22}^{aniso} based on Re_λ . Data from five different airfoil BL measurements at Reynolds number range $0.8 \times 10^6 - 3.0 \times 10^6$, varying AOA and BL tripping applied. Source (Kamruzzaman M. , Lutz, Herrig, & Krämer, 2012a), p. 56.

By comparing the results of the RANS shear stress transport (SST) k, ω turbulence model (Wilcox, 2010) employed in RNoise for this research, with wind tunnel measurement data, the authors found the wall-normal velocity distribution U_1 to be reasonably good, with an increasing overestimation shift for higher AOA, resulting in a corresponding underestimation of the TBL integral parameters that also increases for higher AOA. In the case of $\langle u_i^2 \rangle$ the use of the anisotropic model just discussed led to reasonable agreement for zero AOA, but underpredicted the measured data for the 4°

⁸⁶ In the case of a full RSM-based RANS simulation, there is no need for the semi-empirical function $f_{22}^{aniso}(Re_\lambda)$ (Kamruzzaman M. , Lutz, Herrig, & Krämer, 2012a), p. 56.

AOA, both in the streamwise Reynolds stress $\langle u_1^2 \rangle$ as in the normal Reynolds stress $\langle u_2^2 \rangle$. This decrease in Reynolds stress estimation was attributed to the underestimation of the kinetic energy, $\frac{2}{3}k_T$. All calculated data is shown compared to experimental values in Fig. E-15.

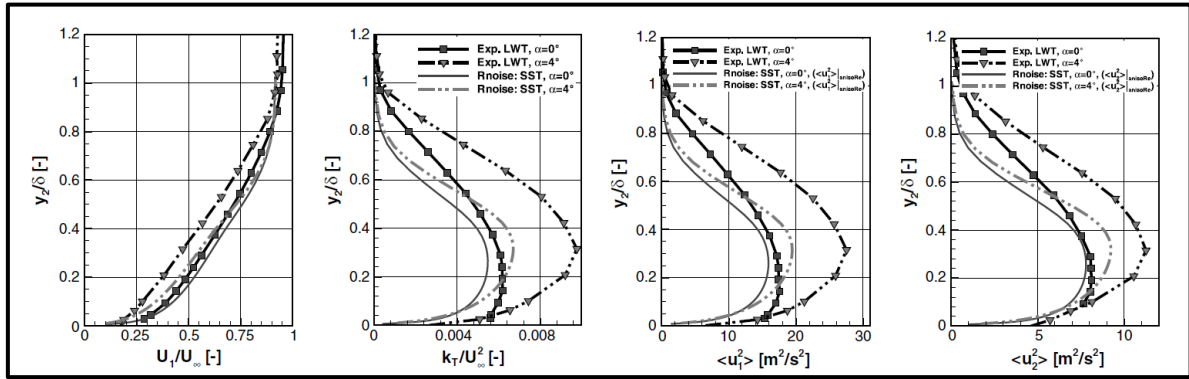


Figure E-15 – Wind Tunnel TBL data (Exp. LWT) for a NACA 0012 at $Re = 1.5 \times 10^6$; $M = 0.166$; $y_1/c = 0.999$ and AOA of 0° and 4° , against RANS calculation by RNoise (Rnoise:SST), employing Menter's $SST k, \omega$ two-equation turbulence model. Source (Kamruzzaman M. , Lutz, Herrig, & Krämer, 2012a), p. 57.

Since $\langle u_2^2 \rangle$ depends upon the anisotropy scaling function Eqn. (E-4) and the RANS-predicted $\frac{2}{3}k_T$, the authors concluded that any inaccuracy of the RANS-predicted k_T and ε results would directly impact the proposed anisotropy scaling model. By examining the wall-normal ε distribution against experimental data, they found that the $SST k, \omega$ model estimates (ε^*) would also significantly overestimate the data, especially close to the wall, at the inner region of the BL. As a consequence, the RANS-predicted integral longitudinal length scale $(\Lambda_f|_*)$ is very low compared with measurements (see Fig. E-16). This behavior or RANS near-wall dissipation is considered a common limitation of the two-equation turbulence models (Wilcox, 2010), since they rely on the log layer region of the BL, i.e. the turbulence production is equal to the scalar isotropic mean dissipation rate, ε^* used in the models

$$\varepsilon^* = -\langle u_1 u_2 \rangle \frac{dU_1}{dy_2} \quad (E - 7)$$

while for isotropic homogeneous flow

$$\varepsilon = \frac{1}{2} \epsilon_{ij} = 2\nu \left\langle \frac{du_i}{dx_k} \frac{du_j}{dx_k} \right\rangle \quad (E - 8)$$

The authors point out that this difference in definition make the two-equations models fail to agree satisfactorily with experiments in the viscous sublayer, unless the coefficients are made empirical functions of as appropriate Reynolds Number. Therefore, a function relating ε and ε^* was introduced

$$\frac{\varepsilon}{\varepsilon^*} = f(y^+) = c_5 \cdot \left(\frac{c_1}{c_3}\right) \cdot (y^+)^{c_2 - c_4} \quad (E - 9)$$

Since the equation was derived empirically for TBL measurements over a flat plate, some of the original values of the constants ($c_1 = 1.2$; $c_2 = 1.1$; $c_3 = 0.03$; $c_4 = 0.8$; $c_5 = 15$) were dropped in favor of values that would consider the pressure gradient effect ($c_2 - c_4 = 0.28$; $c_5 = 12$), although such values were only “initial guesses” as described by the authors. The application of this corrected dissipation to the *SST* k, ω two-equation turbulence model resulted in a better capture of the turbulent mean dissipation ε , as shown in Fig. E-16, with better improvements for lower AOA measurements.

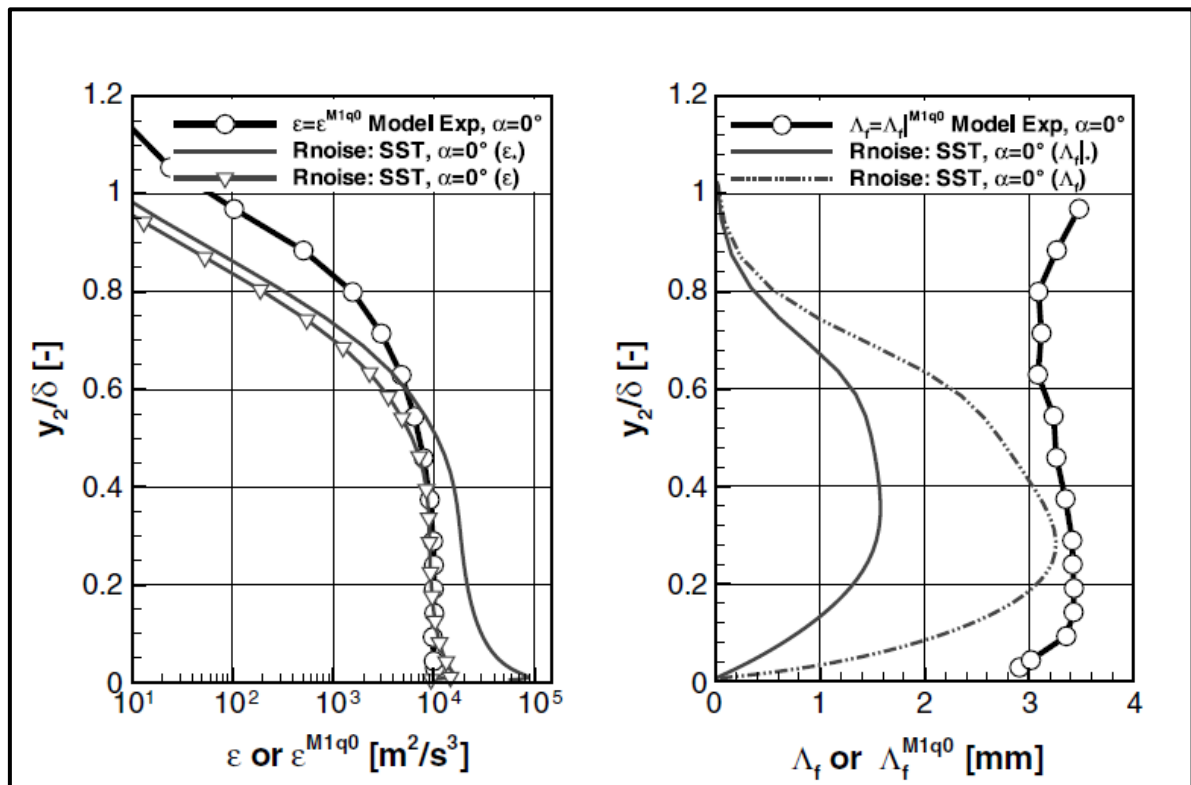


Figure E-16 – Wind Tunnel TBL data (Model Exp.) for a NACA 0012 at $Re = 1.5 \times 10^6$; $M = 0.166$; $y_1/c \approx 1.004$, against RANS calculation by RNoise (Rnoise:SST), employing Menter's *SST* k, ω two-equation turbulence model. ε_* and $\Lambda_f|_*$ values are direct RANS-calculated values. ε and Λ_f values use a near-wall correction formula. Figures shown are for 0° AOA only, for clarity. Figures for 4° show similar trends, although authors state the correction presented better results for lower AOA. Source (Kamruzzaman M. , Lutz, Herrig, & Krämer, 2012a), p. 57.

All improvements discussed (dissipation and length scale correction) were adopted by the authors (Kamruzzaman M. , Lutz, Herrig, & Krämer, 2012a). Substitution of anisotropic relations Eqns. (E-4) and (E-5) on the Eqn. (E-1) for the spectrum of the wall pressure fluctuations (*WPF*) underneath a *TBL*, results:

$$\mathbf{P}(k_1, k_3, \omega) = 4\rho^2 \left(\frac{k_1^2}{k_1^2 + k_3^2} \right) \int_0^\infty \Lambda_2(y_2) \left[\frac{dU_1}{dy_2} \right]^2 \cdot \Lambda_2|_{iso} \cdot \tilde{\phi}_{22}^{iso}(y_2, k_1, k_3) \cdot \left[\frac{2}{3} k_T \right] \cdot \phi_m^{iso} \cdot e^{-2|K|y_2} [f_{22}^{aniso}(y_2)]^4 dy_2 \quad (E - 10)$$

where $\tilde{\phi}_{22}(y_2, k_1, k_3) = \phi_{22}(y_2, k_1, k_3)/\langle u_2^2(y_2) \rangle$ is the normalized wavenumber spectrum of the vertical velocity fluctuations $\langle u_2^2(y_2) \rangle$, Λ_2 is the integral length scale for the eddy field, ϕ_m is the moving axis spectrum, $U_1(y_2)$ is the streamwise mean velocity, $U_c \cong 0.8U$ is the mean convective velocity of wall pressure fluctuations and y_2 is the normal wall coordinate.

For $f_{22}^{aniso}(y_2) = 1$, Eqn. (E-10) decays into the isotropic case, Eqn. (E-1)

The far field sound pressure power density spectrum can be evaluated by the TNO-Blake model diffraction integral for a semi-infinite flat plate, already presented, and reproduced here for convenience:

$$S(\omega) = \frac{L}{2\pi r^2} \int_0^\infty \frac{\omega}{c_0 k_1} \mathbf{P}(k_1, 0, \omega) dk_1 \quad (E - 2)$$

where $S(\omega)$ is the far field spectra (power spectral density) of the scattering pressure, L is the airfoil span (wetted length of the TE), r is the distance from the TE to the observer, k_1 is the wavenumber in the y_1 (streamwise) coordinate direction and $\mathbf{P}(k_1, 0, \omega)$ is the wavenumber-frequency ($k - \omega$) spectrum.

By assuming $f_{22}^{aniso} = constant$ (the very small variation of f_{22}^{aniso} with Re_λ is shown in Fig. E-14), the far field spectrum in terms of sound pressure level may be approximated in the following manner, after Eqn. (E-10) has been combined with Eqn. (E-2):

$$SPL(f) = 10 \cdot \log \left[\frac{(f_{22}^{aniso})^4 \cdot S(\omega) \cdot df}{4 \times 10^{-10}} \right] \quad [dB] \quad (E - 11)$$

The following figure (Figure 17) reveals the results from this IAG second, enhanced anisotropic model (Kamruzzaman M. , Lutz, Herrig, & Krämer, 2012a), which are essentially the same types of plots discussed previously by Kamruzzaman et al. (Kamruzzaman M. , Lutz, Nübler, & Krämer, 2011), except for the exclusion of the Xnoise, NAFnoise and XEnoise methods, and focus on the Rnoise, which incorporated the enhanced anisotropy modeling.

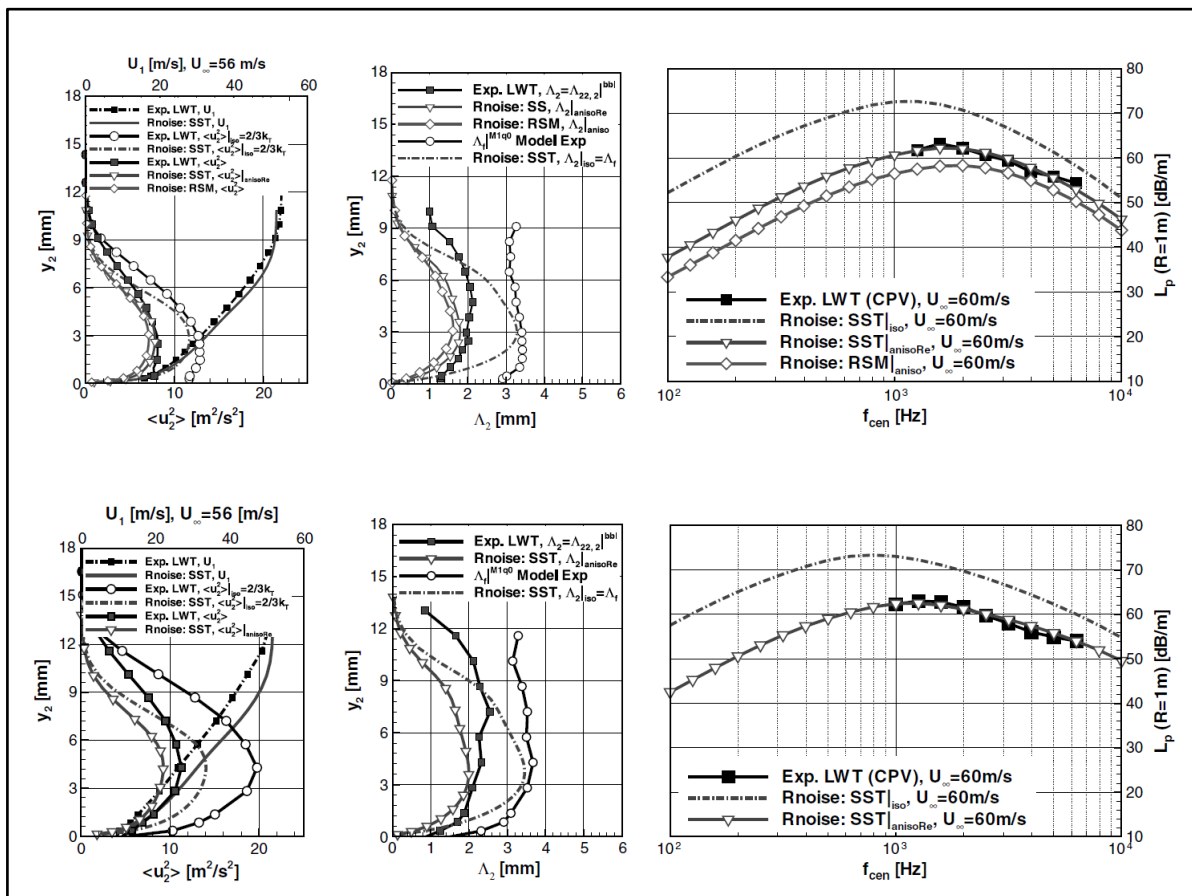


Figure E-17 – Noise sources parameters. Validation of the enhanced anisotropy scale function for TBL-TE noise prediction. NACA 0012 at $Re = 1.5 \times 10^6$; $M = 0.166$. $AOA=0^\circ$ (upper figure) and $AOA=4^\circ$ (lower figure). Experimental values (Exp. LWT); direct $SST k, \omega$ RANS-calculated values (Rnoise:SST/iso); $SST k, \omega$ RANS-calculated values corrected for both anisotropy and dissipation (Rnoise:SST/anisoRe); *Reynolds Stress Modeling RSM* RANS-calculated values (Rnoise:RSM/aniso). Source (Kamruzzaman M. , Lutz, Herrig, & Krämer, 2012a), p. 58-59.

From the right-hand plots on Fig. E-17 it can be seen that feeding Rnoise with RANS isotropic data from the SST turbulence model will lead to an overprediction of the far field noise spectra (for directivity function $D_h = 1$), of about 10 dB, however, the Rnoise

fed by the RSM-RANS anisotropic data (which renders the anisotropy corrections unnecessary), underpredicts the measured spectrum by only 2 to 4 dB and by applying the *SST* k, ω RANS model, corrected not only for velocity fluctuation anisotropy but also for the turbulent dissipation rate, ε , the results are very good compared to measured data. The main conclusion of the authors is that accuracy and consistency of TBL-TE noise prediction is highly dependent upon the accurate modeling of the turbulent flow structure near the airfoil TE. The corrections developed are helpful in the CAA steady-RANS-based stochastic noise generation prediction method, where accurate evaluation of the turbulence length scale and anisotropic Reynolds stresses are important.

In a paper developed concurrently and published at about the same time, Kamruzzaman et al. (Kamruzzaman M., et al., 2012b) also published measurements (Figure E-18) for the non-symmetrical NACA 643-418 airfoil, at $Re = 2.5 \times 10^6$; $M = 0.184$, plotted against numerical solutions from the Rnoise and from the RISO-developed RANS solver (RISOE), both employing isotropic turbulence modeling for the *SST* $k - \omega$ turbulence model. However, no result was published comparing the measured spectra against the results from RANS-based methods corrected with the enhanced anisotropy model.

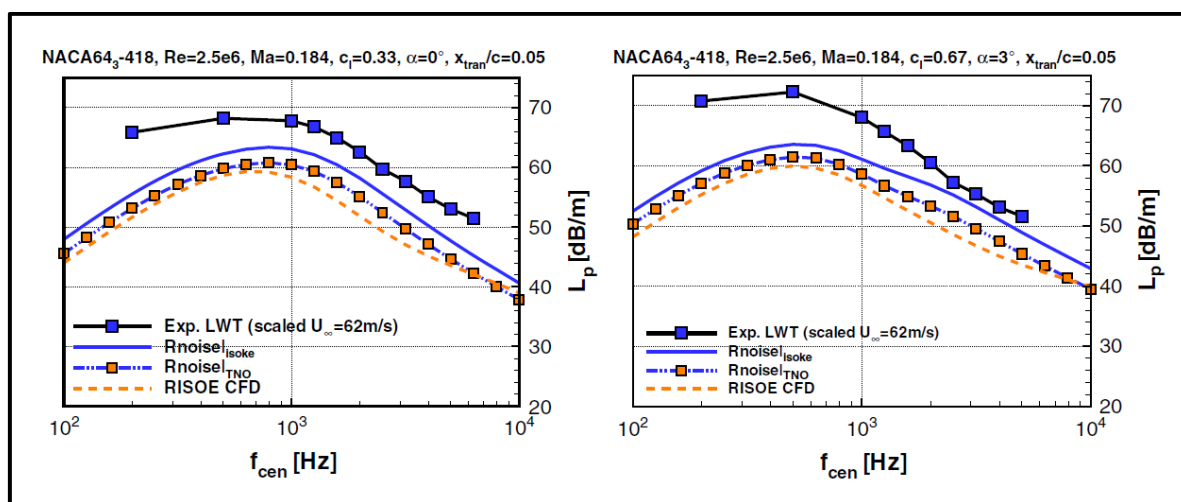


Figure E-18 – Comparison of the 1/3 octave band far-field noise spectrum measured (Exp. LWT), with that predicted by Rnoise with original TNO modeling (Rnoise/TNO); Rnoise with isotropic turbulence modeling (Rnoise/isoke) and RISOE with isotropic turbulence modeling (RISOE CFD). Airfoil: NACA 643-418. Source (Kamruzzaman M., et al., 2012b), p. 56.

Therefore, the performance of the TNO-model-based noise prediction methods remain unclear regarding airfoils other than the NACA 0012.

APPENDIX F - THE “QUASI 3-D” METHOD FOR BLADE AND ROTOR NOISE PREDICTION FROM 2-D METHODS.

Since most airfoil self-noise methods based on semi-empirical or simplified theoretical models are suitable for 2-D section noise prediction only, their application to a rotor must follow a procedure generally referred to as “quasi 3-D” method. This procedure has been applied, with some variations, in the works of Glegg (Glegg S. , Significance of Unsteady Thickness Noise Sources, 1987), Brooks et al. (Brooks, Pope, & Marcolini, Airfoil Self-Noise and Prediction, 1989), Moriarty and Migliore (Moriarty & Migliore, Semi-Empirical Aeroacoustic Noise Prediction Code for Wind Turbines, 2003), Fuglsang and Bak (Fuglsang & Bak, Development of the Risø Wind Turbine Airfoils, 2004), Zhu (Zhu, 2004), Vargas (Vargas L. d., 2008), and Kamruzzaman et al. (Kamruzzaman M. , Lutz, Nübler, & Krämer, 2011).

In the procedure a 2-D method is employed for noise emission prediction from different sections of the blade and the blade is positioned in some different angles of the azimuthal plane. The total OASPL determination for the rotor is computed from the contributions of all sections, properly averaged over the rotor area, and summed up in an observer position close to the hub. If the observer position is distant in the far-field, as required by some applicable measurement standards, a propagation model shall be employed.

The method was first devised for the calculation of torque and later adapted for noise prediction. For precision, the contribution from each 2-D blade segment must be calculated with the local flow, i.e., the flow corrected with the locally induced parameters. For this reason, the quasi 3-D method needs additional flow information that may be provided by the BEM method, for instance. Some methods may have corrections for tip loss, 3-D rotational augmentation, etc., which may be triggered by blade segment position.

The quasi 3-D method employed by Kamruzzaman et al. (Kamruzzaman M. , Lutz, Nübler, & Krämer, 2011), is:

- The blade is divided into N_s spanwise segments.

- By determining iteratively the axial and radial induction factors with the aid of a BEM method the relative speed, Reynolds number, Mach number and AOA are calculated.
- The tip correction method and other corrections elected are applied.
- One TBL 2-D calculation process (e.g. TBL-FP correlation, XFOIL, CFD, Experiment) provides the data necessary to calculate the source parameters of the model.
- The TE source spectrum in 1/3 octave bands is obtained for each radial blade segment, at a fixed observer position with respect to the blade segment (i.e. an observer rotating with the blade and positioned at $(\theta = 90^\circ, \phi = 90^\circ)$, according to the reference frame of Figure 3-5.
- A more physical situation of a rotating blade but with the observer fixed relative to the ground is then introduced with the aid of a coordinate systems transformation and use of a directivity function.
- The total spectrum and OASPL can then be calculated from the logarithmic sum of all contributions at the observer position, fixed relative to the ground.
- Propagation models may or may not be employed.

For practical application purposes, Glegg (Glegg S. , Significance of Unsteady Thickness Noise Sources, 1987), p. 842, employed the average of 20 azimuthal angles and 5 radial positions, for each blade, in the application of the quai-3D method.

Vargas (Vargas L. d., 2008) accomplished a sensitivity study on the number of optimal positions of the blade in the azimuthal plane N_β , versus the OASPL predicted. For this purpose, the blade was split in $N_s = 13$ segments and the frequency spectrum was divided in $N_f = 29$ center frequencies⁸⁷.

Table F-1 - Sensitivity studies of SPL_W (A-Weighted SPL) as a function of the number of positions of the blade in the azimuthal plane. The total number of computed pressure values is $N_p = N_\beta \cdot N_s \cdot N_f$. Source: (Vargas L. d., 2008), p.43.

⁸⁷ The standard 1/3 octave spectra is made up of 33 center frequencies, from 12.5 Hz up to 20 kHz (Bistafa, 2011), p. 96.

β step (°):	360	320	250	130	80	60	45	20	1
N_β :	1	2	2	3	5	6	8	18	360
N_p :	377	754	754	1131	1885	2262	3016	6786	135720
processing time (s):	0	0	0	0	1	1	1	3	59
SPL_W (dBA):	94.31	93.82	94.72	98.43	97.93	98.30	98.29	98.30	98.29

Based on the results from Table F-1, Vargas concluded that OASPL variation for more than 8 blade positions on the azimuthal plane was negligible and this number of positions also kept the calculation time very low.

APPENDIX G – CONSIDERATIONS ON DESIGNING-FOR-NOISE AND SUGGESTIONS FOR LOCAL NOISE-REGULATIONS IMPROVEMENTS.

It was shown in Eqn. (1-1), that *WT* mechanical power output scales with the approaching wind speed cubed, $P_{mech} \approx U_{\infty}^3$, and we have also seen in Eqn. (B-77) that the acoustic power for a dipole-type source, for instance, scales with the sixth power of the local flow velocity $P \approx U^6$.

The monotonic increase in local flow velocity and Mach number found from root to tip in the Wind Turbines (see Figure 4-3, for instance) confirms the concentration of stronger noise sources towards the tip of the blades, as shown in Figure 2-6 (Section 2.1.5.2).

Similarly to the design challenge on the performance side, one very important aspect of designing for noise is that there is no single operating point for a WT.

Because the Rayleigh distribution is positively skewed, the wind may attain very high velocity values associated with low probability and it was shown that the modern WT has mechanisms to prevent it from going outside an acceptable operating range (over speeding), from the standpoints of performance and structural integrity, such as the *pitch control*. Power regulation can be achieved either by pitching to promote stalling or pitching to feather which reduces the lift force on the blades by reducing the angle of attack (Burton, Sharpe, Jenkins, & Bossanyi, 2008), p. 181.

While designing-for-noise, pitch control by stalling is certainly not desirable, since it may worsen the noise problem, and there are currently no applicable noise models for stalled flows over airfoils, as discussed in Section 2.

For an efficient design-to-noise it is also necessary that the local noise regulations are efficiently designed. Although the WT must be safely operated at wind cut-out speed, it will be operating most of the time in speeds below that limit. As an example, suppose that modal value of the wind speed, σ , is 10 m/s, at a site and that the wind follows a Rayleigh distribution. The average wind speed may be calculated from:

$$\mu(v) = \sigma \cdot \sqrt{\pi/2} = 12.5 \frac{m}{s} \quad (G - 1)$$

The time the WT would spend subjected to 25 m/s winds, above which the equipment is cut-out, would be only 1% of the time. Also the total cumulative time spend above cut-out would be:

$$F(v > 25m/s) = -e^{-\frac{v^2}{2\sigma^2}} = 0.0436 \text{ or } 4.36\% \quad (G - 2)$$

Even then, speeds above cut-out-speed would not be attained due to the WT pitch control mechanism. It may be seen that designing the equipment for noise emissions at the extreme condition, i.e., the 1% time it will be facing a 25m/s wind, may prove uneconomical.

This is probably the reason why most countries where the Wind Energy Industry is more developed have migrated from peak-maximum noise (sound pressure level) allowable limits to equivalent levels allowable limits (e.g. in Denmark, Netherlands), expressed as L_{eq} , or exceedance levels (e.g. California), expressed as L_{60} , L_{90} , etc, (see section 1.1.6 for details). The issuing of a specific noise standard concerning WTN would be also desirable in Brazil, and the noise limits should be stated in energy equivalence methods as those described above, not absolute maximum levels.

APPENDIX H - THE TYPICAL OPERATING CONDITIONS FOR THE POLI-180 AND POLI-220 WIND TURBINES.

The detailed premises and aerodynamic geometry selected for the Poli-180 and Poli-220 Wind Turbines were explained in detail in Section 3.1.1.

The resulting flow conditions calculated with the BEM method and after twist optimization procedure with the aid of QBlade, are shown in Tables H.1 and H.2.

Table H.1 – Airfoil distribution, with Reynolds and Mach numbers for the local flow as a function of radial station for the Poli-180, 177.10 m diameter, 10 MW (nominal) horizontal axis wind turbine.

Poli-180			iter 1			iter 2	
Airfoil	pos [m]	Chord [m]	Reynolds	Mach	V_loc(m/s)	Reynolds	
1 Cyl1	2.64	5.011	2,941,090	0.03	10.44	2,977,460	
2 Cyl1	4.23	5.011	3,198,420	0.03	11.36	3,225,930	
3 Cyl2	6.84	5.089	3,536,050	0.04	12.36	3,568,490	
4 DU 99-W-405	10.41	5.496	4,337,100	0.04	14.04	4,380,240	
5 DU 350	14.84	6.003	5,615,330	0.05	16.64	5,668,280	
6 DU 350	20.03	6.477	7,311,180	0.06	20.09	7,371,920	
7 DU 300	25.85	6.518	8,870,840	0.07	24.22	8,927,350	
8 DU 250	32.15	6.213	10,146,700	0.09	29.07	10,197,500	
9 DU 250	38.79	5.853	11,275,700	0.10	34.29	11,319,700	
10 DU 210	45.59	5.436	12,135,900	0.12	39.74	12,171,700	
11 DU 210	52.40	5.021	12,767,400	0.13	45.26	12,795,600	
12 NACA64(3)418	59.04	4.623	13,159,800	0.15	50.67	13,181,200	
13 NACA64(3)418	65.34	4.244	13,325,800	0.16	55.88	13,341,400	
14 NACA64(3)418	71.16	3.895	13,279,600	0.18	60.68	13,290,500	
15 NACA64(3)418	76.35	3.584	13,080,900	0.19	64.97	13,088,000	
16 NACA64(3)418	80.78	3.318	12,792,200	0.20	68.63	12,796,400	
17 NACA64(3)418	84.35	3.039	12,218,300	0.21	71.56	12,221,100	
18 NACA64(3)418	86.96	2.200	9,113,830	0.22	73.73	9,114,440	
19 NACA64(3)418	88.55	2.056	8,655,190	0.22	74.94	8,655,290	

Table H.2 – Airfoil distribution, with Reynolds and Mach numbers for the local flow as a function of radial station for the Poli-220, 217.84 m diameter, 15 MW (nominal) horizontal axis wind turbine.

Poli-220				iter 1		iter 2	
Airfoil	pos [m]	Chord [m]	Reynolds	Mach	V_loc(m/s)	Reynolds	
1	Cyl1	3.06	6.134	3,572,870	0.03	10.361	3,631,940
2	Cyl1	5.02	6.134	3,887,190	0.03	11.274	3,930,790
3	Cyl2	8.24	6.229	4,282,370	0.04	12.230	4,333,160
4	DU 99-W-405	12.63	6.728	5,223,980	0.04	13.814	5,291,900
5	DU 350	18.10	7.349	6,729,940	0.05	16.294	6,813,890
6	DU 350	24.49	7.929	8,735,680	0.06	19.608	8,830,150
7	DU 300	31.66	7.979	10,568,000	0.07	23.573	10,660,200
8	DU 250	39.43	7.605	12,073,400	0.08	28.255	12,156,100
9	DU 250	47.61	7.165	13,411,600	0.10	33.317	13,482,800
10	DU 210	55.99	6.655	14,430,300	0.11	38.598	14,488,400
11	DU 210	64.37	6.146	15,179,500	0.13	43.958	15,225,100
12	NACA64(3)418	72.55	5.659	15,645,500	0.14	49.211	15,680,300
13	NACA64(3)418	80.32	5.196	15,842,500	0.16	54.273	15,867,700
14	NACA64(3)418	87.49	4.768	15,787,700	0.17	58.934	15,805,200
15	NACA64(3)418	93.88	4.387	15,551,800	0.19	63.098	15,563,200
16	NACA64(3)418	99.34	4.062	15,208,600	0.20	66.652	15,215,500
17	NACA64(3)418	103.74	3.720	14,526,300	0.20	69.499	14,530,000
18	NACA64(3)418	106.96	2.693	10,837,900	0.21	71.612	10,839,100
19	NACA64(3)418	108.92	2.517	10,289,300	0.21	72.775	10,289,600

APPENDIX I - VERIFICATION OF THE AIRFOIL TRAILING-EDGE NOISE PREDICTION MODULE (PNOISE) INSIDE QBLADE V0.8

Validation of the spectra output of the PNoise module inside QBlade v0.8 was shown in Section 4.3 and also the tables that summarizes the calculation procedure verification.

The details of the extensive verification procedure are shown in this Appendix.

I1 - Verification case for TBL data calculated by XFLR5 (inside QBlade) for AOA=0°.

A) PNoise calculation:

Baseline case simulated: Figure 11 of BPM original paper.

- NACA 0012, Sharp Trailing Edge.
- Reynolds: 1,500,000
- Mach: 0.21
- Chord: 0.3048 m
- Wetted TE span: 0.4572 m
- Reference Spreadsheet output data:
- Chord Station for D* measurement: 0.98C
- Input file name: Teste Revisão 8 28_ago_2015.WPA
- Output file name: Modified_QBlade_output_for_validation_Aug_28_2015_zero_AOA.txt

The PNoise input and output screens are shown in Figures I-1 and I-2.

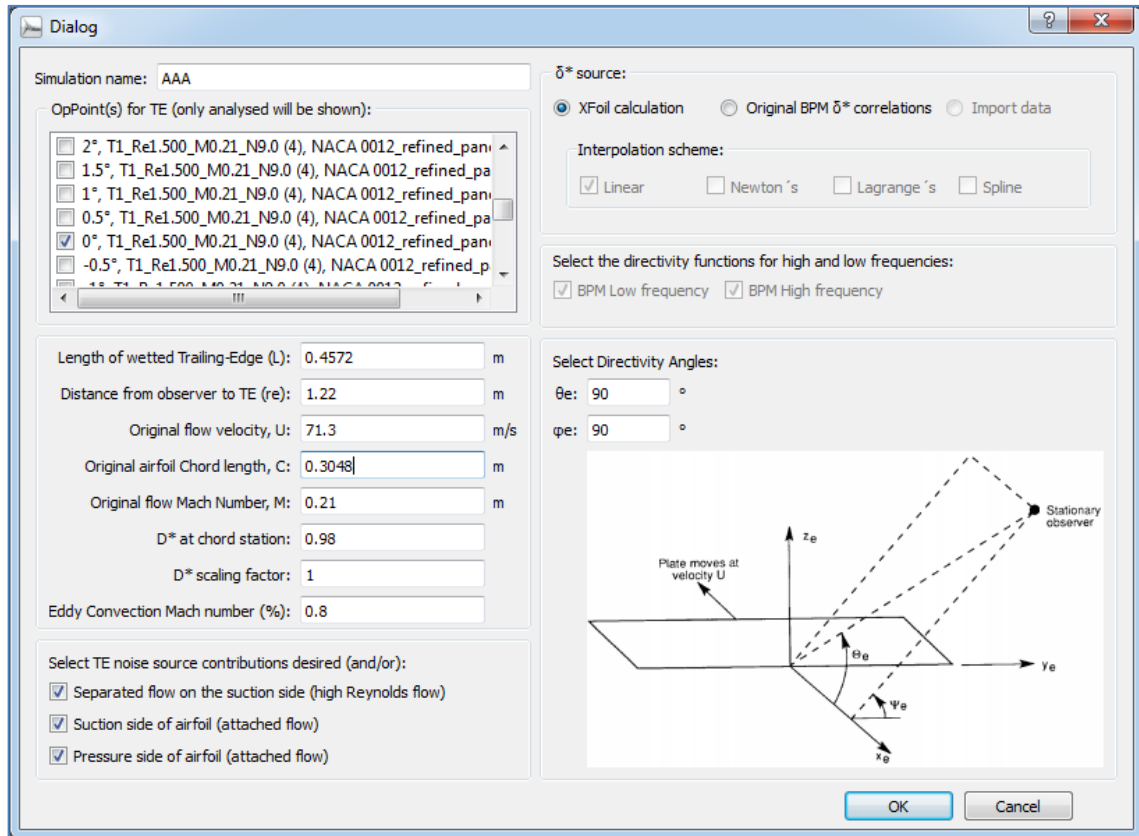


Figure I-1 – Typical input screen of the PNoise for zero AOA calculation.

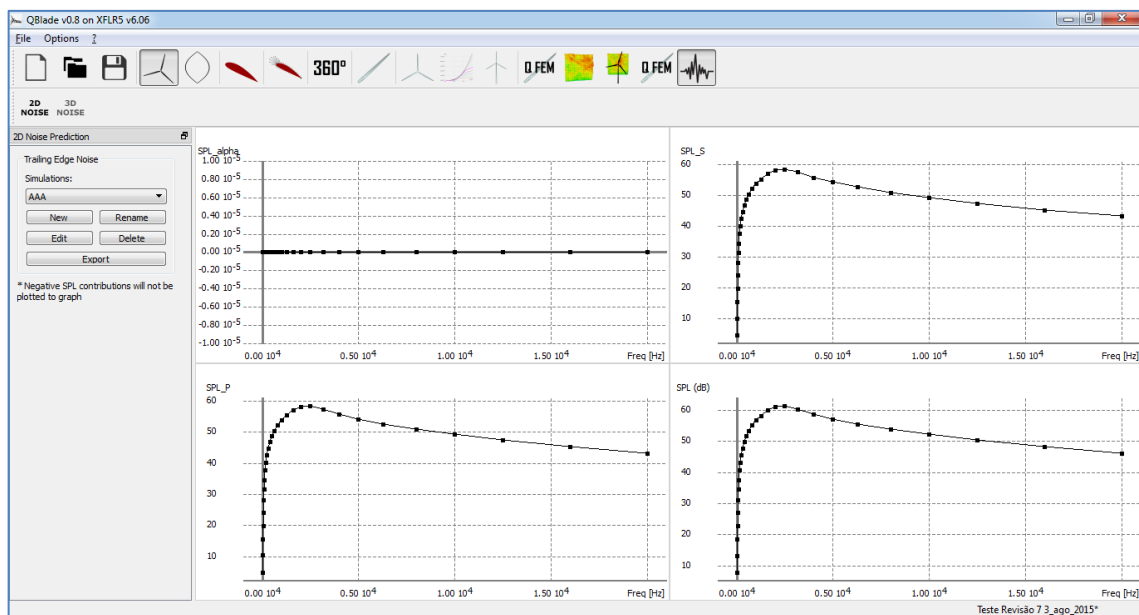


Figure I-2 – Typical output screen of the PNoise for zero AOA calculation.

Table I-1 – Text output with spectral data for the zero AOA simulation.

Noise prediction file export

Alpha: 0, Re = 1.5e+06

OASPL: 69.6254 dB

OASPL (A): 70.1545 dB(A)

OASPL (B): 69.1096 dB(B)

OASPL (C): 69.0692 dB(C)

SPL_a: -933.115

SPL_s: 66.6053

SPL_p: 66.6248

Freq [Hz]	SPL (dB)	SPLa	SPLs	SPLp	SPL (dB(A))	SPL (dB(B))	SPL (dB(C))
25	7.75788	-1456.2	4.68165	4.81253	-36.9421	-12.6421	3.35788
31.5	13.2548	-1380.07	10.1832	10.3049	-26.1452	-3.84521	10.2548
40	18.4575	-1309.99	15.3904	15.5033	-16.1425	4.25753	16.4575
50	22.9046	-1251.97	19.8414	19.9465	-7.29542	11.3046	21.6046
63	27.118	-1198.97	24.0586	24.1562	0.918006	17.818	26.318
80	31.0833	-1151.26	28.0276	28.118	8.58333	23.6833	30.5833
100	34.4565	-1112.71	31.4039	31.4882	15.3565	28.8565	34.1565
125	37.5363	-1079.53	34.4865	34.5652	21.4363	33.3363	37.3363
160	40.6324	-1048.55	37.5855	37.6585	27.2324	37.6324	40.5324
200	43.1777	-1025.24	40.133	40.2015	32.2777	41.1777	43.1777
250	45.5088	-1005.93	42.4661	42.5305	36.9088	44.2088	45.5088
315	47.7245	-989.684	44.6837	44.7444	41.1245	46.9245	47.7245
400	49.8321	-976.383	46.7929	46.8505	45.0321	49.3321	49.8321
500	51.6604	-966.699	48.6224	48.6775	48.4604	51.3604	51.6604
630	53.4388	-958.977	50.4019	50.455	51.5388	53.3388	53.4388
800	55.1837	-952.951	52.1475	52.1991	54.3837	55.1837	55.1837
1000	56.7552	-948.647	53.7194	53.7701	56.7552	56.7552	56.7552
1250	58.2983	-945.173	55.2627	55.3132	58.8983	58.2983	58.2983
1600	60.003	-943.925	56.9673	57.0178	61.003	60.003	59.903
2000	61.2358	-939.04	58.2088	58.2421	62.4358	61.1358	61.0358
2500	61.3966	-938.677	58.3801	58.3926	62.6966	61.1966	61.0966
3150	60.4289	-941.522	57.4243	57.4128	61.6289	60.0289	59.9289
4000	58.7792	-944.127	55.7747	55.7632	59.7792	58.0792	57.9792
5000	57.2382	-947.423	54.2337	54.2221	57.7382	56.0382	55.9382
6300	55.6226	-951.562	52.6184	52.6061	55.5226	53.7226	53.6226
8000	53.8972	-957.131	50.8937	50.88	52.7972	50.9972	50.8972
10000	52.2074	-963.988	49.2048	49.1893	49.7074	47.9074	47.8074
12500	50.416	-972.895	47.4146	47.3968	46.116	44.316	44.216
16000	48.2852	-985.666	45.2853	45.2644	41.6852	39.8852	39.7852
20000	46.1965	-1000.33	43.1983	43.174	36.8965	35.0965	34.9965

B) Spreadsheet calculation:

Data input is same as in case A, above.

- Output file name: File: D_star_files_for 28_aug_2015 validation_Re_1_5.txt

XFLR5 output file with displacement thickness data is shown in Table I-2.

Table I-2 – XFLR5 output with displacement thickness.

XFOil (inside QBlade) calculations:								
QBlade v0.8 on XFLR5 v6.06								
NACA 0012_refined_panels_STE								
Alpha = 0.0, Re = 1500000, Ma= 0.2100, ACrit= 9.0								
Top Side								
x	Hk	Ue/Vinf	Cf	Cd	A/A0	D*	Theta	CTq
0.976198	1.58883	0.91131	0.00170	0.00109	0.04185	0.00496	0.00309	0.04674
0.983339	1.61857	0.89997	0.00156	0.00106	0.04239	0.00530	0.00324	0.04818
Bottom Side								
x	Hk	Ue/Vinf	Cf	Cd	A/A0	D*	Theta	CTq
0.976201	1.59008	0.91122	0.00169	0.00109	0.04188	0.00499	0.00310	0.04680
0.983341	1.61996	0.89987	0.00155	0.00106	0.04242	0.00532	0.00325	0.04825

When the Spreadsheet developed for verification was fed with D* highlighted above,

Table I-3 – Spreadsheet displacement thickness input cells.

Suction Side (superior para alfa positivos, inferior para alfas negativos)	Location	Chord Station	D* (δ^*s)
	Upstream	0.976198	0.00496
	Specified Station	0.98000	0.00514
	Downstream	0.983339	0.00530
	D* Value (XFOIL)		0.00157
Pressure Side (inferior para alfas positivos, superior para alfas negativos)	Location	Chord Station	D* (δ^*p)
	Upstream	0.976201	0.00499
	Specified Station	0.980000	0.00517
	Downstream	0.983341	0.00532
	D* Value (XFOIL)		0.00157
			1.57E-03

the Spectrum returned from the Spreadsheet is shown below:

Table I-4 – Spreadsheet output with spectral data for the zero AOA case.

Freq [Hz]	SPL_alpha	SPL_S	SPL_P	SPL (dB)
25	-1456.78	4.59	4.73	7.67
31.5	-1380.59	10.10	10.23	13.17
40	-1310.46	15.31	15.43	18.38
50	-1252.39	19.76	19.88	22.83
63	-1199.34	23.98	24.09	27.05
80	-1151.58	27.96	28.05	31.02
100	-1113.00	31.34	31.43	34.39
125	-1079.79	34.42	34.50	37.47
160	-1048.77	37.52	37.60	40.57
200	-1025.43	40.07	40.14	43.12
250	-1006.10	42.41	42.47	45.45
315	-989.82	44.62	44.69	47.67
400	-976.50	46.74	46.80	49.78
500	-966.80	48.57	48.62	51.61
630	-959.07	50.35	50.40	53.38
800	-953.03	52.09	52.15	55.13
1000	-948.72	53.66	53.72	56.70
1250	-945.24	55.21	55.26	58.24
1600	-941.83	56.91	56.97	59.95
2000	-939.10	58.16	58.19	61.19

2500	-938.72	58.34	58.35	61.35
3150	-940.89	57.39	57.38	60.39
4000	-944.15	55.74	55.73	58.74
5000	-947.44	54.20	54.19	57.20
6300	-951.58	52.58	52.57	55.59
8000	-957.14	50.86	50.85	53.86
10000	-963.98	49.17	49.16	52.17
12500	-972.87	47.38	47.36	50.38
16000	-985.62	45.25	45.23	48.25
20000	-1000.26	43.17	43.14	46.17

Table I-5 – SPL contributions by source for zero AOA case (from the spreadsheet).

TE noise contributions			
Sep	Suction Side	Pressure-Side	Total SPL
OASPL-----> 69.6	70.1	69.1	69.0
dB	dB(A)	dB(B)	dB(C)

Table I-6 – Final SPL comparison (overall and by source), in three selected 1/3 octave frequencies, including the peak frequency.

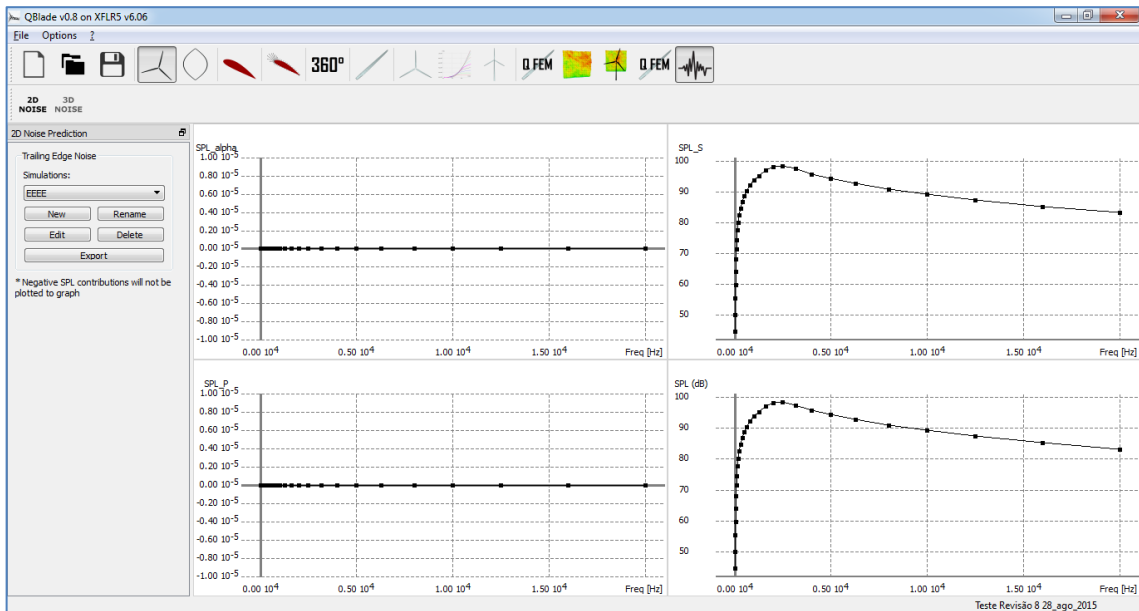
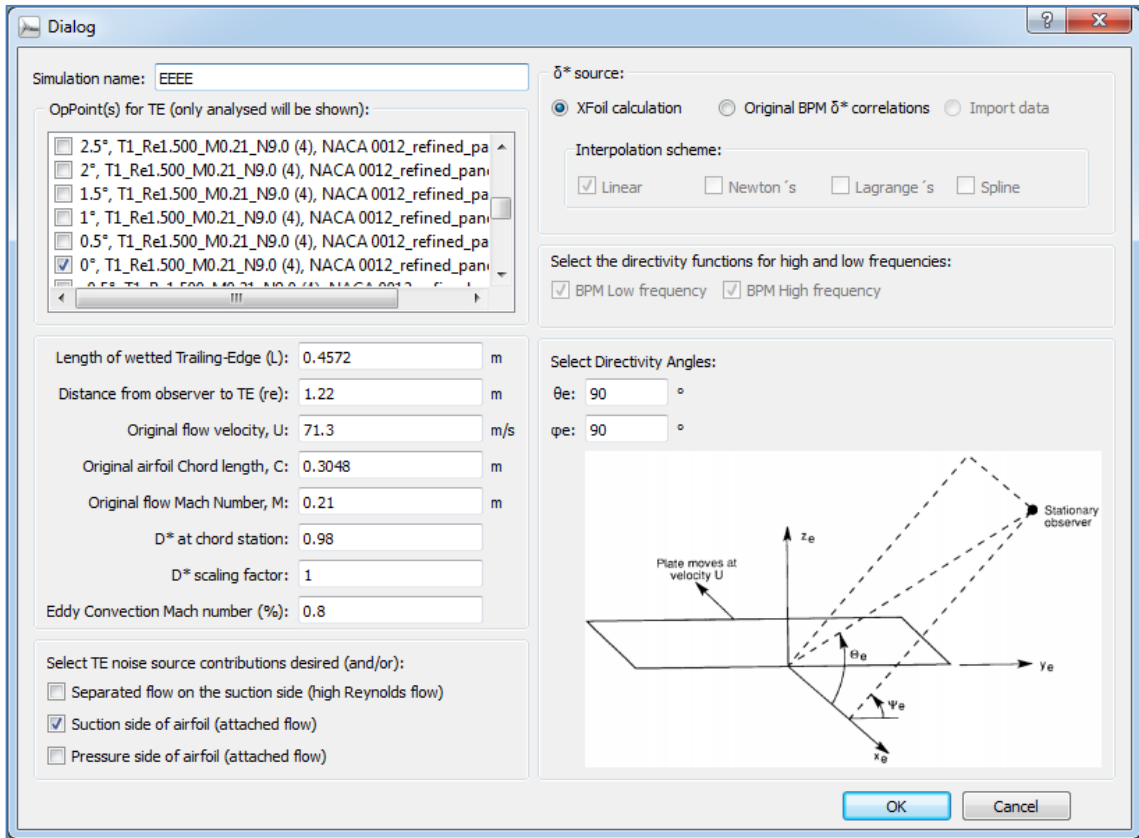
Frequency (Hz)	Source	SPL_alpha (dB)	SPL_S (dB)	SPL_P (dB)	SPL (dB)	Diff.(dB)
50	Spreadsheet	-1252.39	19.76	19.88	22.83	-0.07
	Code	-1251.97	19.84	19.95	22.90	
1.000	Spreadsheet	-948.72	53.66	53.72	56.70	-0.06
	Code	-948.65	53.72	53.77	56.76	
2.500	Spreadsheet	-938.72	58.34	58.35	61.35	-0.05
	Code	-938.68	58.38	58.39	61.40	

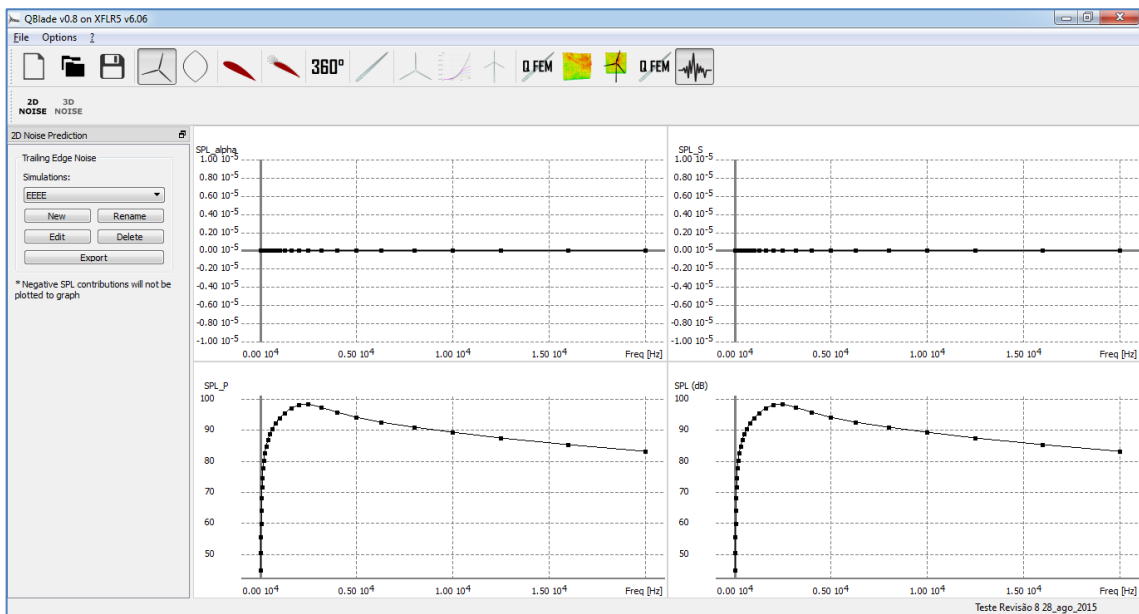
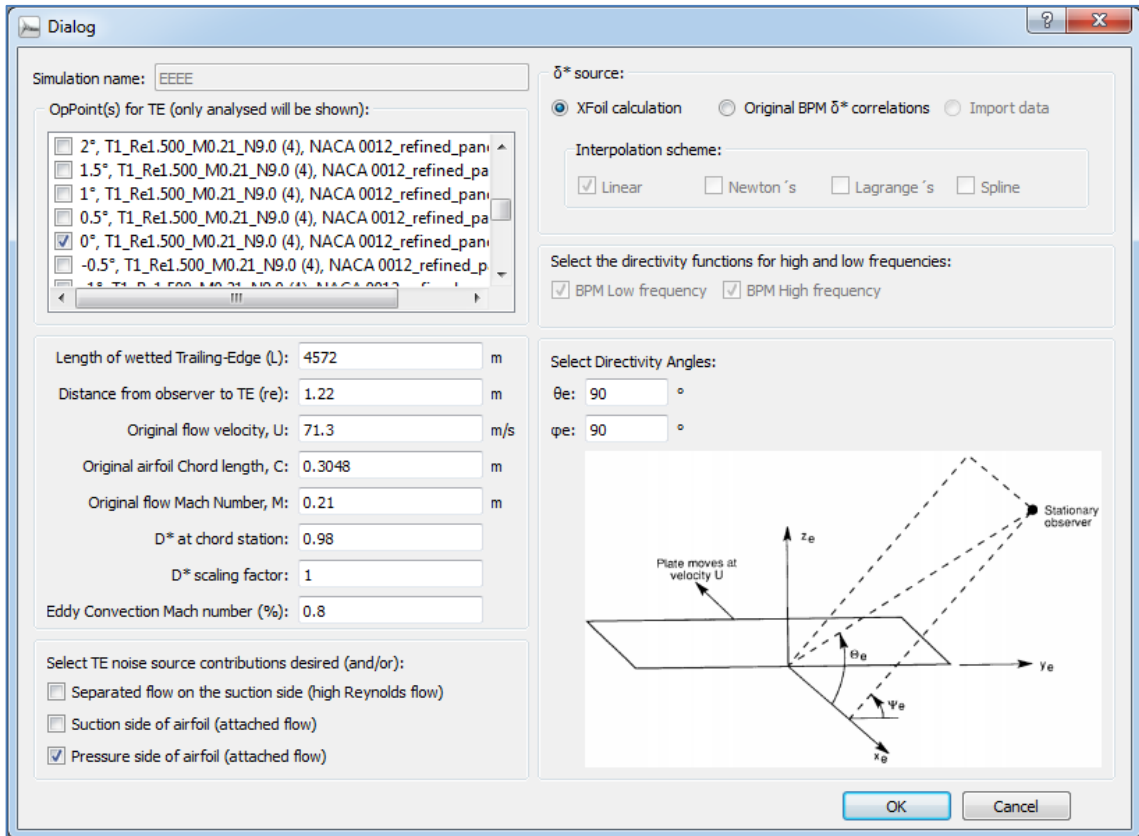
The result was very close for the PNoise and the Spreadsheet, completing the calculation verification process for zero AOA. The small result difference was attributed to different number precision between the different processes and the result improved towards the peak frequency of 2,500 Hz.

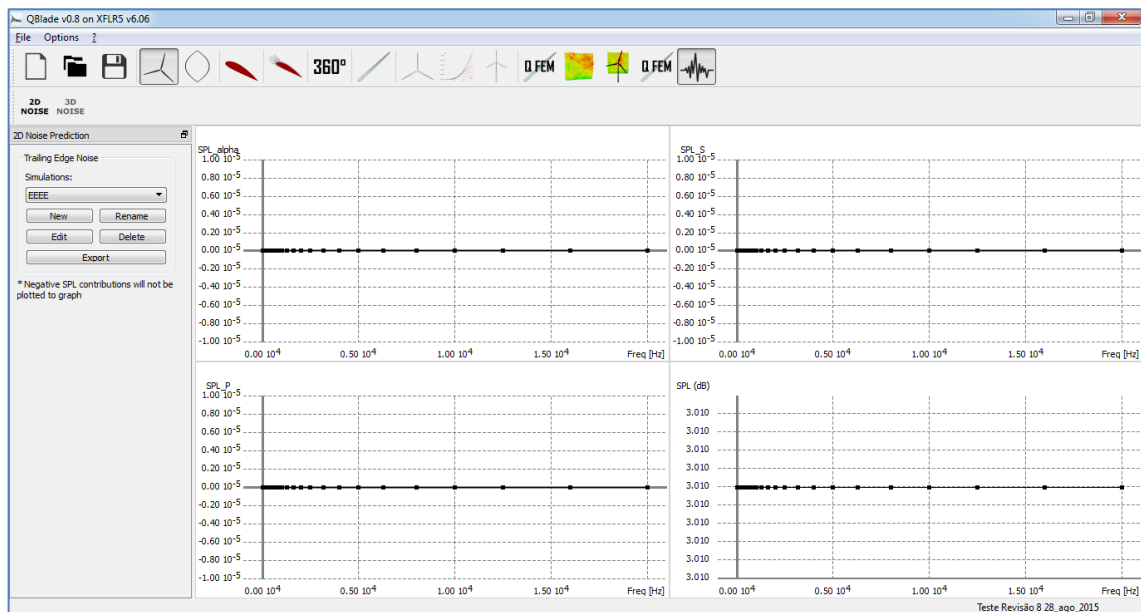
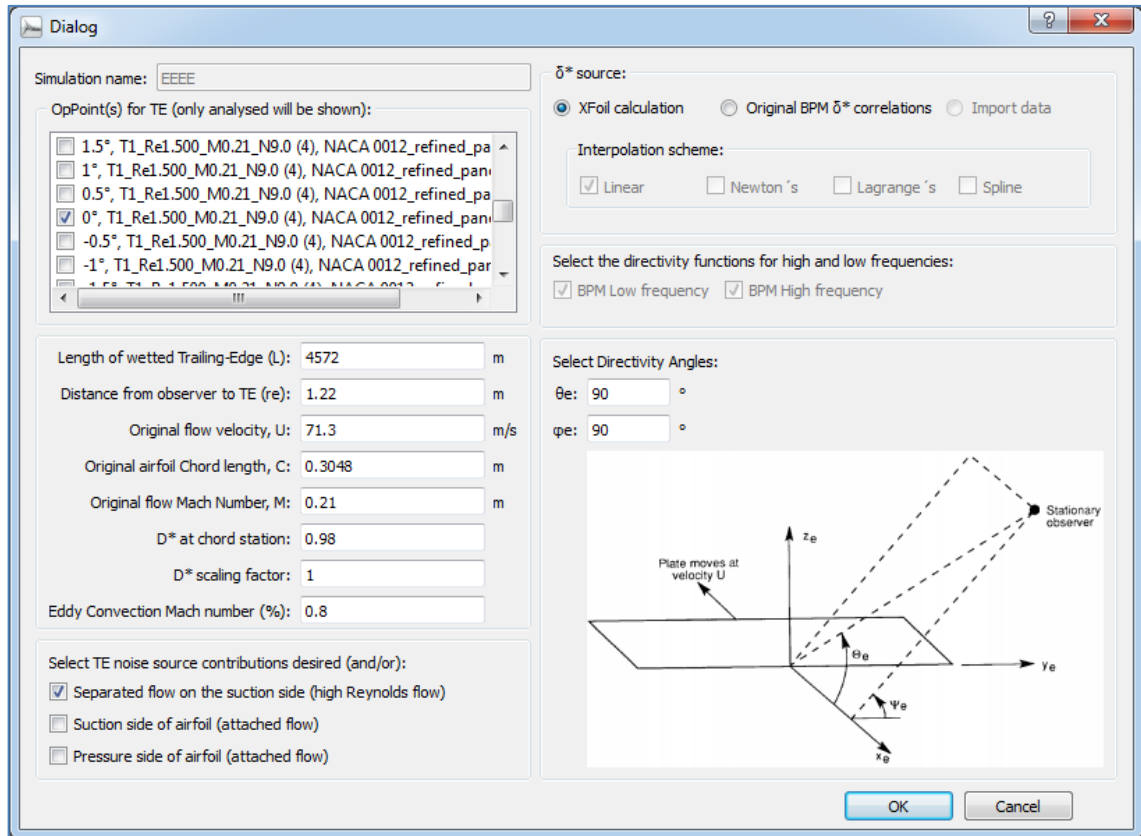
Also the OASPL is 69.6 dB for the Spreadsheet and 69.6 for the Code.

Also, some “what if” cases are verified:

- What if only one source is selected at the dialog screen?

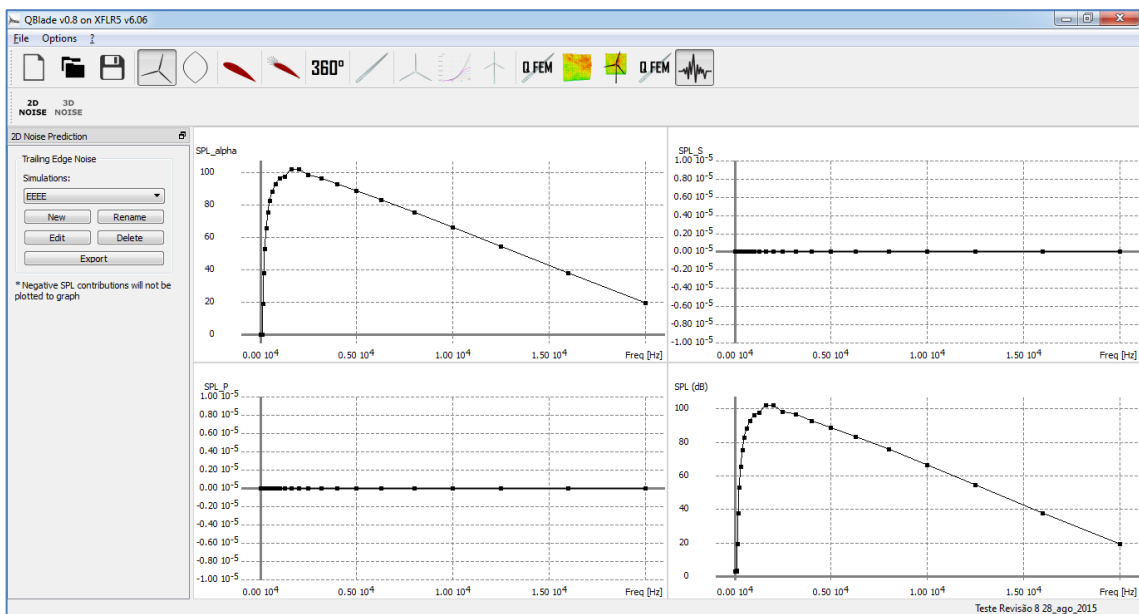
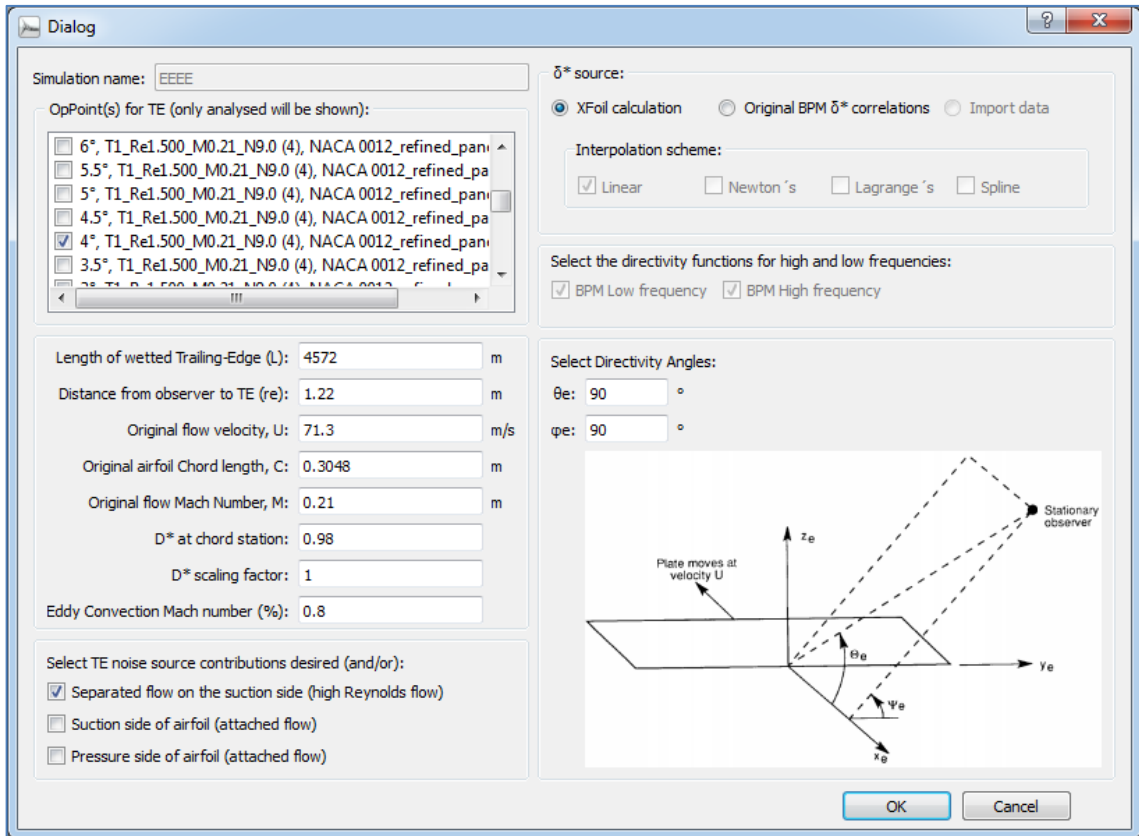






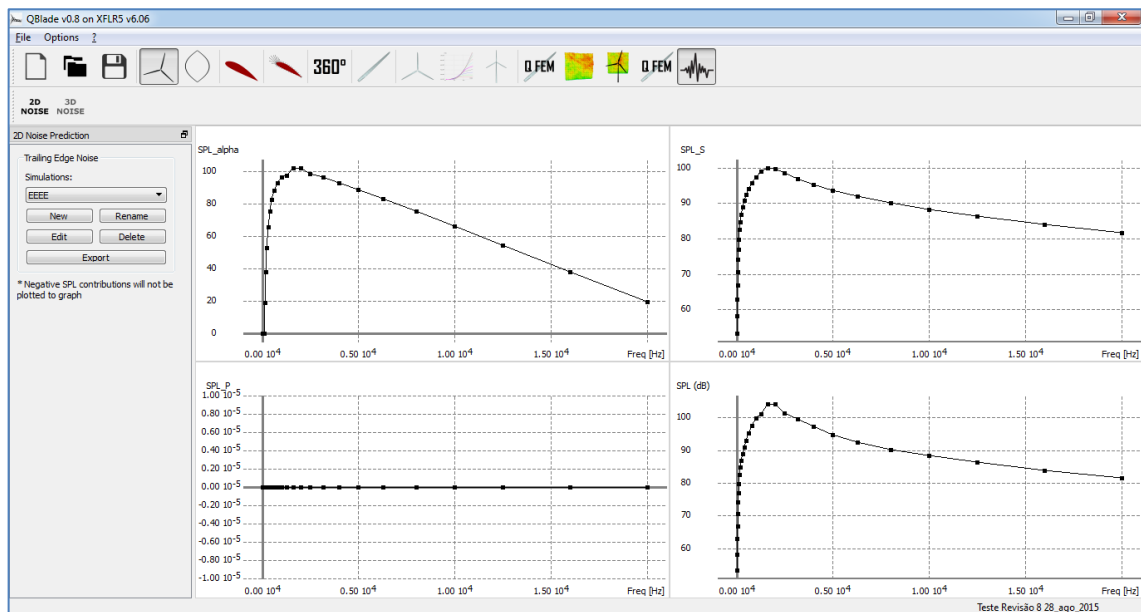
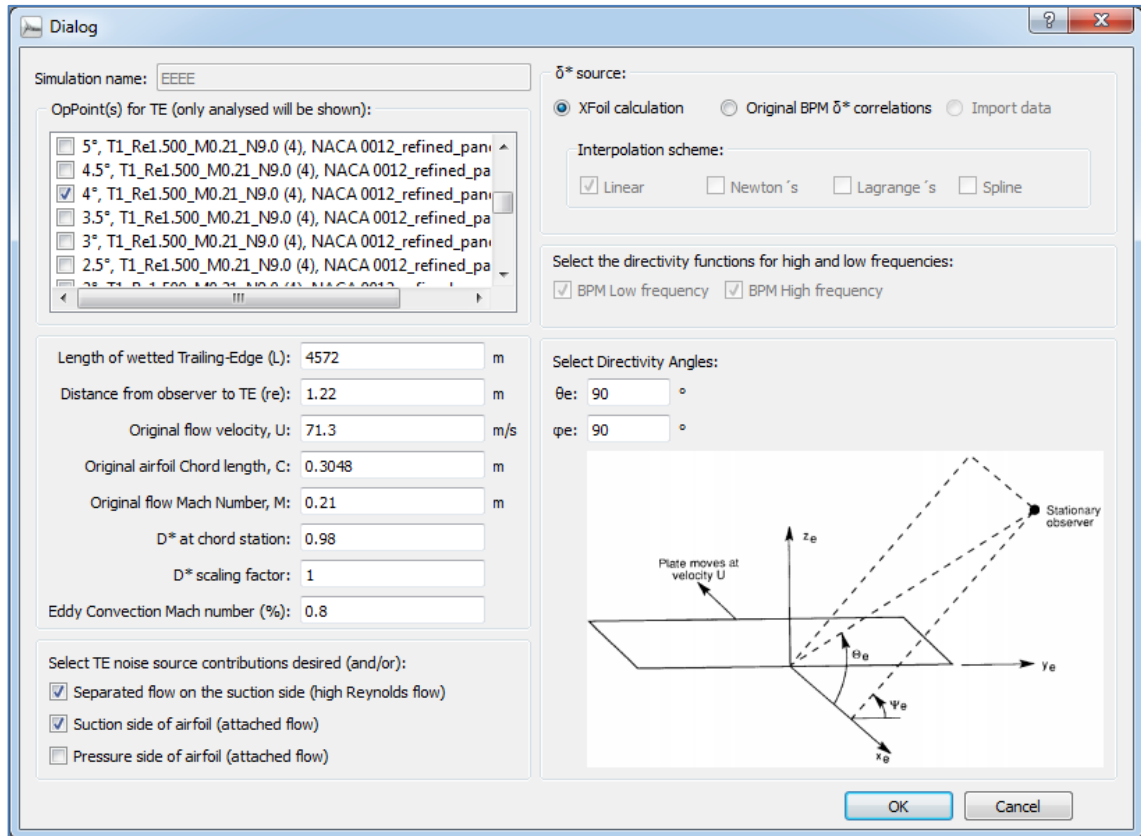
Ok! Separated flow SPL contribution is negative (shown as zero in the output graph) for zero AOA.

- What if separated flow only had been selected and AOA other than zero?



It showed correct behavior

- Does source combination works?



Thus the SPL and peak frequency for zero AOA is very good. The source selection combination works fine (tested for zero and other than zero AOA). The numerical verification was accomplished between the modified QBlade calculation and the spreadsheet baseline calculation validated against the BPM model.

The verification process in the next subsections will cover AOA other than zero (both below and above the switching angle), and the displacement thicknesses will be provided by both the XFLR5 embedded inside QBlade and by the original BPM correlations .

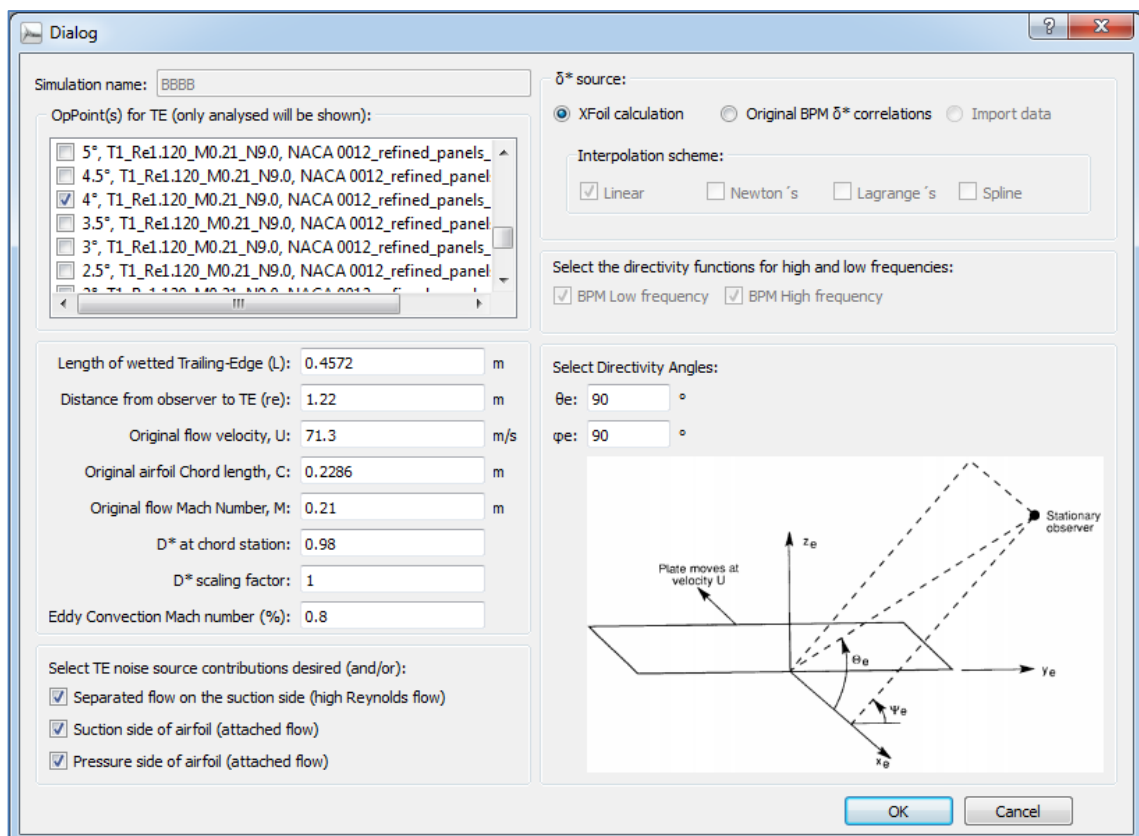
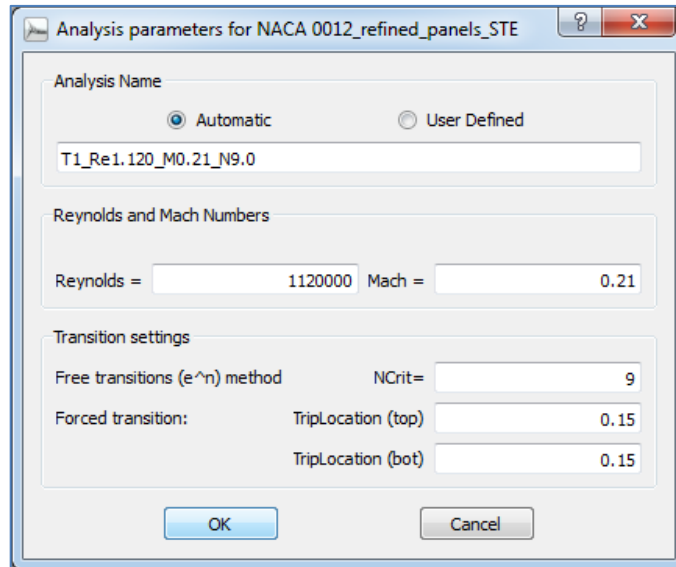
I2 - Verification cases for TBL data calculated by XFOIL (inside QBlade) for AOA other than zero.

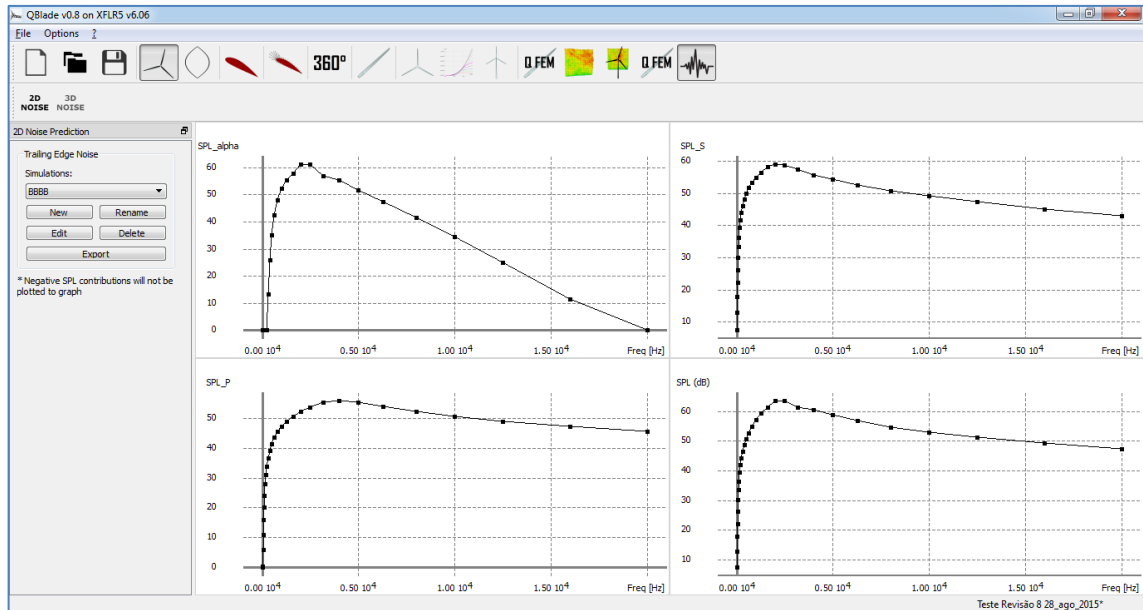
Since the model has different calculation procedures for AoA below and above the “switching angle”, estimated for the Reynolds of 1,120 Million to be at 9.5°, one test was chosen to be made below the switching angle (4°) and the other above it (12.5°).

Verification for angle below the switching angle.

All verification cases from this point on will be displayed in the following sequence, without individual figure and table numbering:

- Input file name.
- PNoise simulation for the case.
- XFLR5 calculated displacement thickness output file.
- Spreadsheet input of displacement thickness.
- Spreadsheet spectral output (1/3 octave spectra).
- Spreadsheet overall SPL.
- PNoise output spectra.
- Comparison table.
- Conclusions.





Notice that the SPL_Alpha contribution now is positive, as it should be.

Output TBL file: D_star_files_for_28_aug_2015 Validation_Re_1_12.txt

QBlade v0.8 on XFLRS v6.06

NACA 0012_refined_panels_STE

Alpha = 4.0, Re = 1120000, Ma= 0.2100, ACrit= 9.0

Top Side

x	Hk	Ue/Vinf	Cf	Cd	A/A0	D*	Theta	CTq
0.976198	1.72954	0.90628	0.00130	0.00120	0.04550	0.00757	0.00433	0.05311
0.983339	1.77050	0.89580	0.00117	0.00118	0.04608	0.00810	0.00453	0.05477

Bottom Side

x	Hk	Ue/Vinf	Cf	Cd	A/A0	D*	Theta	CTq
0.976201	1.52901	0.91918	0.00219	0.00115	0.04053	0.00389	0.00251	0.04355
0.983341	1.54931	0.90950	0.00205	0.00111	0.04095	0.00410	0.00262	0.04463

2_BPM Calculation Procedure_alpha_below_critical_4_28_Aug_15_XFOIL.XLSX

Displacement Thickness Spreadsheet input:

Suction Side (superior para alfa positivos, inferior para alfas negativos)	Location	Chord Station	D* (δ^*s)
	Upstream	0.976198	0.00757
	Specified Station	0.98000	0.00785
	Downstream	0.983339	0.00810
	D* Value (XFOIL)		0.00180
			1.80E-03
Pressure Side (inferior para alfas positivos, superior para alfas negativos)	Location	Chord Station	D* (δ^*p)
	Upstream	0.976201	0.00389
	Specified Station	0.980000	0.00400
	Downstream	0.983341	0.00410
	D* Value (XFOIL)		0.00091
			9.15E-04

Spreadsheet Output:

Freq [Hz]	TE noise contributions			
	Sep	Suction Side	Pressure-Side	Total SPL
	SPL_alpha	SPL_S	SPL_P	SPL (dB)
25	-440.50	7.40	-12.76	7.44
31.5	-366.03	12.72	-6.08	12.78
40	-297.57	17.75	0.27	17.83
50	-240.96	22.05	5.73	22.15
63	-189.33	26.13	10.93	26.25
80	-142.93	29.95	15.84	30.12
100	-105.52	33.21	20.03	33.42
125	-73.39	36.18	23.87	36.43
160	-43.46	39.17	27.73	39.47
200	-21.00	41.63	30.90	41.99
250	-2.46	43.89	33.80	44.29
315	13.09	46.03	36.53	46.50
400	25.77	48.08	39.11	48.62
500	34.97	49.87	41.31	50.55
630	42.29	51.61	43.41	52.64
800	47.99	53.33	45.41	54.95
1000	52.09	54.88	47.16	57.17
1250	55.45	56.42	48.82	59.37
1600	58.83	58.12	50.58	61.84
2000	61.19	58.95	52.13	63.55
2500	61.10	58.71	53.67	63.55
3150	58.48	57.35	55.21	61.99
4000	55.21	55.71	55.78	60.34

5000	51.80	54.16	55.24	58.73
6300	47.46	52.53	53.71	56.72
8000	41.58	50.78	52.06	54.69
10000	34.34	49.05	50.51	52.91
12500	24.96	47.21	48.92	51.17
16000	11.56	45.02	47.09	49.19
20000	-3.77	42.86	45.33	47.28

OASPL----->

71.1	71.8	70.6	70.6
dB	dB(A)	dB(B)	dB(C)

QBlade data: Modified_QBlade_output_for_validation_Aug_28_2015_4_AOA.txt

Noise prediction file export

Alpha: 4, Re = 1.12e+06

OASPL: 71.0019 dB

OASPL (A): 71.6838 dB(A)

OASPL (B): 70.5184 dB(B)

OASPL (C): 70.4573 dB(C)

SPL_a: 66.882

SPL_s: 67.2023

SPL_p: 63.9204

Freq [Hz]	SPL (dB)	SPLa	SPLs	SPLp	SPL (dB(A))	SPL (dB(B))	SPL (dB(C))
25	7.51371	-440.017	7.4721	-12.6929	-37.1863	-12.8863	3.11371
31.5	12.8494	-365.594	12.7927	-6.01601	-26.5506	-4.25058	9.84942
40	17.9011	-297.175	17.8243	0.336621	-16.6989	3.70111	15.9011
50	22.2219	-240.606	22.1219	5.79367	-7.97807	10.6219	20.9219
63	26.3202	-189.014	26.1911	10.9879	0.120222	17.0202	25.5202
80	30.1835	-142.652	30.0186	15.8973	7.68352	22.7835	29.6835
100	33.477	-105.274	33.2733	20.0882	14.377	27.877	33.177
125	36.492	-73.1712	36.2447	23.9238	20.392	32.292	36.292
160	39.5329	-43.271	39.2324	27.784	26.1329	36.5329	39.4329
200	42.0423	-20.8394	41.6903	30.9548	31.1423	40.0423	42.0423
250	44.3496	-2.31659	43.9441	33.8496	35.7496	43.0496	44.3496
315	46.5534	13.2162	46.0902	36.5838	39.9534	45.7534	46.5534
400	48.6774	25.88	48.1372	39.1578	43.8774	48.1774	48.6774
500	50.6085	35.066	49.9193	41.3576	47.4085	50.3085	50.6085
630	52.6947	42.3686	51.6605	43.4556	50.7947	52.5947	52.6947
800	55.0092	48.0655	53.3782	45.4612	54.2092	55.0092	55.0092
1000	57.2304	52.158	54.9346	47.2121	57.2304	57.2304	57.2304

1250	59.4311	55.5138	56.4755	48.8708	60.0311	59.4311	59.4311
1600	61.3841	57.8011	58.1759	50.6292	62.3841	61.3841	61.2841
2000	63.5957	61.241	58.9912	52.1776	64.7957	63.4957	63.3957
2500	63.5907	61.1447	58.7446	53.7185	64.8907	63.3907	63.2907
3150	61.3391	56.7914	57.3896	55.2535	62.5391	60.9391	60.8391
4000	60.379	55.2339	55.7399	55.8263	61.379	59.679	59.579
5000	58.7627	51.8304	54.1958	55.2751	59.2627	57.5627	57.4627
6300	56.753	47.482	52.5635	53.748	56.653	54.853	54.753
8000	54.7281	41.5931	50.8095	52.0983	53.6281	51.8281	51.7281
10000	52.9479	34.3409	49.0826	50.5488	50.4479	48.6479	48.5479
12500	51.2066	24.9467	47.2441	48.9596	46.9066	45.1066	45.0066
16000	49.2207	11.5279	45.0493	47.1245	42.6207	40.8207	40.7207
20000	47.3146	-3.81656	42.8921	45.3681	38.0146	36.2146	36.1146

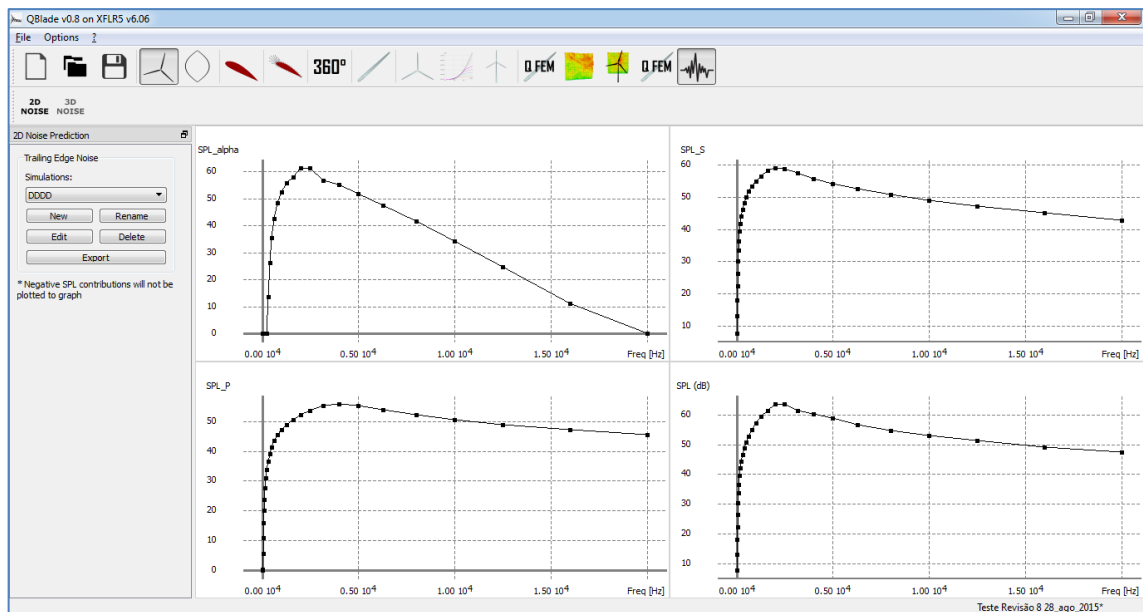
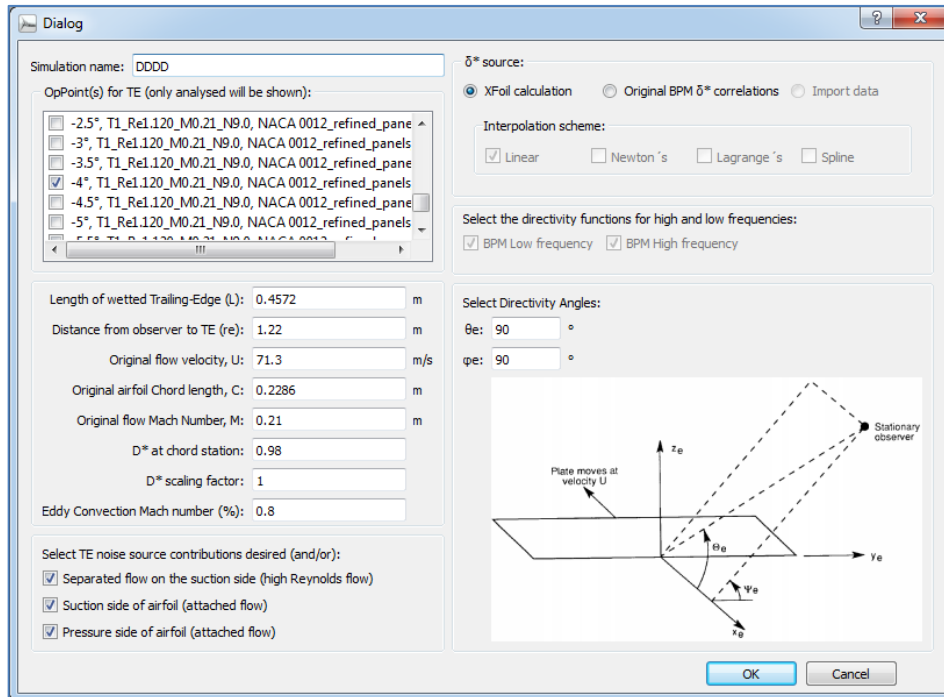
Frequency (Hz)	Source	SPL_alpha (dB)	SPL_S (dB)	SPL_P (dB)	SPL (dB)	Diff.(dB)
50	Spreadsheet	-240.96	22.05	5.73	22.15	-0.07
	Code	-240.61	22.12	5.79	22.22	
1.000	Spreadsheet	52.09	54.88	47.16	57.17	-0.06
	Code	52.16	54.93	47.21	57.23	
2.000	Spreadsheet	61.10	58.95	52.13	63.55	-0.05
	Code	61.24	58.99	52.18	63.60	

The result is very good and improves toward the peak frequency of 2 KHz.

Also the OASPL is 71.1 dB for the Spreadsheet and 71.0 dB for the code or a 0.1 dB difference.

What if the AOA angle is negative? Is the code switching the Pressure and Suction side and making the correct D* reading as it should?

Now the results for -4° was verified:



In negative AOA, the upper surface, initially a suction side, becomes a pressure side and the lower surface, initially a pressure side, becomes a suction side. Since the graphs are for the “pressure” and “suction” sides, not for “upper” and “lower” sides of the airfoil, the output is correct in shape (no change from +4 degrees, since we have tested with a symmetrical -4 degrees).

The calculations are verified below:

File (output from XFOil): D_star_files_for_28_aug_2015 Validation_Re_1_12.txt

QBlade v0.8 on XFLR5 v6.06

NACA 0012_refined_panels_STE

Alpha = -4.0, Re = 1120000, Ma= 0.2100, ACrit= 9.0

Top Side

x	Hk	Ue/Vinf	Cf	Cd	A/A0	D*	Theta	CTq
0.976198	1.52810	0.91928	0.00219	0.00115	0.04050	0.00387	0.00250	0.04350
0.983339	1.54828	0.90963	0.00206	0.00111	0.04092	0.00408	0.00261	0.04457

Bottom Side

x	Hk	Ue/Vinf	Cf	Cd	A/A0	D*	Theta	CTq
0.976201	1.73171	0.90619	0.00129	0.00120	0.04554	0.00761	0.00435	0.05320
0.983341	1.77285	0.89573	0.00117	0.00119	0.04612	0.00814	0.00455	0.05486

By comparing numbers above with those for + 4 AOA, we conclude that they have been correctly inverted, apart from minor rounding (computation difference due to minor airfoil asymmetry or panel asymmetry).

Spreadsheet output is the same as before (for +4 degrees), as it should be for a symmetrical airfoil.

File output from the Noise Module:

Modified_QBlade_output_for_validation_Aug_28_2015_minus4_AOA.txt

Noise prediction file export

Alpha: -4, Re = 1.12e+06

OASPL: 71.0171 dB

OASPL (A): 71.6975 dB(A)

OASPL (B): 70.5374 dB(B)

OASPL (C): 70.4766 dB(C)

SPL_a: 66.9106

SPL_s: 67.2263

SPL_p: 63.8903

Freq [Hz]	SPL (dB)	SPLa	SPLs	SPLp	SPL (dB(A))	SPL (dB(B))	SPL (dB(C))
25	7.66323	-438.167	7.62447	-12.8505	-37.0368	-12.7368	3.26323

31.5	12.9875	-363.938	12.9343	-6.16373	-26.4125	-4.11253	9.98747
40	18.0279	-295.707	17.9557	0.198608	-16.5721	3.82787	16.0279
50	22.3387	-239.304	22.2442	5.66422	-7.86133	10.7387	21.0387
63	26.4271	-187.871	26.3047	10.8668	0.227116	17.1271	25.6271
80	30.2809	-141.663	30.1238	15.7843	7.78086	22.8809	29.7809
100	33.566	-104.417	33.3715	19.9822	14.466	27.966	33.266
125	36.5733	-72.4359	36.3363	23.8244	20.4733	32.3733	36.3733
160	39.6064	-42.6579	39.3176	27.6913	26.2064	36.6064	39.5064
200	42.1095	-20.3257	41.7703	30.8676	31.2095	40.1095	42.1095
250	44.4111	-1.89158	44.0194	33.7674	35.8111	43.1111	44.4111
315	46.61	13.5605	46.1614	36.5064	40.01	45.81	46.61
400	48.7306	26.1528	48.2049	39.0847	43.9306	48.2306	48.7306
500	50.662	35.2829	49.9843	41.288	47.462	50.362	50.662
630	52.7525	42.5389	51.7233	43.3892	50.8525	52.6525	52.7525
800	55.0716	48.1995	53.4395	45.3974	54.2716	55.0716	55.0716
1000	57.2947	52.2691	54.9951	47.1504	57.2947	57.2947	57.2947
1250	59.4967	55.6125	56.536	48.8106	60.0967	59.4967	59.4967
1600	61.5033	58.0196	58.2332	50.5702	62.5033	61.5033	61.4033
2000	63.6285	61.2871	59.0207	52.1189	64.8285	63.5285	63.4285
2500	63.5826	61.1385	58.749	53.6599	64.8826	63.3826	63.2826
3150	61.2612	56.6195	57.3759	55.2023	62.4612	60.8612	60.7612
4000	60.348	55.181	55.7261	55.7974	61.348	59.648	59.548
5000	58.7408	51.764	54.1816	55.267	59.2408	57.5408	57.4408
6300	56.7366	47.3904	52.5482	53.7484	56.6366	54.8366	54.7366
8000	54.7152	41.4635	50.7924	52.0987	53.6152	51.8152	51.7152
10000	52.9379	34.1648	49.0631	50.5496	50.4379	48.6379	48.5379
12500	51.1981	24.7136	47.2215	48.9614	46.8981	45.0981	44.9981
16000	49.2126	11.2195	45.0227	47.1279	42.6126	40.8126	40.7126
20000	47.307	-4.20437	42.8612	45.3736	38.007	36.207	36.107

By comparing the OASPL we may see that the overall result is OK. The OASPL for +4 AOA is 71.0019 dB, while for -4 AOA is 71.0171 dB.

The individual source contributions were compared at three different frequencies:

+4 AOA

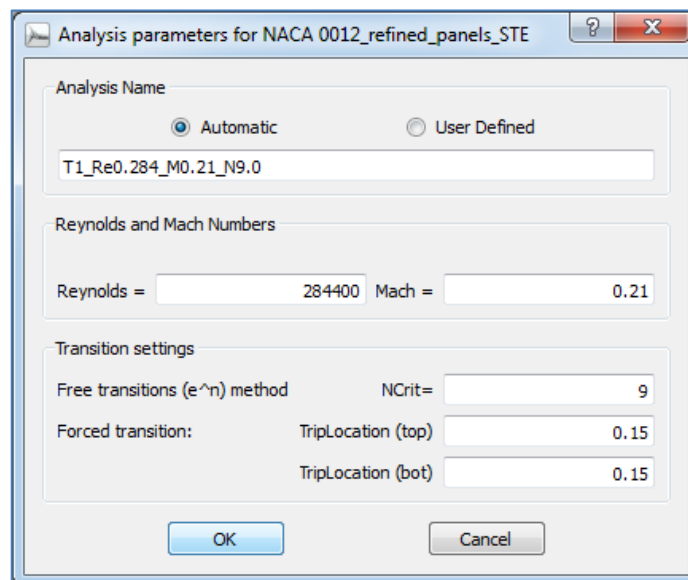
Freq [Hz]	SPL (dB)	SPLa	SPLs	SPLp
50	22.2248	-240.606	22.1248	5.7984
1000	57.2304	52.158	54.9347	47.2122
2000	63.5957	61.241	58.9912	52.1776

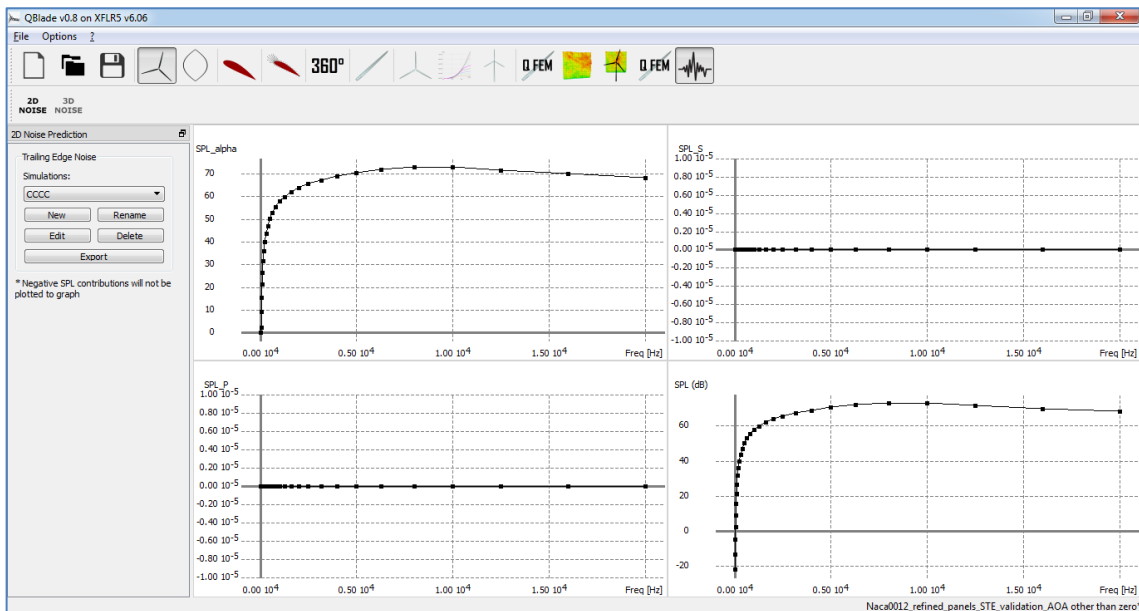
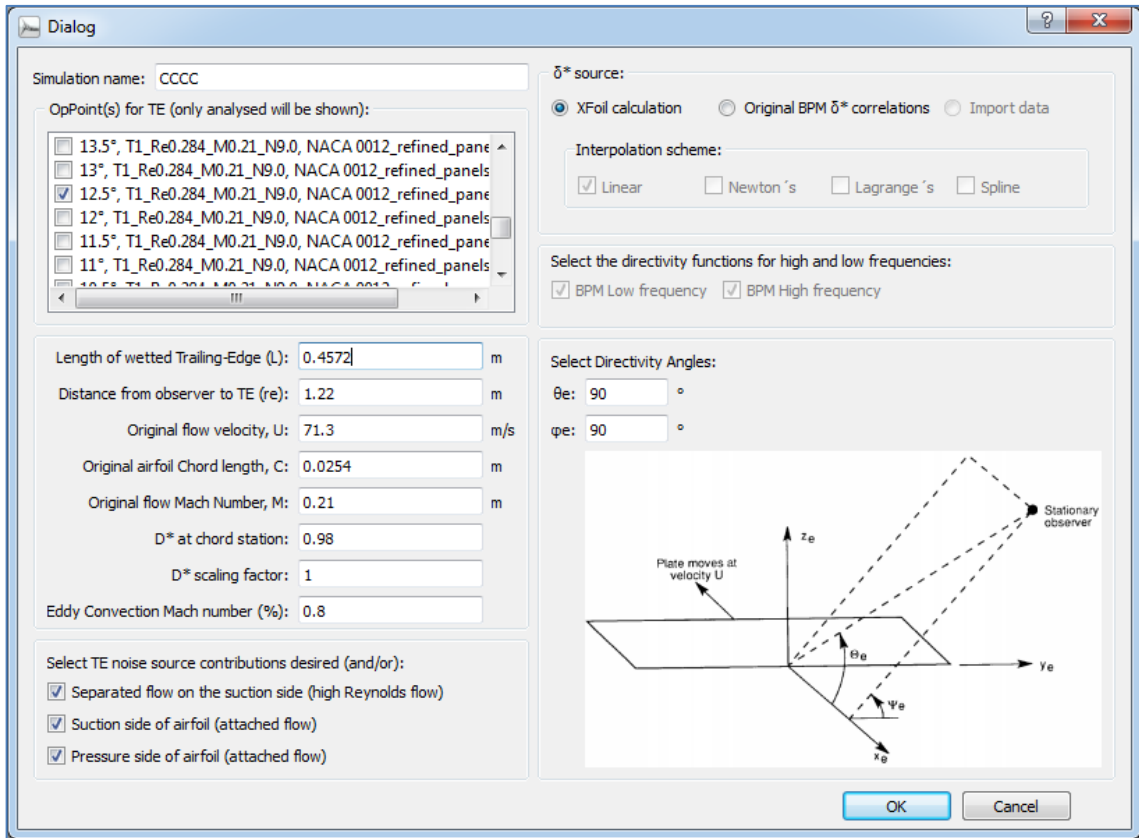
-4 AOA

Freq [Hz]	SPL (dB)	SPLa	SPLs	SPLp
50	22.3387	-239.304	22.2442	5.6642
1000	57.2947	52.2691	54.9951	47.1504
2000	63.6285	61.2871	59.0207	52.1189

The differences are very small and due only to the minor XFOIL asymmetric calculation results for the pressure and suction sides for +4 and -4 degrees. Ok.

Verification for AOA larger than the Switching Angle:





SPL_Alpha should be the sole contributor for this AOA, which is exactly the behavior displayed.

Export File (from QBlade): Modified_QBlade_output_for_validation_Jan_15_2016_12_5_AOA.txt

Noise prediction file export

Alpha: 12.5, Re = 284400

OASPL: 80.8124 dB

OASPL (A): 79.6286 dB(A)

OASPL (B): 77.9802 dB(B)

OASPL (C): 77.8858 dB(C)

SPL_a: 80.8124

SPL_s: 14.7712

SPL_p: 14.7712

Freq [Hz]	SPL (dB)	SPLa	SPLs	SPLp	SPL (dB(A))	SPL (dB(B))	SPL (dB(C))
25	-21.9211	-21.9211	0	0	-66.6211	-42.3211	-26.3211
31.5	-13.2904	-13.2904	0	0	-52.6904	-30.3904	-16.2904
40	-5.01777	-5.01777	0	0	-39.6178	-19.2178	-7.01777
50	2.14124	2.14124	0	0	-28.0588	-9.45876	0.84124
63	9.00508	9.00508	0	0	-17.1949	-0.294915	8.20508
80	15.5407	15.5407	0	0	-6.95933	8.14067	15.0407
100	21.1592	21.1592	0	0	2.05916	15.5592	20.8592
125	26.3341	26.3341	0	0	10.2341	22.1341	26.1341
160	31.5729	31.5729	0	0	18.1729	28.5729	31.4729
200	35.8969	35.8969	0	0	24.9969	33.8969	35.8969
250	39.8565	39.8565	0	0	31.2565	38.5565	39.8565
315	43.6006	43.6006	0	0	37.0006	42.8006	43.6006
400	47.1188	47.1188	0	0	42.3188	46.6188	47.1188
500	50.1091	50.1091	0	0	46.9091	49.8091	50.1091
630	52.9329	52.9329	0	0	51.0329	52.8329	52.9329
800	55.589	55.589	0	0	54.789	55.589	55.589
1000	57.8561	57.8561	0	0	57.8561	57.8561	57.8561
1250	59.9428	59.9428	0	0	60.5428	59.9428	59.9428
1600	62.0717	62.0717	0	0	63.0717	62.0717	61.9717
2000	63.8617	63.8617	0	0	65.0617	63.7617	63.6617
2500	65.5504	65.5504	0	0	66.8504	65.3504	65.2504
3150	67.2198	67.2198	0	0	68.4198	66.8198	66.7198
4000	68.8902	68.8902	0	0	69.8902	68.1902	68.0902
5000	70.4312	70.4312	0	0	70.9312	69.2312	69.1312
6300	72.0272	72.0272	0	0	71.9272	70.1272	70.0272
8000	73.033	73.033	0	0	71.933	70.133	70.033

10000	72.8584	72.8584	0	0	70.3584	68.5584	68.4584
12500	71.6143	71.6143	0	0	67.3143	65.5143	65.4143
16000	69.9096	69.9096	0	0	63.3096	61.5096	61.4096
20000	68.3663	68.3663	0	0	59.0663	57.2663	57.1663

Spreadsheet data for the 12.5° AOA calculation, using XFOIL Input.

Output TBL file (run inside modified Qblade):

D_star_files_for_28_aug_2015_Validation_Re_284k.txt

QBlade v0.8 on XFLR5 v6.06

NACA 0012_refined_panels_STE

Alpha = 12.5, Re = 284400, Ma= 0.2100, ACrit= 9.0

Top Side

x	Hk	Ue/Vinf	Cf	Cd	A/A0	D*	Theta	CTq	
0.976198	4.66799	1.01129	-0.00001	0.00580	0.07373	0.07764		0.01650	0.10341
0.983339	4.73892	1.01066	-0.00001	0.00587	0.07410	0.07915		0.01657	0.10392

Bottom Side

x	Hk	Ue/Vinf	Cf	Cd	A/A0	D*	Theta	CTq	
0.976201	1.43445	1.05659	0.00568	0.00237	0.03847	0.00238		0.00164	0.03617
0.983341	1.42816	1.06325	0.00582	0.00242	0.03825	0.00235		0.00162	0.03575

Spreadsheet displacement thickness input:

Suction Side (superior para alfa positivos, inferior para alfas negativos)	Location	Chord Station	D* (δ^*s)
	Upstream	0.976198	0.07764
	Specified Station	0.98000	0.07844
	Downstream	0.983339	0.07915
	D* Value (XFOIL)		0.00199
Pressure Side (inferior para alfas positivos, superior para alfas negativos)	Location	Chord Station	D* (δ^*p)
	Upstream	0.976201	0.00238
	Specified Station	0.980000	0.00236
	Downstream	0.983341	0.00235
	D* Value (XFOIL)		0.00006
			6.00E-05

Spectrum output from the spreadsheet.

TE noise contributions				
	Sep	Suction Side	Pressure-Side	Total SPL
Freq [Hz]	SPL_alpha	SPL_S	SPL_P	SPL (dB)
25	-22.04	-9999999999	-9999999999	-22.04
31.5	-13.41	-9999999999	-9999999999	-13.41
40	-5.13	-9999999999	-9999999999	-5.13
50	2.03	-9999999999	-9999999999	2.03
63	8.90	-9999999999	-9999999999	8.90
80	15.44	-9999999999	-9999999999	15.44
100	21.06	-9999999999	-9999999999	21.06
125	26.24	-9999999999	-9999999999	26.24
160	31.48	-9999999999	-9999999999	31.48
200	35.80	-9999999999	-9999999999	35.80
250	39.76	-9999999999	-9999999999	39.76
315	43.51	-9999999999	-9999999999	43.51
400	47.03	-9999999999	-9999999999	47.03
500	50.02	-9999999999	-9999999999	50.02
630	52.85	-9999999999	-9999999999	52.85
800	55.50	-9999999999	-9999999999	55.50
1000	57.77	-9999999999	-9999999999	57.77
1250	59.86	-9999999999	-9999999999	59.86
1600	61.99	-9999999999	-9999999999	61.99
2000	63.78	-9999999999	-9999999999	63.78
2500	65.47	-9999999999	-9999999999	65.47
3150	67.14	-9999999999	-9999999999	67.14
4000	68.81	-9999999999	-9999999999	68.81
5000	70.35	-9999999999	-9999999999	70.35
6300	71.95	-9999999999	-9999999999	71.95
8000	72.96	-9999999999	-9999999999	72.96
10000	72.79	-9999999999	-9999999999	72.79
12500	71.55	-9999999999	-9999999999	71.55
16000	69.85	-9999999999	-9999999999	69.85
20000	68.30	-9999999999	-9999999999	68.30

Verification table:

Frequency (Hz)	Source	SPL_alpha (dB)	SPL_S (dB)	SPL_P (dB)	SPL (dB)	Diff.(dB)
50	Spreadsheet	2.03	-∞	-∞	2.03	-0.11
	Code	2.14	0	0	2.14	
1.000	Spreadsheet	57.77	-∞	-∞	57.77	-0.09
	Code	57.86	0	0	57.86	

8.000	Spreadsheet	72.96	$-\infty$	$-\infty$	72.96	-0.07
	Code	73.03	0	0	73.03	

Ok, the numbers are very close and improve towards the peak frequency.

13- Verification cases for displacement thickness calculated via original BPM correlations:

The same three cases will be validated: $AOA=0^\circ$, $AOA=4^\circ$, $AOA=12.5^\circ$, with further testing for negative AOA and one source selection, only:

AOA=0°

Input screen for the case where the original BPM correlations will be used for displacement thickness evaluation:

Dialog

Simulation name: BPM_AAAA

OpPoint(s) for TE (only analysed will be shown):

- 2°, T1_Re1.500_M0.21_N9.0 (4), NACA 0012_refined_pani
- 1.5°, T1_Re1.500_M0.21_N9.0 (4), NACA 0012_refined_pa
- 1°, T1_Re1.500_M0.21_N9.0 (4), NACA 0012_refined_pani
- 0.5°, T1_Re1.500_M0.21_N9.0 (4), NACA 0012_refined_pa
- 0°, T1_Re1.500_M0.21_N9.0 (4), NACA 0012_refined_pani
- 0.5°, T1_Re1.500_M0.21_N9.0 (4), NACA 0012_refined_p

δ* source:

XFoil calculation Original BPM δ* correlations Import data

AOA, α: 0 °

Chord based Reynolds number, Rc: 1500000

Type of transition: Fully turbulent

Select the directivity functions for high and low frequencies:

BPM Low frequency BPM High frequency

Select Directivity Angles:

θe: 90 °

φe: 90 °

Length of wetted Trailing-Edge (L): 0.4572 m

Distance from observer to TE (re): 1.22 m

Original flow velocity, U: 71.3 m/s

Original airfoil Chord length, C: 0.3048 m

Original flow Mach Number, M: 0.21 m

D* at chord station: 0.98

D* scaling factor: 1

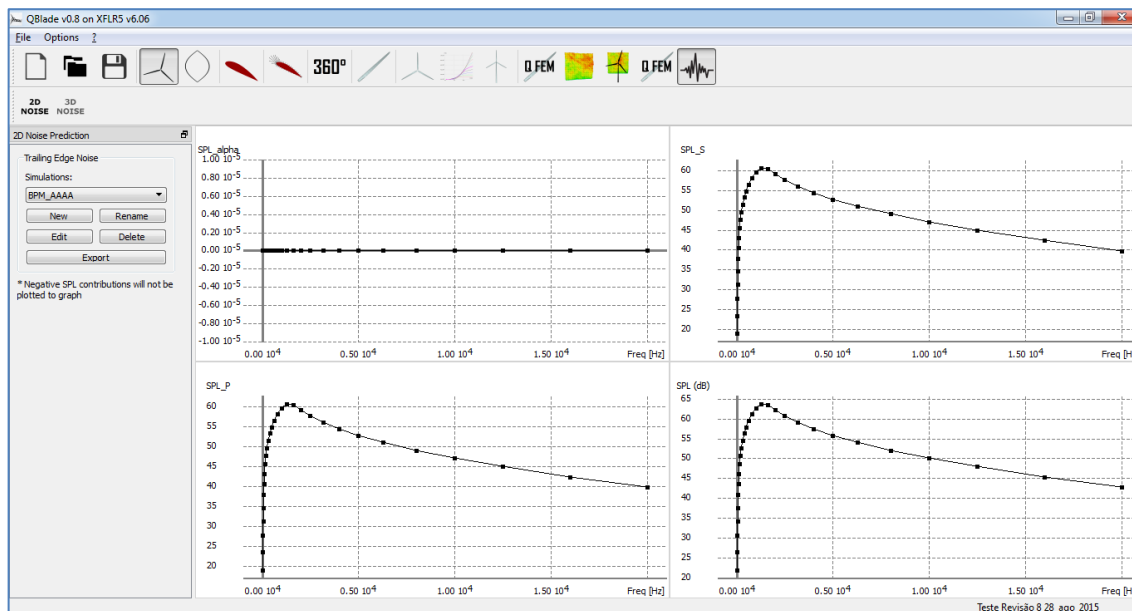
Eddy Convection Mach number (%): 0.8

Select TE noise source contributions desired (and/or):

- Separated flow on the suction side (high Reynolds flow)
- Suction side of airfoil (attached flow)
- Pressure side of airfoil (attached flow)

OK Cancel

When the Original BPM correlations for displacement thickness are selected, the dialog opens three new fields for the user to enter AOA data, chord-based Reynolds Number and Transition of Fully Turbulent Flow.



Output File:

Modified_QBlade_output_for_validation_Aug_28_2015_zero_AOA_BPM_corr.txt

Noise prediction file export

Alpha: 0, Re = 1.5e+06

OASPL: 71.9245 dB

OASPL (A): 72.0246 dB(A)

OASPL (B): 71.6365 dB(B)

OASPL (C): 71.6894 dB(C)

SPL_a: -930.887

SPL_s: 68.9142

SPL_p: 68.9142

Freq [Hz]	SPL (dB)	SPLa	SPLs	SPLp	SPL (dB(A))	SPL (dB(B))	SPL (dB(C))
25	21.9242	-1291.55	18.9139	18.9139	-22.7758	1.52417	17.5242
31.5	26.4217	-1233.48	23.4114	23.4114	-12.9783	9.32169	23.4217
40	30.6593	-1180.9	27.649	27.649	-3.9407	16.4593	28.6593
50	34.2672	-1138.14	31.2569	31.2569	4.06718	22.6672	32.9672
63	37.675	-1099.84	34.6647	34.6647	11.475	28.375	36.875
80	40.8754	-1066.15	37.8651	37.8651	18.3754	33.4754	40.3754
100	43.5965	-1039.63	40.5862	40.5862	24.4965	37.9965	43.2965
125	46.0844	-1017.43	43.0741	43.0741	29.9844	41.8844	45.8844
160	48.5959	-997.371	45.5856	45.5856	35.1959	45.5959	48.4959

200	50.6761	-982.839	47.6658	47.6658	39.7761	48.6761	50.6761
250	52.6024	-971.264	49.5921	49.5921	44.0024	51.3024	52.6024
315	54.4623	-961.925	51.452	51.452	47.8623	53.6623	54.4623
400	56.2701	-954.591	53.2598	53.2598	51.4701	55.7701	56.2701
500	57.8806	-949.399	54.8703	54.8703	54.6806	57.5806	57.8806
630	59.497	-945.231	56.4867	56.4867	57.597	59.397	59.497
800	61.1468	-941.702	58.1365	58.1365	60.3468	61.1468	61.1468
1000	62.6877	-939.466	59.6774	59.6774	62.6877	62.6877	62.6877
1250	63.6652	-936.428	60.6549	60.6549	64.2652	63.6652	63.6652
1600	63.4895	-936.805	60.4792	60.4792	64.4895	63.4895	63.3895
2000	62.2147	-941.953	59.2044	59.2044	63.4147	62.1147	62.0147
2500	60.6738	-942.664	57.6635	57.6635	61.9738	60.4738	60.3738
3150	59.0759	-946.234	56.0656	56.0656	60.2759	58.6759	58.5759
4000	57.3926	-950.85	54.3823	54.3823	58.3926	56.6926	56.5926
5000	55.7618	-956.483	52.7515	52.7515	56.2618	54.5618	54.4618
6300	53.9854	-964.144	50.9751	50.9751	53.8854	52.0854	51.9854
8000	52.0259	-974.529	49.0156	49.0156	50.9259	49.1259	49.0259
10000	50.0551	-986.965	47.0448	47.0448	47.5551	45.7551	45.6551
12500	47.9225	-1002.49	44.9122	44.9122	43.6225	41.8225	41.7225
16000	45.3439	-1023.81	42.3336	42.3336	38.7439	36.9439	36.8439
20000	42.7872	-1047.29	39.7769	39.7769	33.4872	31.6872	31.5872

The spreadsheet for zero AOA was then fed with the D^* correlations from the Model ($D^* = 2.66E-3$), in order to reproduce the original model intended spectrum:

Original BPM correlations for displacement thickenss				
Airfoil Chord	0,3048	m		
Reynolds Number	1.500.000	[] of the actual flow		
Type of Flow	H	H for Heavy-tripping, N for Natural transition		
For Alpha = 0 flows:				
For Heavy Tripping				
D*/C =	8,73E-03	[] , for both Pressure and Suction sides		
D* =	2,66E-03	[m] , for both Pressure and Suction sides		
For natural transition				
D*/C =	3,54E-03	[] , for both Pressure and Suction sides		
D* =	1,08E-03	[m] , for both Pressure and Suction sides		
For Alpha ≠ 0 flows:				
Alpha=	0	Graus(°)		
For the PRESSURE SIDE only				
Correction factor for D*: D*p/D*= 1 []				
Tripped flow				
D*p =	2,66E-03	[m]		
Natural transition flow				
D*p =	1,08E-03	[m]		
For the SUCTION SIDE, for Tripped flow				
Valor absoluto de alpha entre 0 e 5 graus	D*s/D=	1 []	D*s=	2,66E-03 [m]
Valor absoluto de alpha entre 5 e 12,5 graus	D*s/D=	0,381 []	D*s=	1,01E-03 [m]
Valor absoluto de alpha entre 12,5 e 25 graus	D*s/D=	14,296 []	D*s=	3,81E-02 [m]
For the SUCTION SIDE, for natural transition flow				
Valor absoluto de alpha entre 0 e 7,5 graus	D*s/D=	1 []	D*s=	1,08E-03 [m]
Valor absoluto de alpha entre 7,5 e 12,5 graus	D*s/D=	0,0162 []	D*s=	1,75E-05 [m]
Valor absoluto de alpha entre 12,5 e 25 graus	D*s/D=	54,42 []	D*s=	5,87E-02 [m]

Spreadsheet file:

1_BPM_Calculation_Procedure_zero_alpha_28_Aug_15_BPM_Corr.XLSX

Freq [Hz]	SPL_alpha	SPL_S	SPL_P	SPL (dB)
25	-1291.91	18.84	18.84	21.85
31.5	-1233.81	23.34	23.34	26.35
40	-1181.19	27.58	27.58	30.59
50	-1138.39	31.19	31.19	34.20
63	-1100.07	34.60	34.60	37.61
80	-1066.35	37.81	37.81	40.82
100	-1039.80	40.53	40.53	43.54
125	-1017.58	43.02	43.02	46.03
160	-997.50	45.53	45.53	48.54
200	-982.95	47.61	47.61	50.62
250	-971.36	49.54	49.54	52.55

315	-962.01	51.40	51.40	54.41
400	-954.67	53.21	53.21	56.22
500	-949.47	54.82	54.82	57.83
630	-945.29	56.43	56.43	59.45
800	-941.76	58.08	58.08	61.10
1000	-938.72	59.63	59.63	62.64
1250	-936.48	60.61	60.61	63.62
1600	-936.84	60.44	60.44	63.45
2000	-939.62	59.17	59.17	62.18
2500	-942.69	57.63	57.63	60.64
3150	-946.26	56.03	56.03	59.04
4000	-950.87	54.35	54.35	57.36
5000	-956.49	52.72	52.72	55.73
6300	-964.14	50.94	50.94	53.95
8000	-974.51	48.98	48.98	51.99
10000	-986.93	47.01	47.01	50.02
12500	-1002.44	44.88	44.88	47.89
16000	-1023.74	42.30	42.30	45.31
20000	-1047.19	39.75	39.75	42.76

TE noise contributions			
Sep	Suction Side	Pressure-Side	Total SPL
71.9	72.0	71.6	71.6
dB	dB(A)	dB(B)	dB(C)

OASPL value (unweighted and weighted) are in excellent agreement.

Verification table:

Frequency (Hz)	Source	SPL_alpha (dB)	SPL_S (dB)	SPL_P (dB)	SPL (dB)	Diff.(dB)
50	Spreadsheet	-1138.39	31.19	31.19	34.20	-0.07
	Code	-1138.14	31.26	31.26	34.27	
1.000	Spreadsheet	-938.72	59.63	59.63	62.64	-0.05
	Code	-939.47	59.68	59.68	62.69	
1.250	Spreadsheet	-936.48	60.61	60.61	63.62	-0.05
	Code	-936.43	60.65	60.65	63.67	

All the results are in excellent agreement, including the peak frequency of 1,250 Hz, which shifted in the fully turbulent flow, from the value previously calculated with the aid of XFLR5, for transition flow, when the peak was @ 1,500 Hz.

AOA=4°

Dialog

Simulation name: BPM_BBBB

OpPoint(s) for TE (only analysed will be shown):

- 20°, T1_Re1.500_M0.21_N9.0 (4), NACA 0012_refined_par
- 19.5°, T1_Re1.500_M0.21_N9.0 (4), NACA 0012_refined_p
- 19°, T1_Re1.500_M0.21_N9.0 (4), NACA 0012_refined_par
- 18.5°, T1_Re1.500_M0.21_N9.0 (4), NACA 0012_refined_p
- 18°, T1_Re1.500_M0.21_N9.0 (4), NACA 0012_refined_par
- 17.5°, T1_Re1.500_M0.21_N9.0 (4), NACA 0012_refined_p

δ* source:

XFoil calculation Original BPM δ* correlations Import data

AOA, α: 4 °

Chord based Reynolds number, R_c: 1120000

Type of transition: Fully turbulent

Select the directivity functions for high and low frequencies:

BPM Low frequency BPM High frequency

Select Directivity Angles:

θ_e: 90 °

φ_e: 90 °

Length of wetted Trailing-Edge (L): 0.4582 m

Distance from observer to TE (r_e): 1.22 m

Original flow velocity, U: 71.3 m/s

Original airfoil Chord length, C: 0.2286 m

Original flow Mach Number, M: 0.21 m

D* at chord station: 0.98

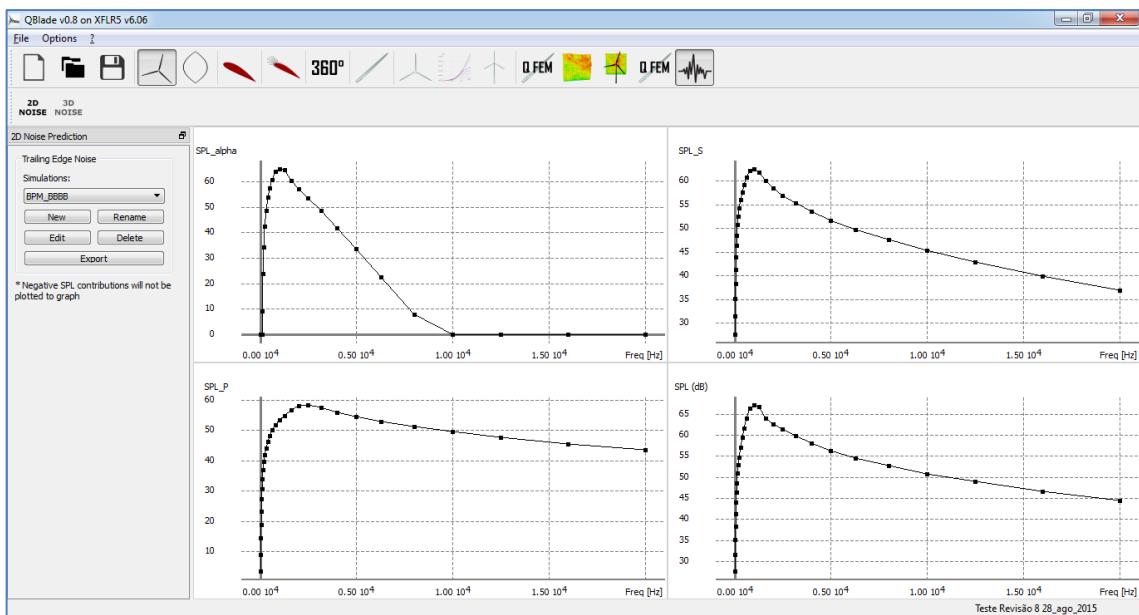
D* scaling factor: 1

Eddy Convection Mach number (%): 0.8

Select TE noise source contributions desired (and/or):

- Separated flow on the suction side (high Reynolds flow)
- Suction side of airfoil (attached flow)
- Pressure side of airfoil (attached flow)

OK Cancel



QBlade output file:

Modified_QBlade_output_for_validation_Aug_28_2015_4AOA_BPM_corr.txt

Noise prediction file export

Alpha: 4, Re = 1.12e+06

OASPL: 74.556 dB

OASPL (A): 74.3578 dB(A)

OASPL (B): 74.3336 dB(B)

OASPL (C): 74.4072 dB(C)

SPL_a: 70.9374

SPL_s: 70.7028

SPL_p: 66.4185

Freq [Hz]	SPL (dB)	SPLa	SPLs	SPLp	SPL (dB(A))	SPL (dB(B))	SPL (dB(C))
25	27.6121	-211.71	27.5955	3.42206	-17.0879	7.21207	23.2121
31.5	31.5135	-163.336	31.489	9.01143	-7.88652	14.4135	28.5135
40	35.1848	-120.056	35.1492	14.3039	0.584753	20.9848	33.1848
50	38.3099	-85.333	38.2607	18.8295	8.10992	26.7099	37.0099
63	41.2653	-54.6964	41.1982	23.1188	15.0653	31.9653	40.4653
80	44.0492	-28.2119	43.9595	27.1567	21.5492	36.6492	43.5492
100	46.4282	-7.76166	46.3134	30.5923	27.3282	40.8282	46.1282
125	48.6194	8.99657	48.4757	33.7294	32.5194	44.4194	48.4194
160	50.8616	23.765	50.6754	36.8829	37.4616	47.8616	50.7616
200	52.7883	34.1855	52.5176	39.4746	41.8883	50.7883	52.7883
250	54.7439	42.2801	54.2474	41.847	46.1439	53.4439	54.7439
315	56.9272	48.6809	55.9477	44.1	50.3272	56.1272	56.9272
400	59.3266	53.69	57.6373	46.2403	54.5266	58.8266	59.3266
500	61.5771	57.3645	59.1819	48.0939	58.3771	61.2771	61.5771
630	63.8902	60.6275	60.7778	49.893	61.9902	63.7902	63.8902
800	66.2772	63.8634	62.2089	51.6536	65.4772	66.2772	66.2772
1000	67.0797	64.9434	62.4866	53.2342	67.0797	67.0797	67.0797
1250	66.7374	64.6778	61.7056	54.7803	67.3374	66.7374	66.7374
1600	64.0085	60.2919	60.0094	56.4849	65.0085	64.0085	63.9085
2000	62.6232	57.1138	58.4685	57.8684	63.8232	62.5232	62.4232
2500	61.3863	53.3829	56.9131	58.2404	62.6863	61.1863	61.0863
3150	59.8672	48.4669	55.2543	57.5153	61.0672	59.4672	59.3672
4000	57.9545	41.7469	53.4588	55.8846	58.9545	57.2545	57.1545
5000	56.2464	33.494	51.6801	54.3436	56.7464	55.0464	54.9464
6300	54.4926	22.4543	49.7067	52.735	54.3926	52.5926	52.4926
8000	52.6185	7.86433	47.4967	51.0225	51.5185	49.7185	49.6185
10000	50.777	-9.15409	45.2489	49.3502	48.277	46.477	46.377
12500	48.8277	-29.8973	42.7976	47.5814	44.5277	42.7277	42.6277
16000	46.5245	-57.7154	39.8182	45.4816	39.9245	38.1245	38.0245
20000	44.2908	-87.7429	36.8552	43.4263	34.9908	33.1908	33.0908

Baseline spreadsheet calculation:

2_BPM Calculation Procedure_alpha_below_critical_4_Aug_15_BPM_Corr.XLSX

Original BPM correlations for displacement thickenss				
Airfoil Chord	0,2286	m		
Reynolds Number	1.120.000	[]	of the actual flow	
Type of Flow	H	H for Heavy-tripping, N for Natural transition		
For Alpha = 0 flows:				
For Heavy Tripping				
D*/C =	9,38E-03	[]	, for both Pressure and Suction sides	
D* =	2,14E-03	[m]	, for both Pressure and Suction sides	
For natural transition				
D*/C =	3,80E-03	[]	, for both Pressure and Suction sides	
D* =	8,69E-04	[m]	, for both Pressure and Suction sides	
For Alpha ≠ 0 flows:				
Alpha=	4	Graus(°)		
For the PRESSURE SIDE only				
Correction factor for D*:	D*p/D*=	0,700293	[]	
Tripped flow				
D*p =	1,50E-03	[m]		
Natural transition flow				
D*p =	6,09E-04	[m]		
For the SUCTION SIDE, for Tripped flow				
Valor absoluto de alpha entre 0 e 5 graus	D*s/D=	1,86896	[]	D*S= 4,01E-03 [m]
Valor absoluto de alpha entre 5 e 12,5 graus	D*s/D=	1,539306	[]	D*S= 3,30E-03 [m]
Valor absoluto de alpha entre 12,5 e 25 graus	D*s/D=	18,1307	[]	D*S= 3,89E-02 [m]
For the SUCTION SIDE, for natural transition flow				
Valor absoluto de alpha entre 0 e 7,5 graus	D*s/D=	1,86896	[]	D*S= 1,62E-03 [m]
Valor absoluto de alpha entre 7,5 e 12,5 graus	D*s/D=	0,272844	[]	D*S= 2,37E-04 [m]
Valor absoluto de alpha entre 12,5 e 25 graus	D*s/D=	69,01739	[]	D*S= 6,00E-02 [m]

Freq [Hz]	SPL_alpha	SPL_S	SPL_P	SPL (dB)
25	-212.03	27.53	3.34	27.54
31.5	-163.62	31.42	8.94	31.45
40	-120.30	35.09	14.23	35.12
50	-85.55	38.20	18.76	38.25
63	-54.89	41.14	23.05	41.21
80	-28.38	43.90	27.09	43.99
100	-7.91	46.26	30.53	46.37
125	8.87	48.42	33.67	48.56

160	23.66	50.62	36.82	50.81
200	34.09	52.46	39.42	52.73
250	42.20	54.19	41.79	54.69
315	48.61	55.90	44.04	56.87
400	53.62	57.59	46.19	59.27
500	57.30	59.13	48.04	61.52
630	60.56	60.73	49.84	63.83
800	63.80	62.16	51.60	66.22
1000	64.90	62.44	53.18	67.03
1250	63.62	61.67	54.73	66.09
1600	60.26	59.97	56.43	63.97
2000	57.09	58.43	57.82	62.59
2500	53.36	56.88	58.20	61.35
3150	48.45	55.22	57.48	59.83
4000	41.74	53.42	55.85	57.92
5000	33.50	51.65	54.31	56.21
6300	22.47	49.67	52.70	54.46
8000	7.90	47.46	50.99	52.58
10000	-9.10	45.22	49.32	50.74
12500	-29.82	42.77	47.55	48.79
16000	-57.61	39.79	45.45	46.49
20000	-87.61	36.83	43.39	44.26

OASPL----->	74.4	74.2	74.2	74.3
	dB	dB(A)	dB(B)	dB(C)

Frequency (Hz)	Source	SPL_alpha (dB)	SPL_S (dB)	SPL_P (dB)	SPL (dB)	Diff.(dB)
50	Spreadsheet	-85.55	38.20	18.76	38.25	-0.06
	Code	-85.33	38.26	18.83	38.31	
1.000	Spreadsheet	64.90	62.44	53.18	67.03	-0.05
	Code	64.94	62.49	53.23	67.08	

The comparison yields excellent results, both for OASPL and for peak frequency of 1,000 Hz.

AOA=-4° (negative)

Dialog

Simulation name: BPM_DDDD

OpPoint(s) for TE (only analysed will be shown):

Length of wetted Trailing-Edge (L): 0.4572 m

Distance from observer to TE (re): 1.22 m

Original flow velocity, U: 71.3 m/s

Original airfoil Chord length, C: 0.2286 m

Original flow Mach Number, M: 0.21

D* at chord station: 0.98

D* scaling factor: 1

Eddy Convection Mach number (%): 0.8

Select TE noise source contributions desired (and/or):

- Separated flow on the suction side (high Reynolds flow)
- Suction side of airfoil (attached flow)
- Pressure side of airfoil (attached flow)

δ^* source:

XFOil calculation Original BPM δ^* correlations Import data

AOA, α : -4 °

Chord based Reynolds number, R_c: 1120000

Type of transition: Fully turbulent

Select the directivity functions for high and low frequencies:

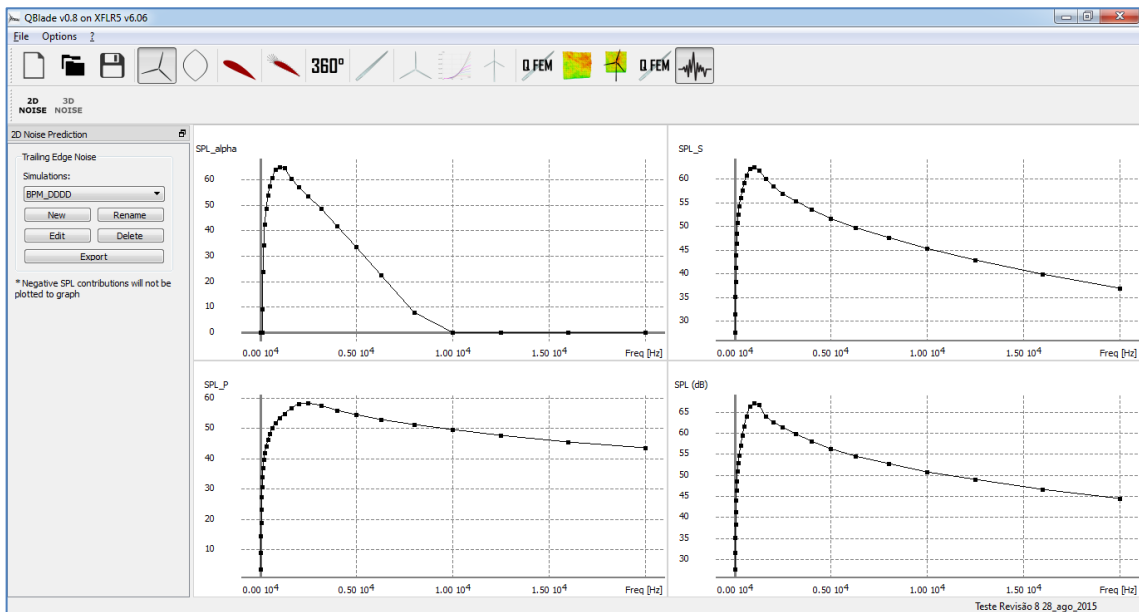
BPM Low frequency BPM High frequency

Select Directivity Angles:

θ_e : 90 °

φ_e : 90 °

OK Cancel



The pressure side and suction sides are now different but kept the same positions on the output screen, ok.

Modified_QBlade_output_for_validation_Aug_28_2015_minus4AOA_BPM_corr.txt

Noise prediction file export

Alpha: -4, Re = 1.12e+06

OASPL: 74.556 dB

OASPL (A): 74.3578 dB(A)

OASPL (B): 74.3336 dB(B)

OASPL (C): 74.4072 dB(C)

SPL_a: 70.9374

SPL_s: 70.7028

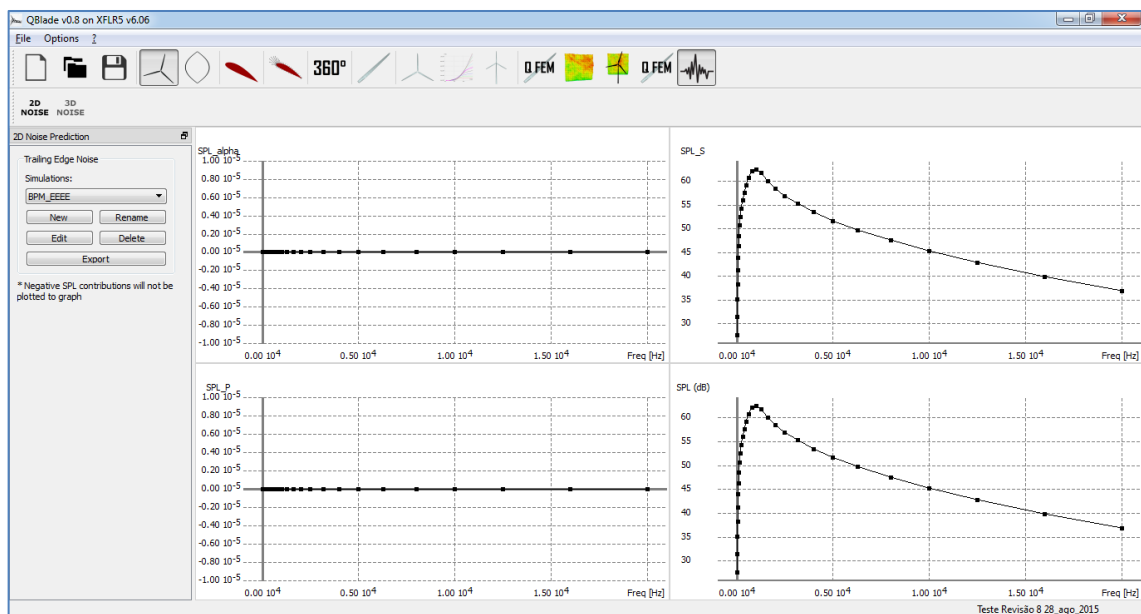
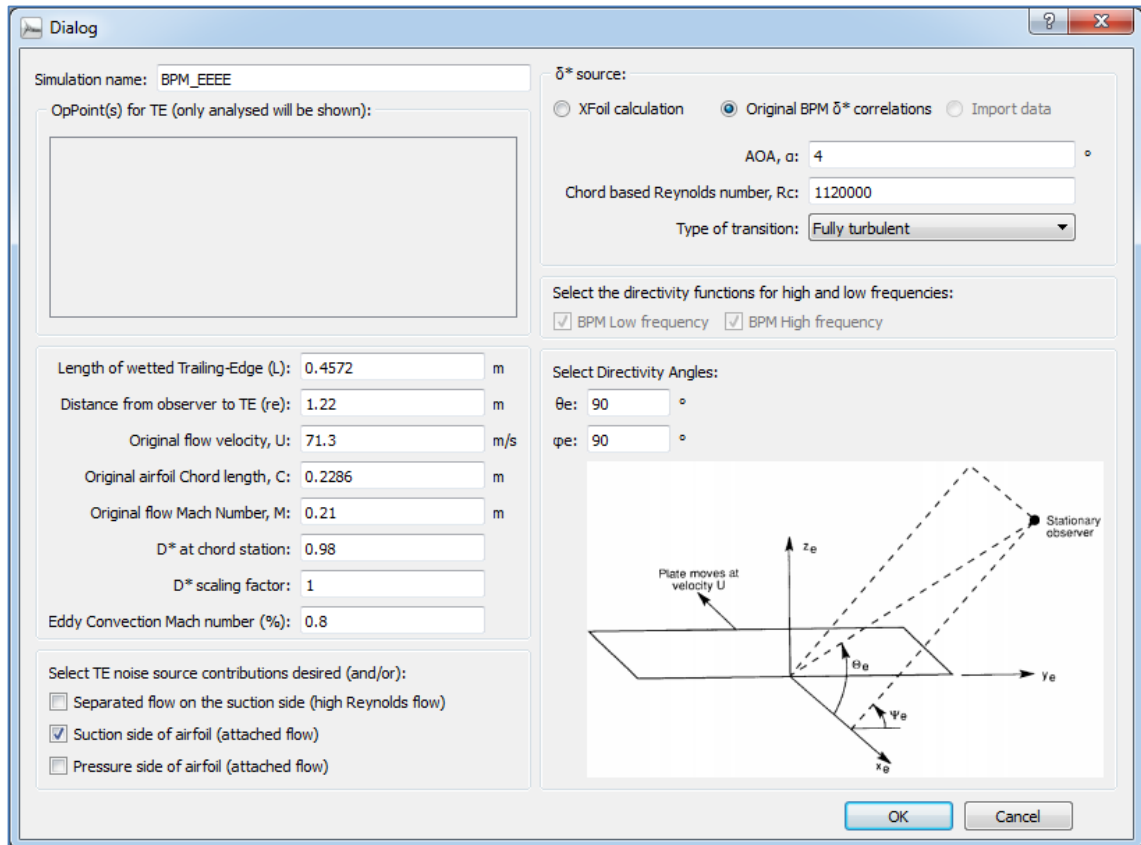
SPL_p: 66.4185

Freq [Hz]	SPL (dB)	SPLa	SPLs	SPLp	SPL (dB(A))	SPL (dB(B))	SPL (dB(C))
25	27.6095	-211.71	27.5929	3.41649	-17.0905	7.20947	23.2095
31.5	31.5114	-163.336	31.4869	9.00674	-7.8886	14.4114	28.5114
40	35.1831	-120.056	35.1475	14.3	0.583117	20.9831	33.1831
50	38.3086	-85.333	38.2594	18.8263	8.10864	26.7086	37.0086
63	41.2643	-54.6964	41.1973	23.1161	15.0643	31.9643	40.4643
80	44.0485	-28.2119	43.9588	27.1546	21.5485	36.6485	43.5485
100	46.4277	-7.76166	46.3129	30.5907	27.3277	40.8277	46.1277
125	48.619	8.99657	48.4754	33.7281	32.519	44.419	48.419
160	50.8613	23.765	50.6752	36.8819	37.4613	47.8613	50.7613
200	52.7881	34.1855	52.5175	39.4739	41.8881	50.7881	52.7881
250	54.7438	42.2801	54.2473	41.8464	46.1438	53.4438	54.7438
315	56.9271	48.6809	55.9476	44.0996	50.3271	56.1271	56.9271
400	59.3266	53.69	57.6373	46.2401	54.5266	58.8266	59.3266
500	61.5771	57.3645	59.1819	48.0937	58.3771	61.2771	61.5771
630	63.8902	60.6275	60.7779	49.8929	61.9902	63.7902	63.8902
800	66.2772	63.8634	62.2089	51.6535	65.4772	66.2772	66.2772
1000	67.0797	64.9434	62.4866	53.2342	67.0797	67.0797	67.0797
1250	66.7375	64.6778	61.7057	54.7803	67.3375	66.7375	66.7375
1600	64.0085	60.2919	60.0094	56.485	65.0085	64.0085	63.9085
2000	62.6232	57.1138	58.4685	57.8685	63.8232	62.5232	62.4232
2500	61.3863	53.3829	56.913	58.2404	62.6863	61.1863	61.0863
3150	59.8672	48.4669	55.2542	57.5154	61.0672	59.4672	59.3672
4000	57.9544	41.7469	53.4587	55.8846	58.9544	57.2544	57.1544
5000	56.2463	33.494	51.68	54.3436	56.7463	55.0463	54.9463
6300	54.4925	22.4543	49.7064	52.7349	54.3925	52.5925	52.4925
8000	52.6183	7.86433	47.4963	51.0225	51.5183	49.7183	49.6183
10000	50.7767	-9.15409	45.2483	49.3501	48.2767	46.4767	46.3767
12500	48.8273	-29.8973	42.7968	47.5813	44.5273	42.7273	42.6273
16000	46.5241	-57.7154	39.8171	45.4813	39.9241	38.1241	38.0241
20000	44.2902	-87.7429	36.8538	43.4259	34.9902	33.1902	33.0902

The OAPLS for +4 and -4 degrees is the same 74.56 dB for both calculations (Ok).

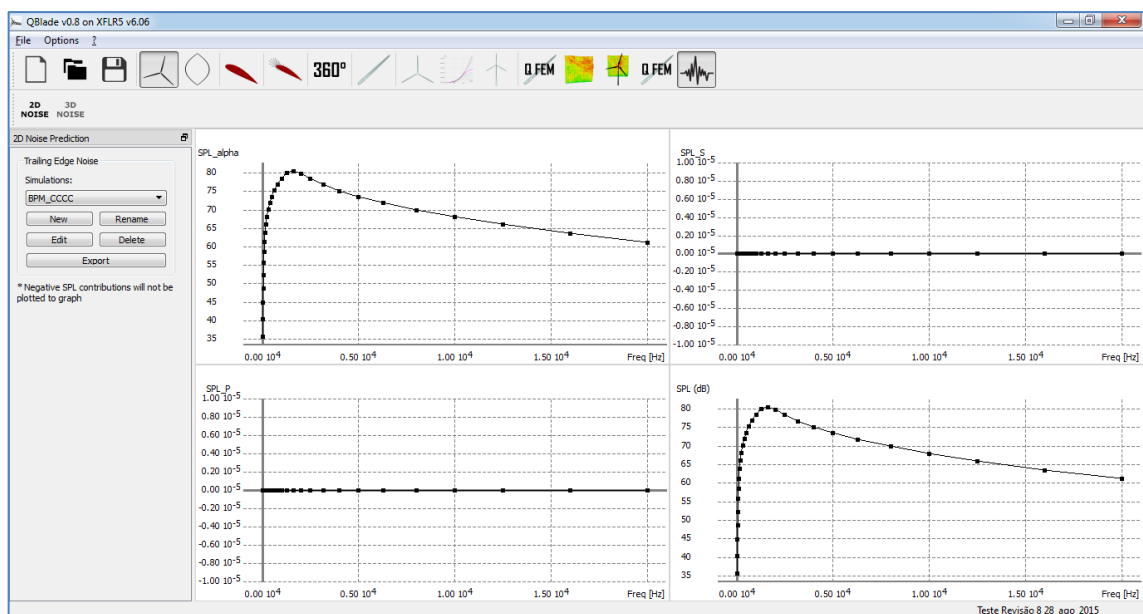
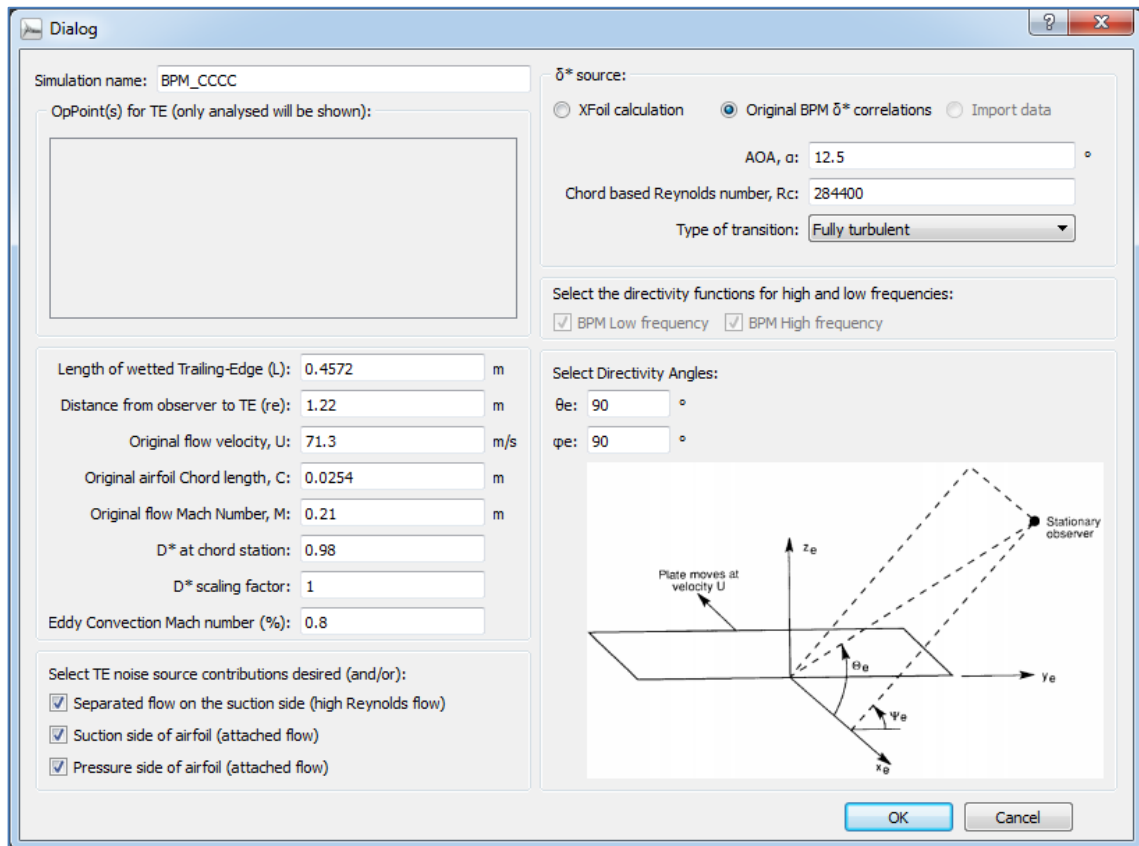
The values for 50 Hz and 1,000 Hz are ok.

What if on source only is checked:



Consistent output

Verification case: $AOA = 12.5^\circ$ (larger than Switching Angle):



QBlade output file:

Modified_QBlade_output_for_validation_Aug_28_2015_12_5AOA_BPM_corr.txt

Noise prediction file export

Alpha: 12.5, Re = 284400

OASPL: 88.6544 dB

OASPL (A): 88.9345 dB(A)

OASPL (B): 88.3343 dB(B)

OASPL (C): 88.3545 dB(C)

SPL_a: 88.6544

SPL_s: 14.7712

SPL_p: 14.7712

Freq [Hz]	SPL (dB)	SPLa	SPLs	SPLp	SPL (dB(A))	SPL (dB(B))	SPL (dB(C))
25	35.7101	35.7078	0	0	-8.98991	15.3101	31.3101
31.5	40.459	40.4582	0	0	1.059	23.359	37.459
40	44.9393	44.939	0	0	10.3393	30.7393	42.9393
50	48.7575	48.7574	0	0	18.5575	37.1575	47.4575
63	52.3662	52.3661	0	0	26.1662	43.0662	51.5662
80	55.7561	55.7561	0	0	33.2561	48.3561	55.2561
100	58.6375	58.6375	0	0	39.5375	53.0375	58.3375
125	61.2696	61.2696	0	0	45.1696	57.0696	61.0696
160	63.9218	63.9218	0	0	50.5218	60.9218	63.8218
200	66.1123	66.1123	0	0	55.2123	64.1123	66.1123
250	68.1327	68.1327	0	0	59.5327	66.8327	68.1327
315	70.0731	70.0731	0	0	63.4731	69.2731	70.0731
400	71.946	71.946	0	0	67.146	71.446	71.946
500	73.6007	73.6007	0	0	70.4007	73.3007	73.6007
630	75.2459	75.2459	0	0	73.3459	75.1459	75.2459
800	76.9035	76.9035	0	0	76.1035	76.9035	76.9035
1000	78.4445	78.4445	0	0	78.4445	78.4445	78.4445
1250	79.918	79.918	0	0	80.518	79.918	79.918
1600	80.4705	80.4705	0	0	81.4705	80.4705	80.3705
2000	79.8631	79.8631	0	0	81.0631	79.7631	79.6631
2500	78.3708	78.3708	0	0	79.6708	78.1708	78.0708
3150	76.7748	76.7748	0	0	77.9748	76.3748	76.2748
4000	75.1152	75.1152	0	0	76.1152	74.4152	74.3152
5000	73.5233	73.5233	0	0	74.0233	72.3233	72.2233
6300	71.8041	71.8041	0	0	71.7041	69.9041	69.8041
8000	69.9218	69.9218	0	0	68.8218	67.0218	66.9218
10000	68.0396	68.0396	0	0	65.5396	63.7396	63.6396
12500	66.0117	66.0117	0	0	61.7117	59.9117	59.8117
16000	63.5676	63.5676	0	0	56.9676	55.1676	55.0676
20000	61.1491	61.1491	0	0	51.8491	50.0491	49.9491

Baseline spreadsheet calculation:

3_BPM Calculation Procedure_alpha_above_critical_28_aug_15_BPM_Corr.xlsx

Original BPM correlations for displacement thickness			
Airfoil Chord	0,0254	m	
Reynolds Number	284.400	[]	of the actual flow
Type of Flow	H	H for Heavy-tripping, N for Natural transition	
For Alpha = 0 flows:			
For Heavy Tripping			
D*/C =	1,44E-02	[]	for both Pressure and Suction sides
D* =	3,65E-04	[m]	for both Pressure and Suction sides
For natural transition			
D*/C =	5,91E-03	[]	for both Pressure and Suction sides
D* =	1,50E-04	[m]	for both Pressure and Suction sides
For Alpha ≠ 0 flows:			
Alpha =	12,5	Graus(°)	
For the PRESSURE SIDE only			
Correction factor for D*:	D*p/D* =	0,433074	[]
Tripped flow			
D*p =	1,58E-04	[m]	
Natural transition flow			
D*p =	6,50E-05	[m]	
For the SUCTION SIDE, for Tripped flow			
Valor absoluto de alpha entre 0 e 5 graus	D*s/D =	7,059111	[]
	D*s =	2,57E-03	[m]
Valor absoluto de alpha entre 5 e 12,5 graus	D*s/D =	29,91748	[]
	D*s =	1,09E-02	[m]
Valor absoluto de alpha entre 12,5 e 25 graus	D*s/D =	30,04101	[]
	D*s =	1,10E-02	[m]
For the SUCTION SIDE, for natural transition flow			
Valor absoluto de alpha entre 0 e 7,5 graus	D*s/D =	7,059111	[]
	D*s =	1,06E-03	[m]
Valor absoluto de alpha entre 7,5 e 12,5 graus	D*s/D =	110,1577	[]
	D*s =	1,65E-02	[m]
Valor absoluto de alpha entre 12,5 e 25 graus	D*s/D =	114,3559	[]
	D*s =	1,72E-02	[m]

Freq [Hz]	TE noise contributions			
	Sep	Suction Side	Pressure-Side	Total SPL
	SPL_alpha	SPL_S	SPL_P	SPL (dB)
25	35.72	-999999999999	-999999999999	35.72
31.5	40.46	-999999999999	-999999999999	40.46
40	44.94	-999999999999	-999999999999	44.94
50	48.75	-999999999999	-999999999999	48.75
63	52.36	-999999999999	-999999999999	52.36
80	55.74	-999999999999	-999999999999	55.74
100	58.62	-999999999999	-999999999999	58.62
125	61.25	-999999999999	-999999999999	61.25

160	63.90	-999999999999	-999999999999	63.90
200	66.09	-999999999999	-999999999999	66.09
250	68.10	-999999999999	-999999999999	68.10
315	70.04	-999999999999	-999999999999	70.04
400	71.91	-999999999999	-999999999999	71.91
500	73.57	-999999999999	-999999999999	73.57
630	75.21	-999999999999	-999999999999	75.21
800	76.87	-999999999999	-999999999999	76.87
1000	78.41	-999999999999	-999999999999	78.41
1250	79.88	-999999999999	-999999999999	79.88
1600	80.42	-999999999999	-999999999999	80.42
2000	79.79	-999999999999	-999999999999	79.79
2500	78.30	-999999999999	-999999999999	78.30
3150	76.70	-999999999999	-999999999999	76.70
4000	75.04	-999999999999	-999999999999	75.04
5000	73.45	-999999999999	-999999999999	73.45
6300	71.73	-999999999999	-999999999999	71.73
8000	69.84	-999999999999	-999999999999	69.84
10000	67.96	-999999999999	-999999999999	67.96
12500	65.93	-999999999999	-999999999999	65.93
16000	63.48	-999999999999	-999999999999	63.48
20000	61.06	-999999999999	-999999999999	61.06

OASPL----->

88.6	88.9	88.3	88.3
dB	dB(A)	dB(B)	dB(C)

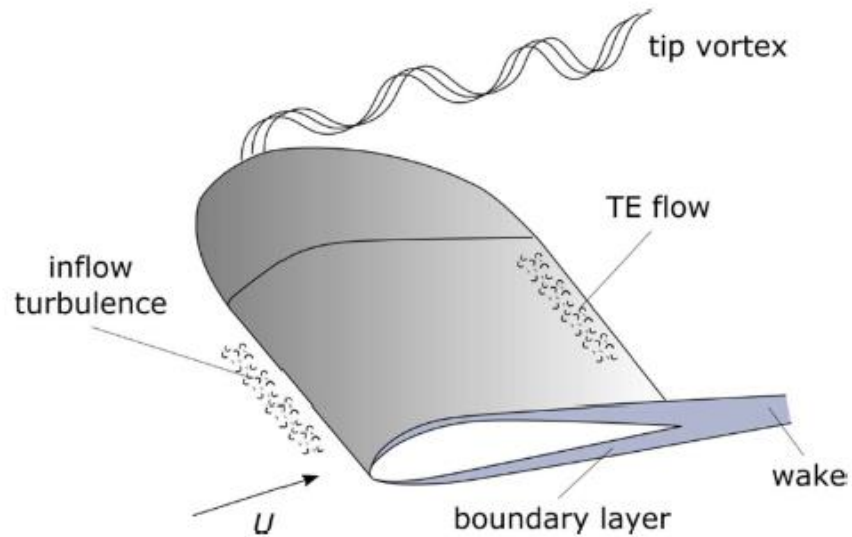
The OASPL is consistent (88.6 for the spreadsheet and 88,6 for the calculation).

Verification table:

Frequency (Hz)	Source	SPL_alpha (dB)	SPL_S (dB)	SPL_P (dB)	SPL (dB)	Diff.(dB)
50	Spreadsheet	48.75	-∞	-∞	48.75	
	Code	48.75	0	0	48.75	
1.000	Spreadsheet	78.41	-∞	-∞	78.41	
	Code	78.44	0	0	78.44	
1.600	Spreadsheet	80.42	-∞	-∞	80.42	
	Code	80.47	0	0	80.47	

All the results are in excellent agreement, including the peak frequency of 1,600 Hz.

APPENDIX J - VERIFICATION AND VALIDATION OF THE AIRFOIL TRAILING-EDGE NOISE PREDICTION MODULE (PNOISE) INSIDE QBLADE V0.95



Poli-USP – TU-Berlin Collaboration



POLI USP

**Technische
Universität
Berlin**



June, 2016.

Collaboration team members:

At Poli-USP⁸⁸: Module conception, development and integration into QBlade v0.8; V&V for both integrations.

Prof. M. Eng. Joseph Youssif Saab Jr. (corresponding author: joseph.saab@usp.br).

Prof. Dr. Eng. Marcos de Mattos Pimenta.

Prof. Dr. Eng. José Roberto Castilho Piqueira, Director, EPUSP.

Ricardo Marques Augusto (Programming).

At TU-Berlin⁸⁹: Output improvements, code clean-up and integration into Qblade v0.95.

Prof. Dipl.- Ing. David Marten.

Dr. George Pechlivanoglou, Head, HFI Institute.

Dr. Christian Navid Nayeri.

Prof. Dr. Christian Oliver Pachereit.

Nikolai Moesus (Programming).

⁸⁸ Escola Politécnica da Universidade de São Paulo, Brasil. Departamento de Engenharia Mecânica, área de Energia e Fluidos (<http://www.poli.usp.br/>)

⁸⁹ Technische Universität Berlin. Institut für Strömungsmechanik und Technische Akustik (<http://fd.tu-berlin.de/>)

1 Introduction

The new airfoil TE noise module was developed under a Poli-USP and TU-Berlin collaboration project.

The TE noise module is based on a modified BPM TE noise model (Brooks, Pope, & Marcolini, Airfoil Self-Noise and Prediction, 1989) with the XFLR5 (Drela, Youngren, & Deperrois, XFOIL/XFLR5, 2009) providing the turbulent boundary layer data, both integrated inside the unique wind-turbine-design, graphical interface and user-friendly environment provided by the QBlade software (Pechlivanoglou, Marten, G., N., & Wendler, 2009), (Marten D. , Extension of an Aerodynamic Simulator for Wind Turbine Blade Design and Performance Analysis, 2010), (Marten & Wendler, Qblade Guidelines v0.6, 2013), (Marten D. , Qblade Short Manual V0.8, 2014).

Other self-noise sources as well as inflow noise models will be added in the future as part of the collaboration scope. Also a “quasi-3D rotor” noise prediction tool is planned.

The 2D TE noise module was developed and integrated in a beta version into QBlade V0.8, when it was thoroughly verified and validated.

The module was later integrated into the newer QBlade V0.95 for public release. In this re-integration process, some improvements were made to the output graphs and files and also to the internal structure of the code. Despite the effort to keep the calculation routines intact, it was considered necessary once more to verify and validate the new integration prior to public release, which is the purpose of the present text.

This text is not a rigorous technical paper in format nor is it intended to be a detailed manual on the airfoil TE noise module inside QBlade v0.95.

2 Definitions

The following definitions were extracted from Oberkampf and Roy (Oberkampf & Roy, 2012) and applied throughout the verification and validation (V&V) procedure:

Prediction: use of a computational model to foretell the state of a physical system under conditions for which the computational model has not been validated.

Code verification: the process of determining that the numerical algorithms are correctly implemented in the computer code and of identifying errors in the software.

Solution verification: the process of determining the correctness of the input data, the numerical accuracy of the solution obtained and the correctness of output data for a particular simulation.

Model validation: quantification of the accuracy of the computational model results by comparing the computed system response quantities of interest with experimentally measured quantities of interest. It becomes a mathematical model validation only if code and solution verification were satisfactorily accomplished.

3 Verification and Validation range.

The code and solution verifications were accomplished within the original limitations of the BPM model (Brooks, Pope, & Marcolini, Airfoil Self-Noise and Prediction, 1989).

The validation of the results was accomplished against the original BPM experimental spectra provided in the seminal BPM paper (Brooks, Pope, & Marcolini, Airfoil Self-Noise and Prediction, 1989).

The use of the model for assessing the TE noise of a generic airfoil geometry at large Reynolds and Mach number flows has become a practical reality with the current integration of the BPM model to the XFLR5 and QBlade functionalities. As defined earlier, the use of model beyond the original validation scope is called a PREDICTION and, by definition, implies that it shall be made at the user own responsibility and risk, particularly in the case of absolute noise value assessment.

For improved performance, when using TBL displacement thickness reading over the TE from a XFLR5 output file, a recommendation is made for the data to be taken at 98% chord station (Saab Jr & Pimenta, 2016) as a *compromise station* among fully turbulent and transition flows, but the number is provided as a default value that may and should be altered at the discretion of the user. The same reasoning applies to the default eddy-convection Mach number ($0.8 \cdot M$) and other default input data, like the observer distance from the source and the directivity angles, for instance.

4 Model validity range and scope.

The BPM model (Brooks, Pope, & Marcolini, Airfoil Self-Noise and Prediction, 1989) is based on previous experimental work by (Brooks & Hodgson, 1981), (Brooks & Marcolini, 1985), (Brooks & Marcolini, Airfoil Trailing-Edge Flow Measurements, 1986).

The experimental cases which provided the database for the 2D TE noise are:

	Reference	Chord-Based Reynolds Number Range	Mach Number Range	AOA (α)	TU	Type of flow	TE Type
1	(Brooks & Hodgson, 1981)	$9.5 \times 10^5 < Re_c < 2.5 \times 10^6$	$M < 0.19$	$0^\circ, 5^\circ, 10^\circ$	N/A	Tripped	From blunt to sharp variations
2	(Brooks & Marcolini, 1985)	$4.8 \times 10^4 < Re_c < 2.5 \times 10^6$	$M \leq 0.208$	0°	$< 0.05\%$	Tripped and untripped	Very Sharp
3	(Brooks & Marcolini, 1986)	$Re_c < 3.0 \times 10^6$	$M \leq 0.208$	Up to 19.8°	$\sim 0.03\% / < 0.54\%$ Uniform flow / TE	Tripped and untripped	Very Sharp
4	(Brooks, Pope, & Marcolini, Airfoil Self-Noise and Prediction, 1989)	$Re_c \leq 1.5 \times 10^6$	$M \leq 0.208$	Up to 19.8°	Low turbulence	Tripped and untripped	Very Sharp

In the seminal BPM paper (Brooks, Pope, & Marcolini, Airfoil Self-Noise and Prediction, 1989), the TE noise model was introduced and validated for turbulent (tripped) flow up to $Re_c \leq 1.5 \times 10^6$, $M < 0.21$ and 19.8° AOA. All experiments and thus, the resulting model validation, were made for the NACA 0012 airfoil, based on the acoustic spectra measured in this range. For further details, see page 51 of the BPM report.

Also, the BPM authors, in page 99 of their report, state that:

“For the turbulent-boundary-layer-trailing-edge noise and separation noise sources, an accurate and generally applicable predictive capability is demonstrated, especially for the important conditions of high Reynolds numbers and low to moderate angle of attack”

“The unique prediction capability presented should prove useful for the determination of broadband noise for helicopter rotors, wind turbines, airframe

noise and other cases where airfoil shapes encounter low-to-moderate speed flow”

A later NREL validation study for the BPM TE noise model (Moriarty & Migliore, Semi-Empirical Aeroacoustic Noise Prediction Code for Wind Turbines, 2003) showed good agreement of the BPM prediction model with data taken from a series of wind tunnel tests performed at the NLR, The Netherlands (Oerlemans, Wind Tunnel Aeroacoustic Tests of Six Airfoils for Use on Small Wind Turbines., 2003). The comparison was made at $M=0.21$ and AOA ranging from 0° to 13.1° . The agreement was good for frequencies near 3 kHz but for lower frequencies (~ 800 Hz) the differences found were up to 6 dB. The study did not expand the validation range of the model.

More recently, Doolan and Moreau (Doolan & Moreau, 2013) have plotted SPL spectra as a function of Strouhal number for some experiments, against BPM predictions. For the case of the IAG Wind tunnel data (Herrig & Würz, 2008) at $Re_c \sim 2.9 \times 10^6$ (graphic (d) of Fig. 3, at page 6 of D&M), it is shown good agreement with BPM prediction at $M=0.20$, for peak Strouhal number and higher frequencies.

By verifying directly the IAG Wind Tunnel Data, on the other hand, it seems that the Reynolds number of the experiments tops at $Re_c \sim 2.4 \times 10^6$ (see page 2 of (Herrig & Würz, 2008)).

Further attempts on extending the validation of the BPM-based tool integrated into QBlade are being made under the Poli-USP - TU-Berlin collaboration, using the research of (Devenport W. , et al., 2010) based on data from the Virginia Tech Aeroacoustic Tunnel, and will be published eventually.

5 Results

5.1 Displacement thickness data writing.

A preliminary modification had to be made to the XFLR5 output routines embedded into the QBlade, in order to save displacement thickness (D^*) data along with each OpPoint (polar operational point object). This information was not previously saved to file, which became necessary since it is employed as the transversal turbulence scale at the TE noise model. It is also employed as a turbulence scale for other self-noise sources that are intended to be implemented in the future.

Table I below shows the results of the displacement thickness calculations made with some versions of the reference and QBlade software for the calculation procedure verification. All calculations are made for the NACA0012 airfoil modified with a sharp trailing edge, 300 panels and TE/LE point density ratio of 0.30, at a Reynolds number of 1,500,000, Mach number of 0.21 and tripping at 15% chord for upper and lower sides:

D* calculation Table					
Version	AOA	# of data points	D* at 1C, Upper	D* at 1C, Lower	symmetry
XFLR5 V6.06	0	188	0.00686	0.00689	acceptable
	10	213	0.02383	0.00297	N/A
	20	220	0.29850	0.00140	
QBlade V0.8	0	188	0.00686	0.00689	acceptable
	10	212	0.02383	0.00297	N/A
	20	220	0.29850	0.00140	
QBlade V0.95 32 bits	0	188	0.00686	0.00689	acceptable
	10	212	0.02383	0.00297	N/A
	20	220	0.29850	0.00140	

Table I – Calculation procedure verification for the displacement thickness value returned by different codes, measured over the Trailing Edge (1C). N/A = non applicable.

There are no differences among the values of D^* for the three versions tested. For a study of the impact of the quality of the D^* value assessment on a BPM-type TE noise prediction method, see (Saab Jr & Pimenta, 2016).

The path for exporting D^* calculated data for visual inspection, is:

Operating Points -> Cp Graph -> Current Xfoil Results -> Export Cur. Xfoil Results.

5.2 TE noise spectra generation procedure verification and validation.

5.2.1 Flow conditions and methodology.

Three different TE noise calculations procedures are provided for in the original BPM model:

- For zero angle-of-attack (AOA).
- For AOA below the switching angle.
- For AOA above the switching angle.

The specific switching angle, for AOA under 12.5° , is calculated as a function of the Mach number and describes the angle above which the noise contribution of the detached flow over the suction side of the airfoil becomes dominant. Below this angle, the attached flow over the pressure and the suction sides plus the unattached flow portion over the suction sides are all considered as contributive sources to the overall noise. For each of the mentioned cases, there are different calculation procedures and different displacement thickness correlations provided along with the original model.

However, since the implementation of the modified-BPM model allowed more flexibility, derived from the use of TBL data extracted from the XFLR5 calculations, the verification and validation process involved analyzing the results of six different situations, displayed in table II:

NACA0012 Sharp TE airfoil		
Transversal turbulence scale source		
Flow Angle	BPM correlations	XFLR5 data
Zero AOA	1	4
Below Switching angle	2	5
Above Switching angle	3	6

Table II – Combinations (cases) of flow data sources and angles of attack for the verification and validation process.

The calculation procedure verification for all six cases was accomplished against step-by-step calculations carried out in spreadsheets for each one of them. The verification cases requiring XFLR5 output data were run in a non-integrated fashion, with displacement thickness data calculated, exported to file, linearly interpolated to the desired chord station and then inputted in the spreadsheet for the remainder of the BPM calculation.

The verification and validation of the reference spreadsheets themselves was accomplished simultaneously against peak frequency, peak level and roll-off compared to graphical output (TE noise spectra), both experimental and calculated, provided in the original BPM paper (Brooks, Pope, & Marcolini, Airfoil Self-Noise and Prediction, 1989).

An important description of the experimental spectra presented in the BPM paper is reproduced below:

“The self-noise spectra for the 2D NACA 0012 airfoil models with sharp TE are presented in a 1/3-octave format in figures 11 to 74. Figures 11 to 43 are for airfoils where the boundary layers have been tripped and figures 44 to 74 are for smooth surface airfoils where the boundary layers are untripped (natural transition). Each figure contains spectra for a model at a specific angle of attack for various tunnel speeds. Note that the spectra are truncated at upper and lower frequencies. This editing of the spectra was done because, as described in appendix A, a review of the narrow-band amplitude and phase for all cases revealed regions where extraneous noise affected the spectra in a significant way (2 dB or more). These regions were removed from the 1/3-octave presentations.

The spectra levels have been corrected for shear-layer diffraction and TE noise directivity effects, as detailed in appendix B. The noise should be that for an observer positioned perpendicular to, and 1.22 m from, the TE and the model midspan. In terms of the directivity definitions of appendix B, $r_e = 1.22$ m, $\theta_e = 90^\circ$ and $\phi_e = 90^\circ$.” (Brooks, Pope, & Marcolini, Airfoil Self-Noise and Prediction, 1989), p. 17.

Once verified and validated, the worksheets were used to generate detailed individual source contribution at each 1/3-octave frequency, which could be compared to the detailed output of the code.

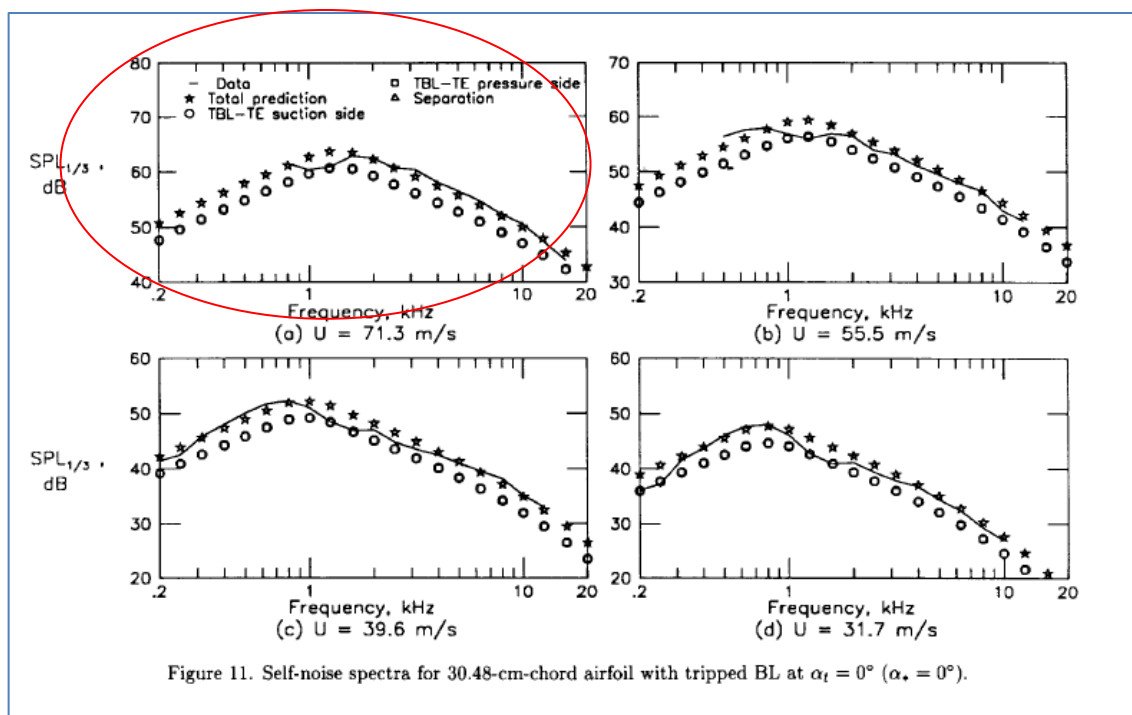
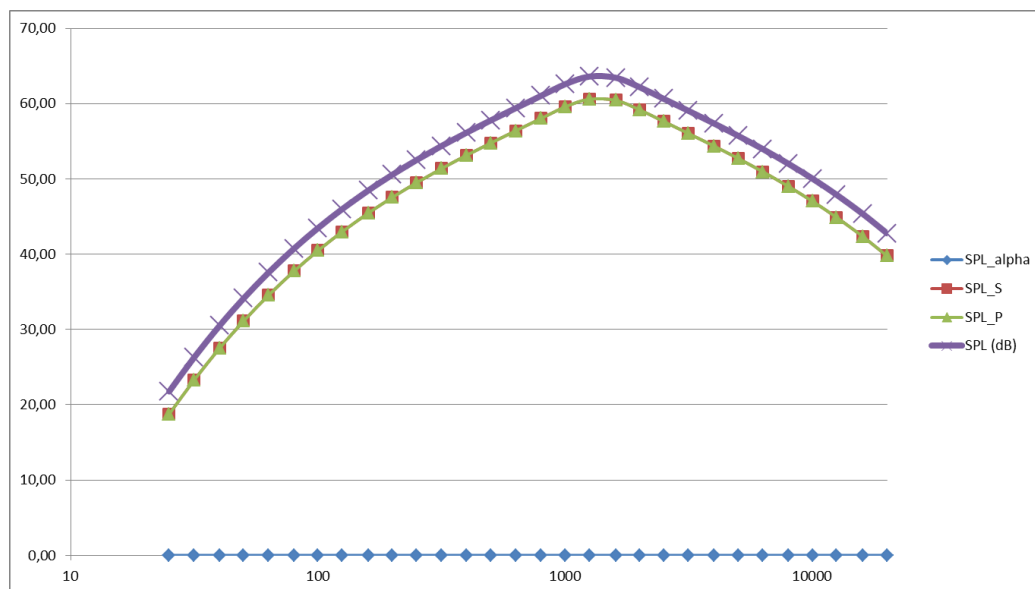
The spreadsheet-generated spectra were calculated and saved for the following key flow angles:

- Zero AOA flow, tripped BL.
- Flow below the switching angle (4°), tripped BL.
- Flow above the switching angle (17.4°), tripped BL.

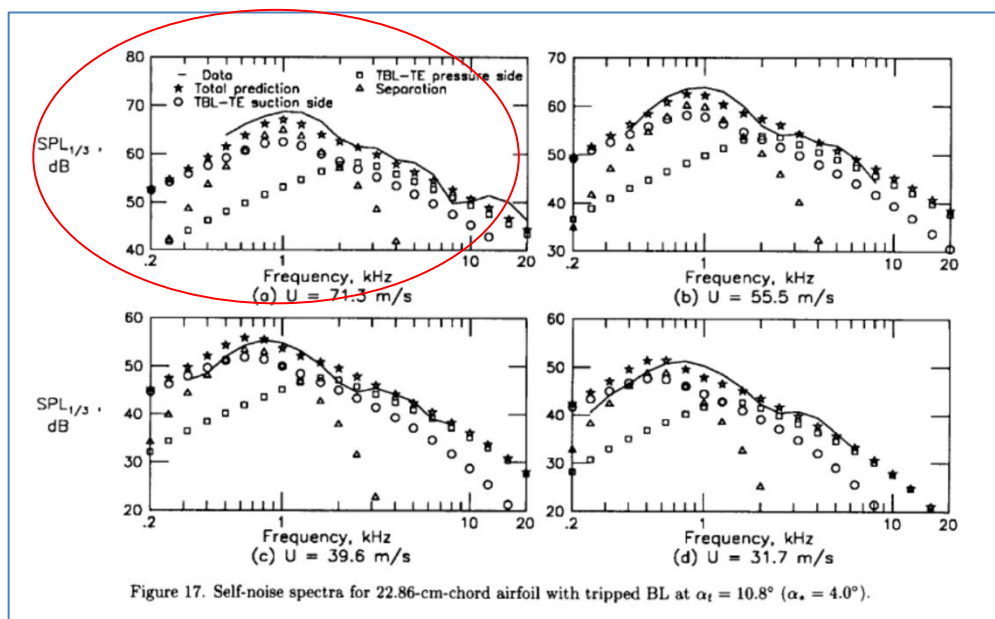
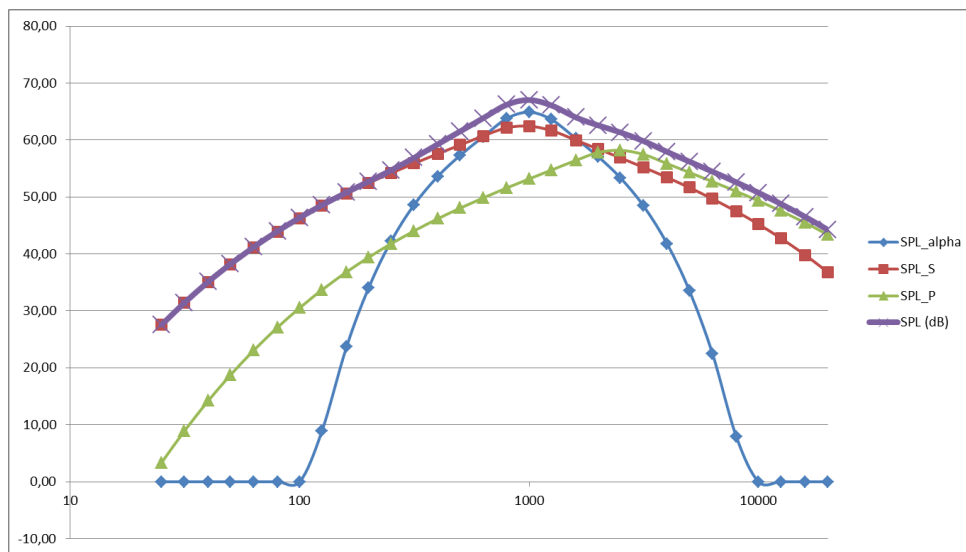
Examples of the spreadsheet-generated output spectra are shown below for 71.3 m/s flow, next to the original experimental measurements and the original BPM model calculations, all in graphical format.

5.2.2 Examples of the spreadsheet graphical output compared with original BPM output graphs:

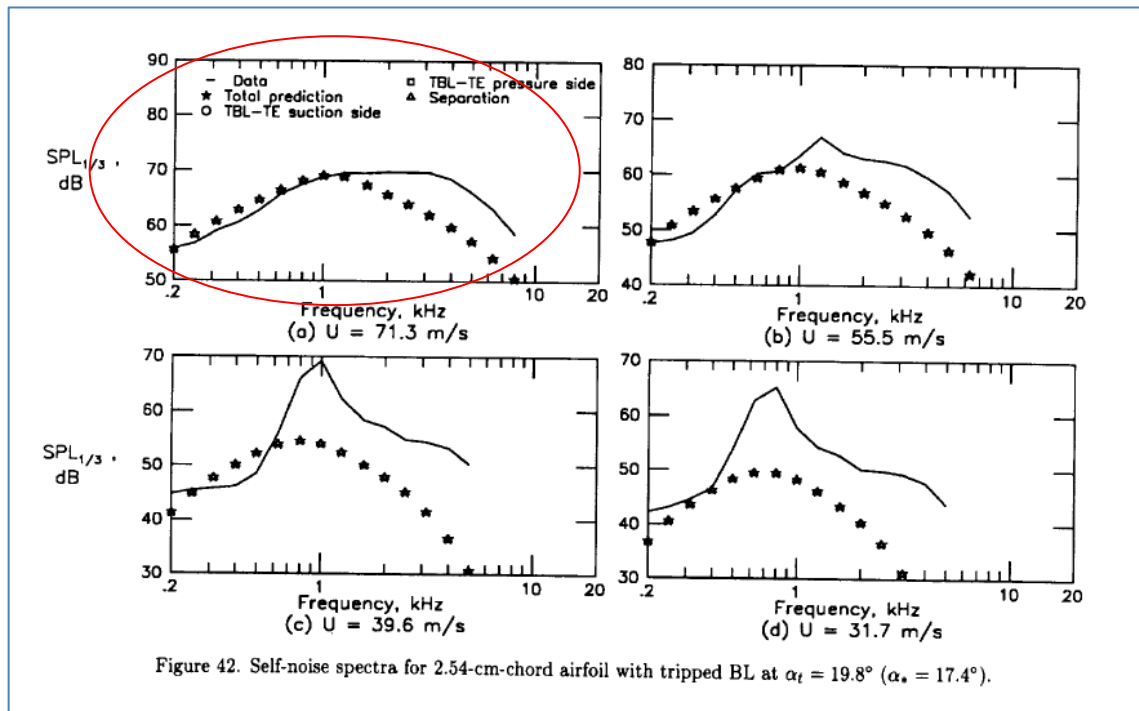
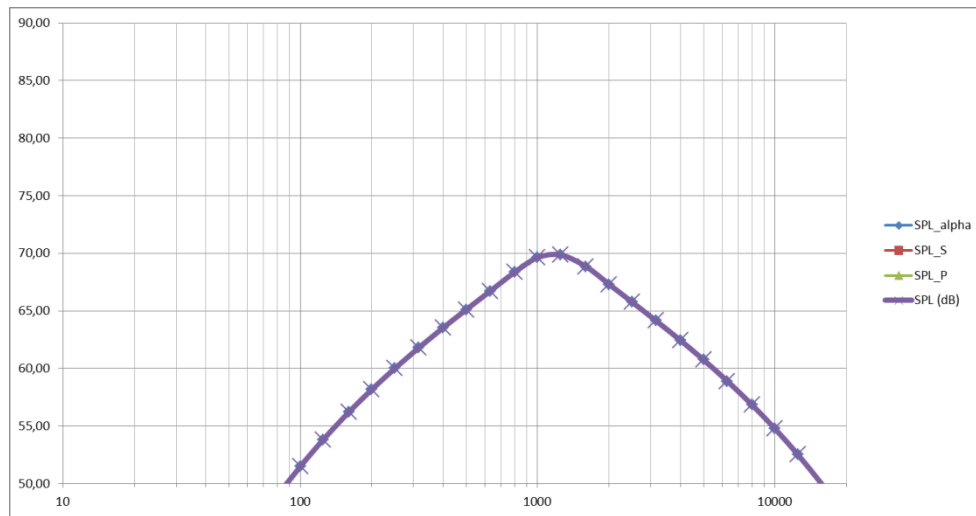
i) For zero AOA flow and same conditions as in figure 11, item (a) of BPM paper:



- ii) For $AOA=4^\circ$ (below the switching angle) flow and same conditions as in figure 17, item (a) of BPM paper:



- iii) For $\text{AOA}=17,4^\circ$ flow (above the switching angle) and same conditions as in figure 42, item (a) of BPM paper:



5.2.3 Working Procedure.

In the following pages, the procedure for using the new module will be described along the simulation for generating code verification data. For the 3 original BPM correlation cases considered (flow at zero AOA (i); below switching angle (ii) and; above switching angle (iii)), only case iii had a different angle from the previous validation plots. The reason is that, for a Reynolds Number of 284,000, the XFLR5 did not converge above 14.5° so the validation graph used earlier (@ 17.4°) had to be replaced by another validation chart at 12.7° geometrical AOA, still above the switching angle.

Step 1

Open the QBlade with the 2D TE noise module.

Open your working airfoil profile.

Globally refine your airfoil from 160 to 300 panels and set the TE/LE panel density to 0.30. Normalize and de-rotate the airfoil, then save it.

It is recommended that the V_{Accel} parameter in XFLR5 be set to 0.0001 value or less, when using the QBlade v0.95 64 bit version, before generating TBL data associated with TE noise calculations (path: Analysis->XFoil Advanced Settings-> V_{Accel}).

Define an XFOIL analysis by the Reynolds and Mach numbers, plus transition details to simulate the experimental case the user wants to replicate.

Analysis parameters for NACA 0012_160_panels_STE

Analysis Name

Automatic User Defined

T1_Re1.500_M0.21_N9.0

Reynolds and Mach Numbers

Reynolds = 1500000 Mach = 0.21

Transition settings

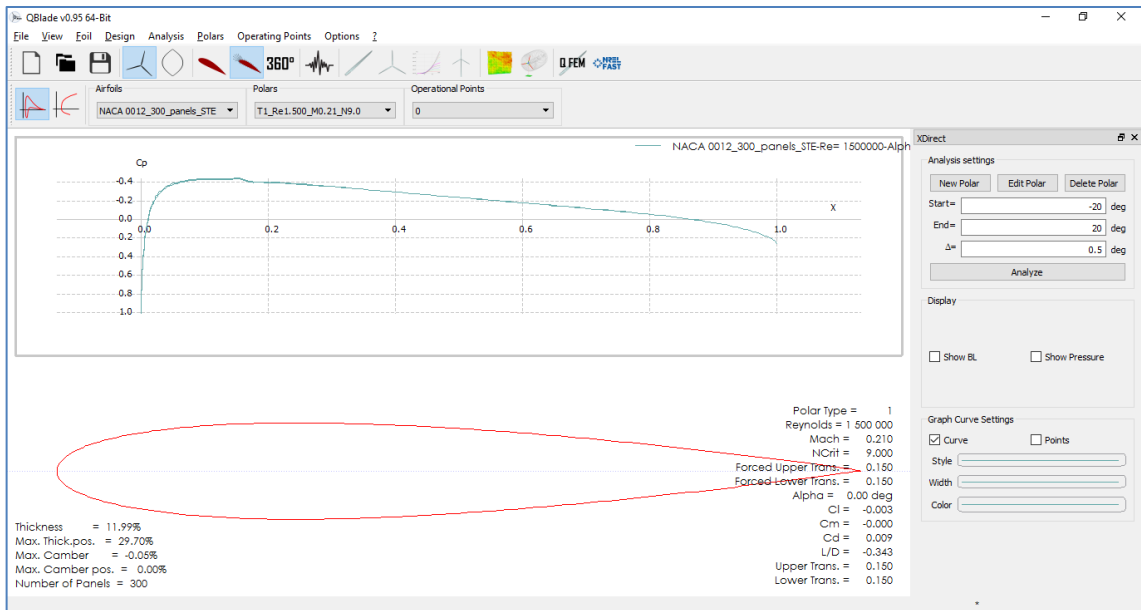
Free transitions (eⁿ) method NCrit= 9

Forced transition: TripLocation (top) 0.15

TripLocation (bot) 0.15

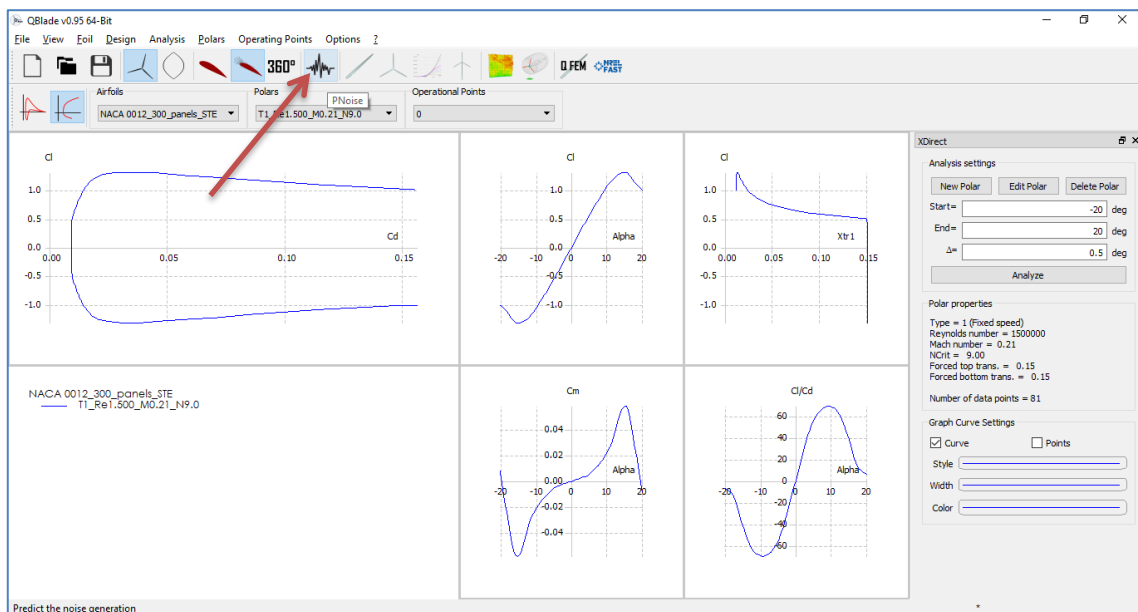
OK Cancel

Run the analysis along an AOA or angle range to meet the user specific needs, generating one or more Operational Points.



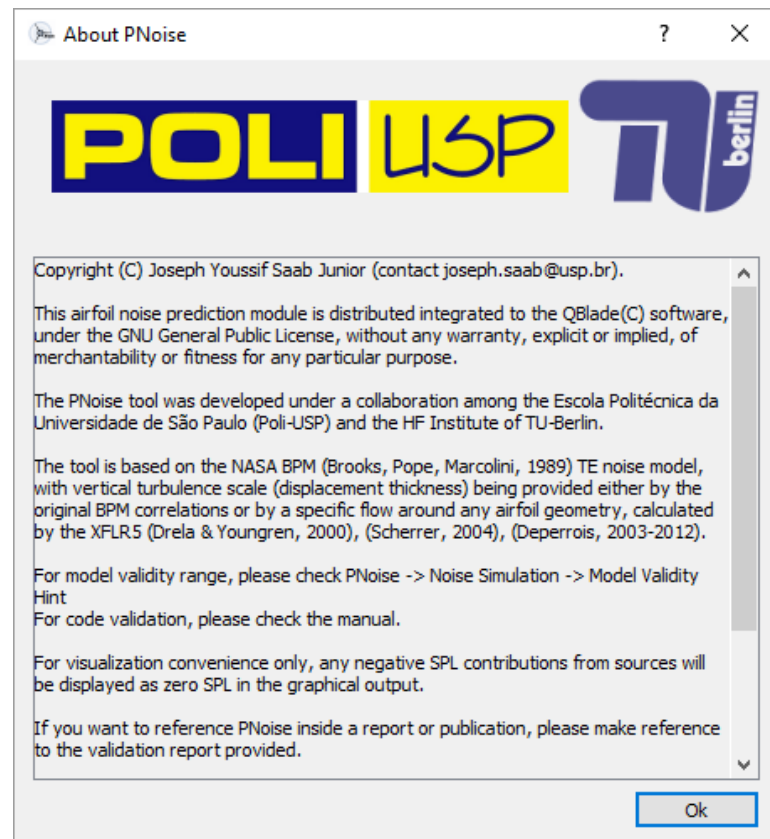
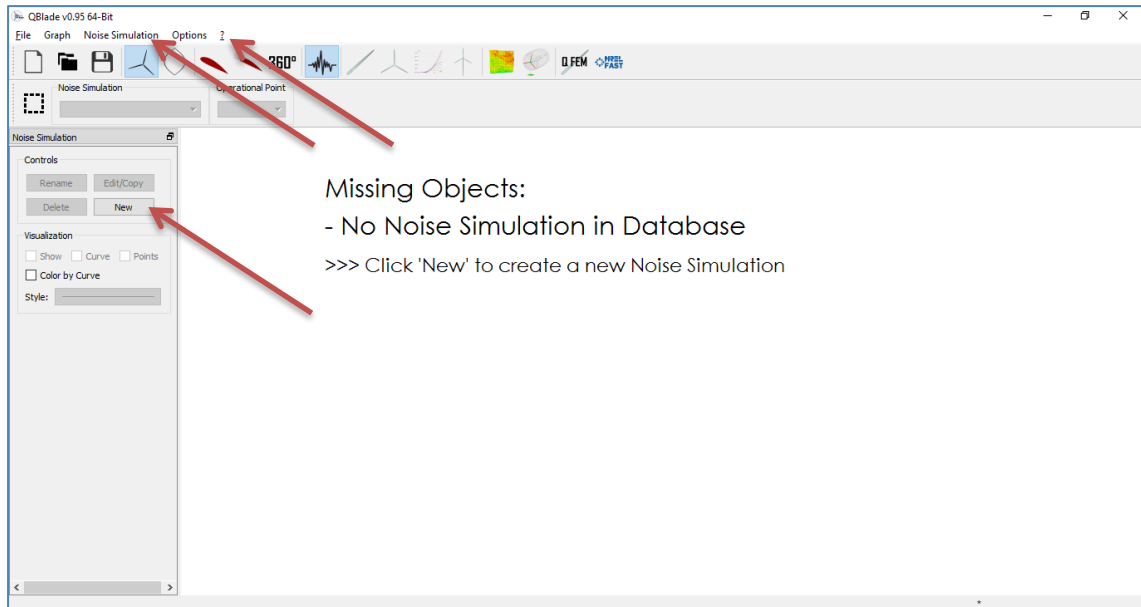
Step 2

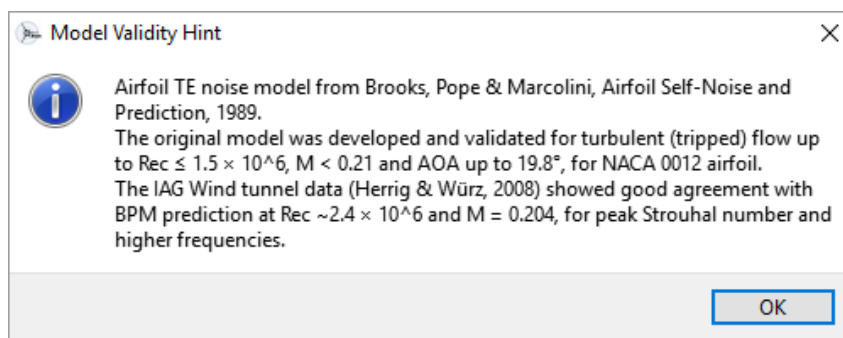
Click in the NOISE module icon (indicated by the red arrow in the picture below), to open the TE noise module:



Step 3

For important information on the model and the validity range, please check the “?” menu, option “About Qnoise” and also “Noise Simulation” menu, option “Model Validity Hint”.



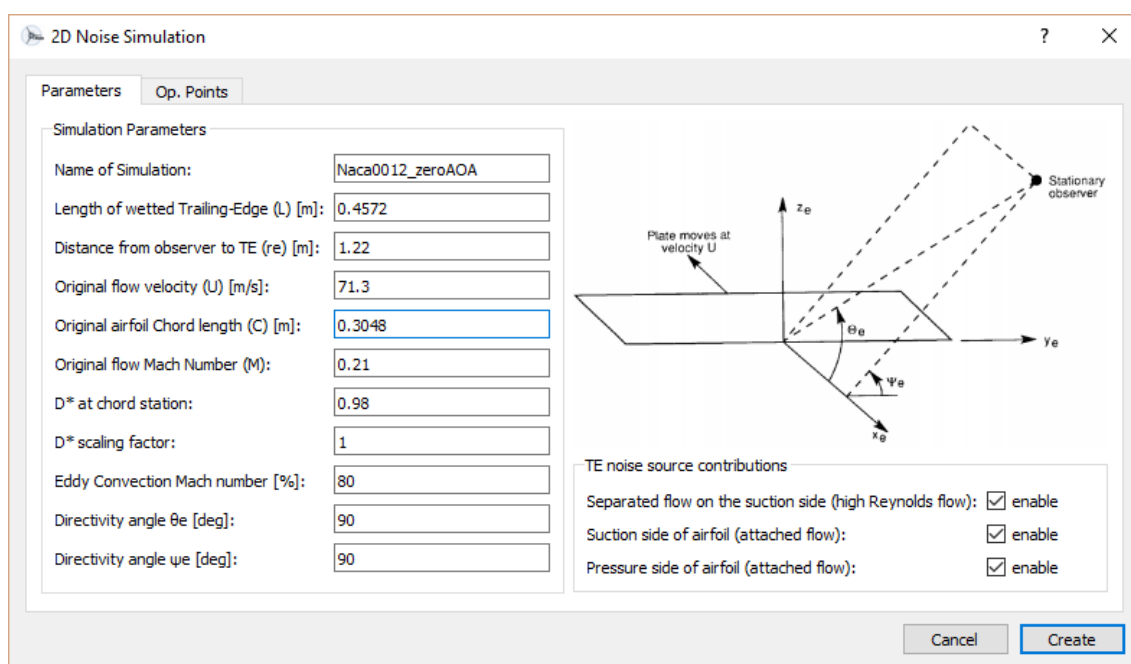


The user should read it carefully and review the definition of PREDICTION presented earlier. The result of any prediction should be declared alongside the limitations of the model employed.

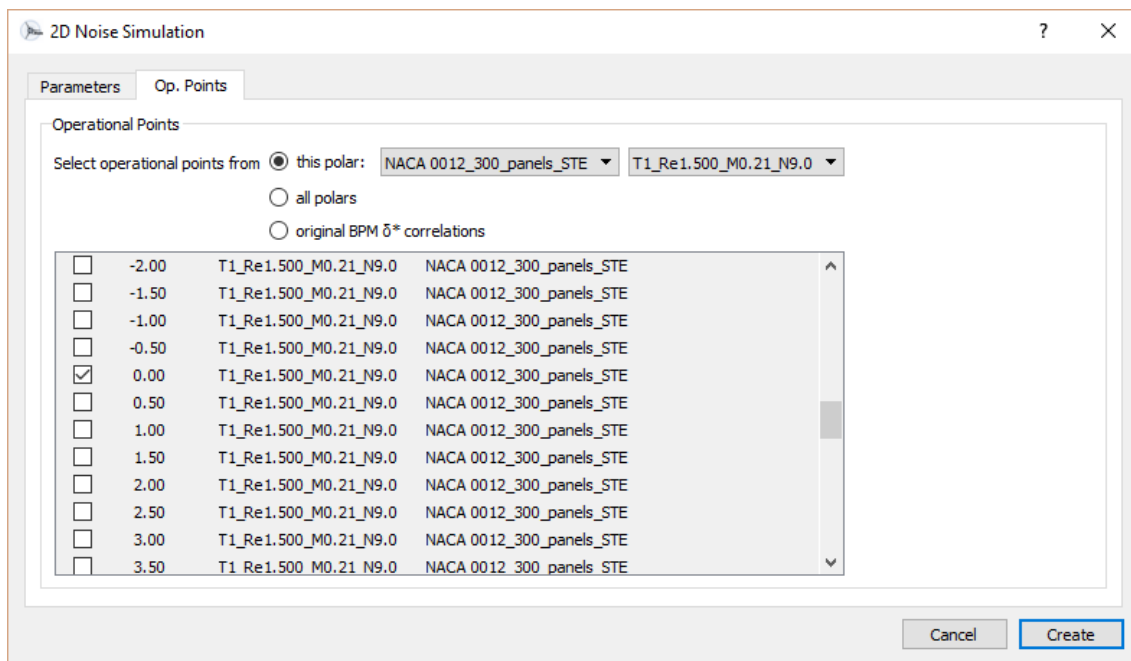
Step 4

Click the NEW simulation button.

The input screen will appear. The screen below shows the input screen that must be completed prior to any airfoil TE noise simulation. The snapshot is displayed with zero AOA data employed both in the MS Excel spreadsheet for that angle and also in the original BPM graph of Fig. 11, case a.



The next step is to open the second tab **Op.Points** and select the model (modified or original BPM TE noise models) and the angle of attack for the calculation.



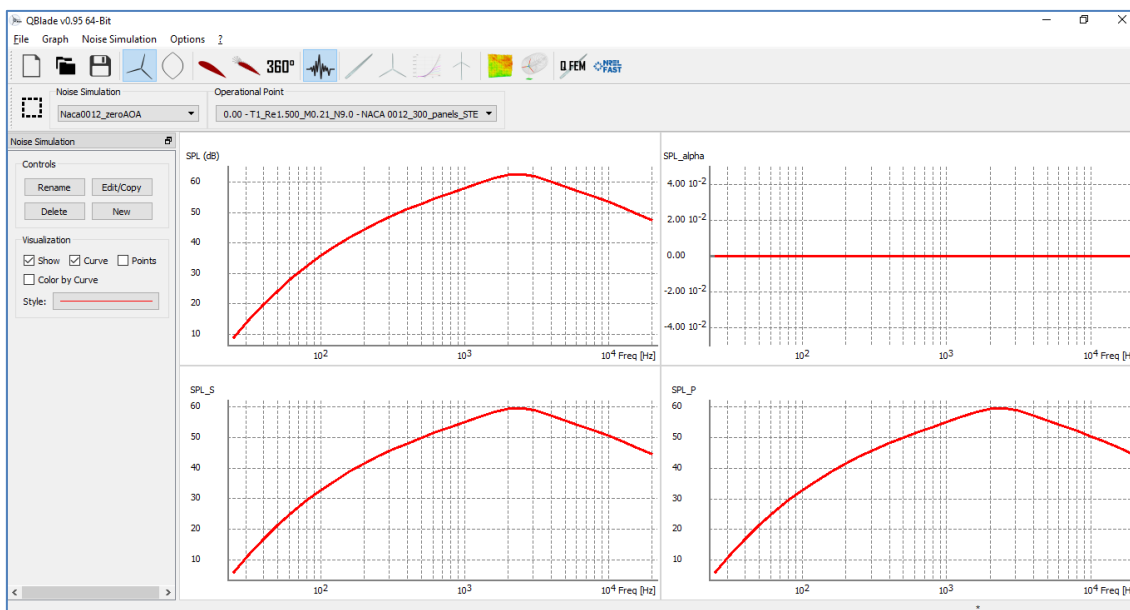
The user may select more than one angle for direct comparison of results.

Notice that the default option is to use boundary layer data (displacement thickness) calculated by the XFLR5, by selection a specific airfoil + polar combination. The user should select the “*original BPM δ^* correlations*” option to run the unmodified BPM model.

Click **Create**.

Step 5

The individual contributions of each source and the total SPL are displayed in different quadrants of the screen.



The original BPM model calculates the SPL_alpha contribution (unattached flow on the suction side) for zero AOA as a negative value. Since the negative values have no overall contribution to the OASPL and their absolute number is large and distorts the graph scale making it difficult to read other curves (for other angles) in the same set of axis, it was decided that negative SPL contributions of the model would be plotted as zero values (see RH upper graph).

Also notice that, at zero AOA, the TE noise contributions should be the same for the pressure and the suction sides of the airfoil, which is confirmed above, and also, the logarithmic sum of two uncorrelated sources of the same strength should increase the total SPL by 3 dB, which can also be visually verified above and numerically confirmed in the “save to file” output option described next.

STEP 6

The TE noise overall data may be saved to file by selecting the “Noise Simulation” menu, “Export Current Noise Simulation” option.

Example of file output (file NACA0012_zeroAOA_noise.txt)

Noise prediction file export

Alpha: 0.00, Re = 1500000
 OASPL: 70.82949 dB
 OASPL (A): 71.35975 dB(A)
 OASPL (B): 70.30961 dB(B)
 OASPL (C): 70.26860 dB(C)
 SPL_a: -931.90020
 SPL_s: 67.80969
 SPL_p: 67.82868

Freq [Hz]	SPL (dB)	SPLa	SPLs	SPLp	SPL (dB(A))	SPL (dB(B))	SPL (dB(C))
25	8.81529	-1456.96154	5.74057	5.86847	-35.88471	-11.58471	4.41529
31.5	14.32465	-1380.62597	11.25446	11.37343	-25.07535	-2.77535	11.32465
40	19.53943	-1310.34594	16.47362	16.58393	-15.06057	5.33943	17.53943
50	23.99696	-1252.14763	20.93499	21.03772	-6.20304	12.39696	22.69696
63	28.22047	-1198.97585	25.16220	25.25762	2.02047	18.92047	27.42047
80	32.19540	-1151.09917	29.14067	29.22908	9.69540	24.79540	31.69540
100	35.57681	-1112.41303	32.52512	32.60752	16.47681	29.97681	35.27681
125	38.66414	-1079.10545	35.61523	35.69210	22.56414	34.46414	38.46414
160	41.76772	-1047.99372	38.72160	38.79294	28.36772	38.76772	41.66772
200	44.31901	-1024.57624	41.27514	41.34202	33.41901	42.31901	44.31901
250	46.65542	-1005.17122	43.61354	43.67646	38.05542	45.35542	46.65542
315	48.87591	-988.83409	45.83584	45.89517	42.27591	48.07591	48.87591
400	50.98772	-975.45574	47.94923	48.00542	46.18772	50.48772	50.98772
500	52.81920	-965.70980	49.78193	49.83571	49.61920	52.51920	52.81920
630	54.60024	-957.93649	51.56396	51.61577	52.70024	54.50024	54.60024
800	56.34709	-951.87004	53.31155	53.36189	55.54709	56.34709	56.34709
1000	57.91968	-947.53966	54.88456	54.93405	57.91968	57.91968	57.91968
1250	59.46311	-944.04976	56.42812	56.47737	60.06311	59.46311	59.46311
1600	61.16785	-942.92492	58.13285	58.18210	62.16785	61.16785	61.06785
2000	62.42217	-937.87515	59.39535	59.42832	63.62217	62.32217	62.22217
2500	62.60944	-937.45596	59.59281	59.60545	63.90944	62.40944	62.30944
3150	61.67233	-940.11304	58.66764	58.65642	62.87233	61.27233	61.17233
4000	60.02262	-942.84396	57.01793	57.00671	61.02262	59.32262	59.22262
5000	58.48165	-946.12855	55.47698	55.46572	58.98165	57.28165	57.18165
6300	56.86691	-950.24452	53.86259	53.85061	56.76691	54.96691	54.86691
8000	55.14318	-955.77619	52.13951	52.12623	54.04318	52.24318	52.14318
10000	53.45559	-962.58736	50.45279	50.43778	50.95559	49.15559	49.05559
12500	51.66706	-971.43678	48.66537	48.64814	47.36706	45.56706	45.46706
16000	49.54008	-984.13200	46.53991	46.51963	42.94008	41.14008	41.04008
20000	47.45553	-998.71325	44.45700	44.43343	38.15553	36.35553	36.25553

Also, any of the individual plots may be exported by pressing RMC, “Export Graph” option over the selected graph.

5.2.4 Code verification with TBL data calculated by XFLR5 (inside QBlade) for zero AOA (Case 1).

For all cases, the procedure will be to verify the calculation output for three specific frequencies, including the peak one, and then the overall Sound Pressure Levels.

VV project file name: QbladeV095_32b_validation.wpa

Baseline case: Figure 11 of BPM original paper.

NACA 0012, Sharp Trailing Edge.
 Reynolds: 1,500,000
 Mach: 0.21
 Tripping: @15% chord, both sides
 Chord: 0.3048 m

Wetted TE span: 0.4572 m
 Reference Spreadsheet output data:
 Chord Station for D* measurement: 0.98C

See the working procedure figures for illustration on this case input and output files.

The results for zero AOA are shown in table III below:

Frequency(Hz)	Source	SPL_alpha(dB)	SPL_S (dB)	SPL_P (dB)	SPL (dB)	Diff.(dB)
50	Spreadsheet	-1252.71	19.64	19.74	22.70	+1.2
	Code	-1252.15	20.93	21.04	24.00	
1,000	Spreadsheet	-948.83	53.60	53.65	56.64	+1.3
	Code	-947.54	54.88	54.93	57.92	
2,500	Spreadsheet	-938.72	58.32	58.33	61.34	+1.3
	Code	-937.46	59.59	59.61	62.60	

TABLE III – RESULTS FROM QBLADE V0.95 CODE CALCULATION AGAINST VERIFICATION SPREADSHEET, FOR ZERO AOA.

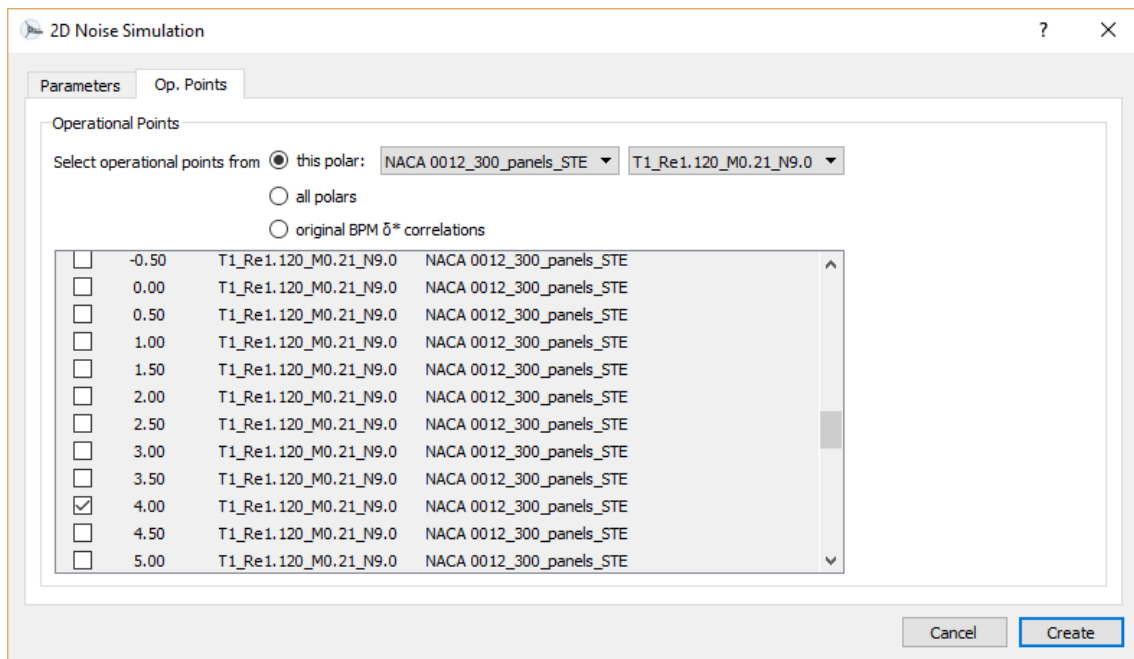
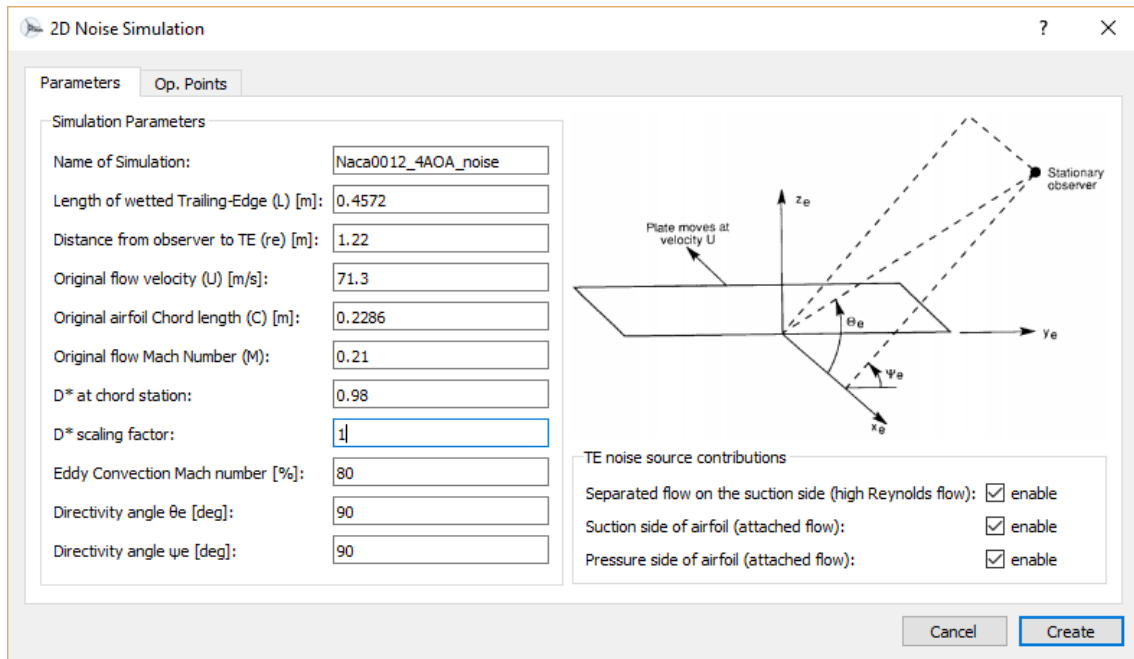
The differences are systemic and around 1.3 dB, which was considered acceptable. The peak frequency is within the 2,500 Hz band for both spectra.

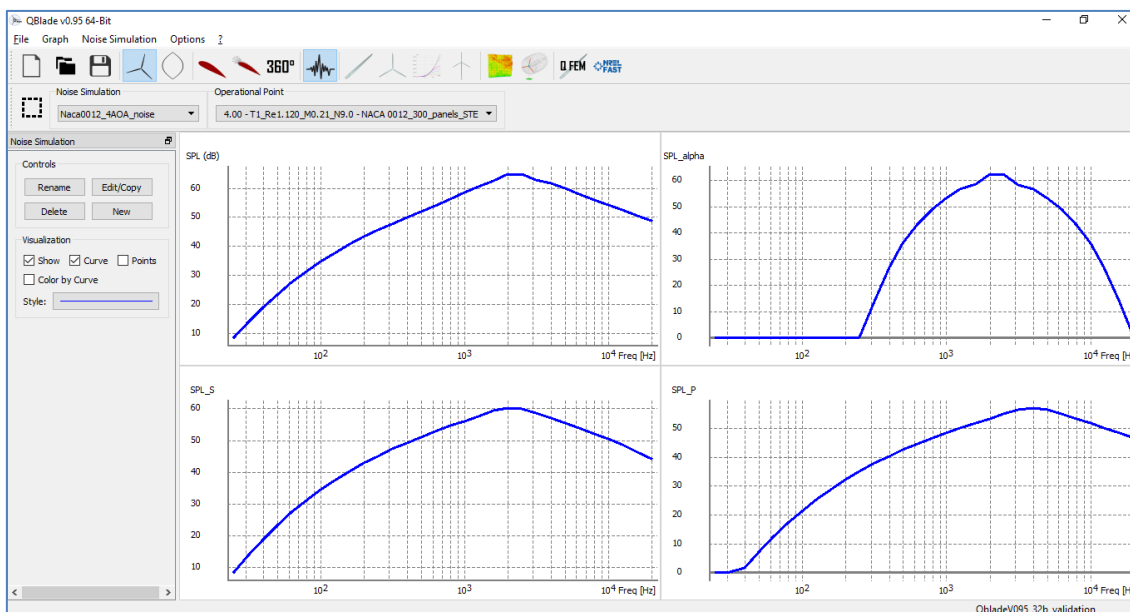
The overall unweighted sound pressure level is 69.6 dB for the Spreadsheet and 70.8 dB for the Code, a 1.2 dB difference over prediction by the code.

5.2.5 Code verification with TBL data calculated by XFLR5 (inside QBlade) for AOA other than zero.

The BPM model has different calculation procedures for AOA below and above the “switching angle”. The switching angle calculated to match the experimental conditions for the 22.86 cm–chord BPM airfoil at a Reynolds number flow of 1,120 Million, is 9.5°. Thus, one verification shall be made below the switching angle (4°) and another one above it (12.5°).

5.2.5.1 Code verification with TBL data calculated by XFLR5 (inside QBlade) for AOA below the switching angle (4° - Case 2).





The results for some frequencies at 4° AOA (below the switching angle), are shown in table IV below:

Frequency (Hz)	Source	SPL_alpha (dB)	SPL_S (dB)	SPL_P (dB)	SPL (dB)	Diff.(dB)
50	Spreadsheet	-243.38	21.83	5.67	21.93	+1.3
	Code	-241.81	23.12	6.97	23.23	
1,000	Spreadsheet	51.88	54.77	47.13	57.04	+1.3
	Code	53.18	56.05	48.42	58.33	
2,500	Spreadsheet	61.10	58.89	52.10	63.47	+1.4
	Code	62.38	59.96	54.92	64.82	

TABLE IV – RESULTS FROM QBLADE V0.95 CODE CALCULATION AGAINST VERIFICATION SPREADSHEET, FOR 4° AOA.

The differences are systemic and of the order of 1.3 dB, which was considered acceptable. The peak frequency is contained within the 2,500 Hz band for both spectra.

Also the OASPL is 71.1 dB for the Spreadsheet and 72.2 dB for the code or a 1.1 dB difference.

The user should be warned that for negative AOA, the upper surface, initially a suction side, becomes a pressure side and the lower surface, initially a pressure side, becomes a suction side. Since the graphs are labelled “pressure” and “suction” sides, not “upper” and “lower” sides of the airfoil, the output will appear overlapped in such cases as symmetrical angles (e.g., $+4^\circ$ and -4° AOA) are simultaneously selected.

5.2.5.2 Code verification with TBL data calculated by XFLR5 (inside QBlade) for AOA above the switching angle (12.5° - Case 3).

2D Noise Simulation

Parameters Op. Points

Simulation Parameters

Name of Simulation: Naca0012_12_5AOA_noise

Length of wetted Trailing-Edge (L) [m]: 0.4572

Distance from observer to TE (re) [m]: 1.22

Original flow velocity (U) [m/s]: 71.3

Original airfoil Chord length (C) [m]: 0.0254

Original flow Mach Number (M): 0.21

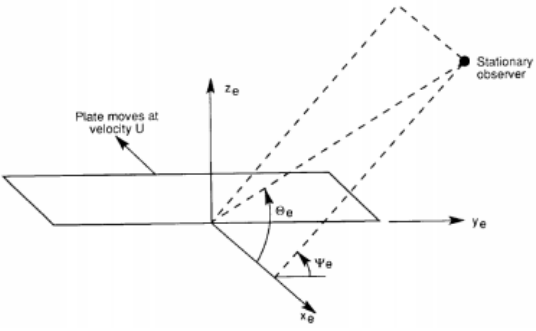
D* at chord station: 0.98

D* scaling factor: 1

Eddy Convection Mach number [%]: 80

Directivity angle θ_e [deg]: 90

Directivity angle ψ_e [deg]: 90



TE noise source contributions

Separated flow on the suction side (high Reynolds flow): enable

Suction side of airfoil (attached flow): enable

Pressure side of airfoil (attached flow): enable

Cancel Create

2D Noise Simulation

Parameters Op. Points

Operational Points

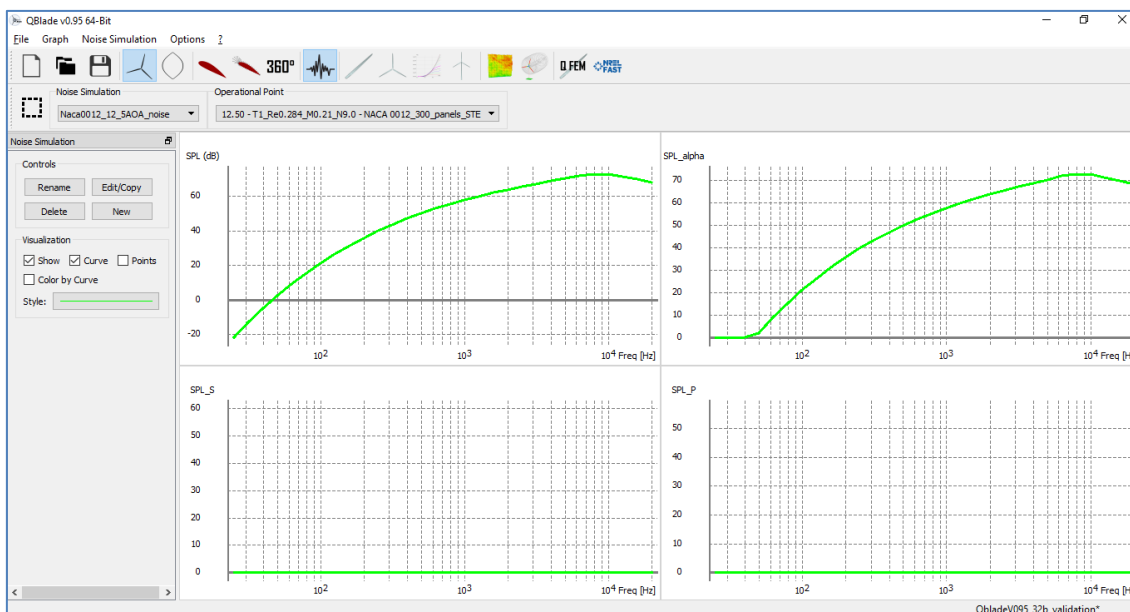
Select operational points from this polar: NACA 0012_300_panels_STE T1_Re0.284_M0.21_N9.0

all polars

original BPM 5* correlations

<input type="checkbox"/>	9.00	T1_Re0.284_M0.21_N9.0	NACA 0012_300_panels_STE
<input type="checkbox"/>	9.50	T1_Re0.284_M0.21_N9.0	NACA 0012_300_panels_STE
<input type="checkbox"/>	10.00	T1_Re0.284_M0.21_N9.0	NACA 0012_300_panels_STE
<input type="checkbox"/>	10.50	T1_Re0.284_M0.21_N9.0	NACA 0012_300_panels_STE
<input type="checkbox"/>	11.00	T1_Re0.284_M0.21_N9.0	NACA 0012_300_panels_STE
<input type="checkbox"/>	11.50	T1_Re0.284_M0.21_N9.0	NACA 0012_300_panels_STE
<input type="checkbox"/>	12.00	T1_Re0.284_M0.21_N9.0	NACA 0012_300_panels_STE
<input checked="" type="checkbox"/>	12.50	T1_Re0.284_M0.21_N9.0	NACA 0012_300_panels_STE
<input type="checkbox"/>	13.00	T1_Re0.284_M0.21_N9.0	NACA 0012_300_panels_STE
<input type="checkbox"/>	13.50	T1_Re0.284_M0.21_N9.0	NACA 0012_300_panels_STE
<input type="checkbox"/>	14.00	T1_Re0.284_M0.21_N9.0	NACA 0012_300_panels_STE
<input type="checkbox"/>	14.50	T1_Re0.284_M0.21_N9.0	NACA 0012_300_panels_STE

Cancel Create



The results for some frequencies at 12.5° AOA (above the switching angle), are shown in table V below:

Frequency (Hz)	Source	SPL_alpha (dB)	SPL_S (dB)	SPL_P (dB)	SPL (dB)	Diff.(dB)
50	Spreadsheet	1.78	-∞	-∞	1.78	+0.3
	Code	2.03	-2.1E+9	-2.1E+9	2.03	
1,000	Spreadsheet	57.67	-∞	-∞	57.67	0.0
	Code	57.67	-2.1E+9	-2.1E+9	57.67	
8,000	Spreadsheet	72.92	-∞	-∞	72.92	-0.1
	Code	72.82	-2.1E+9	-2.1E+9	72.82	

TABLE V – RESULTS FROM QBLADE V0.95 CODE CALCULATION AGAINST VERIFICATION SPREADSHEET, FOR 12.5° AOA.

SPL_Alpha should be the sole positive noise source contributor for an angle above the switching angle, which is exactly the behavior displayed.

The OASPL is 80.7 dB for the Spreadsheet and 80.6 dB for the code or a 0.1 dB difference.

5.2.6 Code verification with TBL displacement thickness calculated with the original BPM correlations (Cases 4, 5 and 6):

The same three conditions of cases 1, 2 and 3 will be verified in this section, with the original BPM displacement thickness correlations applied instead of the XFLR5 calculation results, i.e., the original BPM procedure, without modification shall be applied.

AOA=0° (Case 4)

Input screen for the case where the original BPM correlations will be used for displacement thickness evaluation:

2D Noise Simulation

Parameters Op. Points

Simulation Parameters

Name of Simulation:

Length of wetted Trailing-Edge (L) [m]:

Distance from observer to TE (re) [m]:

Original flow velocity (U) [m/s]:

Original airfoil Chord length (C) [m]:

Original flow Mach Number (M):

D* at chord station:

D* scaling factor:

Eddy Convection Mach number [%]:

Directivity angle θ_e [deg]:

Directivity angle ψ_e [deg]:

TE noise source contributions

Separated flow on the suction side (high Reynolds flow): enable

Suction side of airfoil (attached flow): enable

Pressure side of airfoil (attached flow): enable

Cancel Create

2D Noise Simulation

Parameters Op. Points

Operational Points

Select operational points from this polar:

all polars

original BPM δ^* correlations

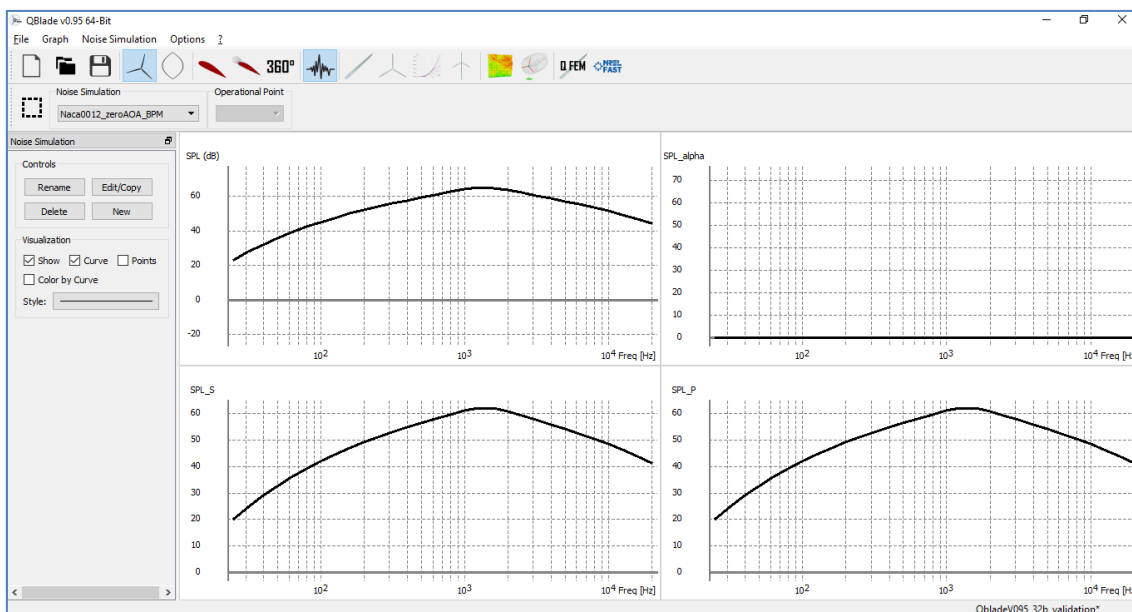
AOA (α) [deg]:

Chord based Reynolds number (Rc):

Type of Transition:

Cancel Create

When the Original BPM correlations for displacement thickness are selected, the dialog opens three new fields for the user to enter AOA data, chord-based Reynolds Number and Transition of Fully Turbulent Flow.



The verification was once again made with the aid of a calculation spreadsheet, fed with the BPM D^* correlations ($D = 2.66E-3$ m is this particular case), in order to reproduce the original model intended spectrum.

Frequency (Hz)	Source	SPL_alpha (dB)	SPL_S (dB)	SPL_P (dB)	SPL (dB)	Diff.(dB)
50	Spreadsheet	-1138.39	31.19	31.19	34.20	+1.29
	Code	-1136.90	32.48	32.48	35.49	
1,000	Spreadsheet	-938.72	59.63	59.63	62.64	+1.28
	Code	-938.24	60.91	60.91	63.92	
1,250	Spreadsheet	-936.48	60.61	60.61	63.62	+1.27
	Code	-935.20	61.88	61.88	64.89	

The peak frequency of 1,250 is correctly predicted by the code and the overall SPL is 73.2 dB against 71.9 dB for the spreadsheet, a difference of 1.25 dB. The same kind of systemic difference is seen on the 3 frequencies compared.

AOA=4° (case 5)

2D Noise Simulation

Parameters Op. Points

Simulation Parameters

Name of Simulation:

Length of wetted Trailing-Edge (L) [m]:

Distance from observer to TE (re) [m]:

Original flow velocity (U) [m/s]:

Original airfoil Chord length (C) [m]:

Original flow Mach Number (M):

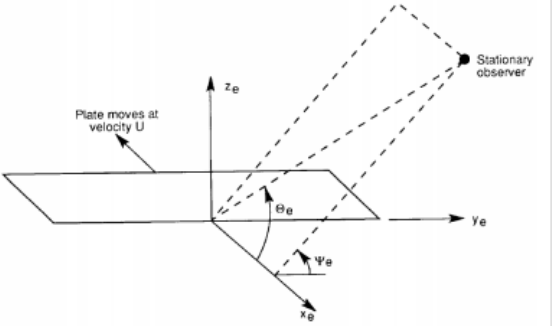
D* at chord station:

D* scaling factor:

Eddy Convection Mach number [%]:

Directivity angle θ_e [deg]:

Directivity angle ψ_e [deg]:



TE noise source contributions

Separated flow on the suction side (high Reynolds flow): enable

Suction side of airfoil (attached flow): enable

Pressure side of airfoil (attached flow): enable

Cancel Create

2D Noise Simulation

Parameters Op. Points

Operational Points

Select operational points from this polar:

all polars

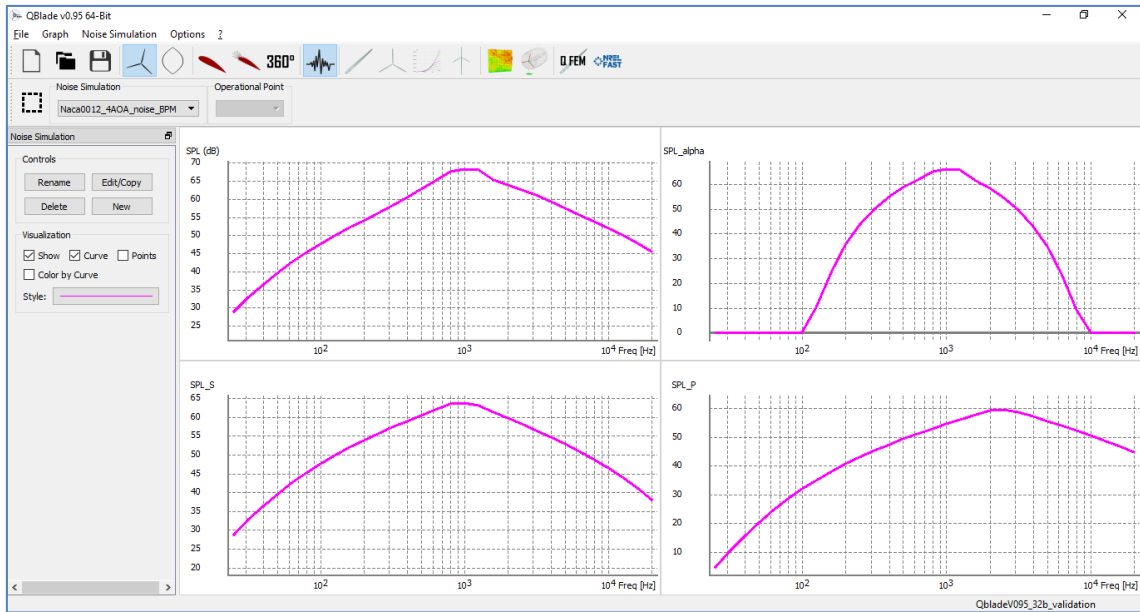
original BPM 5* correlations

AOA (a) [deg]:

Chord based Reynolds number (Rc):

Type of Transition:

Cancel Create



Frequency (Hz)	Source	SPL_alpha (dB)	SPL_S (dB)	SPL_P (dB)	SPL (dB)	Diff.(dB)
50	Spreadsheet	-85.55	38.20	18.76	38.25	+1.29
	Code	-84.10	39.49	20.06	39.54	
1,000	Spreadsheet	64.90	62.44	53.18	67.03	+1.28
	Code	66.17	63.72	54.46	68.31	

The peak frequency of 1,000 is correctly predicted by the code and the overall SPL is 75.8 dB against 74.4 dB for the spreadsheet, a difference of 1.4 dB. A systemic difference close to +1.3 dB is seen for both frequencies compared.

AOA=12,5° (Case6)

2D Noise Simulation

Parameters Op. Points

Simulation Parameters

Name of Simulation:

Length of wetted Trailing-Edge (L) [m]:

Distance from observer to TE (re) [m]:

Original flow velocity (U) [m/s]:

Original airfoil Chord length (C) [m]:

Original flow Mach Number (M):

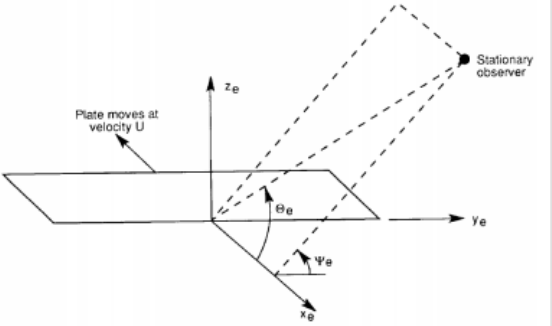
D* at chord station:

D* scaling factor:

Eddy Convection Mach number [%]:

Directivity angle θ_e [deg]:

Directivity angle ψ_e [deg]:



TE noise source contributions

Separated flow on the suction side (high Reynolds flow): enable

Suction side of airfoil (attached flow): enable

Pressure side of airfoil (attached flow): enable

Cancel Create

2D Noise Simulation

Parameters Op. Points

Operational Points

Select operational points from this polar:

all polars

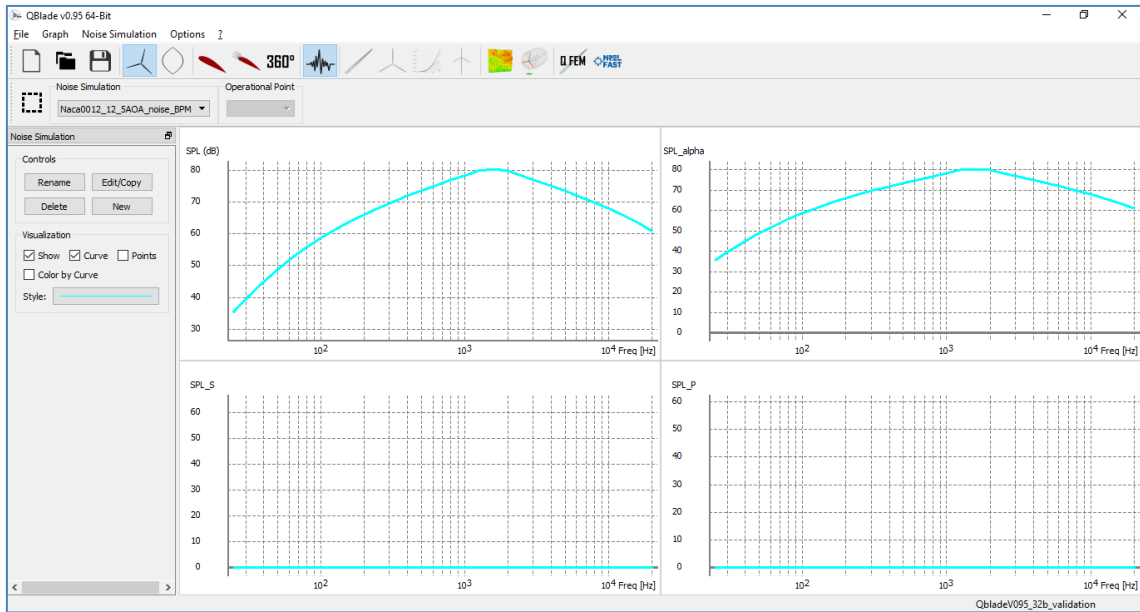
original BPM 5* correlations

AOA (a) [deg]:

Chord based Reynolds number (Rc):

Type of Transition:

Cancel Create



Frequency (Hz)	Source	SPL_alpha (dB)	SPL_S (dB)	SPL_P (dB)	SPL (dB)	Diff.(dB)
50	Spreadsheet	48.75	-∞	-∞	48.75	-0.22
	Code	48.53	-2.1E+9	-2.1E+9	48.53	
1,000	Spreadsheet	78.41	-∞	-∞	78.41	-0.20
	Code	78.21	-2.1E+9	-2.1E+9	78.21	
1,600	Spreadsheet	80.42	-∞	-∞	80.42	-0.18
	Code	80.24	-2.1E+9	-2.1E+9	80.24	

The OASPL is 88.6 dB for the spreadsheet and 88.4 dB for the code calculation, a -0.2 dB difference and the peak frequency is in the band of the 1,600 Hz central frequency for both calculations.

6 Conclusions

The calculation procedure verification for the code was made for 6 cases, covering the zero, below and above the switching angle conditions, with turbulent boundary layer data provided by the XFLR5 or by the original BPM correlations, depending on the case.

The code calculation verification procedure was made for all cases against spreadsheet (manual) calculation, prepared as per the original model and previously verified against the original BPM-calculated spectra.

The code calculations displayed a systemic, positive overprediction of about 1.3 dB for the cases below the switching angle (0° , 4°). This applies to sample frequencies selected for comparison, which included the peak frequency for each case and also to the overall SPL.

The code calculations displayed a closer adhesion to manual calculation in the cases for AOA above the switching angle (12.5°), where the differences ranged in the $[-0.2,+0.1]$ dB interval, for selected frequencies and for the overall SPL.

The +1.3 dB systemic difference perceived in some of the cases was considered acceptable for the first release of the PNoise module, but improvements in calculation accuracy will be made for follow-up releases.

All correspondence and suggestions for improvements are welcome and should be addressed to the corresponding author, which is the sole responsible for any bugs and mistakes found.

APPENDIX K - S830 AIRFOIL AERODYNAMIC AND AEROACOUSTIC PERFORMANCE IN RELATION TO OTHER NREL S-SERIES AIRFOILS

In this appendix, some simulations accomplished in order to compare the S830 aerodynamic and acoustic performance with other NREL 21% thickness airfoils is reported. The flow conditions are those from the Poli-100m WT operating conditions at 85% blade span. The results are show in Table (K-1).

Table K-1 – Aerodynamic and Acoustic performance of NREL/Sommers 21% thick airfoils.

Airfoil	S830 Splined	S808	S819	S823	S835
Airfoil number	9	22	27	29	31
thickness-->	21.05%	21%	21%	21.19%	21.05%
camber-->	4.47%	2.37%	1.44%	2.51%	2.47%
Aerodynamic/ Aero acoustic Characteristic	POLI_100 WT at 85% span				
Reynolds number:	7,700,000	7,700,000	7,700,000	7,700,000	7,700,000
Mach number:	0.21	0.21	0.21	0.21	0.21
cl max:	1.8	1.93	1.53	1.78	1.70
angle of cl max	20	17	16	19	20
Max cl/cd value:	92.2	113.5	101	99.6	82
Angle of max cl/cd	6	10	8	8	7
cl at max efficiency point:	1.25	1.5	1.13	1.21	0.97
AOA test range:	-6 to +25				
Convergence range	-6 to +25				
OASPL (dB), @ (cl/cd)max.	94	98.5	92.1	93.2	94.4
Peak Frequency:	100 Hz (87.5 dB)	250 Hz (90.2 dB)	250 Hz (85.8 dB)	200 Hz (86.9 dB)	125 Hz (88.1 dB)
OASPL (dB(A)):	81.0	92.8	85.5	84.8	82.1
OASPL (dB(B)):	89.0	96.9	90.6	91.1	90.0
OASPL (dB(C)):	93.5	98.4	92.0	93.1	94.1

The S830 airfoil was not the most silent overall airfoil, however, it was the most silent in the audible range (A-weighted SPL), which justifies the selection as a reference airfoil.